CHARACTERIZING THE EFFECTS OF SIMULATED INJURY ON THE STRUCTURE AND FUNCTION OF THE GLENOHUMERAL CAPSULE

by

Carrie Ann Voycheck

BS, University of Rochester, 2006

Submitted to the Graduate Faculty of

Swanson School of Engineering in partial fulfillment

of the requirements for the degree of

Doctor of Philosophy

University of Pittsburgh

2011

UNIVERSITY OF PITTSBURGH

SWANSON SCHOOL OF ENGINEERING

This dissertation was presented

by

Carrie Ann Voycheck

It was defended on

March 14th, 2011

and approved by

Steven D. Abramowitch, PhD, Assistant Professor, Departments of Bioengineering and Obstetrics, Gynecology, and Reproductive Sciences

John C. Brigham, PhD, Assistant Professor, Departments of Civil and Environmental Engineering and Bioengineering

Patrick J. McMahon, MD, Adjunct Associate Professor, Department of Bioengineering

Michael S. Sacks, PhD, Professor, J.A. Swanson Endowed Chair, Departments of Bioengineering, Civil Engineering, Mechanical Engineering/Materials Science, McGowan Institute for Regenerative Medicine

Jeffrey A. Weiss, PhD, Professor, Departments of Bioengineering and Orthopaedics, University of Utah

Dissertation Director: Richard E. Debski, PhD, Associate Professor, Departments of Bioengineering and Orthopaedics

CHARACTERIZING THE EFFECTS OF SIMULATED INJURY ON THE STRUCTURE AND FUNCTION OF THE GLENOHUMERAL CAPSULE

Carrie Ann Voycheck, PhD

University of Pittsburgh, 2011

Anterior glenohumeral dislocation is a significant clinical problem, which can result in the glenohumeral capsule being loaded beyond its elastic limit (permanently deformed). Diagnosing and treating this pathology is difficult as currently no reliable method for determining the location and extent of capsular damage exists. Consequently, following repair ~20% of patients experience recurrent dislocations and ~50% are at risk for developing osteoarthritis. Existing knowledge of the structure and function of the capsule following permanent deformation is minimal and may be the root cause behind these issues. A greater awareness of how injury affects this structure will enable specific at-risk locations to be targeted during repair. Additionally, validated finite element models of the glenohumeral joint may be able to improve patient treatments; but require adequate constitutive models to describe normal and injured capsule behavior. Therefore, the goal of this work was to evaluate the effect of anterior dislocation on the structure and function of the capsule from three levels: microstructure, tissue, and joint; and to suggest improvements to a constitutive model for the capsule. At the microstructural level, collagen fiber alignment increased with uniaxial extension and was able to predict the location of tissue failure. Following simulated injury of tissue samples from the capsule, the stiffness and modulus of stress-stretch curves increased by 47% and 128%, respectively, but changes were not detectable in the parameters of a phenomenological constitutive model. Anterior dislocation permanently deformed the capsule and resulted in

increased anterior translations and glenohumeral contact forces of 18-48% and 41-148% at three joint positions. Finally, a structural constitutive model was found to better predict the complex capsule behavior than the phenomenological model; but accounting for non-affine fiber kinematics may further improve the accuracy of computational models. This work suggests that surgical repair procedures targeting the anterior capsule based on increased anterior translation during pre-operative physical exams are not addressing the appropriate region of the capsule; rather the posterior axillary pouch suffers the most damage following anterior dislocation. Therefore, current physical examinations may not be capable of identifying specific locations of tissue damage and future research to standardize physical exams is warranted.

TABLE OF CONTENTS

LIST OF TABLES

LIST OF FIGURES

NOMENCLATURE

Abbreviations

AB-IGHL – Anterior Band of the Inferior Glenohumeral Ligament

PB-IGHL – Posterior Band of the Inferior Glenohumeral Ligament

MCL – Medial Collateral Ligament

ACL – Anterior Cruciate Ligament

SALS – Small Angle Light Scattering

IR/ER – Internal / External Rotation

Ab – Abduction

UFS – universal force-moment sensor

Q-Q Plot – Quantile – Quantile Plot

Computational

W – Strain energy density

F_1, F_2, F_3 – Sub-functions representing the ground substance, collagen fibers, and interaction terms contributing to the strain energy function

C_1, C_2, C_3, C_4, C_5 – Coefficients of the strain energy density functions

F – Deformation gradient tensor

B – Left Cauchy-Green deformation tensor

C – Right Cauchy-Green deformation tensor

$(\tilde{I}_{1-5})$ – Modified Invariants of the right Cauchy-Green deformation tensor

λ – Stretch tensor

T – Cauchy stress tensor

J – Jacobian matrix

K – bulk modulus

p - hydrostatic pressure

y_i – experimental clamp reaction force

f_i – clamp reaction force from finite element model

a – fiber direction

θ - experimentally measured fiber direction

θ_p – affine-predicted fiber direction

PREFACE

Five years ago I began this journey towards a PhD. I had just graduated from college but felt that I had so much more to learn. So I moved to Pittsburgh with three of my UR BME classmates and after spending about a week at the MSRC I realized that I was right…I had so much more to learn. Little did I know that the seemingly insurmountable task of obtaining a PhD would teach me more about myself and life in general than the field of biomechanics. My experiences here have greatly influenced the person I have become but I certainly did not get here on my own and I owe significant thanks to those who have helped me along the way.

Looking back now I really had no idea what I was getting myself into by going to graduate school, and to this day I'm not sure exactly how I ended up in this lab, but I consider myself extremely lucky to have studied under Dr. Richard Debski. The time and energy he has spent teaching me far exceeds the training provided by typical mentors and the work presented in this dissertation is a tribute to his efforts. Although I have developed as a researcher and experimentalist you have taught me more than I ever expected about life. I truly admire your ability to balance family and research and aspire to maintain similar values as I venture through my career. I thank you for your constant loyalty and support and am truly grateful for the numerous opportunities and wealth of knowledge you have bestowed upon me. I only hope that in the future I can be a fraction of the educator you have been to me.

I would like to acknowledge Dr. Patrick McMahon for his clinical contributions to this dissertation which help remind me why we, as bioengineers, do the work that we do. Your

commitment to the education of the next generation and to excellent, meaningful research is truly an inspiration. To the remainder of my dissertation committee, Drs. Abramowitch, Brigham, Sacks, and Weiss I cannot thank you enough for your contributions to this work and to my education. Dr. Abramowitch, from the day I started at the MSRC you have taken a vested interest in my learning and always pushed me to think critically and ask tough questions. Although I may not have seemed grateful at first, I am now able to appreciate the tools you have given me. Dr. Brigham, your finite element modeling expertise has been invaluable to my education and I thank you for the time you have spent with me. Dr. Sacks, I will never forget your lessons in soft tissue mechanics which have played a critical role in this dissertation and my knowledge base for the years to come. Finally, a special thanks to Dr. Weiss and his staff, especially Steve Maas, for the generous use of your computational tools as well as your advice and collaborations on this dissertation work.

I would also like to thank Dr. Savio Woo for always taking the time to teach me as if I were his own graduate student. The most meaningful knowledge and advice you have given me is not presented in this dissertation but is in the form of reflections and life lesions which I will carry with me wherever I go. I am grateful for the time I have spent at the MSRC and the opportunity to have known and learned from you.

These past five years, while filled with hard work and sacrifice, have also been the most enjoyable years of my life thus far as I have made many life-long friends. To my MSRC family: there are far too many of you to name but I thank you all for your endless support. To the Shoulder Group, especially those who have come before me, particularly Susan, Eric, Nick and John: I would not have been able to complete this dissertation without the foundations you all established and I deeply appreciate your willingness to teach me and troubleshoot problems

when I called or emailed you at various hours of the day or night. To all of my undergraduates: thank you so much for your contributions to this dissertation and I hope that I was able to teach you a bit about research along the way. To Andrew: we've gone through this journey together and somehow managed to come out unscathed. I cannot think of anyone who I'd rather have shared this experience with then you. Thank you for your friendship and the countless memories.

Finally, I thank my best friend and fiancé, Eric. I wish that dissertations could have coauthors because as far as I'm concerned this degree, like everything else in our lives, is half yours. From all of the mechanical testing and strain tracking you taught me when I first joined the lab, to the support you provided when I took the prelim, to the countless shoulders you helped me dissect, to the numerous times I called you at work because I broke something, to the hours at the robot, to the random conference presentations you listened to, to the proofreading of this 500 page document, and to the million other things… you have been by my side and kept me grounded the entire time. Your endless patience, love and support have been vital to my success and I look forward to the rest of our lives together.

There is no doubt in my mind that I would not have accomplished such a tremendous task as obtaining this degree if it were not for the endless love and support of my family. To my sister Erica, you have shown me that, while life is never easy, with hard work and dedication things that never seemed possible can be achieved. I am so proud that you are my sister. Mom and Dad, words cannot express how thankful I am for everything you have done for me. You have always encouraged me to pursue my dreams, given me endless support, and pushed me to be better. Because of you I have achieved this remarkable goal. I thank you from the bottom of my heart for never believing that your little girl could not be an engineer and for that I dedicate this dissertation to you.

1.0 INTRODUCTION AND BACKGROUND

The glenohumeral joint, is a diarthrodial joint stabilized by a complex combination of active and passive structures. Bony stability is provided by contact between the head of the humerus and glenoid of the scapula. The humeral head articulates on the glenoid much like a golf ball on a tee and rests on a circular soft tissue structure, similar to the meniscus at the knee, known as the glenoid labrum. Additional stability in the normal functioning shoulder is provided actively by the musculature surrounding the joint. These muscles include the rotator cuff (supraspinatus, infraspinatus, subscapularis and teres minor) and deltoid. Passive stability is maintained by other soft tissue structures such as the glenoid labrum, coracoacromial and coracohumeral ligaments, and the glenohumeral capsule. Problems arise when the ability of one or more of these structures to stabilize the glenohumeral joint is compromised. This can result in joint instability as the rest of the structures cannot always fully account for the deficit of another. The focus of this dissertation is on the glenohumeral capsule and how injury to this passive stabilizer may alter its structure and function thereby weakening its ability to stabilize the glenohumeral joint. The structure and function of the normal glenohumeral capsule have been examined extensively and will be discussed in detail in Sections 1.2 and 1.3. However, little research has examined the properties of the injured glenohumeral capsule. This lack of knowledge likely results from the complexity of the glenohumeral joint due to its wide range of motion compared to other joints,

such as the knee, which transmit loads primarily in one direction. In addition, the mechanisms behind glenohumeral dislocation are not well understood.

1.1 GENERAL COMPOSITION OF BIOLOGIC TISSUES

Although biologic soft tissues can have very different functions, they are all comprised of the same building blocks. One of the most important components of soft tissues is a protein known as collagen. Currently about 12 types of collagen have been identified [1] and can be combined in different amounts to create numerous biologic tissues with very different functions. The structural hierarchy varies from tissue to tissue but in general collagen molecules are bundled together to form a collagen fibril. [2] A bundle of fibrils is called a collagen fiber which formulates the basic mechanical unit in biologic soft tissues. The collagen fibers are initially wavy (collagen crimp) when unloaded and arranged in such a way that when asked to bear load, an increasing force results in the recruitment of more fibers. In addition to collagen, soft tissues contain other, non-collagen components that make up the tissue ground substance in which the collagen fibers are embedded. The ground substance is comprised of cells and intercellular substance, the composition of which varies with tissue type but usually contains glycosaminoglycans and water. The motion of the water through the ground substance contributes to the viscoelastic properties of soft tissues.

Collagen fibers are the supporting structures of biologic tissues, however, differences in the amount, type, and arrangement of these fibers creates tissues whose functions are different. This dissertation focuses on musculoskeletal soft tissues, i.e. ligaments and tendons. Ligaments are a sheet or band of collagenous tissue connecting bone to bone where as tendons connect

muscle to bone. However, even within this subset of biologic tissues their function can be quite different. For example, in the medial collateral ligament (MCL) the collagen fibers are aligned parallel in order to transmit tensile loads between the femur and tibia. The anterior cruciate ligament (ACL) consists of two bundles whose individual predominate fiber orientations are along the long axis of the ligament. These bundles are woven together in such a way that different collagen fibers are loaded when the knee is at different joint positions. In contrast, ligaments that function to transmit loads in multiple directions, like the glenohumeral capsule, have no predominant fiber direction. [3-5] Thus, the arrangement of collagen fibers yields tissues with different the mechanical properties.

As ligaments function to transmit loads across joints, researchers have examined their tensile properties. Due to numerous factors, such as collagen crimp, fiber recruitment, and viscoelastic properties, the load-elongation response of ligaments and tendons is nonlinear. Parameters such as stiffness, ultimate load, and energy absorbed to failure can provide structural information on the bone-ligament-bone complex. [6] (Figure 1.1) Where stiffness is defined as the slope of the linear region of the load-elongation curve, ultimate load is the load at which the tissue fails and is typically the largest load achieved, and energy absorbed to failure is the area under the load-elongation curve up to the ultimate elongation.

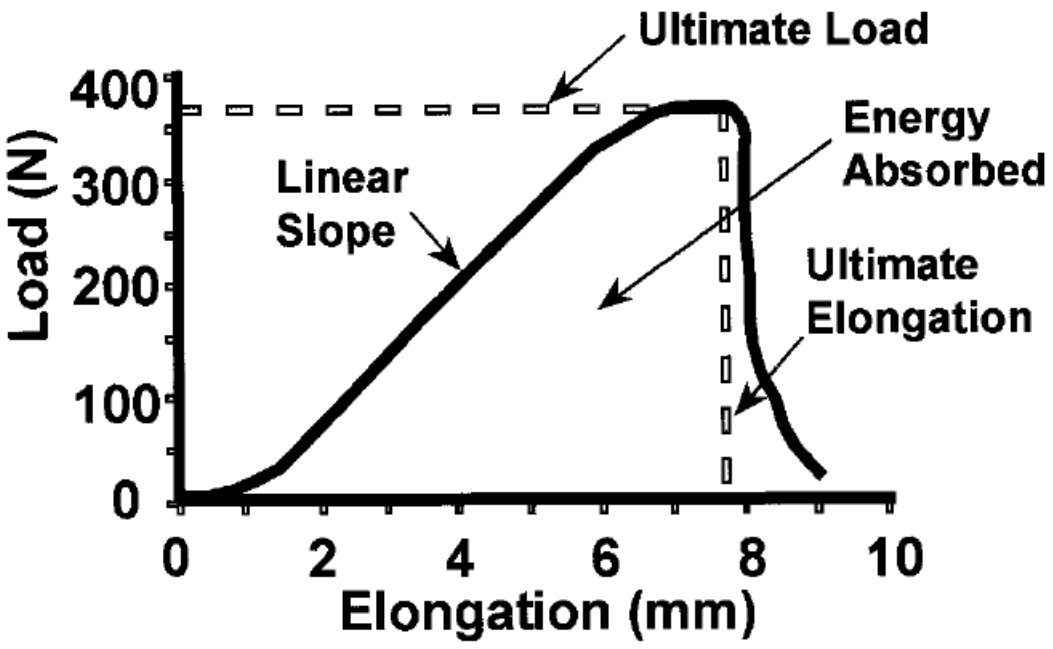

Figure 1.1 A schematic load-elongation curve for ligament. (Used with Permission [6])

Similarly, the mechanical properties of the ligament midsubstance can be obtained from the stress-strain curve. [6] (Figure 1.2) The tangent modulus, tensile strength, ultimate strain, and strain energy density provide a measure of tissue quality. The tangent modulus is the slope of the linear portion of the stress-strain curve, ultimate stress is the maximum amount of stress before failure, ultimate strain is the strain corresponding to the ultimate stress, and the strain energy density is the area under the stress-strain curve until ultimate strain.

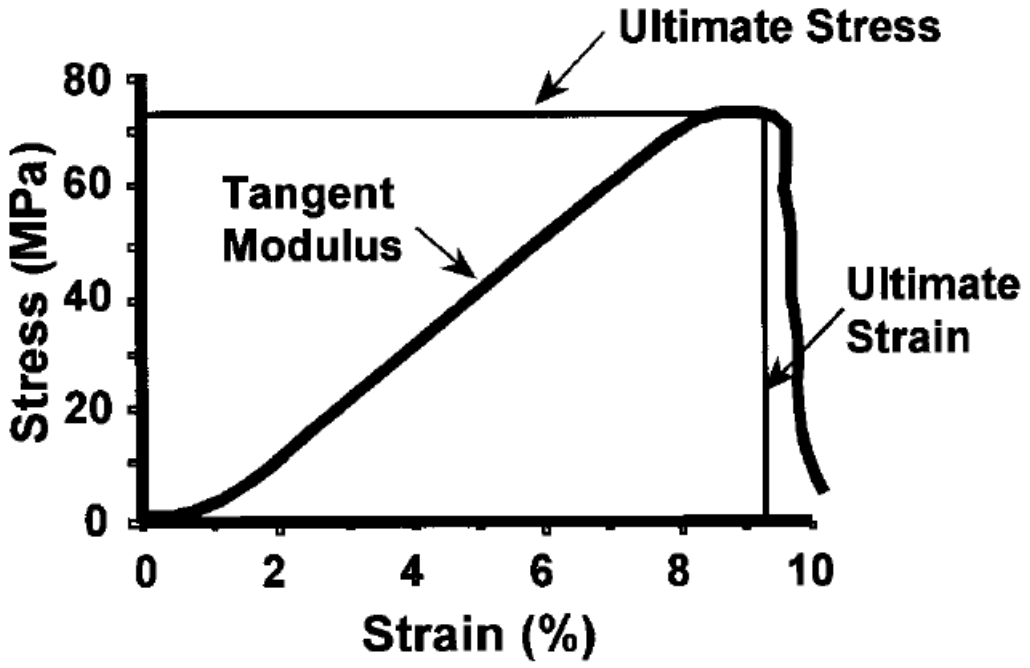

Figure 1.2 A schematic stress-strain curve for a ligament. (Used with Permission [6])

Using these parameters, researchers can compare the structural and mechanical properties between different ligaments as well as between normal, injured and healing ligaments in order to address certain research questions. These concepts will be applied throughout the dissertation when examining the structure and function of the glenohumeral capsule.

1.2 STRUCTURE OF THE GLENOHUMERAL CAPSULE

The glenohumeral capsule is a continuous sheet of ligamentous tissue [7-9] connecting the glenoid of the scapula to the head of the humerus. The capsule is composed of several regions (superior glenohumeral ligament, middle glenohumeral ligament, inferior glenohumeral ligament which is comprised of the anterior and posterior bands (AB-IGHL, PG-IGHL) and axillary pouch

(Figure 1.3), and the posterior capsule) that function collectively to stabilize the joint. [5, 10] The variability of the capsule is similar to other ligamentous structures at the major diarthrodial joints in the musculoskeletal system [11] with the thickness of the capsule varying 1 mm between regions and over 2 mm between subjects. [12-14]

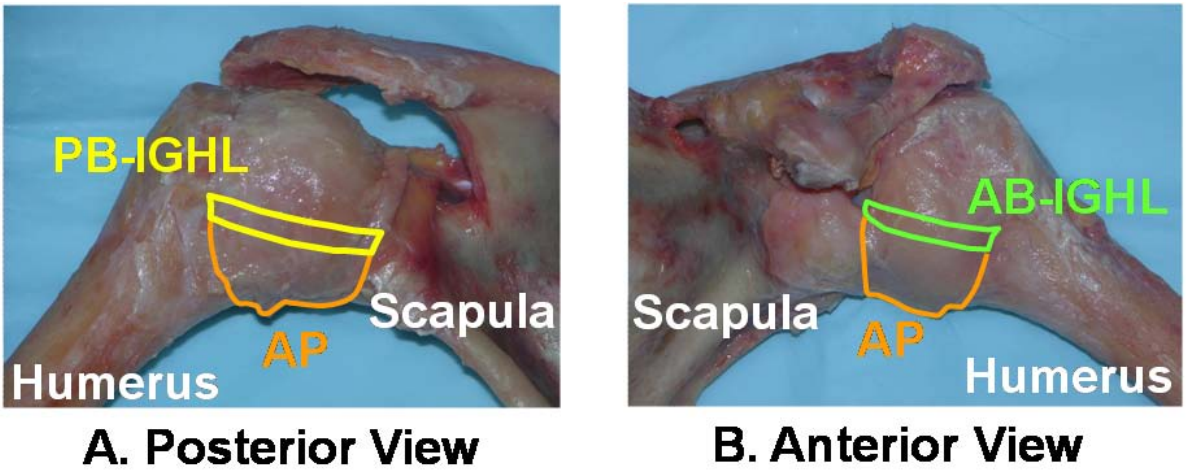

Figure 1.3 A) Posterior and B) anterior views of the glenohumeral capsule in a human cadaveric shoulder depicting the inferior glenohumeral ligament complex: AB-IGHL (green), axillary pouch (orange), PB-IGHL (yellow), (Voycheck, C. A. et al., J of Appl Physiol, 2010, Am Physiol Soc, used with permission). [15]

In the past, these regions of the glenohumeral capsule have been termed the glenohumeral ligaments; however, more recent research has shown that this may not be the most appropriate terminology. Previously, engineers and clinicians have interpreted the mechanical function of this complex structure by making two assumptions, first that the glenohumeral ligaments are structures that primarily transmit uniaxial loads and second, that they are the primary contributors to joint stability. For decades researchers have focused on these structures utilizing studies of cadaveric specimens [16-18] and observations during surgery [19-21] as the most common methods to clarify their anatomy.

In an effort to better understand the structure of the glenohumeral capsule, numerous studies have qualitatively examined the collagen fiber organization using standard and polarized light microscopy. [4, 5, 22, 23] The collagen fiber organization of most capsule regions: posterior capsule, superior glenohumeral ligament, and inferior glenohumeral ligament complex (AB-IGHL, axillary pouch, PB-IGHL) have been examined previously. [3-5, 12] The posterior capsule was not shown to have a preferred fiber orientation. [12] Cooper and associates [23] demonstrated that the superior glenohumeral ligament had a ligamentous structure, and that the collagen fibers were organized in a longitudinal fashion. O'Brien et al. [5] reported that the axillary pouch was less organized than either the AB-IGHL or PB-IGHL, and demonstrated a great deal of intermingling of the fibers. In contrast, Gohlke et al. [4] found an organized pattern of collagen fibers in the axillary pouch, as the collagen fibers were found to be predominately oriented in the longitudinal direction of the ligaments. Both investigations [4, 5] reported that the collagen fibers in the AB-IGHL were more aligned than in the axillary pouch. Using a small angle light scattering (SALS) technique the collagen fibers alignment in the axillary pouch and AB-IGHL were quantified and found to be randomly oriented with local areas of alignment. [3]

1.3 FUNCTION OF THE GLENOHUMERAL CAPSULE

The contribution to joint stability provided by the glenohumeral capsule is highly dependent on joint position. In general, the capsule functions to stabilize the joint during extreme ranges of motion. For example, throwing athletes such as baseball or football players constantly have their arm positioned over and behind their head in a position of extreme abduction and external rotation known as the apprehension position. Glenohumeral dislocation most commonly occurs

when the joint is in this position. [24] Here the AB-IGHL and axillary pouch (Figure 1.3 (B)) are the dominant stabilizers, becoming tight as they wrap around the humeral head with increasing external rotation. Ovesen and coworkers reported that the axillary pouch stabilizes the joint more as abduction is increased, and this function increases even more with external rotation of the humerus. [25] Even when active stabilizers such as the rotator cuff muscle forces were included, the anteroinferior capsule was the dominant stabilizer in positions of external rotation. [26] Similarly, the posterior capsule (Figure 1.3(A)) functions to stabilize the joint during positions of extreme internal rotation. [25]

The glenohumeral capsule does not contribute to joint stability at the mid-range of motion as most regions of the capsule are unloaded. [24, 27] In these positions, the deltoid and rotator cuff muscles play a significant role in joint stability. The coracohumeral and superior glenohumeral ligaments have been shown to limit external rotation in the lower range of abduction. [24] During the mid-range of abduction, the middle glenohumeral ligament and AB-IGHL provide anterior restraint. All of these initial studies to understand the function of the glenohumeral capsule were assuming that the capsule acts as discrete uniaxial ligaments rather than a continuous sheet of tissue.

The contribution of individual regions of the glenohumeral capsule to joint stability has been examined by treating the capsule as discrete ligaments. These studies examined the strain in localized capsule regions, or length changes in the entire bone-ligament-bone complex using a variety of methodologies including radiographic markers [24, 28], electromagnetic tracking devices [29], Hall effect strain transducers [30], mercury strain gauges [31], and simple mathematical models [32].

The first study to treat the capsule as a continuous structure examined the strain distribution in the anteroinferior glenohumeral capsule during joint subluxation. [33] A grid of lead spheres was attached to the surface of the anteroinferior capsule and tracked using a stereoradiogrammetric technique. Strain was determined by comparing the positions of the lead spheres during a nominal state, in which the capsule was inflated with compressed air, and during joint subluxation. This work was the first to find that the strain distribution in the anteroinferior capsule did not match the anatomic description of the capsule as discrete uniaxial ligaments and that maximum principal strains were greater on the glenoid side than the humeral side of the capsule during joint subluxation.

In contrast to the extensive literature describing elongation or strain in the capsule, less work has been done examining the forces in the glenohumeral capsule. This is likely due to the fact that direct measurement of the force in the glenohumeral capsule presents an experimental challenge due to the complexity of the joint geometry. [34] Initially qualitative studies attempted to evaluate forces in the capsule by simple observation and palpation of cadaveric shoulders [35, 36]. Other studies mounted mercury strain gauges to the surface of the capsule in order to indirectly measure the force. [31] Two additional models of the glenohumeral joint have been developed to investigate the joint stability provided by the capsule [27, 37, 38], however, these models treated the capsule as discrete uniaxial ligaments as each region of the capsule was modeled as uni-axial springs that wrapped around the articular surface of the humeral head. Thus, the continuous structure and function of the capsule was not captured in these models.

1.4 TENSILE PROPERTIES OF THE GLENOHUMERAL CAPSULE

The structural and mechanical properties of discrete capsule regions have been evaluated previously. One study examined bone-ligament-bone complexes taken from three regions of the anteroinferior capsule (AB-IGHL, anterior axillary pouch, and posterior axillary pouch). [13] Each specimen was preloaded, preconditioned, and loaded to failure in tension at a rate of 0.04 mm/sec. No differences were found in the ultimate stress between regions (5.2 ± 2.7 MPa for the AB-IHGL, 5.5 ± 2.0 MPa for the anterior axillary pouch, and 5.6 ± 1.9 MPa for the posterior axillary pouch). However, bone-ligament-bone complex strain and midsubstance tissue strain were found to be significantly larger in the anterior axillary pouch compared to the other two regions but the stiffness was less.

The mechanical properties of the posterior capsule have also been examined via similar methods. [12] The posterior capsule was found to be significantly thinner and have lower strain at failure compared to the AB-IGHL; however, no differences were found in the other mechanical properties. These studies found little difference in the material properties of various capsule regions which suggests that the capsule functions as a continuous sheet rather than discrete regions.

The effect of age on the structural properties of the capsule has also been evaluated. [39] Tensile tests were performed on glenoid-AB-IGHL-humerus complexes with the joint in the apprehension position. The age of the specimens was found to significantly affect the failure mode, ultimate load, and ultimate stress. In younger shoulders failure tended to occur at the glenoid-labrum insertion whereas in the older group failure most often occurred in the tissue midsubstance. In addition, younger specimens exhibited larger ultimate load and ultimate stress

compared to the older specimens. Therefore, the structural and mechanical properties of the AB-IGHL decrease with age.

1.5 CHARACTERIZING THE NORMAL GLENOHUMERAL CAPSULE

In order to fully characterize the structure and function of the glenohumeral capsule our research group has group has performed numerous studies examining the capsule from three different levels: microstructural [3], tissue [15, 40-42], and joint [9]. The ultimate goal of characterizing the capsule was to develop and validate subject-specific finite element models of the glenohumeral joint. [8, 43, 44] These models could then be used to provide insight regarding function of the capsule and injury diagnosis. The properties of the glenohumeral capsule at each level are discussed in the next three sections.

1.5.1 Microstructural Level: Collagen Fiber Organization

Previous research has examined the collagen fiber alignment in several regions of the glenohumeral capsule. However, as discussed in Section 1.2 there was some discrepancy in the literature as to the collagen fiber alignment of the anteroinferior capsule, specifically between studies performed by O'Brien et al. and Gohlke et al. [4, 5] These controversial results may be due to the methodology used to examine the tissue microstructure. Both studies utilized polarized light microscopy which requires that the tissue be sliced into very thin sections, on the order of a few micrometers. However, slicing of the tissue disrupts the collagen fiber architecture and may explain why differences have been reported in the literature when

examining such thin sections. Recently, our research group has studied the collagen fiber alignment of the anteroinferior capsule using a small angle light scattering (SALS) technique. [3] This technique is advantageous as it is capable of examining tissues up to 500 μm thick [45, 46], two orders of magnitude greater than the slices used by O'Brien and Gohlke [4, 5]. Using the SALS technique, the collagen fibers were shown to be randomly oriented throughout the anteroinferior capsule, but do have local areas of alignment (Figure 1.4). [3] This finding is consistent with the function of the glenohumeral capsule to stabilize the joint multi-axially. The SALS technique is used in the current work and is discussed in detail in Section 3.1.1.

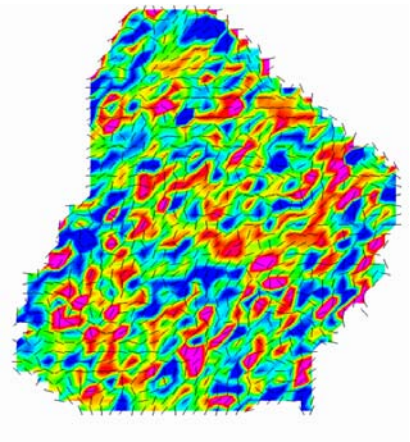

Figure 1.4 Plot of collagen fiber alignment in the axillary pouch. Blue represents regions of randomly aligned collagen fibers and pink represents regions of highly aligned collagen fibers.

1.5.2 Tissue Level: Bi-Directional Mechanical Properties

Characterizing the glenohumeral capsule on a microstructural level showed that the collagen fibers in the anteroinferior capsule do not have a preferred direction of alignment. [3] This suggests that the material properties of the capsule may be directionally independent. Moore and coworkers tested this hypothesis by characterizing the bi-directional mechanical properties in both the axillary pouch and posterior capsule. [40, 41] Longitudinal and transverse samples

(parallel and perpendicular to the longitudinal axis of the AB-IGHL and PB-IGHL) were extracted from the axillary pouch and posterior capsule. (Figure 1.5) The samples were then dog-boned, placed in custom soft tissue clamps, preconditioned, and loaded to failure.

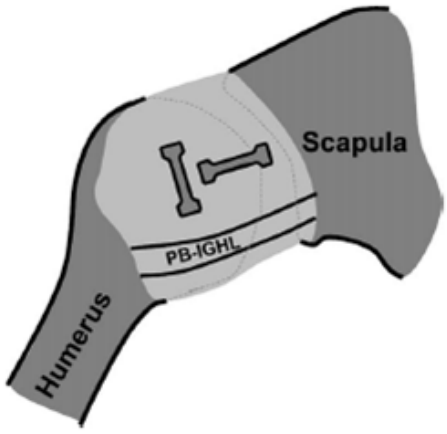

Figure 1.5 Posterior view of the glenohumeral capsule illustrating the orientation of the dog-bone shaped longitudinal and transverse tissue samples with respect to the PB-IGHL (Used with permission) [40]

Significant differences in the ultimate stress and tangent modulus were reported between the longitudinal and transverse samples in both capsule regions. The ratio of moduli between the longitudinal and transverse samples was similar between the axillary pouch (3.3 ± 2.8) [41] and posterior capsule (4.8 ± 4.2) [40]. Although differences do exist between the longitudinal and transverse samples in both capsule regions, these differences are much smaller than typical uniaxial ligaments such as the MCL which has a ratio of moduli of ~30. [47] Therefore, this study further demonstrates the axillary pouch and posterior capsule function multi-axially to stabilize the shoulder.

1.5.3 Tissue Level: Material Symmetry

The microstructural analysis depicted no preferred collagen fiber orientation in the axillary pouch (Section 1.5.1) and the bi-directional mechanical tests yielded relatively small differences in the ratio of longitudinal to transverse moduli in both the axillary pouch and posterior capsule (Section 1.5.2). Together these studies suggest that isotropic material symmetry may be an appropriate way to describe the behavior of the glenohumeral capsule in finite element models. Our research group developed a combined experimental and computational approach to characterize the mechanical properties of the axillary pouch and posterior capsule in order to determine if isotropic material symmetry would effectively describe the function of the glenohumeral capsule. [42] The same methodology was utilized in the current work and is described in detail in Section 4.2. Briefly, square sheets of tissue (25mm x 25mm) were extracted from the axillary pouch and posterior capsule and each tissue sample was placed in custom designed soft tissue clamps. Each sample was subjected to four non-destructive loading conditions: (1) tensile elongation applied in the direction parallel to the longitudinal axis of the AB-IGHL (tensile longitudinal), (2) tensile elongation applied in the direction perpendicular to the longitudinal axis of the AB-IGHL (tensile transverse), (3) shear elongation applied in the direction parallel to the longitudinal axis of the AB-IGHL (shear longitudinal), and (4) shear elongation applied in the direction perpendicular to the longitudinal axis of the AB-IGHL (shear transverse).

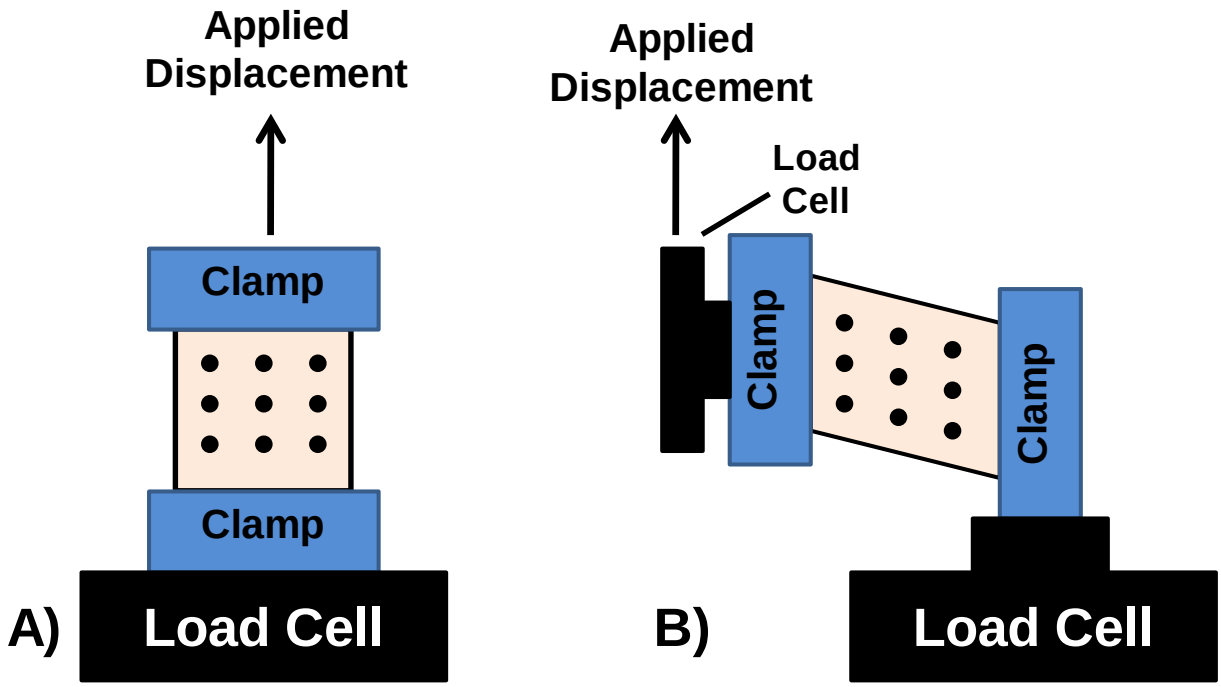

Figure 1.6 Mechanical testing set up for A) tensile and B) shear loading conditions showing the load cell and clamp relationships and 3x3 grid of strain markers on tissue surface.

A specimen-specific finite element model was then generated to simulate each loading condition for each tissue sample. An isotropic phenomenological constitutive model (Equation 1, Section 4.2.3) was used to describe the material behavior of the capsule and an inverse finite element optimization routine [48] was used to determine the optimized material coefficients of the constitutive model for each loading condition for each tissue sample. The two perpendicular tensile elongations yielded similar optimized material coefficients for both the axillary pouch (Table 1.1) and posterior capsule (Table 1.2).

Table 1.1 Material coefficients of the isotropic phenomenological constitutive model for the axillary pouch under four loading conditions.

Axillary Pouch (n = 20)	C_1 (MPa)	C_2
Tensile Longitudinal	0.27 ± 0.20	8.4 ± 4.5
Tensile Transverse	0.28 ± 0.46	7.3 ± 3.7
Shear Longitudinal	0.29 ± 0.31	4.8 ± 3.5
Shear Transverse	0.32 ± 0.39	4.3 ± 2.8

Table 1.2 Material coefficients of the isotropic phenomenological constitutive model for the posterior capsule under four loading conditions.

Posterior Capsule (n = 18)	C_1 (MPa)	C_2
Tensile Longitudinal	0.40 ± 0.38	7.9 ± 4.5
Tensile Transverse	0.45 ± 0.32	7.0 ± 2.8
Shear Longitudinal	0.31 ± 0.43	5.6 ± 3.4
Shear Transverse	0.38 ± 0.34	6.1 ± 4.9

Further, the two perpendicular shear elongations also yielded similar material coefficients for both capsule regions. The similarities between the mechanical properties of the two perpendicular directions imply that the capsule may be considered isotropic. However, when comparing the tensile and shear material coefficients, the C_2 coefficient from the tensile elongations could not predict the C_2 coefficient from the shear elongations. Therefore, a more advanced constitutive model is necessary to predict both tensile and shear responses.

1.5.3.1 Effects of Region and Gender

In order to further characterize the material properties of the glenohumeral capsule, the effects of region and gender were examined. [15] As discussed in Section 1.3 each region of the capsule contributes differently to joint stability as they are loaded at different joint positions. The axillary pouch and posterior capsule function to stabilize the joint in different positions. The axillary pouch stabilizes the joint during external rotation and is commonly injured during anterior dislocation. [10, 25, 49-52] The posterior capsule stabilizes the joint during internal

rotation [25] and is responsible for the decreased internal rotation in throwing athletes. [53-55] The collagen fibers in both regions do not exhibit a preferred orientation. [3, 12]

Previous studies [12, 13, 40-42] have generated conflicting results regarding the relative structural and material properties of these regions. Further, it has been suggested that increased joint translations, stiffness, and range of motion exist in women compared to men; however, contradictory data have been reported. [56-63]

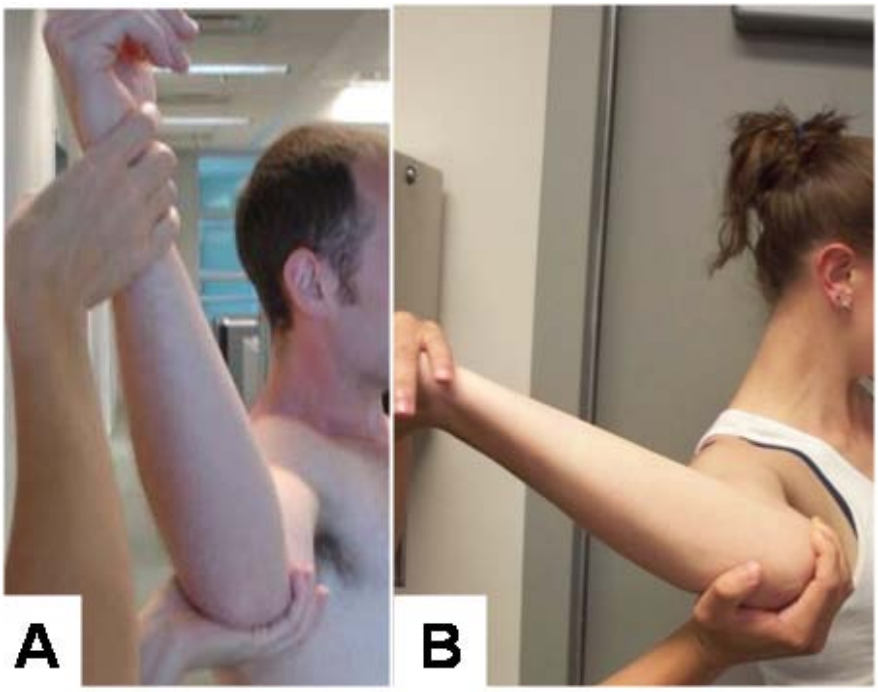

Figure 1.7 Lateral views of male (A) and female (B) glenohumeral joints demonstrating the possibility of gender differences in the overall range of motion. (Voycheck, C. A. et al., J of Appl Physiol, 2010, Am Physiol Soc, used with permission) [15]

The same methodology used to characterize the material symmetry of the glenohumeral capsule described in Section 1.5.3 was used to compare the material properties of the capsule based on region and gender. The material coefficients of the isotropic phenomenological constitutive model (Equation 1, Section 4.2.3) were determined via inverse finite-element

optimization. [48] These material coefficients were then used to create stress-stretch curves representing the material properties of each capsule region for each gender in response to uniaxial extension. (Section 4.2.4) No differences were found in the material coefficients of the constitutive model between regions or genders (Table 1.3).

Table 1.3 Optimized material coefficients for the axillary pouch and posterior capsule.

	C_1 (MPa)		C_2	
	Female	**Male**	**Female**	**Male**
Axillary Pouch				
Mean ± SD	0.23 ± 0.12	0.28 ± 0.39	7.7 ± 3.0	8.2 ± 4.1
Range	0.09 – 0.48	0.08 – 1.35	4.1 – 11.8	2.7 – 13.4
Posterior Capsule				
Mean ± SD	0.34 ± 0.20	0.49 ± 0.26	7.2 ± 3.0	7.8 ± 2.9
Range	0.15 – 0.64	0.17 – 0.87	4.3 – 13.6	4.3 – 13.0

Further, when comparing the average stress-stretch curves, no differences were found between genders within each region.

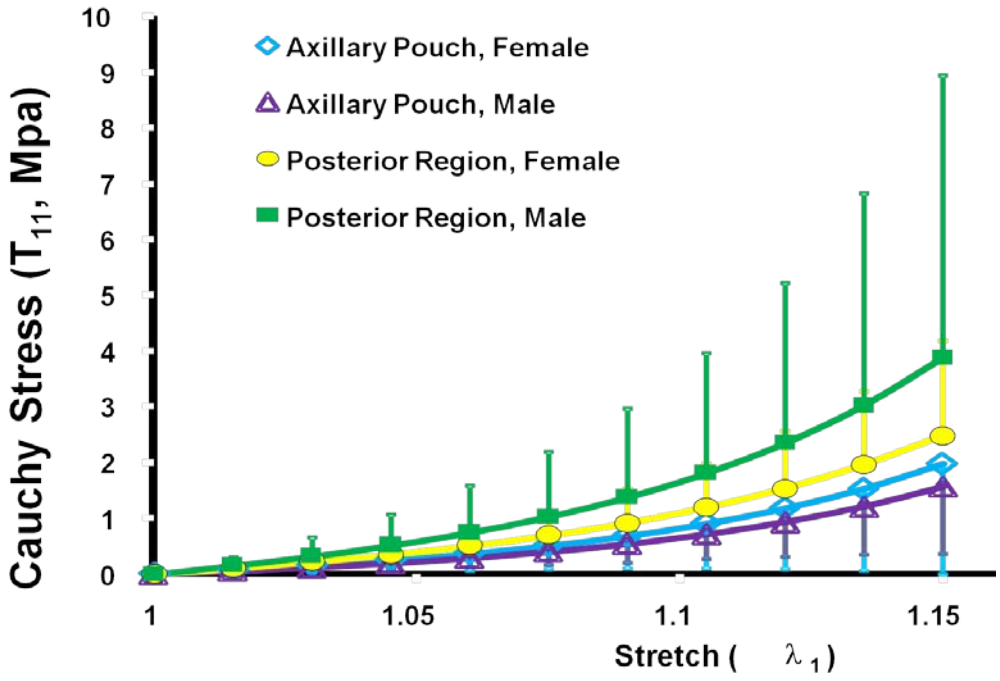

Figure 1.8 Stress-Stretch curves for the axillary pouch and posterior capsule under uniaxial extension for each gender (mean ± SD). (Voycheck, C. A. et al., J of Appl Physiol, 2010, Am Physiol Soc, used with permission) [15]

These results support current repair techniques, which ignore regional boundaries of the capsule during plication. As no differences in the material properties of the capsule exist between regions, it is unlikely that plicating along regional boundaries would improve patient outcome. These results further imply that in models of the glenohumeral joint, the axillary pouch and posterior capsule could be represented using the same material coefficients when using this isotropic hyperelastic constitutive model. Similarly, no differences were found in the material properties between genders. Therefore, gender specific repair procedures or material coefficients are not necessary for this constitutive model.

1.5.4 Joint Level: Treat as Sheet

1.5.4.1 Experimental Strains

The last step in characterizing the normal glenohumeral capsule was to evaluate its functional role in clinically relevant joint positions. The strain distribution in various sections of the glenohumeral capsule can be used to understand the function of this soft tissue structure and how it transmits loads between the humerus and scapula. As discussed previously (Section 1.3) the capsule was treated as discrete uniaxial ligaments until Malicky and coworkers examined the strain distribution in the anteroinferior capsule during joint subluxation. [33] Results of this study showed that the average peak maximum principal strain in both the AB-IGHL and axillary pouch was ~20% larger than what had been reported as the failure strain from uniaxial tests of the individual capsule regions. Therefore, when determining strain distributions in the glenohumeral capsule in future studies, the capsule should be left intact.

Similar methodologies to those used by Malicky were used to determine the strain distribution in the anteroinferior glenohumeral capsule during a simulated clinical exam 60° of abduction and 0°, 30° and 60° of external rotation. [9] Cadaveric shoulders were dissected down to the glenohumeral capsule and a 7 x 11 grid of strain markers was fixed to the surface of the anteroinferior capsule. The reference state was determined by inflating the capsule with compressed air. Joints were then mounted on a 6-degree-of-freedom robotic/universal force moment sensor (UFS) testing system which was used to simulate clinical exams by positioning the joint at 60° of abduction and 0°, 30° and 60° of external rotation and applying a 25 N anterior load. The positions of the strain markers were captured at all three joint positions with the 25 N anterior load applied. The magnitude and direction of maximum principal strain was then

determined by comparing the marker positions during the simulated clinical exams to the reference state.

The strain distribution in the anteroinferior capsule varied greatly among specimens and did not exhibit the individual regions of the anteroinferior capsule (AB-IGHL, axillary pouch) as would have been visible if the previous anatomic description of the capsule as discrete uniaxial ligaments were appropriate. The maximum principal strains were found to be greater on the glenoid side compared to the humeral side and their magnitude increased with increasing external rotation. Further, the direction of the maximum principal strains became more aligned with the AB-IGHL as external rotation was increased.

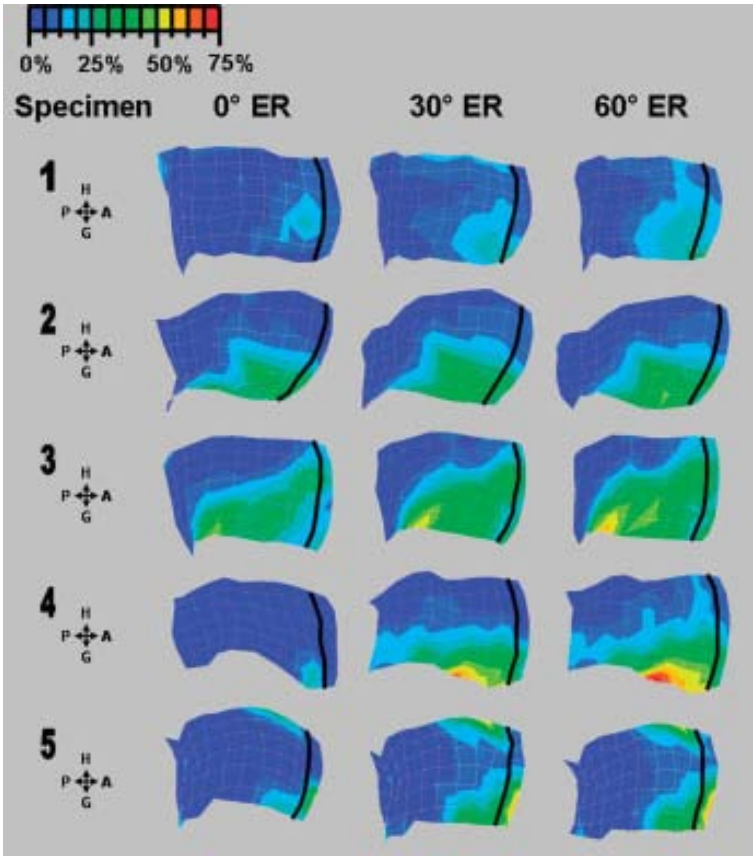

Figure 1.9 Magnitude of maximum principal strain distribution for five specimens at 0°, 30°, and 60° of external rotation (ER). The key indicates the orientation of the tissue with respect to the humerus (H), glenoid (G), and the anterior (A) and posterior (P) aspects of the joint. The black line indicates the location of the AB-IGHL. (Used with Permission) [9]

The results of this study indicate that the description of the regions of the inferior glenohumeral ligament does not correspond with its functional role. The continuous strain distribution in the anteroinferior glenohumeral capsule demonstrates that the capsule should be treated as a continuous sheet of tissue rather than discrete uniaxial ligaments.

1.5.4.2 Finite Element Models of the Glenohumeral Joint

Finite element models can be a powerful tool to evaluate a variety of research questions; however, they must be developed and validated appropriately so that legitimate conclusions can be made from their results. Therefore, in order to develop finite element models of the glenohumeral joint, it is essential to understand how the capsule functions such that the appropriate boundary conditions can be placed on the capsule to yield results representative of in vivo scenarios. In the past, computational models of the glenohumeral capsule have treated the capsule as discrete structures. [15, 32, 37, 38, 42, 64] As the capsule functions multi-axially to resist loads in a variety of joint positions, excluding neighboring capsule regions may significantly impact stress and strain distributions predicted by the models. A recent study in our laboratory evaluated the strain distributions in the anteroinferior capsule predicted by two finite element models of the glenohumeral joint. [8] The first model represented the inferior glenohumeral ligament as a discrete uniaxial ligament and the second model treated the capsule as a continuous sheet of ligamentous tissue. (Figure 1.10) Experimental strain distributions in the inferior glenohumeral ligament were used to validate the finite element models.

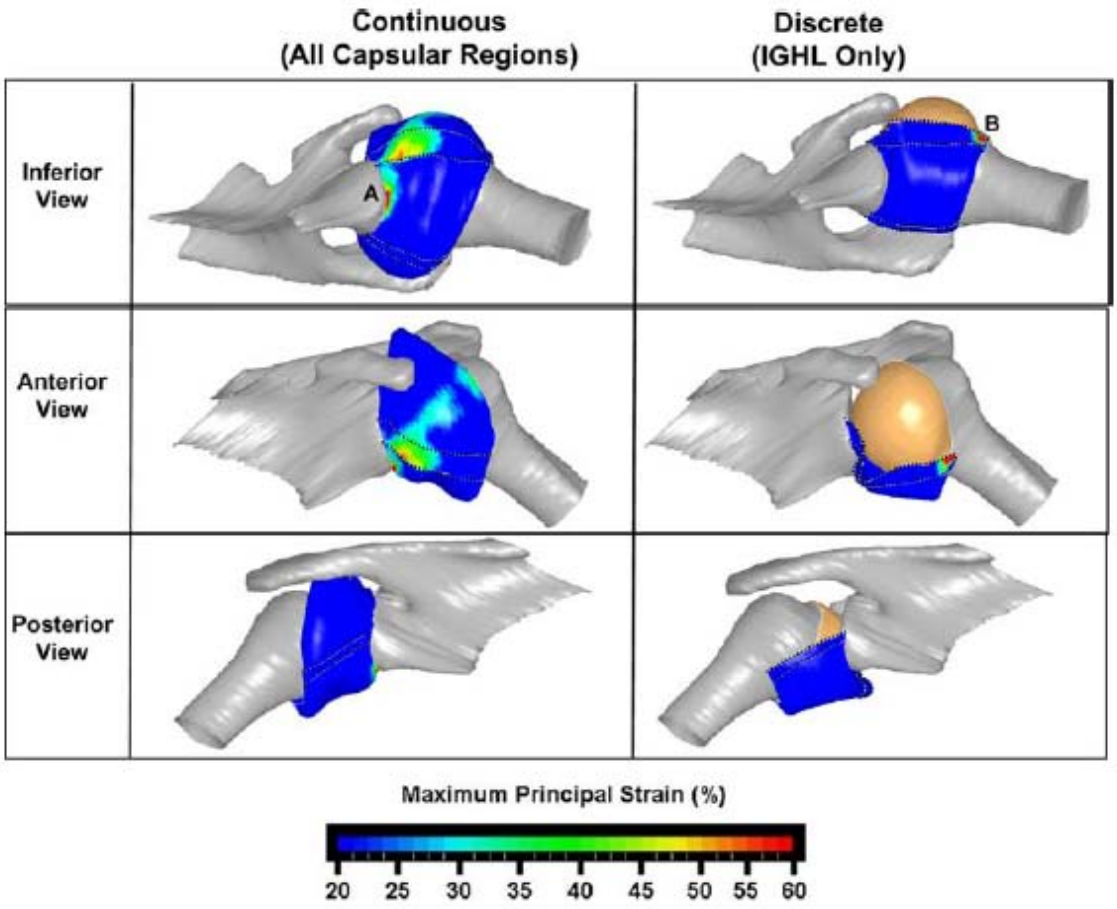

Figure 1.10 Inferior, anterior, and posterior views of maximum principal strains and deformed shapes for the left shoulder predicted by continuous and discrete finite element models. (Used with permission) [8]

Under the same prescribed kinematics, the average difference between the maximum principal strains predicted by the continuous model (5%) and the experimental strains was much less than the discrete model (20%). In addition, the deformed shape predicted by the continuous model was more representative of the in vivo situation with the inferior glenohumeral ligament clearly wrapping around the humeral head. The differences in the predictions of the continuous and discrete finite element models of the glenohumeral joint are likely due to the differences in boundary conditions applied to the glenohumeral capsule. In the discrete model, the complex interactions between capsule regions is neglected and results in model predictions which were not validated by experimental data. This study further exemplifies the continuous structure and

function of the glenohumeral capsule and emphasizes its treatment as a sheet of tissue in computational models of the glenohumeral joint.

1.6 GLENOHUMERAL DISLOCATION

1.6.1 Demographics

The glenohumeral joint is the most dislocated major diarthrodial joint in the human body. Glenohumeral dislocation occurs across all age groups, with approximately 2% of the population between the ages of 18 and 70 suffering a dislocation. [65] This equates to nearly 5.6 million people in the United States alone. [66] Despite the wide range of shoulder motion, the vast majority of dislocations (80%) occur in the anterior direction. [67] The ability of the capsule to maintain joint stability is compromised following dislocation, typically resulting in anterior instability.

1.6.2 Mechanisms for Dislocation

Approximately 80% of glenohumeral dislocations occur in the anterior direction. [67] However, the mechanism behind an anterior dislocation can be quite different from patient to patient and is dependent upon the loading conditions applied to the joint forcing it to dislocate. Anterior dislocation typically occurs when the joint is in the apprehension position, extreme abduction and external rotation, and causes the humeral head to translate anteriorly and inferiorly over the glenoid rim. One mechanism for dislocation from this joint position is a large anteriorly-directed

force which pushes the humeral head over the glenoid rim. In vivo this may occur if an athlete's arm is forced forward with respect to their torso, perhaps by an opponent. This dissertation will develop a dislocation model to simulate this mechanism for dislocation. While no model has applied an excessive force to the humerus to cause dislocation, previous injury models have been developed to simulate joint kinematics which may occur during this type of anterior dislocation. Malicky and coworkers subluxed the glenohumeral joint by translating the humeral head anteriorly and inferiorly [68, 69], however, this model only allowed the joint 2-degrees-of-freedom and thus may not have completely simulated in vivo loading conditions.

Anterior dislocation may also occur from the apprehension position if the humerus is forced into a position of horizontal abduction. In this situation, it may be possible that the shoulder muscles are contributing to dislocation. A cadaveric model was developed to simulate this in vivo mechanism by placing the glenohumeral joint in the apprehension position and forcing the humerus to translate resulting in horizontal abduction. [70] Rotator cuff and deltoid muscle forces were simulated and the resulting passive force in the pectoralis major was recorded. The joints dislocated anterior-inferiorly all with some form of capsular pathology found in vivo following anterior dislocation.

A third mechanism for anterior dislocation is excessive external rotation. When the glenohumeral joint is in the apprehension position and the humerus is forced to externally rotate dislocation may result. This could occur when a person falls on their shoulder with their arm rotated behind them. Researchers have created models using excessive external rotation of the humerus to simulate a particular capsular state: the thrower's shoulder. This state is characterized by increased external rotation and decreased internal rotation compared to normal shoulders [54, 71-73] This model was not used to simulate joint dislocation.

1.6.3 Pathology Associated with Dislocation

When dislocation occurs any of the joint stabilizers may be affected. Hill-Sachs lesions and glenoid defects are compression injuries that occur when the soft posterolateral humeral head contacts the harder glenoid rim following glenohumeral dislocation. [74] This results in large indentations on the humeral head or glenoid, respectively.

Injuries to the glenohumeral capsule can also result from dislocation and typically result in joint instability. For example, Bankart lesions occur when the AB-IGHL and the glenoid labrum tear away from the glenoid [75] and humeral avulsions involve the lateral capsule tearing away from its insertion to the humerus. [76] Previous research has examined the effects of these lesions on glenohumeral joint kinematics. Speer and coworkers simulated Bankart lesions, via surgical incisions in cadaveric specimens. The AB-IGHL, axillary pouch and labrum were transected from the glenoid and the humerus was translated anteriorly and inferiorly at three abduction angles. The simulated Bankart lesion resulted in a small increase in anterior and inferior translation at all joint positions but no dislocation. [77] A second study simulated the Bankart lesion by detaching various combinations of four capsular regions and again the humerus was subjected to anterior and inferior translations. [78] Both studies found that glenohumeral dislocation could not occur if the only injury present was a Bankart lesion. Similarly, four sections of the capsule insertion on the humerus were consecutively transected in order to simulate a humeral avulsion. Resulting joint kinematics were examined and dislocation was only observed after three of the four sections had been transected. [79] These studies prove that the presence of capsular lesions alone does not enable the glenohumeral joint to dislocate and that tissue damage must be present for dislocation to occur.

A common injury resulting from dislocation is permanent deformation of the capsular tissue as dislocation cannot occur from capsular lesions alone. [77, 79] This occurs when the capsule is loaded beyond its elastic limit and has been shown to be the primary contributor to anterior instability. [77-79] Nonrecoverable strain has been used as a method to quantify this permanent deformation and will be discussed in detail in Section 1.6.3.2.

1.6.3.1 Capsule Strains during Dislocation

Computing strain in the glenohumeral capsule is much more complex than computing strain in a uniaxial ligament such as the MCL. Measuring strain requires a reference state that reflects a position of the tissue in which very minimal strain (or load) is applied. For a uniaxial ligament, a small tensile preload is typically applied to serve as the reference state. However, for a three-dimensional structure such as the capsule, determining a configuration in which minimal strain is applied to the tissue is more difficult. Malicky and coworkers developed a method of determining a reference strain state for the glenohumeral capsule in which the capsule is inflated with air to eliminate any wrinkles in the tissue. [69] This methodology was used in the current work and is described in more detail in Section 5.1.1.5.

Once a reference state is established marker positions on the surface of the capsule can be compared between the reference state and other joint positions in order to compute three-dimensional strain fields. Using this concept, maximum principal strain distributions in the intact anteroinferior glenohumeral capsule (AB-IGHL and axillary pouch) during glenohumeral subluxation have been quantified. [69] Average and peak maximum principal strains in the anteroinferior capsule were found to be greater on the glenoid side when compared to the humeral side. Glenohumeral subluxation ranging from 7 mm to 18 mm resulted in average and

peak maximum principal strains that ranged from 13% to 14% and 25% to 31% on the glenoid side compared to 9% to 15% and 18% to 28% on the humeral side, respectively.

1.6.3.2 Nonrecoverable Strain

Prior to the realization that the glenohumeral capsule should be treated as a continuous sheet of tissue, attempts were made to quantify the amount of permanent deformation in discrete capsule regions. Initially, cyclic elongations were applied at increasing levels of sub-failure strain to the glenoid-anteroinferior capsule-humeral complexes in order to simulate permanent deformation of the capsule that occurs due to repetitive motion. [80] A permanent increase in tissue elongation from ~5% to 7% was found depending on the level of applied sub-failure strains. Although permanent deformation was reported following cyclic loading, the mechanism behind permanent deformation resulting from joint dislocation is much different as it results from a single traumatic event. McMahon and coworkers evaluated the permanent deformation of glenoid-AB-IGHL-humerus complexes during load-to-failure tests [81] by quantifying the difference in elongation between the yield and ultimate deformation, or the length of the plastic region of the load-elongation curve. The difference between the yield and ultimate strain was also calculated. However, these definitions of permanent deformation yielded very small amounts of damage and do not provide the most clinically relevant information as the capsule was separated into discrete sections.

Nonrecoverable strain can be used as a way to quantify permanent tissue deformation that results from the glenohumeral capsule being loaded beyond its elastic limit during joint dislocation. This concept is best illustrated by comparison to a balloon. When a balloon is inflated a small amount and the air is released, it will return to its initial shape. In other words, it will still hold the same volume of air at an equal pressure before and after inflation. However, if

the balloon is inflated a large amount it becomes permanently deformed once the air is released and therefore it takes a greater volume of air to fill the balloon to the same pressure. Similarly, when the capsule is loaded beyond its elastic limit it becomes permanently deformed. In this deformed state, the capsule cannot function properly to stabilize the joint leading to increased joint rotations and translations, instability and recurrent dislocations. [71-73, 77, 78] Nonrecoverable strain is a method of quantifying the permanent increase in surface area of the capsule following glenohumeral dislocation.

Until recently clinicians had only suspected permanent tissue deformation of the capsule following glenohumeral dislocation based on their observations of increased capsular volume and joint instability, particularly when no capsular tears were present. In the cadaveric model of glenohumeral subluxation, Malicky and coworkers also quantified the resulting nonrecoverable strain by comparing the positions of 60 lead markers on the anteroinferior capsule (axillary pouch and AB-IGHL) in an inflated reference strain state before and after glenohumeral subluxation. Nonrecoverable strains in the anteroinferior capsule were found to be greater on the glenoid side when compared to the humeral side. Glenohumeral joint subluxation ranged from 7 mm to 18 mm and resulted in average and peak maximum principal nonrecoverable strains ranging from 3% to 10% and 8% to 25% on the glenoid side and 2% to 4% and 5% to 14% on the humeral side, respectively. The results of this study quantified and thereby supported the existence of nonrecoverable strain following glenohumeral subluxation.

1.6.3.3 Structural Changes

In addition to the presence of nonrecoverable strain in the capsule following joint dislocation, it is likely that structural changes occur in the tissue as well. The microstructure of the glenohumeral capsule is composed primarily of type I collagen, collagen fiber cross-links and

elastin. [82] Rodeo and coworkers have shown that increases in collagen fibril diameter are associated with greater tensile strength of soft tissue. Capsular tissue from unstable shoulders show greater fiber diameter and increased number of collagen cross-links when compared to tissue from normal shoulders. [82] These changes are representative of a healing response, increased tissue strength, and disruption of the collagen fibers and their orientation within the tissue. These findings demonstrate that capsular tissue is altered with injury. The tissue following injury is not structurally consistent with normal tissue and these changes may be indicative of altered material properties from normal to injured tissue.

1.7 CLINICAL TREATMENT

Once dislocation occurs, patients may need to seek medical attention either to reduce the joint back into the socket or due to pain, instability, and recurrent dislocations following the initial incident. Clinicians will then try to diagnose and repair any injuries caused by the dislocation.

1.7.1 Diagnosis

Diagnosis of glenohumeral joint pathology includes many techniques such as discussion of patient history, imaging of the joint via radiographs or magnetic resonance imaging (MRI), physical examinations and even arthroscopic evaluation. Certain capsular pathologies are more easily identified using these techniques than others. Imaging techniques can be used to identify soft tissue tears or bony lesions [52], however they depend upon the experience of radiologists [83] and are not capable of detecting the most common form of injury and the focus of this

dissertation, permanent deformation of the capsule. Although not visible via imaging, permanent deformation of the anteroinferior capsule can lead to anterior instability. Therefore, surgeons typically turn to the physical examination as the primary means for identifying the location and extent of permanent capsular deformation. [84-86]

Physical examinations require surgeons to hold the scapula as stationary as possible while applying manual loads to the humerus at various joint positions. Typically patients will lie supine on the edge of a table in order to limit translation of the scapula. While translating the humerus, surgeons will attempt to measure the resulting motions with respect to the humerus and compare these motions between the injured and contralateral joint. [87] These translations are then used to provide insight into the joint stability provided by the capsule. However, these exams are extremely subjective as they are dependent on examiner skill and experience and are not standardized for joint position. [88-90] The lack of standardized joint positions for physical exams is particularly problematic as the function of the glenohumeral capsule is highly dependent upon joint position. [9, 27, 84, 91] This makes diagnosing localized capsular injuries extremely difficult. The combination of these issues makes clinical exams to diagnose anterior instability due to permanent capsular deformation not reliable [92] which may lead to misdiagnosis and poor patient outcome.

In an attempt to standardized physical examinations, validated subject specific finite element models were used to suggest joint positions which consistently loaded the anteroinferior glenohumeral capsule. [93] Joint positions with 60° of glenohumeral abduction and a mid-range (20°-40°) of external rotation consistently loaded the glenoid side of the anteroinferior capsule. This work suggests that standardizing physical exams to specific joint positions to diagnose localized capsular injury may be possible and could be used to improve patient outcome.

1.7.2 Rehabilitation

Conservative treatment following shoulder dislocation involves a period of immobilization followed by rehabilitation to strengthen the shoulder muscles surrounding the joint. However, the effectiveness and proper treatment protocols are controversial. For example, following a first-time shoulder dislocation immobilization in internal rotation has been performed for years. [94] However, high recurrence rates following this treatment have been reported. [95-97] More recently, studies have shown that immobilization in external rotation may yield better results. [98-104] One study found that 42% of patients with internal immobilization experienced recurrent dislocations compared to only 26% of patients with external immobilization at a two-year follow-up. [99] Regardless of the position of immobilization, recurrence rates are still unacceptably high following conservative treatment with rates from 60 – 94% being reported for patients less than 25 years of age. [52, 105-110] In addition, physical exams to determine if patients require surgery following conservative treatment are not reliable predictors of recurrence. [111] The ineffectiveness of conservative treatments could be due to the fact that these treatments do not address the damage that occurs to the capsule during dislocation. Thus, surgical repair to target the capsule is often performed.

1.7.3 Surgical Repair

Due to the poor patient outcome following conservative treatment, about 23% will need surgery. [11]. These repairs specifically target the glenohumeral capsule in an attempt to tighten the excessive capsular tissue and restore normal joint kinematics. Initially, surgeons performed an open repair, known as the capsular shift, which was used to treat multi-directional instability.

[21, 112, 113] This procedure involved making two incisions in the capsule, one along the anterior rim of the glenoid and the other parallel to the margins of the AB-IGHL running from the glenoid to humeral insertion. These incisions create two leaflets in the capsule which can then be folded upon one another and sutured in place. (Figure 1.11)

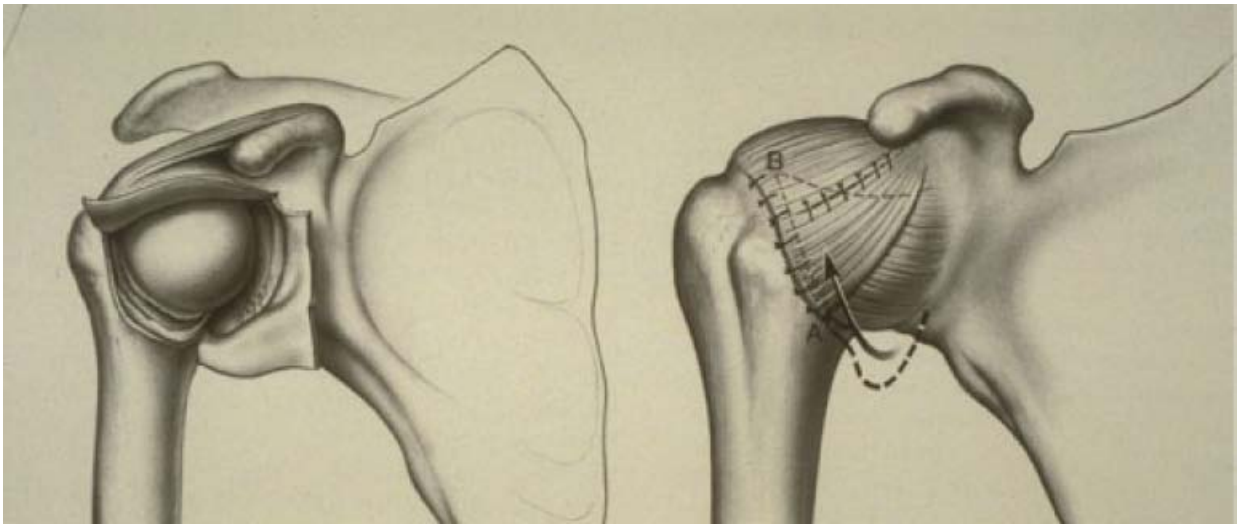

Figure 1.11 Anterior view (right shoulder) of the capsular shift indicating the "T" incision followed by a shift of the capsule tissue. (Neer, C. S. and C. R. Foster, J Bone Joint Surg Am, 1980, used with permission, www.rockwaterinc.com) [21]

Recently, arthroscopic procedures have become the most common form of repair in which the redundant (permanently deformed) capsular tissue is bunched up and sutured to the glenoid. This procedure allows for selective tightening in various capsule regions to treat uni-directional or multi-directional instability as needed. In order to determine where and how many plications to perform, surgeons will perform physical exams just prior to surgery while the patient is anesthetized. [114-117] Surgeons will attempt to translate the humeral head in the anterior, posterior, and inferior direction and compare these translations to the contralateral joint. Based on the direction of excessive joint translation the surgeon will assess the location and amount of plication required. However, this may not be the most appropriate method for

quantifying injury to the capsule as the direction of excessive joint translation may not correspond to injury in that particular portion of the capsule due to its continuous nature. For example, excessive anterior translation may not imply that the anterior portion of the capsule requires plication.

The glenohumeral joint may also be evaluated via an arthroscope in order to assess injury to the capsule. [118, 119] In one study “the condition of the capsular laxity was evaluated with direct visualization and palpation with a probe”. [118] Although this method is capable of detecting capsular tears, identifying the location and amount of permanent deformation of the capsule is somewhat subjective as the specific capsule regions are difficult to identify through the scope.

These repair techniques ignore changes in the structure of localized areas of the capsule that may have occurred as a result of joint dislocation. It is often unclear where or how much of the tissue should be plicated or shifted and is left up to the interpretation of the surgeon. The specific location and extent of capsular injury is not taken into account during repair procedures. This is probably because the location and extent of repair depend on the capsule pathology diagnosed using the physical exams. [87, 88, 120] Understanding how the structure and function of the glenohumeral capsule are altered following joint dislocation could provide information as to the location and extent of capsular injuries thereby decreasing the subjectivity of rehabilitation and repair procedures.

1.8 CLINICAL OUTCOMES

The subjective nature of diagnostic and repair procedures leads to patient outcome which is less than adequate. Following capsular shift procedures, patients are at risk for the development of glenohumeral osteoarthritis which may be present in over 50% of cases, with an older age at the first dislocation increasing the risk of osteoarthritis development. [121] Although the shift from open to arthroscopic repair techniques was advantageous to the patient, problems still exist following repair. Studies examining arthroscopic plication procedures following traumatic anterior dislocation have reported recurrence in up to 18% and fair to poor functional outcomes in up to 24% of patients. Further, 10% of patients do not return to their previous activity level. [114, 116, 118, 121]

In many cases, poor patient outcome following surgical repair may be due to misdiagnosis. Misdiagnosis of the type of instability (uni-directional or multi-directional) has been reported to be responsible for 38% of recurrent dislocations and 35% of recurrent dislocations may result from the wrong surgical procedure being performed. [122] These issues are linked together as the type of repair procedure performed is based on the diagnosis made from the physical exam and probably result from the clinician having a poor understanding of the location and extent of capsular damage in a particular patient. Therefore, there is a need to improve current diagnostic and repair techniques. Characterization of the structure and function of the glenohumeral capsule following anterior dislocation can aid surgeons in improving repair techniques by identifying specific locations and amounts of the capsule to be targeted during repair. In addition, quantifying the differences in kinematics between normal and injured joints in multiple positions may help identify joint positions in which changes in translation can be detected during physical exams.

2.0 MOTIVATION

Permanent deformation of the glenohumeral capsule is a common injury associated with anterior dislocation as glenohumeral dislocation cannot occur in the presence of lesions alone. [77, 79] However, diagnosing and treating this pathology is extremely difficult as there is currently no reliable method for determining the location and extent of capsular damage. [88-90] Current diagnostic and repair techniques are subjective and unreliable [92] thereby contributing to poor patient outcome following anterior dislocation. Existing knowledge of the structure and function of the glenohumeral capsule following permanent deformation is minimal and may be the root cause behind these issues. A greater awareness of how this structure changes following injury will enable specific locations of the capsule which are at risk for injury to be identified so that they can be targeted during repair procedures. Surgeons may need to account for changes in the material properties of the capsule following injury as simply plicating redundant tissue may not be sufficient to restore the joint to a normal functioning state. Further, relating capsular damage to changes in other measures of joint function such as joint kinematics could help explain why current physical exams are misdiagnosing the location and extent of capsular damage.

Validated finite element models of the glenohumeral capsule may also be able to improve diagnostic and repair techniques; however, improving the accuracy of these models requires adequate constitutive models to describe the behavior of both normal and injured capsular tissue. As the normal capsule can withstand loading in any direction, the collagen fibers in the

anteroinferior capsule are randomly oriented. [3-5, 123] Therefore, an isotropic hyperelastic phenomenological constitutive model was initially used to characterize the material properties of the normal glenohumeral capsule. [42, 124]

As collagen fibers are the primary load bearing components in the capsule, changes in their orientation as a result of dislocation would affect the mechanical properties and thus the function of the glenohumeral capsule in vivo. Collagen fibers in other biologic tissues have been shown to align with applied load. [125-127] In addition, changes in the rate of fiber rotation have been associated with the location of tissue damage in the cervical capsular ligament and damage was found to occur well before rupture. [127] While this study was able to predict the location of tissue damage, it was predicted from a point on the load-elongation curve at which the tissue was already damaged. It is possible that changes in collagen fiber alignment may be indicative of permanent deformation of the capsule and being able to predict the location of tissue damage before damage has occurred would be beneficial. Therefore, this work requires an understanding of the collagen fiber kinematics in the glenohumeral capsule during uniaxial extension to failure.

If the collagen fiber alignment aligns under loading, then the capsule may exhibit a more aligned reference state following injury resulting in a more anisotropic tissue. The same constitutive model may not be capable of describing the behavior of both normal and injured capsular tissue. Therefore, a method for simulating injury in tissue samples from the glenohumeral capsule should be developed and used to determine if the previously used isotropic constitutive model is capable of detecting changes in the material behavior of the capsule via changes in the material parameters. Clearly, a model that is capable of describing the collagen fiber kinematics of the glenohumeral capsule throughout the entire load-elongation curve would

be ideal for development of finite element models of glenohumeral dislocation that could be used to examine rehabilitation and repair techniques.

Developing an experimental model to simulate injury in tissue samples from the capsule will demonstrate that permanent deformation can be created and related to changes in material properties. However, in order to fully understand how anterior dislocation affects the function of the glenohumeral capsule, it must also be evaluated from the joint level. Permanent deformation has been created in the capsule of cadaveric shoulders by means of excessive internal and external rotation and was used to simulate the increased joint mobility found in thrower's shoulders. [54, 71-73]. While other models have quantified the permanent deformation during joint subluxation using nonrecoverable strain [68], no model has correlated the amount of tissue damage to altered capsule function. Understanding the relationship between the extent of tissue damage and changes in capsule function following anterior dislocation could aid surgeons in diagnosing and treating anterior instability. Therefore, an experimental model to dislocate the glenohumeral joint anteriorly and create permanent deformation of the capsule needs to be developed. The experimental model can then be used to relate the location and extent of tissue damage to changes in capsule function in clinically relevant joint positions.

In addition to enhancing clinical knowledge, the results of the microstructural-, tissue-, and joint-level analyses to examine the effect of anterior dislocation on the structure and function of the glenohumeral capsule can be used to suggest improvements to the previously developed isotropic constitutive model for the glenohumeral capsule. [42] Structural constitutive models are based on specific tissue constituents, such as the collagen fiber alignment and ground substance. As the collagen fiber kinematics are a link between the normal and injured capsule it is likely that a structural model will better describe its complex behavior compared to the isotropic

phenomenological model. Understanding the collagen fiber kinematics is imperative for developing an appropriate structural constitutive model to describe capsule behavior. Many structural models make the affine assumption, i.e. that the local fiber kinematics follow the global tissue deformation. Conversely, an approach to account for non-affine fiber kinematics in structural models has been recently developed. [128] Determining whether the affine assumption can be applied to the collagen fiber kinematics of the glenohumeral capsule would aid in the development of an adequate constitutive model to be used in finite element models of the glenohumeral joint.

2.1 RESEARCH QUESTION

Therefore, this dissertation addresses the following research question.

Research Question: How does anterior glenohumeral dislocation affect the structure and function of the glenohumeral capsule?

2.2 HYPOTHESIS

As collagen fiber alignment has been linked to tissue damage in other biologic tissues [127], it may be an indicator of permanent deformation of the capsule. Changes in fiber alignment as a result of anterior dislocation would affect the mechanical properties, and therefore the function of the glenohumeral capsule. Simply plicating redundant tissue will not address changes in collagen fiber alignment which could be the source of its loss in the stabilizing function. This

may explain some of the recurrent dislocations following capsular plication for anterior instability. [114, 116, 118, 121] As a result, the current work aims to address the following hypothesis.

Hypothesis: Anterior glenohumeral dislocation causes permanent deformation of the anteroinferior glenohumeral capsule that can be characterized by changes in collagen fiber alignment. These changes will result in altered material properties thereby diminishing the joint stability provided by the capsule.

The anteroinferior glenohumeral capsule (specifically AB-IGHL and axillary pouch) was selected as the primary focus of this work as it is the region of the capsule most commonly injured during anterior dislocations. [39, 105, 129-132] Consequently, it is the region of the capsule targeted by surgical repair techniques [45, 115, 117, 133] and evaluated in finite element models of the normal glenohumeral capsule [43, 44, 134-136]. Investigating the effects of anterior dislocation on the structure and function of this region of the glenohumeral capsule will provide valuable insight into an appropriate constitutive model to describe the behavior of the normal and injured glenohumeral capsule. Such a model can then be implemented into finite element models of the glenohumeral joint.

2.3 SPECIFIC AIMS

The hypothesis was tested using the following specific aims (Figure 2.1):

Specific Aim 1: Quantify the collagen fiber alignment and maximum principal strain in the glenohumeral capsule during uniaxial extension to failure and determine if these properties can predict the location of tissue failure.

Specific Aim 2: Develop an experimental model to create permanent deformation in tissue samples excised from the glenohumeral capsule via sub-failure loading. Use this model to:

a) Quantify the magnitude of strain that results in permanent deformation of the AB-IGHL, as evidenced by the creation of nonrecoverable strain.

b) Determine the effect of the permanent deformation on the stiffness and material properties of the AB-IGHL during tensile deformation.

Specific Aim 3: Develop an experimental model to create permanent deformation (nonrecoverable strain) in the anteroinferior glenohumeral capsule by dislocating the joint anteriorly using robotic technology. Use this model to:

a) Quantify the magnitude of strain during anterior dislocation and the resulting nonrecoverable strain in the anteroinferior glenohumeral capsule.

b) Identify specific sub-regions of the anteroinferior glenohumeral capsule which are at risk for injury during anterior dislocation.

c) Evaluate the effect of anterior dislocation on the function of the glenohumeral capsule by examining the strain distribution in the anteroinferior capsule, joint kinematics, and *in situ* force in the capsule during a simulated clinical exam at three clinically relevant joint positions in the intact and injured joint.

Specific Aim 4: Suggest improvements to a hyperelastic constitutive model for the glenohumeral capsule that could increase the accuracy of finite element models of the glenohumeral joint and potentially be used to model the injured glenohumeral capsule.

a) Compare the ability of an isotropic phenomenological model and a structural model which accounts for the random fiber organization in the plane of the tissue to describe

and predict the material behavior of the glenohumeral capsule in response to tensile and shear loading.

b) Evaluate the affine assumption for the fiber kinematics of the anteroinferior glenohumeral capsule by comparing experimentally measured preferred fiber directions to the fiber directions predicted by the affine model.

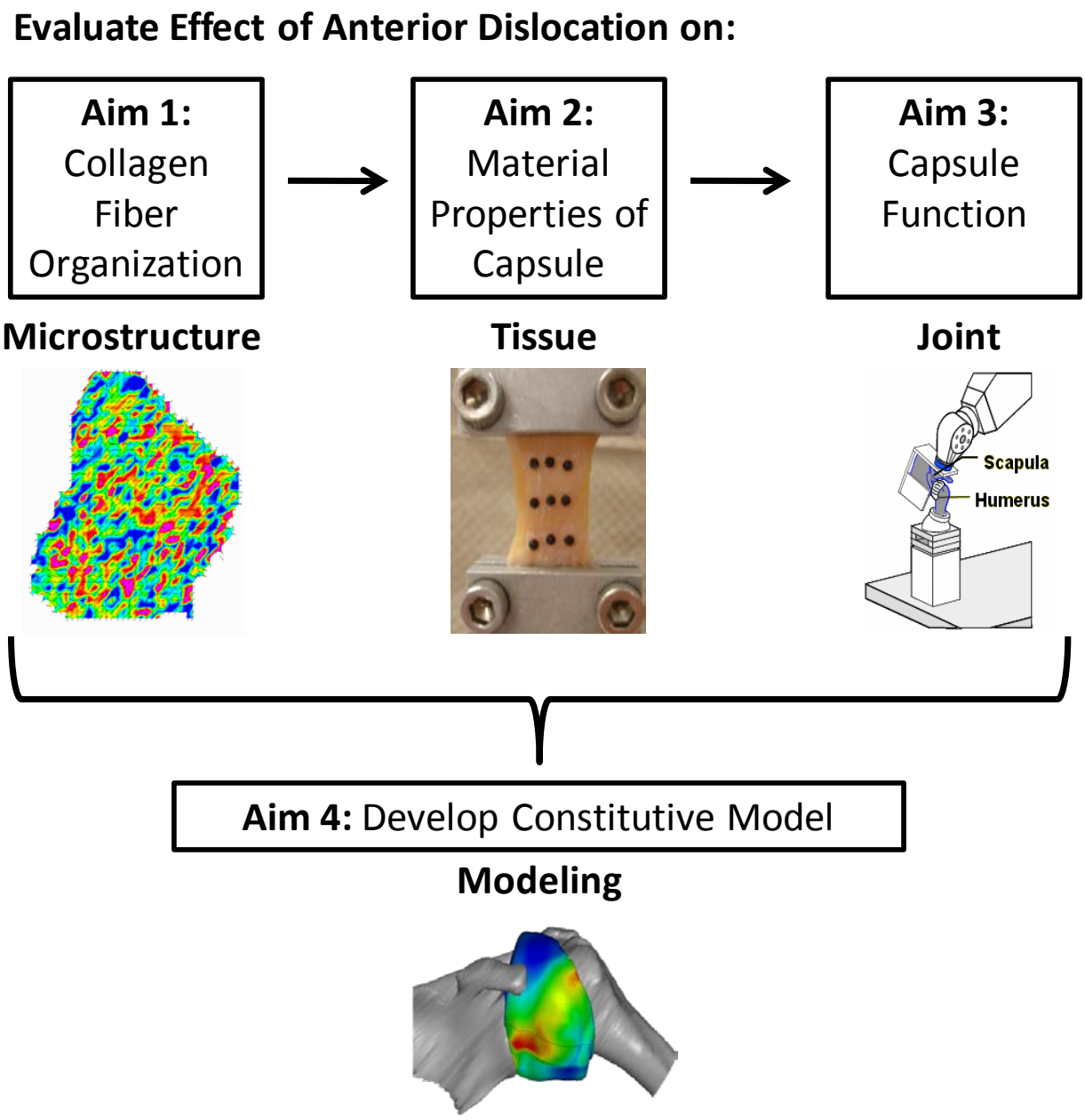

Figure 2.1 Flowchart demonstrating the objective of the dissertation and the relative relation of the Specific Aims.

3.0 MICROSTRUCTURAL LEVEL: COLLAGEN FIBER ORGANIZATION

3.1 INTRODUCTION

In an effort to understand the load-bearing capabilities of the glenohumeral capsule, researchers have investigated the collagen fiber alignment in each region using quantitative polarized light imaging. [3-5] In general, the collagen fibers in the capsule do not have a preferred orientation. O'Brien and coworkers [5] found the AB-IGHL and PB-IGHL to be more organized than the axillary pouch, and demonstrated a great deal of intermingling of the fibers. Gohlke et al. [4] agreed that the AB-IGHL was more aligned than the axillary pouch, but also reported that the collagen fibers in the axillary pouch were organized along the longitudinal direction of the ligaments. More recently, using a small angle light scattering (SALS) technique, it was found that the collagen fiber alignment in the axillary pouch and AB-IGHL demonstrated no evidence of alignment and only moderate organization within a largely unorganized tissue, respectively. [3] In addition, the posterior capsule was not shown to have a preferred fiber orientation. [12] All of these studies demonstrate that the collagen fibers in the glenohumeral capsule are designed to support loads in multiple directions thus allowing for the wide range of motion at the shoulder.

Recently the maximum principal strain distribution in the anteroinferior capsule with humeral external rotation has been examined. [137] The magnitude of maximum principal strains on the anterior glenoid side of the anteroinferior capsule was found to increase with humeral

external rotation. (Figure 1.9) This region of the capsule corresponds to the location of a common capsular tear known as the Bankart Lesion. [137] In addition, the strain directions in the capsule became more aligned with the AB-IGHL with increasing humeral external rotation. This study suggests that increases in strain magnitude and collagen fiber alignment may be able to predict injury locations.

Increases in fiber alignment with load have been shown in biologic soft tissues other than the capsule. [125, 127, 138-142] For example, an increase in collagen fiber alignment with load in the supraspinatus tendon has been shown in the toe-region of the load-elongation curve. [137] Quinn and coworkers examined the collagen fiber alignment in the cervical capsular ligament during loading to failure. [137] They found that the location of tissue failure could be predicted from the linear region of the load-elongation curve when a high rate of fiber rotation was used to indicate tissue damage. Thus collagen fiber alignment may be able to predict potential injury locations in the glenohumeral capsule as well.

Due to the correspondence of high strains to the location of common clinical injuries in the intact glenohumeral capsule as well as the successful prediction of the location of failure from collagen fiber alignment in other biologic soft tissues, it was believed that these parameters could predict the location of tissue failure in the capsule. Therefore, it was hypothesized that increases in the maximum principal strain and collagen fiber alignment would correlate with the location of tissue failure in the glenohumeral capsule. The objective of this section of the work was to quantify the collagen fiber alignment and maximum principal strain in the glenohumeral capsule during uniaxial extension to failure and determine if these parameters can predict the location of tissue failure.

3.1.1 Small Angle Light Scattering Technique

The first step to addressing the objective was to choose a method for quantifying fiber alignment. As the gross fiber orientation can provide valuable information regarding the mechanical properties of soft tissues, numerous techniques have been developed to examine the collagen fiber architecture in biologic soft tissues. Microscopic techniques are common for examining small tissue sections but are unable to quantify the gross fiber structure in a timely manner. Quantitative techniques to process optical [143, 144] or scanning electron microscopy [145-147] images have been utilized to determine the size and orientation of collagen fibers but the tissue preparation is destructive and very time consuming. Similar problems arise with the use of Small Angle X-Ray Scattering (SAXS) which is used to analyze collagen molecular architecture and involves collecting scattering patterns on film over a long exposure time. [148] A very common method which takes advantage of the birefringence of collagen fibers is known as polarized light microscopy. This method allows for the visualization of fiber direction as well as crimp. [149] However, a major limitation of polarized light microscopy is its inability to distinguish the fibers at multiple layers within the tissue and therefore limits measurements to superficial fibers. This technique was modified [150, 151] to generate polarized light retardation and alignment from single images of the tissue. This allows fiber directions and an index of the strength of orientation to be directly quantified without scanning the entire tissue. However, it is not capable of providing the actual fiber angular distribution. One final technique, known as small-angle light scattering (SALS) shines a laser through the tissue sample and provides a map of the collagen fiber alignment based on the spatial intensity distribution of the scattered light. This method is capable of determining the preferred fiber direction as well as the angular fiber distribution. However, it requires sufficient time to scan the entire tissue sample, which would

not allow for continuous data collection throughout elongation of a tissue sample as polarized light imaging would.

As the objective of this work required the collection of accurate, gross, rapid collagen fiber alignment information only two techniques were appropriate: polarized light imaging and SALS. The thickness of the capsule can vary 1 mm between regions and over 2 mm between subjects [12-14]; therefore it is necessary to section it into smaller slices before either of these techniques can be employed. Tissue slicing damages collagen fibers, thus a thicker sample would allow more collagen fibers to remain intact. This is particularly important for this work as the collagen fiber alignment will be quantified as the tissue is loaded. Since collagen fibers are the primary load barring constituents in the capsule, it is necessary to have as many intact fibers as possible so that they function as they would in the intact capsule. As polarized light imaging is limited to quantifying fibers only in superficial layers, the SALS technique was chosen as it is capable of capturing the collagen fiber orientation throughout tissues as thick as 500 μm.

SALS has been used extensively in the past to investigate the collagen fiber organization in biologic soft tissues and detailed descriptions have been reported. [3, 46, 152-163] A 4 mW continuous unpolarized laser (λ = 632.8 nm) is passed through tissue samples with a spatial resolution of 250 μm and the resulting angular distribution of the scattered light pattern is examined. From this scattered light pattern the angular fiber distribution can be determined. [160] The local preferred fiber direction is calculated as the centroid of the angular fiber distribution and represents the distribution of fiber angles within the light beam at any given point on the tissue sample. The orientation index (OI) is a quantitative measure of the fiber distribution and is defined as the angle that contains one half of the total area under the scattered light intensity-versus-fiber angle curve. [46, 156] The Normalized orientation index (NOI) can

be computed as a percentage to simplify physical interpretation [125, 154] such that a higher NOI value indicates a higher fiber alignment.

$$NOI = \frac{90 - OI}{90} \times 100\% \quad (1)$$

As described previously [125, 154], the NOI ranges from 0% to 100% representing a completely random to perfectly aligned fiber organization, respectively.

3.1.2 Preliminary Studies

The SALS technique has been used previously to examine the collagen fiber alignment in soft tissues under uniaxial and biaxial loading [125, 161, 164, 165], and it has been used to quantify the collagen fiber alignment in the unloaded glenohumeral capsule [3]. However, the collagen fiber alignment in the capsule has never been examined under load using the SALS technique; therefore, several preliminary analyses were necessary in order to establish an appropriate protocol to meet the desired objective.

3.1.2.1 Collagen Fibers Align with Load

A preliminary study was performed to prove that the collagen fibers in the glenohumeral capsule would become more aligned under load. Two tissue samples were harvested from the axillary pouch of the glenohumeral capsule. The samples (20 x 5 mm) were taken side-by-side with the long dimension corresponding to the longitudinal axis of the AB-IGHL. A stretching device was designed to hold tissue samples at various elongations while submerged it in a fixative.

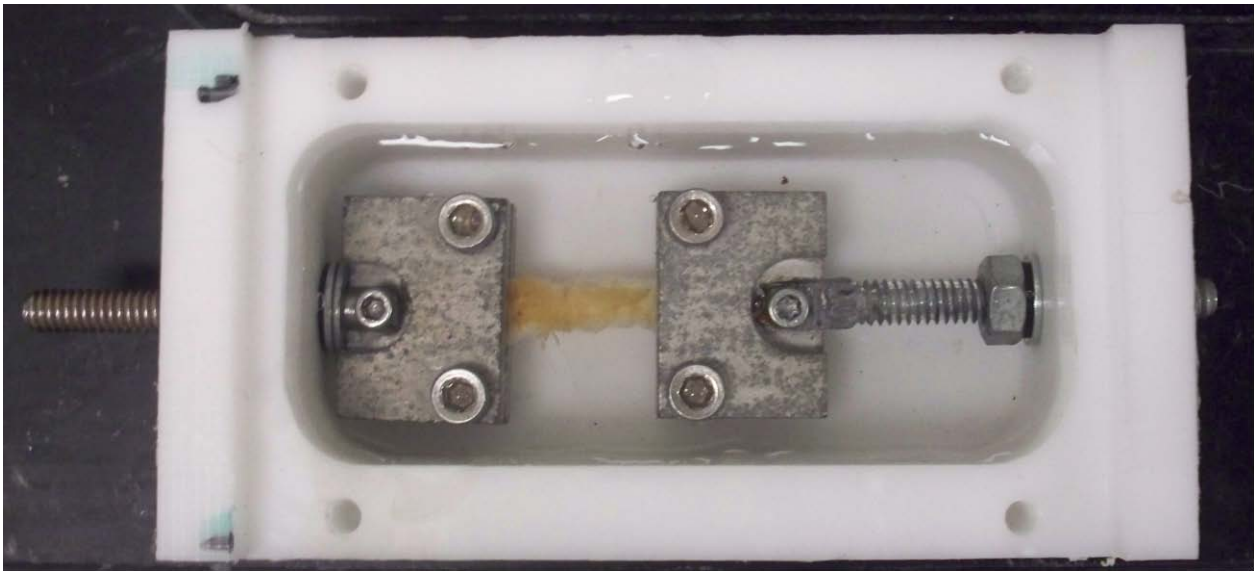

Figure 3.1 Custom designed stretching chamber.

One axillary pouch sample was placed in the stretching chamber and subjected to ~40% stretch (6 mm). The other tissue sample (control) was not stretched. Both samples were fixed with formalin for 24 hours, sectioned (25μm), and prepared appropriately for use in the SALS device.

The stretched axillary pouch showed higher fiber alignment compared to the control sample. (Figure 3.2) There are some local areas of alignment in the control tissue, but in general, the NOI is lower compared to the stretched tissue sample. The average NOI values for the control and stretched tissue samples were 45° ± 12° and 53° ± 8°, respectively, indicating increased alignment in the tissue that was stretched. Further, the lower standard deviation of the NOI values in the stretched tissue demonstrates that more fibers are aligned when the tissue is stretched.

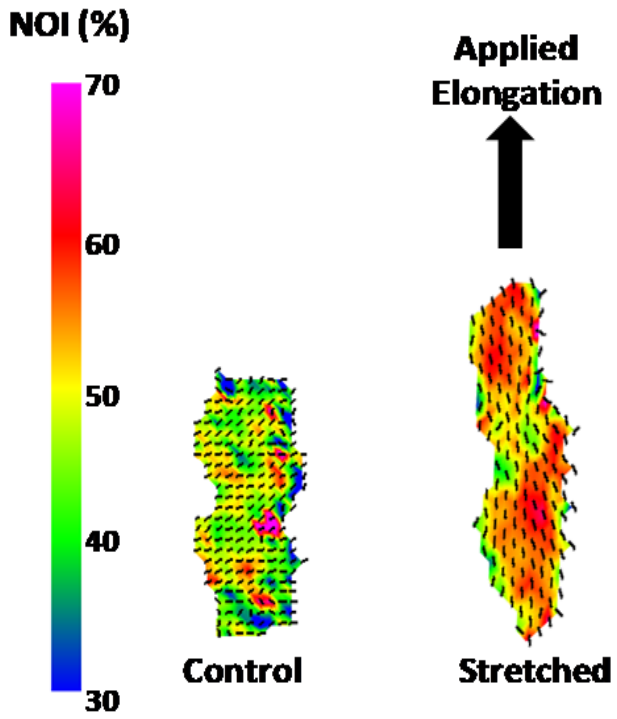

Figure 3.2 Normalized Orientation Index (NOI) distribution in two axillary pouch samples: one sample was unloaded (control) and the other was subjected to 40% stretch. High NOI values (pink) represent areas of highly aligned collagen fibers and low NOI values (blue) represent regions of randomly aligned fibers. The black lines represent the dominant fiber direction.

Figure 3.3 shows NOI histograms for the control and stretched tissue. The center of the stretched distribution is shifted toward higher NOI values and the peak is taller and thinner compared to the control distribution indicating an increase in collagen fiber alignment in the stretched axillary pouch. The results of this preliminary study indicate the possibility that the collagen fibers in the glenohumeral capsule become more aligned when loaded and that differences in the alignment between normal and stretched tissue may be detected using the SALS device.

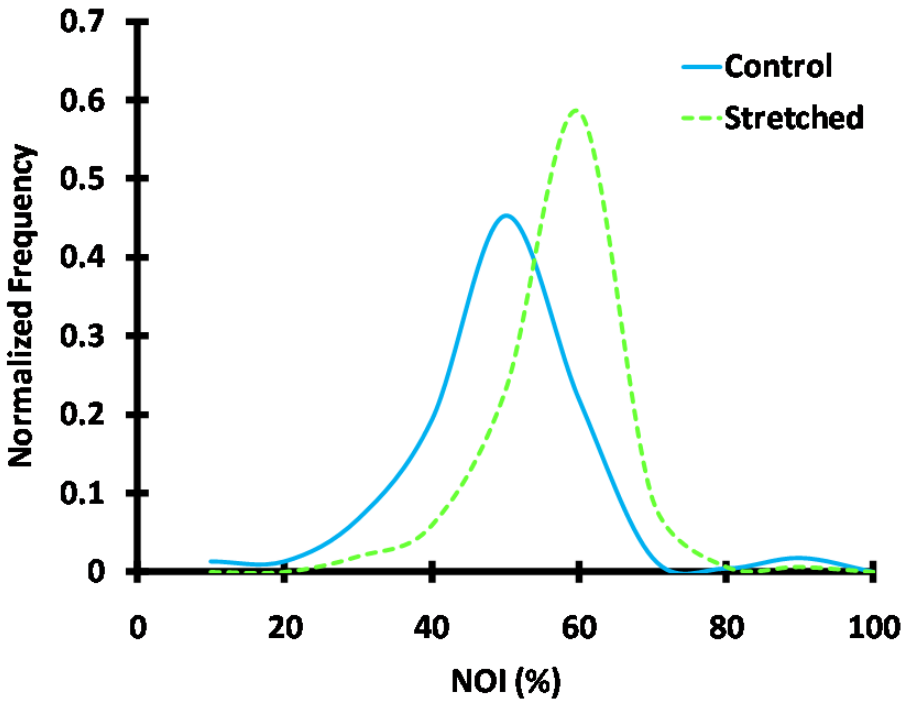

Figure 3.3 NOI histogram for the control and stretched axillary pouch.

3.1.2.2 Effect of Freezing on Collagen Fiber Alignment

The SALS device is capable of accurately measuring the collagen fiber alignment in tissues up to 500 μm in thickness. As the glenohumeral capsule is much thicker than this, it would have to be sectioned prior to measuring the collagen fiber alignment. The slicing process requires that the tissue be frozen in order to achieve uniform slices. In addition, since the tissues could not be sliced in our own laboratory due to the limitations of our cryostat (can only slice up to 25 μm); they would have to be taken to a different laboratory (Center for Biological Imaging) for slicing. This means that the tissue samples would be dissected from the cadavers, frozen and sliced one day and then tested on the SALS device the following day. The tissue would be kept frozen after

slicing and thawed prior to testing the next day. Therefore, the effect of freezing on the collagen fiber alignment of the glenohumeral capsule was evaluated.

Two tissue samples (10 mm x 10 mm) were excised from the axillary pouch of the glenohumeral capsule, embedded in OCT compound, frozen with liquid nitrogen, and sliced to 300 μm thick sections. These sections were placed on a slide and allowed to thaw. The collagen fiber alignment data was collected using the SALS device and the tissue was re-frozen. This process was repeated three times.

The collagen fiber alignment was not affected by the freeze-thaw cycles. (Figure 3.4, Figure 3.5) The NOI in the tissue sample was 42 ± 12%, 42 ± 12%, and 43 ± 11% following each cycle, respectively. Therefore, freezing and thawing of the tissue samples up to three times prior to testing would not affect the collagen fiber alignment data.

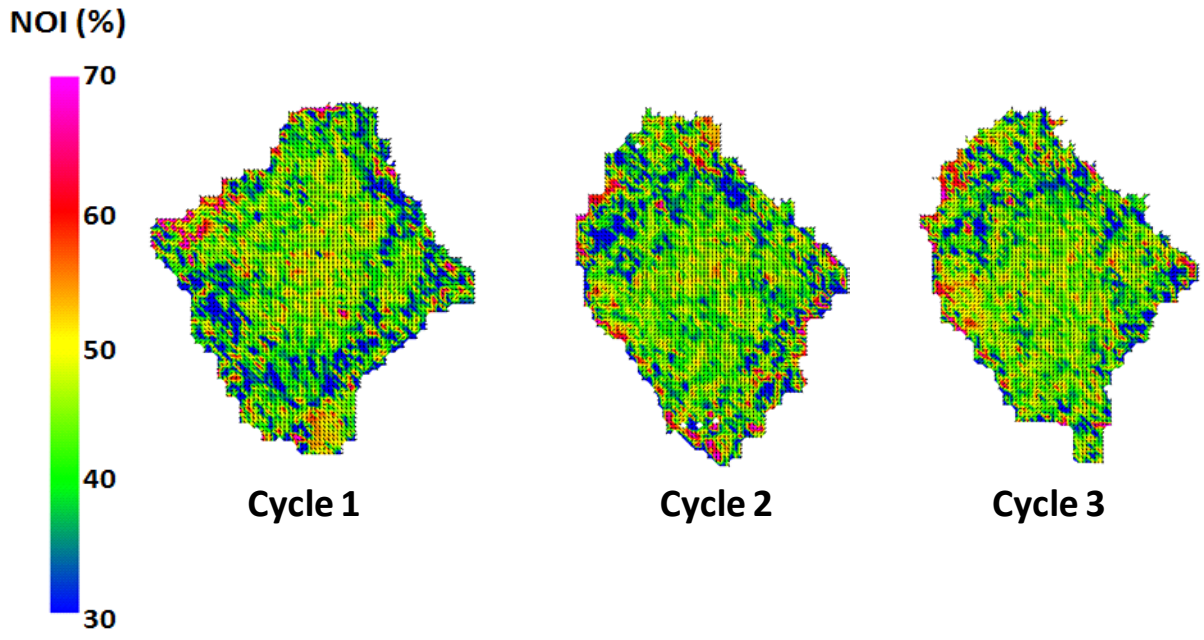

Figure 3.4 NOI distribution in a sample from the axillary pouch following each of three freeze-thaw cycles

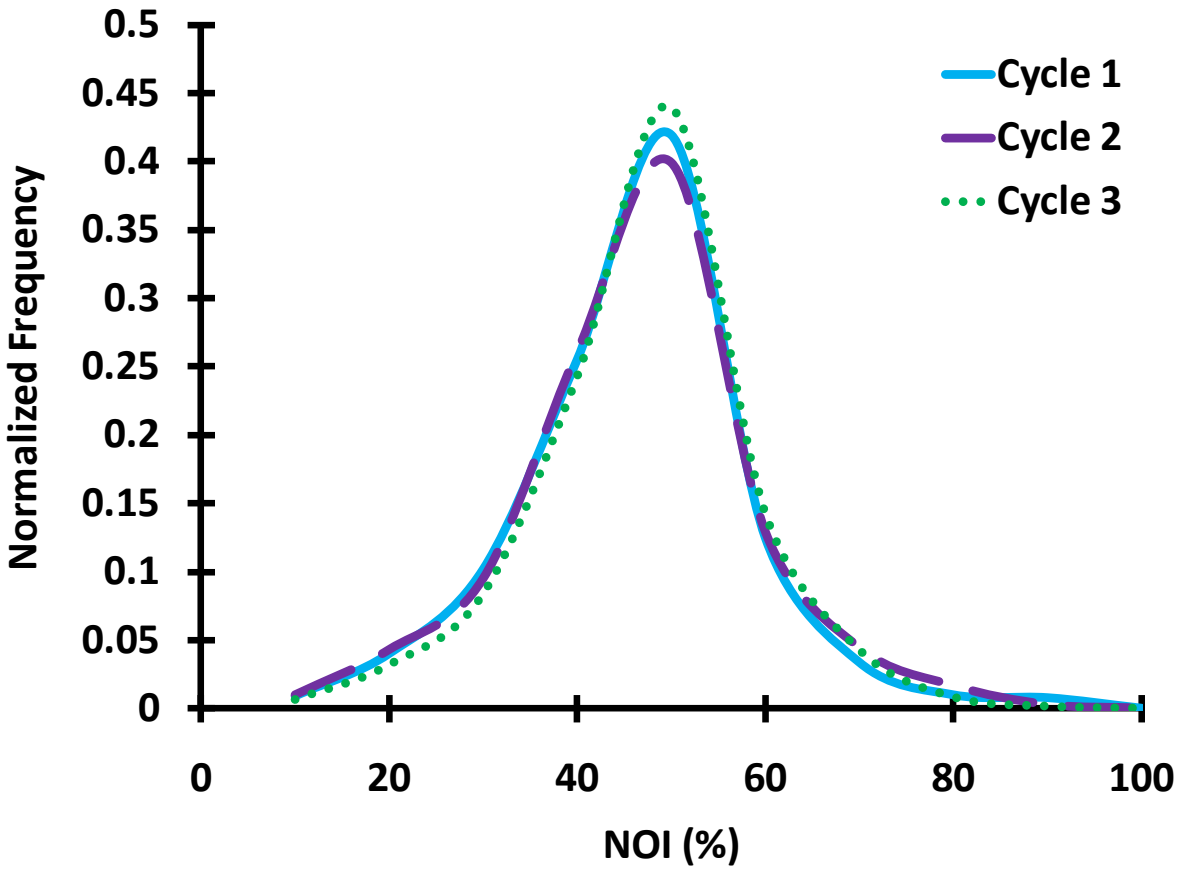

Figure 3.5 NOI histogram in a representative sample from the axillary pouch following three freeze-thaw cycles.

3.1.2.3 Modification of Stretching Device

The collagen fiber alignment of soft tissues under load has been examined several times using the SALS technique. [125, 155, 161, 164] A stretching device was previously developed to apply uniaxial and biaxial loads to tissue samples.

Figure 3.6 Stretching device designed to integrate with the SALS device and previously used to apply uniaxial and biaxial loads to soft tissues.

This device consisted of four lead screws coupled via gears to a stepper motor in the horizontal and vertical direction. [125] Tissue samples were attached to the device using sutures threaded over pulleys which could rotate freely. For this work, only the vertical loading direction was required so the horizontal pulleys, screws and motor were removed from the device. Initial attempts were made to attach tissue samples from the glenohumeral capsule to the device using sutures. However, due to the lack of load applied to the tissue in the horizontal direction the sample did not remain flat under loading. Thus, it was decided to remove the pulley system from the stretching device and replace them with custom soft tissue clamps. (Figure 3.7) This modification allowed the tissue sample to remain flat during elongation so that it could be accurately scanned using the SALS device.

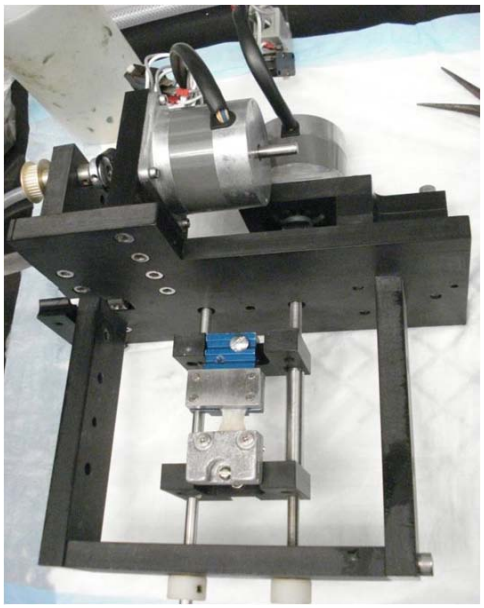

Figure 3.7 Stretching device modified to incorporate soft tissue clamps.

3.1.2.4 Appropriate Sample Thickness

The SALS device is capable of accurately measuring the collagen fiber alignment in tissue samples as thick as 500 μm. Once the stretching device was modified it was necessary to determine an appropriate sample thickness for this work. It is important that the sample is as thick as possible to allow the greatest number of collagen fibers to remain intact; however, slicing thick samples on the cryostat is extremely difficult so a compromise would have to be made. Further, the sample had to be thick enough so that it would not fail or be damaged during the handling required to mount the sample into the soft tissue clamps.

Three tissue samples from were excised from the axillary pouch, embedded in OCT compound, and frozen with liquid nitrogen. Slices of thickness 250 μm, 300 μm and 400 μm were taken from each sample. After slicing, the samples were placed in the custom soft tissue clamps and mounted into the stretching device. The 250 μm slices were too thin and failed under handling or when mounting the soft tissue clamps into the stretching device. Slices of thickness

300 μm were easier to handle and could be mounted into the stretching device however these samples failed as soon a small amount of load was applied to them. The 400 mm slices were the easiest to handle and mount into the soft tissue clamps and stretching device. These slices were also able to be elongated several millimeters before showing any signs of damage. Therefore, tissue samples taken from the glenohumeral capsule were sliced into 400 μm thick sections for the remainder of this work as it was thin enough for accurate data collection in the SALS device [46, 156] and still maintained as many intact collagen fibers as possible, and it was thick enough to be handled without damage

3.1.2.5 Repeatability of Fiber Alignment Measurements

After modification of the stretching device the repeatability of the SALS device to accurately measure the collagen fiber alignment in the new set-up was determined. A tissue sample from the axillary pouch was sliced to 400 μm, placed in custom soft tissue clamps, and attached to the stretching device. A small load was applied to the tissue sample and the same section of the tissue was scanned five times. The average NOI (Table 3.1) and preferred fiber direction (Table 3.2) were computed for each of the five trials and histograms were generated of the NOI (Figure 3.8) and preferred fiber direction (Figure 3.9) distributions. The range of average NOI and preferred fiber direction values were 0.9% and 1.9°, respectively.

Table 3.1 NOI (mean SD) for five scans using the SALS device of a tissue sample from the axillary pouch.

Trial	Mean ± SD (%)
1	45.8 ± 7.0
2	45.4 ± 7.1
3	46.3 ± 7.0
4	46.0 ± 6.9
5	45.7 ± 7.3
RANGE	0.9

Table 3.2 Preferred fiber direction for five scans using the SALS device of a tissue sample from the axillary pouch.

Trial	Mean ± SD (°)
1	0.4 ± 18.1
2	0.3 ± 17.5
3	1.8 ± 20.0
4	2.2 ± 21.1
5	1.5 ± 19.8
RANGE	1.9

Further, a very close agreement was found between the NOI and preferred fiber direction distributions for the five trials. Therefore, the SALS device is capable of measuring the NOI and preferred fiber direction of tissue samples in the modified stretching device with a repeatability of 1% and 2°.

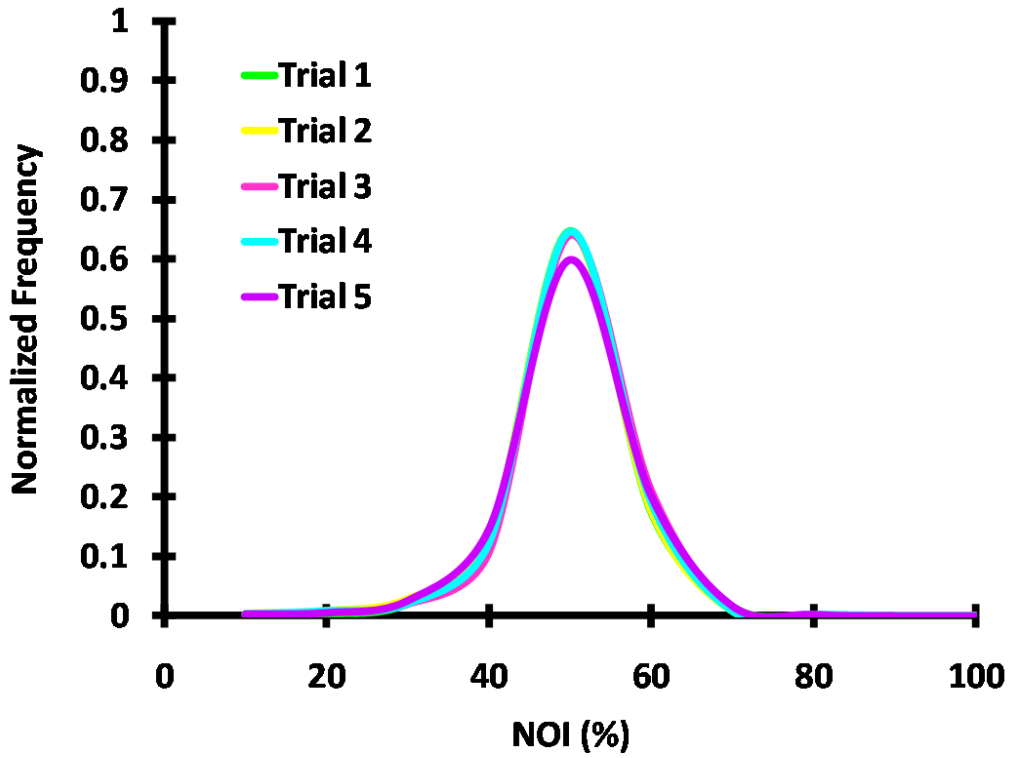

Figure 3.8 NOI histogram for five scans using the SALS device of a tissue sample from the axillary pouch

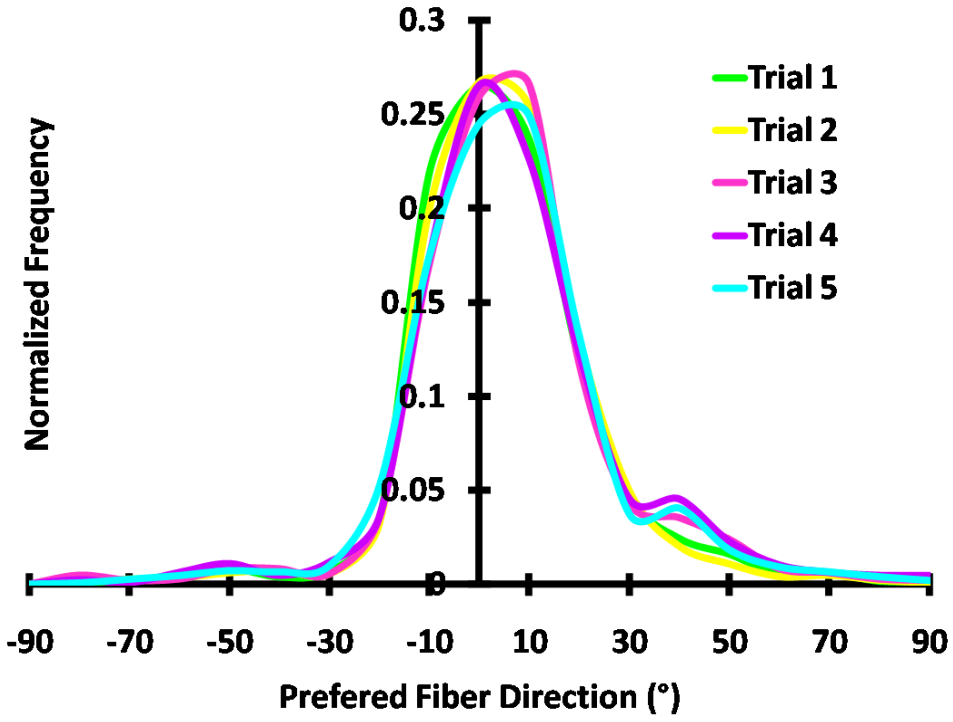

Figure 3.9 Preferred fiber direction histogram for five scans using the SALS device of a tissue sample from the axillary pouch.

3.1.2.6 Choice of Strain Markers

At the commencement of this project, the SALS device was not capable of measuring simultaneous stress-strain and collagen fiber alignment data. Therefore, a digital camera was used to track strain on the surface of each tissue sample during elongation. When tracking strain on tissue samples during mechanical testing, black, spherical, delrin markers are typically used. These markers were initially used for this study, however, when scanning the tissue to collect collagen fiber alignment data it was discovered that the laser light scatters in all directions when it hits the spherical marker. Therefore the strain makers could not be distinguished from the collagen fiber alignment data and as a result could not be used. To avoid this issue, graphite chips were used as strain markers since their surface is irregular and would not scatter light directly behind the marker. The graphite chips can be easily distinguished in the collagen fiber alignment data and were used for the remainder of this section of the work.

3.1.2.7 Accuracy of Distance Measurements with Digital Camera

The accuracy of the strain tracking procedure was assessed by comparing strain measurements to a gold standard. A piece of white cardboard was used to represent a tissue sample and was placed between two soft tissue clamps. The clamp-to-clamp distance (L_0) was measured (digital calipers, accuracy: 0.03mm) and four graphite strain markers were fixed to the cardboard sample using cyanoacrylate. (Figure 3.10)

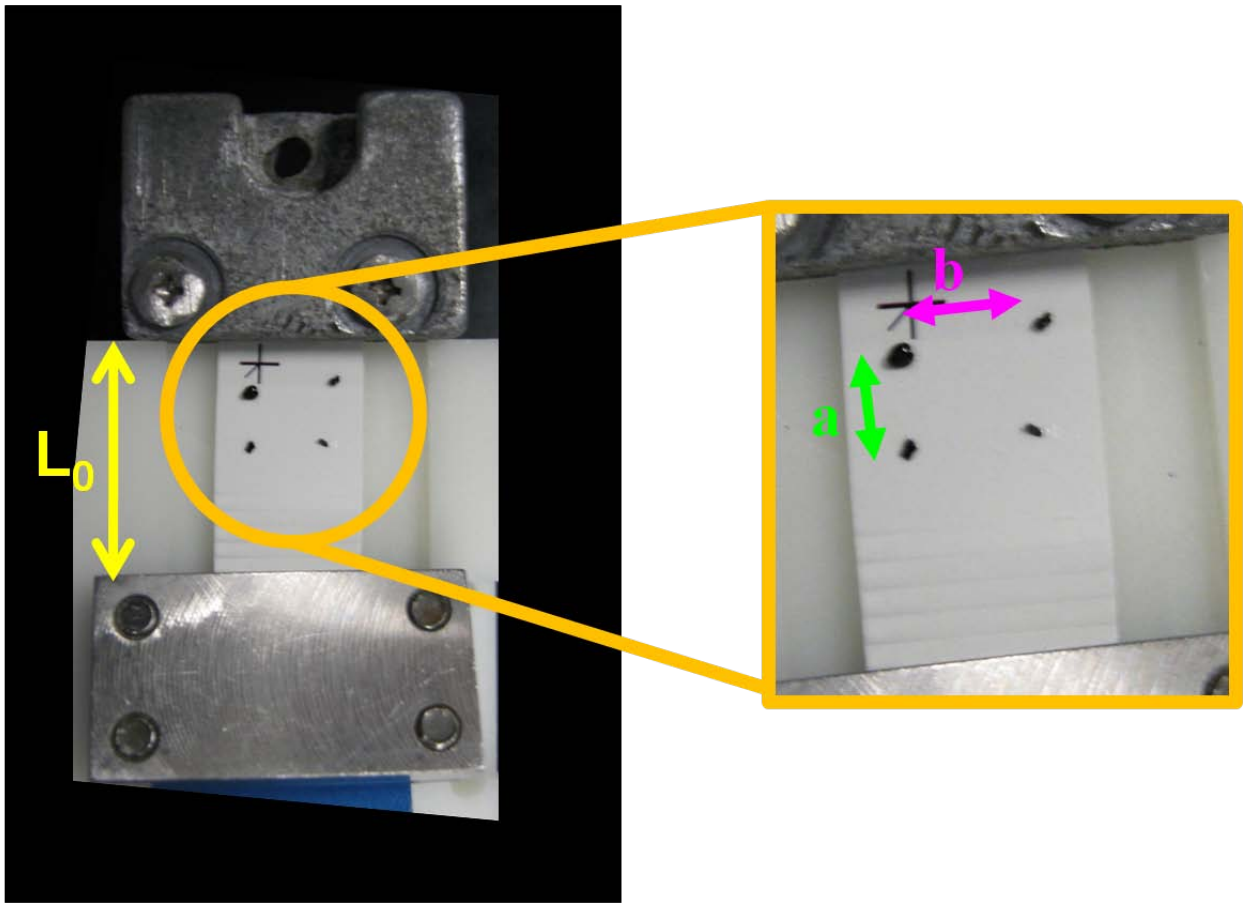

Figure 3.10 Experimental set-up for determining the accuracy of strain measurements using a digital camera showing the grid of graphite strain markers on the cardboard sample, clamp-to-clamp distance (L_0), and the relative distances between three of the strain markers (*a* & *b*).

An external digitizer (Microscribe 3DX © 2002, Immersion Corporation, San Jose CA, accuracy: 0.10 mm) was used to record the 3D positions of the four strain markers. The position of each marker was determined as the average of five measurements of the 3D coordinates. The relative distances between three strain markers (*a* & *b*, Figure 3.10) were computed from the marker coordinates. This process was repeated again for a total of two Trials.

The clamp-cardboard sample-clamp complex was then placed in the stretching device and fixed into the SALS device as if the collagen fiber alignment data were to be collected. The digital camera was placed on a stand at the 51 cm mark on the ruler on the base of the SALS device. (Figure 3.11) This position was chosen as it was able to get the digital camera close

enough to the stretching device to detect the strain markers on the tissue sample but was not in the way of the optics of the SALS device. Using the digital camera, two pictures were then taken of the strain makers on the cardboard sample.

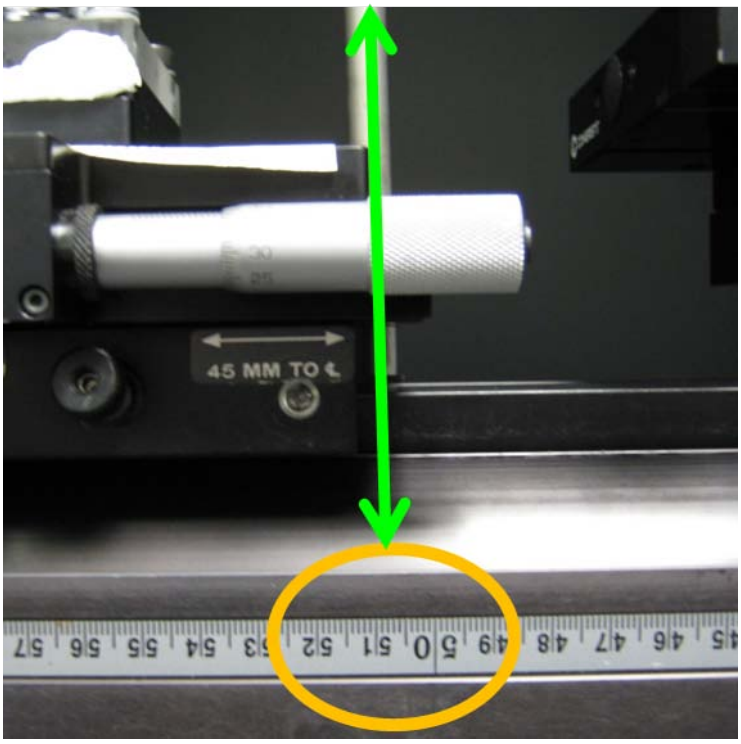

Figure 3.11 The main track of the SALS device on which all of the optics are located, showing the 51 cm mark at which the digital camera was placed to capture the positions of the strain makers.

Imaging processing software (ImageJ) was used to identify the 2D pixel locations of the three strain markers in each image taken with the digital camera. Using the known clamp-to-clamp distance and the number of pixels between the clamps, a ratio can be computed for each image (mm/pix). This ratio was then used to compute the relative distances, *a* and *b*, between the three strain markers. The distances between the strain markers determined using this method were then compared to those determined by the external digitizer and the accuracy of measuring distances with the digital camera was calculated.

The distances *a* and *b* between the three strain markers as measured by each technique were compared. (Table 3.3) The distance *a* was calculated to be 5.79 mm using the digital camera and 5.29 mm using the external digitizer. The distance *b* was calculated to be 8.64 mm and 8.19 mm using the digital camera and external digitizer, respectively. The difference between the digital camera and external digitizer measurements was computed to be 0.5 mm for both distances. Therefore, the accuracy of measuring distances using the digital camera set-up necessary to meet the objective of this section of the work is 0.5 mm.

Table 3.3 Distances a and b measured between three strain markers using the digital camera and external digitizer (Microscribe) to compute the accuracy of measuring distances with the digital camera.

	Digital Camera (Average of 2 Trials)	Microscribe (Average of 2 Trials)	Difference
a (mm)	5.79	5.29	0.5
b (mm)	8.64	8.19	0.5

3.1.2.8 Repeatability of Strain Measurements

Although the accuracy of measuring distances with the digital camera is 0.5 mm, other error may arise in the image processing which could lead to differences in the maximum principal strain computed between four strain makers. Therefore, the repeatability of the image processing procedure was determined.

The largest source of error associated with this process is identifying the pixel locations of the center of each strain marker. Two observers were asked to identify the x- and y-coordinates of pixels for twelve strain markers in an image of a tissue sample taken with the digital camera in the same set-up as described in the previous section. The maximum difference between the x- and y-coordinates of the two observers was six pixels. Therefore, an observer is

able to repeatably identify the pixel locations of the center of strain markers using the digital camera set up within six pixels.

Once the pixel locations are identified they are input into a finite element solver (ABAQUS) in order to determine the maximum principal strain in elements defined by four strain markers. The next step was to determine the effect of a 6 pixel difference in marker position on the maximum principal strain in that element. A four-node element representative in size of one placed on a tissue sample, was created that was 125 x 125 pixels. A random number generator was used to identify a number between 0 and 6 for each of the four strain markers to represent the repeatability of an observer choosing the location of the center of the strain markers. A second random number generator was used to identify the x- or y-axis. The initial 125 x 125 pixel element was used as the reference state for strain calculations. The deformed state was created by adding the randomly generated number between 0 and 6 in the randomly chosen axis to each of respective element. This process was repeated twenty times creating twenty different deformed elements. The maximum principal strain at the centroid of each element was computed.

Table 3.4 Maximum principal strain for each trial.

Trial #	Maximum principal Strain (%)
1	0.0
2	1.9
3	0.4
4	0.0
5	2.5
6	0.6
7	0.0
8	0.8
9	0.0
10	0.4
11	3.8
12	0.6
13	1.4
14	1.9
15	0.0
16	0.4
17	1.6
18	3.3
19	2.2
20	1.1
MEAN	1.1
SD	1.1
MINIMUM	0.0
MAXIMUM	3.8

The highest maximum principal strain created in an element was 3.8%. Therefore, the repeatability of measuring strain in tissue samples in the stretching device, while integrated into the SALS device, using a digital camera is 3.8%. This implies that the set-up used in this section of the work is not able to detect any differences in strain smaller than 3.8%.

3.2 METHODS

3.2.1 Specimen Preparation

Seven fresh-frozen cadaveric shoulders (69 ± 4 yrs, 3 females, 4 males) were stored at -20°C and thawed for 24 hours at room temperature prior to testing. The protocol was approved by the University of Pittsburgh Committee for Oversight of Research Involving the Dead (CORID no. 131). The shoulders were dissected down to the scapula, humerus, and glenohumeral capsule. Each joint was examined using radiographs and dissection, and determined to be free of pathology, osteoarthritis and any visible signs of injury. The capsule regions were identified by first determining the margins of the AB-IGHL and PB-IGHL, whose locations were determined by applying distraction and external or internal rotation, respectively, to the joint. These positions were chosen as they are the positions in which the bands are most visible. [166] A 20 x 10 mm section was excised from the AB-IGHL, axillary pouch, PB-IGHL, posterior capsule, and anterosuperior capsule, embedded in OCT compound, and frozen with liquid nitrogen. [3] Each sample was then sliced into 400 μm thick sections using a cryostat (MICROM, Model #: HM 505 E). This thickness was chosen as described in Section 3.1.2.4, as it was thin enough for accurate data collection in the SALS device [46, 156] while still maintaining as many intact collagen fibers as possible.

3.2.2 Difficulties with Tissue Slicing

Six of the thirty-five tissue samples (one from the axillary pouch, two from the posterior capsule, two from the PB-IGHL, and one from the anterosuperior capsule) were damaged prior to testing

as a result of the difficulties associated with slicing thick samples. As the posterior capsule can be as thin as 1 mm [137], obtaining 400 μm slices of sufficient size was extremely difficult. In addition, one sample from the axillary pouch the tissue pulled out of the OCT during slicing and was not salvageable. In addition, the one sample from the anterosuperior capsule slipped from the soft tissue clamps before failure but was already damaged so the test could not be repeated. Therefore, a total of twenty-nine samples were tested (six from the axillary pouch, five from the posterior capsule, seven from the AB-IGHL, five from the PB-IGHL, and six from the anterosuperior capsule).

3.2.3 Effect of Sample Depth

The effect of sample depth on the collagen fiber alignment of the glenohumeral capsule was evaluated. It was not expected that the collagen fibers would behave differently throughout the sample depth as previous research found no differences in the collagen fiber alignment at three depths within the anteroinferior capsule (articular, middle, bursal). [3] However, this study only examined the unloaded axillary pouch and AB-IGHL and the collagen fibers may behave differently under load. The axillary pouch was chosen to evaluate the collagen fiber alignment under load at different depths within the sample as it is one of the thickest regions of the capsule [137] and would allow the greatest number of slices to be taken from each sample. Due to the 400 μm thickness chosen for this study it would be impossible to obtain multiple samples through the tissue depth from the thinner regions such as the posterior capsule. Slices were taken from the first four samples of the axillary pouch at two or three locations through the tissue depth (depending on the initial thickness of the sample) in order to determine if the collagen fibers behaved differently during loading throughout the thickness of the tissue.

3.2.4 Elongation Protocol

Only one 400 μm slice was taken from the remaining axillary pouch samples (two) and only one slice was taken from all samples from the other four capsule regions. Tissue samples were placed in custom soft tissue clamps and a 3 x 4 grid of graphite strain markers was attached to the surface of each sample using cyanoacrylate for strain tracking.

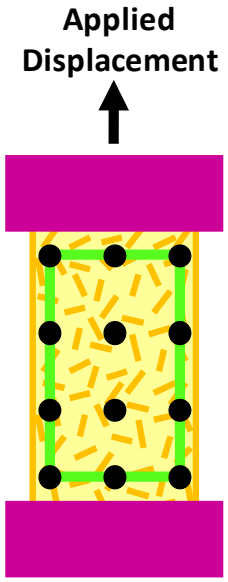

Figure 3.12 Mechanical testing set-up for tensile elongations showing the direction of applied elongation and the 3 x 4 grid of graphite strain markers.

Each sample was then elongated in the longitudinal direction using a materials testing machine (Thumler, Model #TH2730) with load cell (Interface, Scottsdale, AZ, Model #SM-1000N, range: 0 – 1000 N, resolution: 0.015 N) until a 0.1 N preload was achieved. The tissue width (average of three measurements along the length of the tissue sample) and clamp-to-clamp distance were then measured using a ruler. The clamp-tissue sample-clamp complex was mounted in the custom stretching device. [46, 156] As a load cell is not currently incorporated into the SALS device, the preload was re-established in the stretching chamber by restoring the clamp-to-clamp

distance. Tissue samples were kept hydrated using physiologic saline solution throughout the entire testing protocol. Each tissue sample was elongated in increments of 5% of the clamp-to-clamp distance at preload and the collagen fiber alignment data was collected using the SALS device following each increment. This process was repeated until visible tissue failure (hole) occurred. The location of tissue failure was noted.

3.2.5 Data Analysis

The effect of sample depth was assessed on four tissue samples from the axillary pouch in order to determine if the collagen fibers behaved differently during loading throughout the thickness of the tissue. The NOI distributions were visually examined for similar patterns in the way the collagen fiber alignment changed throughout elongation to failure.

3.2.5.1 Tissue Sample Geometry

The width and clamp-to-clamp distance measured when each tissue was preloaded to 0.1N was used to compute the aspect ratio for each tissue sample. The tissue sample geometry was then compared between regions to make sure that no differences in initial sample size existed. The width, clamp-to-clamp distance, and aspect ratio data were normally distributed; therefore, a one-way ANOVA was used to compare between the five capsule regions. Similarly, the clamp-to-clamp distance at failure was also compared between the five capsule regions using a one-way ANOVA.

3.2.5.2 Maximum principal Strain

The graphite strain markers were used to divide the midsubstance of each tissue sample into six elements: two elements across the width and three elements along the length. (Figure 3.13) Each element was approximately 3 x 4 mm.

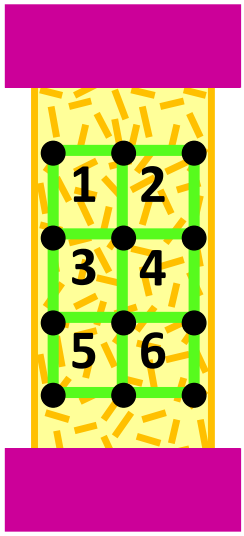

Figure 3.13 The midsubstance of the tissue samples divided into six elements based on the 3 x 4 grid of strain markers.

To determine the amount of strain in each tissue sample, the 2D coordinates of the markers at each 5% increment of elongation were determined as pixel coordinates using the image processing software (ImageJ). The top left corner of the top plate on the stretching device was used as the origin of the x-y coordinate system and pixel coordinates of each strain marker were identified with respect to this point.

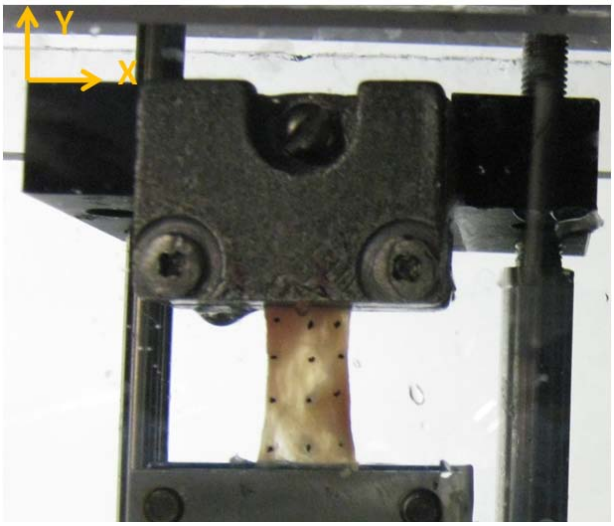

Figure 3.14 Origin of coordinate system used to determine the pixel coordinates of the strain markers at each increment of elongation.

The coordinates of the markers at each 5% increment of elongation were input into a finite element software (ABAQUS, Simulia, Providence, RI) and compared to their initial coordinates in the reference (preloaded) state. The maximum principal strain was determined at the centroid of each element for all tissue samples.

3.2.5.3 Collagen Fiber Alignment

The peak and minimum NOI were determined in each element at the 5% increment of elongation just prior to the increment resulting in failure (plastic region of the load-elongation curve) and at the preloaded state (the beginning of the toe-region of the load-elongation curve). All parameters were non-normally distributed so nonparametric statistical analyses were preformed. At the 5% increment just prior to failure, the peak NOI and maximum principal strain in the element of failure were compared between capsule regions using a Kruskal-Wallis Test with Mann-Whitney post-hoc tests. At the preloaded state, the peak and minimum NOI were

compared between regions of the inferior glenohumeral ligament complex using a Kruskal-Wallis Test with Mann-Whitney post-hoc tests. Significance was set at $\alpha = 0.05$ for all analyses.

3.2.5.4 Predicting the Location of Tissue Failure

The peak NOI at the 5% increment just prior to failure was correlated to the element of tissue failure. All of the elements from all tissue samples were considered and a contingency table was generated. A Fisher's exact test was then used to compare the location of peak NOI at the 5% increment just prior to failure to the location of visible tissue failure. [127] Significance was set at $\alpha = 0.05$. The results of this analysis would demonstrate the ability of the collagen fiber alignment just prior to failure to predict the location of tissue failure. However, by this point on the load-elongation curve, the tissue has already been permanently deformed. [127, 167] Predicting potential locations of tissue failure while the capsule is functioning under normal ranges of motion (in the toe-region of the load-elongation curve) would be much more useful clinically as potential injury locations could be identified before tissue damage has even occurred. Therefore, a second analysis was performed in order to determine if the collagen fiber alignment from the toe-region of the load-elongation curve could predict the location of tissue failure. This analysis was only performed on the inferior glenohumeral ligament complex (AB-IGHL, axillary pouch, and PB-IGHL).

The peak and minimum NOI at the preloaded state were correlated to the element of tissue failure. All of the elements from all tissue samples from the inferior glenohumeral ligament complex were considered and a contingency table was generated. A Fisher's exact test was then used to compare the location of peak NOI in the preloaded state to the location of visible tissue failure. [127] Significance was set at $\alpha = 0.05$. When high fiber alignment in the

preloaded state was correlated with tissue failure, the local preferred fiber direction was computed in the same location as the peak NOI occurred in order to see if the fibers were aligned in the direction of applied elongation. In instances where there were multiple locations of the peak NOI within the failure element, the preferred fiber direction was computed for all locations. The local preferred fiber direction ranges from -90° to 90°, where 0° is along the axis of loading. (Figure 3.15)

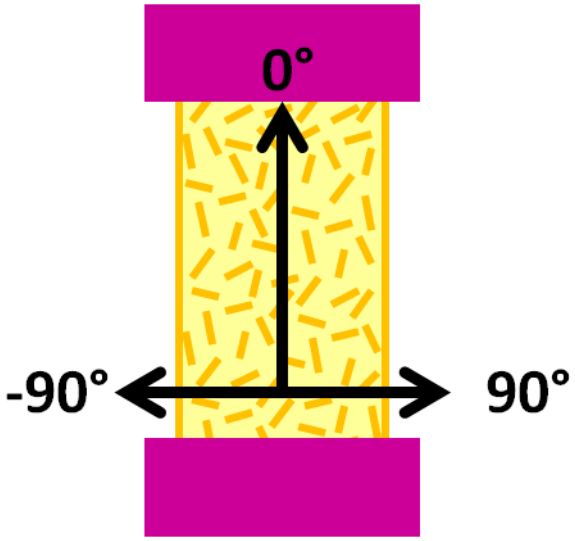

Figure 3.15 The preferred fiber direction coordinate system where 0° is parallel to the direction of applied loading.

The local preferred fiber direction at every location of the peak NOI was then placed in one of three groups: 1) parallel to the direction of applied elongation (0° to ±30°), 2) neither parallel nor perpendicular to the direction of applied loading (±30° to ±60°), or 3) perpendicular to the direction of applied elongation (±60° to ±90°).

3.3 RESULTS

3.3.1 Effect of Sample Depth

The collagen fiber alignment throughout elongation to failure was examined throughout the depth of four samples from the axillary pouch. For two of the samples, two slices were obtained throughout the tissue depth (from the bursal and articular locations of the sample). The other two samples were thick enough to allow for three slices to be taken and these slices were from the bursal, middle, and articular areas of the axillary pouch samples. The NOI distributions for all four tissue samples from the axillary pouch at each sample depth are shown below.

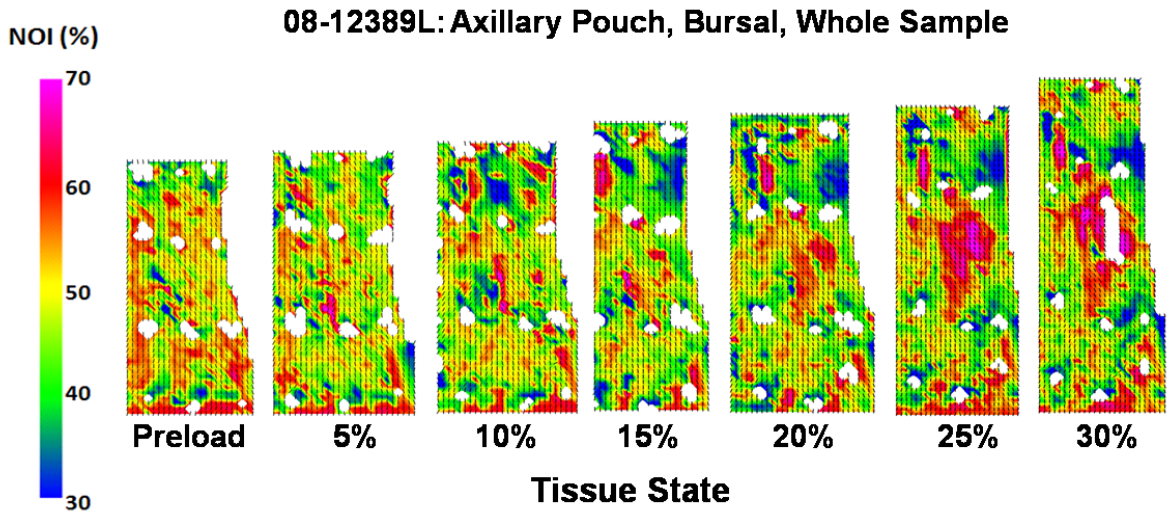

Figure 3.16 NOI distribution at each increment of elongation for Specimen 08-12389L: bursal Axillary Pouch.

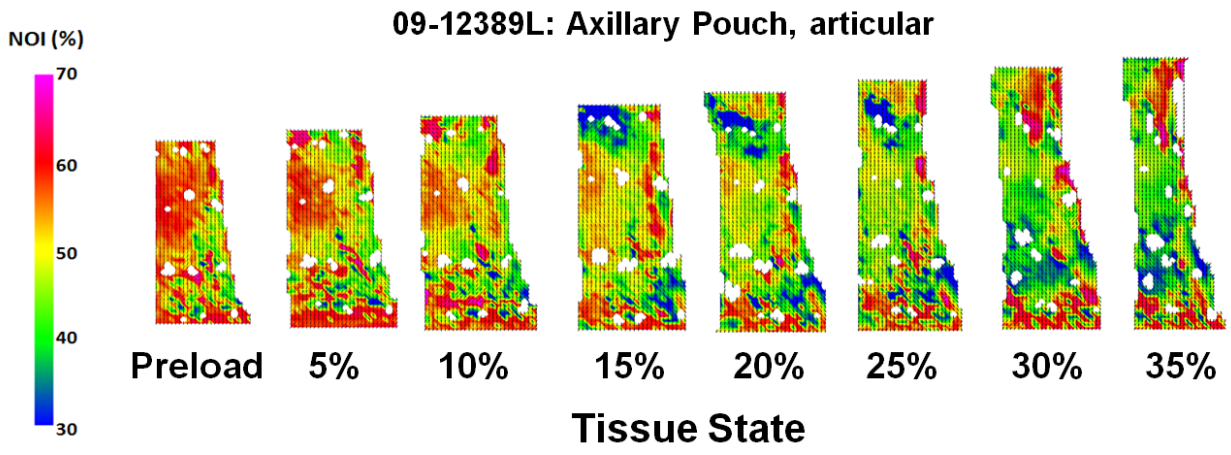

Figure 3.17 NOI distribution at each increment of elongation for Specimen 08-12389L: articular Axillary Pouch.

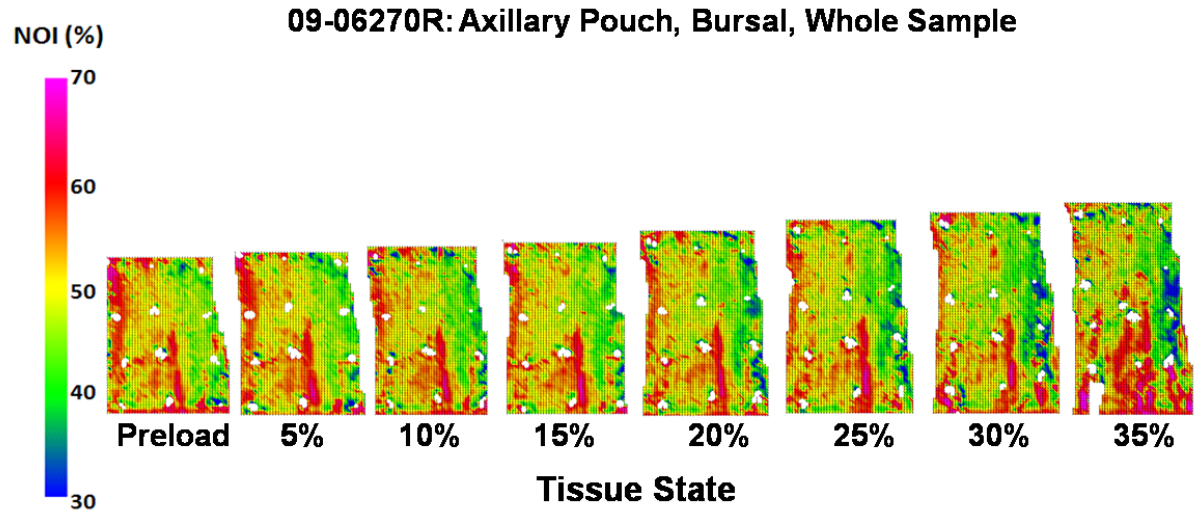

Figure 3.18 NOI distribution at each increment of elongation for Specimen 09-06270R: bursal Axillary Pouch.

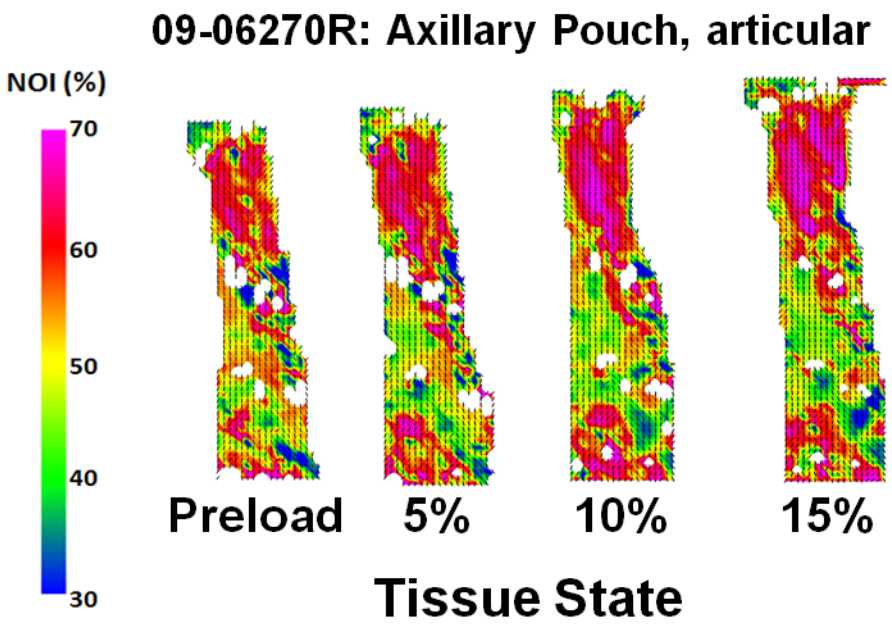

Figure 3.19 NOI distribution at each increment of elongation for Specimen 09-06270R: articular Axillary Pouch.

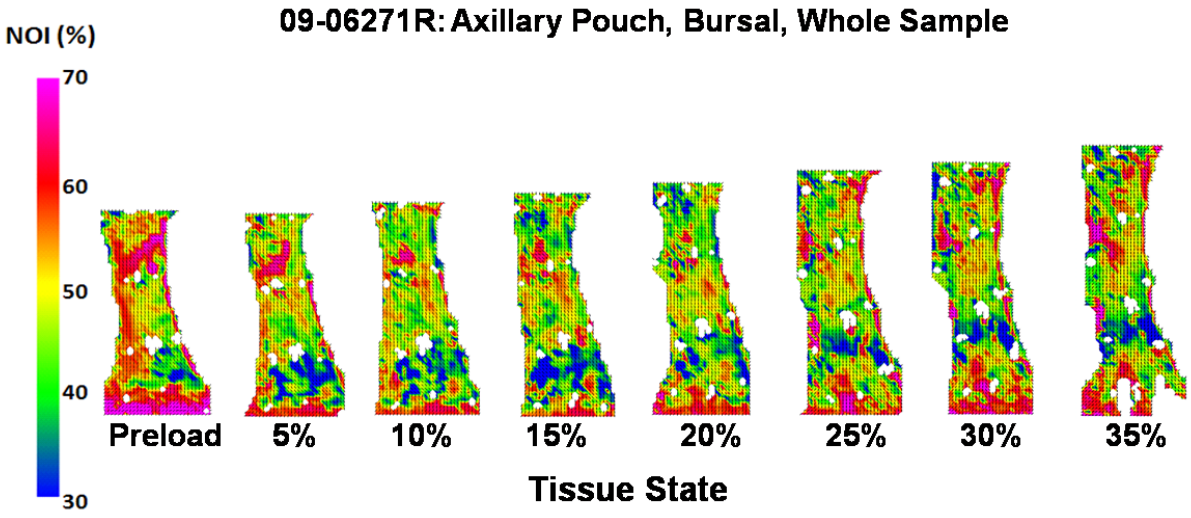

Figure 3.20 NOI distribution at each increment of elongation for Specimen 09-06271R: bursal Axillary Pouch.

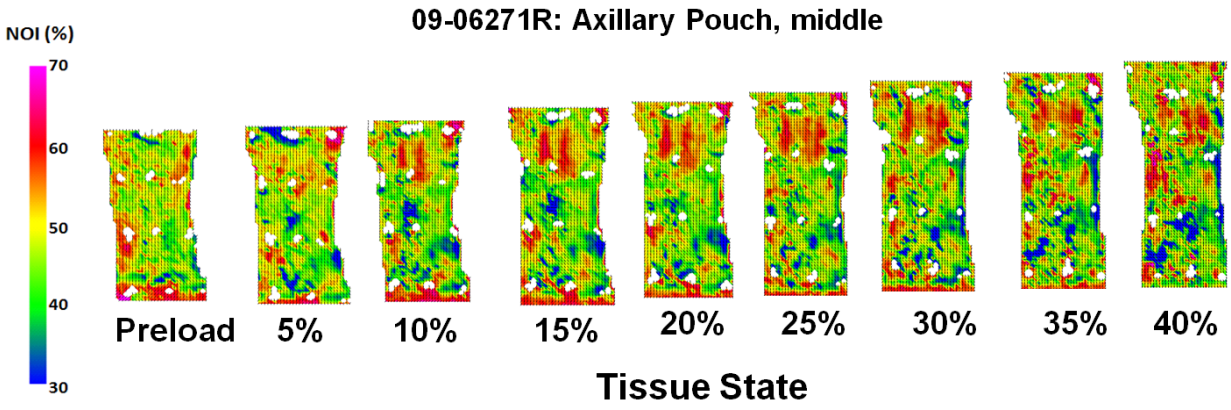

Figure 3.21 NOI distribution at each increment of elongation for Specimen 09-06271R: middle Axillary Pouch.

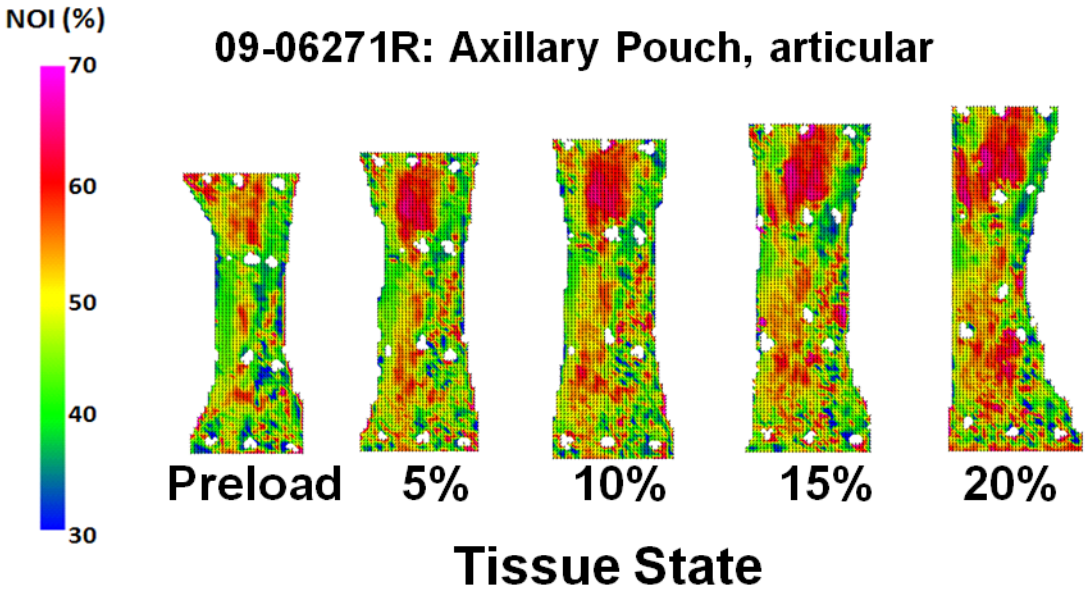

Figure 3.22 NOI distribution at each increment of elongation for Specimen 09-06271R: articular Axillary Pouch.

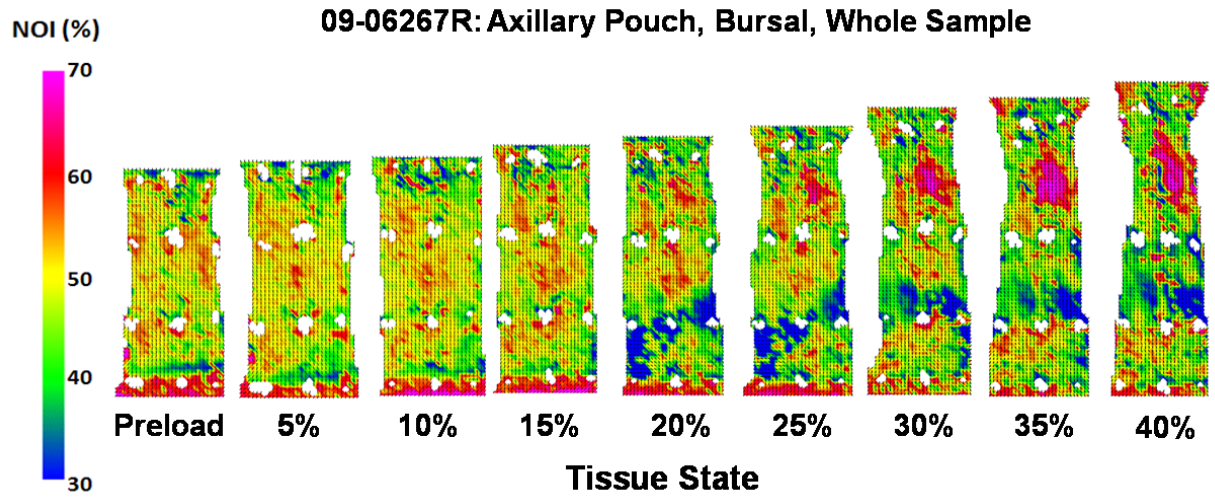

Figure 3.23 NOI distribution at each increment of elongation for Specimen 09-06267R: bursal Axillary Pouch.

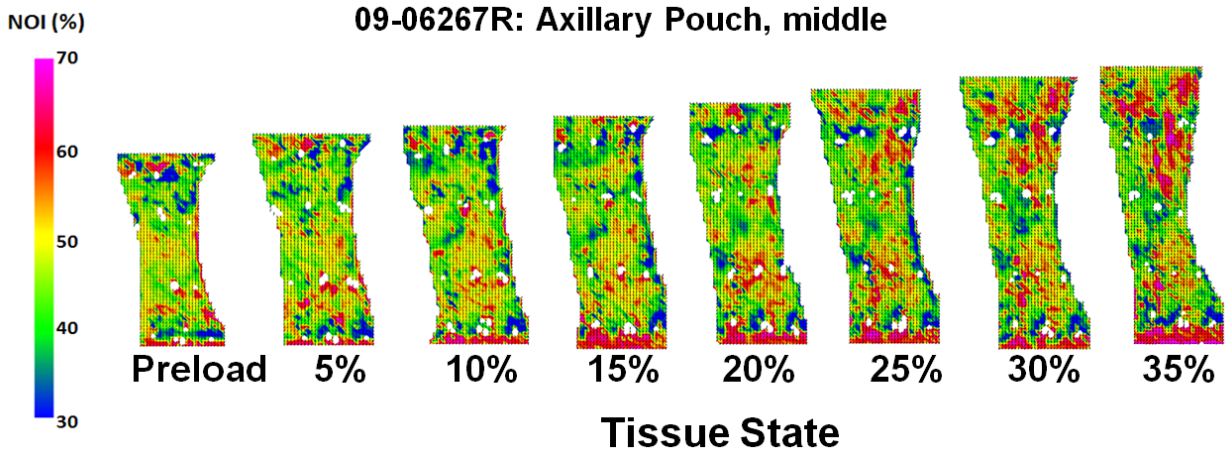

Figure 3.24 NOI distribution at each increment of elongation for Specimen 09-06267R: middle Axillary Pouch.

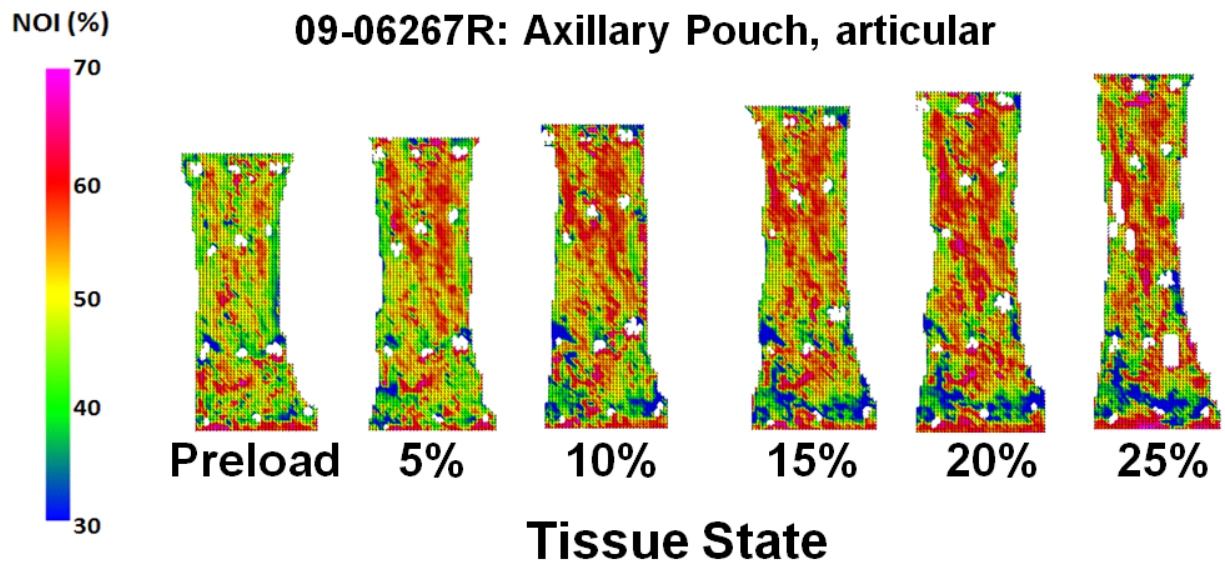

Figure 3.25 NOI distribution at each increment of elongation for Specimen 09-06267R: articular Axillary Pouch.

The location of tissue failure varied between samples of the axillary pouch and between tissue depths. However, changes in the collagen fiber alignment with elongation were the same regardless of tissue depth. As the tissue samples were elongated, some localized regions became more aligned (increased NOI) while others became less aligned (decreased NOI). For all tissue samples the locations of the tissue exhibiting areas of increasing fiber alignment eventually led to tissue failure. The location of greatest fiber alignment in the 5% increment of elongation just prior to failure corresponded to the location of tissue failure for all tissue samples regardless of tissue depth. Therefore, obtaining slices throughout the depth of the other capsule regions was not necessary to meet the objective of this section of the work as the same conclusions could be drawn regardless of tissue depth.

3.3.2 Tissue Sample Geometry

The clamp-to-clamp distance at the preloaded state was 15.4 ± 1.2 mm, 15.3 ± 2.1 mm, 16.9 ± 1.6 mm, 17.6 ± 3.8 mm, and 17.2 ± 1.9 mm for the axillary pouch, posterior capsule, AB-IGHL, PB-IGHL, and anterosuperior capsule, respectively. (Table 3.5) The width of the tissue samples was 6.9 ± 2.1 mm, 6.8 ± 2.5 mm, 8.1 ± 1.0 mm, 7.2 ± 1.5 mm, and 7.2 ± 0.7 mm yielding aspect ratios of 2.4 ± 0.6, 2.4 ± 0.7, 2.1 ± 0.2, 2.5 ± 0.7, and 2.4 ± 0.4 for the axillary pouch, posterior capsule, AB-IGHL, PB-IGHL, and anterosuperior capsule, respectively. No differences were found in the tissue sample geometry at the preloaded state between any of the capsule regions with p-values of 0.27, 0.66, and 0.73 when comparing the clamp-to-clamp distances, widths, and aspect ratios, respectively. The clamp-to-clamp distance at failure was also similar between all capsule regions ($p = 0.23$) with values of 21.0 ± 2.8 mm, 19.8 ± 1.9 mm, 21.0 ± 2.7 mm, 24.1 ± 4.5 mm, and 22.5 ± 3.0 mm for the axillary pouch, posterior capsule, AB-IGHL, PB-IGHL, and anterosuperior capsule, respectively. Failure occurred at 37 ± 10%, 27 ± 9%, 24 ± 8%, 40 ± 27%, and 31 ± 13% elongation, respectively. (Table 3.6)

Table 3.5 Tissue sample geometry for all samples tested.

Region	Specimen #	Clamp-to-Clamp @ Preload	Width	Aspect Ratio	Clamp-to-Clamp @ Failure
Axillary Pouch	08-12389L	13.51	5.65	2.4	17.55
	09-06270R	15.81	9.49	1.7	21.34
	09-06271R	14.38	4.91	2.9	19.41
	09-06267R	15.82	7.19	2.2	22.15
	07-10874L	16.56	9.23	1.8	25.67
	08-12366R	X	X	X	X
	09-06278R	16.1	5.0	3.2	20.1
Posterior Capsule	08-12389L	13.56	4.14	3.3	20.34
	09-06270R	14.71	4.67	3.1	19.86
	09-06271R	18.91	10.22	1.9	21.75
	09-06267R	13.89	7.92	1.8	16.67
	07-10874L	X	X	X	X
	08-12366R	15.25	7.16	2.1	20.59
	09-06278R	X	X	X	X
AB-IGHL	08-12389L	15.68	7.48	2.1	18.81
	09-06270R	17.24	7.78	2.2	19.83
	09-06271R	16.93	7.16	2.4	20.32
	09-06267R	19.99	9.55	2.1	25.99
	07-10874L	16.51	6.88	2.4	23.11
	08-12366R	16.54	9.27	1.8	20.68
	09-06278R	15.11	8.46	1.8	18.13
PB-IGHL	08-12389L	22.82	9.00	2.5	26.24
	09-06270R	20.24	5.55	3.6	27.32
	09-06271R	13.86	6.48	2.1	17.32
	09-06267R	X	X	X	X
	07-10874L	16.15	8.56	1.9	21.80
	08-12366R	15.10	6.46	2.3	27.95
	09-06278R	X	X	X	X
Anterosuperior Capsule	08-12389L	19.40	6.42	3.02	24.25
	09-06270R	14.73	7.78	1.89	17.64
	09-06271R	19.4	8.18	2.37	23.28
	09-06267R	17.2	6.47	2.66	23.22
	07-10874L	15.83	7.13	2.22	20.58
	08-12366R	X	X	X	X
	09-06278R	16.93	7.40	2.29	26.24

Table 3.6 The percent elongation at failure for all tissue samples tested.

SPECIMEN #	Axillary Pouch	Posterior Capsule	AB-IGHL	PB-IGHL	Anterosuperior Capsule
08-12389L	30%	30%	20%	15%	25%
09-06270R	35%	35%	15%	35%	20%
09-06271R	35%	15%	20%	25%	20%
09-06267R	40%	20%	30%	X	35%
07-10874L	55%	X	40%	40%	30%
08-12366R	X	35%	25%	85%	X
09-06278R	25%	X	20%	X	55%

The location of tissue failure varied from sample to sample and occurred in all elements. For the AB-IGHL, all failures occurred in either the superior or inferior elements. Whereas failures in the axillary pouch occurred twice in the midsubstance elements and four times in either the superior or inferior the elements and failures in the PB-IGHL occurred once in the midsubstance elements and five times in the other elements.

3.3.3 Maximum principal Strain

Maximum principal strain was computed in each element for all tissue samples. If the tissue sample failed near the bottom clamp, below element 5 or 6 two additional elements were included (7 and 8). Similarly, if the tissue sample failed near the top clamp, above element 1 or 2, elements 9 and 10 were included. (Figure 3.26) The center point on the top and bottom clamps and the points where the tissue sample inserted into the clamp were used as the boundaries for the additional elements.

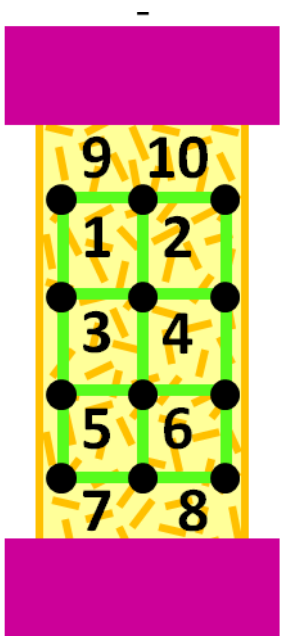

Figure 3.26 Four additional elements included when the tissue sample failed above or below the six initially defined elements.

The digital camera images used to determine the maximum principal strain in each element at each 5% increment of elongation until failure are shown below for one tissue sample from each region. Images for the remaining samples can be found in Appendix A. Visual analysis of these camera images suggests that failure tends to occur in the elements undergoing the most strain.

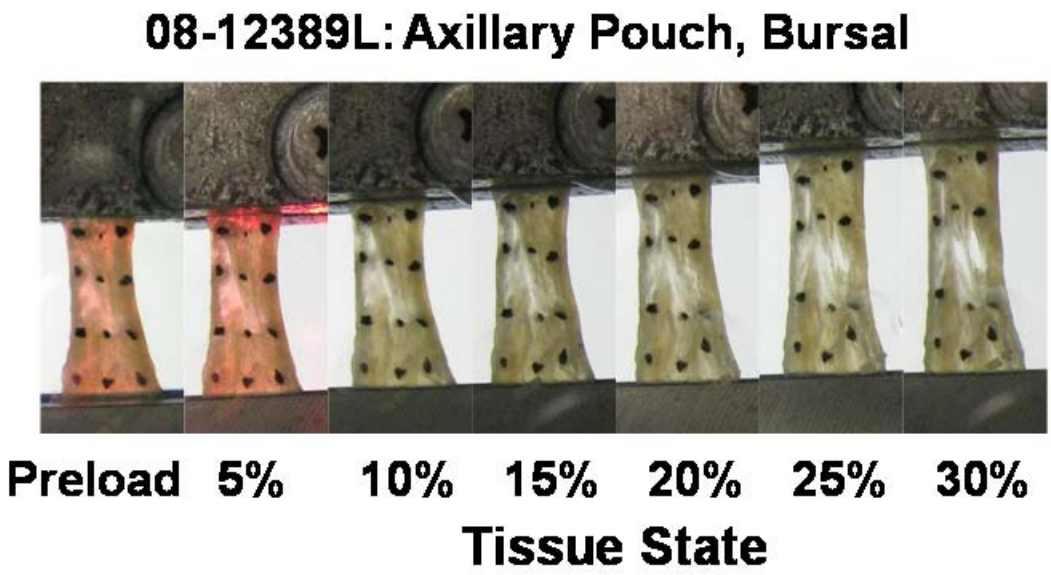

Figure 3.27 Digital camera images for each increment of elongation from which the strain marker coordinates were determined for Specimen 08-12389L: axillary pouch.

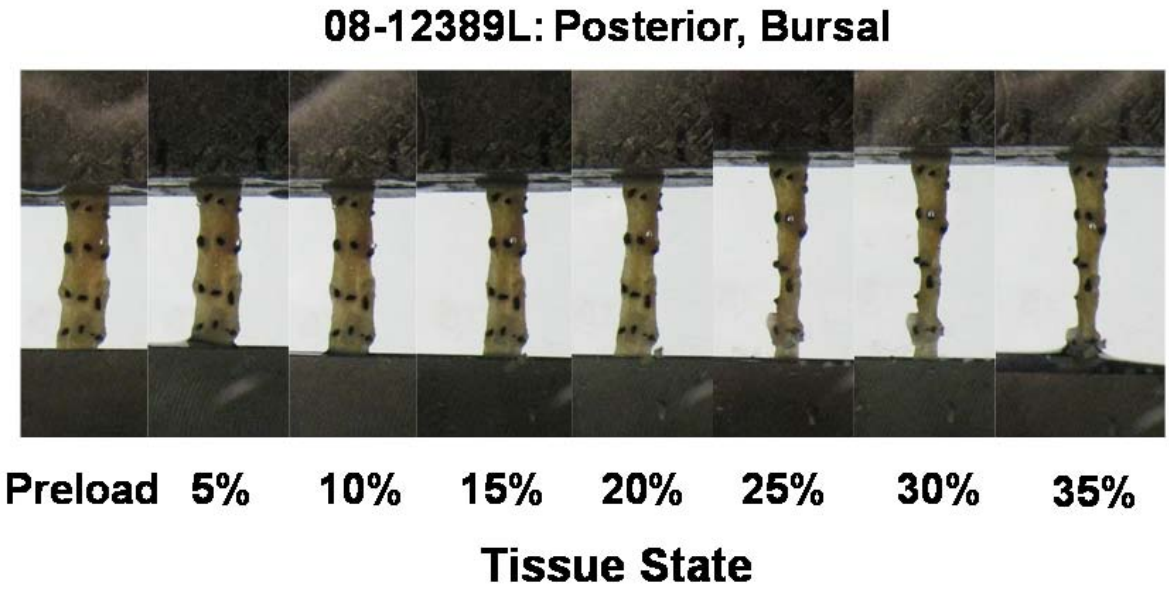

Figure 3.28 Digital camera images for each increment of elongation from which the strain marker coordinates were determined for Specimen 08-12389L: posterior capsule.

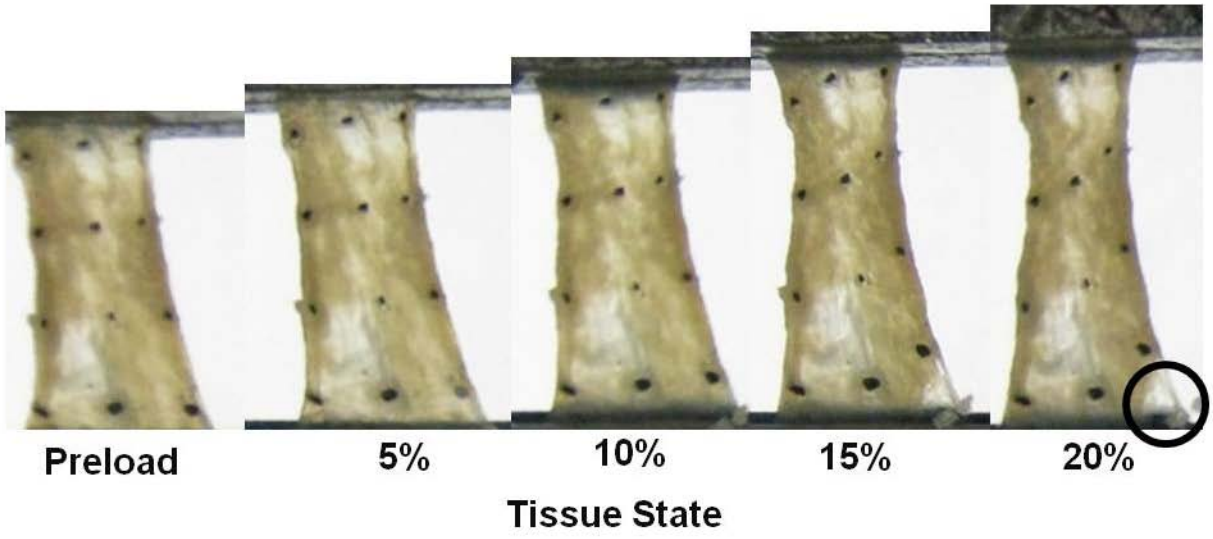

Figure 3.29 Digital camera images for each increment of elongation from which the strain marker coordinates were determined for Specimen 08-12389L: AB-IGHL.

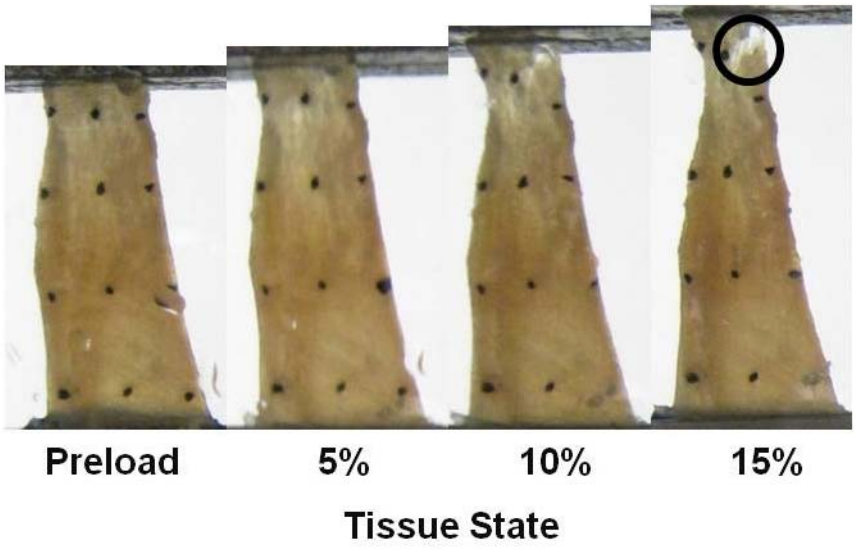

Figure 3.30 Digital camera images for each increment of elongation from which the strain marker coordinates were determined for Specimen 08-12389L: PB-IGHL.

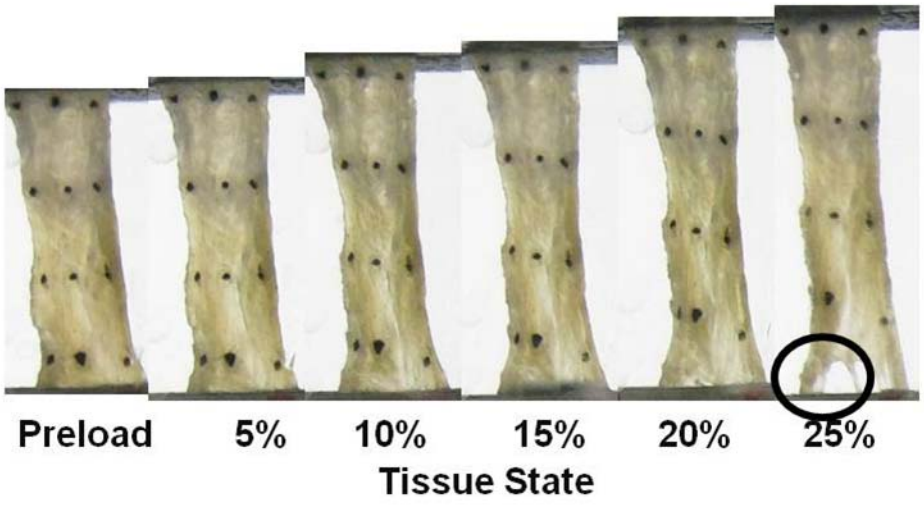

Figure 3.31 Digital camera images for each increment of elongation from which the strain marker coordinates were determined for Specimen 08-12389L: Anterosuperior Capsule.

The quantitative data showing the maximum principal strain in each element at the 5% increment just prior to failure is presented in the tables below for each capsule region. As expected, maximum principal strains were higher in the elements closer to the clamps compared to the elements in the tissue midsubstance.

Table 3.7 Maximum principal strain in each element (1 – 8) for all tissue samples from the axillary pouch. The element of failure for each sample is highlighted in grey.

SPECIMEN #	1	2	3	4	5	6	7	8	9	10
08-12389L	39.2	15.5	33.9	48.2	17.0	8.3	-	-	-	-
09-06270R	27.6	21.1	15.3	21.6	14.3	21.6	128.0	103.4	-	-
09-06271R	75.7	25.8	82.4	26.1	42.6	59.5	159.8	139.5	-	-
09-06267R	54.3	71.1	10.7	20.0	17.0	18.7	-	-	-	-
07-10874L	71.6	9.3	104.3	107.2	24.5	45.8	-	-	-	-
08-12366R	-	-	-	-	-	-	-	-	-	-
09-06278R	11.7	8.8	12.8	0.0	92.0	80.1	-	-	104.9	82.7

Table 3.8 Maximum principal strain in each element (1 – 10) for all tissue samples from the posterior capsule. The element of failure for each sample is highlighted in grey.

SPECIMEN #	1	2	3	4	5	6	7	8	9	10
08-12389L	9.3	27.0	0.0	24.4	48.9	41.1	-	-	-	-
09-06270R	54.0	59.7	7.5	15.6	21.8	11.1	-	-	238.6	228.0
09-06271R	63.3	70.0	40.0	53.3	38.9	53.3	-	-	-	-
09-06267R	7.3	0.7	7.3	22.4	17.3	18.5	28.5	12.9	-	-
07-10874L	-	-	-	-	-	-	-	-	-	-
08-12366R	57.1	66.7	47.2	52.3	30.0	15.4	-	-	-	-
09-06278R	-	-	-	-	-	-	-	-	-	-

Table 3.9 Maximum principal strain in each element (1 – 10) for all tissue samples from the AB-IGHL. The element of failure for each sample is highlighted in grey.

SPECIMEN #	1	2	3	4	5	6	7	8	9	10
08-12389L	21.6	17.2	14.9	24.8	11.4	24.5	19.5	70.5	-	-
09-06270R	2.8	5.6	0.0	18.9	14.7	25.1	30.3	22.7	-	-
09-06271R	4.7	19.1	11.2	17.7	5.8	17.5	-	-	75.2	65.1
09-06267R	48.0	21.1	38.6	14.8	35.8	26.3	-	-	-	-
07-10874L	11.2	0.0	31.0	63.8	68.9	12.1	112.5	70.4	-	-
08-12366R	15.4	24.7	12.0	14.8	23.5	15.2	-	-	-	-
09-06278R	10.8	6.8	5.0	5.3	8.4	4.9	-	-	27.3	36.2

Table 3.10 Maximum principal strain in each element (1 – 10) for all tissue samples from the PB-IGHL. The element of failure for each sample is highlighted in grey.

SPECIMEN #	1	2	3	4	5	6	7	8	9	10
08-12389L	33.8	21.8	0.0	2.4	0.2	1.1	-	-	17.5	49.3
09-06270R	15.0	85.9	44.4	79.0	19.8	3.8	-	-	-	-
09-06271R	1.1	14.0	0.0	27.9	4.4	36.5	98.8	75.5	-	-
09-06267R	-	-	-	-	-	-	-	-	-	-
07-10874L	0.0	3.3	53.4	3.6	78.0	11.4	115.9	131.1	-	-
08-12366R	8.8	35.6	45.4	103.0	103.8	67.4	-	-	-	-
09-06278R	-	-	-	-	-	-	-	-	-	-

Table 3.11 Maximum principal strain in each element (1 – 8) for all tissue samples from the anterosuperior capsule. The element of failure for each sample is highlighted in grey.

SPECIMEN #	1	2	3	4	5	6	7	8
08-12389L	7.5	13.2	8.4	14.0	8.3	13.6	139.3	113.3
09-06270R	15.5	21.1	13.7	25.7	13.0	29.2	51.4	80.7
09-06271R	16.4	9.1	15.8	7.6	13.0	0.0	165.9	158.1
09-06267R	0.9	55.4	50.3	57.6	7.9	13.7	-	-
07-10874L	10.6	5.1	10.4	8.7	53.1	42.9	-	-
08-12366R	-	-	-	-	-	-	-	-
09-06278R	0.2	0.5	0.2	0.7	2.6	2.9	27.3	23.3

For all tissue samples tested the element containing the highest maximum principal strain compared to all other elements corresponded with the element of tissue failure. The maximum principal strain in the element of failure was 101.3 ± 39.9%, 85.5 ± 81.0%, 56.6 ± 31.5%, 93.8 ± 29.8%, and 87.3 ± 54.0% in the axillary pouch, posterior capsule, AB-IGHL, PB-IGHL, and anterosuperior capsule, respectively. No significant differences were found between the maximum principal strain in the element of failure between the capsule regions ($p = 0.26$).

3.3.4 Collagen Fiber Alignment

The NOI distribution under the 0.1 N preload was highly variable from sample to sample and this variation did not depend on cadaveric donor or region of the glenohumeral capsule. In general, most tissue samples were moderately aligned (green) when preloaded, with localized areas of decreased (blue) or increased (pink) alignment. Throughout elongation, all regions of the glenohumeral capsule behaved similarly. As the tissue samples were elongated, some localized regions became more aligned (increased NOI) while others became less aligned (decreased NOI). The regions experiencing the highest strains exhibited areas of increasing fiber alignment and finally tissue failure. The NOI distributions for one tissue sample from each capsule region are presented below. The remaining NOI distributions can be found in Appendix B.

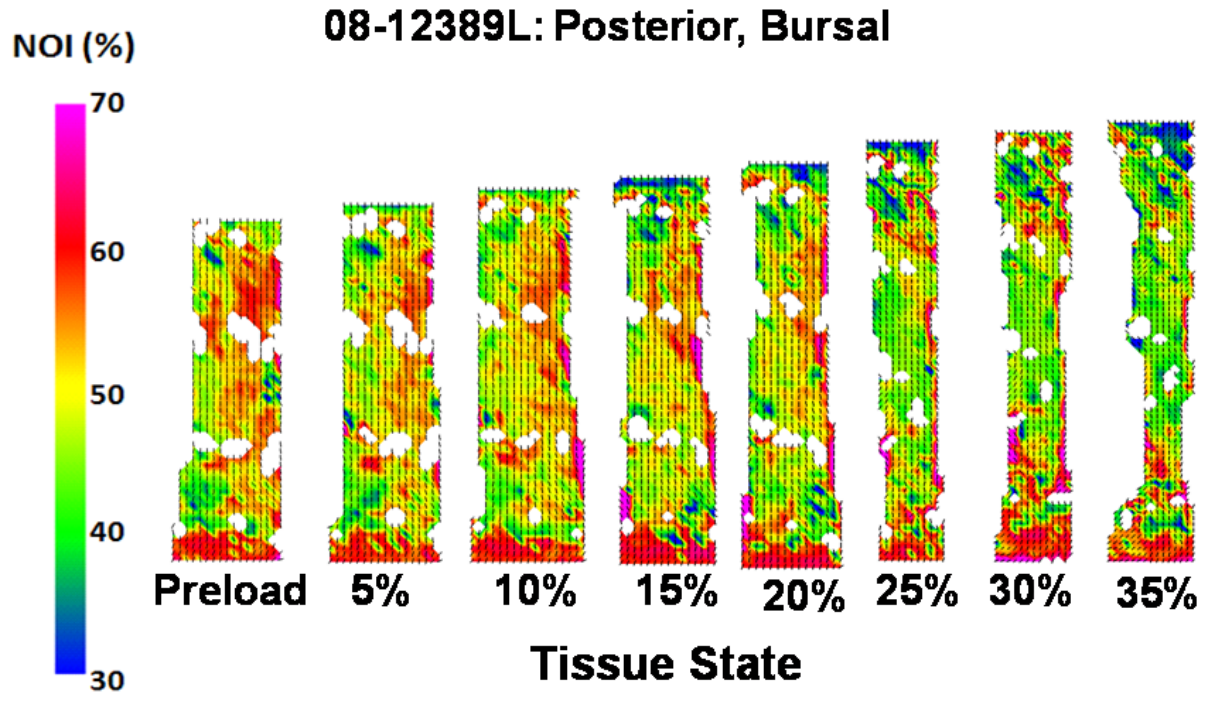

Figure 3.32 NOI distribution at each increment of elongation for Specimen 08-12389L: Posterior Capsule.

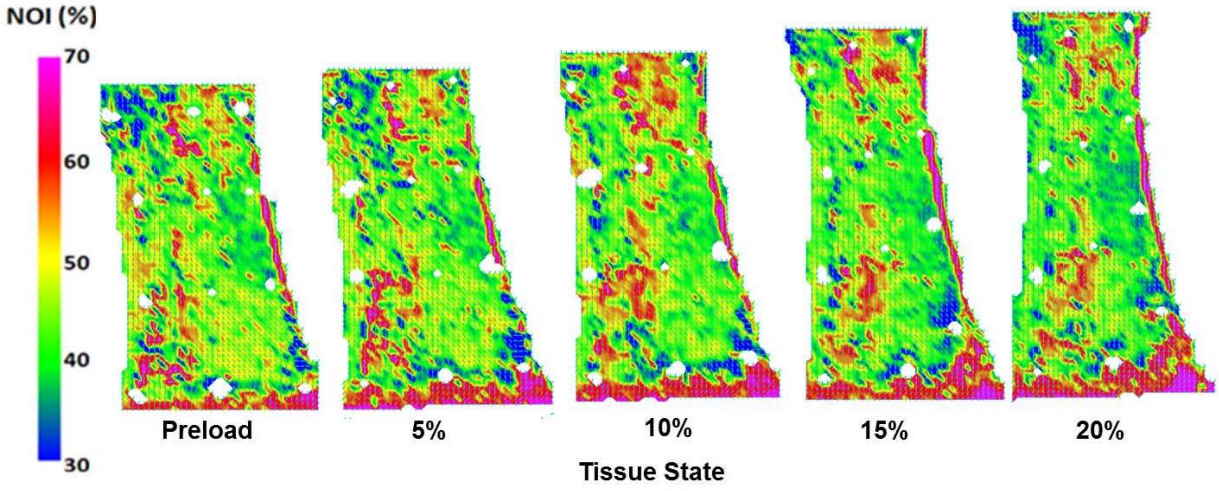

Figure 3.33 NOI distribution at each increment of elongation for Specimen 08-12389L: AB-IGHL.

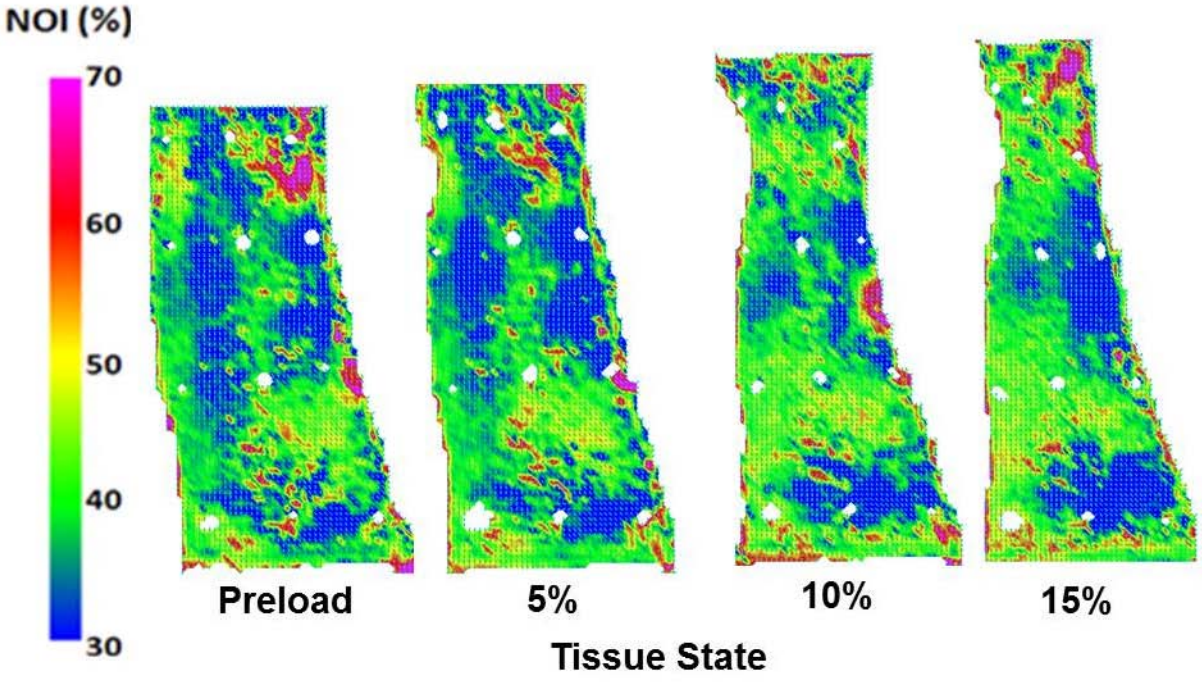

Figure 3.34 NOI distribution at each increment of elongation for Specimen 08-12389L: PB-IGHL.

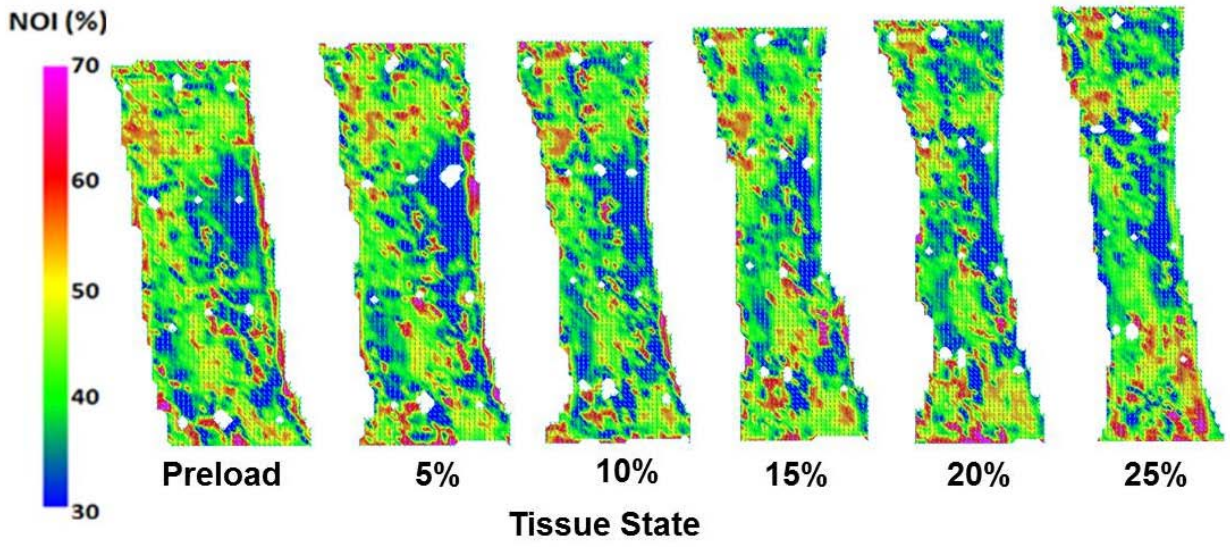

Figure 3.35 NOI distribution at each increment of elongation for Specimen 08-12389L: Anterosuperior Capsule.

The quantitative data showing the peak NOI in each element at the 5% increment just prior to failure is presented in the tables below for each capsule region. Peak NOI values were similar between all regions.

Table 3.12 Peak NOI in each element (1-8) at the 5% increment just prior to failure for all tissue samples from the axillary pouch. The element of failure for each sample is in grey.

SPECIMEN #	1	2	3	4	5	6	7	8	9	10
08-12389L	73	69	72	79	66	68	-	-	-	-
09-06270R	67	67	72	64	71	72	77	76	-	-
09-06271R	76	73	76	76	79	80	82	81	-	-
09-06267R	76	80	68	69	67	66	-	-	-	-
07-10874L	74	67	74	84	69	69	-	-	-	-
08-12366R	-	-	-	-	-	-	-	-	-	-
09-06278R	77	78	76	78	78	69	-	-	78	77

Table 3.13 Peak NOI in each element (1-8) at the 5% increment just prior to failure for all tissue samples from the posterior capsule. The element of failure for each sample is in grey.

SPECIMEN #	1	2	3	4	5	6	7	8	10
08-12389L	69	79	54	73	82	78	-	-	-
09-06270R	79	79	70	70	78	69	-	-	80
09-06271R	74	77	67	72	73	68	-	-	-
09-06267R	69	64	57	66	64	69	72	66	-
07-10874L	-	-	-	-	-	-	-	-	-
08-12366R	72	74	78	78	66	67	-	-	-
09-06278R	-	-	-	-	-	-	-	-	-

Table 3.14 Peak NOI in each element (1-10) at the 5% increment just prior to failure for all tissue samples from the AB-IGHL. The element of failure for each sample is in grey.

SPECIMEN #	1	2	3	4	5	6	7	8	9	10
08-12389L	82	82	71	77	74	70	74	84	-	-
09-06270R	72	71	66	67	70	71	74	77	-	-
09-06271R	64	67	57	72	73	77	-	-	79	78
09-06267R	81	77	64	77	66	72	-	-	-	-
07-10874L	66	63	71	71	66	73	83	73	-	-
08-12366R	70	68	74	59	76	69	-	-	-	-
09-06278R	72	70	72	72	71	72	-	-	68	76

Table 3.15 Peak NOI in each element (1-10) at the 5% increment just prior to failure for all tissue samples from the PB-IGHL. The element of failure for each sample is in grey.

SPECIMEN #	1	2	3	4	5	6	7	8	9	10
08-12389L	64	63	60	68	71	66	-	-	70	88
09-06270R	68	74	71	66	71	70	-	-	-	-
09-06271R	64	59	64	72	67	67	73	63	-	-
09-06267R	-	-	-	-	-	-	-	-	-	-
07-10874L	67	68	63	63	63	63	64	79	-	-
08-12366R	69	69	69	78	86	74	-	-	-	-
09-06278R	-	-	-	-	-	-	-	-	-	-

Table 3.16 Peak NOI in each element (1-8) at the 5% increment just prior to failure for all tissue samples from the anterosuperior capsule. The element of failure for each sample is in grey.

SPECIMEN #	1	2	3	4	5	6	7	8
08-12389L	68	0	72	70	61	76	77	71
09-06270R	64	68	68	71	69	72	67	73
09-06271R	77	76	44	52	66	77	69	83
09-06267R	72	78	78	78	71	69	-	-
07-10874L	72	70	73	70	78	76	-	-
08-12366R	-	-	-	-	-	-	-	-
09-06278R	67	66	64	64	70	73	78	80

For all tissue samples tested the element containing the highest peak NOI compared to all other elements corresponded with the element of tissue failure. The peak NOI in the element of failure was 80 ± 3%, 78 ± 4%, 79 ± 3%, 80 ± 7%, and 78 ± 3% in the axillary pouch, posterior capsule, AB-IGHL, PB-IGHL, and anterosuperior capsule, respectively. No significant differences were found between the maximum principal strain in the element of failure between the capsule regions ($p = 0.88$).

3.3.5 Predicting the Location of Tissue Failure

The maximum principal strain and NOI values at the 5% increment of elongation just prior to tissue failure and the peak and minimum NOI values at the preloaded state were evaluated in each element and correlated to the element of tissue failure. These parameters were able to predict the location of tissue failure from the plastic region of the load-elongation curve as well as the toe-region of the load-elongation curve.

3.3.5.1 Plastic Region of Load-Elongation Curve

For all tissue samples tested from all five capsule regions, the element containing the location of tissue failure also contained the highest peak NOI (highest degree of alignment) and high maximum principal strain in the 5% increment of elongation just prior to failure. Further, the maximum principal strain and peak NOI at the 5% increment of elongation just prior to failure were found to be statistically significant predictors of the location of tissue failure ($p < 0.001$).

3.3.5.2 Toe-Region of Load-Elongation Curve

No significant differences were found in the peak NOI values at the preloaded state between capsule regions. However, the minimum NOI were significantly lower in the AB-IGHL compared to the axillary pouch ($p = 0.01$). No differences were found between the axillary pouch and AB-IGHL or between the AB-IGHL and PB-IGHL. For all tissue samples in the AB-IGHL, axillary pouch and PB-IGHL, the element of failure could be predicted by examining the peak and minimum NOI in each element at the preloaded state. Two different NOI configurations in the preloaded state led to tissue failure.

Configuration 1: if the lowest peak NOI and lowest minimum NOI (lowest degree of alignment) compared to all other elements, occurred within the same element, then failure occurred in that element. (Table 3.17)

Table 3.17 A representative tissue sample from the AB-IGHL in which failure occurred in Element 1 via *Configuration 1*.

ELEMENT	1	2	3	4	5	6
PEAK NOI (%)	72	79	76	83	77	77
MIN NOI (%)	3	12	19	6	12	28

Configuration 2: if the lowest peak NOI and lowest minimum NOI did not occur within the same element, then the sample failed in the element that contained the highest peak NOI (greatest degree of alignment) at the preloaded state. (Table 3.18)

Table 3.18 A representative tissue sample from the axillary pouch in which failure occurred in Element 4 via *Configuration 2*.

ELEMENT	1	2	3	4	5	6
PEAK NOI (%)	62	69	70	80	64	67
MIN NOI (%)	28	29	2	31	24	23

When samples failed via configuration 2, the local preferred fiber direction was computed in the same point on the tissue sample as the peak NOI occurred.

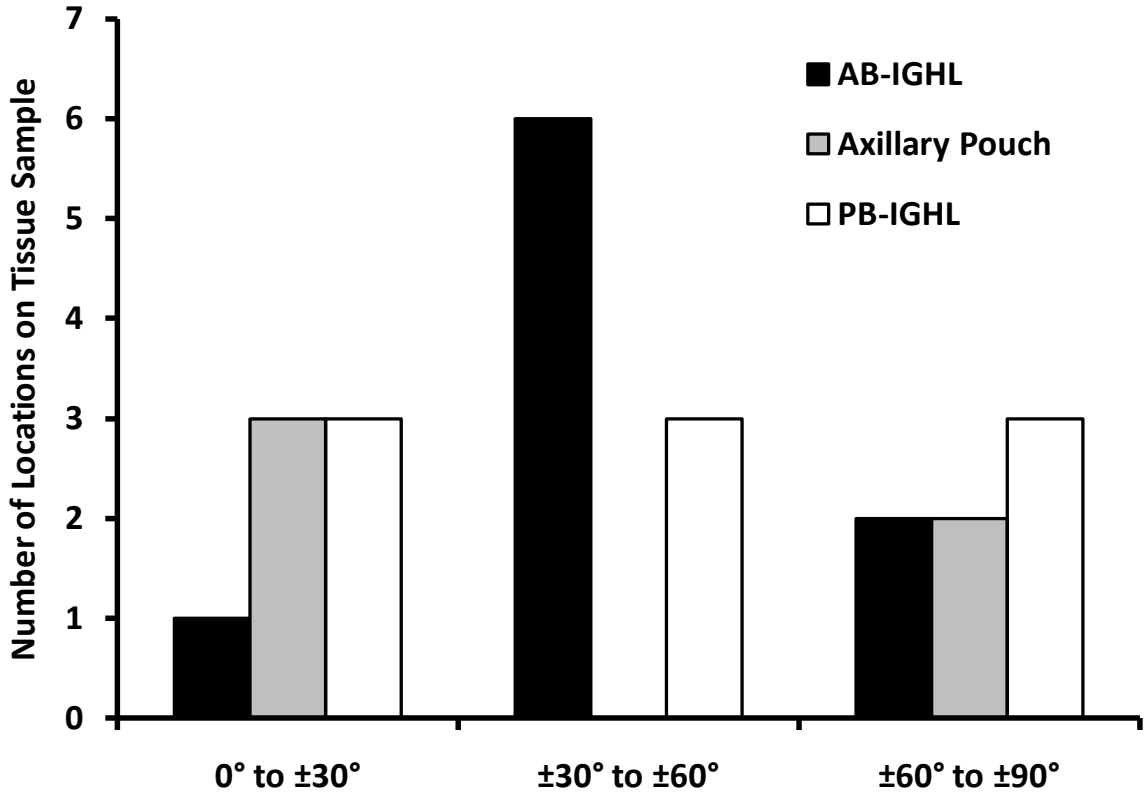

Figure 3.36 The number of times the local preferred fiber direction was parallel (0° to 30°), neither parallel nor perpendicular (30° to 60°), or perpendicular (60° to 90°) to the direction of applied elongation at the location of peak NOI values for all tissue samples from the inferior glenohumeral ligament complex (AB-IGHL, axillary pouch, and PB-IGHL)

For both configurations, the element containing the highest or lowest peak NOI was significantly associated with the element containing the location of visible failure ($p < 0.05$) for all regions of the inferior glenohumeral ligament.

AB-IGHL

Failure of the AB-IGHL was split evenly between the two configurations. (Table 3.19)

Table 3.19 The failure configuration, peak and minimum NOI, and local preferred fiber direction at the location of the peak NOI values for the AB-IGHL. The "-" denotes tissue samples which failed according to *Configuration 1* and thus the preferred fiber direction was not determined.

SPECIMEN #	CONFIGURATION	PEAK NOI (%)	MIN NOI (%)	Fiber Direction (°)
08-12389L	2	83	21	-59, -60, -62
09-06270R	2	70	23	-15, -59, -53
09-06271R	1	67	4	-
09-06267R	1	72	3	-
07-10874L	2	71	17	-40, -55
08-12366R	1	74	6	-
09-06278R	2	79	9	-70

For the samples that failed according to C*onfiguration 1*, the average peak and minimum NOI was 71 ± 4% and 4 ± 2%, respectively. The samples that failed via *Configuration 2*, had a peak and minimum NOI of 75 ± 7% and 20 ± 3%, respectively. When the sample failed due to a high degree of fiber alignment (*Configuration 2*), the peak NOI was 5% higher and the minimum NOI was 370% higher compared to when the sample failed due to an extremely low degree of fiber alignment (C*onfiguration 1*). The local preferred fiber direction at the location of the peak NOI that correlated with failure in *configuration 2* was in group 1 (parallel) in one instance and in group 3 (perpendicular) in one instance. The remaining fiber directions associated with tissue failure (six) fell into group 2 (neither parallel nor perpendicular).

Table 3.20 The range (minimum – peak) of NOI values in each element (1-10) for each tissue sample from the AB-IGHL. The element of failure is in grey.

SPECIMEN #	1	2	3	4	5	6	7	8	9	10
08-12389L	2-81	2-78	12-79	27-64	9-79	3-74	18-80	21-83	-	-
09-06270R	16-67	28-70	17-64	36-67	32-69	28-67	23-70	24-77	-	-
09-06271R	4-68	22-77	31-68	12-73	24-74	33-81	-	-	4-67	22-72
09-06267R	3-72	12-79	19-76	6-83	12-77	28-77	-	-	-	-
07-10874L	21-69	13-67	22-64	6-69	10-64	10-64	17-71	21-68	-	-
08-12366R	18-77	22-77	13-82	29-80	6-74	13-80	-	-	-	-
09-06278R	3-76	9-67	2-69	24-68	2-74	18-67	-	-	9-73	9-79

Axillary Pouch

Only one sample from the axillary pouch failed due to low fiber alignment (*Configuration 1*) and the peak and minimum NOI values were 60% and 38%, respectively. (Table 3.21)

Table 3.21 The failure configuration, peak and minimum NOI, and local preferred fiber direction at the location of the peak NOI values for the axillary pouch. The "-" denotes tissue samples which failed according to *Configuration 1* and thus the preferred fiber direction was not determined.

SPECIMEN #	CONFIGURATION	PEAK NOI (%)	MIN NOI (%)	Fiber Direction (°)
1	2	80	31	-6
2	2	71	36	-14
3	2	90	43	-75
4	2	80	22	9
5	1	60	38	-
6	2	80	18	61

For the samples that failed in the region of highest fiber alignment at the preloaded state (*Configuration 2*) the peak and minimum NOI was 80 ± 7% and 30 ± 10%, respectively. Samples that failed via C*onfiguration 2* had a peak NOI that was 34% higher and a minimum

NOI that was 21% lower than the sample that failed via *Configuration 1*. The preferred fiber direction associated with tissue failure was in group 1 (parallel) for three tissue samples from the axillary pouch and in group 3 (perpendicular) to the direction of applied elongation for two tissue samples.

Table 3.22 The range (minimum – peak) of NOI values in each element (1-10) for each tissue sample from the axillary pouch. The element of failure is in grey.

SPECIMEN #	1	2	3	4	5	6	7	8	9	10
08-12389L	28-62	29-69	2-70	31-80	24-64	23-67	-	-	-	-
09-06270R	27-71	29-57	31-66	26-66	27-66	23-68	36-71	26-69	-	-
09-06271R	22-69	37-82	32-66	24-77	17-67	17-84	43-90	40-88	-	-
09-06267R	23-68	22-80	23-67	31-67	31-67	24-66	-	-	-	-
07-10874L	40-63	38-66	47-60	38-60	38-62	38-76	-	-	-	-
08-12366R	-	-	-	-	-	-	-	-	-	-
09-06278R	8-78	3-78	17-76	14-76	9-68	17-76	-	-	14-74	18-80

PB-IGHL

The PB-IGHL only failed according to *Configuration 2*. (Table 3.23)

Table 3.23 The failure configuration, peak and minimum NOI, and local preferred fiber direction at the location of the peak NOI values for the PB-IGHL.

SPECIMEN #	CONFIGURATION	PEAK NOI (%)	MIN NOI (%)	Fiber Direction (°)
1	2	79	17	-88
2	2	73	16	23
3	2	74	23	-34
4	2	84	20	-70
5	2	78	12	-11, -33, -9, -46

The peak and minimum NOI values were 79 ± 5% and 19 ± 5%, respectively. The preferred fiber direction at the location of the peak NOI was well distributed and failed three times in each group (1) parallel, 2) neither parallel nor perpendicular, and 3) perpendicular).

The minimum and peak NOI in each element for all tissue samples from the PB-IGHL are shown in Table 3.24.

Table 3.24 The range (minimum – peak) of NOI values in each element (1-10) for each tissue sample from the PB-IGHL. The element of failure is in grey.

SPECIMEN #	1	2	3	4	5	6	7	8	9	10
08-12389L	9-66	18-77	18-71	11-68	11-71	10-74	-	-	18-62	17-79
09-06270R	1-66	16-73	26-64	20-67	20-72	23-67	-	-	-	-
09-06271R	22-64	14-64	19-59	10-61	23-66	6-66	23-74	10-62	-	-
09-06267R	-	-	-	-	-	-	-	-	-	-
07-10874L	6-76	14-62	11-78	14-68	4-78	28-67	20-72	20-84	-	-
08-12366R	19-62	16-68	18-59	12-78	23-71	17-77	-	-	-	-
09-06278R	-	-	-	-	-	-	-	-	-	-

3.4 SIGNIFICANCE OF RESULTS

3.4.1 Predicting from Plastic Region

The first part of this section of the work utilized the SALS technique to quantify the collagen fiber alignment and maximum principal strain in the glenohumeral capsule during uniaxial extension to failure. Despite regional differences in the collagen fiber alignment of the glenohumeral capsule [3-5, 12] in the unloaded state, all elements containing the location of failure in all regions also included the highest peak NOI and maximum principal strain just prior to tissue failure.

3.4.1.1 Discussion of Results

The direct correlation between the maximum principal strain and collagen fiber alignment just prior to failure can be used to predict the location of failure for the entire glenohumeral capsule. Further no differences were found in the maximum principal strain or collagen fiber alignment just prior to failure between the five capsule regions. This result supports the concept that the glenohumeral capsule functions as a continuous sheet of tissue rather than discrete uniaxial ligaments. [9] The initial random distribution of fibers in the glenohumeral capsule functions to resist loads in multiple directions. After loading of the tissue into the plastic region of the load-elongation curve, the initial reference state may then contain more aligned collagen fibers. In such a state, the glenohumeral capsule suffers from a loss of its multidirectional stabilizing function. As a result, following injury, the glenohumeral capsule could lack the ability to properly stabilize the glenohumeral joint.

3.4.1.2 Comparison to Literature

Quinn et al. examined the collagen fiber alignment in the cervical capsular ligament during loading to failure using quantitative polarized light imaging. [127] Failure was predicted by a high rate of fiber rotation which was used to indicate tissue damage. The damaged cervical capsular ligament exhibited less aligned fibers than the normal ligament and the location of maximum principal or shear strain did not predict tissue damage. Differences in the results shown here are likely due to the different deformations applied to the tissue samples in each study. Further, the collagen fiber alignment and maximum principal strain in the cervical capsular ligament were recorded continuously as opposed to discrete increments of elongation as was done in this study.

3.4.2 Predicting from Toe-Region

This second part of this section of the work utilized the SALS technique to quantify the collagen fiber alignment in the inferior glenohumeral ligament complex during the toe-region of the load-elongation curve. In all three regions (AB-IGHL, axillary pouch, and PB-IGHL), the collagen fiber alignment in the initial preloaded state was able to predict the location of tissue failure.

3.4.2.1 Discussion of Results

There were two different patterns of collagen fiber alignment in the preloaded state that led to tissue failure. In *Configuration 1*, failure occurred in the elements initially containing the lowest degree of fiber alignment. The collagen fibers were less organized in the preloaded state with a minimal amount of fibers aligned in the direction of elongation. One mechanism for this configuration leading to failure could be that not enough fibers could align during elongation,

leaving the weaker ground substance to support the load and making this area of the tissue prone to failure.

In contrast, if a location of relatively low fiber alignment did not exist, the tissue sample failed according to *Configuration 2*, i.e. in the element containing highest fiber alignment in the preloaded state. Failure via this mechanism occurred in 78% of all tissue samples tested. Further, although failure occurred in the locations of highest fiber alignment, this alignment was not always parallel to the direction of applied elongation; it also occurred when the highest fiber alignment was perpendicular or at an intermediate angle. When the collagen fibers in the preloaded state were aligned with the direction of applied loading they could not rotate substantially to support the increase in load during excessive elongation. Most of the load was carried by the majority of these fibers and the higher fiber strains in this area of the tissue eventually led to tissue failure. When the collagen fibers are aligned perpendicular or at an intermediate angle, the results are similar to when they are randomly oriented; in this case there are not enough fibers aligned with the axis of elongation to support the load created.

These results suggest that areas of extreme high or low collagen fiber alignment are at risk for injury under high strains. In addition, the location of tissue failure may be independent of loading direction as failure occurred in locations of high fiber alignment even when the fibers were not aligned in the direction of applied elongation. This further supports the notion that the random orientation of collagen fibers in the glenohumeral capsule contributes to its multi-axial loading capabilities. The direction of loading applied to the capsule may not affect the location at which failure occurs. Therefore, the degree of collagen fiber alignment in the glenohumeral capsule under small loads may be used to identify regions of the capsule that could potentially be damaged or torn under extreme multi-axial loading conditions.

No significant differences were found in the peak and minimum NOI values between regions of the inferior glenohumeral ligament complex except for the minimum NOI values between the AB-IGHL and axillary pouch. In addition, the average peak NOI was also higher in the axillary pouch compared to the AB-IGHL, although this difference was not statistically significant. This difference could be due to the collagen fibers in the unloaded axillary pouch being somewhat less organized than in the unloaded AB-IGHL. [3] The randomly oriented fibers in the axillary pouch may be able to rotate to the direction of elongation more easily than those in the AB-IGHL resulting in more organized fibers in the preloaded tissue.

3.4.2.2 Comparison to Literature

Failure of ligamentous tissue has been predicted from collagen fiber alignment at the middle and end of the load-elongation curve. [127, 139] Quinn and coworkers examined the collagen fiber alignment in the cervical capsular ligament during loading to failure using quantitative polarized light imaging. [127] Failure was predicted by a high rate of fiber rotation which was used to indicate tissue damage. This damage occurred in the middle of the load elongation curve. In addition, the collagen fiber alignment and maximum principal strain just before failure was able to predict the location of tissue damage in the glenohumeral capsule. [139] Examining the collagen fiber alignment of the inferior glenohumeral ligament complex in the toe-region of the load-elongation curve allows potential failure sites to be identified prior to tissue damage. Locating regions of the capsule at risk for injury and determining joint positions which would apply excessive strains to these regions would enable rehabilitation techniques to be developed to strengthen the muscles that stabilize the joint at these positions. This may help limit injury to the glenohumeral capsule.

3.4.3 Limitations

Due to the inability of the SALS device to quantify the collagen fiber orientation of the entire tissue sample, instantaneously, maximum principal strain and collagen fiber alignment data were obtained at discrete increments of elongation. Further the device is not capable of capturing simultaneous load-elongation data, thus uniaxial stress-strain data could not be examined.

This second part of this section of the work described possible collagen fiber alignment configurations in the anteroinferior capsule that led to tissue failure but other configurations may exist in this region, or other regions of the glenohumeral capsule. Due to capsule thickness, tissue slicing was required for proper use of the SALS device. However, most collagen fibers remained intact and changes in alignment with elongation were detected. In vivo, the capsule functions as a continuous sheet of tissue rather than discrete uniaxial ligaments and therefore experiences more complex loading conditions than applied to the tissue samples in this study. In the future, bi-axial elongation of the capsule should be examined to enhance understanding of collagen fiber kinematics in the glenohumeral capsule. However, the low aspect ratio utilized in this work allowed better simulation of the sheet-like properties of the capsule as the collagen fiber alignment in a larger amount of the tissue could be examined. Due to the low aspect ratio, a majority of the tissue samples failed in elements closer to the clamps as opposed to in the tissue midsubstance but changes in the collagen fiber alignment with elongation still occurred and the initial collagen fiber alignment was correlated with the location of tissue failure.

3.4.4 Implications

The results of this section have implications for the way engineers and clinicians understand structural changes in the glenohumeral capsule following joint dislocation, as well as potential rehabilitation and repair techniques. This work suggests that areas of extreme high or low collagen fiber alignment are at risk for injury under high strains. Further, the location of tissue failure may be independent of loading direction as failure occurred in locations of high fiber alignment even when the fibers were not aligned in the direction of applied elongation. The random orientation of collagen fibers in the glenohumeral capsule contributes to its multi-axial loading capabilities and failure occurs in locations which are not capable of supporting large multi-axial loads. Therefore, the degree of collagen fiber alignment in the glenohumeral capsule under small loads may be used to identify regions of the capsule that could potentially be damaged or torn under extreme multi-axial loading conditions. If a device was developed to allow surgeons to examine the collagen fiber alignment of the capsule *in vivo*, they may be able to identify regions of the capsule that have high or low collagen fiber alignment. Although development of this technology is probably a long ways away this work provides a deeper understanding of the link between structure and function of the glenohumeral capsule. Locating regions of the capsule at risk for injury and determining joint positions which would apply excessive strains to these regions would enable rehabilitation techniques to be developed to strengthen the muscles that stabilize the joint at these positions. This may help limit injury to the glenohumeral capsule.

4.0 TISSUE LEVEL: MATERIAL PROPERTIES OF CAPSULE

4.1 INTRODUCTION

The glenohumeral joint suffers more dislocations than any other major diarthrodial joint, most of which occur in the anterior direction. [65, 67] The glenohumeral capsule, a complex sheet of ligamentous tissue, functions to stabilize the glenohumeral joint in end ranges of motion. [166, 168] During dislocation, a common injury to the capsule is permanent tissue deformation. This tissue deformation has been quantified by measuring the amount of nonrecoverable strain in the capsule. [68, 81, 169] Injury, or nonrecoverable strain, results in permanently elongated tissue as well as increased joint rotations and translations which contribute to recurrent instability. [71-73, 77, 79, 80, 170] Despite the countless studies examining injuries resulting from dislocation, research on the properties of the injured glenohumeral capsule is not nearly as prevalent. It is likely that this lack of knowledge regarding injury to the capsule during dislocation contributes to recurrent dislocations in up to 18% of patients following surgical repair for traumatic anterior instability. [114, 116, 171]

Of all the capsule regions, the anteroinferior capsule (anterior band of the inferior glenohumeral ligament (AB-IHGL) and axillary pouch) is the primary restraint to anterior dislocation and experiences the highest strains during these events. [24, 27, 69, 172] As a result, this region is commonly injured during joint dislocation. The collagen fibers of the

anteroinferior capsule do not exhibit a global preferred orientation despite localized areas of alignment, thus the capsule can withstand loading in any direction. [4, 5, 123] Therefore, an isotropic hyperelastic constitutive model has been used to characterize the material properties of the normal glenohumeral capsule. [42] As the collagen fibers of other biologic soft tissues have been shown to become more aligned under loading [125-127] an isotropic constitutive model may not appropriately describe the potentially anisotropic behavior of the injured glenohumeral capsule.

The previously used isotropic hyperelastic constitutive model utilizes a phenomenological strain energy function which does not distinguish between matrix and collagen fiber responses, thus the material coefficients of the model do not have direct physical meaning. Therefore, changes in the material properties of the glenohumeral capsule following injury may not correspond to detectable differences in the material coefficients of this phenomenological isotropic constitutive model. A method for simulating injury (creating nonrecoverable strain) in the glenohumeral capsule should be developed and used to determine if the previously utilized isotropic constitutive model is capable of detecting changes in the material behavior of the capsule via changes in the material parameters following simulated injury. Therefore, the objective of this study was to determine the effect of the simulated injury on the stiffness and material properties of the AB-IGHL during tensile deformation. A combined experimental-computational protocol has been developed and used to characterize the material properties of the glenohumeral capsule. [42, 124]

4.1.1 Preliminary Studies

The following preliminary studies were performed in order to establish a mechanical testing protocol to simulate injury in tissue samples from the AB-IGHL. The protocol was then be used to examine the effect of simulated injury on the stiffness and material properties of the AB-IGHL during uniaxial extension utilizing previously developed methodologies.

4.1.1.1 Non-destructive Elongation

Previously, non-destructive mechanical tests have been performed to determine the material properties of 25 mm x 25 mm samples from the axillary pouch and posterior capsule. [42, 173] Extensive preliminary studies were performed in order to determine an appropriate elongation to consistently capture the toe- and linear-region of the load-elongation curve without causing permanent damage to the tissue, as indicated by repeatable load-elongation curves. It is important to capture a sufficient portion of the linear-region as this curve will serve as input into the finite element optimization routine used to determine the material properties of each tissue sample. The same process was performed in order to determine an appropriate elongation for tissue samples from the AB-IGHL. The same protocol that was applied to the axillary pouch was used as a starting point. A 10 mm x 15 mm sample from the AB-IGHL was excised from a cadaveric shoulder, mounted in custom soft tissue clamps and placed in a materials testing machine (Thumler, Model #TH2730) with load cell (Interface, Scottsdale, AZ, Model #SM-1000N, range: 0 – 1000 N, resolution: 0.015 N). A 0.5 N preload was applied followed by 10 cycles of preconditioning from 0 to 1.5 mm at a rate of 10 mm/min. The tissue sample was then elongated to 2.25 mm. Following this protocol the load-elongation curve was examined and

found to include only the beginning of the linear-region. (Figure 4.1) Therefore, in order to capture more of the linear region a greater elongation was needed for the AB-IGHL samples.

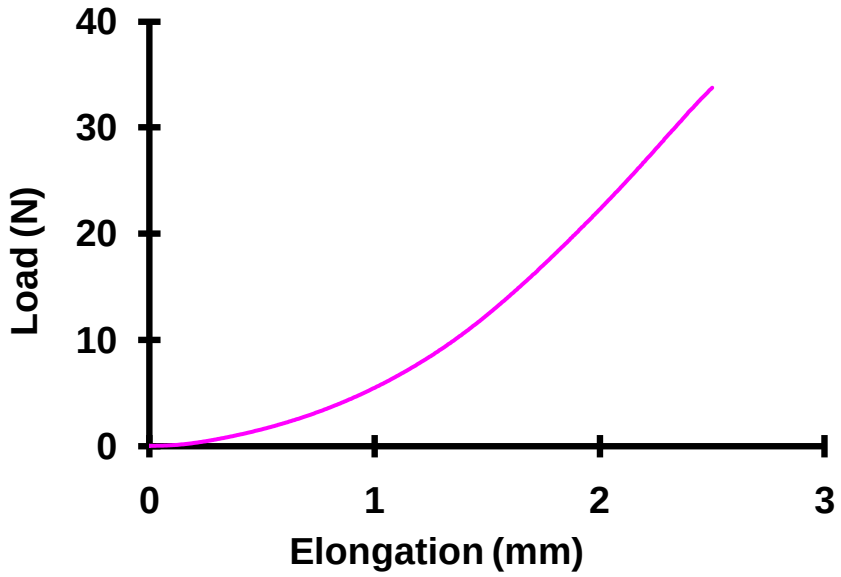

Figure 4.1 Load-elongation curve for a non-destructive elongation of the AB-IGHL to 2.25 mm.

The preload and preconditioning regime was repeated and the non-destructive elongation was increased to 2.75 mm. This elongation was able to capture more of the linear region of the load-elongation curve.

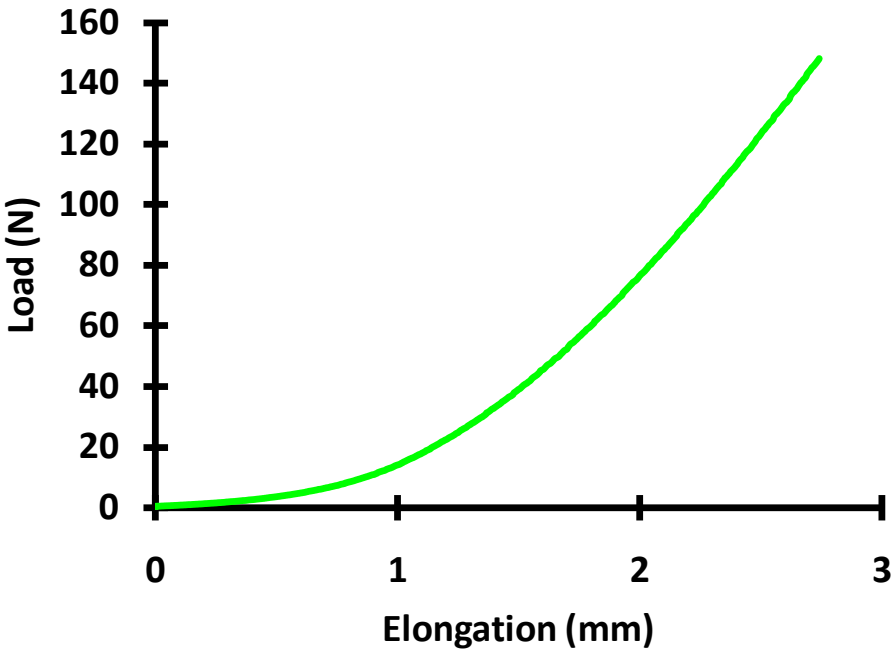

Figure 4.2 Load-elongation curve for a non-destructive elongation of the AB-IGHL to 2.75 mm including more of the linear-region.

Finally, it had to be shown that elongating tissue samples from the AB-IGHL to 2.75 mm would not result in tissue damage. As described previously for the axillary pouch and posterior capsule, the AB-IGHL was elongated to 2.75 mm and then allowed to recover for 30 minutes following. The mechanical testing protocol was then repeated and the resulting load-elongation curves compared. The curves were considered to be the same if the squared correlation coefficient (R^2) was greater than 0.95. [42, 173]

The elongation of 2.75 mm proved to be non-destructive as indicated by the repeatable load-elongation curves. The squared correlation coefficient between the two consecutive curves was $R^2 = 0.997$. Therefore, 2.75 mm was used as the non-destructive elongation for the following work.

4.1.1.2 Destructive Elongation

Next a method for repeatability determining the amount of elongation necessary to injure the AB-IGHL was determined. Several tissue samples from the AB-IGHL were preloaded to 0.5 N and subjected to 10 cycles of preconditioning from 0 to 1.5 mm. The samples were then loaded to failure at a rate of 10 mm/min. The resulting load-elongation curves were examined in order to determine the location of the plastic region. The transition point between the toe and linear region was defined as the point at which the R^2 value between the load and elongation data deviated from 0.999. It was determined that twice the percent elongation at the start of the linear region was required to consistently load the tissue into the plastic region of the load-elongation curve. (Figure 4.3)

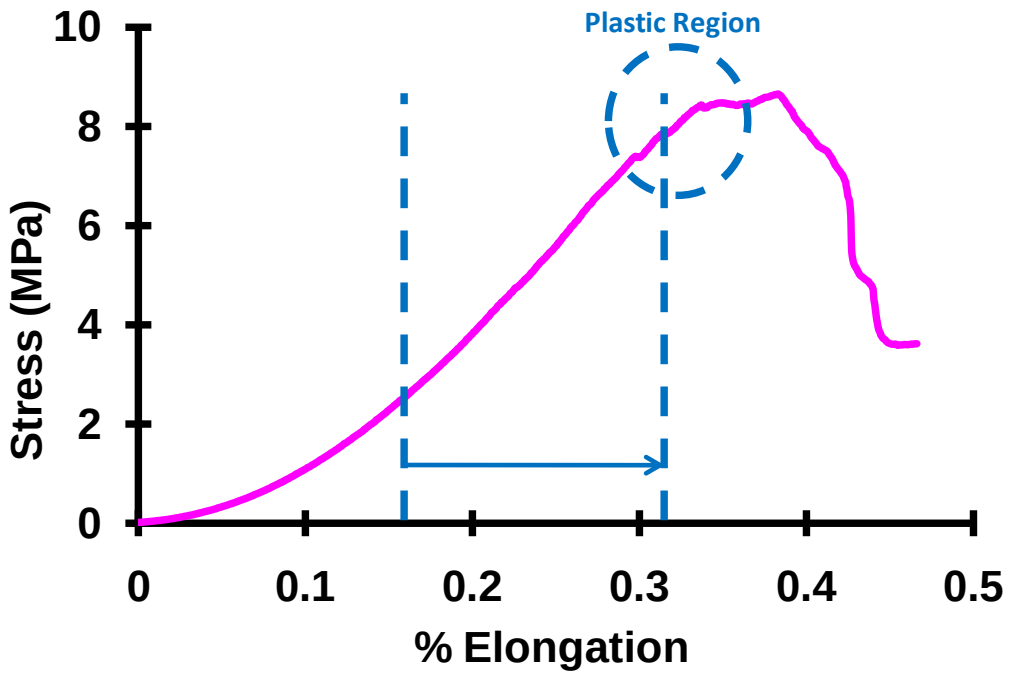

Figure 4.3 Load-elongation curve for a tissue sample from the AB-IGHL loaded to failure.

4.1.1.3 Repeatability

The repeatability of the motion tracking system (Spicatek, Inc.) used in this work has been previously determined to be 0.01 mm. [173] However, the experimental set-up used for the current work was slightly different (materials testing machine, and soft tissue clamps) than the set-up used to determine the initial repeatability of the system, thus, it needed to be reassessed. In addition, the sensitivity of the average maximum principal strain to the repeatability was determined as this parameter was to be used to quantify tissue damage.

A 10 mm x 15 mm sample was excised from the axillary pouch, placed in custom soft tissue clamps and a 3x3 grid of black delrin markers were fixed to the surface of the tissue using cyanoacrylate. The clamp-tissue sample-clamp complex was then mounted into the materials testing machine. A 0.5 N preload was applied to the tissue sample and the position of the strain markers recorded and served as the *reference state* for strain calculations. The clamp-tissue sample-clamp complex was then removed from the materials testing machine, the cross-head was moved, and the whole process was repeated four additional times. The marker coordinates (x, y) of all nine strain markers were averaged over the five trials. (Table 4.1)

Table 4.1 Average marker coordinates over five trials for nine strain markers.

Marker	X (mean ± SD)			Y (mean ± SD)		
1	14.562	±	0.028	12.862	±	0.039
2	12.651	±	0.033	12.875	±	0.001
3	10.085	±	0.032	11.924	±	0.033
4	13.560	±	0.001	16.864	±	0.039
5	12.035	±	0.001	16.349	±	0.029
6	9.907	±	0.031	15.942	±	0.030
7	14.280	±	0.029	20.380	±	0.001
8	11.456	±	0.001	20.148	±	0.001
9	9.350	±	0.002	20.203	±	0.036

The average standard deviation for all nine markers was 0.02 ± 0.02 mm in the x-direction and 0.02 ± 0.02 mm in the y-direction. Therefore, the motion tracking system is repeatable to 0.02 mm in both the x- and y-directions for this experimental set-up.

The tissue sample was then subject to the non-destructive elongation of 2.75 mm at a rate of 10 mm/min and the position of the strain markers were recorded for the normal AB-IGHL. Next, the sample was elongated into the plastic region of the load-elongation curve to simulate injury as described in the previous section and the position of the strain markers were captured and served as the *injured strain state*. Finally, the AB-IGHL was allowed to recover for 30 minutes [173] and the 0.5 N preload was re-applied. The position of the strain markers were recorded and served as the *nonrecoverable strain state*.

The maximum principal strain at the centroid of each element was determined by comparing the coordinates of the strain markers for the normal AB-IGHL as well as in the *injure*d and *nonrecoverable strain states* to the *reference state*. The x- and y-coordinates of each marker in the normal AB-IGHL, *injured strain stat*e, and *nonrecoverable strain state* were then

increased by 0.02 mm, the repeatability of the motion tracking system for the current experimental set-up. The maximum principal strain at the centroid of each element was then re-calculated for each strain state. In all three states, the change in average and peak maximum principal strain was less than 0.25%. (Table 4.2) Therefore, the sensitivity of the maximum principal strains to the repeatability of the motion tracking system was found to be less than 0.25%.

Table 4.2 Maximum principal strain (%) in the AB-IGHL tissue sample at each strain state before and after inducing an error based on the repeatability.

	Initial Strain Values		Strain Values w/ Error Added	
	Average (Mean ± SD)	Peak	Average (Mean ± SD)	Peak
Normal AB-IGHL	9.84 ± 2.63	11.32	9.61 ± 2.76	11.41
Injured Strain State	13.51 ± 5.69	18.36	13.28 ± 5.71	18.17
Nonrecoverable Strain State	3.96 ± 2.73	7.09	3.83 ± 2.87	7.03

4.2 METHODS

4.2.1 Specimen Preparation

Six cadaveric shoulders (57 ± 8 yrs., 4 males, 2 females) were stored at -20°C and thawed for 24 hours at room temperature prior to testing. A power analysis, based on data collected for other regions of the normal glenohumeral capsule, with significance set at $\alpha = 0.05$, revealed that six specimens would be required to detect desired differences, with 80% power, in the material coefficients of the average stress-stretch curves of the normal and injured AB-IGHL using a

paired t-test. The shoulders were dissected free of all skin and musculature leaving only the scapula, humerus and glenohumeral capsule. Each joint was examined using radiographs and dissection, and determined to be free of pathology, osteoarthritis and any visible signs of injury. The AB-IGHL was identified by applying distraction and external rotation to the joint as the band is most visible in this position. [166] Tissue samples (20 x 15 mm) were then excised from the AB-IGHL, mounted in custom soft tissue clamps, and a 3x3 grid of black delrin markers (diameter: 1.6 mm) was attached to each tissue sample for strain tracking using a small amount of cyanoacrylate. Strain tracking was performed optically with a custom designed motion analysis system (Spicatek, Inc., Accuracy: 0.01mm). [8, 9, 135, 174] Tissue samples were hydrated using physiologic saline solution throughout the entire testing protocol.

4.2.2 Mechanical Testing Protocol

An overview of the mechanical testing protocol is provided.

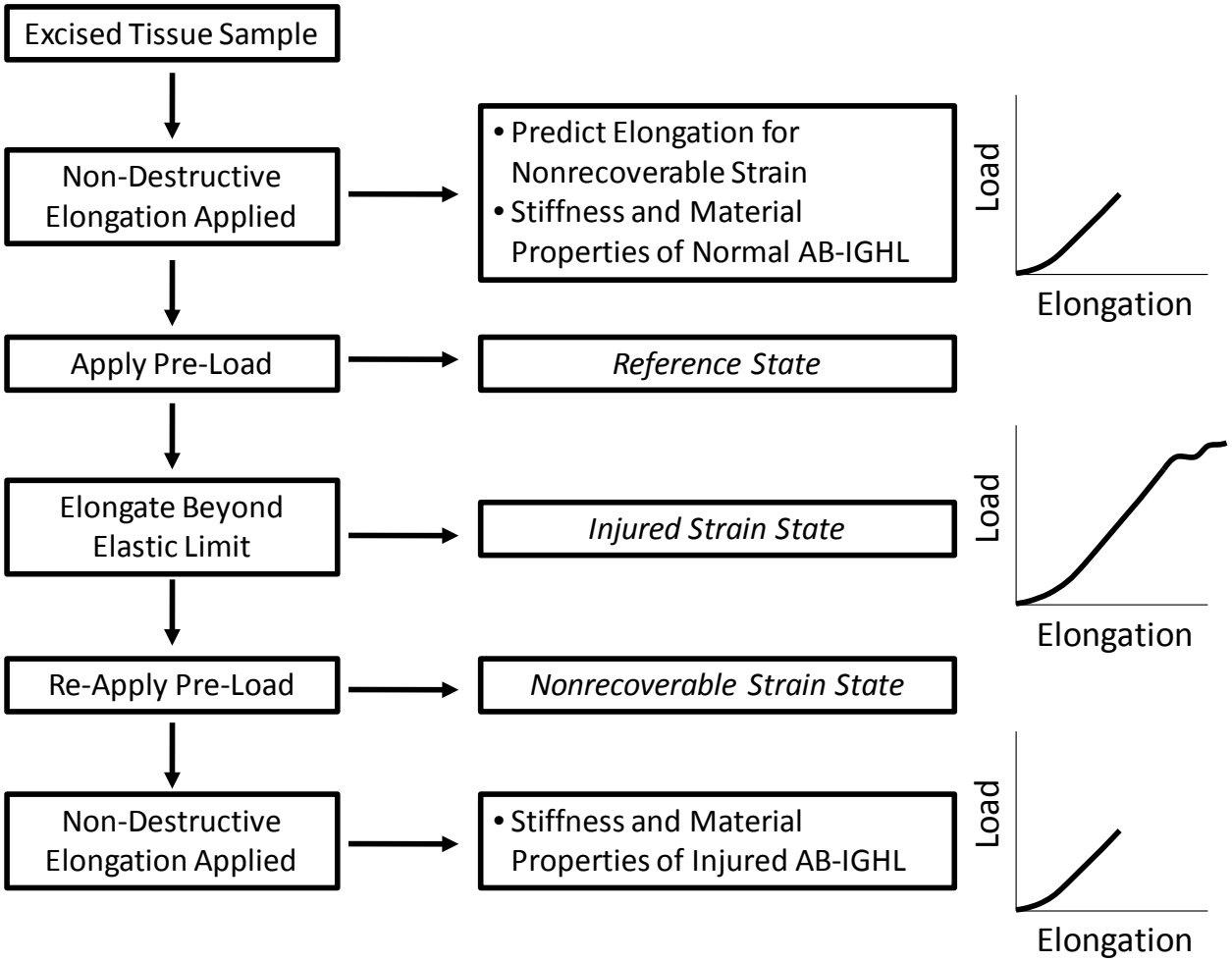

Figure 4.4 Over view of methodology used to determine the stiffness and material properties of the normal and injured AB-IGHL.

Each AB-IGHL was then elongated in the longitudinal direction parallel to the longitudinal axis of the AB-IGHL using a materials testing machine (Thumler, Model #TH2730) with load cell (Interface, Scottsdale, AZ, Model #SM-1000N, range: 0 – 1000 N, resolution: 0.015 N) to determine the stiffness and material properties of the normal tissue sample. (Figure 4.5)

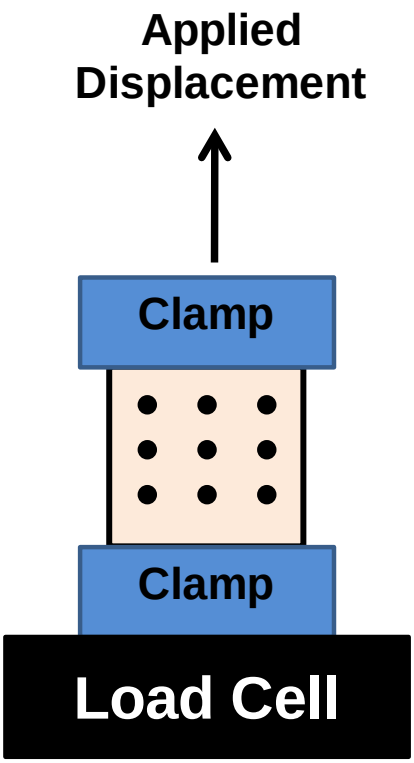

Figure 4.5 Mechanical testing set-up for tensile elongations showing the load cell and clamp relationships and the 3x3 grid of strain markers on the surface of the tissue sample.

This non-destructive loading protocol consisted of applying a 0.5 N pre-load and measuring tissue sample geometry using a ruler (width and clamp-to-clamp distance, accuracy: 0.5 mm)) and digital calipers (thickness, accuracy: 0.03 mm). Width and thickness measurements were made three times and averaged together in three places along the length of the tissue. Each tissue sample then underwent preconditioning consisting of ten cycles of elongation to 1.5 mm at a rate of 10 mm/min. Immediately following preconditioning the tissue sample was elongated to 2.75 mm again at a rate of 10 mm/min. This elongation was chosen to elongate the tissue sample into the linear region of the load-elongation curve. Preliminary studies have shown that the AB-IGHL can be consistently elongated 2.75 mm without altering the experimental load-elongation curve. The tissue was then allowed to recover for 30 minutes at an unstrained state. This was the shortest recovery time between two applications of the same loading condition required to

produce repeatable load-elongation curves. [42] This non-destructive tensile deformation was used to determine the amount of elongation needed to produce nonrecoverable strain (simulated injury) as well as determine the stiffness and material properties of the normal AB-IGHL. Based on preliminary experiments, the percent elongation required to injure the tissue sample is approximately twice that at the end of the toe region of the load-elongation curve.

Following the 30 minute recovery period, the tissue samples were subjected to the simulated injury in order to create nonrecoverable strain. To achieve this, the same preconditioning and pre-load protocol was applied to each tissue sample extracted from the AB-IGHL. The positions of the strain markers were captured in the pre-loaded state and served as the *reference state* for the strain calculations. The tissue sample was then injured by elongating it to twice the percent elongation at the end of the toe region of the non-destructive load-elongation curve, which was consistently enough to elongate the tissue into the plastic region of the load-elongation curve in order to produce nonrecoverable strain. The positions of the strain markers were also captured at the maximum elongation for each tissue sample and served as the *injured strain state* for the strain calculations. Following simulated injury the tissue sample was returned to an unstrained state and allowed to recover for 30 minutes.

Once fully recovered, the tissue sample was again pre-loaded to 0.5 N. The positions of the strain markers were captured at this pre-load and served as the *nonrecoverable strain state*. The presence of nonrecoverable strain was verified before proceeding. Finally, the same pre-load, preconditioning, and non-destructive elongation protocol previously applied to the normal tissue was repeated on the injured AB-IGHL.

4.2.3 Computational Parameter Optimization

The material coefficients of the normal and injured AB-IGHL were determined computationally utilizing previously developed methodology. [42, 124] Since the experimental tests produced inhomogeneous deformations, specimen-specific finite element models were used to predict the response of the tissue. The tissue sample geometry, applied elongation and clamp reaction forces from the non-destructive tests were used as boundary conditions to create finite element models of each tissue sample (normal and injured).

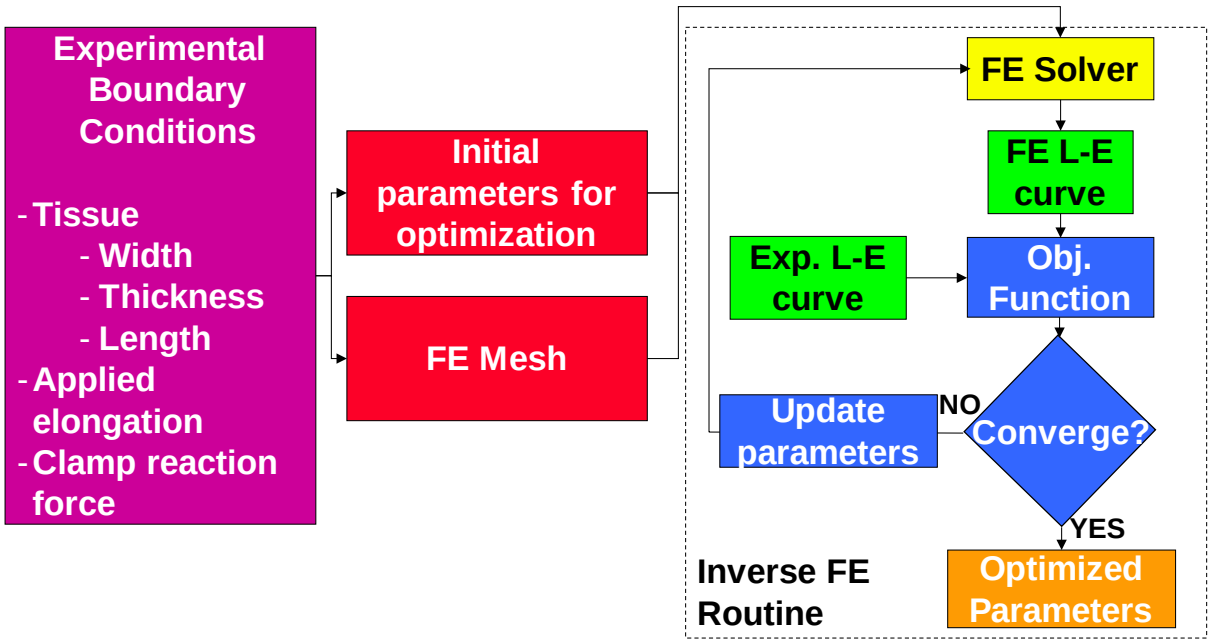

Figure 4.6 Flowchart of inverse finite element optimization methodology used to determine the optimized material coefficients.

An image obtained using a high-speed video camera (model 1000m, Adimec, Stoneham, MA, resolution: 1,000 x 1,000 pixels) from each loading condition with the tissue sample in the preloaded state, was used to create a finite-element mesh (1200 elements) by adjusting nodal points of the mesh until they were aligned with the edges of the tissue samples. A hyperelastic

isotropic strain energy function was used to describe the response of the tissue to the applied elongation and the material coefficients were determined using an inverse finite element optimization technique. [48] The strain energy was based on the form originally used by Veronda and Westmann [175], but with an uncoupled dilatational and deviatoric response. [42, 124, 176]

$$W = C_1[e^{C_2(\tilde{I}_1-3)} - 1] - \frac{C_1 C_2}{2}(\tilde{I}_2 - 3) + \frac{1}{2}K[\ln(J)]^2 \quad (1)$$

Where $\tilde{I}_1$ and $\tilde{I}_2$ are the deviatoric invariants of the right Cauchy-Green deformation tensor C, $\frac{1}{2}K[\ln(J)]^2$ governs the dilatational response of the tissue (where J is the volume ratio). C_1 and C_2 are the material coefficients that were determined using the inverse finite element optimization routine, where C_1 scales the magnitude of the stress-stretch curve and C_2 governs the magnitude and nonlinearity of the stress-stretch curve. The strain energy is convex and exhibits physically reasonable behavior under tension, compression, and shear. [48, 176] Initial estimates for the material coefficients of C_1 = 0.1 MPa and C_2 = 10 were used consistently for the parameter optimization. Previous work in our research group has shown that the optimized material parameters were not sensitive to the initial guesses. [173] All finite element calculations were performed using the nonlinear code FEBio (http://mrl.sci.utah.edu/software.php?soft_id=7, Musculoskeletal Research Laboratory, University of Utah).

The inverse finite element optimization routine used a sequential quadratic programming method (E04UNF, Numerical Algorithms Group, Oxford, UK). The NAG routine minimized a smooth objective function subject to a set of constraints on the following variables:

$$F(C_1, C_2) = \frac{1}{2}\sum_{i=1}^{m}\{y_i - f_i(C_1, C_2)\}^2 \tag{2}$$

Where $F(C_1, C_2)$ is the objective function, y is the experimental clamp reaction force, $f(C_1,C_2)$ is the clamp reaction force from the finite element simulation, *i* represents a particular clamp displacement level, and *m* is the number of discrete clamp displacement levels. Eleven points were used in the present study, based on previous work performed on the medial collateral ligament [177] and glenohumeral capsule [42]. Both material coefficients were constrained to be greater than 0 to ensure physically reasonable behavior and strong ellipticity but less than 5 (C_1) or 50 (C_2). [42, 124, 178]

The optimized coefficients for the normal and injured AB-IGHL were then used to generate stress-stretch curves for uniaxial extension, respectively, using the deformation gradient for uniaxial extension and the isotropic hyperelastic constitutive model. [42, 124] The stress-stretch relationship was derived from the appropriate deformation gradient tensor. For uniaxial extension and assuming incompressibility, the deformation gradient (**F**) and Cauchy Stress (T) were as follows:

$$F = \begin{bmatrix} \lambda_1 & 0 & 0 \\ 0 & \frac{1}{\sqrt{\lambda_1}} & 0 \\ 0 & 0 & \frac{1}{\sqrt{\lambda_1}} \end{bmatrix} \tag{3}$$

$$T_{11} = \frac{C_1 C_2 (\lambda_1 - 1)(\lambda_1^2 + \lambda_1 + 1)\left[2\lambda_1 e^{\frac{C_2(\lambda_1+2)(\lambda_1-1)^2}{\lambda_1}} - 1 \right]}{\lambda_1^2} \quad (4)$$

where λ is stretch. Stress-stretch curves from λ = 1.0 to λ = 1.3 and were discretized into twenty-one points and averaged across all tissue samples generating an average curve for the normal and injured AB-IGHL. [42, 124, 179] It is important to note that the stress-stretch curves are more representative of the mechanical properties of the tissue rather than the structural response provided by the load-elongation curves. At the same time, these curves are not representative of what is induced in the tissue sample during the experiment but represent the response of each tissue to pure tensile elongations. Since the aspect ratio of the samples used in this work was very low, the pure tension assumptions are valid.

4.2.4 Data Analysis

The tissue sample geometry (width, thickness, clamp-to-clamp distance and cross-sectional area) at the pre-loaded (*reference*) state, toe region and linear region stiffness, as well as the material coefficients of the normal and injured tissue samples were compared using paired t-tests as all data was normally distributed. Significance was set at $\alpha = 0.05$ for all statistical analyses.

In order to verify that the simulated injury was successful (presence of nonrecoverable strain), the average maximum principal strain for each tissue sample in the *injured* and *nonrecoverable strain states* was determined. The coordinates of the markers at each strain state were input into a finite element software package (ABAQUS, Simulia, Providence, RI). The magnitude of the maximum principal strain at the centroid of each element was calculated and

averaged over the four elements for the *injured* and *nonrecoverable strain states* for each tissue sample. This average maximum principal strain was then averaged again over all tissue samples at the *injured* and *nonrecoverable strain states*. The strains in the AB-IGHL midsubstance were an order of magnitude greater than the experimental repeatability of the strain calculations (0.25%). The directions of the maximum principal strains in the *injured* and *nonrecoverable strain states* were also computed at four integration points within each element. Strain directions were qualitatively examined in order to verify that their alignment was consistent with the direction of elongation applied to the tissue samples.

Pearson's correlation coefficient was used to compare the average and peak maximum principal strain for the AB-IGHL in the *injured* and *nonrecoverable strain states* as well as to compare these strain values to the linear region stiffness of the load–elongation curves and modulus of the stress-stress curves between the normal and injured states. The critical value for Pearson's correlation coefficients for a sample size of $n = 6$ is $r = 0.8$. [180] Therefore, correlations were considered statistically significant when $0.8 \leq |r| < 1.0$. Further, the correlation was considered moderate for $0.5 \leq |r| < 0.8$, weak for $0.0 \leq |r| < 0.5$. [181] The stiffness of the initial toe region and linear region was determined from the load-elongation curves of the normal and injured states for each tissue sample. The stiffness of the initial toe region was computed between 0 and 0.5 mm of elongation, while the stiffness of the linear region was computed as the maximum slope of the entire load-elongation curve over a running window of 1% elongation, respectively.

A single statistical comparison of the material coefficients may not be enough to reveal differences in the material properties of the normal and injured AB-IGHL as the constitutive model is nonlinear and the material coefficients are not linearly independent. Therefore,

averaging the individual material coefficients does not yield the same stress-stretch response as averaging the individual stress-stretch curves and determining a set of average material coefficients. In order to determine if differences existed between the normal and injured stress-stretch curves at each of the twenty-one discretized points, a repeated measures ANOVA and paired t-test post-hoc analyses were performed. The average stress-stretch curves were fit to the stress-stretch relationship for uniaxial extension using the non-linear Levenberg-Marquardt algorithm with a tolerance of 0.001 to obtain a set of material coefficients representing the average stress-stretch curves for each region. The same initial guesses of 0.1 for C_1 and 10 for C_2 were used. These material coefficients representing the average stress-stretch curves were compared as previously reported. [42, 124] Based on preliminary analyses to determine the sensitivity of the stress-stretch curves to the constitutive coefficients, a difference of greater than 0.30 for C_1 or greater than 3.0 for C_2 was considered significant. Changes in the average coefficients greater than these values indicate that the squared correlation coefficient between two curves was less than 0.9 and the curves would be significantly different.

Further, the modulus of each tissue sample in the normal and injured states was determined as the slope of the Cauchy stress-stretch curves between a stretch of $\lambda = 1.2$ and $\lambda = 1.3$. As the moduli were normally distributed, a paired t-test was used to compare between the normal and injured AB-IGHL.

4.3 RESULTS

4.3.1 Tissue Sample Geometry

No statistically significant differences were found in the tissue sample geometery (width: $p = 0.75$, thickness: $p = 0.52$) or cross-sectional area ($p = 0.96$) between normal and injured capsular tissue. (Figure 4.7) The differences in width, thickness and cross-sectional area between normal and injured tissue were <1%, 5%, and <1%, respectively. An elongation of 3.78 ± 0.70 mm was applied to simulate injury and cause nonrecoverable strain in each AB-IGHL. Further, the clamp-to-clamp distance with the preload applied (*reference state*) increased significantly ($p = 0.01$) following simulated injury by 1.7 ± 1.0 mm (11.0 ± 7.6%).

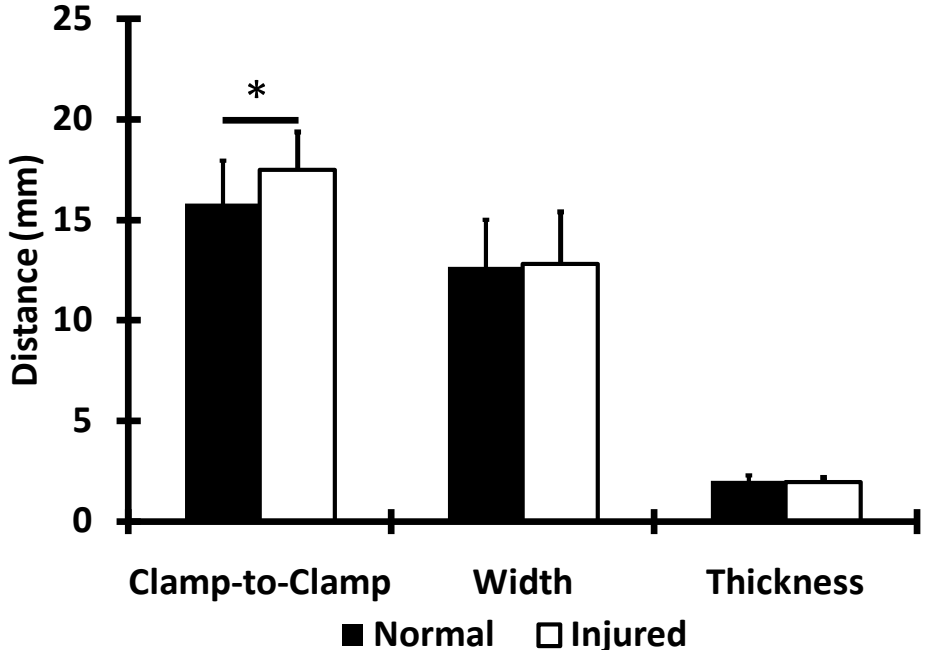

Figure 4.7 Tissue sample geometry for the normal and injured AB-IHGL.

4.3.2 Maximum principal Strains

At the *injured strain state* (AB-IGHL elongated into plastic region of load-elongation curve), the average and peak maximum principal strain in the AB-IGHL were 12.7 ± 3.2% (Range: 8.3% to 16.9%) and 19.2 ± 5.6% (Range: 12.8% to 27.1%), respectively. (Table 4.3)

Table 4.3 Elongation and Maximum principal Strain in the *Injured Strain State*.

Specimen #	Elongation (mm)	Average Strain (%)	Peak Strain (%)
05-11007R	3.57	13.1 ± 2.8	16.8
05-10043R	3.42	8.3 ± 5.9	14.9
05-08022L	3.94	12.7 ± 7.9	24.7
05-08041R	3.91	16.9 ± 7.4	27.1
07-03471L	2.88	9.7 ± 3.0	12.8
07-03472R	4.98	15.2 ± 4.7	19.1
MEAN ± SD	3.78 ± 0.70	12.7 ± 3.2	19.2 ± 5.6

Nonrecoverable strain was created in each AB-IGHL following the destructive elongation. The experimentally measured average and peak maximum principal nonrecoverable strain in the tissue midsubstance was 2.5 ± 0.9% (Range: 1.5% to 4.0%) and 5.4 ± 1.8% (Range: 3.6% to 7.7%), respectively. (Table 4.4)

Table 4.4 Experimentally measured maximum principal Strain in the *Nonrecoverable Strain State*.

Specimen #	Average Strain (%)	Peak Strain (%)
05-11007R	2.9 ± 1.4	4.1
05-10043R	1.9 ± 2.2	4.0
05-08022L	2.6 ± 3.3	7.3
05-08041R	4.0 ± 2.9	7.7
07-03471L	2.0 ± 2.6	5.7
07-03472R	1.5 ± 1.6	3.6
MEAN ± SD	2.5 ± 0.9	5.4 ± 1.8

The strain directions at both the *injured* and *nonrecoverable strain states* were aligned with the direction of loading. (Figure 4.8)

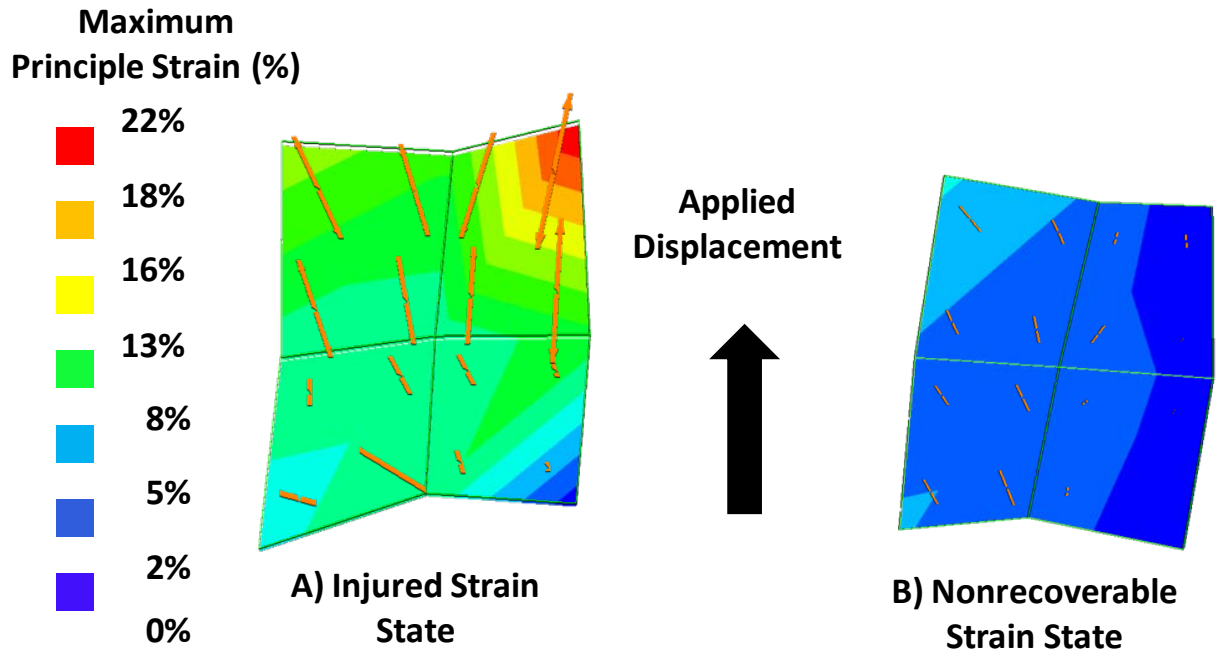

Figure 4.8 Experimentally measured maximum principal strain for a typical tissue sample at A) injured state and B) nonrecoverable strain state with directions denoted by the orange vectors. The black arrow indicates the direction of loading.

The correlation coefficients between the average and peak maximum priniciple nonrecoverable strain and maximum principal strain at the *injured strain state* were 0.5 and 0.7, respectively (Figure 4.9).

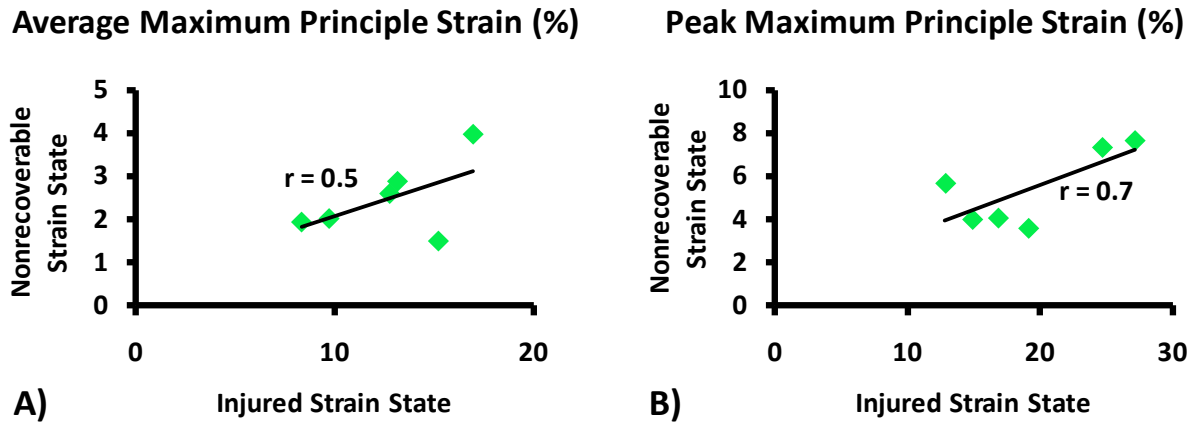

Figure 4.9 Correlations between the average (A) and peak (B) maximum principal strain in the *nonrecoverable* and *injured strain states*.

4.3.2.1 Stiffness

The load-elongation curves for each tissue sample in the normal and injured states exhibited the non-linear behavior typical of biologic tissues.

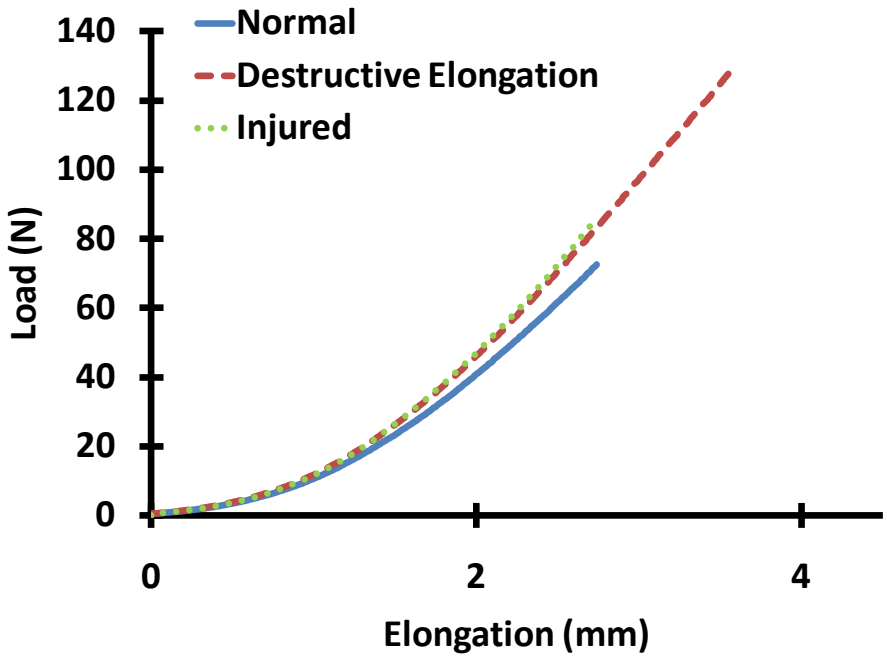

Figure 4.10 Load-elongation curves for the normal and injured AB-IGHL of Specimen 05-11007R as well as the load-elongation curve for the destructive elongation used to create the permanent deformation.

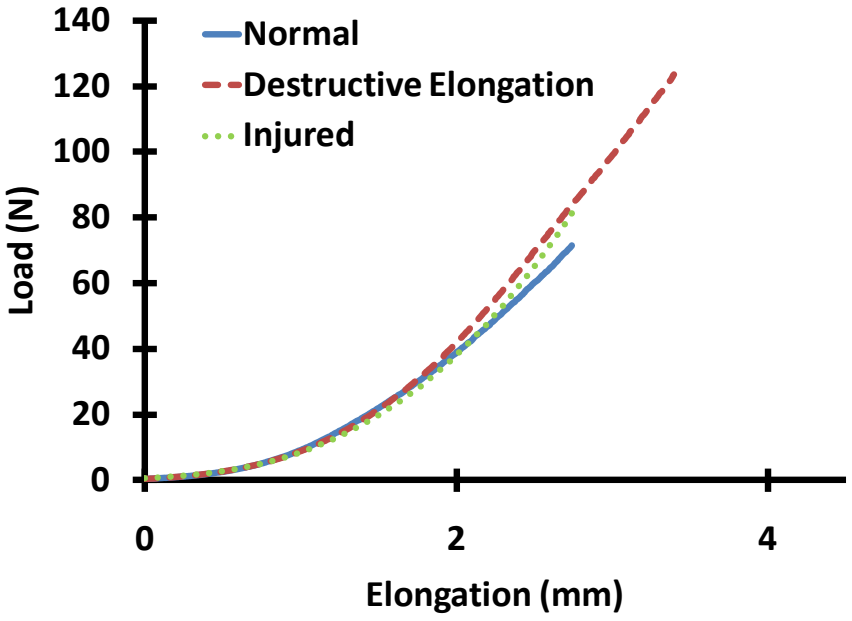

Figure 4.11 Load-elongation curves for the normal and injured AB-IGHL of Specimen 05-10043R as well as the load-elongation curve for the destructive elongation used to create the permanent deformation.

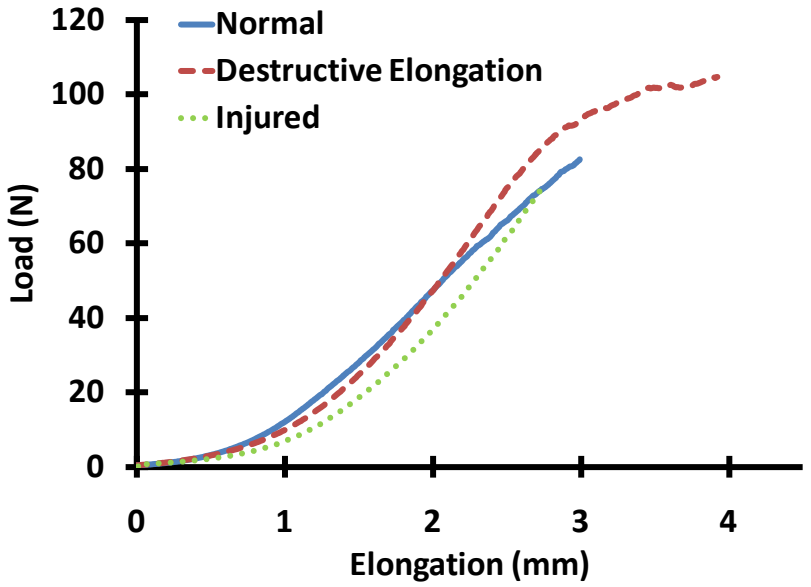

Figure 4.12 Load-elongation curves for the normal and injured AB-IGHL of Specimen 05-08022L as well as the load-elongation curve for the destructive elongation used to create the permanent deformation.

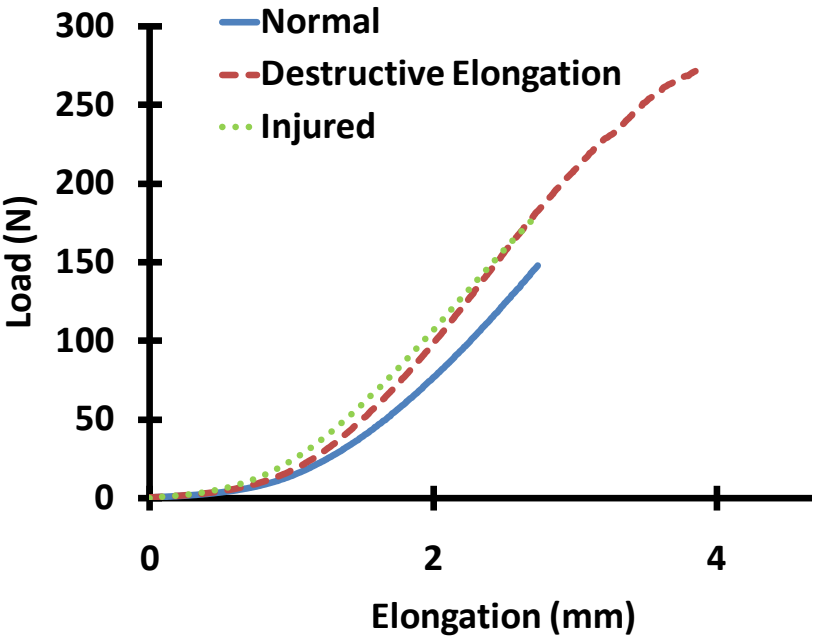

Figure 4.13 Load-elongation curves for the normal and injured AB-IGHL of Specimen 05-08041R as well as the load-elongation curve for the destructive elongation used to create the permanent deformation.

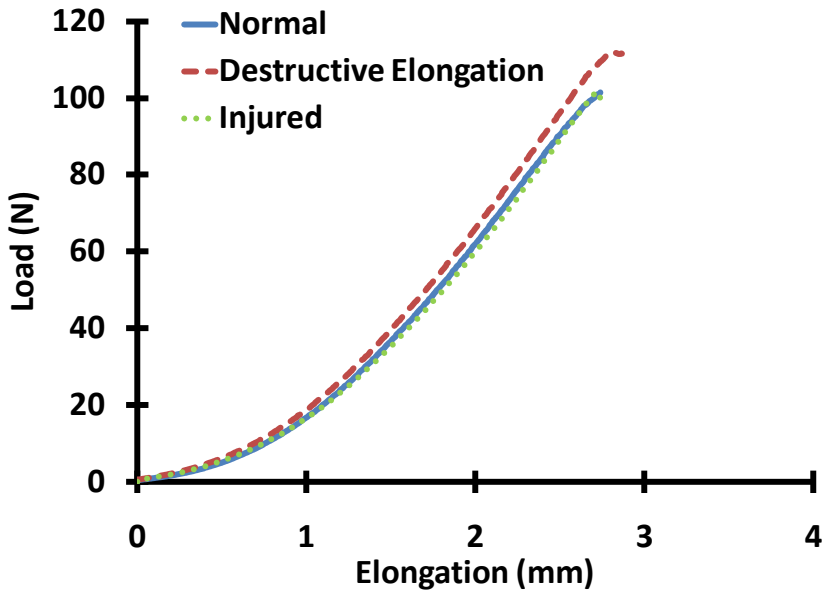

Figure 4.14 Load-elongation curves for the normal and injured AB-IGHL of Specimen 07-03471L as well as the load-elongation curve for the destructive elongation used to create the permanent deformation.

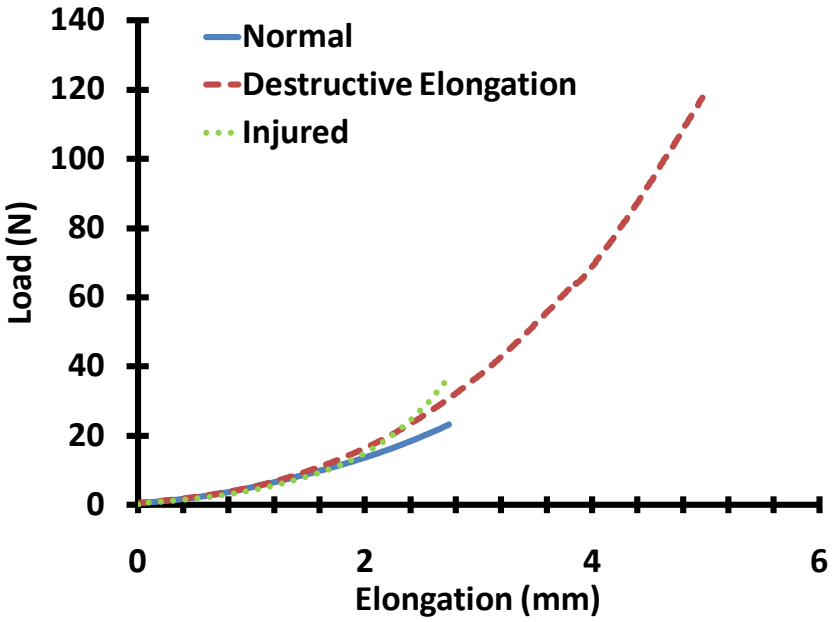

Figure 4.15 Load-elongation curves for the normal and injured AB-IGHL of Specimen 07-03472R as well as the load-elongation curve for the destructive elongation used to create the permanent deformation.

No statistical difference was found when comparing the initial toe region stiffness of the load-elongation curves for the normal and injured AB-IGHL ($p = 0.70$). (Table 4.5) Initial toe region stiffness was 5.7 ± 1.9 N/mm and 6.1 ± 3.3 N/mm for the normal and injured AB-IGHL, respectively.

Table 4.5 Initial toe-region stiffness for the normal and injured AB-IGHL.

SPECIMEN #	NORMAL	INJURED
05-11007R	5.5	3.2
05-10043R	6.2	10.2
05-08022L	4.3	4.2
05-08041R	5.9	6.3
07-03471L	9.0	9.8
07-03472R	3.3	2.6
MEAN ± SD	5.7 ± 1.9	6.1 ± 3.3

The linear region stiffness was significantly different between the normal (52.4 ± 30.0 N/mm) and injured (64.7 ± 21.3 N/mm) AB-IGHL ($p = 0.03$). The increase in linear region stiffness following simulated injury was computed for all AB-IGHL samples; the average increase was 47%. (Table 4.6)

Table 4.6 Linear-region stiffness for the normal and injured AB-IGHL.

SPECIMEN #	NORMAL	INJURED
05-11007R	39.8	56.9
05-10043R	105.7	103.9
05-08022L	49.2	67.8
05-08041R	45.8	57.9
07-03471L	59.2	61.6
07-03472R	15.0	40.0
MEAN ± SD	52.4 ± 30.0	64.7 ± 21.3

Linear region stiffness in both the normal and injured states was significantly correlated to the average (normal & injured: $r = 0.8$, $p = 0.04$, Figure 4.16(A)) and moderately correlated to the peak (normal: $r = 0.7$, injured: $r = 0.6$, Figure 4.16(B)) maximum principal nonrecoverable strain in the tissue midsubstance. However, the change in linear region stiffness between the normal and injured states was negatively correlated to the average ($r = -0.7$, Figure 4.16(C)) and peak ($r = -0.6$, Figure 4.16(D)) maximum principal nonrecoverable strain in the tissue midsubstance.

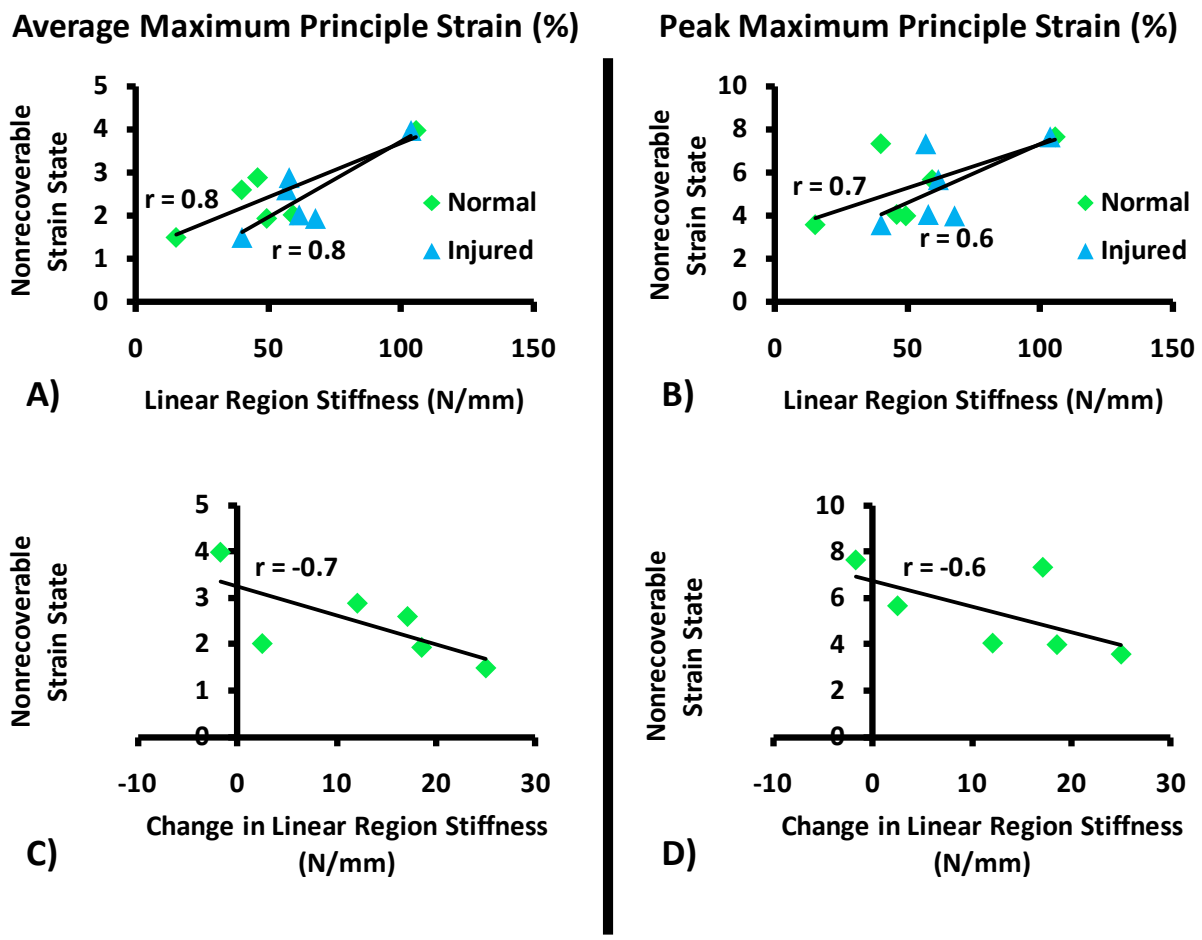

Figure 4.16 Correlations between average and peak maximum principal nonrecoverable strain and the linear region stiffness of the normal and injured AB-IGHL (A, B) and between the change in linear region stiffness between the normal and injured AB-IGHL (C, D).

4.3.2.2 Material Properties

No statistical difference was found when comparing the material coefficients for the normal and injured AB-IGHL ($p = 0.59$ for C_1; $p = 0.07$ for C_2). (Table 4.7) The values of C_1 and C_2 were 0.71 ± 0.51 MPa (Range: 0.21 MPa to 1.36 MPa) and 3.2 ± 1.8 (Range: 1.4 to 6.3), respectively for the normal tissue samples. Following injury, the values of C_1 and C_2 were 0.56 ± 0.59 MPa (Range: 0.12 MPa to 1.45 MPa) and 5.0 ± 1.7 (Range: 3.3 to 7.6), respectively. When compared to the normal AB-IGHL, the value of C_1 was 20% lower (by 0.15 MPa) and the value of C_2 was 56% higher (by 1.8) in the injured AB-IGHL.

Table 4.7 Material coefficients of the constitutive model for the normal and injured AB-IGHL.

SPECIMEN #	NORMAL		INJURED	
	C_1 MPa	C_2	C_1 MPa	C_2
05-11007R	0.21	6.3	0.27	7.6
05-10043R	0.40	3.0	0.17	4.6
05-08022L	1.36	1.4	0.18	4.2
05-08041R	0.52	3.9	1.19	3.5
07-03471L	1.34	2.8	1.45	3.3
07-03472R	0.42	1.7	0.12	6.5
MEAN ± SD	0.71 ± 0.51	3.2 ± 1.8	0.56 ± 0.59	5.0 ± 1.7

Stress-stretch curves for uniaxial extension were generated up to a stretch of $\lambda = 1.3$ using the optimized material coefficients for each AB-IGHL in the normal and injured states. Average curves were then generated representing the response of the normal and injured AB-IGHL to uniaxial extension. The stress-stretch curves exhibited a non-linear shape, typical of soft tissues and are similar with a correlation coefficient between the curves of R=0.998. (Figure 4.23)

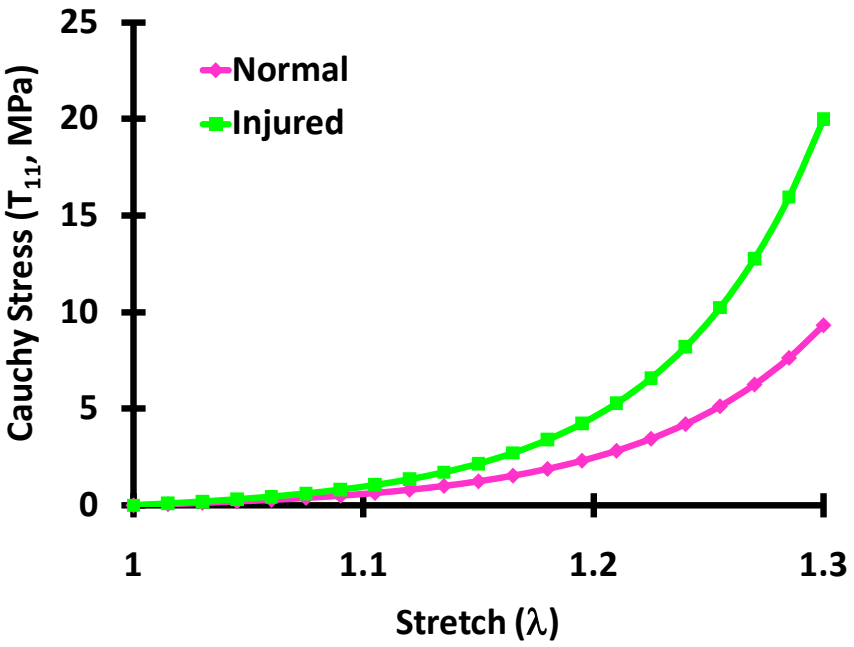

Figure 4.17 Cauchy stress-stretch curves for the normal and injured AB-IGHL from specimen 05-11007R.

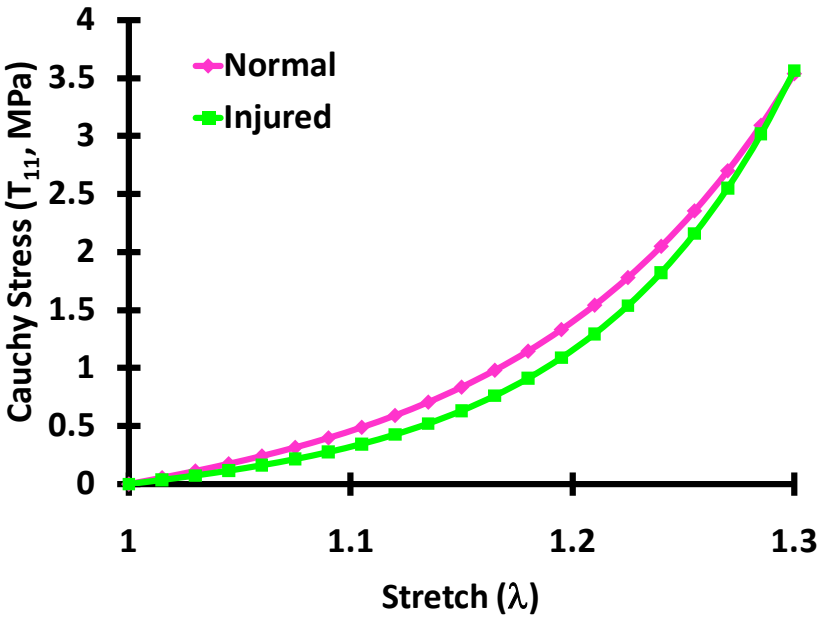

Figure 4.18 Cauchy stress-stretch curves for the normal and injured AB-IGHL from specimen 05-10043R.

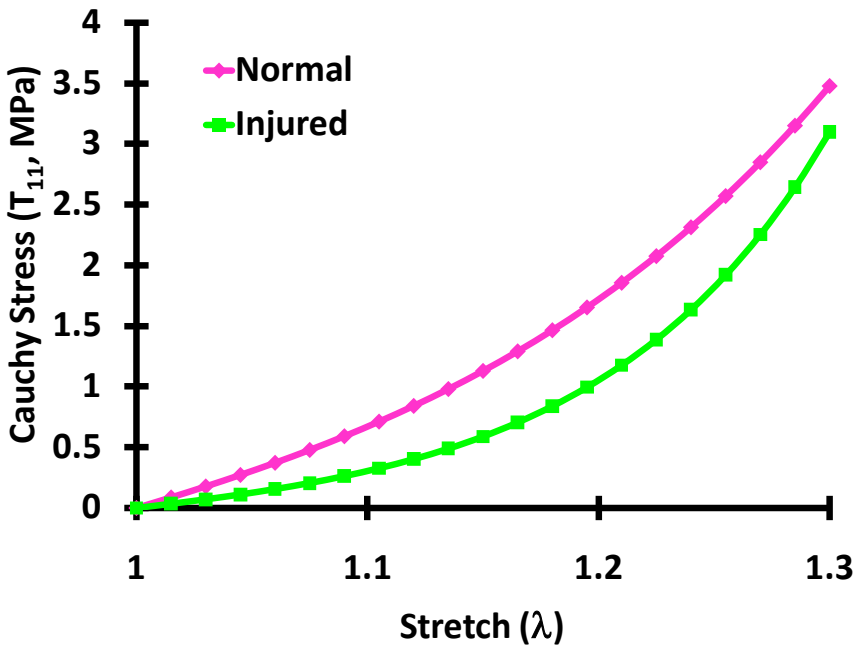

Figure 4.19 Cauchy stress-stretch curves for the normal and injured AB-IGHL from specimen 05-08022L.

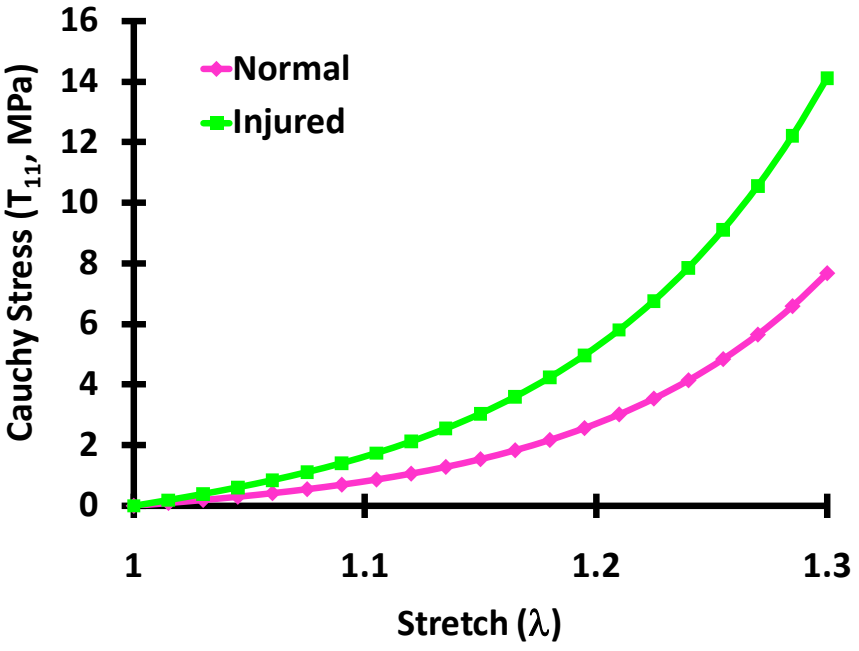

Figure 4.20 Cauchy stress-stretch curves for the normal and injured AB-IGHL from specimen 05-08041R.

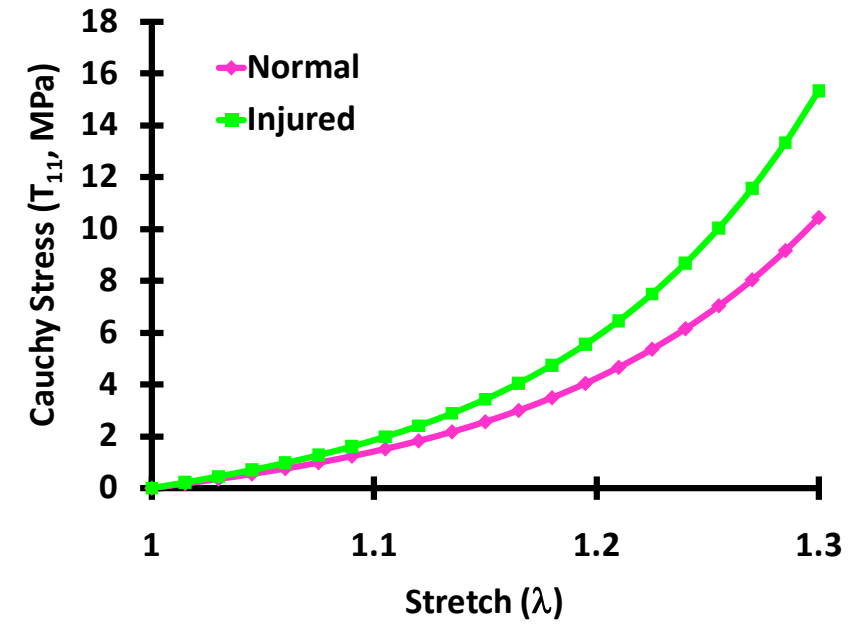

Figure 4.21 Cauchy stress-stretch curves for the normal and injured AB-IGHL from specimen 07-03471L.

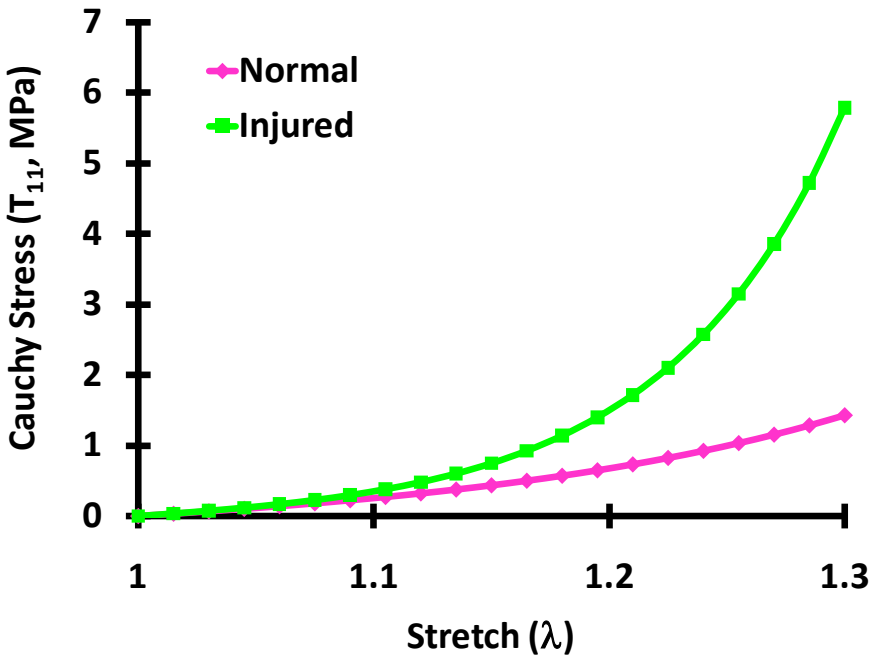

Figure 4.22 Cauchy stress-stretch curves for the normal and injured AB-IGHL from specimen 07-03472R.

The average stress-stretch curves for all specimens were generated. (Figure 4.23)

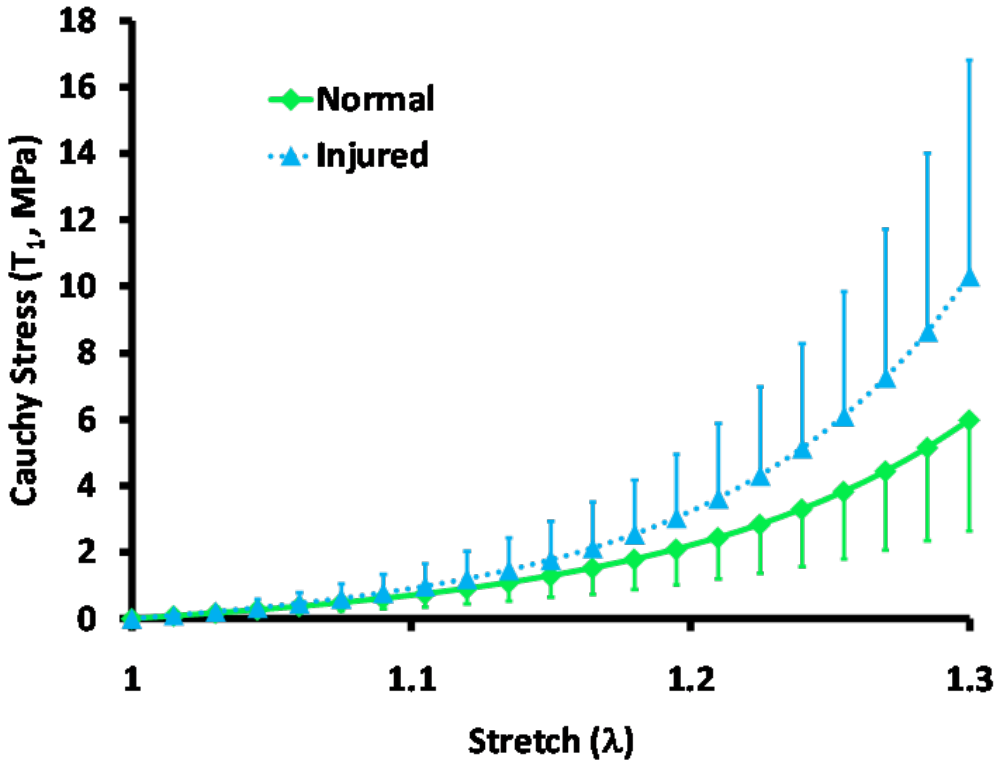

Figure 4.23 Stress-stretch curves (mean SD) for the normal and injured AB-IGHL under uniaxial extension.

No significant differences were found between the normal and injured AB-IGHL when comparing the stress values at each of the twenty-one discretized points of the stress-stretch curve for uniaxial extension ($p \geq 0.05$). However, the stress -stretch curves exhibited a trend towards significance with individual comparisons between the normal and injured stress values at the twenty-one discretized stretch values yielding p-values ranging from $p = 0.43$ at $\lambda = 1.02$ to $p = 0.05$ at $\lambda = 1.3$. At the maximum stretch of $\lambda = 1.3$, the stress in the injured AB-IGHL was 72% higher than the normal AB-IGHL.

The values of C_1 and C_2 representing the average stress-stretch curves were 0.36 MPa and 4.6 for the normal tissue, and 0.39 MPa and 5.4 for the injured tissue. The values of C_1 and C_2 were 0.03 MPa and 0.7 higher in the injured than the normal AB-IGHL. Again, differences

of less than 0.3 for C_1 and less than 3 for C_2 are considered insignificant. [42, 173] Therefore, the coefficients representing the average stress-stretch curves are not significantly different using this constitutive model.

Significant differences were found between the modulus of the normal (39.1 ± 26.6 MPa) and injured (73.5 ± 53.8 MPa) AB-IGHL ($p = 0.04$). (Table 4.8)

Table 4.8 Modulus of the Cauchy stress-stretch curves for the normal and injured AB-IGHL.

SPECIMEN #	NORMAL	INJURED
05-11007R	71.4	160.6
05-10043R	22.0	25.0
05-08022L	18.0	21.2
05-08041R	51.3	91.7
07-03471L	63.9	98.1
07-03472R	7.7	44.6
MEAN ± SD	31.9 ± 26.6	73.5 ± 53.8

The average increase in modulus between the normal and injured tissue states was 34.5 ± 31.7 MPa (128%). Correlation coefficients between the modulus of the normal and injured AB-IGHL and the average maximum principal nonrecoverable strain in the tissue midsubstance were $r = 0.5$ for the normal AB-IGHL and $r = 0.4$ for the injured AB-IGHL (Figure 4.24(A)). Further, a weak correlation was found between the change in modulus between the normal and injured states and the average maximum principal nonrecoverable strain in the tissue midsubstance ($r = 0.3$, Figure 4.24(C)) as well as the average maximum principal strain in the tissue midsubstance at the *injured strain state* ($r = 0.4$, Figure 4.24(D)).

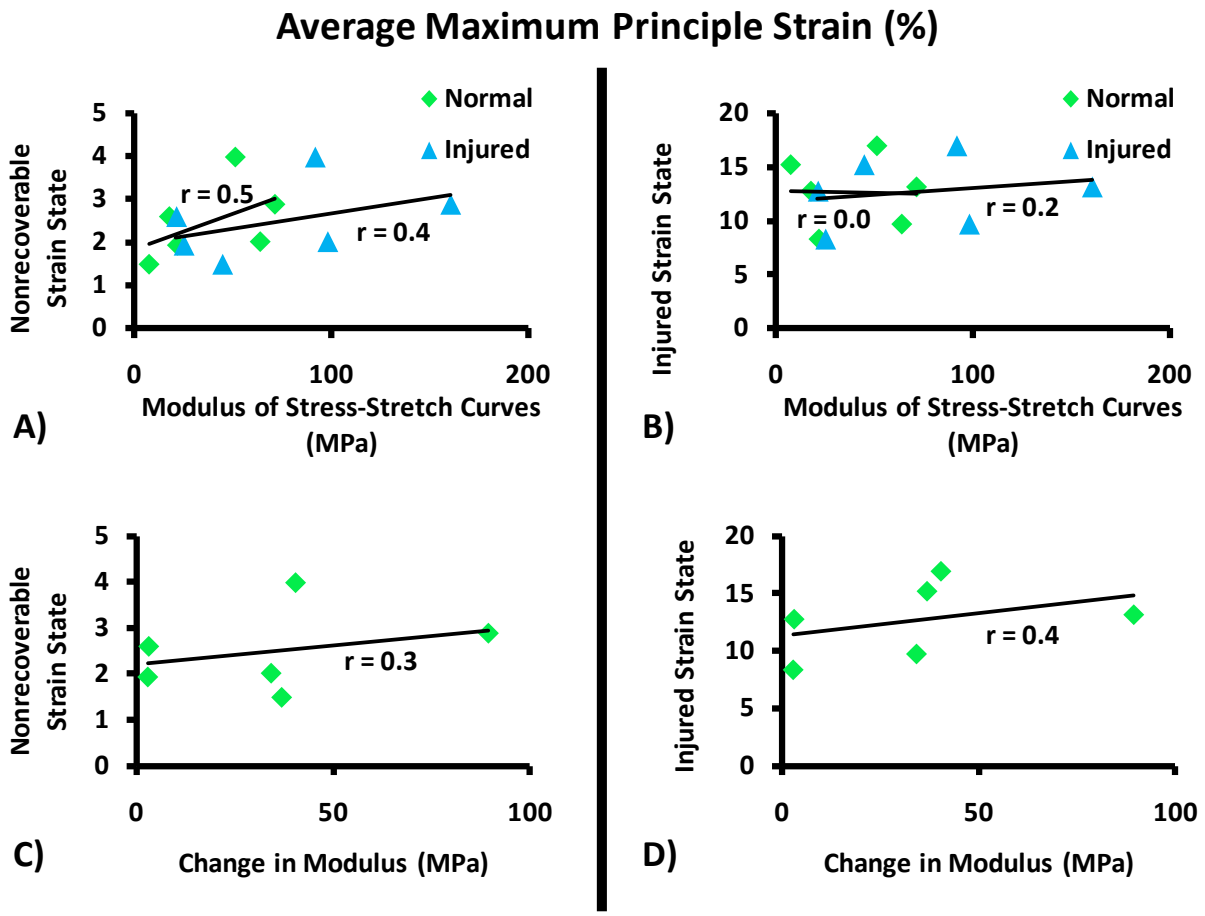

Figure 4.24 Correlations between average maximum principal strain at the nonrecoverable and injured strain states and the modulus of the stress-stretch curves of the normal and injured AB-IGHL (A, B) and between the change in modulus of the stress-stretch curves between the normal and injured AB-IGHL (C, D).

4.4 SIGNIFICANCE OF RESULTS

In this study a method for simulating injury by creating nonrecoverable strain in a tissue sample excised from the glenohumeral capsule was developed. The average maximum principal strain during the simulated injury and the corresponding average maximum principal nonrecoverable strain produced in the midsubstance of each AB-IGHL sample were quantified. The effects of the simulated injury on the stiffness and material properties of the AB-IGHL were determined

using a hyperelastic isotropic constitutive model to describe the material response of each tissue sample to tensile deformations.

4.4.1 Discussion of Results: Maximum principal Strains

Simulated injury of the AB-IGHL resulted in nonrecoverable strain and increased tissue elongation thereby confirming that permanent tissue deformation occurred. The maximum priniple strain produced in the tissue samples from the AB-IGHL in the *injured strain state* and *nonrecoverable strain state* compare well with other injury models. [33, 68, 69] For example, varying degrees of subluxation of the glenohumeral joint resulted in 9% - 15% maximum principal strain during injury [69] and 5% - 7% nonrecoverable strain [68] in the anteroinferior glenohumeral capsule. Our tensile elongations of the AB-IGHL into the plastic region of the load-elongation curve yielded 12.7% strain in the tissue sample at the maximum elongation and resulted in 2.5% nonrecoverable strain. It is expected that strains produced in a tissue sample extracted from the AB-IGHL would be less than that produced in an injury model of the intact joint because of the continous structure and function of the glenohumeral capsule. Nonetheless, the simulated injury model developed in this work is capable of creating maximum principal strains in tissue samples from the glenohumeral capsule that are similar to those experienced by the intact capsule during joint subluxation.

In this injury model, tissue samples from the AB-IGHL were elongated into the plastic region of the load-elongation curve in order to consistently create nonrecoverable strain. Although this model consistently injures the AB-IGHL, the amount of damage is variable between tissue samples, as indicated by the standard deviation in the maximum principal strain in the tissue sample in the *injured strain state*. Future studies should base injury on strains

applied to the tissue midsubstance rather than elongation to produce consistent damage to each tissue sample.

The positive correlation between the strain at the *injured strain state* and the resulting nonrecoverable strain in the AB-IGHL suggests that more severe injuries may result in higher amounts of nonrecoverable strain. Similar results were found when a univariate regression model was used to examine the relationship between the maximum principal strain at the *injured* and *nonrecoverable strain states* produced by applying varying degrees of glenohumeral subluxation ($R^2 = 0.35$, $r = 0.6$). [33]

4.4.2 Discussion of Results: Stiffness

The injury protocol was used to examine the effect of simulated injury on the initial toe region and linear region stiffness of the AB-IGHL. The increase in linear region stiffness following simulated injury compares well with a sub-failure injury model in the rabbit anterior cruciate ligament. [170] The correlations between the linear region stiffness and nonrecoverable strain suggests that in tissue samples where the fibers are only able to rotate a small amount between the normal and injured states (small change in linear region stiffness), damage is likely to occur at an earlier elongation compared to tissue samples where the fibers can rotate substantially (large change in linear region stiffness) to support applied loads. Therefore, tissue samples which are more aligned initially are more likely to be damaged during the simulated injury than those with dispersed fibers. Further examination of collagen fiber kinematics in the glenohumeral capsule during tissue elongation is necessary to investigate this hypothesis.

4.4.3 Discussion of Results: Mechanical Properties

The material coefficients of the normal AB-IGHL compare well with those reported for other capsule regions. [42, 173] Despite differences in the material properties of the AB-IGHL following injury, no statistical differences were found in the constitutive model parameters. These finding suggest that the constitutive model used in this work is not able to detect changes in the material coefficients, for the small amount of nonrecoverable strain created. This could be attributed to the phenomenological form of the strain energy function, which does not distinguish between matrix and collagen fiber responses. Changes in the material coefficients affect the entire stress-stretch response, as opposed to the toe or linear regions independently, making changes in tissue microstructure, which primarily affect the linear region, difficult to detect. Therefore, a constitutive model which includes terms describing the contributions of the fibers and ground substance separately may more appropriately describe the behavior of the tissue following injury and will be utilized in the future.

4.4.4 Limitations

In addition to a significant increase in clamp-to-clamp distance following simulated injury, an increase in the toe-region of the load-elongation curve was observed. However, it was not quantified as the same preload had to be applied to the normal and injured AB-IGHL samples in order to quantify the nonrecoverable strain produced during simulated injury. Had this extended toe region been included in the stress-stretch response differences in the material parameters may have been detected. This concept should be examined in the future in order to fully characterize the properties of the injured AB-IGHL. In vivo, the capsule acts as a continuous sheet of fibrous

tissue rather than a uniaxial ligament [8] and thus experiences more complex loadings and strains than reported here. However, a low aspect ratio was used to simulate these complex loading conditions by creating inhomogeneous deformations during loading. Tissue properties were then determined from the theoretical case of uniaxial extension.

4.4.5 Implications

The simulated injury model examined here is capable of creating nonrecoverable strain in capsular tissue that is similar to damage experienced by the intact capsule during injury. Following permanent deformation, changes in the stiffness and material properties of the AB-IGHL were found. These changes could be due to permanent changes in the collagen fiber architecture following simulated injury. Since the tissue is stiffer, its reference state may contain more aligned collagen fibers following injury that shift the tissue towards anisotropy. Therefore, surgical repair techniques which simply tighten the capsule to eliminate excessive tissue elongation may only be addressing part of the problem and changes in tissue properties may still affect the ability of the capsule to support the wide range of motion at the glenohumeral joint. Surgeons should be cognizant of these changes when they are performing repair procedures to tighten the capsule following dislocation in order to fully restore the joint to a normal functioning state.

5.0 JOINT LEVEL: GLENOHUMERAL DISLOCATION

5.1 INTRODUCTION

The previous sections of this work evaluated injury to the glenohumeral capsule on the microstructural and tissue levels. On the microstructural level, it was found that collagen fiber alignment and maximum principal strain in the glenohumeral capsule can predict the location of tissue failure. Permanent deformation of the capsule was then shown to result in an increase in material properties during uniaxial extension. Specific Aim 3 of this dissertation will evaluate the effect of permanent deformation resulting from anterior dislocation on the function of the glenohumeral capsule from the joint level.

As described previously, other researchers have developed models to create permanent deformation in the glenohumeral capsule. One group developed a cadaveric injury model to simulate the thrower's shoulder which is characterized by excessive external rotation and very little internal rotation. [71] Permanent deformation of the capsule was created by forcing the humeral head into external rotation beyond the normal range of motion to simulate the increase in external rotation found in overhead athletes. Increases in anterior translation and external rotation were found following the creation of this injury. [71] This model was modified to create permanent deformation in the capsule by applying excessive internal and external rotation and used to evaluate capsular plication procedures. [72, 73] Although these permanent

deformation models no doubt created injury to the capsule as seen by the increased joint translations and rotations, the amount of permanent deformation was not quantified.

Malicky and coworkers were the first to quantify the amount of permanent deformation in the anteroinferior capsule resulting from glenohumeral subluxation. [68] In this work a method for determining a reference strain state in the glenohumeral capsule was developed [69] and used to quantify permanent deformation in the capsule via nonrecoverable strain. The maximum principal strain in the anteroinferior capsule during subluxation was also quantified [69] and later related to the resulting nonrecoverable strain [33]. Maximum principal strains during subluxation and the resulting nonrecoverable strains were found to be greater on the glenoid side of the anteroinferior capsule when compared to the humeral side. This is consistent with the location of clinical pathology such as the Bankart lesion. Although this model quantified the permanent deformation in the capsule, the effect of this dislocation on the function of the capsule was not evaluated.

The current work aims to combine concepts from these two previously described models in order to evaluate the effect of permanent deformation on the function of the glenohumeral capsule. Therefore, the overall goal of this section of the work was to develop an experimental injury model of the glenohumeral joint to create permanent deformation in the anteroinferior capsule by dislocating the joint anteriorly using robotic technology. This model will then be used to address Specific Aims 3a-c.

The magnitude of strain during anterior dislocation and the resulting nonrecoverable strain in the anteroinferior capsule will be quantified. Specific locations on the anteroinferior capsule experiencing the greatest damage will be identified as at-risk regions that should be targeted during repair procedures. Finally, the effect of anterior dislocation on the function of

the glenohumeral capsule will be evaluated by examining the strain distribution in the anteroinferior capsule, joint kinematics, in situ force in the capsule, and glenohumeral contact force during simulated clinical exams at three joint positions in the *intact* and *injured* joint.

5.1.1 Preliminary Studies

Glenohumeral dislocation had never been intentionally achieved on the robotic/UFS testing system in a controlled manner. Therefore, several preliminary studies were performed in order to determine the most appropriate and safe way to achieve this task. Initial intentions were that the robotic/UFS testing system would be used to translate the humeral head to the edge of the glenoid of each glenohumeral joint.

5.1.1.1 Repeatability of Anatomic Measurements

As the amount of translation to achieve glenohumeral dislocation is based on the anatomy of the humeral head and glenoid of each individual specimen, anatomic measurements needed to be made in order to determine how much translation was necessary to dislocate the joint. Typical definitions of glenohumeral dislocation are based on the anterior-posterior width of the glenoid. Therefore, the inter- and intra-observer repeatability was determined for the glenoid width measurement. Three observers were asked to measure the glenoid width from the inferior side of the joint using digital calipers (accuracy: 0.03 mm) on two glenohumeral joints. The capsule was still intact and the results were recorded by a fourth observer. Each observer measured the glenoid width four times in each shoulder and the results are shown in Table 5.1and Table 5.2. The glenoid width of the first shoulder was measured to be 30.2 ± 0.3 mm, 31.9 ± 1.2 mm, and 30.1 ± 0.4 mm by each of the three observers. For the second shoulder, the observers measured

the widths to be 31.1 ± 0.8 mm, 31.5 ± 1.1 mm, and 30.6 ± 0.5 mm. The difference between the maximum and minimum measurement made by each observer was computed. The maximum difference across all three observers for both shoulders was 2.4 mm. Therefore, the repeatability of the glenoid width measurement is 2.4 mm.

Table 5.1 Measurements of the glenoid width of specimen BRC1006037L by three observers.

	OBSERVER 1	OBSERVER 2	OBSERVER 3
MEASUREMENT 1	30.1	30.6	30.7
MEASUREMENT 2	29.9	32.9	29.6
MEASUREMENT 3	30.0	32.9	30.0
MEASUREMENT 4	30.7	31.2	30.1
MAXIMUM	30.7	32.9	30.7
MINIMUM	29.9	30.6	29.6
DIFFERENCE	0.8	2.4	1.0

Table 5.2 Measurements of the glenoid width of specimen 09-06250L by three observers.

	OBSERVER 1	OBSERVER 2	OBSERVER 3
MEASUREMENT 1	30.8	32.5	30.2
MEASUREMENT 2	32.0	32.3	30.7
MEASUREMENT 3	31.5	31.2	31.2
MEASUREMENT 4	30.3	30.1	30.2
MAXIMUM	32.0	32.5	31.2
MINIMUM	30.3	30.1	30.2
DIFFERENCE	1.7	2.4	1.0

5.1.1.2 Definition of Dislocation

Based on the repeatability of the glenoid width measurements, the definition of dislocation used in this work was when the humeral head has translated one half the maximum anterior-posterior width of the glenoid plus three millimeters in the anterior direction. The additional three millimeters is enough to account for the repeatability of the anatomic measurements as well as to ensure that the humeral head translated to the edge of the glenoid rim while accounting for any variability in the thickness of the glenoid labrum. This definition of dislocation moves the humeral head out of the glenoid but does not translate it over the glenoid rim. This is important because it allows the robotic/UFS testing system to repeat this motion without damaging other structures or the load cell. It also ensures that permanent deformation of the capsule will occur without creating a Bankart lesion or other capsular tear.

5.1.1.3 Modification of Robotic Code

The robotic/UFS sensor testing system has been used previously to apply forces and moments to the humerus, however, it had never been used to dislocate the glenohumeral joint. Therefore, modifications to the code had to be made to meet the objective of this section of the work based on the definition of dislocation. When running in force-control mode the robotic/UFS testing system moves the scapula with respect to the humerus in twenty steps to reach the applied force target in the first loading direction (anterior or posterior, depending upon shoulder side: right or left). The joint is then moved back to its initial position and the scapula is translated in the opposite direction. During this motion, the joint forces in all three directions (AP, SI, ML) are outputted to the screen. As the definition of dislocation is based on the translation of the humeral head, the code had to be modified to output the anterior translation values at each step along the loading path. The entire anterior-posterior path of motion is repeated three times to find the best

path to reach the applied force targets. When dislocating the joint, the translation must only occur once in the anterior direction and then the joint must be moved back to its initial position. In order to achieve this, the code was modified such that after each step along the loading path an option to stop and exit the program appears on the screen. Thus, after each loading step, the user can look at the anterior translation and decide if the joint has translated enough to meet the definition of dislocation. Once the anterior translation is sufficient, the user can stop the program and manually move the joint back to its initial position. The modified code can be found in Appendix C.

5.1.1.4 Force Required to Achieve Dislocation

The force limits on the universal force moment sensor which is attached to the end effecter of the robotic manipulator are ±450 N in the x- and y-directions and ±900 N in the z-direction. [182] When a glenohumeral joint is mounted in the system, the anterior-posterior direction corresponds to the x-direction. Therefore, when dislocating the joint, anterior-posterior forces must not exceed about ±330 N. In addition, safety checks are written in the code which will stop joint motion and exit the program when forces above this level are recorded. Therefore, a maximum of 300 N was applied in the anterior direction to dislocate each shoulder, as sometimes the force target can be overshot, particularly as the motion is occurring along the first loading path.

5.1.1.5 Reference Strain Configuration

The strain distribution in the anteroinferior capsule will be used to quantify the amount of tissue damage by computing the nonrecoverable strain, as well as to evaluate capsule function before and after glenohumeral dislocation. In order to compute strain, the reference strain configuration must be determined; however, this had never been done on the robotic/UFS testing system prior

to this work. Initial attempts were made to inflate the capsule at various points along the path of external rotation. However, when the 22 N compressive force is applied to the joint in order to center the humeral head on the glenoid, it is impossible to get the end of the hose from the air tank into the joint through the rotator interval to inflate the capsule. Therefore, a new reference path was established and termed the “Reference Strain Path”. This path was achieved by applying a 10 N distractive force and a 1 N-m torque to the humerus. This small distractive force created enough space between the humeral head and glenoid to insert the hose from the air tank and create a seal between the hose and the capsule. In order to determine the reference strain configuration the joint was moved to the positions along the Reference Strain Path which were closest to the previously established joint positions of 0°, ±5°, ±10°, ±15° internal/external rotation. All other aspects of the methodology used to determine the reference strain configuration were kept the same as previously reported. [9]

5.2 METHODS

Most of the methods utilized in this section of the work have been previously described in the literature. [9] An overview of the experimental loading conditions and corresponding strain states is provided**.**

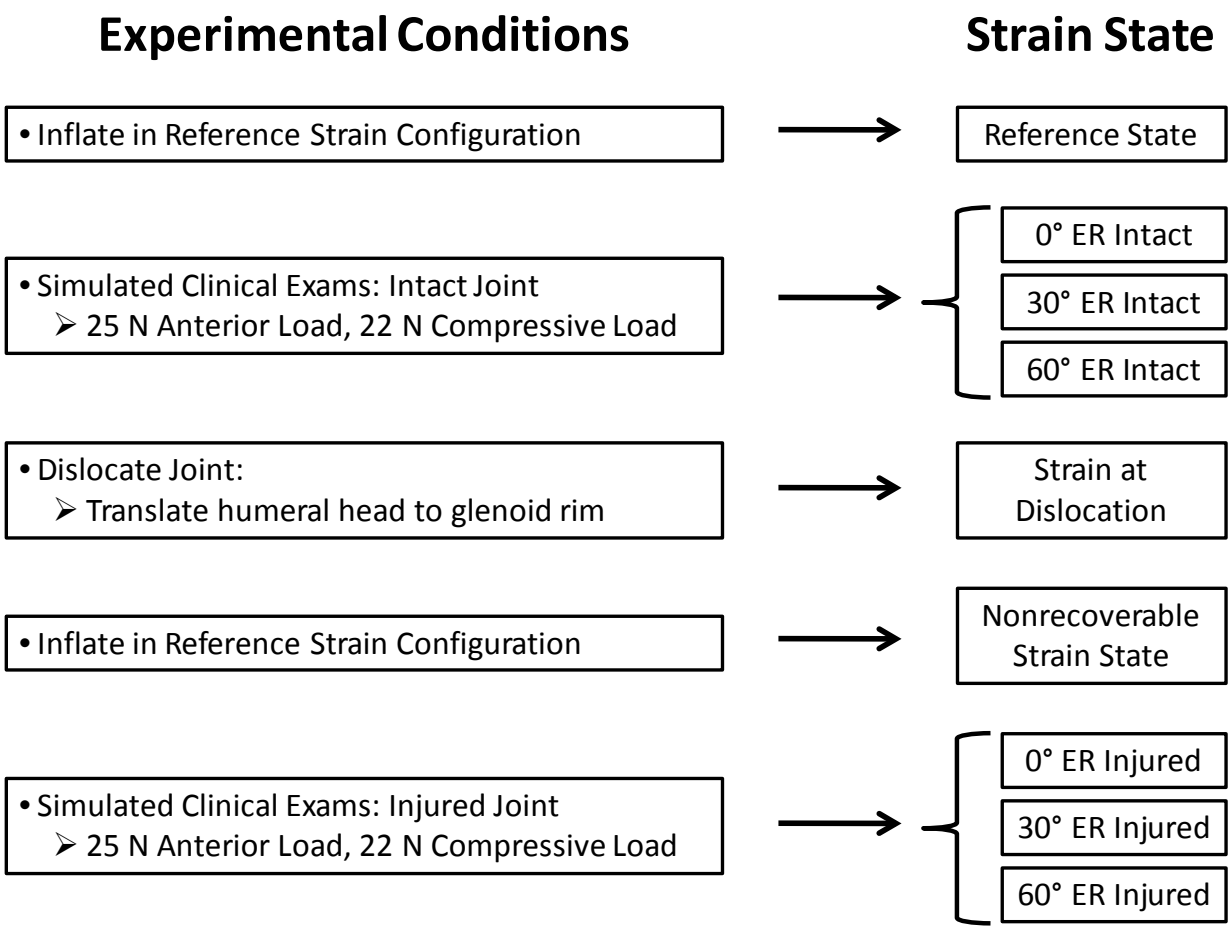

Figure 5.1 Flowchart of experimental loading conditions and corresponding strain states.

5.2.1 Specimen Preparation

Six fresh-frozen cadaveric shoulders (71 ± 8 yrs.) were stored at -20°C and thawed for 24 hours at room temperature prior to testing. The shoulders were dissected free of all skin and musculature leaving only the scapula, humerus, coracoacromial ligament, and glenohumeral capsule. Each joint was examined using radiographs and dissection, and determined to be free of pathology, osteoarthritis and any visible signs of injury. The AB-IGHL and PB-IGHL were identified by applying distraction and external/internal rotation to the joint as the bands are most visible in this position. [166] A 7 x 11 grid of delrin strain markers (1.6 mm diameter), painted

black, was then fixed to the anteroinferior capsule encompassing the AB-IGHL, axillary pouch and PB-IGHL. This divided the anteroinferior capsule into 60 elements. The first row of makers was placed just superior to the AB-IGHL and the last row was placed just superior to the PB-IGHL. Each marker was placed ~5 mm apart and ~10 mm from the insertion sites on the glenoid and humerus to ensure that only the tissue midsubstance was examined. Therefore, one or two columns of elements were placed on each band depending upon its width.

5.2.2 Robotic/Universal Force Moment Sensor Testing System

The humerus and scapula were fixed in epoxy putty and each joint was mounted to a robotic/UFS testing system that was used to apply external loads and torques to the humerus. [27] This 6-degree-of-freedom robotic manipulator (PUMA model 762, Unimate, Inc., Pittsburgh, PA) can run in force control and position control mode. When in position control, the robotic manipulator has a repeatability of 0.2 mm for position and 0.2° for orientation. When collecting force and moment data, the UFS (model 4015, JR3 Inc., Woodland, CA) has a repeatability of 0.2 N and 0.1 N·m, respectively. Custom clamps were designed previously to rigidly fix the humerus and scapula to the base and end effector of the robotic/UFS testing system, respectively. [6, 27, 182-188] When mounted each joint was placed at ~30° glenohumeral abduction, neutral horizontal abduction, and neutral external rotation. Neutral external rotation was achieved by palpating the humeral head articular cartilage and positioning the glenoid such that equal amounts of cartilage were on either side.

The robotic/UFS testing system requires a coordinate system about which motion of the joint can occur. This coordinate system was established using anatomic landmarks of each specimen as previously described. [27, 183, 184] In this testing system, joint forces and moments

are applied to the fixed humerus with respect to the scapula coordinate system. In order to determine the origin of the anatomic coordinate system of the scapula, the most anterior and most posterior point on the humeral head was measured with respect to the origin of the UFS. The point midway between these anatomic landmarks, the approximate center of the humeral head, was set to be the origin of the robotic/UFS testing system. The axes of the scapular coordinate system were defined as follows: the x-axis was perpendicular to the scapular plane with the positive axis pointed anteriorly, the y-axis was parallel to the medial border of the scapula with the positive axis pointed superiorly, and the z-axis was obtained from the cross-product of the x- and y-axes with the positive axis pointed medially. The joint rotations were defined as follows: rotation about the x-axis was abduction in the scapular plane and rotation about the long axis of the humeral head was internal and external rotation.

5.2.3 Reference Paths

Similar to previous studies, the path of passive glenohumeral abduction was achieved by applying a constant 22 N compressive force (in order to center the humeral head on the glenoid) and minimizing the forces applied to the humerus in the anterior/posterior and superior/inferior directions. Under force control mode the scapula was allowed to translate along all three axes in order to achieve the force targets. To determine the path of passive glenohumeral abduction, the robotic/UFS testing system positioned the joint from 10° to 70° of glenohumeral abduction in 1° increments. The joint was then positioned at 60° abduction for all loading conditions applied in this work. Next, the path of internal-external rotation was determined by applying a 3 N-m torque to the humerus while maintaining the constant 22 N joint compressive force. Once the path was achieved, points along the loading path which most closely corresponded to 0°, 30° and

60° of external rotation were identified. Finally, one additional reference path was needed for this work as the reference strain configuration was to be determined with the joint positioned on the robotic/UFS testing system as described in Section 5.1.1.5. The reference strain path was determined by applying a 1 N-m torque to the humerus while maintaining a constant 10 N joint distractive force. Once the path was achieved, points along the loading path which most closely corresponded to 0°, ±5°, ±10° and ±15° of internal and external rotation were identified.

5.2.4 Calibration of the Motion Tracking System

The positions of the 77 strain markers on the surface of the anteroinferior capsule are required to compute strain. A three-camera motion tracking system (Spicatek, Maui, HI; accuracy: 0.05 mm) was used to capture the locations of the strain markers throughout the experimental protocol. Prior to determining the reference strain configuration, the motion tracking system needed to be calibrated for a camera configuration that ensured each strain marker would be visible by at least two cameras at all times. In order to do this, the cameras were initially positioned with the joint at 60° of glenohumeral abduction and neutral external rotation. The joint was then positioned at 5°, 10°, 15°, 30° and 60° of external rotation, and 5°, 10° and 15° of internal rotation and the locations of the cameras were adjusted such that all strain markers could be imaged by at least two cameras in all relevant joint positions. The joint was then removed from the robotic/UFS testing system by detaching the scapular clamp from the end effector and unscrewing and removing the base/humerus. The three dimensional calibration cube (approximate working volume: 0.002 m^3) was then placed on the end effector which was moved to a pre-defined position (#CAMERA). This position was determined during preliminary studies to be a position in which all three cameras could typically image all markers on the calibration cube. If minor

adjustments were needed, the teach pendent was used to move the end effector until all markers were visible by all cameras. The three-camera motion tracking system was then calibrated by identifying the locations of the markers on the calibration cube.

5.2.5 Reference Strain Configuration

Next, the reference strain configuration was determined. The process for determining the reference strain configuration was originally described by Malicky and coworkers [68] and then modified for use in our laboratory [8, 9]. As the glenohumeral capsule is a complex, sheet-like ligament, determining a reference strain configuration is much more complicated than for a uniaxial ligament such as the MCL. Depending on the joint position, portions of the capsule may be wrinkled or folded. In order to eliminate these wrinkles and folds and to establish an appropriate reference strain configuration, the capsule was inflated with compressed air. The joint was positioned at 60° of glenohumeral abduction, neutral horizontal abduction and neutral internal/external rotation. Using the robotic/UFS testing system, the joint was moved along the reference strain path (Section 5.2.3) and inflated at the points along the loading path which most closely corresponded to 0°, ±5°, ±10° and ±15° of internal and external rotation. Specifically, the capsule was inflated to 0.7 kPa (0.7 Psi) and 4.8 kPa (0.9 Psi) in position of internal/external rotation and the positions of the strain markers were recorded for both pressures using a three-camera motion tracking system.

If the wrinkles and folds in the capsule were eliminated, there would be minimal marker motion between the two inflation pressures at a particular joint position. Thus, the joint position in which the smallest average marker motion occurred between the two inflation pressures, with no marker moving more than 1 mm, was selected as the reference strain configuration. The joint

was then positioned in the reference strain configuration and inflated to 1.0 kPa (0.75 Psi). The position of the strain markers under this inflation pressure were used as the reference state for all strain calculations.

5.2.6 Simulated Clinical Exams – *Intact* Capsule

In order to evaluate the function of the *intact* glenohumeral capsule, a simulated clinical exam was performed at three clinically relevant joint positions: 60° of glenohumeral abduction and 0°, 30°, and 60° of external rotation. At these joint positions, a 25 N anterior-posterior load was applied to the humerus, while maintaining the 22 N compressive load. The resulting joint kinematics were recorded. The positions of the strain markers were then captured at the point along the loading path corresponding to the 25 N anterior load for all three joint positions (0° ER *Intact*, 30° ER *Intact*, 60° ER *Intact*). Previous work has shown that an anterior-posterior load of 25 N is enough to translate the humeral head to the edge of the glenoid but not to dislocate the joint, particularly at 0° of external rotation in which the capsule plays a minimal role in joint stability.

5.2.7 Glenohumeral Dislocation

Each joint was dislocated at 60° of abduction and 60° of external rotation by applying a maximum of 300 N anterior load to the humerus (Section 5.1.1.4), while maintaining the 22 N compressive force. The anterior load was applied in order to apply enough force to ensure that the translation target would be reached. The humeral head was allowed to move in all three translational degrees of freedom until the anterior translation reached one half the maximum

anterior-posterior width of the glenoid plus three millimeters. The positions of the strain markers were captured when the joint was dislocated. Following dislocation, the joint was returned to 60° of abduction and 0° of external rotation and allowed to recover for 30 minutes. [42, 173] This recovery period was to be sure that any changes observed in strain, joint kinematics, or joint forces were a result of permanent deformation of the capsule and not due to the viscoelastic properties of the soft tissue.

5.2.8 Nonrecoverable Strain

Following the recovery period, the capsule was positioned in the reference strain configuration and re-inflated to 1.0 kPa (0.75 Psi). The positions of the strain markers were recorded and served as the nonrecoverable strain state.

5.2.9 Simulated Clinical Exams – *Injured* Capsule

In order to evaluate the function of the *injured* glenohumeral capsule, the simulated clinical exams were repeated at 60° of glenohumeral abduction and 0°, 30°, and 60° of external rotation. At these joint positions, a 25 N anterior-posterior load was applied to the humerus, while maintaining the 22 N compressive force and the resulting joint kinematics were recorded. The positions of the strain markers were then captured at the point along the loading path corresponding to the 25 N anterior load for all three joint positions (0° ER *Injured*, 30° ER *Injured*, 60° ER *Injured*).

5.2.10 In Situ Force in Capsule

In order to determine the effect of dislocation on the *in situ* force in the capsule, the previously recorded *intact* kinematics for the simulated clinical exams at 0°, 30° and 60° of ER were reproduced on the *injured* shoulders and the resulting joint forces recorded. The entire glenohumeral capsule was then removed from the joint without damaging the glenoid labrum. In order to determine the glenohumeral contact forces, the previously recorded *intact* and *injured* kinematics for the simulated clinical exams at 0°, 30° and 60° of ER were reproduced on the bones only while recording the resulting joint forces.

Using the principle of superposition, the forces recorded after the capsule was removed were subtracted from the forces obtained before the capsule was removed for the *intact* joint during *intact* kinematics and for the *injured* joint during both the *intact* and *injured* kinematics during the simulated clinical exams. In this manner, the *in situ* forces in the *intact* capsule during *intact* kinematics and in the *injured* capsule during both the *intact* and *injured* kinematics were obtained for each specimen. Significance was set at $\alpha = 0.05$.

5.2.11 Data Analysis

Several analyses were performed in order to address the various sub-aims of Specific Aim 3.

5.2.11.1 Maximum principal Strains

In order to address Specific Aim 3a, the magnitude of maximum principal strain during anterior dislocation and the resulting nonrecoverable strain in the anteroinferior glenohumeral capsule were quantified. The strain marker positions at each strained state were compared to the marker

positions in the reference state using the finite element soft ware package (ABAQUS). Maximum principal strain was computed at the centroid of all elements in the AB-IGHL and axillary pouch for each specimen. Previous work has shown that the repeatability of the maximum principal strains utilizing the entire testing procedure outlined here is 3.5%. [7] Therefore, any maximum principal strains less than 3.5% can be considered negligible (~0%) and any differences less than 3.5% cannot be detected using the current experimental methodology.

Strain at Dislocation

The maximum principal strain at dislocation was determined by comparing the strain marker positions during dislocation to the marker positions in the reference state. The average and peak maximum principal strains in the AB-IGHL and axillary pouch were computed. The strain distributions were not normally distributed therefore nonparametric analyses were performed. In order to compare the strain distribution between the two capsule regions the average and peak maximum principal strains for each of the six specimens were compared between the AB-IGHL and axillary pouch using a Wilcoxon Signed Ranks test. Previous evaluations of the strain distributions in the anteroinferior capsule have shown a wide range of variability between shoulders [7-9, 43, 93, 134]; therefore, it may be more appropriate to compare the strain in the AB-IGHL and axillary pouch on a specimen-by-specimen basis. In order to do this, the maximum principal strains in all elements of the AB-IGHL were compared to the maximum principal strains in all elements of the axillary pouch for each individual shoulder using a Mann-Whitney test.

Nonrecoverable Strain

The maximum principal nonrecoverable strain was determined by comparing the strain marker positions in the nonrecoverable strain state to the marker positions in the reference state and was used to quantify permanent deformation of the capsule resulting from anterior dislocation. The average and peak maximum principal nonrecoverable strains in the AB-IGHL and axillary pouch were computed. Analysis of the nonrecoverable strains was similar to the strain at dislocation. The strain distributions were not normally distributed therefore nonparametric analyses were performed. In order to compare the nonrecoverable strain distribution between the two capsule regions the average and peak maximum principal nonrecoverable strains for each of the six specimens were compared between the AB-IGHL and axillary pouch using a Wilcoxon Signed Ranks test. In order to compare the strain in the AB-IGHL and axillary pouch on a specimen-by-specimen basis, the maximum principal nonrecoverable strain in all elements of the AB-IGHL were compared to the maximum principal strain in all elements of the axillary pouch for each individual shoulder using a Mann-Whitney test. Finally, the Spearman's rho correlation coefficient was computed between average and peak strains at dislocation and the average and peak nonrecoverable strains. The critical value for Spearman's correlation coefficients for a sample size of n = 6 and significance set at $\alpha = 0.05$ is r = 0.81. [180] Therefore, correlations were considered statistically significant when $0.9 \leq |r| < 1.0$. Further, the correlation was considered moderate for $0.5 \leq |r| < 0.8$, weak for $0.0 \leq |r| < 0.5$. [181]

Strain During Simulated Clinical Exams

Finally, the maximum principal strain during the simulated clinical exams was determined by comparing the strain marker positions during the simulated clinical exams on the *intact* and *injured* joints to the marker positions in the reference state. The average and peak maximum principal strains in the AB-IGHL and axillary pouch were computed for all six clinical exams: 0° ER *Intact*, 30° ER *Intact*, 60° ER *Intact*, 0° ER *Injured*, 30° ER *Injured*, 60° ER *Injured*. Comparison between the strain distributions in the *intact* and *injured* capsule at each joint position will be presented in a later section (Section 5.2.11.3)

5.2.11.2 Analysis of Capsule Sub-Region Strains

In order to address Specific Aim 3b, the maximum principal strains in the anteroinferior capsule were divided into six sub-regions to determine if specific locations are at risk for injury during anterior dislocation. These sub-regions were 1) posterior axillary pouch glenoid side (PPG), 2) posterior axillary pouch humeral side (PPH), 3) anterior axillary pouch glenoid side (APG), 4) anterior axillary pouch humeral side (APH), 5) anterior band glenoid side (ABG), and 6) anterior band humeral side (ABH).

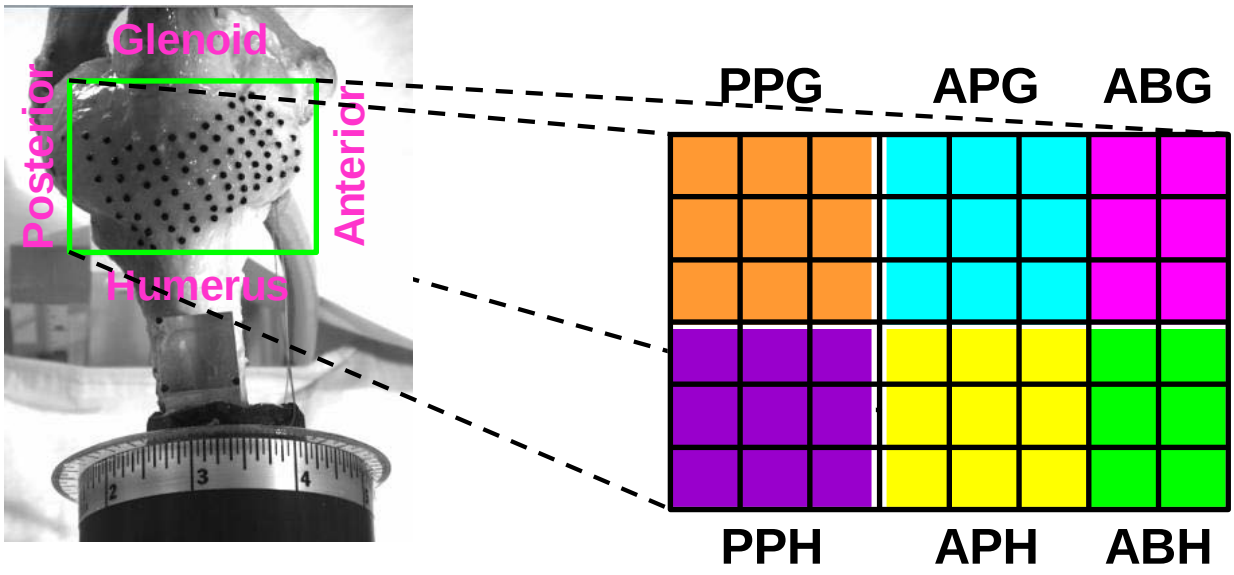

Figure 5.2 Anteroinferior capsule divided into six sub-regions: 1) posterior axillary pouch glenoid side (PPG, orange), 2) posterior axillary pouch humeral side (PPH, purple), 3) anterior axillary pouch glenoid side (APG, blue), 4) anterior axillary pouch humeral side (APH, yellow), 5) anterior band glenoid side (ABG, pink), and 6) anterior band humeral side (ABH, green).

The average and peak maximum principal strains at dislocation and the average and peak maximum principal nonrecoverable strains were determined for each sub-region. Strain data in each capsule sub-region was not normally distributed; therefore, a Friedman test with Wilcoxon Signed Rank post-hoc tests was used to compare the strain at dislocation and the nonrecoverable strain between the glenoid and humeral sides and between capsule sub-regions. Statistical significance was set at $\alpha = 0.05$.

Strain Ratios

As previous evaluations of the strain distributions in the anteroinferior capsule have shown a wide range of variability between shoulders [7-9, 43, 93, 134] the most appropriate comparison would be one in which this variability was eliminated. In order to do this a strain ratio was computed for each element by normalizing the maximum principal strain at dislocation to the peak maximum principal strain at dislocation for each individual specimen. Elements

containing strains less than the experimental repeatability of 3.5% (zero strain) were excluded from analyses. This process was repeated on the nonrecoverable strains. Strain ratios, which were normally distributed, were then compared between capsule sub-regions using an ANOVA with t-test post-hoc tests. Significance was set at $\alpha = 0.05$.

Similarly, strain ratios were computed for the strain distributions in the anteroinferior capsule during the simulated clinical exams and compared between the *intact* and *injured* joint states. However, as paired comparisons need to be made between the two states of each specimen two changes were made to the analysis. First, strain ratios were computed by normalizing the maximum principal strains in each element in the *intact* and *injured* joint states to the peak maximum principal strain in the *intact* state for each specimen. Second, any elements containing strains less than the experimental repeatability of 3.5% were set to zero rather than eliminated from the analysis. This allowed differences to be detected between the *intact* and *injured* states when elements which were initially unloaded became loaded following dislocation. Strain ratios during the simulated clinical exams were not normally distributed and were therefore compared between the *intact* and *injured* joint states using Wilcoxon Signed Rank tests at each joint position. Significance was set at $\alpha = 0.05$ and differences of $p < 0.1$ were also noted.

In order to relate changes in the maximum principal strain between the *intact* and *injured* joint states to the amount of tissue damage the nonrecoverable strain ratios in each capsule sub-region were correlated to the change in strain ratios during the simulated clinical exams at 0°, 30° and 60° of external rotation. The Spearman's Rho correlation coefficient was computed with significance set at $\alpha = 0.05$.

5.2.11.3 Evaluation of Capsule Function

To address Specific Aim 3c, the effect of dislocation on the function of the glenohumeral capsule was evaluated by examining the strain distribution in the anteroinferior capsule, joint kinematics, in situ force in the capsule and glenohumeral contact forces in the *intact* and *injured* joint states.

Strain Distribution in Anteroinferior Capsule

As previously described, maximum principal strain was computed by comparing the 3D marker positions in the reference position to the *nonrecoverable strain state* and to the positions in which the 25 N anterior load was applied at each external rotation angle for both the *intact* and *injured* shoulders using the finite element solver ABAQUS. The strain distributions between the *intact* and *injured* states at 0°, 30° and 60° ER were compared for each shoulder using projection plots. [189, 190] For each distribution, the strain values were grouped into 100 quantiles and projection plots were created by plotting quantile difference values (*injured* - *intact*) vs. average quantile values (paired *intact* and *injured*). The mean (y-axis offset) and range of the quantile differences was computed for each comparison. The range was defined as the difference between the maximum and minimum quantile difference and quantified differences between the *intact* and *injured* strain distributions at 0°, 30° and 60° ER. Therefore, higher mean and range values are indicative of greater differences between two strain distributions. Mean and range values were compared between the three joint positions using Friedman tests with Wilcoxon Signed Rank post-hoc tests. In order to determine if the amount of tissue damage was related to the change in strain distribution between the *intact* and *injured* states, Spearman rank correlation coefficients were computed between the mean and range of the projection plots at 0°, 30° and 60° of external rotation and the peak nonrecoverable strain in the anteroinferior capsule.

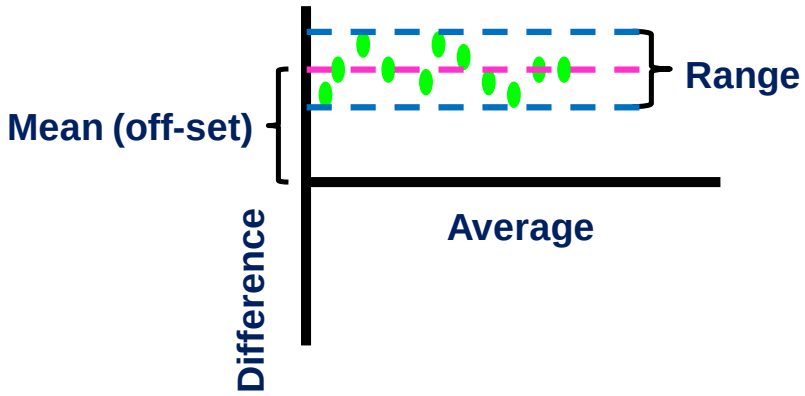

Figure 5.3 Projection plot schematic showing definitions of mean and range of the quantile difference values.

Joint Kinematics

Joint kinematics were recorded during dislocation and in response to the 25 N anterior-posterior load applied during the simulated clinical exams at all three joint positions. The joint translations in all three directions with the 25 N anterior and posterior loads applied were identified. Anterior and posterior joint translations in response to the simulated clinical exam were compared between the *intact* and *injured* joint at 0°, 30° and 60° of external rotation using a paired t-test. Superior-inferior joint translations, with the 25 N anterior load applied, were compared using a Wilcoxon Signed Rank test as they were not normally distributed. Medial-lateral translations, with the 25 N anterior load applied, were normally distributed and were therefore compared using a paired-test. Significance was set at $\alpha = 0.05$.

In Situ Force in Capsule

Friedman tests with Wilcoxon Signed Rank post-hoc tests were used to compare magnitude of the *in situ* force in the *intact* capsule during *intact* kinematics and the *injured* capsule during *intact* and *injured* kinematics at all three joint positions.

Glenohumeral Contact Forces

Wilcoxon Signed Rank tests were also used to compare the magnitude of the resultant glenohumeral contact forces between the *intact* and *injured* joint at 0°, 30° and 60° of external rotation. Significance was set at $\alpha = 0.05$.

5.3 RESULTS & DISCUSSION

5.3.1 Reference Strain Configuration

The reference strain configuration varied between internal and external rotation angles for all six shoulders. The reference strain configurations at 60° of abduction were found to be 5° IR, 10° ER, 15° IR, 15° ER, 15° ER, and 10° ER for each of the six shoulders.

5.3.2 Glenohumeral Dislocation

5.3.2.1 Results

Each glenohumeral joint was considered to be dislocated when the humeral head translated one half the maximum anterior-posterior width of the glenoid plus three additional millimeters. The maximum anterior-posterior glenoid width was 32 ± 4 mm. In order to achieve glenohumeral dislocation, an anterior force of 244 ± 74 N was applied to the shoulders and the resulting anterior translation was 18 ± 2.2 mm. (Table 5.3) As the robotic/UFS testing system was running in force control mode during joint dislocation, the exact anterior translation was not controlled. Joint motion was stopped at the step with an anterior translation closest to the desired target.

One specimen (H01107R) hit the force limit of the robotic/UFS testing system during dislocation just as the anterior translation was within the repeatability of the anatomic measurements.

Table 5.3 Maximum anterior-posterior glenoid width, anterior force required to achieve dislocation and the resulting anterior translation during dislocation for each specimen.

SPECIMEN #	Glenoid Width (mm)	Anterior Force (N)	Anterior Translation (mm)
H00915L	32	258	18.8
H00925R	34	286	21.3
H01015R	32	290	20.1
H01022L	26	115	15.8
H01029L	38	201	20.7
H01107R	32	316	16.9

During dislocation, the joint translated anteriorly and inferiorly. The kinematics during dislocation can be found in Appendix D.

5.3.2.2 Discussion

To address Specific Aim 3, an experimental joint injury model was developed to create permanent deformation (nonrecoverable strain) in the anteroinferior capsule by dislocating the joint anteriorly. This work simulated one mechanism of glenohumeral dislocation: anterior dislocation resulting from an excessive force applied to the humerus in the anterior direction. This mechanism was chosen to create injury to the anteroinferior capsule resulting in anterior instability. In response to the anterior force, all joints translated anteriorly and inferiorly. In order to achieve the anterior translations required to push the humeral head to the edge of the glenoid, anterior forces of around 250 N were required. Therefore, about 56 lbs is required to

dislocate the glenohumeral joint without the shoulder muscles present implying that much larger forces are required to dislocate the shoulder in vivo.

5.3.3 Maximum Principal Strains

In order to address Specific Aim 3a, the maximum principal strain in the anteroinferior capsule during dislocation, the resulting nonrecoverable strain, and the strain distribution during the simulated clinical exams were quantified.

5.3.3.1 Strain at Dislocation: Results

Maximum principal strain distributions in the anteroinferior capsule during joint dislocation varied from specimen to specimen. (Figure 5.4) For all fringe plots anterior is to the right, posterior is to the left, the glenoid side of the capsule is towards the top, and the humeral side is towards the bottom. The AB-IGHL and axillary pouch are separated by the black line. Lower maximum principal strain values are shown in blue and higher values are shown in green.

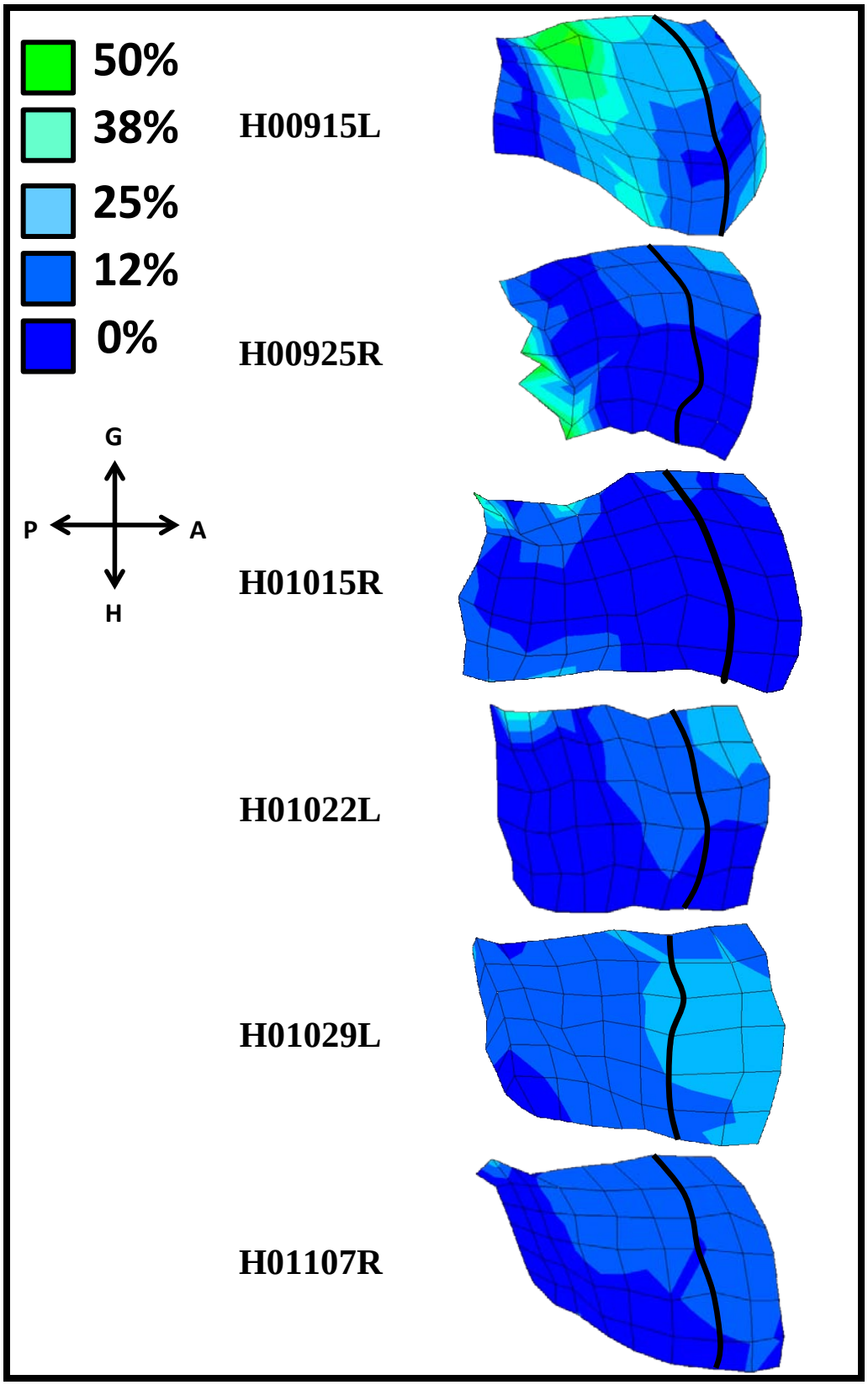

Figure 5.4 Fringe plots of the maximum principal strain distribution in the anteroinferior capsule during dislocation for all six shoulders. The black line separates the AB-IGHL and axillary pouch.

The average maximum principal strain across all specimens was 17.9 ± 4.8% in the AB-IGHL and 14.1 ± 8.1% in the axillary pouch. (Table 5.4). Peak strains in both regions were much larger: 29.9 ± 5.2% in the AB-IGHL and 47.2 ± 31.6 in the axillary pouch.

Table 5.4 Average and peak maximum principal strain in the anteroinferior capsule during joint dislocation at 60° of abduction and 60° of external rotation for all six specimens. The p-values resulting from the individual Mann-Whitney tests comparing strain in the AB-IGHL and axillary pouch for each shoulder are also shown.

SPECIMEN #	AB-IGHL		Axillary Pouch		Mann-Whitney Test
	MEAN ± SD	PEAK	MEAN ± SD	PEAK	p-value
H00915L	16.2 ± 7.7	31.2	29.1 ± 25.3	109.7	0.06
H00925R	11.3 ± 9.7	27.9	11.9 ± 12.4	48.2	0.82
H01015R	21.3 ± 7.5	33.5	10.9 ± 10.5	33.1	0.01
H01022L	17.6 ± 13.6	35.0	7.3 ± 9.5	35.4	0.01
H01029L	25.2 ± 4.0	31.5	17.0 ± 8.0	31.7	0.001
H01107R	15.9 ± 3.5	20.4	8.3 ± 6.7	24.9	0.001

No significant differences were found when comparing the average ($p = 0.46$) and peak ($p = 0.09$) maximum principal strains in each specimen between regions using the Wilcoxon Signed Rank test. Due to the wide variation in strain distributions between specimens the maximum principal strains in each element of the AB-IGHL and axillary pouch were compared on a specimen by specimen basis. These comparisons yielded significant differences between the AB-IGHL and axillary pouch in five of the six specimens. (Table 5.4) Strains in the AB-IGHL during dislocation were significantly higher compared to the axillary pouch in four of the specimens.

5.3.3.2 Strain at Dislocation: Discussion

Compare to Literature

Malicky and coworkers subjected the glenohumeral joint to varying degrees of subluxation, the maximum of which was similar to the anterior translations reached in the current work, 18 mm, based on our definition of dislocation. [69] At this level of subluxation, average and peak maximum principal strains around 15% and 30%, respectively, were reported. In the current work, average and peak strains were slightly higher, with peak strains ranging from 25% to 110%. The difference in strains between these two studies could be due to the different constraints placed on joint motion in each study. Malicky and coworkers constrained the joints to two degrees-of-freedom, one translational and one rotational. In the current work, only the joint orientation was constrained; an anterior force was then applied to the humerus and the joint was allowed to move freely in all three translational degrees of freedom. Therefore, the strain distributions observed in this study may be more representative of the in vivo scenario.

Significance of Results

Initially, the average and peak maximum principal strains across all specimens were compared between regions of the anteroinferior capsule and no differences were found. The average and peak strain in all elements contained within each capsule region was computed for each specimen. These values were then compared between specimens. In this way, the strain values were averaged twice. Taking the average of the average combined with the large variability in strain magnitude within regions and between specimens essentially washed away any differences between the regions within each specimen. For that reason, strain distributions were analyzed on a specimen-by-specimen basis. When the average strain in all elements

contained within the AB-IGHL was compared to the average strain in the axillary pouch of one specimen at a time significant differences were found between the capsule regions. However, the capsule region containing the highest strain varied between specimens. Strains in the AB-IGHL were larger than in the axillary pouch in four of the six specimens. Although one region of the capsule may experience higher strains than another, the region experiencing the highest strains is not the same in all specimens. This supports the recent findings that the anatomic description of the glenohumeral capsule as individual regions, does not correspond to its functional role. In addition, experimental strain distributions in the capsule should be evaluated on a specimen-by-specimen basis, further divided into sub-regions, or normalized in order to counteract the specimen variability.

The strain distributions varied significantly from specimen to specimen. Peak strains during dislocation ranged from 20% to 109% across all specimens. One specimen experienced abnormally large strains (109%) and was further investigated. Several elements in the posterior axillary pouch contained strains over 100% and when compared with photographs taken of this specimen during dislocation these high magnitudes were reasonable. The posterior axillary pouch was clearly being pulled between the humeral head and glenoid for this particular specimen. Large variations in strains make comparing between specimens exteremly difficult. To account for these differences, future analyses will normalize strain magintueds to the peak strain for that specimen when computing the strain ratio. The strain ratios will then be used to make conclusions across all specimens.

5.3.3.3 Nonrecoverable Strain: Results

The amount of nonrecoverable strain resulting from dislocation varied between specimens but was typically less than 12%. (Figure 5.5)

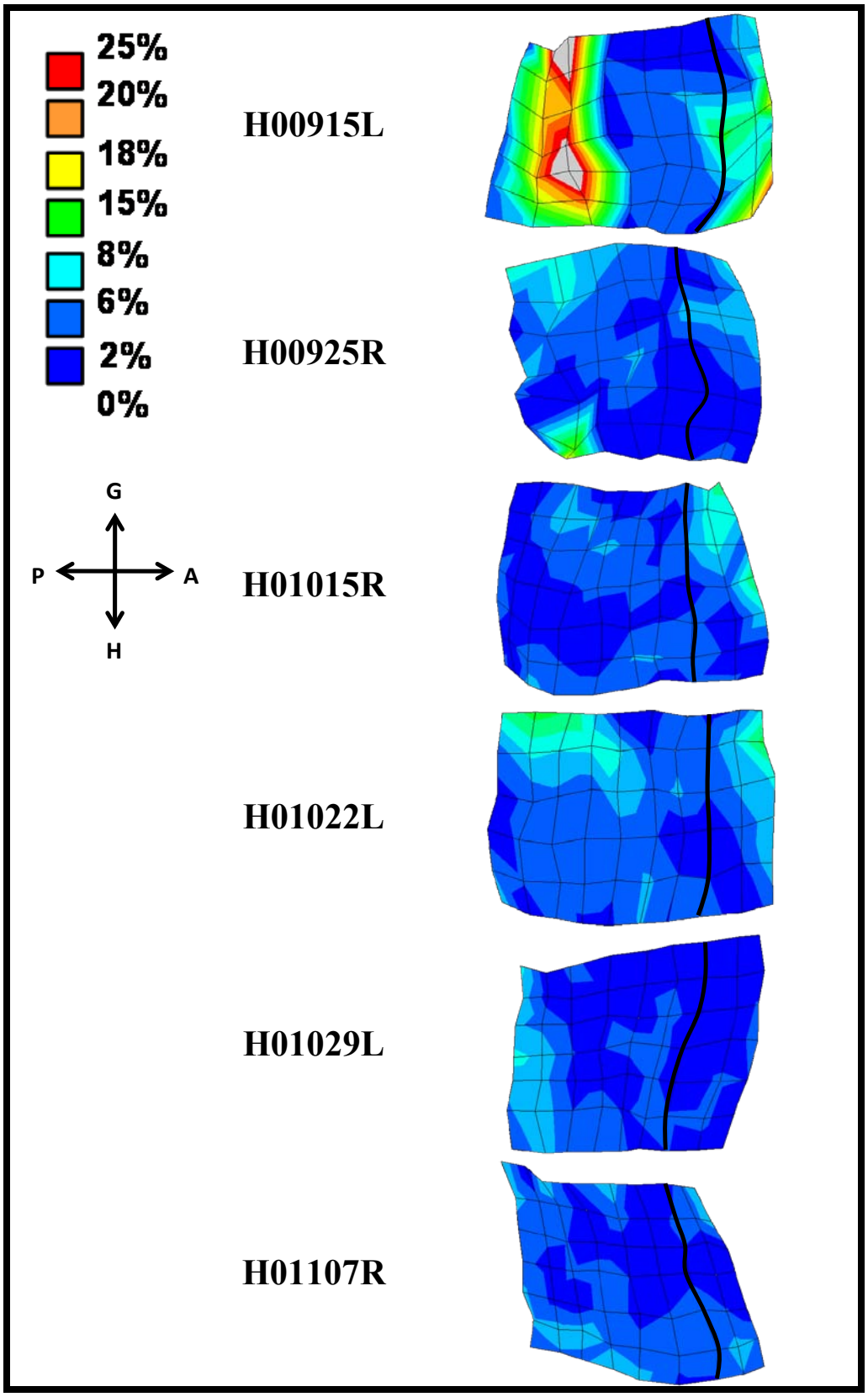

Figure 5.5 Fringe plots of the maximum principal nonrecoverable strain distribution in the anteroinferior capsule for all six shoulders. The black line separates the AB-IGHL and axillary pouch.

The average maximum principal nonrecoverable strain across all specimens was 2.5 ± 1.1% in the AB-IGHL and 3.1 ± 2.5% in the axillary pouch. (Table 5.5). On average, nonrecoverable strains were not larger than the experimental repeatability (3.5%). However, peak nonrecoverable strains were much larger: 7.1 ± 3.6% in the AB-IGHL and 13.9 ± 16.1% in the axillary pouch.

Table 5.5 Average and peak maximum principal nonrecoverable strain in the anteroinferior capsule for all six specimens.

SPECIMEN #	AB-IGHL		Axillary Pouch		Mann-Whitney Test
	MEAN ± SD	PEAK	MEAN ± SD	PEAK	p -value
H00915L	4.2 ± 4.7	12.7	8.2 ± 14.3	46.5	0.92
H00925R	2.1 ± 2.0	5.9	2.3 ± 2.7	11.8	0.88
H01015R	2.7 ± 3.1	7.5	1.4 ± 1.4	5.0	0.54
H01022L	2.9 ± 2.7	9.0	2.6 ± 1.9	7.2	0.97
H01029L	0.8 ± 0.9	2.4	2.2 ± 2.2	7.3	0.07
H01107R	2.0 ± 1.8	4.8	1.8 ± 1.6	5.5	0.83

No significant differences were found when comparing the average ($p = 0.67$) maximum principal nonrecoverable strains in each specimen between regions using the Wilcoxon Signed Rank test. However, peak maximum principal nonrecoverable strains in the axillary pouch were significantly larger than those in the AB-IGHL ($p = 0.03$). Taking the average of an average tends to mask differences that may in fact exist on a specimen-by-specimen basis, especially when dealing with strains so close to the experimental repeatability. Thus the nonrecoverable strains in each element of the AB-IGHL and axillary pouch were compared on a specimen-by-specimen basis. These comparisons yielded no significant differences between the AB-IGHL and axillary pouch in any of the six specimens. (Table 5.5) One specimen had a p-value of 0.07,

exhibiting a trend toward significantly greater nonrecoverable strains in the axillary pouch compared to the AB-IGHL. However, only four of the elements in this specimen had nonrecoverable strain values greater than the experimental reputability, and all of these elements were in the axillary pouch.

In order to determine if there was a correlation between the amount of strain at dislocation and the resulting nonrecoverable strain Spearman's rho correlation coefficients were computed. Correlations between the average strain at dislocation and the average nonrecoverable strain were weak (AB-IGHL: $r = -0.14$, axillary pouch: $r = 0.31$). The peak strain in the AB-IGHL was also weakly correlated to the peak nonrecoverable strain ($r = 0.37$). However, a moderate correlation ($r = 0.71$, $p = 0.11$) between the peak strain in the axillary pouch and the peak nonrecoverable strain was found.

5.3.3.4 Nonrecoverable Strain: Discussion

Compare to Literature

Malicky and coworkers quantified the amount of nonrecoverable strain in the anteroinferior capsule resulting from glenohumeral joint subluxation. [68] At 18 mm of joint subluxation, similar to the anterior translation applied in the current work to achieve dislocation, average and peak nonrecoverable strains between 5 and 10% and 15 and 25%, respectively, were reported. In the current work, nonrecoverable strains of similar magnitudes were observed. Therefore, the amount of damage created in the anteroinferior capsule was similar between the two studies. This implies that the 18 mm translation required for subluxation in some shoulders was probably close to our definition of dislocation, and this experimental injury model is reasonable for producing injury to the capsule. The definition of dislocation used in the current

study moved the humeral head out of the glenoid, but did not push it over the rim, thus allowing the robotic/universal force-moment sensor testing system to repeat this motion without damaging other structures.

Previous studies have shown a decrease in capsule volume of approximately 50% after an open capsular shift procedure [191, 192]. Since surgical procedures often over-tighten the capsule [193], injury from permanent deformation was estimated to increase the capsule volume by 20-40%. Representing the capsule as a sphere, it was determined that a 20-40% volumetric increase from injury would correspond to an average non-recoverable surface strain of 6-12% on the inferior glenohumeral ligament. These calculations support the nonrecoverable strains found in the current work as well as the work by Malicky and coworkers.

Significance of Results

Nonrecoverable strains in the anteroinferior capsule resulting from dislocation varied from specimen to specimen and many elements contained values less than the experimental repeatability. However, specific areas of the capsule experienced large nonrecoverable strains, up to 46%, implying that there were localized regions of the capsule damaged during dislocation. When comparing the average nonrecoverable strain for all specimens between the AB-IGHL and axillary pouch no differences were found. Similar to the strain at dislocation, the nonrecoverable strains in the AB-IGHL and axillary pouch were compared on a specimen-by-specimen basis, however, still no differences were found between capsule regions. This suggests that although certain capsule regions may experience higher strains during dislocation, damage occurs throughout the entire anteroinferior capsule. However, peak maximum principal nonrecoverable strains in the axillary pouch were significantly larger than those in the AB-IGHL indicating that localized regions of the capsule may experience more severe damage.

5.3.3.5 Strain During Simulated Clinical Exams: Results

The maximum principal strain distributions in the anteroinferior glenohumeral capsule during the simulated clinical exams were variable between specimens. As the joint position during the simulated clinical exams increased from 0° to 30° to 60° of external rotation, the deformed shape of the capsule changed. It was clear that the capsule was wrapping around the humeral head in positions of increased external rotation.

The strain distributions during the simulated clinical exams in the *intact* and *injured* joint are shown below for all six specimens. For all fringe plots anterior is to the right, posterior is to the left, the glenoid side of the capsule is towards the top, and the humeral side is towards the bottom. The AB-IGHL and axillary pouch are separated by the black line. Lower maximum principal strain values are shown in blue and higher values are shown in green. Visually, differences in the strain distributions between each state were observed. As the amount of external rotation increased from 0° to 30° to 60° strains increased on the glenoid side as seen by the increasing amount of green and yellow elements towards the top of the fringe plots. Although the amount of increase in strain varied between specimens this trend was always evident and is consistent with previous work. [9] Differences were also observed between the intact and injured joint states. In some specimens strains increased following dislocation while in others strains decreased. In general, regions of high strain tended to shift posteriorly following dislocation at all three joint positions.

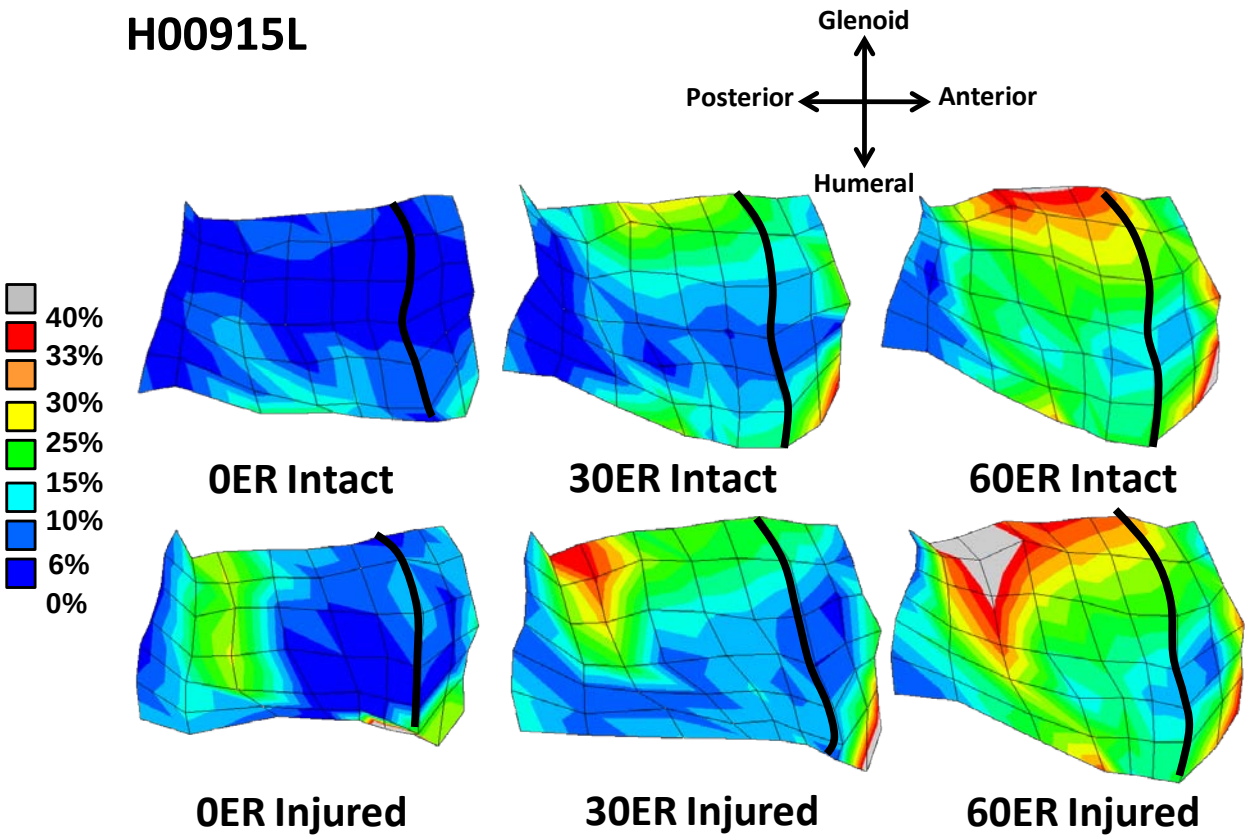

Figure 5.6 Fringe plots of the maximum principal strain distribution in the *intact* and *injured* anteroinferior capsule during the simulated clinical exams for specimen H00915L. The black line separates the AB-IGHL and axillary pouch.

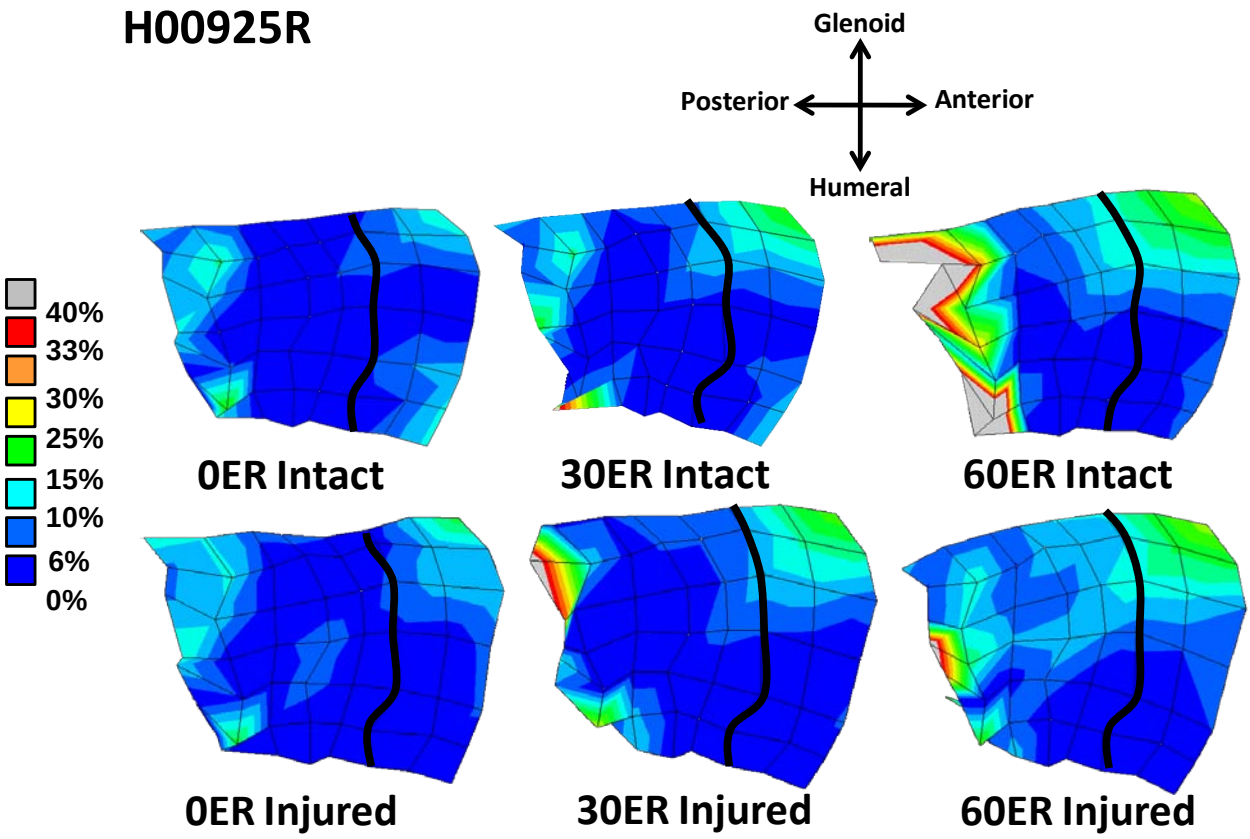

Figure 5.7 Fringe plots of the maximum principal strain distribution in the *intact* and *injured* anteroinferior capsule during the simulated clinical exams for specimen H00925R. The black line separates the AB-IGHL and axillary pouch.

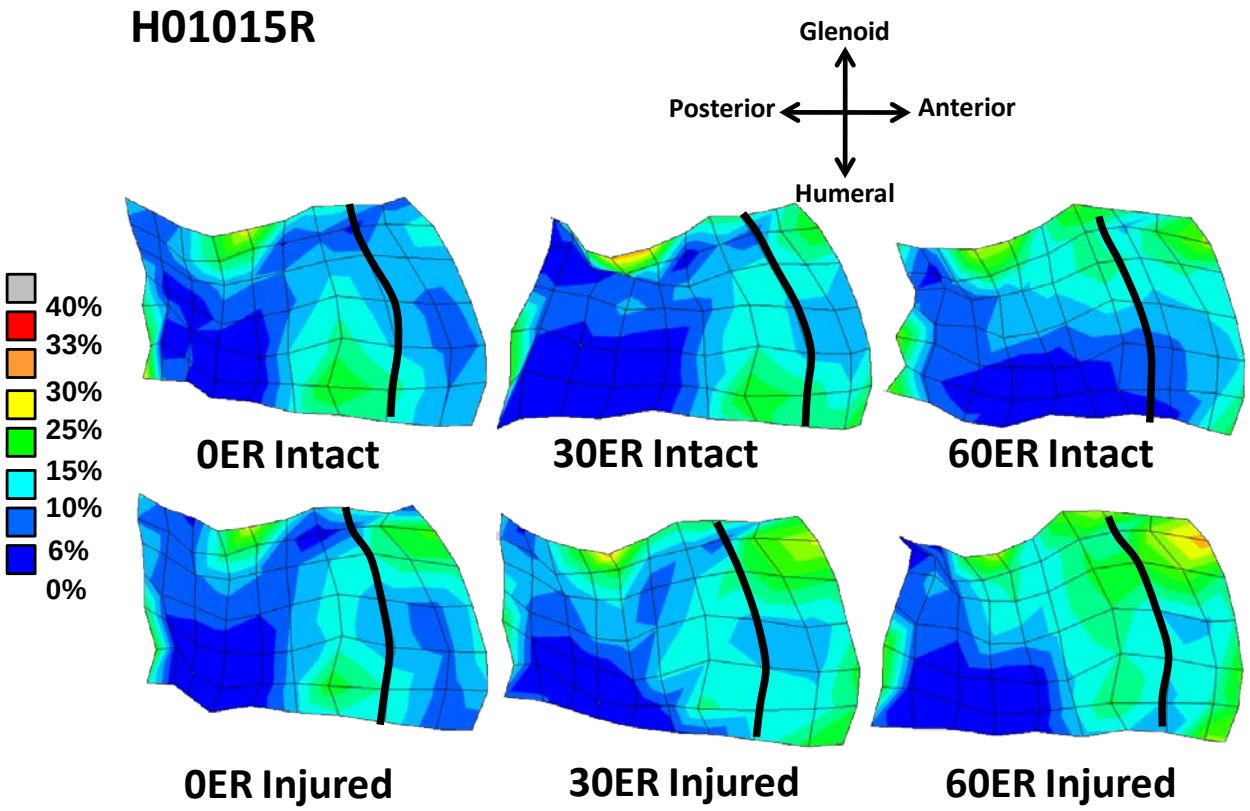

Figure 5.8 Fringe plots of the maximum principal strain distribution in the *intact* and *injured* anteroinferior capsule during the simulated clinical exams for specimen H01015L. The black line separates the AB-IGHL and axillary pouch.

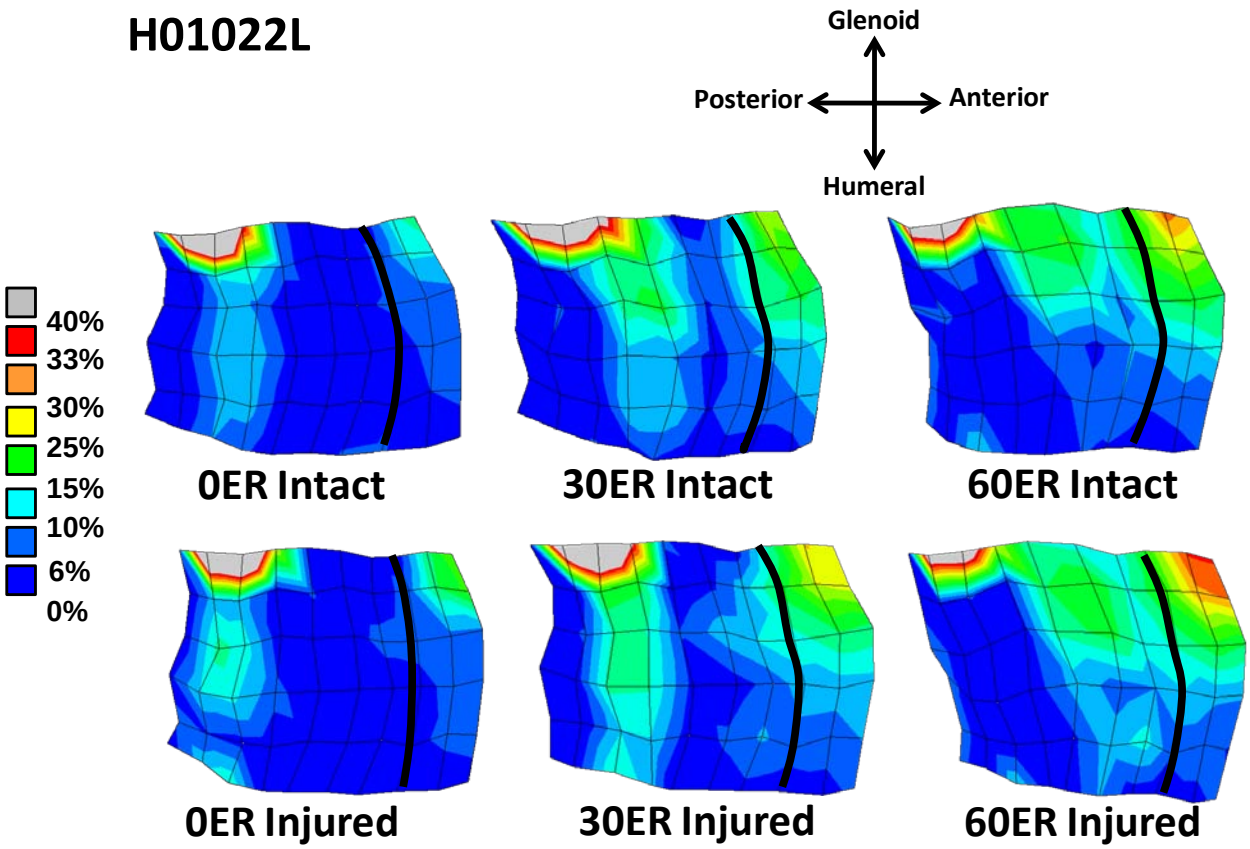

Figure 5.9 Fringe plots of the maximum principal strain distribution in the *intact* and *injured* anteroinferior capsule during the simulated clinical exams for specimen H01022L. The black line separates the AB-IGHL and axillary pouch.

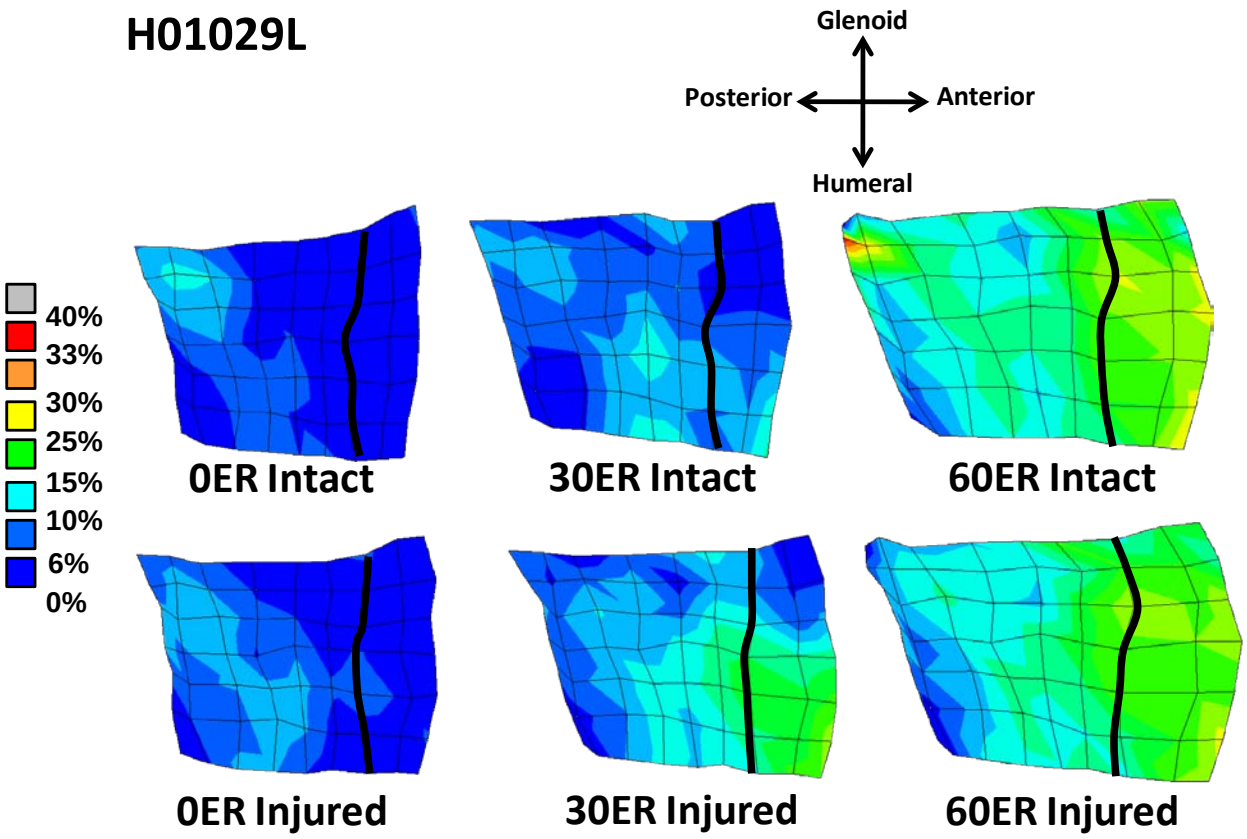

Figure 5.10 Fringe plots of the maximum principal strain distribution in the *intact* and *injured* anteroinferior capsule during the simulated clinical exams for specimen H01029L. The black line separates the AB-IGHL and axillary pouch.

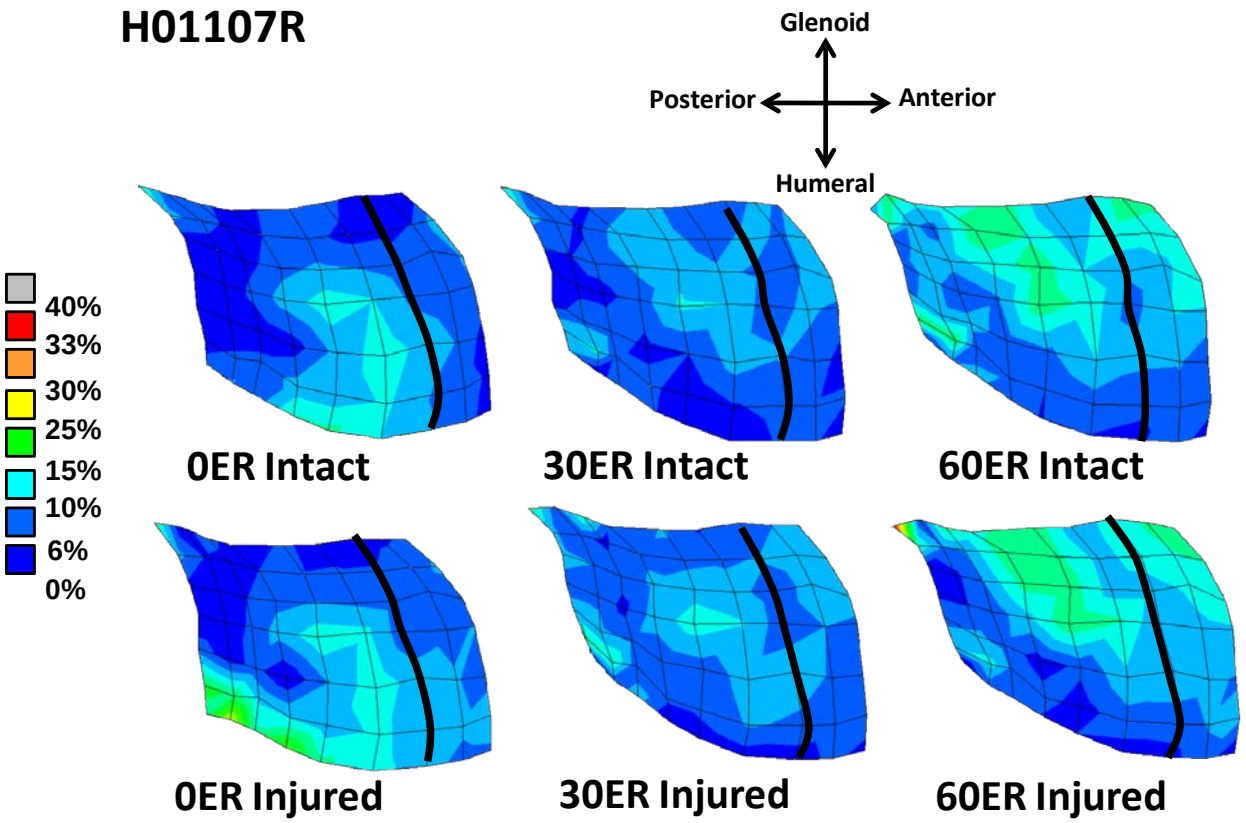

Figure 5.11 Fringe plots of the maximum principal strain distribution in the *intact* and *injured* anteroinferior capsule during the simulated clinical exams for specimen H01107R. The black line separates the AB-IGHL and axillary pouch.

Quantitative data showing the average and peak maximum principal strain in the AB-IGHL and axillary pouch during the simulated clinical exams for the *intact* and *injured* shoulders are shown in the tables below. The quantitative data supports observations made from the fringe plots. Strains in both the AB-IGHL and axillary pouch increased with external rotation. Due to large standard deviations it was difficult to detect differences (greater than the experimental repeatability of 3.5%) in the average maximum principal strains between the normal and injured states at all joint positions. However, differences were easily observed in the peak maximum principal strains following dislocation. At 0° of external rotation, peak strains in the injured AB-IGHL increased in four of the six specimens. In the axillary pouch, strains increased in two of

the six specimens. At 30° of external rotation, peak strains in the AB-IGHL and axillary pouch increased in two and four of the six specimens, respectively, and the peak strain in the axillary pouch of one specimen decreased. Finally, at 60° of external rotation the peak strain increased following dislocation in the AB-IGHL and axillary pouch of one specimen and decreased in the axillary pouch of two specimens. Therefore, the differences in the maximum principal strain magnitudes between the intact and injured capsule were detected in the AB-IGHL and axillary pouch when the simulated clinical exams were performed at 0° and 30° of external rotation, respectively.

Table 5.6 Average and peak maximum principal strain in the normal and *injured* anteroinferior capsule at 60° of abduction and 0° of external rotation for each specimen.

SPECIMEN #	AB-IGHL				Axillary Pouch			
	MEAN ± SD		PEAK		MEAN ± SD		PEAK	
	Intact	Injured	Intact	Injured	Intact	Injured	Intact	Injured
H00915L	0.7 ± 2.2	6.5 ± 10.9	7.5	38.6	2.4 ± 4.2	7.5 ± 12.1	15.1	39.5
H00925R	4.2 ± 3.9	2.7 ± 4.2	11.7	13.4	2.1 ± 4.8	2.3 ± 4.0	18.2	15.9
H01015R	6.1 ± 2.6	7.8 ± 7.1	10.9	24.5	6.4 ± 8.3	5.9 ± 7.5	30.4	26.0
H01022L	4.1 ± 3.4	6.0 ± 6.5	12.2	21.6	3.2 ± 6.1	3.0 ± 5.6	24.3	21.6
H01029L	0.5 ± 1.1	1.0 ± 2.5	3.3	8.6	2.6 ± 3.7	4.1 ± 3.9	12.6	13.2
H01107R	3.7 ± 2.6	4.6 ± 2.5	9.3	7.6	4.5 ± 4.4	5.7 ± 6.3	15.0	25.1

Table 5.7 Average and peak maximum principal strain in the normal and *injured* anteroinferior capsule at 60° of abduction and 30° of external rotation for each specimen.

SPECIMEN #	AB-IGHL				Axillary Pouch			
	MEAN ± SD		PEAK		MEAN ± SD		PEAK	
	Intact	Injured	Intact	Injured	Intact	Injured	Intact	Injured
H00915L	8.4 ± 7.5	7.6 ± 7.9	23.2	20.4	8.0 ± 9.0	11.7 ± 12.6	28.9	58.2
H00925R	5.6 ± 5.7	4.8 ± 6.3	19.3	19.1	2.3 ± 3.5	3.0 ± 6.5	12.7	28.2
H01015R	10.0 ± 4.7	12.4 ± 8.2	16.2	29.2	6.5 ± 8.3	6.7 ± 7.5	35.1	27.3
H01022L	12.7 ± 8.3	13.3 ± 10.0	24.6	25.5	4.8 ± 7.8	5.9 ± 9.5	30.9	35.5
H01029L	3.8 ± 4.4	10.8 ± 8.5	12.1	24.3	5.2 ± 4.0	8.4 ± 6.4	14.1	22.9
H01107R	5.4 ± 1.8	5.9 ± 2.0	8.5	9.1	4.1 ± 3.6	4.7 ± 3.2	11.6	10.7

Table 5.8 Average and peak maximum principal strain in the normal and *injured* anteroinferior capsule at 60° of abduction and 60° of external rotation for each specimen.

SPECIMEN #	AB-IGHL				Axillary Pouch			
	MEAN ± SD		PEAK		MEAN ± SD		PEAK	
	Intact	Injured	Intact	Injured	Intact	Injured	Intact	Injured
H00915L	16.2 ± 7.8	14.3 ± 8.2	29.9	27.8	16.5 ± 11.4	21.6 ± 15.7	42.6	67.8
H00925R	6.4 ± 7.5	6.3 ± 7.4	23.7	22.8	11.3 ± 17.1	5.1 ± 7.0	59.4	31.2
H01015R	10.7 ± 5.6	15.6 ± 9.3	19.0	31.5	6.0 ± 7.6	8.3 ± 8.7	31.0	28.3
H01022L	14.5 ± 11.6	15.3 ± 13.3	34.2	34.1	4.9 ± 6.8	5.2 ± 7.1	27.0	26.7
H01029L	22.3 ± 4.9	20.9 ± 4.5	28.8	26.8	13.2 ± 7.2	11.5 ± 6.3	33.3	26.4
H01107R	8.3 ± 3.5	8.9 ± 3.7	14.0	15.2	7.1 ± 5.0	6.1 ± 5.3	19.2	20.1

The average maximum principal strain in the AB-IGHL and axillary pouch increased from 0° to 30° to 60° of external rotation in both the *intact* and *injured* joints. (Figure 5.12)

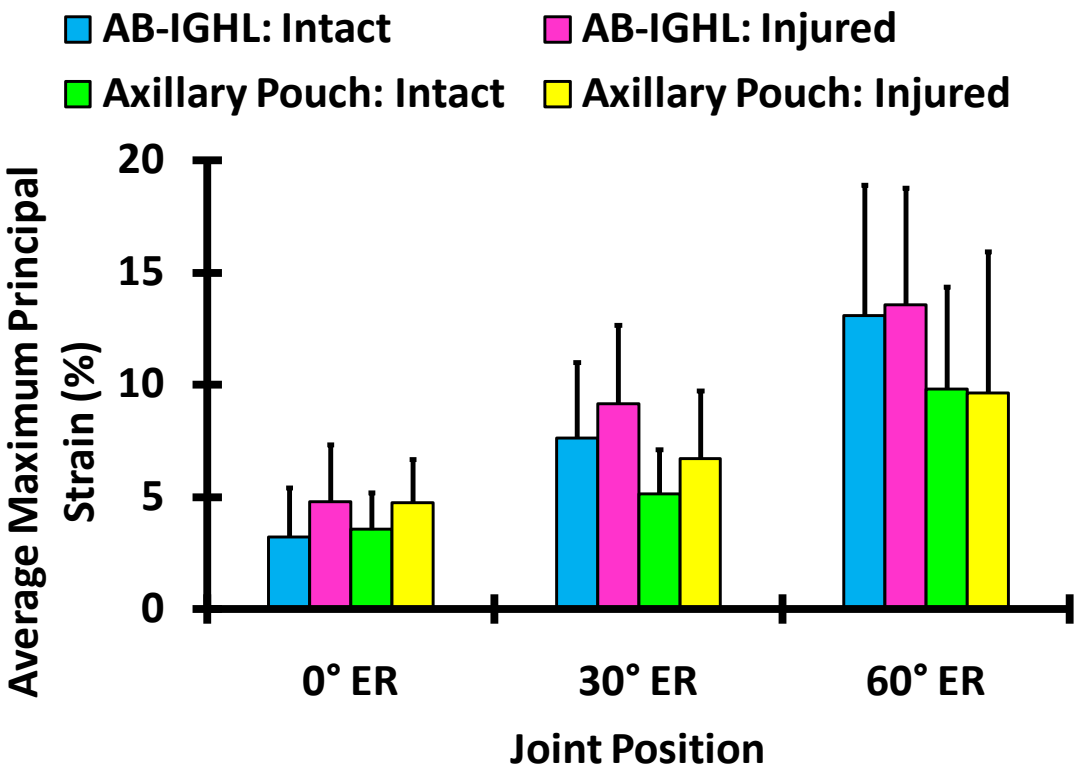

Figure 5.12 Average maximum principal strain (mean ± SD) in the AB-IGHL and axillary pouch during the simulated clinical exams at 60° of abduction and 0°, 30° and 60° of external rotation in the *intact* and *injured* joints.

In the *intact* and *injured* AB-IGHL, respectively, average strains increased from 3.2 ± 2.2% and 4.8 ± 2.6% at 0° to 7.6 ± 3.4% and 9.1 ± 3.5% at 30° and again to 13.1 ± 5.8% and 13.6 ± 5.2% at 60° of external rotation. The average maximum principal strain in the *intact* and *injured* AB-IGHL increased by 350% and 220% from 0° to 30° of external rotation and by 110% and 50% from 30° to 60° of external rotation, respectively. Similarly, in the axillary pouch, average strains at 0°, 30° and 60° of external rotation in the *intact* joint were 3.5 ± 1.6%, 5.1 ± 2.0%, and 9.8 ± 4.6%, and in the *injured* joint were 4.7 ± 2.0%, 6.7 ± 3.0%, and 9.6 ± 6.3%, respectively. From 0° to 30° of external rotation and from 30° to 60° of external rotation the average maximum principal strain in the axillary pouch increased by 60% and 120% in the *intact* joint and by 50% and 40% in the *injured* joint, respectively.

Peak maximum principal strains in the anteroinferior capsule followed similar trends as the average strains. The peak maximum principal strain in the AB-IGHL and axillary pouch increased from 0° to 30° to 60° of external rotation in both the *intact* and *injured* joints. (Figure 5.13)

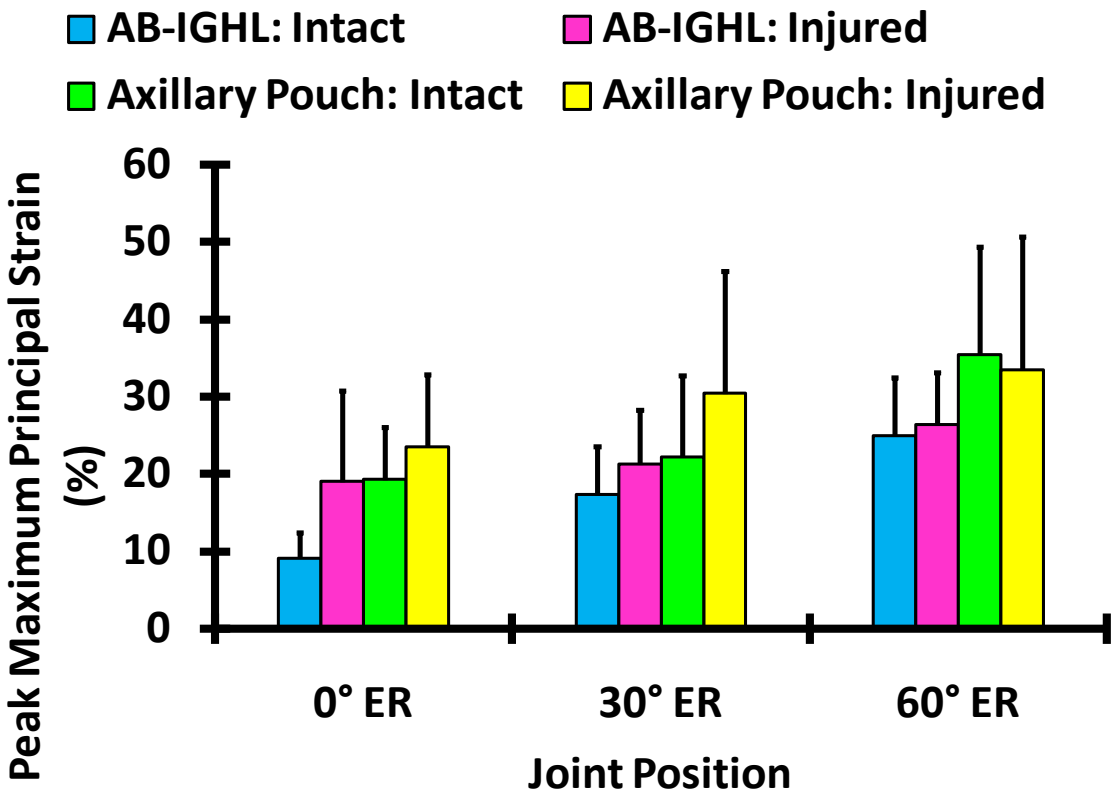

Figure 5.13 Peak maximum principal strain (mean ± SD) in the AB-IGHL and axillary pouch during the simulated clinical exams at 60° of abduction and 0°, 30° and 60° of external rotation in the *intact* and *injured* joints.

In the *intact* and *injured* AB-IGHL, respectively, peak strains increased from 9.1 ± 3.4% and 19.1 ± 11.7% at 0° to 17.3 ± 6.3% and 21.3 ± 7.0% at 30° and again to 24.9 ± 7.5% and 26.4 ± 6.7% at 60° of external rotation. The peak maximum principal strain in the *intact* and *injured* AB-IGHL increased by 630% and 360% from 0° to 30° of external rotation and by 410% and 320% from 30° to 60° of external rotation, respectively. Similarly, in the axillary pouch, peak

strains at 0°, 30° and 60° of external rotation in the *intact* joint were 19.3 ± 6.8%, 22.2 ± 10.5%, and 35.4 ± 14.0%, and in the *injured* joint were 23.6 ± 9.3%, 30.4 ± 15.9%, and 33.4 ± 17.2%, respectively. From 0° to 30° of external rotation and from 30° to 60° of external rotation the peak maximum principal strain in the axillary pouch increased by 15% and 100% in the *intact* joint and by 35% and 18% in the *injured* joint, respectively. Further comparisons between the strain distributions in the *intact* and *injured* states will be made in Section 5.3.5.1.

5.3.3.6 Strain During Simulated Clinical Exams: Discussion

The experimental strain distribution in the *intact* anteroinferior capsule during the simulated clinical exams applied in this work has been reported previously. [9] Moore and coworkers found that average maximum principal strain values in the entire anteroinferior capsule increased with increasing external rotation. Average strains ranged from 1.4 ± 4.8% to 14.1 ± 2.3% at 0°, 7.0 ± 6.7% to 18.2 ± 15.3% at 30°, and 8.5 ± 7.9% to 19.6 ± 16.2% at 60° of external rotation. In the current work, similar results were found with the average and peak maximum principal strains in the AB-IGHL and axillary pouch increasing with external rotation. Following dislocation, the magnitude of maximum principal strain was altered but the same trends were observed from 0° to 30° to 60° of external rotation.

Differences between the magnitudes of maximum principal strain in the each region of the anteroinferior capsule were detected at different joint positions. Changes in strain in the AB-IGHL were most easily detected when the simulated clinical exams were performed at 0° of external rotation whereas changes in the axillary pouch were more easily detected at 30° of external rotation. Previous work using validated subject-specific finite element models suggested that performing simulated clinical exams at 60° of abduction and 20°-40° of external rotation resulted in consistent stability provided by the capsule among patients and high strains in

the AB-IGHL. [93] However, the models used in this work were of the normal glenohumeral joint. The current work suggests that anterior dislocation causes capsule regions to be loaded differently during simulated clinical exams as a result of permanent deformation. In the normal capsule, the AB-IGHL experienced high strains at mid-ranges of external rotation but the current work shows that these strains remain relatively unchanged following permanent deformation. Rather the most change in strain at mid-ranges of external rotation occurs in the axillary pouch. Similarly at low-ranges of external rotation the AB-IGHL experiences the most change in strain during simulated clinical exams and changes in the axillary pouch are minimal. Therefore, by performing simulated clinical exams at 60° of abduction and low-ranges of external rotation clinicians would be most likely to detect injury to the AB-IGHL. On the other hand, physical exams performed at mid-ranges of external rotation can be used to detect injury to the axillary pouch. This suggests that standardizing clinical exams for joint position will help clinicians identify the location of tissue damage.

5.3.4 Analysis of Capsule Sub-Regions

5.3.4.1 Strain at Dislocation & Nonrecoverable Strain

In order to address Specific Aim 3b, and identify specific locations of the anteroinferior capsule which are at risk for injury during anterior dislocation, the anteroinferior capsule was further divided into six sub-regions. These sub-regions were 1) posterior axillary pouch glenoid side (PPG), 2) posterior axillary pouch humeral side (PPH), 3) anterior axillary pouch glenoid side (APG), 4) anterior axillary pouch humeral side (APH), 5) anterior band glenoid side (ABG), and 6) anterior band humeral side (ABH). (Figure 5.2)

The average maximum principal strain during dislocation was 16.1 ± 14.7%, 10.9 ± 10.6%, 20.4 ± 6.5%, 11.2 ± 6.3%, 22.9 ± 5.4%, and 13.8 ± 8.4% in the PPG, PPH, APG, APH, ABG, and APH, respectively. (Table 5.9) The capsule sub-region containing the largest average maximum principal strain at dislocation varied between specimens. The greatest average occurred on the glenoid side of the AB-IGHL in three of the six specimens and never occurred in the anterior axillary pouch. This resulted in average nonrecoverable strains of 4.7 ± 4.9%, 4.5 ± 4.8%, 1.6 ± 0.6%, 1.7 ± 0.7%, 3.1 ± 1.6%, and 1.9 ± 1.3% in each capsule sub-region. (Table 5.10) The capsule sub-region containing the largest average maximum principal nonrecoverable strain did not necessarily correspond to the one experiencing the largest strains during dislocation. The greatest average nonrecoverable strain occurred in the posterior axillary pouch in five of the six specimens. In the remaining specimen, the largest average nonrecoverable strain was on the glenoid side of the AB-IGHL.

Table 5.9 Average maximum principal strain (mean ± SD) in each capsule sub-region during dislocation for each specimen.

Specimen #	PPG	PPH	APG	APH	ABG	ABH
H00915L	43.9 ± 43.1	23.0 ± 19.2	32.9 ± 7.0	16.9 ± 7.7	20.5 ± 7.9	11.9 ± 4.7
H00925R	11.3 ± 6.1	24.7 ± 19.9	14.2 ± 5.5	1.4 ± 2.1	19.5 ± 5.4	3.1 ± 4.2
H01015R	15.7 ± 13.8	1.1 ± 2.1	19.1 ± 4.5	12.5 ± 9.9	22.1 ± 9.8	20.5 ± 5.2
H01022L	2.7 ± 3.1	2.1 ± 2.8	18.4 ± 12.7	11.0 ± 9.8	33.0 ± 2.0	7.3 ± 3.7
H01029L	17.4 ± 9.4	11.2 ± 8.6	21.2 ± 6.6	18.3 ± 4.0	24.5 ± 4.9	26.0 ± 3.2
H01107R	5.8 ± 4.1	3.7 ± 4.1	16.7 ± 4.5	6.9 ± 5.3	18.0 ± 2.4	13.7 ± 3.1

Table 5.10 Average maximum principal nonrecoverable strain (mean ± SD) in each capsule sub-region for each specimen.

Specimen #	PPG	PPH	APG	APH	ABG	ABH
H00915L	14.2 ± 18.8	14.0 ± 19.2	1.9 ± 2.8	2.5 ± 2.1	4.1 ± 5.2	4.3 ± 4.6
H00925R	3.5 ± 2.2	4.4 ± 4.4	2.0 ± 1.2	0.4 ± 0.8	3.2 ± 2.2	1.0 ± 1.1
H01015R	1.2 ± 1.2	1.6 ± 1.4	1.1 ± 1.8	1.8 ± 1.3	4.87 ± 2.7	0.59 ± 1.4
H01022L	5.1 ± 1.9	1.7 ± 1.0	2.4 ± 1.4	1.9 ± 1.4	4.1 ± 3.3	2.2 ± 2.3
H01029L	2.7 ± 2.3	2.9 ± 3.0	1.5 ± 0.9	1.5 ± 1.8	0.6 ± 1.0	1.1 ± 0.9
H01107R	1.6 ± 1.1	2.6 ± 2.0	0.9 ± 1.1	2.0 ± 1.5	1.8 ± 1.7	2.1 ± 2.1

When comparing the average strain at dislocation between capsule sub-regions, statistically significant differences were found between the glenoid and humeral sides of the anterior axillary pouch ($p = 0.03$) and AB-IGHL ($p = 0.046$). (Figure 5.14) Only one statistically significant difference was found when comparing the average nonrecoverable strain, between the glenoid sides of the anterior axillary pouch and AB-IGHL ($p = 0.03$).

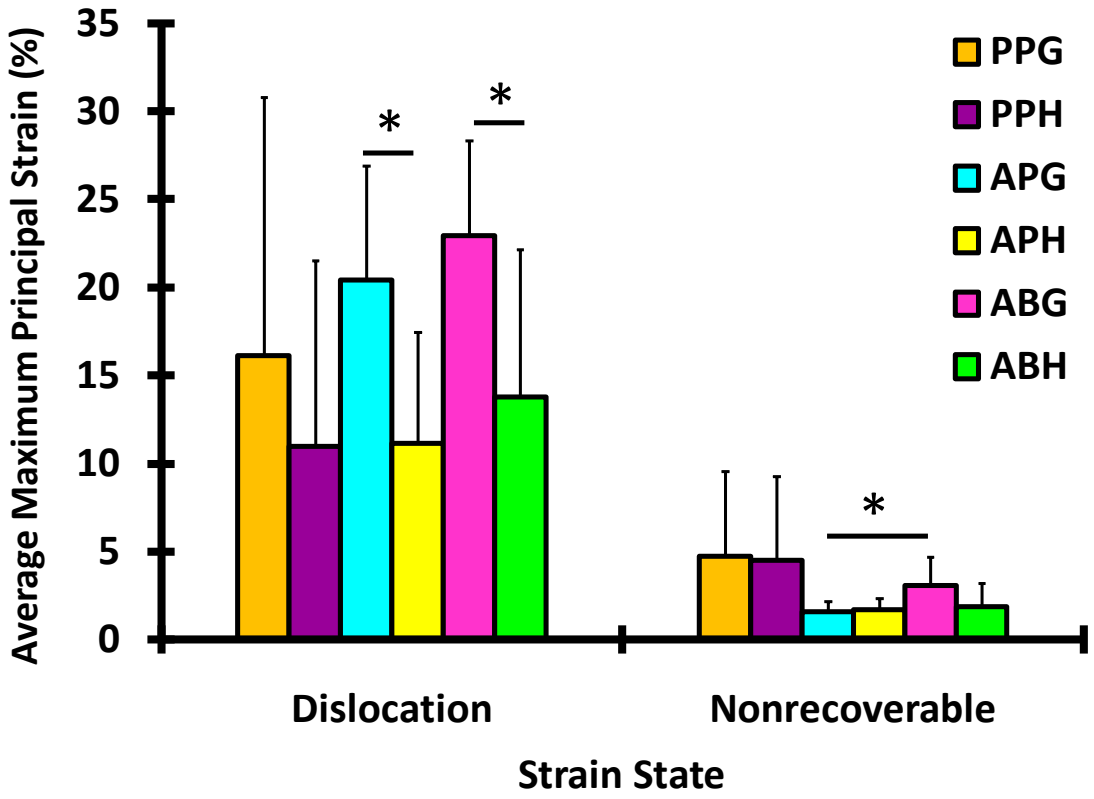

Figure 5.14 Average maximum principal strain (mean ± SD) during dislocation and the resulting nonrecoverable strain in each sub-region of the anteroinferior capsule. * denotes significant differences between the glenoid and humeral sides ($p < 0.05$).

Peak maximum principal strains during dislocation were 35.5 ± 37.8%, 25.0 ± 20.1%, 30.5 ± 9.2%, 21.6 ± 9.6%, 29.9 ± 5.2%, and 19.2 ± 8.1% in the PPG, PPH, APG, APH, ABG, and APH, respectively (Table 5.11) and followed similar trends as the average strains. The capsule sub-region containing the greatest peak maximum principal strain at dislocation varied between specimens. In general, the greatest peaks occurred on the glenoid sides of the AB-IGHL, anterior axillary pouch, and posterior axillary pouch. These high strains at dislocation resulted in peak nonrecoverable strains of 12.3 ± 16.8%, 12.8 ± 16.4%, 4.5 ± 1.8%, 4.2 ± 1.3%, 7.1 ± 3.6%, and 5.2 ± 3.8% in each capsule sub-region, respectively. (Table 5.12) Similar to the average strains, the capsule sub-region containing the greatest peak maximum principal nonrecoverable strain did

not necessarily correspond to the one experiencing the largest strains during dislocation. The greatest average nonrecoverable strain occurred in the posterior axillary pouch in four of the six specimens. In the remaining two specimens, the largest average nonrecoverable strain was on the glenoid side of the AB-IGHL.

Table 5.11 Peak maximum principal strain in each capsule sub-region during dislocation for each specimen.

Specimen #	PPG	PPH	APG	APH	ABG	ABH
H00915L	109.7	50.4	45.6	28.0	31.2	19.4
H00925R	18.7	48.2	20.1	4.7	27.9	9.2
H01015R	33.1	5.5	25.3	24.8	33.5	28.1
H01022L	8.0	8.7	35.4	30.9	35.0	12.6
H01029L	31.7	25.8	31.6	24.9	31.5	29.1
H01107R	11.6	11.4	24.9	16.3	20.4	16.5

Table 5.12 Peak maximum principal nonrecoverable strain in each capsule sub-region for each specimen.

Specimen #	PPG	PPH	APG	APH	ABG	ABH
H00915L	46.5	45.8	8.0	6.1	12.7	12.4
H00925R	6.2	11.8	4.1	2.3	5.9	2.8
H01015R	3.2	3.7	5.1	3.8	7.5	3.5
H01022L	7.2	3.1	4.0	3.8	9.0	5.4
H01029L	7.3	7.2	3.2	4.4	2.4	2.1
H01107R	3.4	5.5	2.9	4.7	4.8	4.8

When comparing the peak strain at dislocation between capsule sub-regions similar trends compared to the average strains were observed. Statistically significant differences were found between the glenoid and humeral sides of the anterior axillary pouch ($p = 0.03$) and AB-IGHL ($p = 0.03$). (Figure 5.15) In addition, a statistically significant difference was found when

comparing the average nonrecoverable strain, between the glenoid sides of the anterior axillary pouch and AB-IGHL ($p = 0.046$).

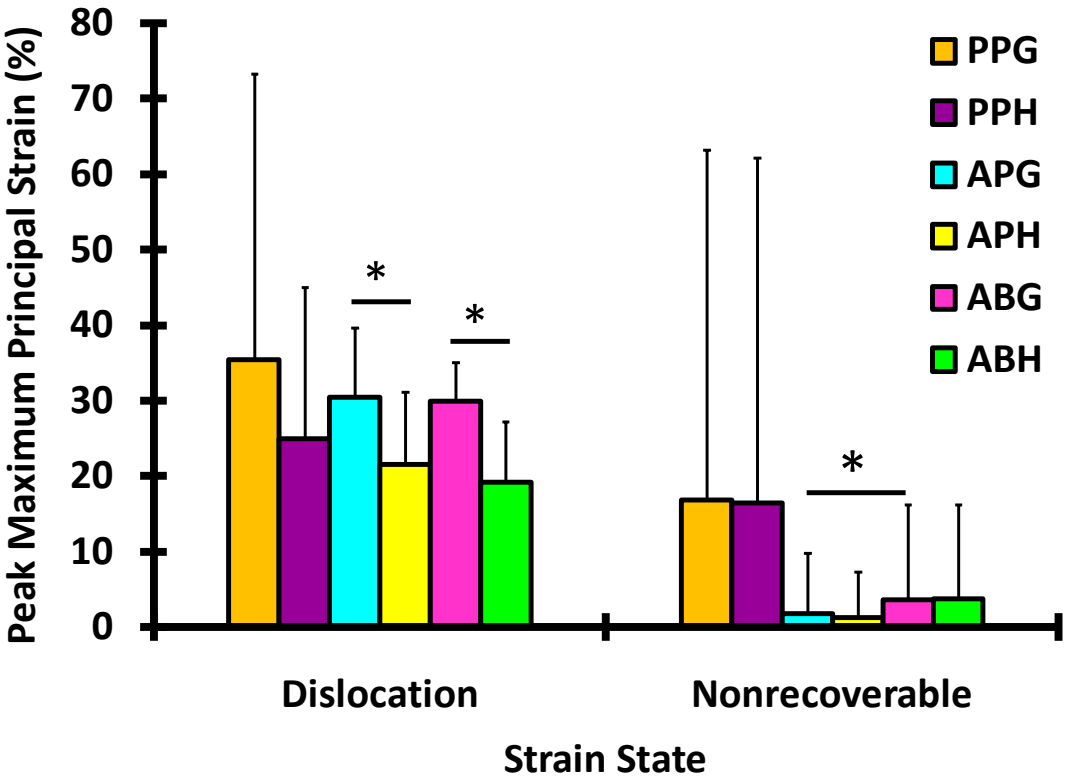

Figure 5.15 Peak maximum principal strain (mean ± SD) during dislocation and the resulting nonrecoverable strain in each sub-region of the anteroinferior capsule. * denotes significant differences between the glenoid and humeral sides ($p < 0.05$).

5.3.4.2 Strain Ratios

Strain at Dislocation and Nonrecoverable Strain

As seen in Figure 5.14 and Figure 5.15 large standard deviations exist in the maximum principal strains between specimens, particularly in the posterior axillary pouch. In order to eliminate

variations in the strain distribution between specimens, strains were normalized as described in Section 5.2.11.2 by computing the strain ratio in each element.

Table 5.13 Strain ratios (mean ± SEM) in each capsule sub-region during dislocation and the nonrecoverable strain state.

	PPG	PPH	APG	APH	ABG	ABH
Dislocation	0.40 ± 0.07	0.39 ± 0.08	0.58 ± 0.08	0.21 ± 0.07	0.21 ± 0.12	0.23 ± 0.10
Nonrecoverable	0.62 ± 0.15	0.73 ± 0.19	0.34 ± 0.14	0.43 ± 0.14	0.61 ± 0.18	0.52 ± 0.20

During dislocation, strain ratios were higher on the glenoid side compared to the humeral side however these differences were only significant in the AB-IGHL ($p = 0.01$) and anterior axillary pouch ($p = 0.003$). No differences were found between the glenoid and humeral sides in the posterior pouch ($p = 0.83$). In addition, the strain ratios in the glenoid side of the AB-IGHL (ABG) was significantly larger than all other capsule regions and the glenoid side of the axillary pouch (APG) was significantly larger than both posterior axillary pouch sub-regions (PPG, PPH) and the humeral side of the anterior axillary pouch (APH).

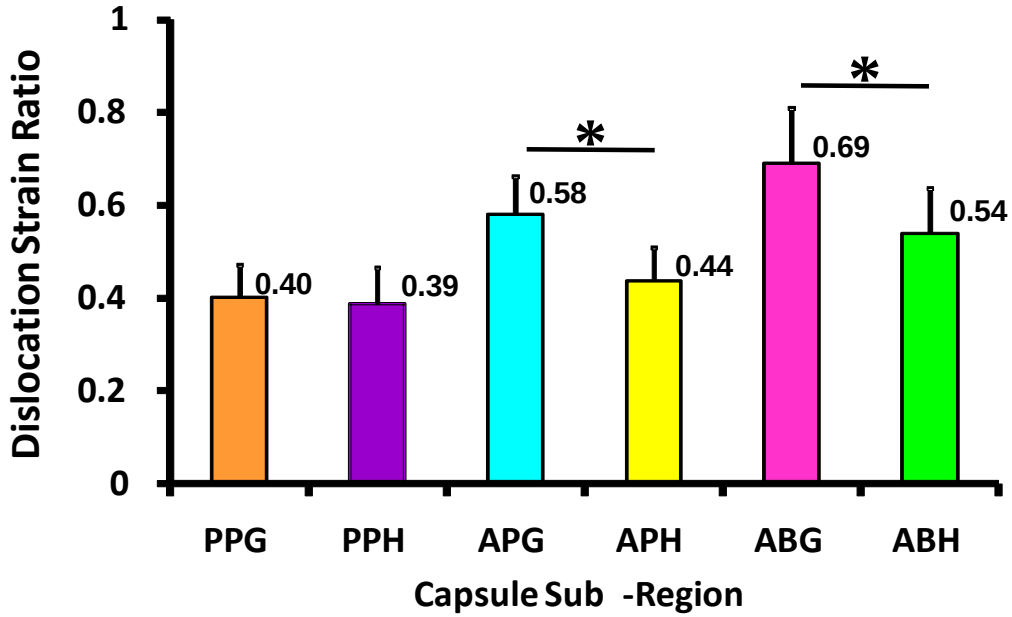

Figure 5.16 Strain ratio (mean ± SEM) in each capsule sub-region during dislocation.

Nonrecoverable strain ratios were largest in the posterior axillary pouch followed by the AB-IGHL. The glenoid side of the axillary pouch (APG) had significantly lower nonrecoverable strain ratios than both sides of the posterior pouch (PPG: $p = 0.02$, PPH: $p = 0.003$) and the glenoid side of the AB-IGHL (ABG: $p = 0.04$).

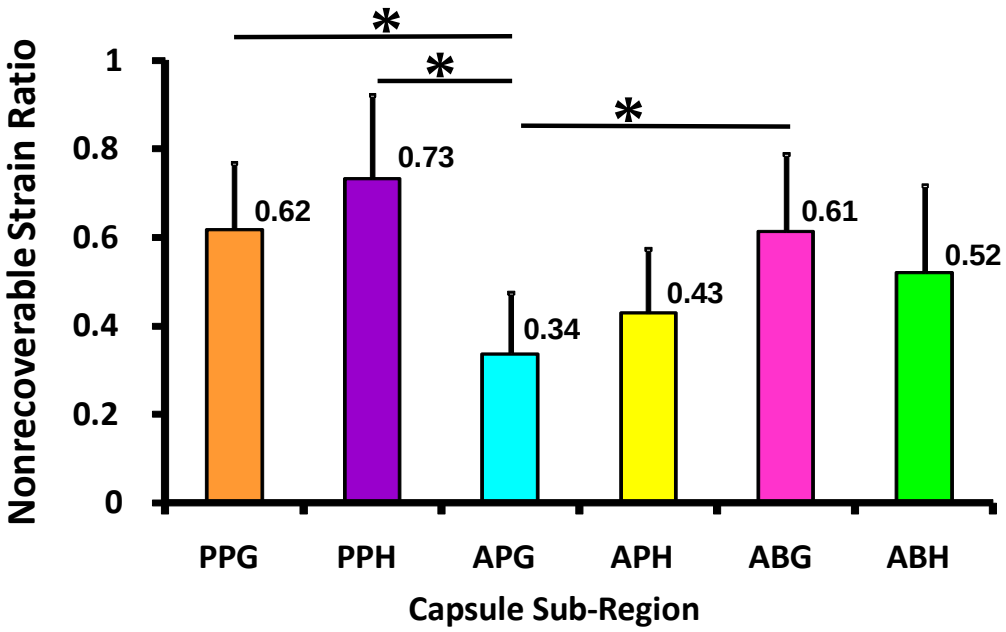

Figure 5.17 Nonrecoverable strain ratio (mean ± SEM) in each capsule sub-region.

Therefore, while the highest strains during dislocation occurred on the glenoid side of the AB-IGHL and anterior axillary pouch, the greatest amount of nonrecoverable strain was found in the posterior axillary pouch.

Strain During Simulated Clinical Exams

In order to eliminate variations in the strain distributions between specimens strain ratios were also computed for the strain distributions during the simulated clinical exams. The strain ratios in each element were then compared between the *intact* and *injured* joints. As the strain

increased in some elements and decreased in others the changes in strain ratios were both positive and negative but the magnitude of change was calculated. (Table 5.14)

Table 5.14 The change in strain ratio (mean ± SEM) between the *intact* and *injured* joint states in each capsule sub-region.

	PPG	PPH	APG	APH	ABG	ABH
0° ER	0.33 ± 0.01	0.26 ± 0.01	0.09 ± 0.003	0.11 ± 0.003	0.13 ± 0.01	0.20 ± 0.01
30° ER	0.32 ± 0.01	0.18 ± 0.005	0.20 ± 0.01	0.15 ± 0.005	0.14 ± 0.004	0.24 ± 0.01
60° ER	0.23 ± 0.01	0.10 ± 0.003	0.07 ± 0.001	0.09 ± 0.002	0.09 ± 0.003	0.07 ± 0.002

The strain ratios between the intact and injured joint states during the simulated clinical exams were found to be significantly different on the humeral side of the posterior axillary pouch (PPH) in all three joint positions ($p = 0.03$ at 0° ER, $p = 0.048$ at 30° ER, and $p = 0.04$ at 60° ER). Also at 0° of external rotation differences were found on the glenoid side of the AB-IGHL (ABG, $p = 0.003$). (Figure 5.18) In addition, differences in the strain ratios on the glenoid side of the posterior axillary pouch (PPG) approached significance ($p = 0.07$). At 30° of external rotation significant differences were also found on the humeral side of the AB-IGHL (ABH, $p = 0.04$). Finally, at 60° of external rotation significant differences in the strain ratios were found on the humeral side of the axillary pouch (APH, $p = 0.03$). Therefore, performing the simulated clinical exams at each joint position allows differences in various capsule sub-regions to be detected.

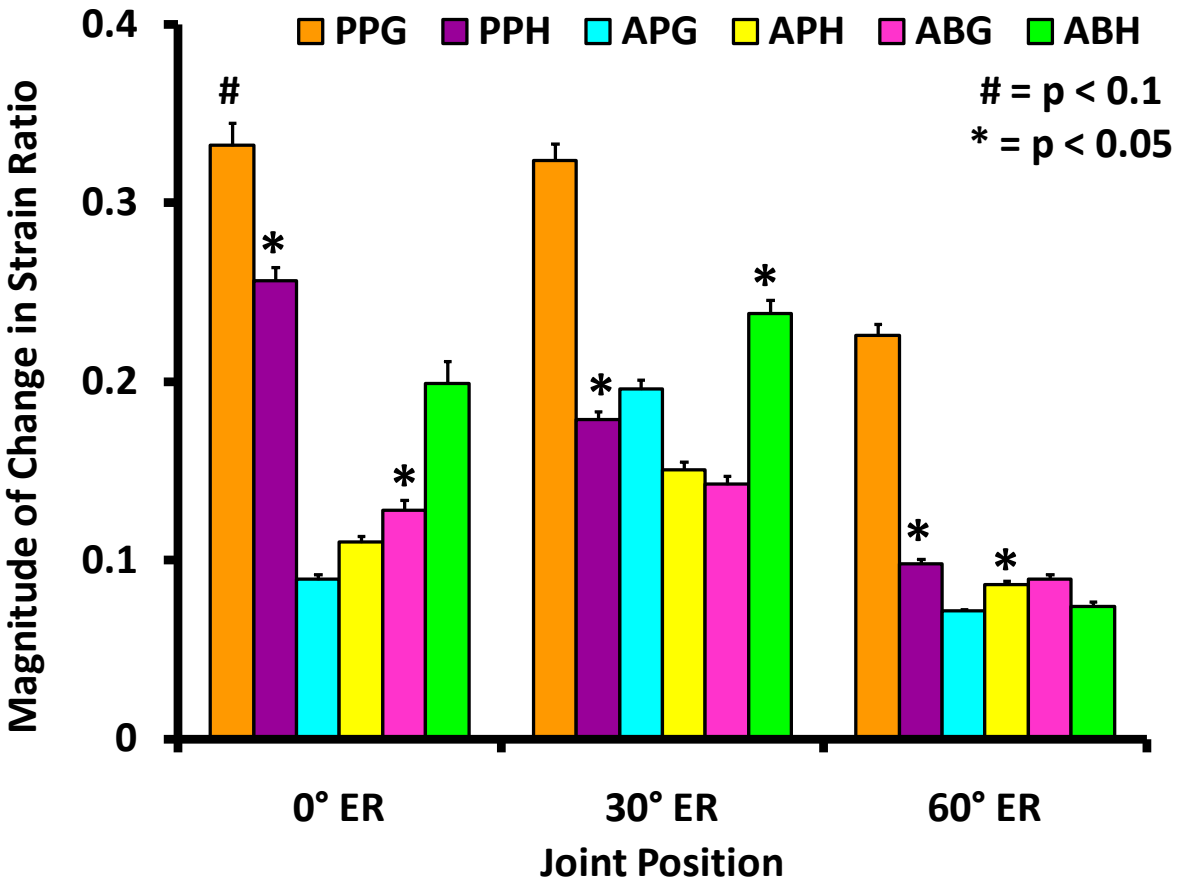

Figure 5.18 Change in strain ratio (mean ± SEM) between the *intact* and *injured* joint states for each capsule sub-region during the simulated clinical exams at 60° of abduction and 0°, 30° and 60° of external rotation.

The largest change in strain ratios occurred on the glenoid side of the posterior axillary pouch at all three joint positions. This was also the capsule sub-region which exhibited the largest nonrecoverable strain ratios, or the most amount of tissue damage. Therefore, the nonrecoverable strain ratios were correlated to the change in strain ratios at each joint position in order to determine if the change in strain distributions during the simulated clinical exams following dislocation was related to the amount of tissue damage. The nonrecoverable strain ratios were found to be significantly correlated to the change in strain ratios at 0° and 60° ($r = 0.89$ and $p = 0.02$ for both joint positions) of external rotation, but not at 30° ($r = 0.09$, $p = 0.87$).

5.3.4.3 Discussion

In order to address Specific Aim 3b, the anteroinferior capsule was divided into six sub-regions and the peak and average maximum principal strain in each region was determined and used to identify specific areas of the capsule that may be at risk for injury during anterior dislocation.

Compare to Literature

Higher strains during dislocation were found on glenoid side of the anteroinferior glenohumeral capsule compared to the humeral side. These results compare well with others reported in the literature. Higher strains have been reported on the glenoid side of the anteroinferior capsule during simulated clinical exams in validated finite element models of the glenohumeral joint during positions of abduction and external rotation. [43] Further, Malicky and coworkers found significantly higher strains on the glenoid side of the anteroinferior capsule compared to the humeral side during joint subluxation. [69] High strains on the glenoid side are consistent with common injuries seen in this region of the capsule such as the Bankart lesion. Nonrecoverable strains have also been reported to be higher on the glenoid side of the anteroinferior capsule [68], however in the current study no significant differences were found. As stated previously, differences in the results of this study and the current work may be due to different constraints placed on joint motion.

Significance of Results

The region of the capsule containing the highest strains varied from specimen-to-specimen and regions experiencing high strains during dislocation did not necessarily correspond to regions experiencing high nonrecoverable strains. High strains during dislocation occurred on the glenoid side of the posterior axillary pouch, anterior axillary pouch and AB-IGHL but the

most nonrecoverable strain was found in both the glenoid and humeral sides of the posterior axillary pouch. This suggests that the injury threshold, or the amount of strain required to create permanent deformation, may be different for different regions of the capsule. Rather than differences in tissue properties being responsible for this phenomenon, as no differences have been found in the material properties of these regions [194], it is likely due to the different boundary conditions placed on the different regions of the capsule during dislocation. The AB-IGHL and anterior axillary pouch wrap around the humeral head in positions of external rotation, particularly when the humeral head is translated anteriorly as it is during dislocation. However, the posterior axillary pouch is typically the region being pulled between the glenoid and humeral head. Wrapping around the humeral head may allow some of the load to be distributed throughout the capsule and to the humerus thereby allowing this area of the capsule to withstand higher strains. On the other hand, the posterior axillary pouch has nothing to rest on as it is pulled between the humerus and scapula thus the high strains experienced in the posterior axillary pouch result in greater damage. The results of this work support current surgical repair procedures which plicate the posterior-inferior capsule [114, 116, 118] following traumatic anterior dislocation.

The strain distributions in the capsule provide an indication of the stability provided by the capsule at each joint position; therefore, changes in the strain distributions indicate that the function of the capsule is being compromised following dislocation. Differences in the strain ratios due to permanent deformation could be detected in various capsule sub-regions by performing simulated clinical exams at each joint position. These results combined with the nonrecoverable strain ratios demonstrate that damage occurred throughout the anteroinferior capsule due to dislocation. When the clinical exams were performed at lower ranges of external

rotation changes in the strain distribution were detected in the AB-IGHL, however, once the joint was placed in extreme external rotation, differences were detected in the axillary pouch. In addition, damage to the posterior axillary pouch was detected by differences in the strain distribution at all three joint positions demonstrating that severe tissue damage can be detected at multiple joint positions. This concept is exemplified by a significant correlation between the change in strain distribution and the amount of tissue damage indicating that capsule sub-regions experiencing the most damage following dislocation exhibited the greatest loss in stabilizing function. This work suggests that while severe damage can be detected at any joint position, standardizing clinical exams for joint position would allow surgeons to identify specific locations of moderate tissue damage in the anteroinferior capsule which may have been previously ignored. Plicating multiple locations in the anteroinferior capsule may be necessary to fully restore glenohumeral joint stability following anterior dislocation and improve patient outcome.

5.3.5 Evaluation of Capsule Function

To address Specific Aim 3c, the effect of anterior dislocation on the function of the glenohumeral capsule was evaluated by examining the strain distribution in the anteroinferior capsule, joint kinematics, *in situ* force in the capsule, and glenohumeral contact force during the simulated clinical exams at 0°, 30° and 60° of external rotation in both the *intact* and *injured* joint.

5.3.5.1 Strain Distribution in Anteroinferior Capsule: Results

Differences in the strain distributions in the anteroinferior capsule during the simulated clinical exams between the *intact* and *injured* joints were detected by computing the strain ratios in the

capsule sub-regions. To supplement this and a technique specifically designed to compare distributions (Projection Plots) was employed to determine if differences exist between the strain distributions in the *intact* and *injured* anteroinferior capsule at each joint position. The projection plots were nonlinear demonstrating differences in the strain distributions, with the 25 N anterior load applied, between the *intact* and *injured* states at all three joint positions. Projection plots for all six specimens are shown below at 0°, 30° and 60° of external rotation. Three lines appear on each projection plot, the mean quantile difference and ±1 standard deviation of the quantile difference.

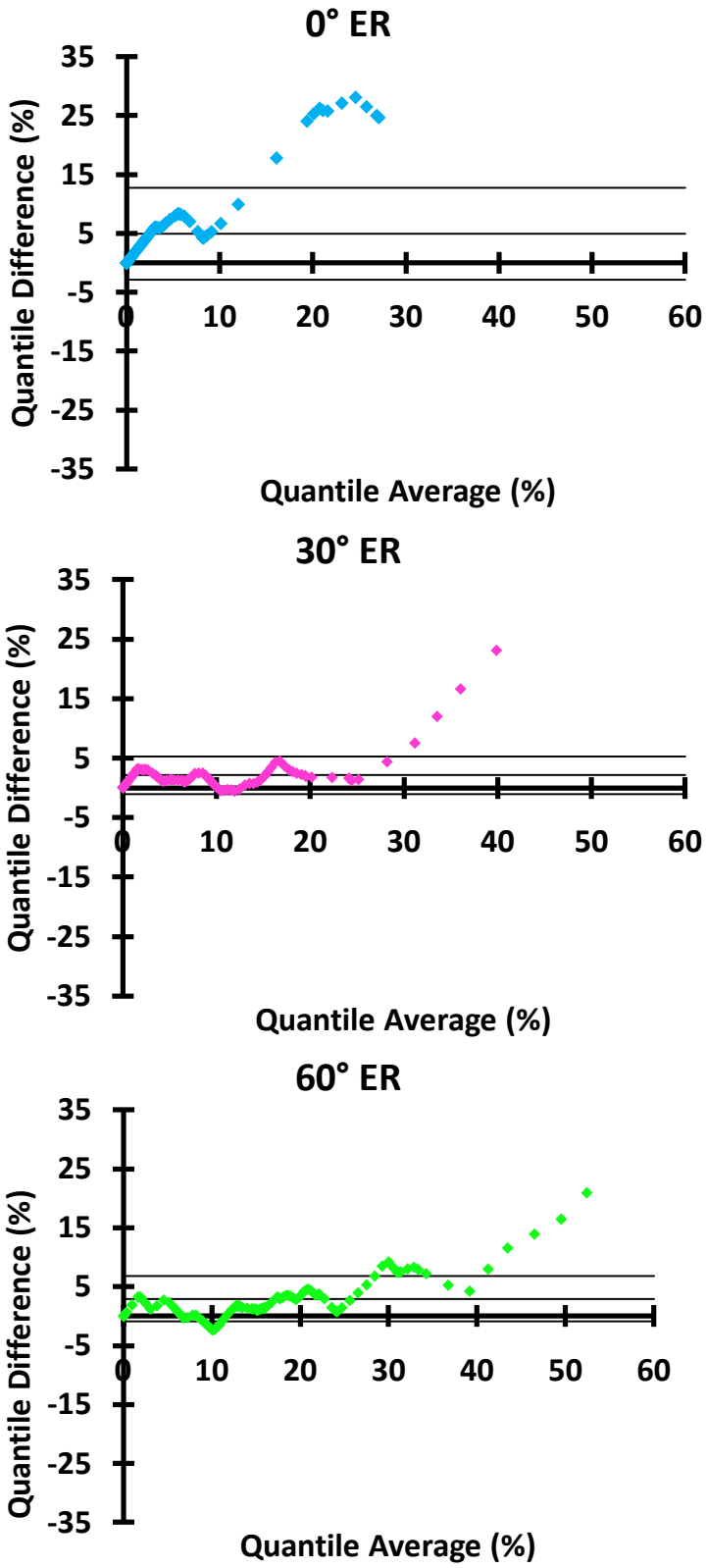

Figure 5.19 Projection plots demonstrating differences in the strain distributions in the *intact* and *injured* anteroinferior capsule during the simulated clinical exams at 0°, 30° and 60° of external rotation for specimen H00915L.

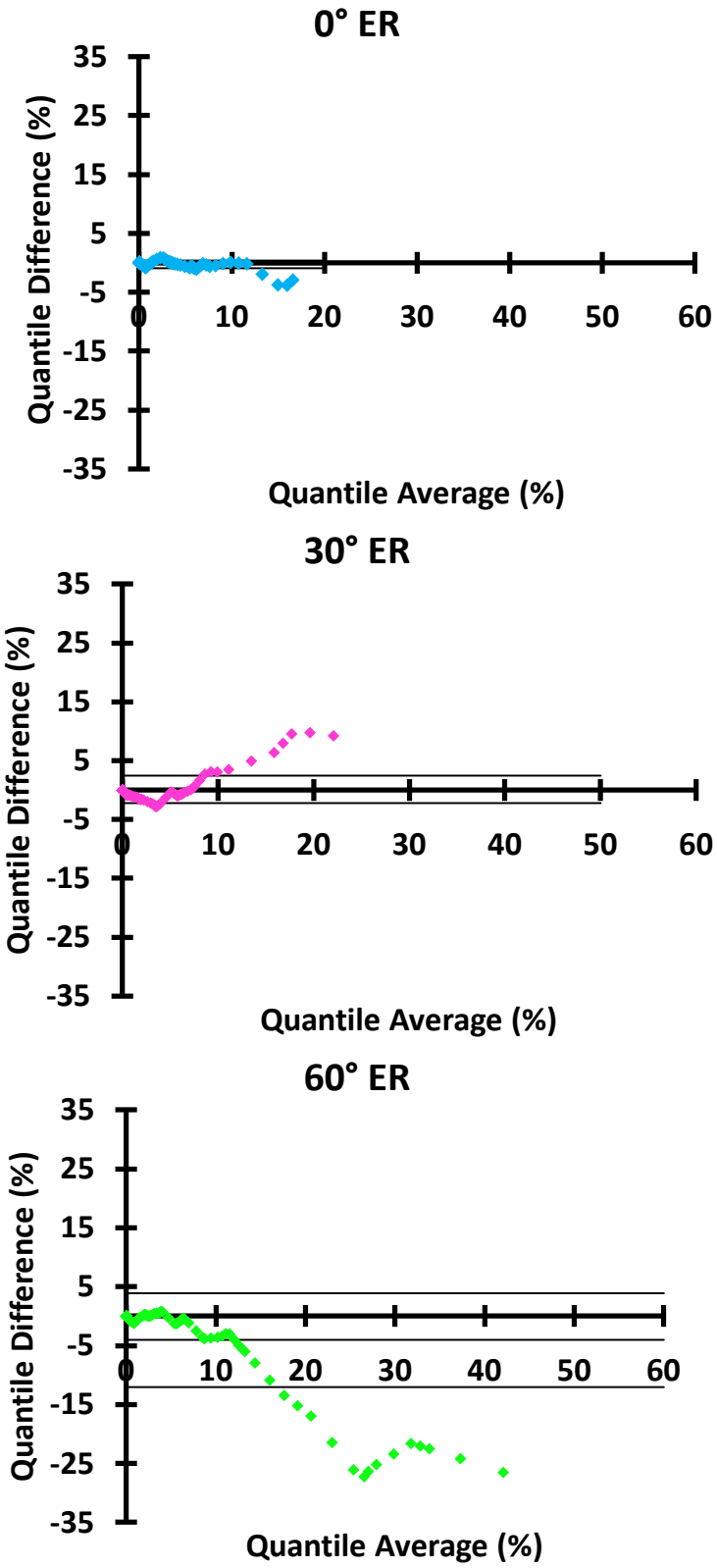

Figure 5.20 Projection plots demonstrating differences in the strain distributions in the *intact* and *injured* anteroinferior capsule during the simulated clinical exams at 0°, 30° and 60° of external rotation for specimen H00925R.

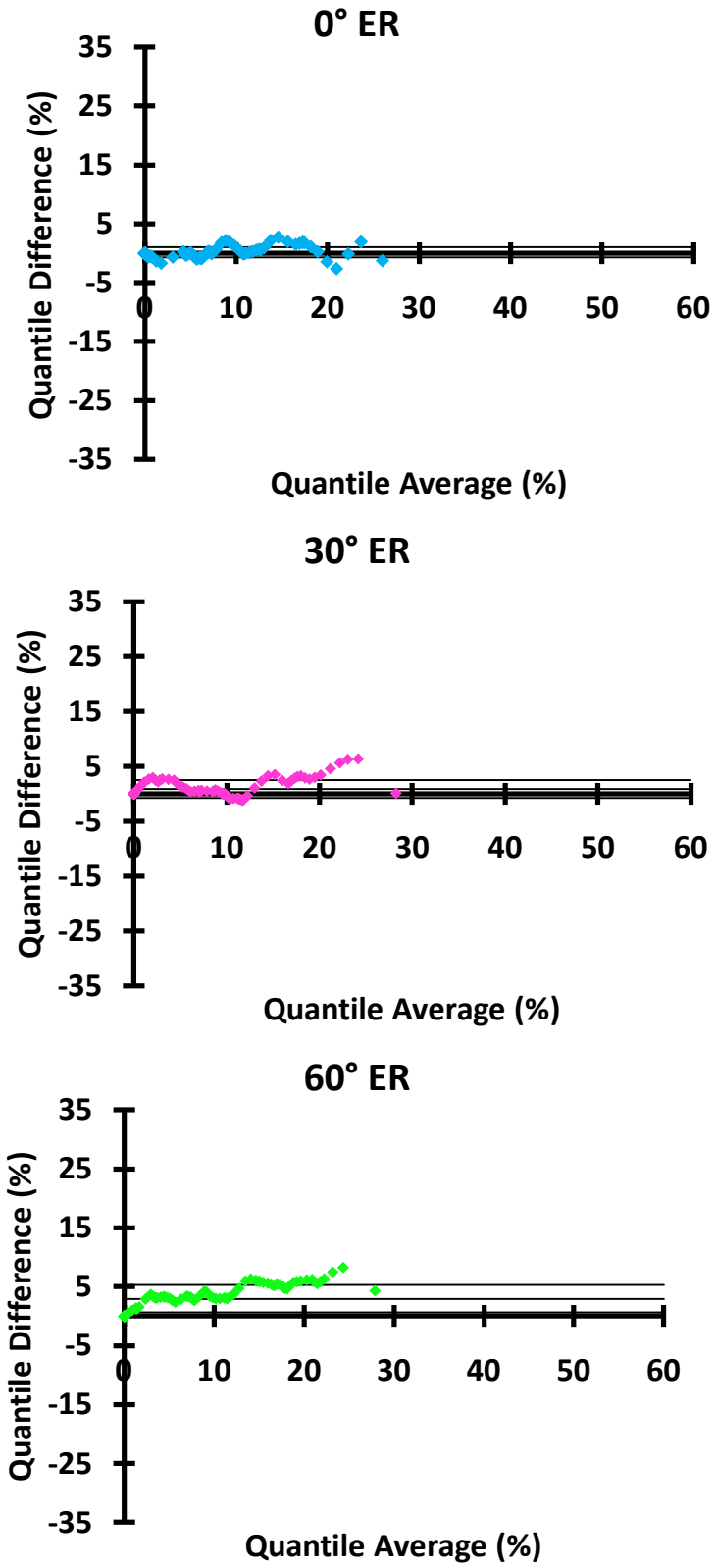

Figure 5.21 Projection plots demonstrating differences in the strain distributions in the *intact* and *injured* anteroinferior capsule during the simulated clinical exams at 0°, 30° and 60° of external rotation for specimen H01015R.

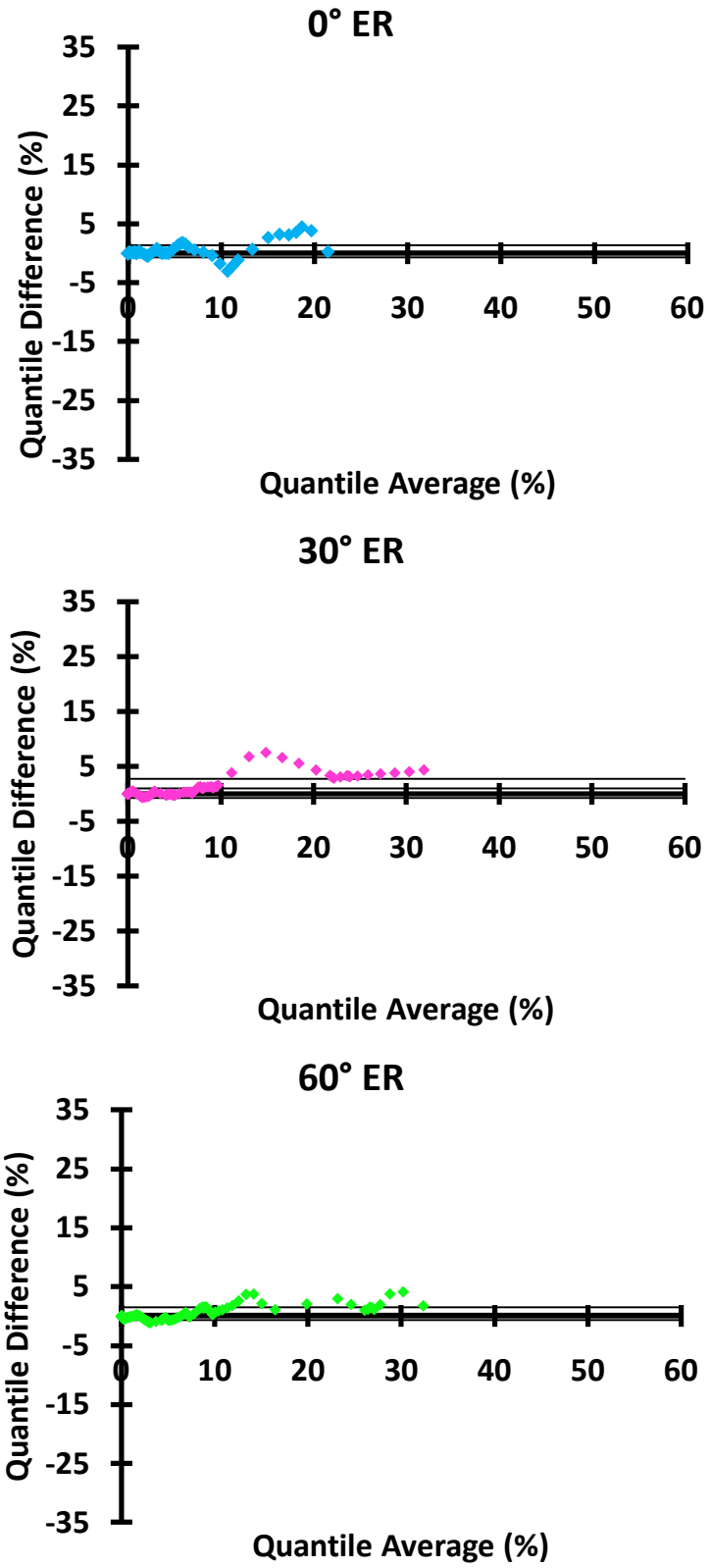

Figure 5.22 Projection plots demonstrating differences in the strain distributions in the *intact* and *injured* anteroinferior capsule during the simulated clinical exams at 0°, 30° and 60° of external rotation for specimen H01022L.

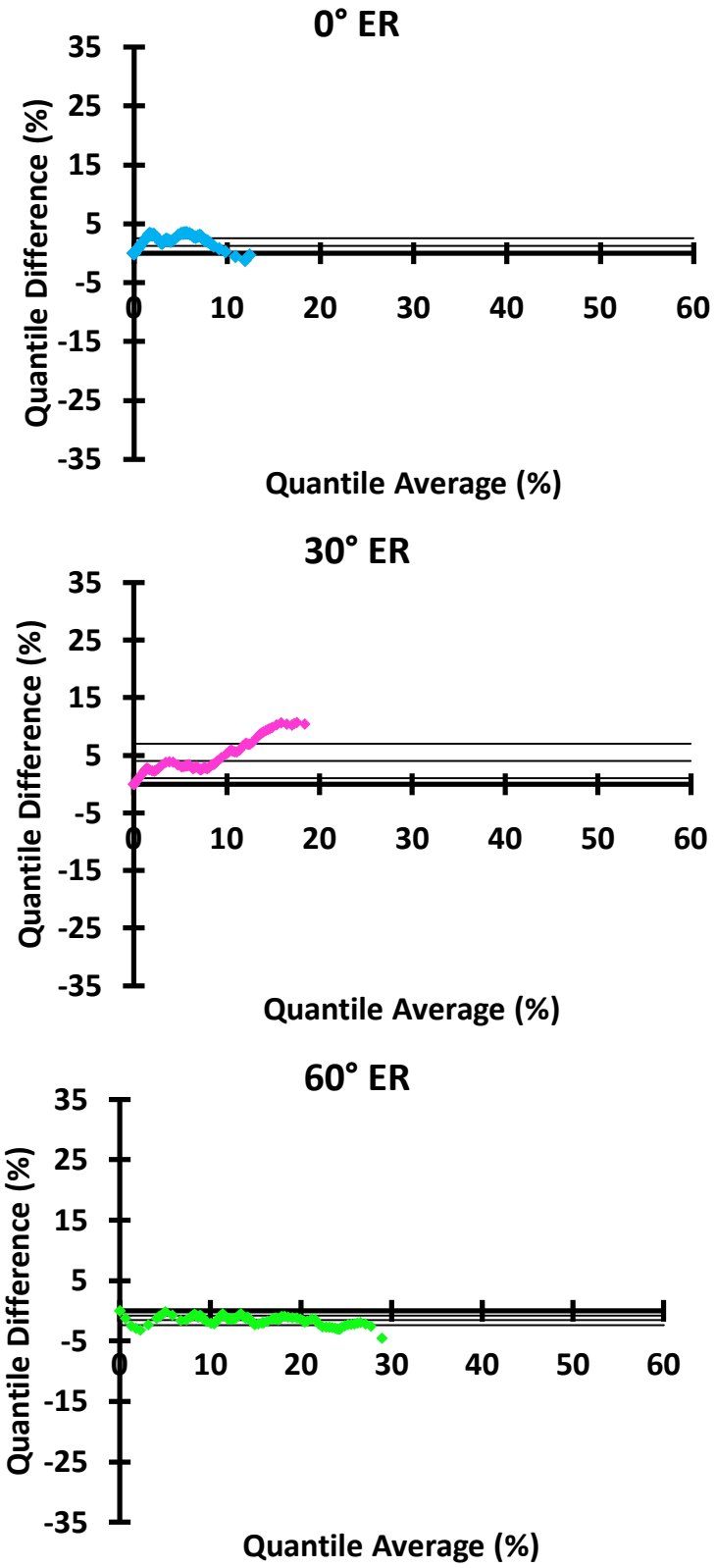

Figure 5.23 Projection plots demonstrating differences in the strain distributions in the *intact* and *injured* anteroinferior capsule during the simulated clinical exams at 0°, 30° and 60° of external rotation for specimen H01029L.

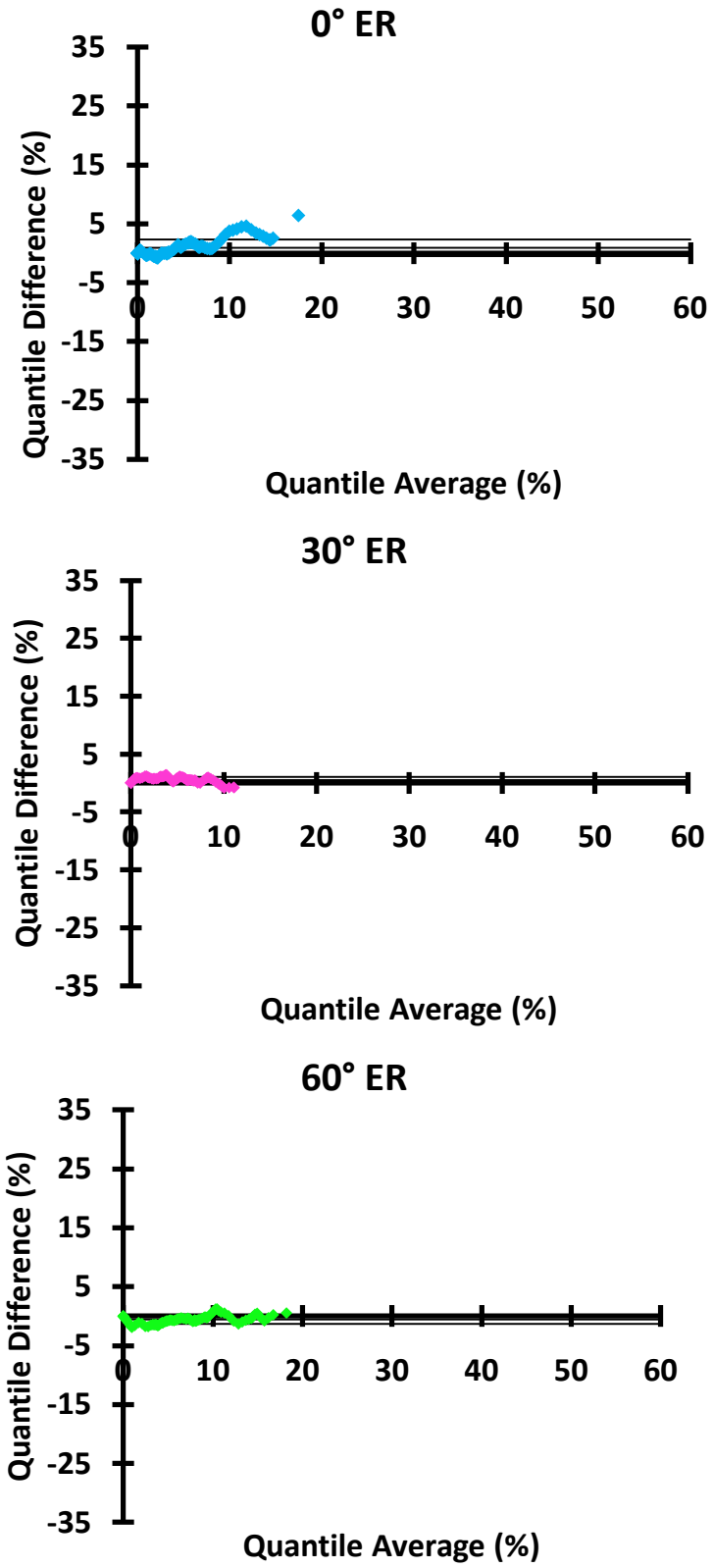

Figure 5.24 Projection plots demonstrating differences in the strain distributions in the *intact* and *injured* anteroinferior capsule during the simulated clinical exams at 0°, 30° and 60° of external rotation for specimen H01007R.

The projection plots demonstrated that elements containing the higher strain (higher quantile average) also exhibited greater changes in strain (quantile difference) between the *intact* and *injured* states. No significant differences were found in mean quantile difference (y-axis offset) at 0° (1.2 ± 1.9%), 30° (1.4 ± 1.4%) and 60° (2.1 ± 1.5%) of external rotation. The mean quantile difference was greater than the experimental repeatability in only three of the eighteen projection plots. (Table 5.15)

Table 5.15 Mean and range of the quantile difference for the projection plots comparing the strain distribution in the *intact* and *injured* anteroinferior capsule during the simulated clinical exams.

SPECIMEN #	0° ER		30° ER		60° ER	
	Mean (%)	Range (%)	Mean (%)	Range (%)	Mean (%)	Range (%)
H00915L	5.0	28.1	2.1	23.7	3.0	23.2
H00925R	-0.3	4.6	0.1	12.5	4.1	28.0
H01015R	0.1	5.4	0.9	7.5	3.0	8.2
H01022L	0.3	7.5	1.0	8.2	0.4	5.2
H01029L	1.2	4.7	4.1	10.7	1.6	4.6
H01107R	0.9	7.2	0.5	2.3	0.6	3.1

Range values showed greater differences in the strain distributions between the *intact* and *injured* anteroinferior capsule than the mean quantile difference at all three joint positions. Range values increased from 0° (9.6 ± 9.2%) to 30° (10.8 ± 7.2%) to 60° (12.1 ± 10.7%) of external rotation but these differences were not statistically significant between each of the joint positions.

As described in Section 5.3.3.3, the amount of nonrecoverable strain in the anteroinferior capsule resulting from anterior dislocation varied greatly between shoulders with peak values of 46.5%, 11.8%, 7.5%, 9.0%, 7.3%, and 5.5% in each shoulder demonstrating localized areas of

increased tissue damage. Further, the peak nonrecoverable strain in the axillary pouch (13.9 ± 16.1%) was greater than the AB-IGHL (7.1 ± 3.6%). Some projection plots showed large differences between the *intact* and *injured* capsule whereas others showed very minimal differences. These differences were found to be related to the amount of tissue damage. No significant correlations were found between the peak nonrecoverable strain in each shoulder and the mean quantile difference values at 0° ($r = -0.03$, $p = 0.96$), 30° ($r = 0.03$, $p = 0.96$) or 60° ($r = 0.23$, $p = 0.66$) of external rotation. However, significant correlations were found between the peak nonrecoverable strain in each shoulder and the range values at 30° ($r = 0.83$, $p = 0.04$) and 60° ($r = 0.89$, $p = 0.02$) of external rotation but not at 0° of external rotation ($r = 0.26$, $p = 0.62$).

5.3.5.2 Strain Distribution in Anteroinferior Capsule: Discussion

In order to assess the effect of dislocation on the strain distribution in the anteroinferior capsule during the simulated clinical exams a modified projection plot analysis was used. [189, 190] Projection plots are a method for comparing two distributions and are an extension of quantile-quantile (Q-Q) plots. They are better suited for statistical comparisons as the asymmetry of Q-Q plots is resolved since projection plots are viewed from the line $y = x$. Other methods, such as comparing means, medians, or standard deviation values, have been employed to compare distributions, however, they may not be the most appropriate as two distributions can have similar means or standard deviations while still differing in shape, especially if the distributions are not normally distributed. Projection plots are able to identify differences in location (mean, median, mode, etc.), spread (dispersion around the location such as standard deviation), and shape (skewness, kurtosis) between two distributions and are also capable of comparing distributions of unequal sample numbers. If two distributions are identical, data will

fall along the line y = 0. Differences in location, shape and spread will be manifested as y-axis offsets, non-linear data, and non-zero slopes, respectively.

Recently, projection plots have been modified in order to make quantitative comparisons between two fiber distributions in the supraspinatus tendon. [190] Lake and coworkers computed the mean quantile difference, or y-axis offset, and range of the quantile difference values as quantitative measures of differences in location and shape/spread of two distributions, respectively. This allows statistical tests to be performed on these parameters in order to determine if two distributions are statistically different. This modified projection plot method was employed in the current work in order to compare the strain distributions in the anteroinferior capsule during the simulated clinical exams for the *intact* and *injured* joints.

Small mean and large range values indicate that the strain distributions in the anteroinferior capsule differ more in shape and spread than location following dislocation. In other words, the area of the anteroinferior capsule experiencing high strains remains the same following injury but the strain values in that area and the surrounding elements were altered. In most cases areas of the capsule experiencing high strains increased following injury, but in some instances decreases in strain were observed further suggesting that injury to the anteroinferior capsule following dislocation should be evaluated on a specimen-by-specimen basis.

Permanent tissue deformation was quantified as nonrecoverable strain in the capsule and was correlated to changes in capsule function following dislocation. Projection plots demonstrated that areas of the *intact* capsule experiencing the greatest strain during the simulated clinical exams were the areas with the most change in strain following injury at all three joint positions. The largest peak maximum principal strains during the simulated clinical exams occurred in the axillary pouch. Thus the greatest change in strain following injury was also in

this region. These changes were found to be significantly correlated to the amount of peak nonrecoverable strain in positions of external rotation, i.e. when the joint is positioned such that the injured region of the capsule is contributing to joint stability, its strain distribution is altered. These results suggest that the posterior axillary pouch, which experiences areas of greater localized damage from dislocation compared to the anterior axillary pouch and AB-IGHL, exhibits a loss in stabilizing function particularly in positions of external rotation. Therefore, plicating the posterior axillary pouch during repair procedures following anterior dislocation may be appropriate.

5.3.5.3 Joint Kinematics: Results

Anterior-Posterior

A 25 N anterior-posterior load was applied to the humerus in order to simulate clinical exams in the *intact* and *injured* joints at 0°, 30° and 60° of external rotation. The resulting anterior-posterior joint kinematics are for each specimen are shown in Appendix E. Anterior translations in the *intact* and *injured* joint during the simulated clinical exams decreased from 17.0 ± 10.4 mm and 18.6 ± 10.4 mm, to 13.3 ± 6.7 mm and 15.3 ± 6.3 mm, and again to 4.4 ± 2.0 mm and 6.4 ± 2.6 mm at 0°, 30°, and 60° of external rotation, respectively. (Table 5.16)

Table 5.16 Anterior translations in the *intact* and *injured* joint in response to a 25 N anterior load applied at 60° of abduction, 0°, 30° and 60° of external rotation.

SPECIMEN #	0° ER		30° ER		60° ER	
	Intact (mm)	Injured (mm)	Intact (mm)	Injured (mm)	Intact (mm)	Injured (mm)
H00915L	5.1	5.5	6.6	7.0	1.8	2.2
H00925R	30.3	32.8	19.9	22.0	5.4	7.4
H01015R	24.8	25.6	18.3	20.3	4.4	8.2
H01022L	20.7	21.8	19.2	20.4	7.4	9.1
H01029L	4.8	8.5	5.0	10.3	4.9	7.2
H01107R	16.5	17.2	10.6	12.0	2.4	4.2

Significant differences were found in anterior translation, with the 25 N anterior load applied, between the *intact* and *injured* states at 0° ($p = 0.03$), 30° ($p = 0.03$), and 60° ($p < 0.01$) of external rotation. (Figure 5.25) Increases in anterior translation were 1.5 ± 1.3 mm, 2.1 ± 1.7 mm, and 2.0 ± 1.1 mm at 0°, 30°, and 60° of external rotation, respectively. The percent increases in anterior translation increased from 17.7 ± 29.2% at 0° to 25.5 ± 39.5% at 30° and again to 48.4 ± 26.9% at 60° of external rotation.

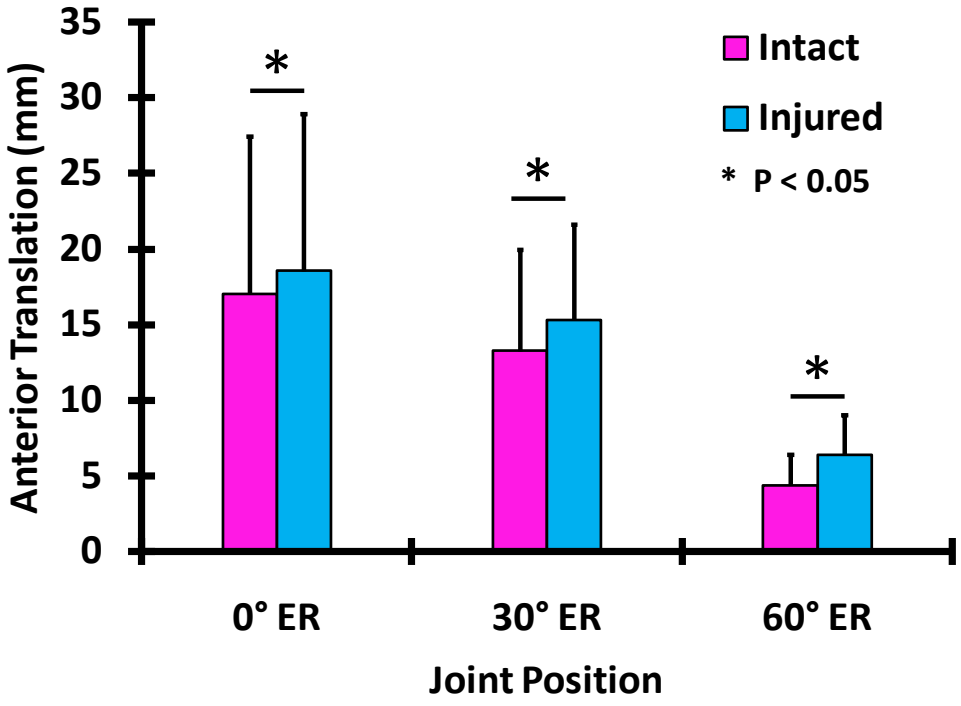

Figure 5.25 Anterior translation (mean ± SD) in response to a 25 N anterior load at 60° of abduction, 0°, 30°, and 60° of external rotation.

Posterior translations in the *intact* and *injured* joint during the simulated clinical exams decreased from 16.9 ± 5.7 mm and 16.1 ± 6.4 mm, to 13.8 ± 8.7 mm and 11.5 ± 8.9 mm, and again to 8.1 ± 6.6 mm and 7.6 ± 7.3 mm at 0°, 30°, and 60° of external rotation, respectively.

Table 5.17 Posterior translations in the *intact* and *injured* joint in response to a 25 N posterior load applied at 60° of abduction and 0°, 30° and 60° of external rotation.

SPECIMEN #	0° ER		30° ER		60° ER	
	Intact (mm)	Injured (mm)	Intact (mm)	Injured (mm)	Intact (mm)	Injured (mm)
H00915L	14.4	11.7	5.3	3.3	2.0	1.1
H00925R	11.0	7.7	3.8	2.9	3.9	2.6
H01015R	27.7	26.3	18.8	6.8	14.1	15.3
H01022L	17.8	18.5	26.1	25.8	18.6	18.3
H01029L	14.9	15.0	17.9	16.8	6.0	4.5
H01107R	15.6	17.1	10.6	13.6	4.2	3.9

No significant differences were found in posterior translation, with the 25 N posterior load applied, between the *intact* and *injured* states at 0° ($p = 0.33$), 30° ($p = 0.34$), and 60° ($p = 0.25$) of external rotation. The increase in anterior translation and no change in posterior translation indicate that this experimental model of glenohumeral dislocation can be used to successfully simulate the state of a joint suffering from anterior instability.

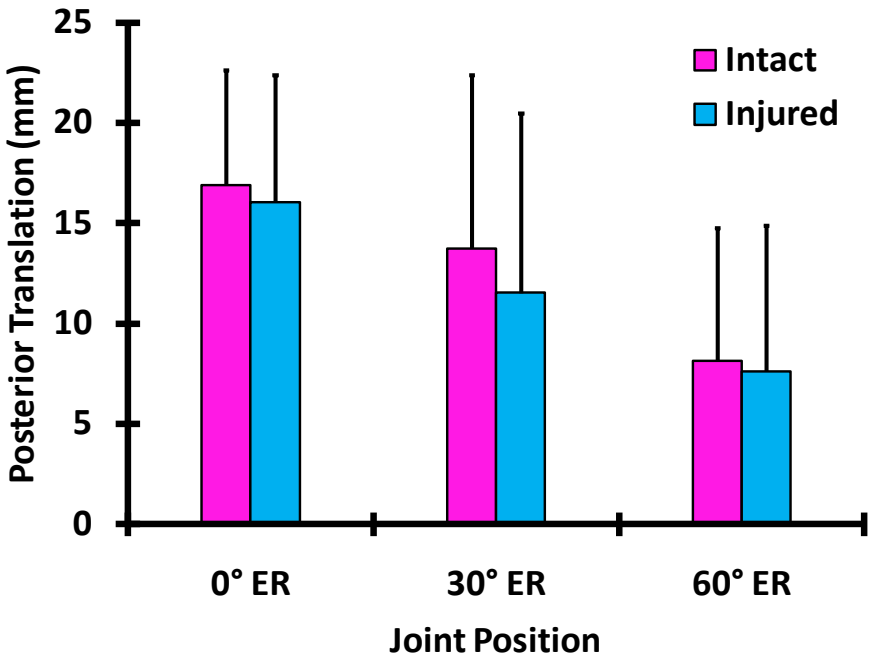

Figure 5.26 Posterior translation (mean ± SD) in response to a 25 N posterior load at 60° of abduction, 0°, 30°, and 60° of external rotation.

Superior-Inferior

As the joint was allowed to translate in all three degrees of freedom during the simulated clinical exams, the resulting superior-inferior joint translations were recorded the *intact* and *injured* joints at 0°, 30° and 60° of external rotation. The resulting superior-inferior joint kinematics are shown Appendix F for each specimen. These joint kinematics indicate that some shoulders translated inferiorly more than others.

Significant differences were found in the superior-inferior translations between the *intact* and *injured* joint at 30° ($p = 0.045$) but not at 0° ($p = 0.17$) or 60° ($p = 0.11$) of external rotation. Superior-inferior translations were 2.5 ± 3.2 mm, 0.0 ± 2.3 mm, and -0.2 ± 0.8 mm in the *intact* joint at 0°, 30°, and 60° of external rotation, respectively. In the *injured* joint, superior-inferior

translations were 2.8 ± 3.1 mm, 0.4 ± 2.6 mm, and -0.4 ± 0.9 mm at 0°, 30°, and 60° of external rotation, respectively.

Table 5.18 Superior-inferior joint translations in the *intact* and *injured* joint in response to a 25 N anterior load applied at 60° of abduction, 0°, 30° and 60° of external rotation.

SPECIMEN #	0° ER		30° ER		60° ER	
	Intact (mm)	Injured (mm)	Intact (mm)	Injured (mm)	Intact (mm)	Injured (mm)
H00915L	-0.9	-0.3	-1.4	-0.9	0.3	0.5
H00925R	0.6	0.1	-3.9	-4.1	-1.6	-1.9
H01015R	5.0	5.2	0.7	1.2	0.2	-0.2
H01022L	6.7	7.0	2.8	3.2	0.3	-0.1
H01029L	-0.4	0.5	0.2	1.3	-0.6	-0.7
H01107R	4.1	4.5	1.3	1.7	0.4	0.3

The change in superior-inferior translation was 0.3 ± 0.5 mm, 0.5 ± 0.4 mm, and -0.2 ± 0.2 mm at 0°, 30°, and 60° of external rotation, respectively. Many of the changes in superior-inferior translations between the *intact* and *injured* joint were within the experimental repeatability of the robotic/UFS testing system, particularly at 60° of external rotation, indicating that the superior-inferior position of the joint between these two states was essentially unchanged. (Table 5.19)

Table 5.19 Change in superior-inferior joint translation (*injured* – *intact*) in response to a 25 N anterior load applied at 60° of abduction, 0°, 30° and 60° of external rotation.

SPECIMEN #	Δ0° (mm)	Δ30° (mm)	Δ60° (mm)
H00915L	0.6	0.5	0.2
H00925R	-0.5	-0.2	-0.3
H01015R	0.2	0.5	-0.4
H01022L	0.3	0.4	-0.4
H01029L	0.9	1.1	-0.1
H01107R	0.4	0.4	-0.1

Medial-Lateral

The medial-lateral joint translations in the *intact* and *injured* joints during the simulated clinical exams at 0°, 30° and 60° of external rotation were also recorded. Plots of these medial-lateral joint kinematics are shown in the tables below for each specimen.

No significant differences were found in the medial-lateral translations between the *intact* and *injured* joint at 0° ($p = 0.15$), 30° ($p = 0.96$), or 60° ($p = 0.66$) of external rotation. Medial-lateral translations were 2.1 ± 0.7 mm, 1.9 ± 0.7 mm, and 0.3 ± 0.5 mm in the *intact* joint at 0°, 30°, and 60° of external rotation, respectively. (Table 5.20) In the *injured* joint, medial-lateral translations were 1.7 ± 0.5 mm, 1.9 ± 0.5 mm, and 0.3 ± 0.6 mm at 0°, 30°, and 60° of external rotation, respectively.

Table 5.20 Medial-lateral joint translations in the *intact* and *injured* joint in response to a 25 N anterior load applied at 60° of abduction, 0°, 30° and 60° of external rotation.

SPECIMEN #	0° ER		30° ER		60° ER	
	Intact (mm)	Injured (mm)	Intact (mm)	Injured (mm)	Intact (mm)	Injured (mm)
H00915L	1.6	1.0	1.6	1.4	-0.3	-0.4
H00925R	1.8	1.0	1.9	1.2	0.7	0.3
H01015R	2.7	1.8	2.1	2.0	0.5	1.1
H01022L	2.9	2.2	2.3	2.0	0.9	1.1
H01029L	1.1	1.9	0.8	2.4	-0.2	0.0
H01107R	2.4	2.0	2.8	2.6	0.0	-0.1

The change in medial-lateral translations was -0.4 ± 0.6 mm, 0.0 ± 0.8 mm, and 0.1 ± 0.3 mm at 0°, 30°, and 60° of external rotation, respectively. Similar to the superior-inferior translations, many of the changes in medical-lateral translations between the *intact* and *injured* joint were within the experimental repeatability of the robotic/UFS testing system indicating that the medial-lateral position of the joint between these two states was essentially unchanged. (Table 5.21)

Table 5.21 Change in medial-lateral joint translation (*injured – intact*) in response to a 25 N anterior load applied at 60° of abduction, 0°, 30° and 60° of external rotation.

SPECIMEN #	Δ0° (mm)	Δ30° (mm)	Δ60° (mm)
H00915L	-0.6	-0.2	-0.1
H00925R	-0.8	-0.7	-0.4
H01015R	-0.9	-0.1	0.6
H01022L	-0.7	-0.3	0.2
H01029L	0.8	1.6	0.2
H01107R	-0.4	-0.2	-0.1

5.3.5.4 Joint Kinematics: Discussion

Compare to Literature

Glenohumeral joint kinematics at 60° of abduction and 0°, 30° and 60° of external rotation have been examined previously using a magnetic tracking system. [120, 195] Decreases in anterior translation as well as coupled inferior translation were found with increasing external rotation and support the results found in the current work. These changes in joint kinematics with external rotation were also found when performing the simulated clinical exams on the robotic/UFS testing system when developing and validating finite element models of the glenohumeral joint. [134] In addition, another group [73] reported increased in anterior translation in the apprehension position following the creation of permanent deformation via excessive external rotation on the same order of magnitude (4.4 mm) as was found in the current work (2.0 mm).

Significance of Results

Following anterior dislocation significant increases in anterior translation but no change in posterior translation during simulated clinical exams were observed. These results demonstrate that this experimental dislocation model successfully simulated the state of a joint suffering from anterior instability. The percent increase in anterior translation almost tripled from 0° to 60° ER further indicating compromised capsule function. Significant increases in anterior translation have been reported for other injury models which create permanent deformation in the capsule [71-73], although the deformation was not created via joint dislocation. The changes in anterior translation, although similar to those reported for other experimental models creating permanent capsular deformation, are on the order of a few millimeters and statistically significant changes

in inferior translation at 30° of external rotation were only around 1 mm. While larger dislocations may result in greater changes in translation, surgeons may not be capable of accurately detecting the small changes in anterior/inferior translation between normal and injured shoulders found here. Further, even if the changes in anterior translation could be detected by clinicians, it was the posterior axillary pouch that was the region of the capsule experiencing the most damage following dislocation. Therefore, repair procedures which target the anterior capsule based on increased anterior translation during pre-operative physical exams are not addressing the appropriate region of the capsule. This may contribute to the poor ability of current clinical examinations to making the correct diagnosis. As larger changes in joint kinematics occur at joint positions where the damaged region of the capsule is most important for maintaining joint stability, developing standardized clinical exams to diagnose damage in specific capsule regions may lead surgeons to repair the appropriate capsule regions, thus improving patient outcome due to misdiagnosis.

5.3.5.5 In Situ Force in Capsule: Results

The in situ force in the capsule during dislocation could only be computed in three of the six specimens (H01015R, H01022L, and H01029L) as not all the necessary data was collected during the first experiments. The in situ force in the capsule during dislocation for these specimens was 169.2N, 90.2 N and 155.8 N, respectively.

The in situ force in the capsule was computed during the simulated clinical exams at three joint states: 1) *intact* capsule during *intact* kinematics, 2) *injured* capsule during *intact* kinematics, and 3) *injured* capsule during *injured* kinematics. Friedman tests yielded significant differences between the *in situ* force in the capsule in the three joint states at 0° ($p = 0.009$), 30° ($p = 0.03$) and 60° ($p = 0.009$) of ER.

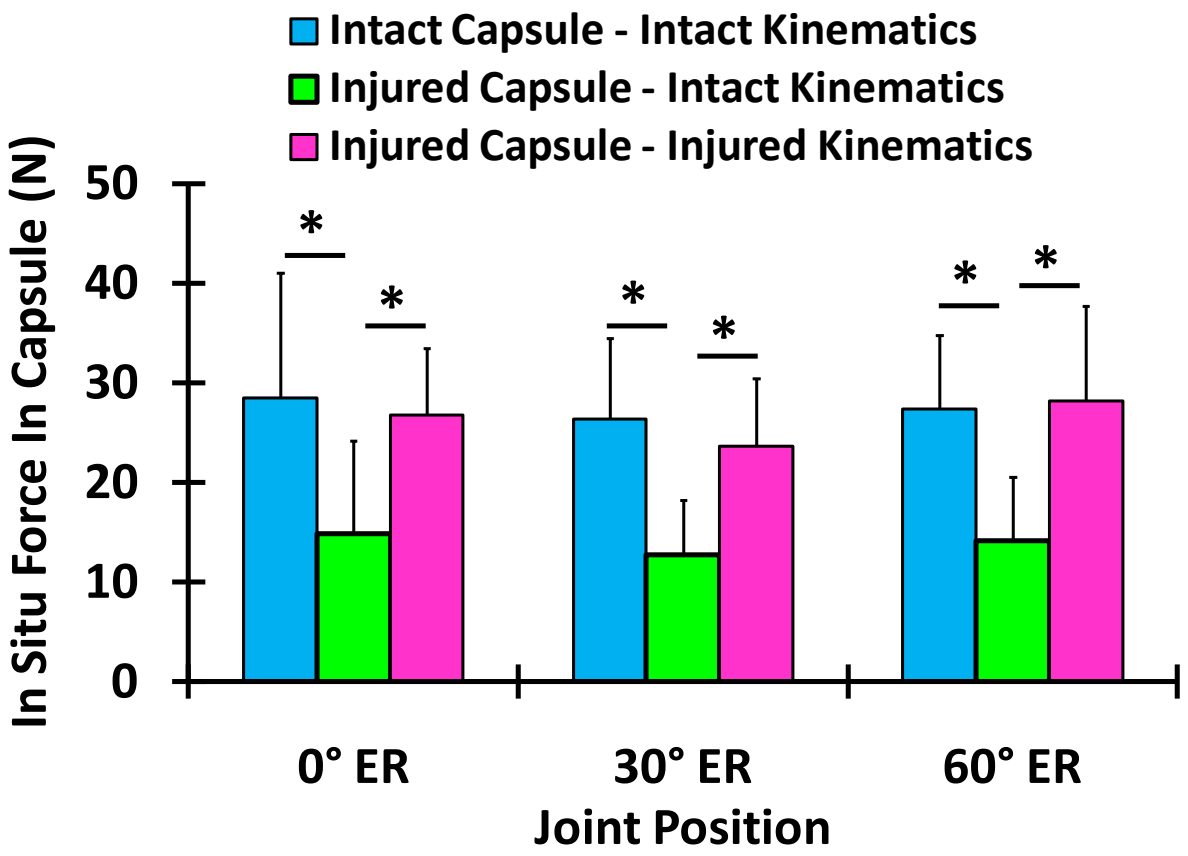

Figure 5.27 In situ force in the *intact* capsule during *intact* kinematics (blue), *injured* capsule during *intact* kinematics (green), and *injured* capsule during *injured* kinematics (pink) in response to a 25 N anterior load applied at 60° of abduction and 0°, 30°, and 60° of external rotation.

The in situ force in the intact capsule during intact kinematics in response to the simulated clinical exam (25 N anterior load) was 28.5 ± 12.5 N, 26.4 ± 8.1 N, and 27.3 ± 7.4 N at 0°, 30° and 60° of external rotation, respectively. Following anterior dislocation, the in situ force in the injured capsule during intact kinematics decreased significantly at all three joint positions to 14.9 ± 9.4 N (48%, p = 0.03), 12.7 ± 5.5 N (52%, p = 0.03), and 14.1 ± 6.4 N (48%, p = 0.03), respectively. Finally, the in situ force in the injured capsule increased significantly during injured compared to intact kinematics to 26.8 ± 6.7 N (80%, p = 0.03) at 0°, 23.6 ± 6.8 N (86%, p = 0.046) at 30° and 28.2 ± 9.5 N (100%, p = 0.03) at 60° of ER. The in situ force in the injured capsule during injured kinematics was not significantly different from the in situ force in the

intact capsule during intact kinematics at any joint position. ($p = 0.75$ at 0°, $p = 0.25$ at 30°, and $p = 0.46$ at 60°).

Table 5.22 In situ force in the capsule at the three joint states in response to a 25 N anterior load at 60° of abduction and 0° of external rotation.

Kinematics:	Intact		Injured
Capsule State:	0° ER Intact (N)	0° ER Injured (N)	0° ER Injured (N)
H00915L	7.7	0.9	20.0
H00925R	45.4	13.2	23.8
H01015R	32.4	26.2	29.7
H01022L	30.7	13.5	29.4
H01029L	22.6	10.7	20.5
H01107R	32.3	24.6	37.4

Table 5.23 In situ force in the capsule at the three joint states in response to a 25 N anterior load at 60° of abduction and 30° of external rotation.

Kinematics:	Intact		Injured
Capsule State:	0° ER Intact (N)	0° ER Injured (N)	0° ER Injured (N)
H00915L	19.9	6.5	17.0
H00925R	39.7	11.6	30.9
H01015R	32.2	21.6	20.0
H01022L	23.2	13.6	20.1
H01029L	18.4	7.7	20.3
H01107R	24.9	15.3	33.5

Table 5.24 In situ force in the capsule at the three joint states in response to a 25 N anterior load at 60° of abduction and 60° of external rotation.

Kinematics:	Intact		Injured
Capsule State:	0° ER Intact (N)	0° ER Injured (N)	0° ER Injured (N)
H00915L	33.8	25.4	37.0
H00925R	31.5	14.7	35.3
H01015R	22.5	9.0	26.9
H01022L	15.6	8.5	26.9
H01029L	26.0	10.2	10.8
H01107R	34.8	16.7	32.4

5.3.5.6 In Situ Force in Capsule: Discussion

This study used robotic technology to simulate injury to the glenohumeral capsule resulting from glenohumeral dislocation due to an excessive force in the anterior direction and to determine the effect of dislocation on the *in situ* force in the glenohumeral capsule during a simulated clinical exam at three joint positions.

Comparison to Literature

The in situ force in each region of the glenohumeral capsule has been reported previously under an 89 N anterior and poster load at four abduction angles. [27] In this work, *in situ* forces between 10 and 20 N were found when the capsule was separated and isolated during anterior loading. Therefore, eliminating the interactions between each of the capsule regions reduces the ability of the capsule to maintain joint stability. It is likely that the in situ forces in the capsule due to separation of the discrete regions would be larger in positions of external rotation. This study, along with more recent literature [9, 69, 136], suggests the capsule should be evaluated as

a continuous structure. Therefore, in the current work, the *in situ* force in the entire capsule was determined rather than separating and isolating various capsule regions in order to determine the *in situ* force in the discrete ligaments.

Significance of Results

The in situ force in the capsule during joint dislocation was nearly four times larger than the *in situ* force in the capsule during the simulated clinical exams demonstrating that the *intact* capsule is capable of withstanding large forces prior to failure.

The *in situ* force in the capsule during *intact* kinematics decreased significantly following anterior dislocation. Along with the presence of nonrecoverable strain, this verifies that permanent deformation of the capsule occurred. During the simulated clinical exams before and after anterior dislocation, the *in situ* force in the *intact* and *injured* capsule was similar; however, the *injured* joint experienced greater anterior translations. These results suggest that if clinicians apply similar loads to the intact and injured joints during clinical exams they should be able to detect differences in translation, particularly when the joint is in positions of external rotation which experienced the greatest change in anterior translation following dislocation. In order to do this a device may need to be developed to provide clinicians with real-time force feedback to train them in appling similar loads to each joint.

5.3.5.7 Glenohumeral Contact Force

Similar to the in situ force in the capsule during dislocation, the glenohumeral contact forces were only computed in three of the six specimens (H01015R, H01022L, and H01029L). The resultant contact force during dislocation for these specimens was 59.6N, 30.6 N and 99.4 N, respectively.

Glenohumeral contact forces in response to the simulated clinical exams in all directions are shown below. Contact forces during the *injured* kinematics were larger in the anterior-posterior (Figure 5.28) and medial-lateral (Figure 5.29) directions were larger compared to during the *intact* kinematics at all three joint positions. In contrast, no changes in the superior-inferior (Figure 5.30) contact forces were observed at any joint position.

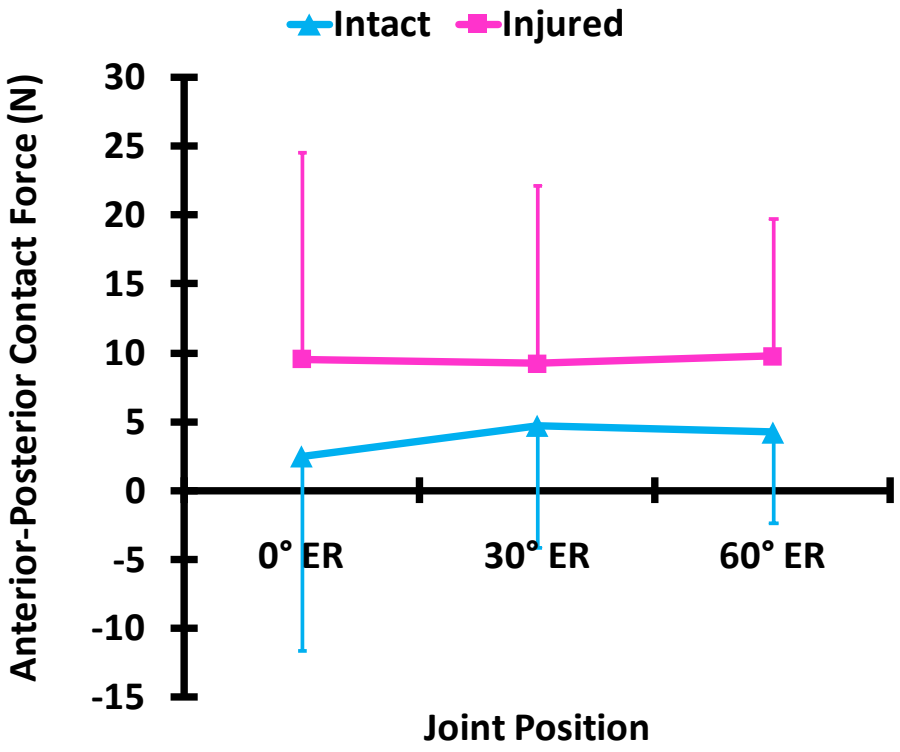

Figure 5.28 Anterior-posterior contact forces between the humerus and scapula during *intact* and *injured* kinematics in response to a 25 N anterior load at 60° of abduction and 0°, 30° and 60° of external rotation.

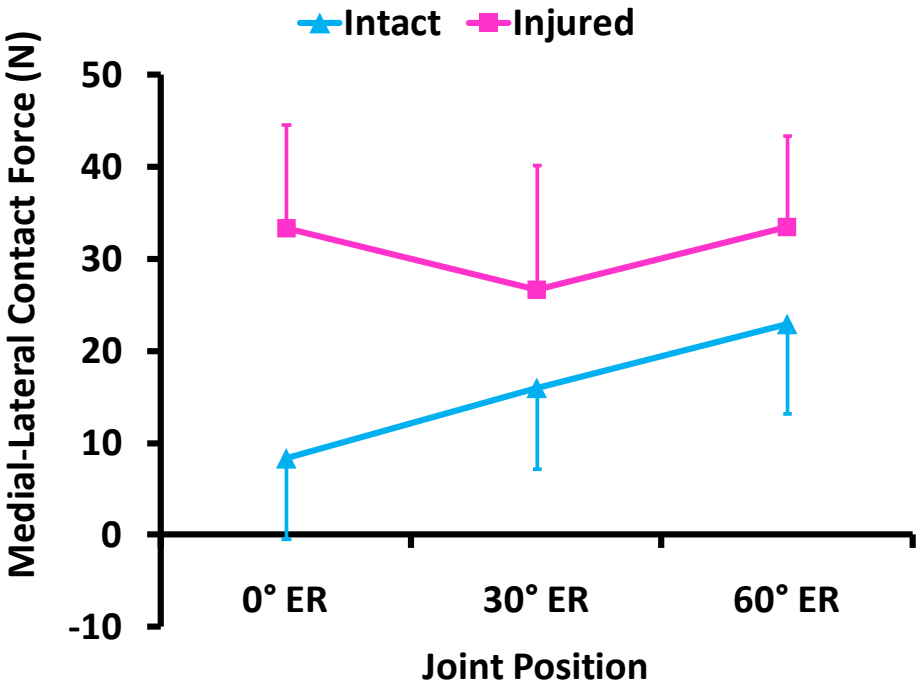

Figure 5.29 Medial-lateral contact forces between the humerus and scapula during *intact* and *injured* kinematics in response to a 25 N anterior load at 60° of abduction and 0°, 30° and 60° of external rotation.

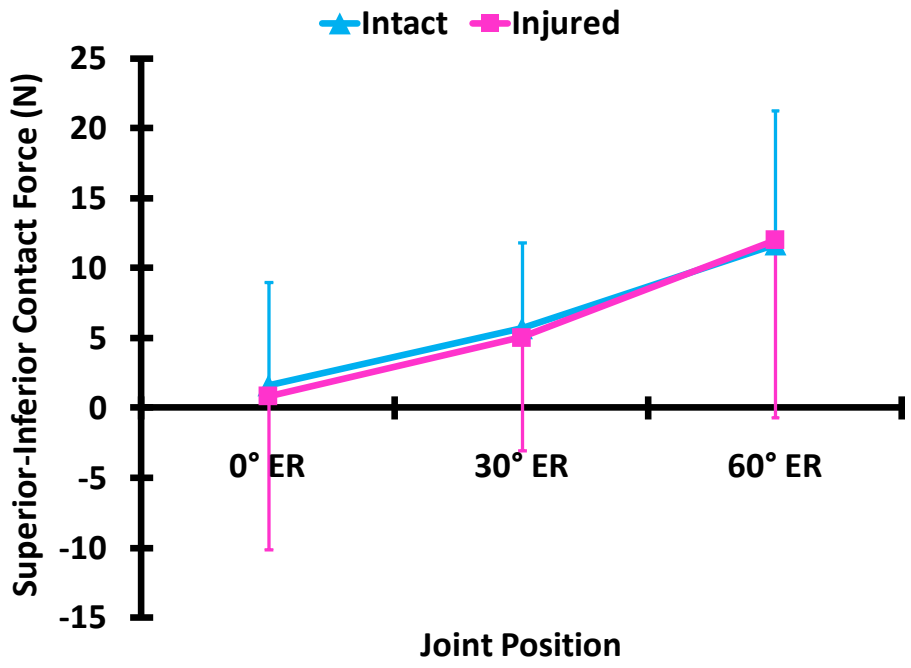

Figure 5.30 Superior-inferior contact forces between the humerus and scapula during *intact* and *injured* kinematics in response to a 25 N anterior load at 60° of abduction and 0°, 30° and 60° of external rotation.

During the *intact* kinematics, the resultant contact forces increased with increasing external rotation (15.3 ± 5.9 N at 0°, 21.2 ± 4.9 N at 30°, and 28.2 ± 9.6 N at 60°), however, this trend was not observed during the *injured* kinematics (37.9 ± 14.2 N at 0°, 30.9 ± 16.0 N at 30°, and 39.8 ± 9.5 N at 60°). Specimen H00925R exhibited very small contact forces, particularly at 30 of external rotation. This could be due to the humeral head translating to the edge of the glenoid rim as shown in the medial lateral translation plots for this specimen.

Table 5.25 Resultant glenohumeral contact forces between the humerus and scapula during *intact* and *injured* kinematics in response to a 25 N anterior load at 60° of abduction, 0°, 30°, and 60° of external rotation.

	0°		30°		60°	
SPECIMEN #	**Intact (N)**	**Injured (N)**	**Intact (N)**	**Injured (N)**	**Intact (N)**	**Injured (N)**
H00915L	24.1	49.2	20.9	44.2	37.9	42.6
H00925R	12.8	36.7	13.5	15.1	23.4	46.9
H01015R	8.8	26.3	26.7	28.5	34.8	39.2
H01022L	9.7	19.9	18.8	27.2	32.1	45.4
H01029L	17.8	58.3	21.6	55.1	29.5	43.4
H01107R	18.7	36.9	26.0	15.4	11.2	21.1

The resultant contact forces between the humerus and scapula during the simulated clinical exams increased by 148% at 0°, 46% at 30° and 41% at 60° of external rotation following dislocation. (Figure 5.31**)** These increases were significant at 0° ($p = 0.03$) and 60° ($p = 0.03$) of external rotation, but not at 30° of external rotation ($p = 0.17$).

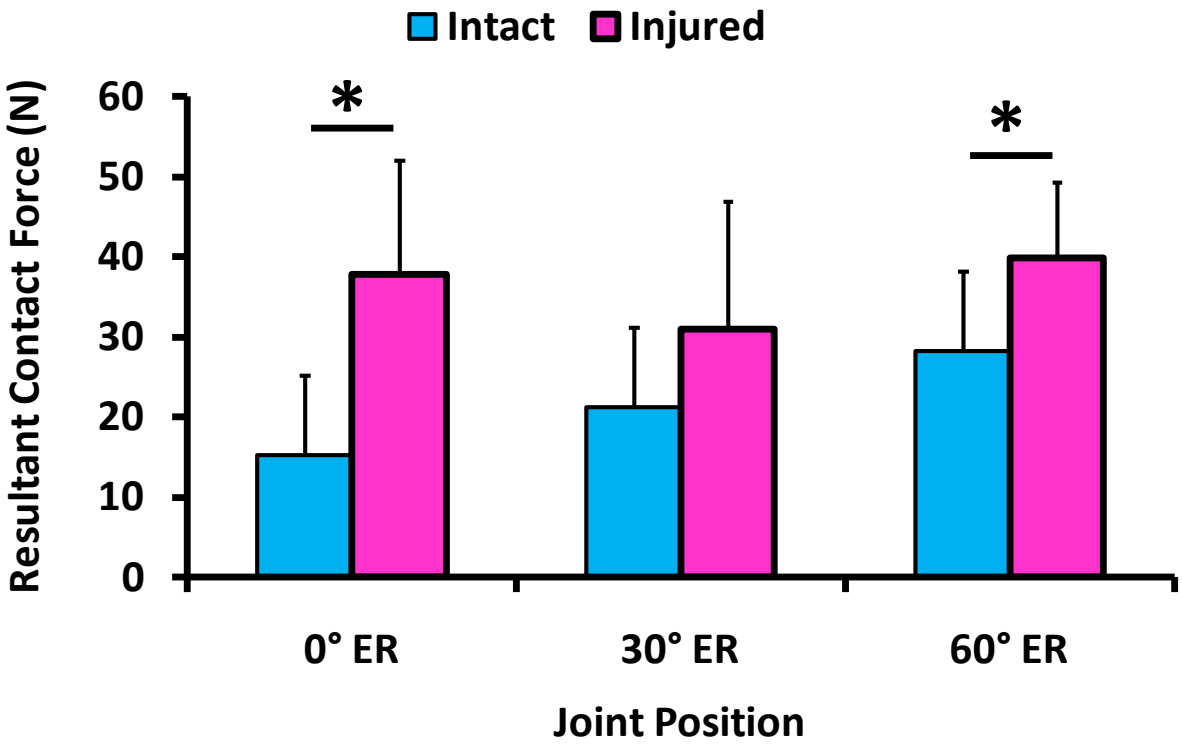

Figure 5.31 Resultant bony contact forces between the humerus and scapula during *intact* and *injured* kinematics in response to a 25 N anterior load at 60° of abduction and 0°, 30° and 60° of external rotation.

5.3.5.8 Glenohumeral Contact Forces: Discussion

Comparison to Literature

The contact forces determined in this study are difficult to compare with the literature as many studies examining glenohumeral joint contact include the active joint stabilizers in their models or examine in vivo subjects [196, 197] and thus are measuring contact forces much larger than reported in this work. However, an analytical model of the glenohumeral joint was constructed to evaluate joint kinematics during external rotation. [37] In order to validate this model, glenohumeral joint contact forces were determined in vitro in four shoulders. Contact forces between the humerus and glenoid were found to increase with external rotation. This

work supports the results found here which exhibited increasing glenohumeral contact forces with external rotation in both the *intact* joint.

Significance of Results

The change in glenohumeral kinematics following anterior dislocation resulted in a significant increase in glenohumeral contact forces between the humerus and scapula. This increase could be due to the shape of the glenoid. As the humeral head is translated towards the geloid rim the contact area may decrease as it no longer sits centered on the glenoid. Rather the humeral head is shifted towards one side of the glenoid and is closer to the edge. The decrease in area should be investigated in the future but could increase the contact force as well as change its direction. In addition, with large increases in anterior translation following dislocation, the humeral head could be contacting other structures such as the coracoid or the coracoacromial arch. The change in contact pattern could lead to impingement or wear of the rotator cuff between the humeral head and coracoid/coracoacromial ligament. Eventually rotator cuff tears may even develop.

This work exemplifies the complex combination of structures that function to maintain stability of the glenohumeral joint. When one structure is injured, joint stability must be maintained by the others. Similar results were found when examining the glenohumeral contact forces in finite element models of normal and supraspinatus-deficient shoulders. [196] Supraspinatus deficiency altered contact locations and resulted in increased contact forces during glenohumeral abduction which could lead to the development of glenohumeral osteoarthritis. The same effects have been reported at the knee with altered tibiofemoral contact biomechanics found in ACL deficient knees compared to the contralateral control. [198] Increased joint stability provided by osteoarticular contact could lead to abnormal wear on the articular cartilage

of the glenohumeral joint. Therefore, patients who do not receive treatment to restore normal joint kinematics following an anterior dislocation may be at risk for the development of glenohumeral osteoarthritis.

5.3.6 Limitations

This work investigated one mechanism of glenohumeral dislocation, an excessive force in the anterior direction with the joint abducted and externally rotated. This quasi-static force was did not simulate the instantaneous nature of glenohumeral dislocations as seen in vivo. Other mechanisms may result in more tissue damage or bony lesions. In addition, the contribution to joint stability provided by the active stabilizers was not included in this dislocation model. The definition of dislocation chosen for this work moves the humeral head out of the glenoid but does not translate it over the glenoid rim. This is important because it allows the robotic/UFS testing system to repeat this motion without damaging other structures or the load cell. It also ensures that permanent deformation of the capsule will occur without creating a Bankart lesion or other capsular tear such that we could isolate the effect of this injury.

Only the strain distributions in the anteroinferior capsule midsubstance were examined. Due to the continuous nature of the capsule, damage may have occurred in other regions or at the insertion sites. The three dimensional shape of the capsule only allows for the anteroinferior portion of the capsule to be visualized by the three-camera motion tracking system available in our laboratory. The addition of a fourth camera to this equipment in the future may allow for additional portions of the capsule to be examined. Nonetheless, insight into the relationship between permanent tissue deformation and capsule function following anterior dislocation was achieved.

This work evaluated the glenohumeral contact forces between the humerus and scapula before and after anterior dislocation, however, specific contact areas were not identified. As permanent deformation of the capsule results in increased joint translations it is likely that the contact areas are quite different in the *intact* and *injured* joints. In addition, with large anterior translations, contact between the humeral head and corocoid process may occur and could contribute to the increased bony contact forces observed. Even so, insight into the effect of anterior dislocation on the *in situ* force in the capsule and bony contact forces was achieved.

5.3.7 Implications

The results reported in this section of the dissertation have extensive clinical implications for diagnostic and repair procedures targeted towards anterior instability resulting from a traumatic dislocation. During anterior dislocation, the anteroinferior glenohumeral capsule experiences high strains on the glenoid side. Even though damage occurs throughout the anteroinferior capsule, the posterior side of the axillary pouch was identified as the specific location most at risk for damage during anterior dislocation. This region experienced the greatest amount of nonrecoverable strain and the most change in strain during simulated clinical exams before and after dislocation. As a result, the ability of this region of the capsule to stabilize the glenohumeral joint in its functional position of abduction and external rotation is compromised. Therefore, plication of the glenohumeral capsule following anterior dislocation should occur in the posterior axillary pouch.

In addition to permanent deformation of the capsule, a significant increase in anterior translation, but no change in posterior translation was found following anterior dislocation. This finding suggests that the dislocation model developed in this dissertation is reasonable for

simulated anterior instability in the glenohumeral joint. Therefore, this model can be utilized in the future to simulate the state of the joint following anterior dislocation when examining other joint pathologies such as Hill-Sachs lesions. This model can also be used to assess the efficacy of various repair techniques. For example, the ability of capsular plication targeted at the posterior axillary pouch to restore joint kinematics and glenohumeral contact forces could be evaluated.

The changes in anterior translation found using this dislocation model were only a few millimeters suggesting that surgeons may not be able to detect such small differences between the injured and contralateral shoulders. Even if increased anterior translation is detected, the specific region of the capsule most at risk for damage following anterior dislocation was identified as the posterior axillary pouch. Therefore, repair procedures which target the anterior capsule based on increased anterior translation during pre-operative physical exams are not addressing the appropriate region of the capsule. Due to the complex, multi-axial function of the capsule current physical examinations which demonstrate increased translations in a particular direction may not be capable of identifying the specific location of tissue damage. This issue may contribute to failed surgical repair due to misdiagnosis. Developing standardized clinical exams to diagnose damage in specific capsule regions may lead surgeons to repair the appropriate capsule regions, thus improving patient outcome following traumatic anterior dislocation.

Glenohumeral contact forces were found to be larger following anterior dislocation. This increased joint stability provided by osteoarticular contact could lead to abnormal wear on the articular cartilage of the glenohumeral joint as weall as on the rotator cuff muscles between the humeral head and coracoid. Therefore, patients who do not receive treatment to restore normal

joint kinematics following an anterior dislocation may be at risk for the development of glenohumeral osteoarthritis as well as other injuries.

6.0 IMPROVED CONSTITUTIVE MODEL FOR CAPSULE

6.1 EVALUATION OF A STRUCTURAL MODEL

6.1.1 Introduction

The glenohumeral capsule is subjected to complex loading during activities of daily living and frequently injured when dislocation occurs. As previously discussed, clinical exams are not standardized to diagnose injury and patients could benefit from improved repair procedures. Validated finite element models of the glenohumeral capsule may be able to identify ways to improve these procedures but need ample constitutive models to describe capsule behavior. The material behavior of biologic tissues can be described with two types of constitutive models: phenomenological and structural models. Phenomenological models are a mathematic expression that relates the stress and strain within the tissue but essentially generalize the overall tissue behavior. On the other hand, structural models are a summation of the response of each tissue constituent (ground substance, collagen fibers, etc.) where the material parameters have direct physical meaning.

Our laboratory has developed and validated several finite element models of the glenohumeral joint using an isotropic phenomenological model to describe the material behavior of the capsule. [43, 93, 134-136] The experimental strain distribution on the surface of the

anteroinferior capsule was compared to the strain distribution predicted by the finite element models for validation. The models were considered to be validated if the average experimental and predicted strain in the AB-IGHL was less than the experimental repeatability. However, when comparing the experimental and predicted strains on a local level (based on the experimental elements defined by the grid of strain markers), differences were much larger than the experimental repeatability. Therefore, in order to use these finite element models appropriately to predict local capsule behavior an improved constitutive model must be developed. This model must be better at predicting the complex capsule behavior than the original isotropic phenomenological model.

Previous work in our research center suggested that the isotropic phenomenological model would be a reasonable first attempt at describing capsule behavior as its collagen fibers are randomly aligned [3-5, 123] and bi-directional mechanical properties are similar [40, 41]. However, using this model to characterize the normal capsule demonstrated that it could not predict tissue response to both tensile and shear elongations (Section 1.5.3) demonstrating its inability to predict complex capsule behavior. [42, 173] In order to improve the accuracy of finite element models of the glenohumeral joint this model will need to be updated. In addition, our research group would like to use these finite element models to predict the behavior of the injured glenohumeral capsule. Therefore, a constitutive model which is capable of describing the behavior of both normal and injured tissue would be ideal.

Specific Aim 1 demonstrated that changes in collagen fiber alignment are related to tissue damage. Specific Aim 2 found increases in the stiffness and material properties of the capsule following injury. These results suggest that the capsule may exhibit a more aligned reference state following injury. A constitutive model which is capable of describing the behavior of both

normal and injured capsule will likely need to account for the change in fiber alignment following injury. As the collagen fiber kinematics are a link between the normal and injured capsule it is likely that a structural model will better describe its complex behavior compared to the isotropic phenomenological model. Therefore, we hypothesize that a structural model, incorporating the ground substance and randomly oriented collagen fibers, will better describe and predict the material behavior of the glenohumeral capsule than the originally used isotropic phenomenological model. The objective of this section of the dissertation was to compare the ability of phenomenological and structural models to describe and predict the material behavior of the axillary pouch in response to tensile and shear loading.

6.1.1.1 Hyperelastic Constitutive Models

Constitutive models used in our research group have been based on the general hyperelastic strain energy, originally proposed by co-investigator Weiss [47, 48, 176, 199]:

$$W = F_1(\tilde{I}_1, \tilde{I}_2) + F_2(\tilde{\lambda}) + F_3(\tilde{\lambda}, \tilde{I}_5) + \frac{1}{2} K \ln(J)^2 \qquad (5)$$

The functions F_1 and F_2 represent the matrix and fiber family strain energies, respectively; while F_3 represents matrix-fiber and/or fiber-fiber coupling that is not used in the current work. Together they compose the entire deviatoric response of the material. Thus there are five deviatoric invariants ($\tilde{I}_{1-5}$) contributing to the strain energy, two of which are governed by $\boldsymbol{a}^0$, the local fiber direction in the undeformed configuration. $\tilde{\lambda}$ is the deviatoric localfiber stretch, and $\tilde{I}_5$ governs fiber-fiber and fiber-matrix coupling. $\frac{1}{2} K \ln(J)^2$ controls the dilatational (volumetric) response of the material, where J=det($\boldsymbol{F}$) is the volume ratio and K represents the effective bulk modulus of the material. As the use of displacement-based finite element methods

to analyze nearly incompressible materials (such as capsule) can be difficult with numerous issues including numerical ill-conditioning of the stiffness matrix due to the larger contributions from the dilational stiffness on the diagonal and locking of the mesh due to overconstraint of the displacement field, among others, an uncoupled deviatoric/dilatational constitutive formulation was used. [176] This formulation significantly simplifies the mathematical relations for finite element implementation and the formulation is identical to the fully coupled strain energy in the limit of incompressibility or for an isochoric deformation (J=1 for both cases). It is also important to note that the invariants used in this formulation of the model ($\tilde{I}_{1-5}$) are the modified deviatoric forms of the invariants of the right Cauchy-Green deformation tensor (I_{1-5}) [176] and the invariants are inherently covariant [200].

In this section of the dissertation, the ability of two constitutive models to predict capsule behavior was evaluated. The first model, an isotropic phenomenological model, which was originally proposed by Veronda and Westmann [175], was described in Section 4.2.3. The second model, a structural model, was chosen for this work because it incorporates the knowledge that the capsular tissue consists of a population of fibers with a random orientation. [3-5, 123] The model consists of an isotropic matrix with fibers randomly aligned throughout the tissue. This approach is based on explicit modeling of the collagen fibers with an exponential-linear strain energy function for $F_2(\lambda)$, and a Neo-Hookean model for the matrix such that the I_2 term is zero.

$$F_1(\tilde{I}_1) = C_1(\tilde{I}_1 - 3) \tag{6}$$

This model assumed that the ground substance is incompressible and isotropic. The response of the collagen fibers was described by the term F_2 and was defined such that:

$$\tilde{\lambda}\frac{\partial F_2}{\partial \lambda} = 0, \tilde{\lambda} < 1;$$
$$\tilde{\lambda}\frac{\partial F_2}{\partial \lambda} = C_3 e^{(C_4(\tilde{\lambda}-1))}, 1 < \tilde{\lambda} < \lambda^* \quad (7)$$
$$\tilde{\lambda}\frac{\partial F_2}{\partial \lambda} = C_5\tilde{\lambda} + C_6, \tilde{\lambda} \geq \lambda^*$$

The fiber stress increases exponentially up to a level of fiber stretch λ^* (the toe region). After this point, the fiber stress–stretch behavior is linear. This is in agreement with the material behavior of collagen fibers that has been observed during tensile testing of ligament and tendons with highly aligned fibers and for isolated tendon fascicles [201]. The material coefficient C_3 scales the exponential fiber stresses, C_4 determines the rate of uncrimping of the collagen fibers, and C_5 is the modulus of the straightened collagen fibers [47]. C_6 follows from the requirement that the fiber stress is C^0 continuous at $\tilde{\lambda} = \lambda^*$.

$$C_6 = C_3(e^{C_4(\lambda^*-1)} - 1) - C_5\lambda^* \quad (8)$$

The Cauchy stress can then be written as:

$$T = 2\left\{(W_1 + \tilde{I}_1 W_2)B^2\right\} + \lambda W_\lambda a \otimes a + p1 \quad (9)$$

Where **B** is the left deformation tensor, W_1, W_2 and W_λ are strain energy derivatives with respect to I_1, I_2, and λ, respectively. **a** is a unit vector field representing the fiber direction in the deformed configuration and *p* is the hydrostatic pressure. As the F_1 term is only a function of I_1, W_2 goes to zero and the Cauchy stress can be reduced to:

$$T = 2\left\{W_1 B^2\right\} + \lambda W_\lambda a \otimes a + p1 \tag{10}$$

The initial fiber direction $\boldsymbol{a}^0$ and its distribution over the domain of the finite element model are generated to yield a random distribution with respect to the sample axes. This model assumes that the collagen does not support compressive load. With this model, the stiffening in both tension and shear is represented by the inherent nonlinearity in the fiber material behavior.

6.1.1.2 Previous Literature – MCL

The structural model to be used in this section of the work has been used previously to describe the transversely isotropic behavior of the MCL. [47] Tissue samples from the MCL were extracted longitudinal and transverse to the predominant fiber orientation and loaded to failure. The structural model was used to describe the response of the MCL. The material parameters of the model were determined from Cauchy stress-stretch curves. Due to the large number of parameters needed to describe the tissue behavior, the parameters were determined in several steps to ensure uniqueness of the parameters. First the material coefficient describing the ground substance was determined using a nonlinear regression of the transverse load-elongation data. This step assumes that since the collagen fibers in the MCL are predominantly aligned in the longitudinal direction their contribution to the transverse tensile data will be negligible compared to the response of the ground substance. The tangent modulus was 30 times larger in the longitudinal compared to the transverse direction implying that this was a valid assumption. Next the value of λ^* was determined from the transition point between the toe- and linear-region of the stress-stretch curve. The toe-region coefficients, C_3 and C_4, and the linear-region coefficient, C_5, were determined via nonlinear regression of the longitudinal tensile data below and above λ^*, respectively.

Using the nonlinear regression protocol described above, the material coefficients (C_1, C_3 – C_5) of seven MCL's were determined to be 4.7 ± 4.8MPa, 1.7 ± 1.1MPa, 47.9 ± 31.0, and 389.3 ± 208.3MPa. More appropriately, average stress-stretch curves were generated by combining the data for each individual MCL and the material coefficients of the average curve were determined to be 4.6 MPa, 2.4 MPa, 30.6, and 323.7 MPa. The value of λ^* for the average curve was 1.055.

The linear regression method for determine the material parameters of the structural model for the MCL was appropriate. However, determining unique material parameters for the glenohumeral capsule will be more difficult. Unlike the MCL, the capsule does not have a predominant fiber direction therefore the load-elongation response from both the longitudinal and transverse directions contains contributions from both the ground substance and collagen fibers. Therefore, another loading condition which separates the response of the ground substance may need to be developed.

6.1.1.3 Preliminary Studies

In order to get an initial understanding of how the structural model would describe the behavior of the glenohumeral capsule the finite element optimization routine described in Section 4.2.3 was employed on previously collected experimental data [15, 42] and all four material coefficients were optimized simultaneously. For all optimizations, initial guesses of the material coefficients for the optimization routine were determined by manually adjusting the material coefficients and running the finite element model until the experimental and model predicted load-elongation curves were similar with an R^2 value of 0.97.

*Value of λ**

The more material parameters optimized simultaneously, the longer the optimization routine will take to find a solution, and the resulting parameters would not be unique. In order to reduce the number of parameters being optimized the value of λ* was held constant. A preliminary sensitivity study was performed in order to determine the appropriate value of λ*. The tensile longitudinal load-elongation data for one representative tissue sample from the axillary pouch was used for this preliminary analysis. The optimized material coefficients were determined for values of λ* ranging from 1.01 to 1.1 in increments of 0.1. The experimental and predicted load-elongation curves were compared using the root-mean-squared error percentage for each value of λ*.

As λ* increased from 1.01 to 1.1 better predictions of the experimental data were achieved. (Figure 6.1)

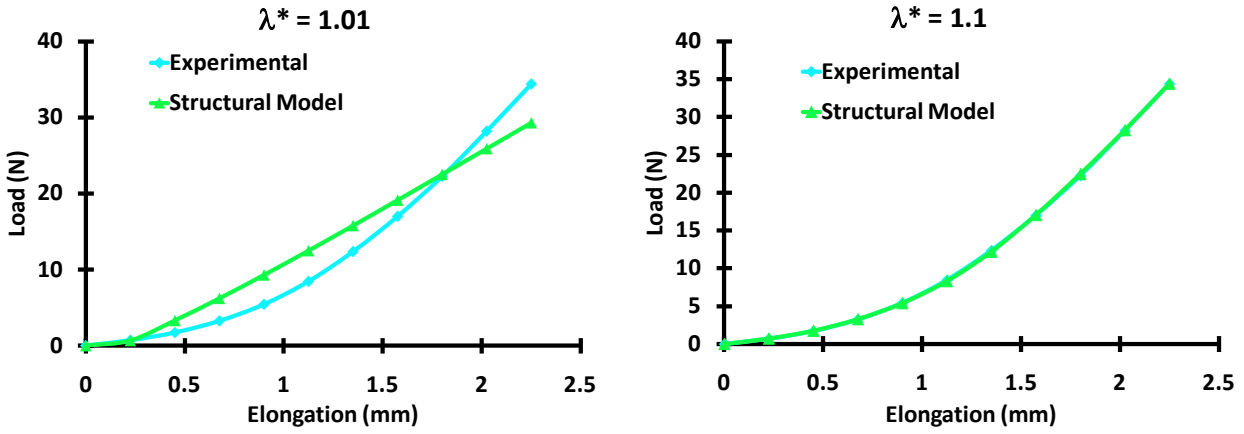

Figure 6.1 Experimental and predicted load-elongation curves for the minimum (1.01) and maximum (1.1) values of λ* demonstrating better model predictions with increasing values of λ*.

RMSE% values comparing the experimental and predicted load-elongation curves ranged from 7.7% for $\lambda^* = 1.01$ to 0.3% for $\lambda^* = 1.1$. A plateau in the change in RMSE% between increasing values of λ^* developed after $\lambda^* = 1.05$ when the RMSE% dropped below 1%. (Figure 6.2)

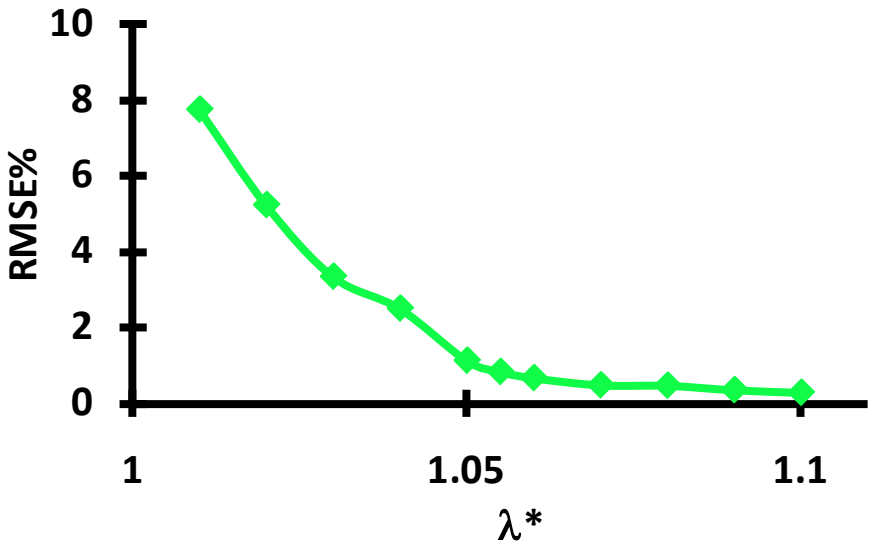

Figure 6.2 RMSE% as a function of λ^*.

The RMSE% values comparing the experimental and predicted load-elongation curves was less than 1% for values of λ^* greater than 1.05. These results compared well with previous work using this structural model to describe the behavior of the MCL in which λ^* for the average stress-stretch curve was found to be 1.055. Therefore, λ^* was set at 1.055 for this work and was not optimized with the other four material parameters.

Which Loading Condition to Predict From

Load-elongation data was previously collected during a total of four nondestructive loading conditions [42]: (1) tensile elongation applied in the direction parallel to the longitudinal axis of the AB-IGHL (tensile longitudinal, TL), (2) tensile elongation applied in the direction

perpendicular to the longitudinal axis of the AB-IGHL (tensile transverse, TT), (3) shear elongation applied in the direction parallel to the longitudinal axis of the AB-IGHL (shear longitudinal, SL), and (4) shear elongation applied in the direction perpendicular to the longitudinal axis of the AB-IGHL (shear transverse, ST). The optimized material parameters of the phenomenological and structural models were to be determined from one loading condition and used to predict the response of the tissue to the other three loading conditions. A preliminary analysis was performed in order to determine which loading condition should be used to predict the other three.

The optimized material parameters of each constitutive model were determined for all four loading conditions applied to one tissue sample from the axillary pouch. These parameters were then used to predict the response of the tissue sample to the other three loading conditions. The experimental and predicted curves were plotted together for all predictions of each loading condition and are shown in the figures below.

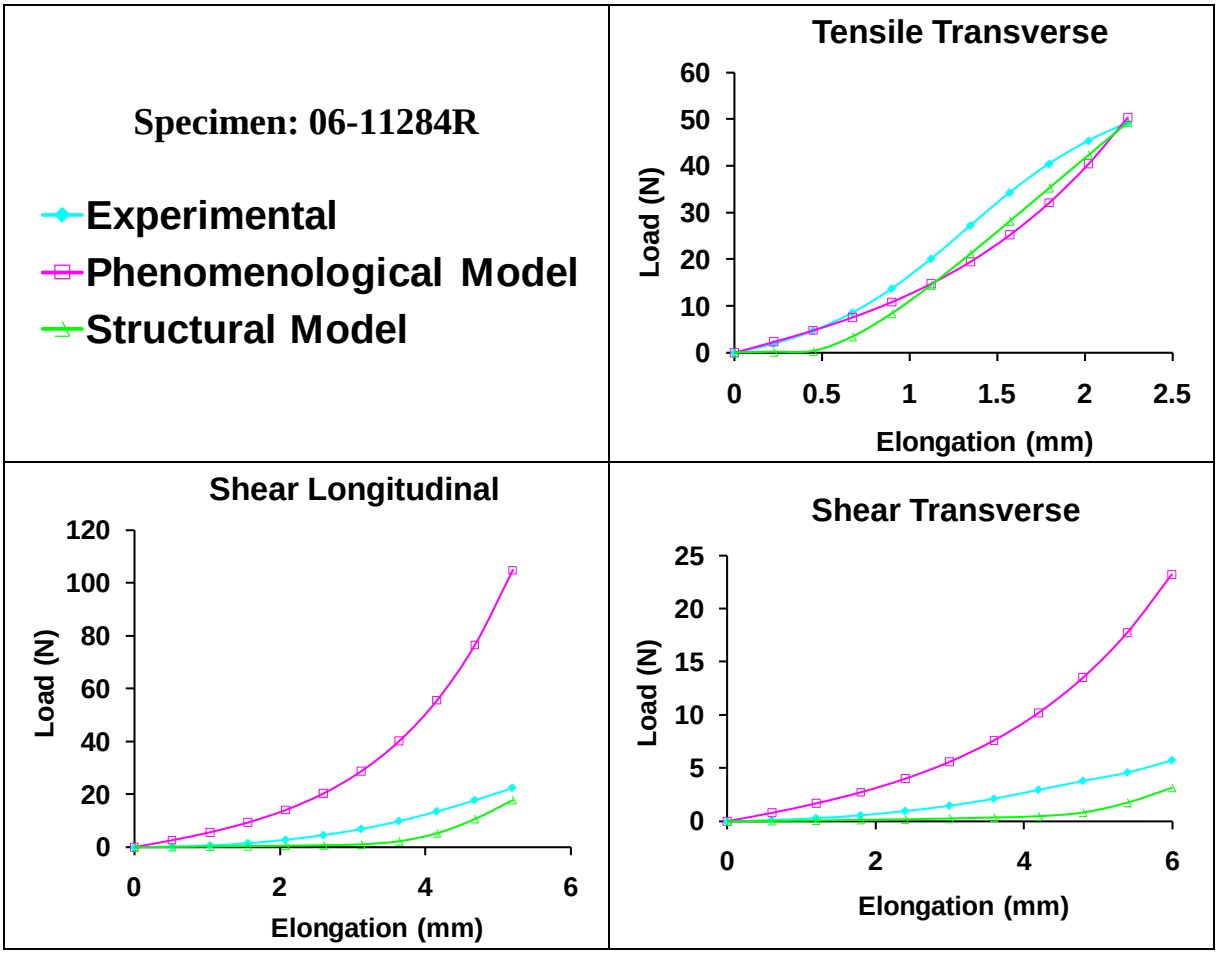

Figure 6.3 The optimized material parameters from the tensile longitudinal loading condition were used to predict the response of the capsule to the 1) tensile transverse (top right), 2) shear longitudinal (bottom left), and 3) shear transverse (bottom right) loading conditions for Specimen 06-11284R.

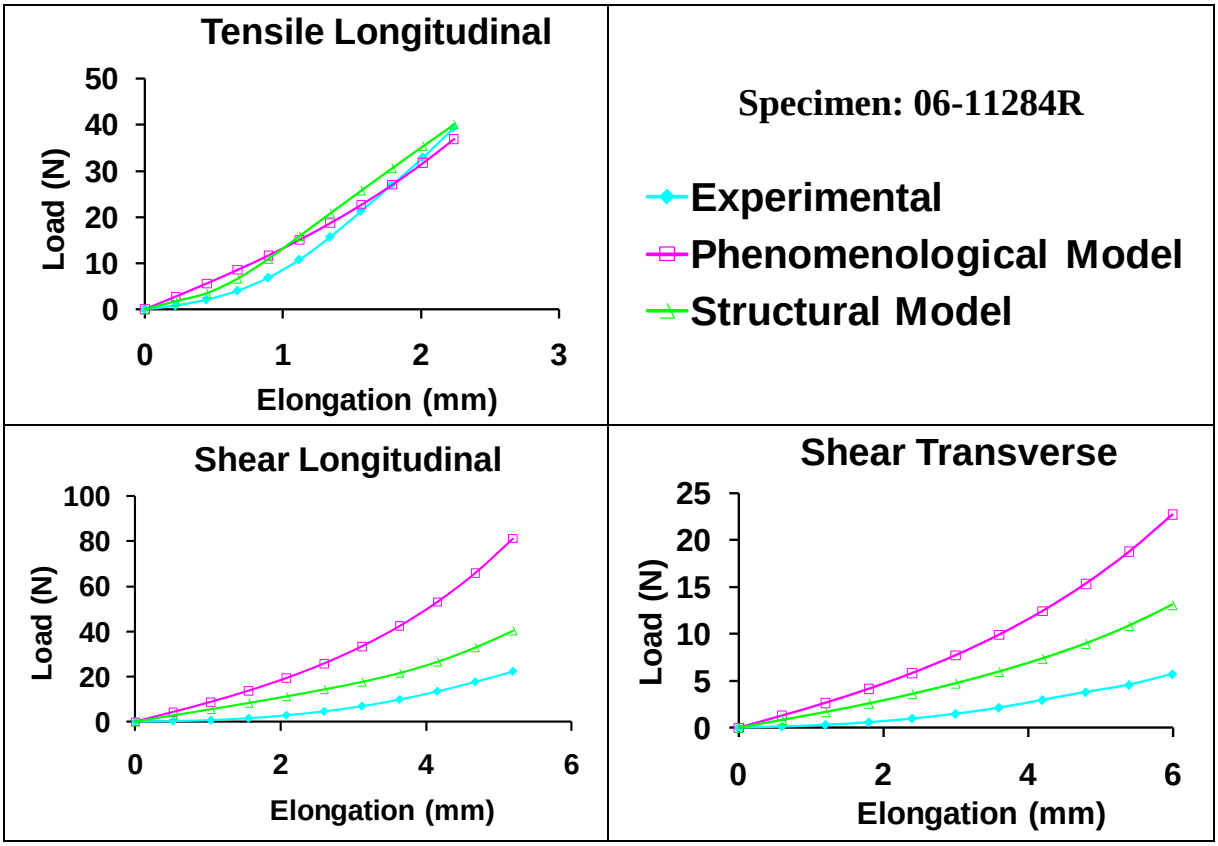

Figure 6.4 The optimized material parameters from the tensile transverse loading condition were used to predict the response of the capsule to the 1) tensile longitudinal (top right), 2) shear longitudinal (bottom left), and 3) shear transverse (bottom right) loading conditions for Specimen 06-11284R.

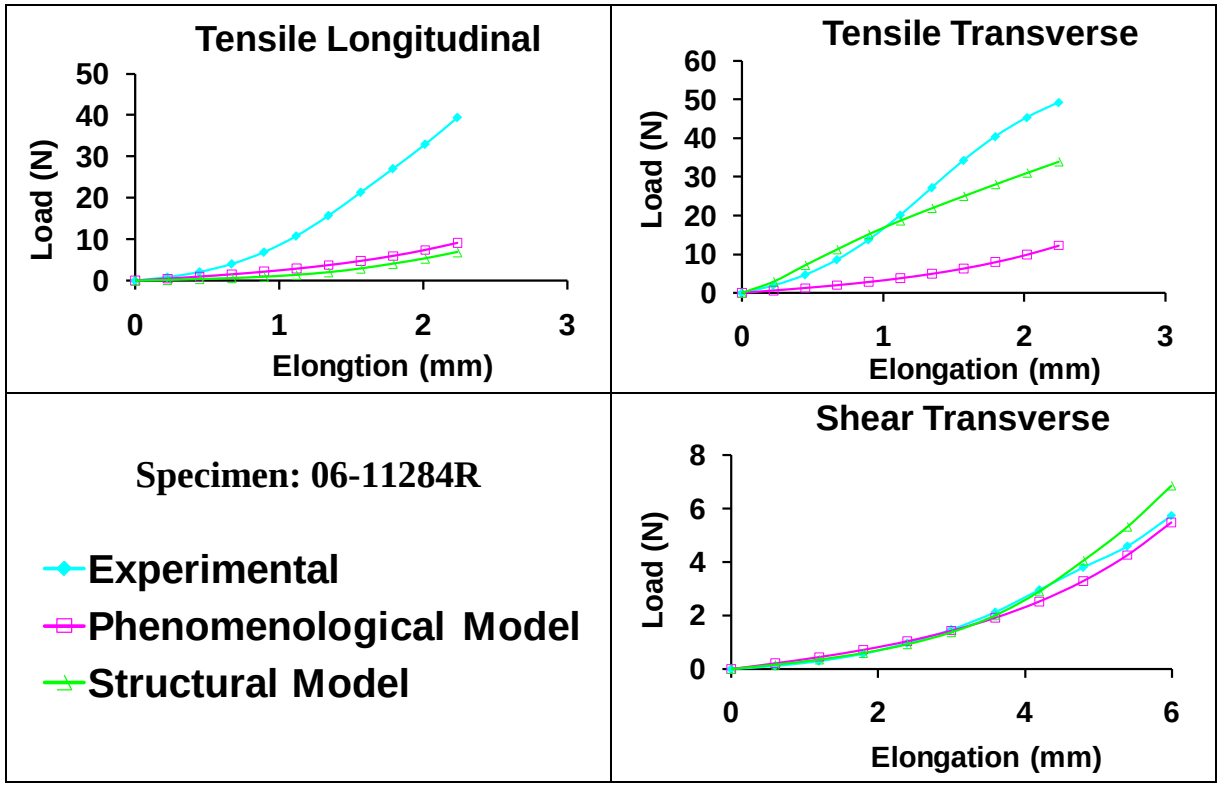

Figure 6.5 The optimized material parameters from the shear longitudinal loading condition were used to predict the response of the capsule to the 1) tensile longitudinal (top left), 2) tensile transverse (top right), and 3) shear transverse (bottom right) loading conditions for Specimen 06-11284R.

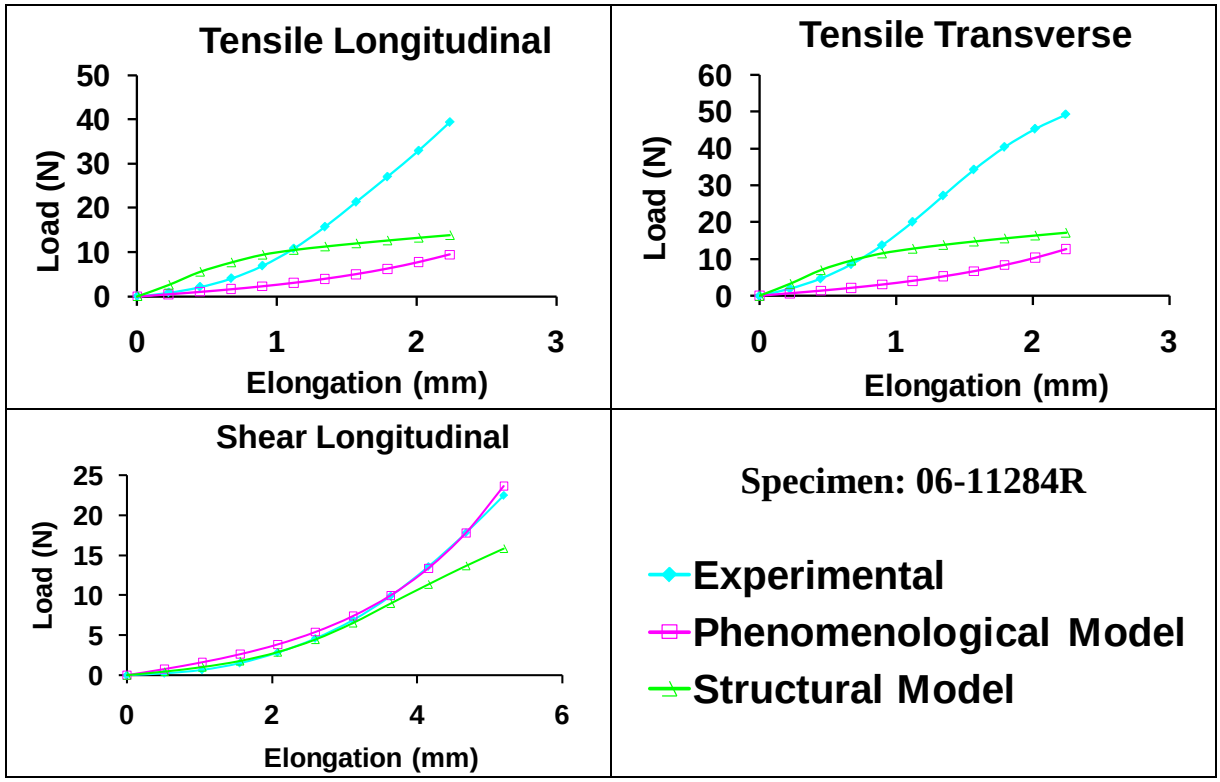

Figure 6.6 The optimized material parameters from the shear transverse loading condition were used to predict the response of the capsule to the 1) tensile longitudinal (top left), 2) tensile transverse (top right), and 3) shear longitudinal (bottom left) loading conditions for Specimen 06-11284R.

When the optimized material coefficients from the tensile longitudinal and tensile transverse loading conditions were used to predict the tissue behavior, similar predictions were made. Predicted curves exhibited typical non-linear behavior and the structural model provided better predictions of the experimental data under shear loading. When the optimized material coefficients from the shear longitudinal and shear transverse loading conditions were used to predict tissue behavior, typical non-linear load-elongation curves were only seen in the shear predictions. When the tissue behavior in response to tensile loading was predicted from the material parameters determined from the tissue response to shear, the shape of the load-elongation curves was not typical of biologic soft tissues. Both models greatly underestimated the stiffness of the capsule under tension.

These results suggest that the contributions of the collagen fibers to the response of the tissue are greater in tension compared to shear. During the applied uniaxial deformations the collagen fibers are axially stretched and the response of the tissue is due to both the ground substance and collagen fibers. However, during the applied shear elongations there is not as much axial stretch but rather the collagen fibers rotate and the tissue response is due mostly to the ground substance. As a result of these differences, the material parameters from shear loading conditions can be used to generate curves similar in shape to the tissue response to the perpendicular shear elongation, but not to either tensile elongation. On the other hand, the material parameters from tensile loading conditions can be used to generate typical non-linear curves in both tension and shear. Therefore, the material parameters from the tensile deformations should be used to predict the response of the tissue to the other loading conditions.

Sensitivity of the Material Coefficients

To better understand the behavior of the structural model, the sensitivity of the fiber parameters ($C_3 - C_5$) in tension and in shear were evaluated. The finite element models for one tissue sample under tensile and shear deformations were used. The material parameters were varied throughout a range of typical optimized values and the resulting load-elongation curves examined. When they were not being varied, each material parameter was set to the following value: $C_1 = 0.07$, $C_3 = 1.7$, $C_4 = 3.5$, and $C_5 = 82.4$. These were the optimized parameters for this particular tissue sample. Plots representing the response of the tissue sample throughout the range of each parameter in shear and in tension are shown below.

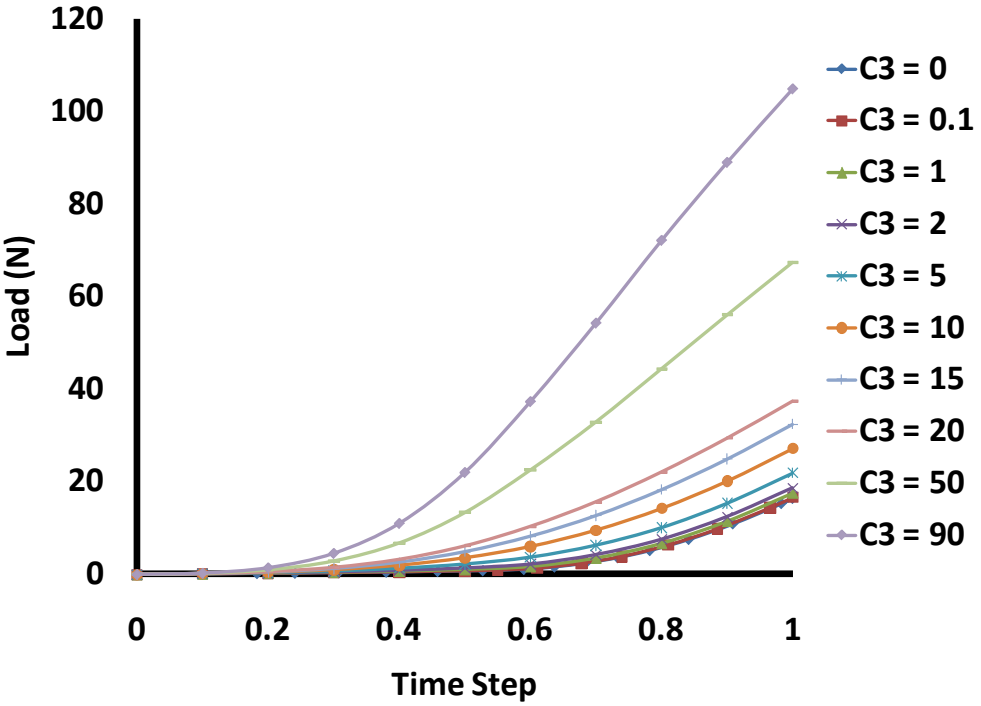

Figure 6.7 Response of a tissue sample from the axillary pouch in shear for each value of C_3.

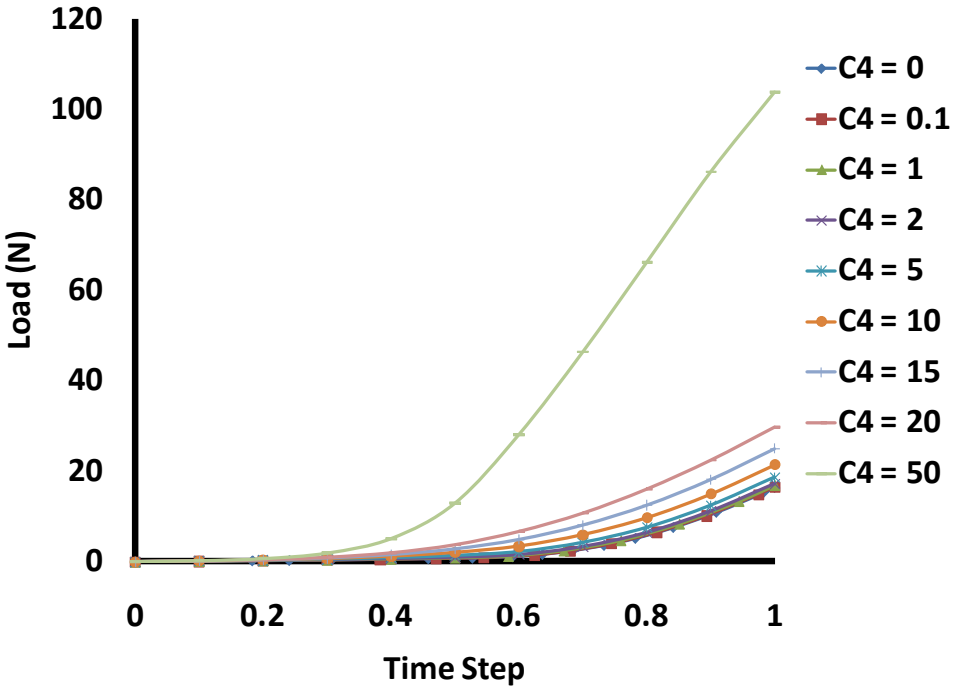

Figure 6.8 Response of a tissue sample from the axillary pouch in shear for each value of C_4.

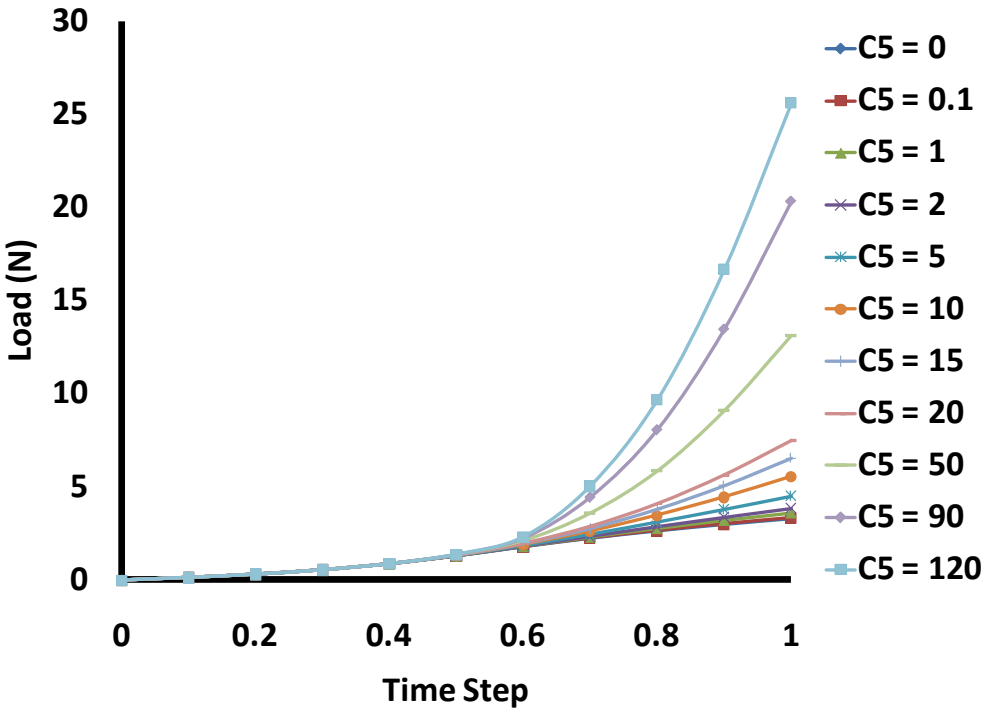

Figure 6.9 Response of a tissue sample from the axillary pouch in shear for each value of C_5.

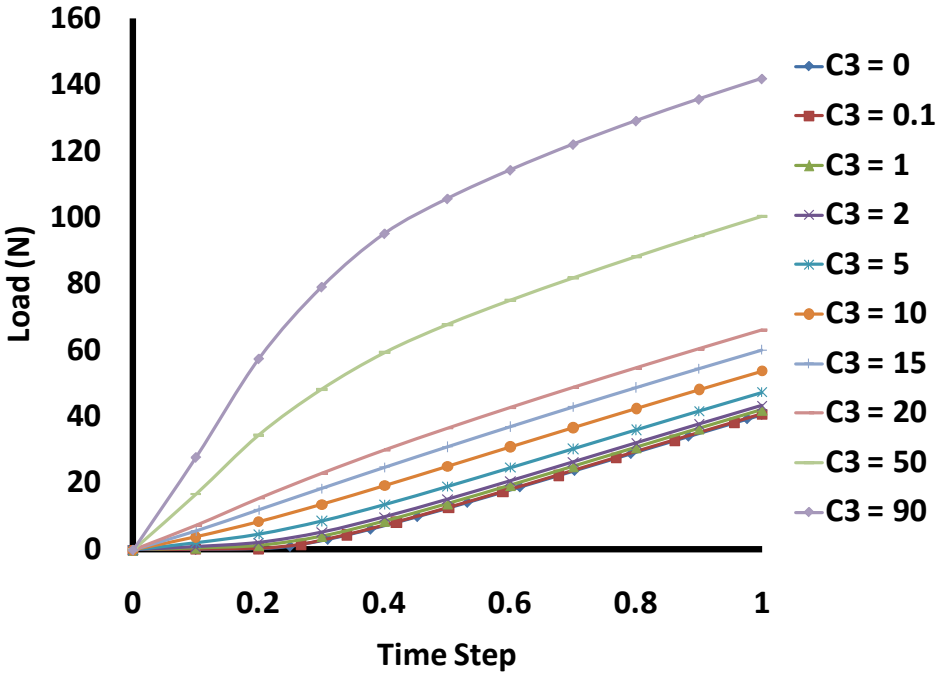

Figure 6.10 Response of a tissue sample from the axillary pouch in tension for each value of C_3.

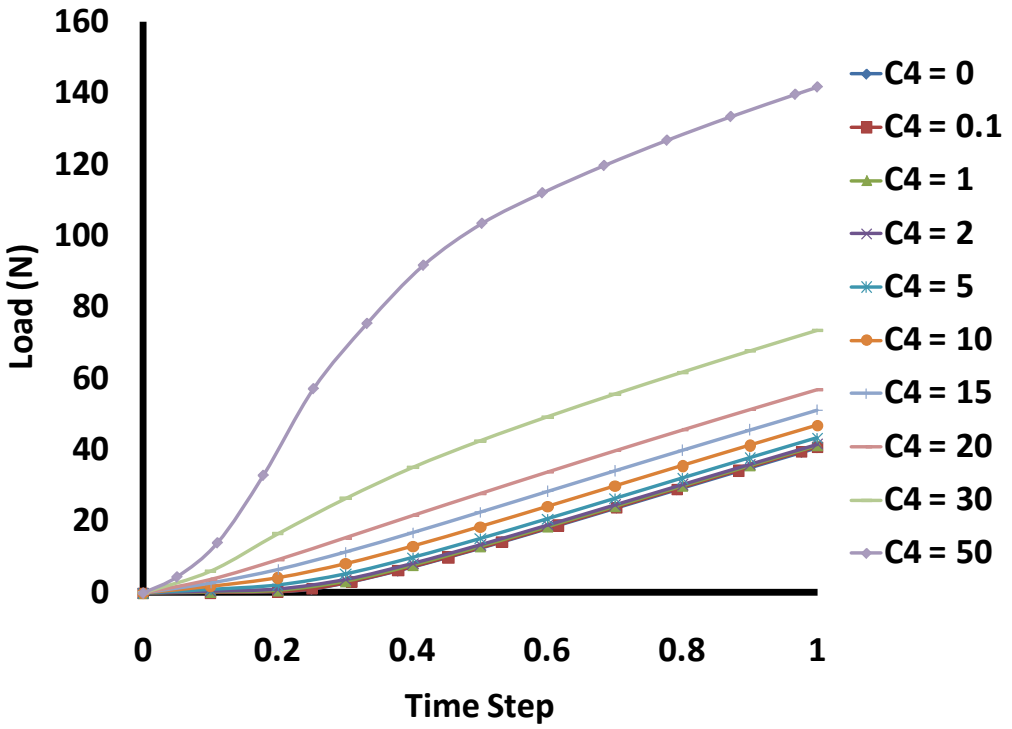

Figure 6.11 Response of a tissue sample from the axillary pouch in tension for each value of C_4.

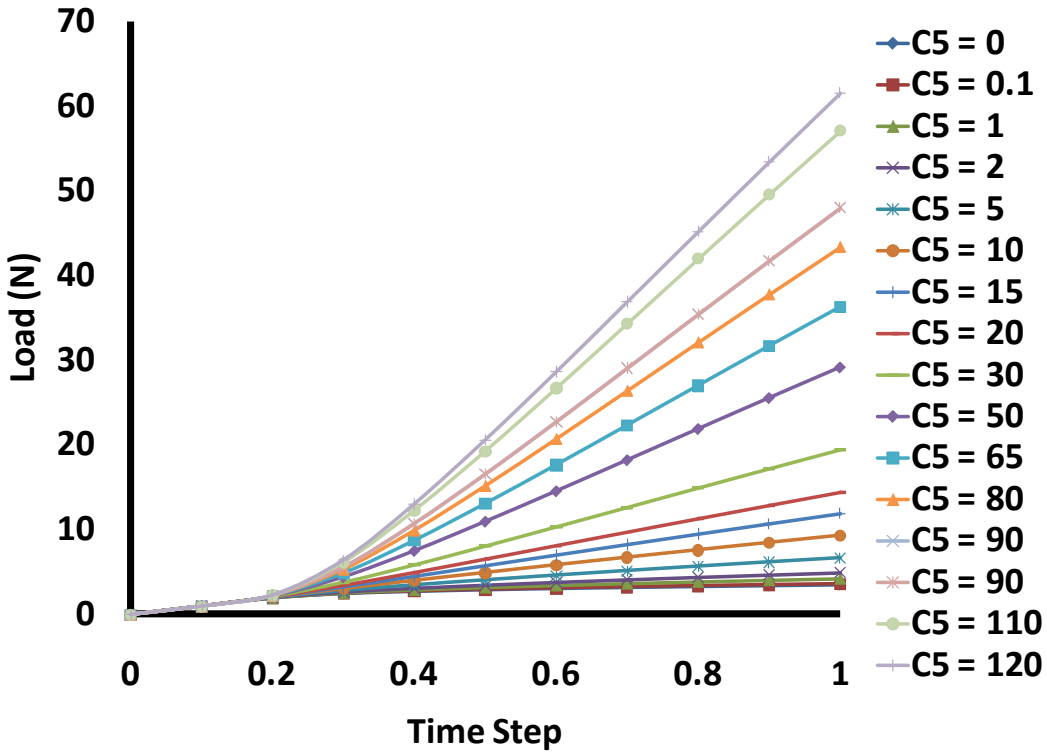

Figure 6.12 Response of a tissue sample from the axillary pouch in tension for each value of C_5.

A greater change in load was observed with changes in the material parameters for the tensile loading condition compared to the shear loading condition. Therefore, the response of the tissue in tension was more sensitive to change in the material parameters than in shear. This further suggests that the optimized material coefficients from the tensile loading conditions should be used to predict the response of the tissue in shear and not vice versa.

Experimental Repeatability

In order to compare the ability of the phenomenological and structural models to predict the experimental load-elongation curves the root-mean-squared error percentage (RMSE%) was computed. As this parameter had not been analyzed previously using the combined experimental and computational protocol, the repeatability of this process in terms of the RMSE% was determined. The accuracy/repeatability of the experimental measurements (vertical load cell accuracy: 0.1N, digital calipers, repeatability: 0.1 mm) which would affect the output parameter (RMSE%) was determined. In addition, the computational protocol requires the user to generate a mesh of each tissue sample by selecting and placing nodes along the edges of the tissue as seen through a photograph of the preloaded sample in each loading condition. Therefore, there were three factors which contributed to the overall repeatability of the combined experimental and computational protocol: accuracy of the vertical load cell, repeatability of tissue thickness measurements, and the mesh generation process. Each of these factors was individually varied for one example specimen by its corresponding accuracy/repeatability and new optimized material parameters were determined for each case. The material parameters were then used to predict the response of the tissue in tension and in shear. Confounding effects were also examined by varying all factors at once and then determining new optimized material parameters.

As expected, the greatest change in optimized material parameters (0.02) occurred when all factors were varied simultaneously. This resulted in a 1.9% change in the RMSE% for tensile predictions and a 9.1% change in the RMSE% for shear predictions. Therefore, the repeatability of the combined experimental and computational methodology used in this section of the work in terms of the RMSE% is ~10%. In other words, differences in RMSE% values of less than 10% are not detectable with our current methodology.

Mesh Density

An extensive mesh density analysis was performed previously for the phenomenological model and it was determined that the optimal mesh density was 1200 elements, with 4 elements through the thickness. [42, 173] Therefore, a preliminary analysis was performed to determine if the number of elements through the tissue thickness was also appropriate for the structural constitutive model. One tissue sample was chosen at random and meshes were generated for a tensile and shear loading condition for that sample. The three mesh densities were evaluated with the number of elements through the tissue thickness being 2, 4 and 6. The number of elements in the plane of the tissue was held constant.

In order to ensure that differences in the material parameters were due to changes in the mesh density and not non-unique parameters the ground substance and fiber parameters were optimized separately. The ground substance parameter, C_1 was determined from the first 1 mm of the shear transverse elongation under the assumption that the contributions from collagen fibers to the tissue response would be negligible under this small shear elongation. The value of λ^* was then set to 3 which was never achieved by the finite element model thereby eliminating the linear region, and C_5, from the optimization. This means that the non-linearity of the load-elongation curves was captured entirely by the toe-region coefficients, C_3 and C_4. As a result the

physical meaning of the parameters is lost but uniqueness is achieved allowing for the detection of changes in the parameters with changes in mesh density.

Changes in the material parameters between mesh densities were very small: 0.004 for C_1, 0.017 for C_3, and 0.096 for C_4. (Table 6.1)

Table 6.1 Optimized material parameters for each mesh density.

# Elements Through Tissue Thickness	C_1 (MPa)	C_3 (MPa)	C_4
2	0.084	0.742	13.676
4	0.087	0.758	13.580
6	0.088	0.759	13.574

These changes in material parameters resulted in negligible changes in the predicted load-elongation curves in tension (Figure 6.13) and shear (Figure 6.14). Therefore, the same mesh density (1200, with 2 elements through the tissue thickness) that was used for the isotropic phenomenological model was also used for the structural model in this section of the dissertation.

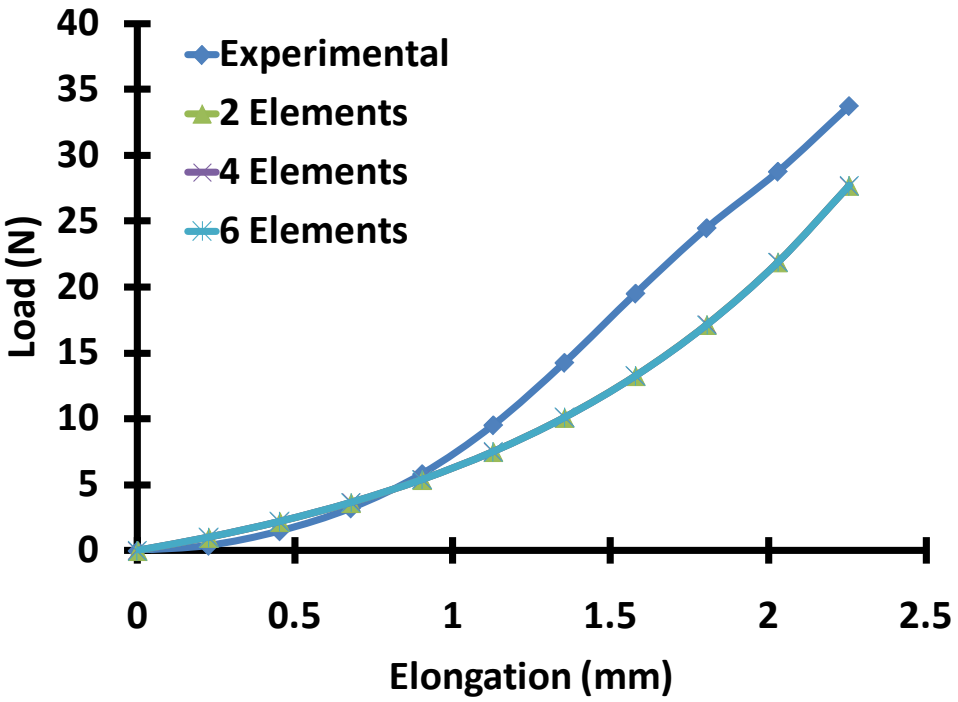

Figure 6.13 Experimental and predicted load-elongation curves for each mesh density for a representative tissue sample in tension.

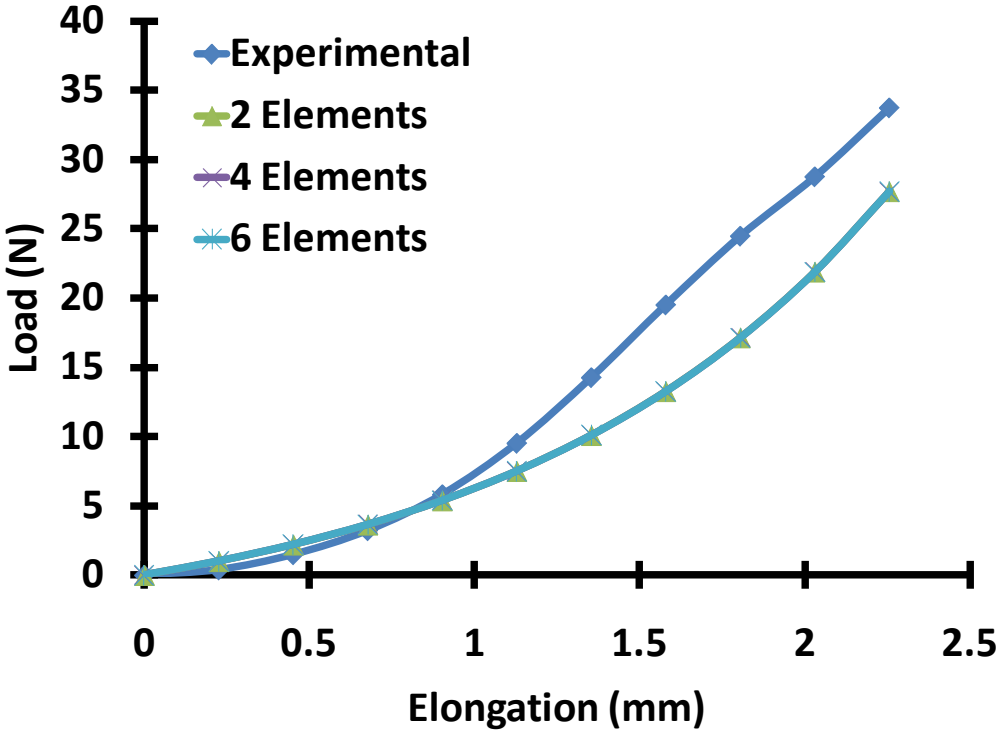

Figure 6.14 Experimental and predicted load-elongation curves for each mesh density for a representative tissue sample in shear.

6.1.2 Methods

The same combined experimental-computational protocol used in Specific Aim 2 was used to determine the material coefficients for phenomenological and microstructural constitutive models. [42, 173] Data was previously obtained from the experiments of twenty tissue samples used to characterize the material properties of the normal glenohumeral capsule. [15, 42] Experimentally, two perpendicular tensile and shear elongations were applied to tissue samples from the axillary pouch. During the experimental elongations the clamp reaction force and clamp displacement were recorded and used in an inverse finite element optimization routine to simulate the experimental conditions (Figure 4.6). This routine optimized the material parameters of the two constitutive models until the sum-of-squares difference between the load-elongation curves from the experimental measurements and finite element model predictions was minimized.

6.1.2.1 Experimental

Sixteen cadaveric shoulders (54 ± 10 yrs.) were dissected down to the glenohumeral capsule. Each joint was examined using radiographs and dissection and determined to be free of osteoarthritis and any signs of previous injury. The AB-IGHL and PB-IGHL were identified by applying distraction and external rotation and internal rotation, respectively, to the joint as the bands are most visible in these position. [166] Tissue samples (25 mm x 25 mm) from the axillary pouch were obtained using a cutting guide and scalpel and were hydrated using physiological saline solution throughout the entire testing protocol.

A total of four nondestructive loading conditions were used in this experimental protocol [42]: (1) tensile elongation applied in the direction parallel to the longitudinal axis of the AB-

IGHL (tensile longitudinal, TL), (2) tensile elongation applied in the direction perpendicular to the longitudinal axis of the AB-IGHL (tensile transverse, TT), (3) shear elongation applied in the direction parallel to the longitudinal axis of the AB-IGHL (shear longitudinal, SL), and (4) shear elongation applied in the direction perpendicular to the longitudinal axis of the AB-IGHL (shear transverse, ST). The testing order was randomized.

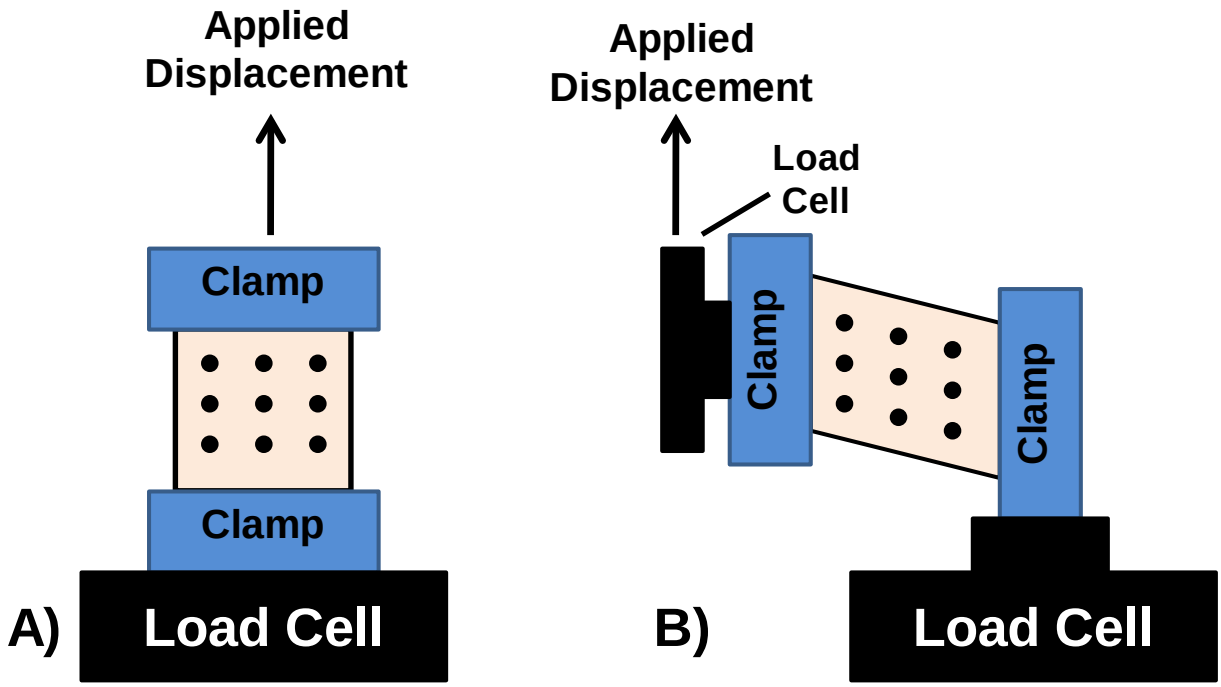

Figure 6.15 Mechanical testing setup for A) tensile and B) shear loading conditions showing the load cell and clamp relationships.

For each *tensile elongation*, the tissue was pre-loaded to 0.5 N. The initial width, length, and thickness of the sample were then recorded as the average of three measurements. The tissue was then preconditioned (10 cycles to 1.5 mm, 10 mm/min) and immediately elongated to 2.25 mm. Samples recovered for 30 minutes between each test. For each *shear elongation*, two pre-loads were applied to the tissue sample: parallel (0.1 N) and perpendicular (0.03 N) to the loading axis. The tissue sample geometry was again measured and the sample was preconditioned (10 cycles to 2 mm, 10 mm/min). Finally, an elongation of $0.4*L_0$ was applied,

where L_0 is the clamp-to-clamp distance. This displacement is equal to a shear ($\kappa = \tan(\theta)$) of 0.4, where θ is the angle between the top edge of the tissue sample and the x-axis.

6.1.2.2 Computational

The same computational methodology outlined in Specific Aim 2 was used to determine the optimized material coefficients of each constitutive model. Since the experimental tests produced inhomogeneous deformations, specimen-specific finite element models were used to predict the response of the tissue when represented with the two constitutive models. Boundary conditions from the experimental tests (geometry, clamp reaction force, applied elongation) were used to create finite element models of the tissue sample for each loading condition. [48] The phenomenological model was an isotropic hyperelastic strain energy function, (Equation 1) [42, 173, 175]. The structural model consisted of an isotropic matrix based on the neo-Hookean constitutive model that was embedded with collagen fibers (Equations 6-7) [47, 177]. The fibers had a random distribution of orientation in the plane of the tissue, yielding an initially isotropic material symmetry that became anisotropic with deformation due to fiber realignment. Overall fiber stress was obtained by integration over the fiber angle distribution [158]. Both models were used to describe the material behavior of each tissue sample. Optimized material coefficients for both constitutive models were determined for each specimen for all four loading conditions using an inverse finite element optimization technique described in Specific Aim 2. [48] For the phenomenological model, initial guess of $C_1 = 0.1$ and $C_2 = 10$ were used as deescribed previously. [42, 173] For the structural model, initial guesses of the material coefficients for the optimization routine were determined by manually adjusting the material coefficients and running the finite element model until the experimental and model predicted

load-elongation curves were similar with an R^2 value of 0.97. Based on the preliminary studies, the material coefficients from the tensile longitudinal (TL) loading condition were used to predict the response of the tissue to the other three elongations.

6.1.2.3 Data Analysis

Root-mean-squared-error percentages (RMSE%) were computed between the experimental and predicted load-elongation curves for each constitutive model. These values were used to compare the ability of each constitutive model to fit predict the response of the capsule to each loading condition.

6.1.3 Results

Both the phenomenological and structural models were able to describe the experimental data for the tensile longitudinal (TL) elongation. (Figure 6.16) The optimized material coefficients for each specimen can be found in Appendix G.

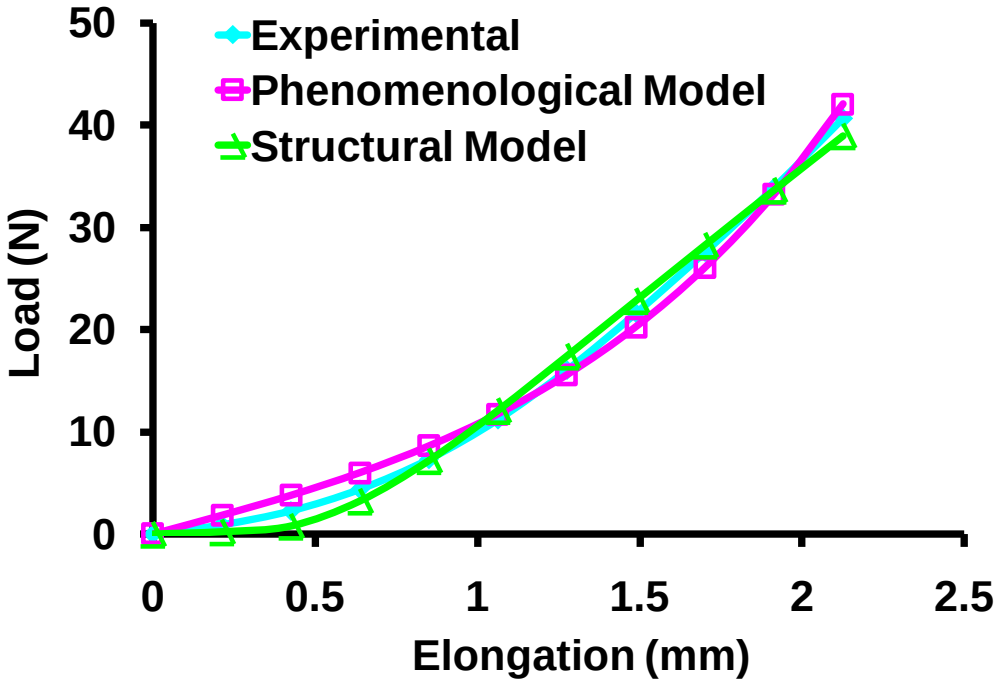

Figure 6.16 Load-elongation data for an example specimen during the tensile longitudinal (TL) elongation showing the ability of the phenomenological and structural models to fit the experimental data.

The structural model provided a slightly better fit than the phenomenological model, with RMS errors between the experimental and optimized load-elongation curves of 1.5 ± 0.8% for the structural model and 3.9 ± 1.2% for the phenomenological model. (Table 6.2)

Table 6.2 Root-mean-squared error percentages (RMSE%) between the experimental and optimized load-elongation data (tensile longitudinal) for the phenomenological and structural constitutive models for each specimen demonstrating the ability of each model to fit the experimental data.

SPECIMEN #	Phenomenological Model (%)	Structural Model (%)
04-09040R	3.9	2.1
05-06046R	3.6	2.1
05-08013L	2.0	2.1
05-08022L	5.5	0.5
05-08024R	3.9	0.9
05-08038L	6.8	1.8
05-10043R	4.4	0.6
05-10071R	5.1	1.7
05-10072R	4.2	0.5
05-11001R	4.6	1.3
05-11007R	3.1	0.4
06-10218L	2.5	0.8
06-11284R	3.2	2.0
07-03466L	3.7	2.7
07-03471L	3.6	2.5
07-03472R	2.8	2.5

The optimized material coefficients for the tensile longitudinal (TL) loading condition were used to predict the response of each tissue to the other three loading conditions. The ability of the models to predict tissue behavior during other loading conditions was sample dependent. The predictions are shown in the figures below for four of the sixteen specimens. Data from the remaining specimens are shown in Appendix I.

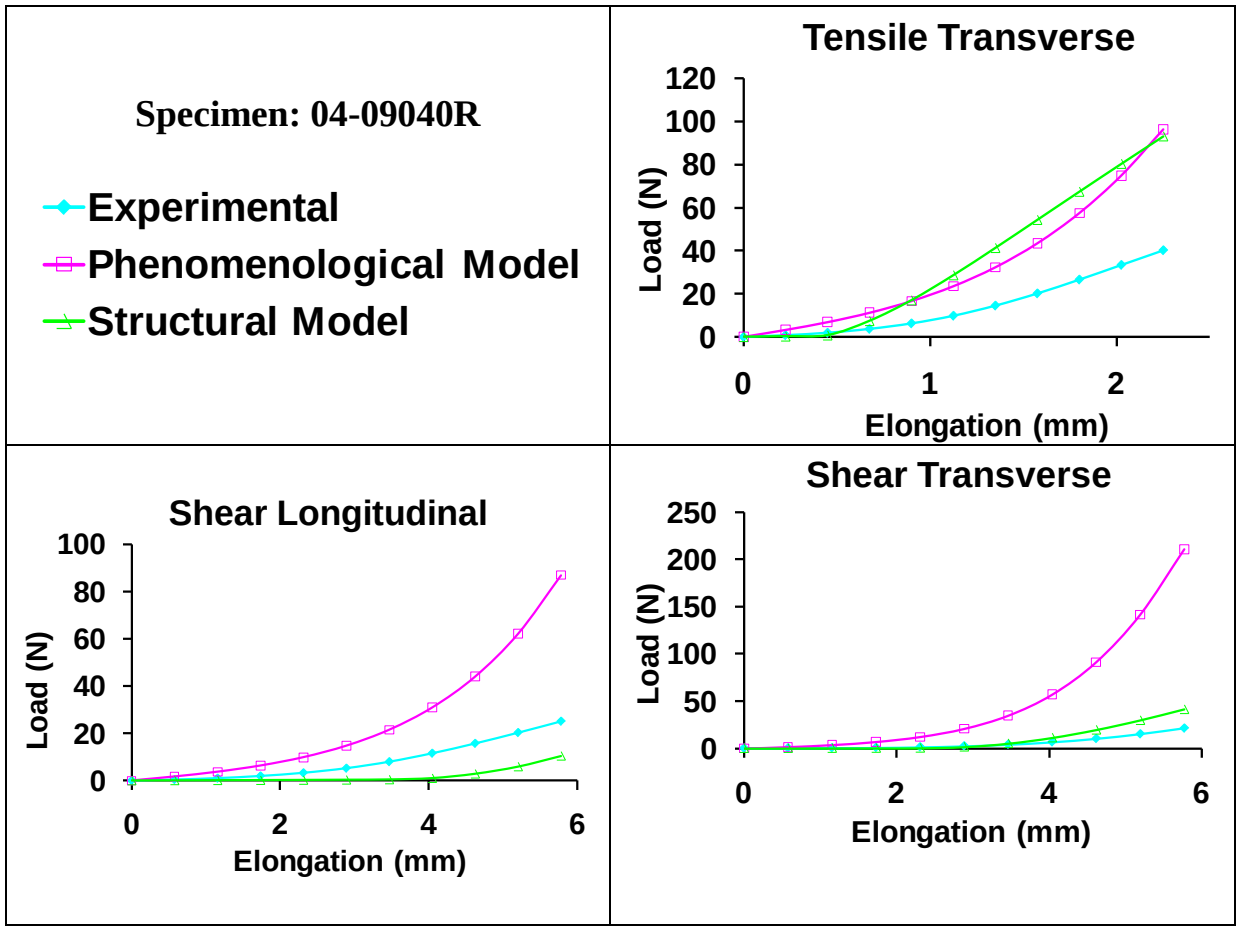

Figure 6.17 The optimized material parameters from the tensile longitudinal loading condition were used to predict the response of the capsule to the 1) tensile transverse (top right), 2) shear longitudinal (bottom left), and 3) shear transverse (bottom right) loading conditions for Specimen 04-09040R.

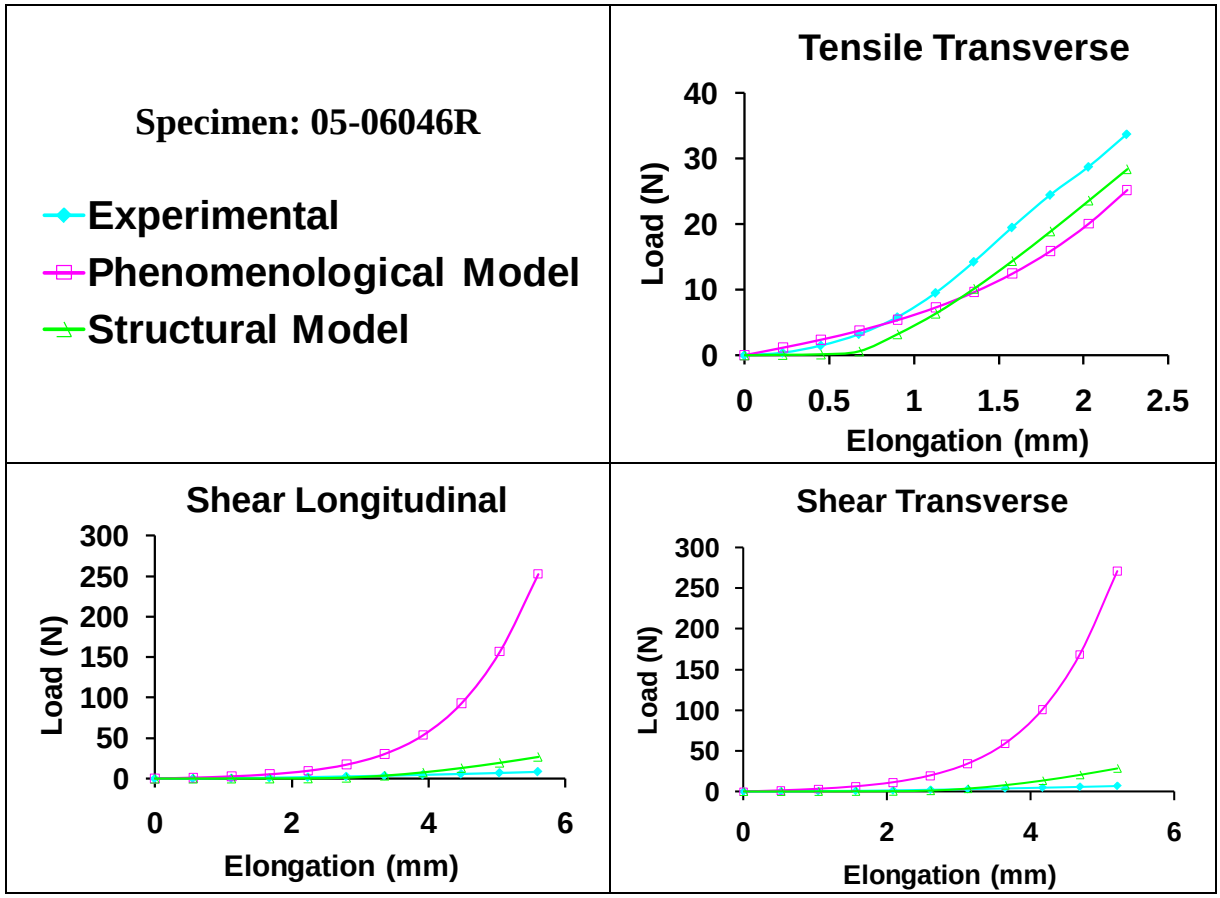

Figure 6.18 The optimized material parameters from the tensile longitudinal loading condition were used to predict the response of the capsule to the 1) tensile transverse (top right), 2) shear longitudinal (bottom left), and 3) shear transverse (bottom right) loading conditions for Specimen 05-06046R.

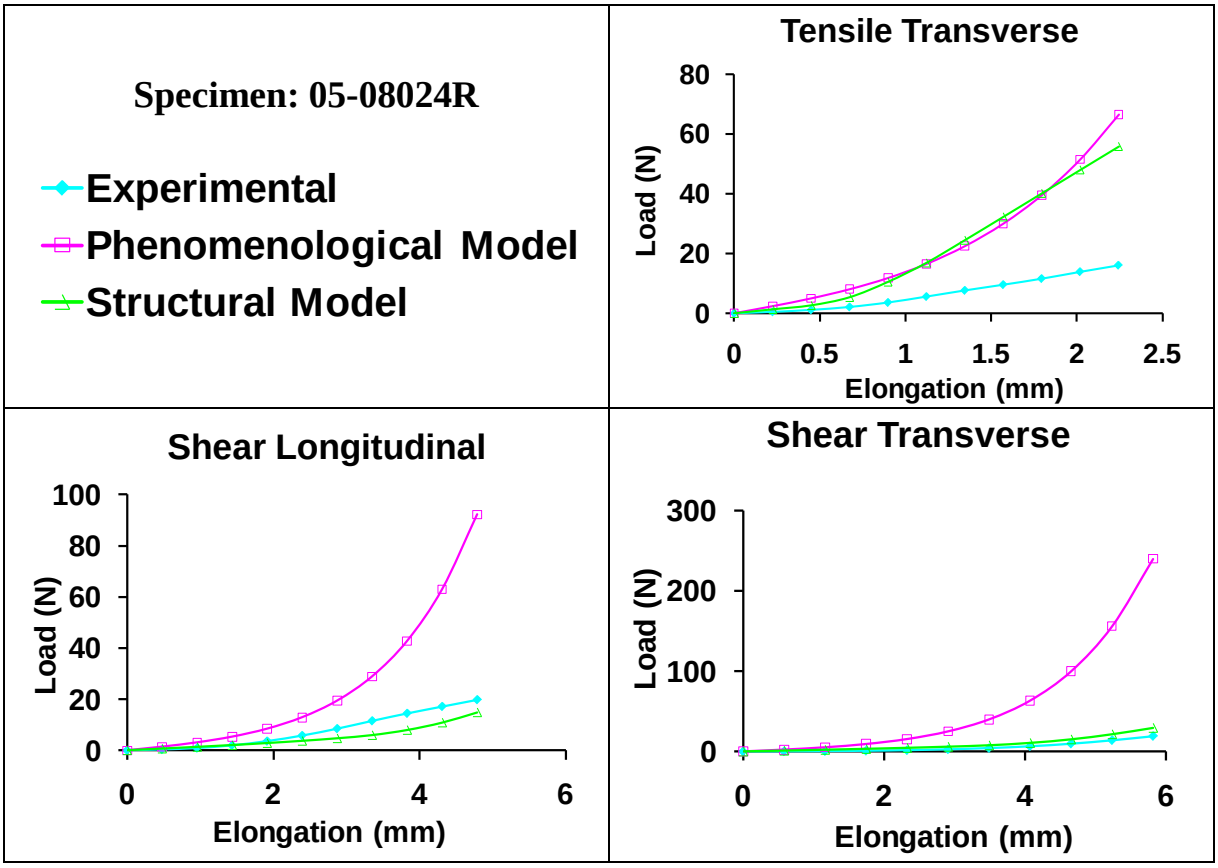

Figure 6.19 The optimized material parameters from the tensile longitudinal loading condition were used to predict the response of the capsule to the 1) tensile transverse (top right), 2) shear longitudinal (bottom left), and 3) shear transverse (bottom right) loading conditions for Specimen 05-08024R.

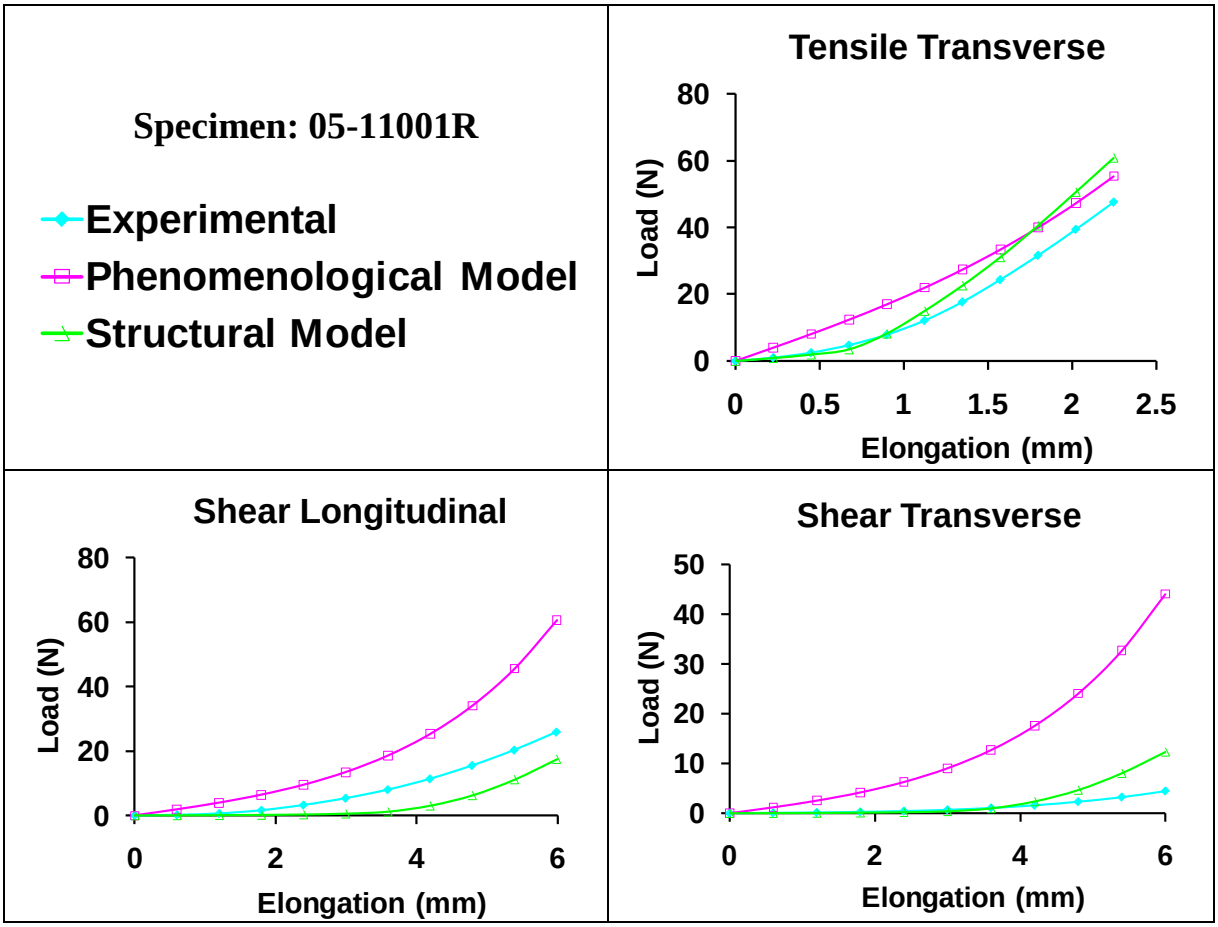

Figure 6.20 The optimized material parameters from the tensile longitudinal loading condition were used to predict the response of the capsule to the 1) tensile transverse (top right), 2) shear longitudinal (bottom left), and 3) shear transverse (bottom right) loading conditions for Specimen 05-11001R.

Both models provided similar predictions of the tensile transverse elongation with RMSE% values of 37.8 ± 45.0% and 44.3 ± 47.3% for the phenomenological and structural models, respectively. (Table 6.3) However, the structural model was better at predicting the response to both shear elongations. The RMSE% between experimental and predicted load-elongation curves for the phenomenological and structural models were 255.5 ± 342.6% and 32.4 ± 15.6% for the shear longitudinal and shear transverse predictions combined. Thus, when predicting the shear elongations, the structural model yielded RMSE% that were about 8 times less than the

phenomenological model. Predictions of shear behavior from the phenomenological model were consistently too stiff in comparison to the experimental measurements.

Table 6.3 Root-mean-squared error percentages (RMSE%) between the experimental and predicted load-elongation data for the phenomenological and structural constitutive models for each specimen.

Specimen #	Tensile Transverse		Shear Longitudinal		Shear Transverse	
	Phenomenological	Structural	Phenomenological	Structural	Phenomenological	Structural
04-09040R	63.5	71.9	101.1	33.7	353.5	38.5
05-06046R	15.5	11.1	1074.3	83.4	1435.2	1.204
05-08013L	142.6	168.2	105.9	33.2	17.7	42.0
05-08022L	4.9	44.1	26.9	22.6	10.9	23.2
05-08024R	141.7	127.7	140.7	19.3	449.2	23.9
05-08038L	67.1	85.9	130.9	39.4	76.9	44.7
05-10043R	43.1	50.1	18.5	42.1	83.4	39.3
05-10071R	11.8	17.9	950.1	21.2	366.9	20.1
05-10072R	10.7	35.8	96.9	34.0	474.2	27.1
05-11001R	16.1	13.5	59.7	23.1	401.0	65.5
05-11007R	7.1	5.6	15.8	36.6	20.8	33.7
06-10218L	4.9	8.6	534.6	12.7	558.5	10.9
06-11284R	10.2	9.0	158.5	21.3	138.6	31.1
07-03466L	19.5	17.3	61.5	38.0	25.0	40.3
07-03471L	16.5	16.0	50.5	40.9	5.0	42.1
07-03472R	28.9	26.1	129.2	14.3	103.4	38.2

6.1.4 Significance of Results

In this study, the structural model that incorporated the individual responses of the ground substance and collagen fibers provided better predictions for the material response of the glenohumeral capsule. Explicit representation of random fibers in the model provides a softer response to shear loading than the isotropic phenomenological model since collagen fibers can realign along the shear plane. Despite the initially isotropic material symmetry of the capsule resulting from the randomly oriented collagen fibers, surgeons may need to be conscious of the existence of the fibers during repair procedures.

The results of this study compare well with other studies that have successfully modeled ligaments [47, 177] and tendons [202] as fiber-reinforced composites. Previous work demonstrated the ability of the structural model to describe the material response of the transversely isotropic human MCL. [47] In the current work, this model was employed in finite element models of tissue samples from the glenohumeral capsule. Using this model, a predominant fiber direction was randomly assigned to each individual element within the finite element model resulting in a globally isotropic material response. For this initial study, all four material coefficients were optimized simultaneously and therefore may not have resulted in unique values. As a result, physical meaning regarding tissue constituents cannot be extracted from their values. The ground substance coefficient was much smaller in the capsule compared to the MCL but the fiber coefficients were typically the same order of magnitude; although a direct comparison between the material parameters of the structural model cannot be made between the MCL and capsule if the parameters are not unique. A method for optimizing the material parameters such that unique values can be obtained should be developed so that these

values can provide insight into the material properties of the capsule and direct comparisons can be made with the behavior of other tissues described using this model.

In the future, a simple test for parameter uniqueness, which was previously performed on the phenomenological model, should be performed for both tensile and shear loading conditions. The values of $C_1 - C_5$ should be defined and using one finite element model of each loading condition, the simulated load-elongation curves should be generated based on the geometry of those specific tissue samples. These load-elongation values can then be used as inputs into the inverse finite element optimization routine as the experimental values. If the optimized material coefficients are unique, they would be identical to the initially defined coefficients. This process should be repeated several times to ensure uniqueness. If the parameters are not unique a protocol or new experiment should be estabilished to determine the matrix and fiber coefficients separately.

6.1.5 Limitations

Hyperelastic models were used in this work due to the non-linear and nearly incompressible behavior of the glenohumeral capsule. Little work has been done to determine the viscoelastic properties of the capsule; however when determining material parameters, the tissue is preconditioned in order to minimize viscoelastic effects prior to application of the non-destructive elongation. Therefore, the viscoelastic response was neglected and did not affect the results of the current work thus the constitutive framework is appropriate given the input data. The question of viscoelastic response of the glenohumeral capsule would be more important under high-rate loading conditions that might simulate injury scenarios. The assumption of uncoupled deviatoric-dilatational response is commonly employed in finite deformation

elasticity for slightly compressible materials [176, 178, 203], since the vast majority of strain energy induced in ligaments is deviatoric due to minimal volumetric confinement of the tissue in physiological loading.

The results of this work demonstrate a significant improvement with the use of the structural model compared to the phenomenological model, particularly when describing the behavior of the capsule in response to shear loading. However, this model was only capable of predicting tensile and shear elongations with ~40% error. The experimental repeatability of ~10% suggests that improvements to the structural model can be made. However, biologic variability can be as much as 50%. In addition, the work using the structural model to describe the behavior of the MCL evaluated the effect of the variation in λ^* on the outcome of the material coefficients. It was found that an error 0.5% strain in determining the location of λ^* could result in up to 20% error in the material coefficients. Considering all assumptions and errors associated with the combined experimental and computational protocol, predicting the material response of the glenohumeral capsule within ~40% may be approaching the limit of this methodology. Small improvements may be possible though, for example, as the value of λ^* was fixed in this study, optimizing for this parameter in each specimen may improve the predictive capability of the structural model. In addition, the structural model makes the assumption of random fiber orientation which was based on fiber alignment studies [3, 173] and the success of the phenomenological model of predicting perpendicular loading conditions [42]. However, as the fiber alignment data suggests, the glenohumeral capsule consists of localized areas of increased fiber alignment in a globally isotropic tissue and fiber distributions and material properties vary from specimen to specimen. Incorporating specimen-specific fiber distributions

into the finite element model on an element by element basis may improve the predictive capability of the structural constitutive model.

6.2 POTENTIAL IMPROVEMENTS TO STRUCTURAL MODEL

6.2.1 Separate Response of Ground Substance and Collagen Fibers

In an attempt to reduce the number of material parameters optimized simultaneously and reduce computational time, an analysis protocol was developed to separate the ground substance and fiber responses.

6.2.1.1 Methods

Based on the preliminary studies, the contribution of the collagen fibers to the response of the tissue in tension was much more than in shear. Therefore, it was decided to use one of the shear loading conditions to determine the ground substance coefficient (C_1). As the strain energy function describing the response of the ground substance was linear it could not provide a good fit to the non-linear experimental load-elongation curve. However, the tissue response during the first 1 mm of elongation in shear was fairly linear. The initial loading of collagen fibers in biologic tissues results in the toe-region of the load-elongation curve due to fiber uncrimping and recruitment. In other words, the collagen fibers were not taking up any load until the toe-region of the load elongation curve. Therefore, it was assumed that during the initial 1 mm of shear elongation the contribution of the collagen fibers to the overall tissue response is very minimal.

The shear transverse loading condition was chosen at random (over the shear longitudinal) and the first 1 mm of the load-elongation curve was used to determine the ground substance coefficient by changing the coefficient until the experimental and finite element model-predicted load-elongation curves matched. This coefficient was then held constant and the tensile longitudinal load-elongation data was used to optimize the fiber coefficients ($C_3 – C_5$). This cut the number of parameters being optimized simultaneously down from four to three. The four optimized parameters were then used to predict the response of the tissue to the tensile transverse and shear longitudinal loading conditions. This protocol was performed on four tissue samples from the axillary pouch in order to determine if any differences were observed between this new technique and the model predictions when all parameters were optimized simultaneously.

6.2.1.2 Results

The optimized material parameters were determined for four tissue samples. (Table 6.4)

Table 6.4 Optimized material coefficients for four specimens. The ground substance coefficient (C_1) was determined from the first 1 mm of the shear transverse elongation and the fiber coefficients ($C_3 – C_5$) were determined from the tensile longitudinal loading condition.

SPECIMEN #	C_1 (MPa)	C_3 (MPa)	C_4	C_5 (MPa)
04-09040R	0.11	0.66	1.06	141.58
05-06046R	0.09	0.10	0.01	65.71
05-08024R	0.06	1.01	8.61	85.53
05-11001R	0.07	1.69	3.47	82.42

The separation of ground substance and collagen fibers resulted in slightly different material parameters compared to when all parameters were optimized simultaneously. The greatest

changes in the material parameters was 0.03 MPa, 1.08 MPa, 32.3, and 14.4 MPa for C_1, C_3, C_4, and C_5, respectively. These maximum changes occurred in samples 04-09040R, 05-11001R, 04-09040R, and 05-08024R, respectively. The ability of the structural model to fit the experimental data when optimizing for the ground substance and fiber coefficients as well as the resulting tensile and shear predictions for each specimen are shown in Figure 6.21-Figure 6.24. In three of the four specimens, separate optimization of the ground substance and fiber coefficients did not affect the model predictions compared to when all parameters were optimized simultaneously. However, in specimen 05-08024R the shear prediction was visibly worse. In this specimen the C_5 coefficient increased by 14 MPa when the ground substance and fiber coefficients were optimized separately, which was the greatest increase in C_5 of any of the tissue samples. As shown in Section 6.1.1.3, when C_5 values are above ~20 MPa, changes in their value greatly affect the response of the tissue in shear. It is likely that parameter uniqueness affected the model predictions for this particular tissue sample when all parameters were optimized simultaneously.

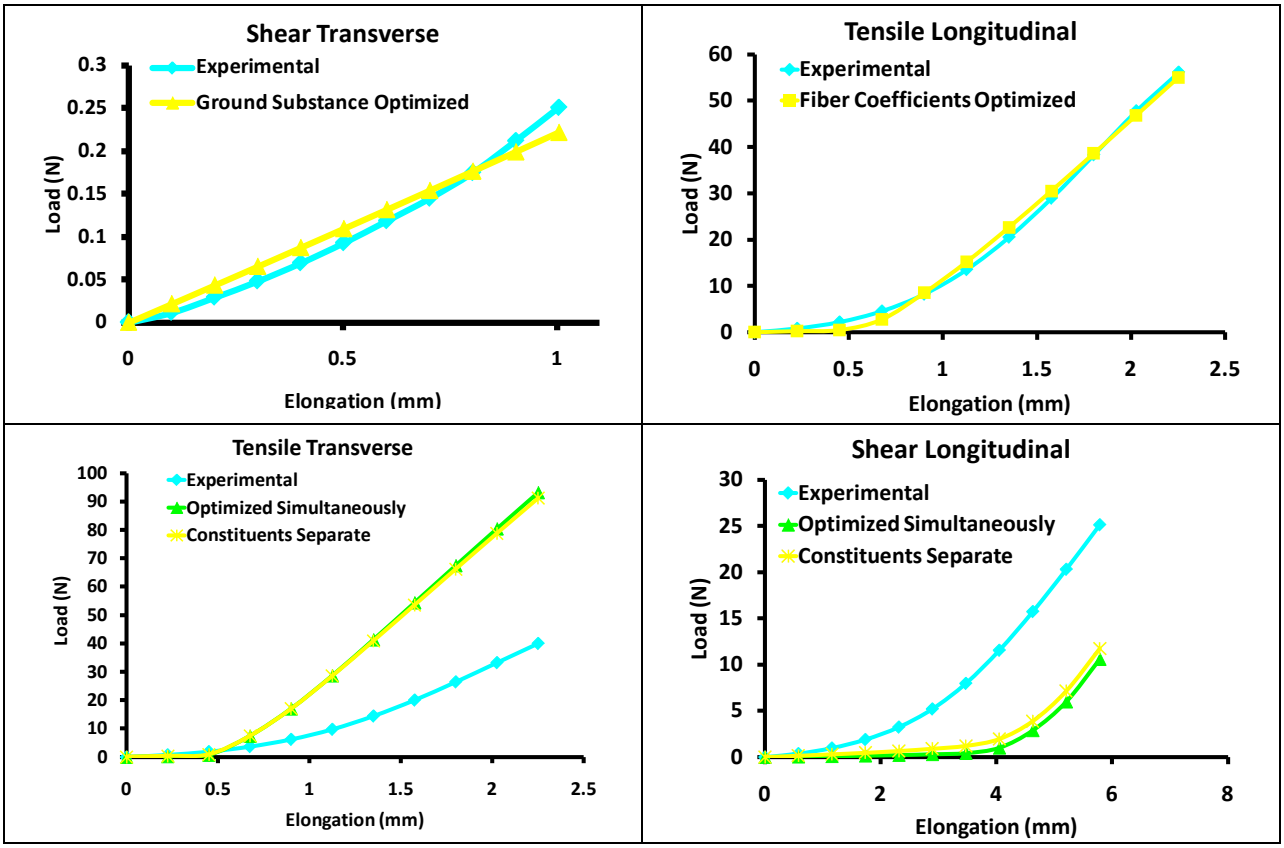

Figure 6.21 Load-elongation curves for Specimen 04-09040R showing the ability of the structural model to fit the experimental data during the optimization of the ground substance (top left) and fiber (top right) coefficients and the ability of these coefficients to predict the tissue response in tension (bottom left) and shear (bottom right).

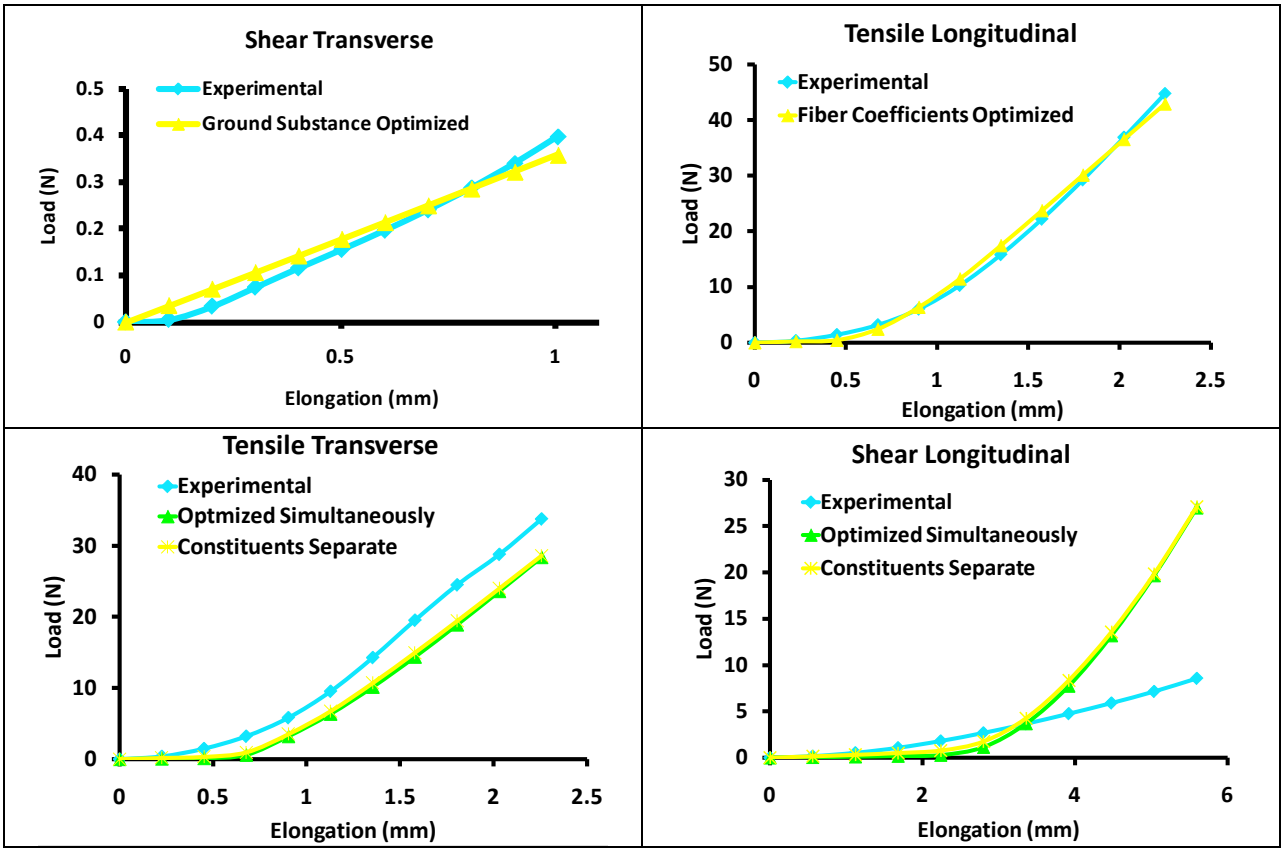

Figure 6.22 Load-elongation curves for Specimen 05-06046R showing the ability of the structural model to fit the experimental data during the optimization of the ground substance (top left) and fiber (top right) coefficients and the ability of these coefficients to predict the tissue response in tension (bottom left) and shear (bottom right).

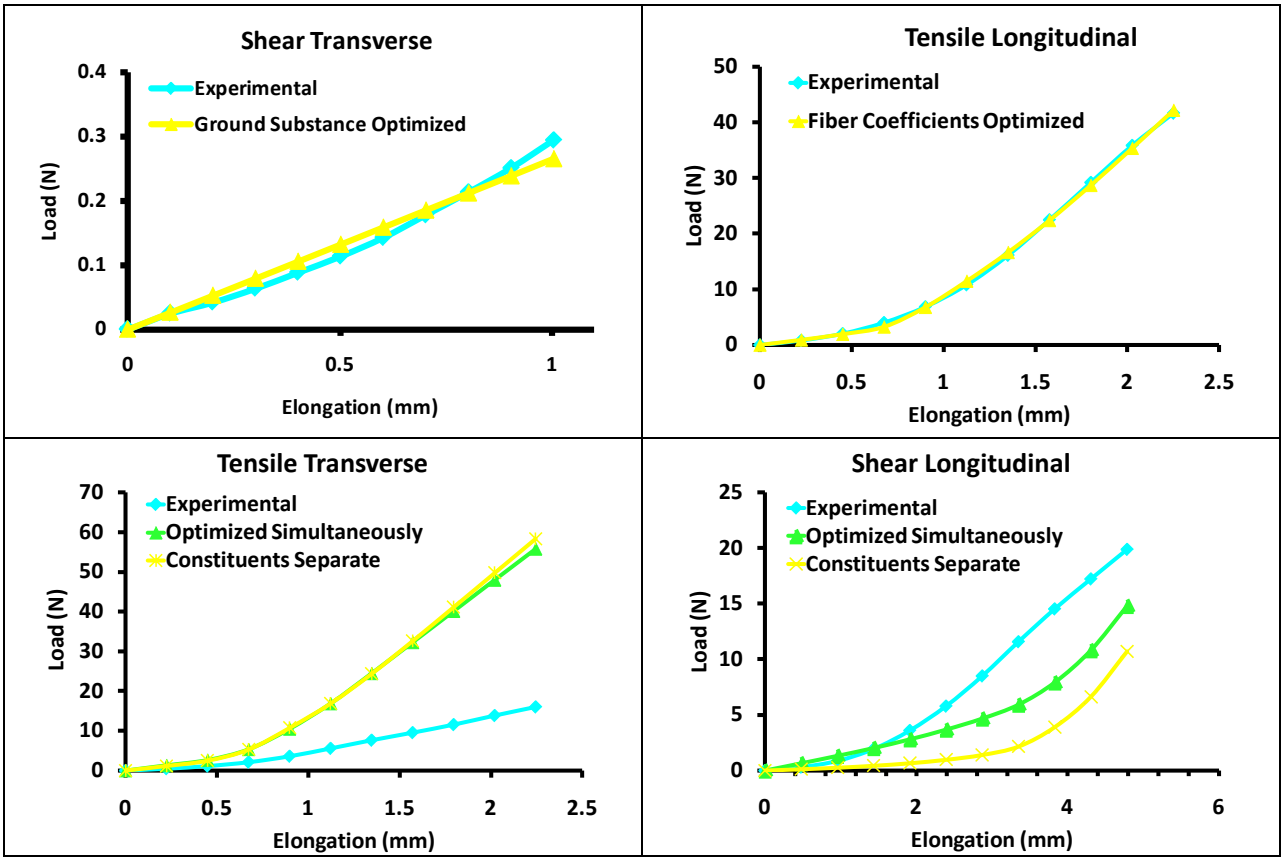

Figure 6.23 Load-elongation curves for Specimen 05-08024R showing the ability of the structural model to fit the experimental data during the optimization of the ground substance (top left) and fiber (top right) coefficients and the ability of these coefficients to predict the tissue response in tension (bottom left) and shear (bottom right).

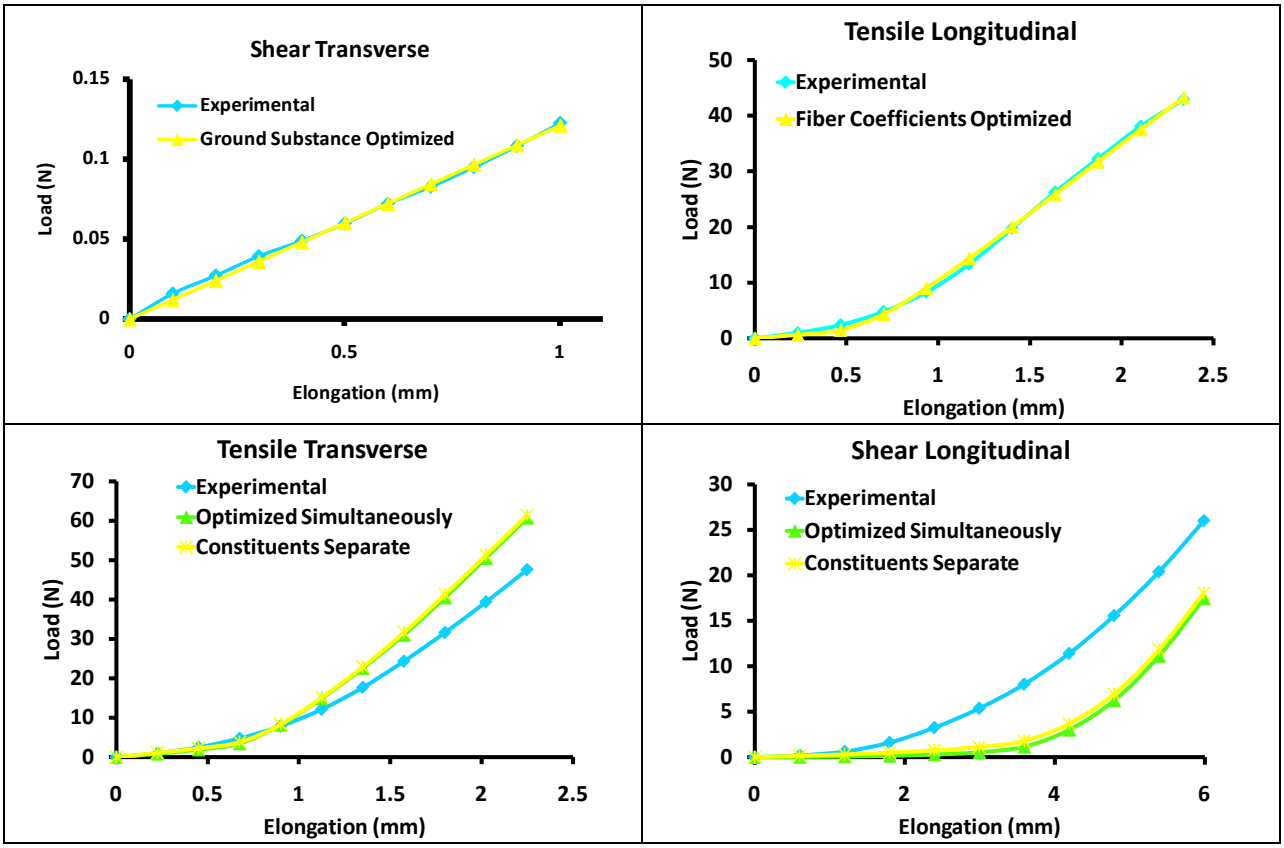

Figure 6.24 Load-elongation curves for Specimen 05-11001R showing the ability of the structural model to fit the experimental data during the optimization of the ground substance (top left) and fiber (top right) coefficients and the ability of these coefficients to predict the tissue response in tension (bottom left) and shear (bottom right).

6.2.2 Eliminate Linear Region from Optimization

In an attempt to further reduce the number of parameters being optimized at once, the linear-region fiber coefficient (C_5) was eliminated from the analysis.

6.2.2.1 Methods

As the entire load-elongation curve is non-linear it could be modeled by the toe-region portion of the F_2 term. This would eliminate the C_5 coefficient from the optimizations and further reduce the number of parameters to two. However, in doing this the assumption that the linear region is not captured in the experimental data and that the fiber contribution to the entire load-elongation response can be characterized by C_3 and C_4 is made. Therefore, the material parameters still may not have direct physical meaning.

The ground substance coefficient was determined from the shear transverse elongation as described in the previous section. In order to eliminate the contribution of C_5 to the tissue response the value of λ^* was set to 3. This stretch value is never reached in the finite element simulations which mean the transition point from toe- to linear-region is never reached and thus, the linear region fiber response in the linear region is never included. C_5 can be set to any value and will not contribute to the load-elongation response predicted by the finite element model. For this work, C_5 was arbitrarily set to 10. The toe-region parameters, C_3 and C_4, were optimized using the tensile longitudinal data and then all three parameters were used to predict the response of each tissue sample in tension and shear. This process was performed on the same four tissue samples as in the previous section.

6.2.2.2 Results

The optimized material parameters were determined for the four tissue samples. (Table 6.5)

Table 6.5 Optimized material coefficients for four specimens. The ground substance coefficient (C_1) was determined from the first 1 mm of the shear transverse elongation and the fiber coefficients ($C_3 – C_4$) were determined from the tensile longitudinal loading condition.

SPECIMEN #	C_1 (MPa)	C_3 (MPa)	C_4
04-09040R	0.11	1.8	12.9
05-06046R	0.09	0.8	13.6
05-08024R	0.06	1.1	14.2
05-11001R	0.07	2.8	8.1

Eliminating the linear region from the model resulted in increased values of C_3 and C_4. The value of C_3 and C_4 increased by 0.8 ± 0.5 MPa and 8.9 ± 4.5, respectively. The ability of the structural model to predict the response of each tissue in tension and shear when using these parameters are shown in Figure 6.25-Figure 6.28. In general, eliminating the linear region did not affect the model predictions in tension or shear, although in some cases a greater stiffness was predicted at higher elongations. This trend could lead to less accurate model predictions under large strains. In addition, the shape of the predicted curves is exponential, as expected, and does not contain the separate toe- and linear-regions typical of biologic soft tissues. Excluding the linear region from the constitutive model eliminates important contributions of the collagen fibers to the overall tissue response. If this structural model is to be used to further understand how the individual constituents contribute to the material behavior of the capsule than both the toe and linear region should be included.

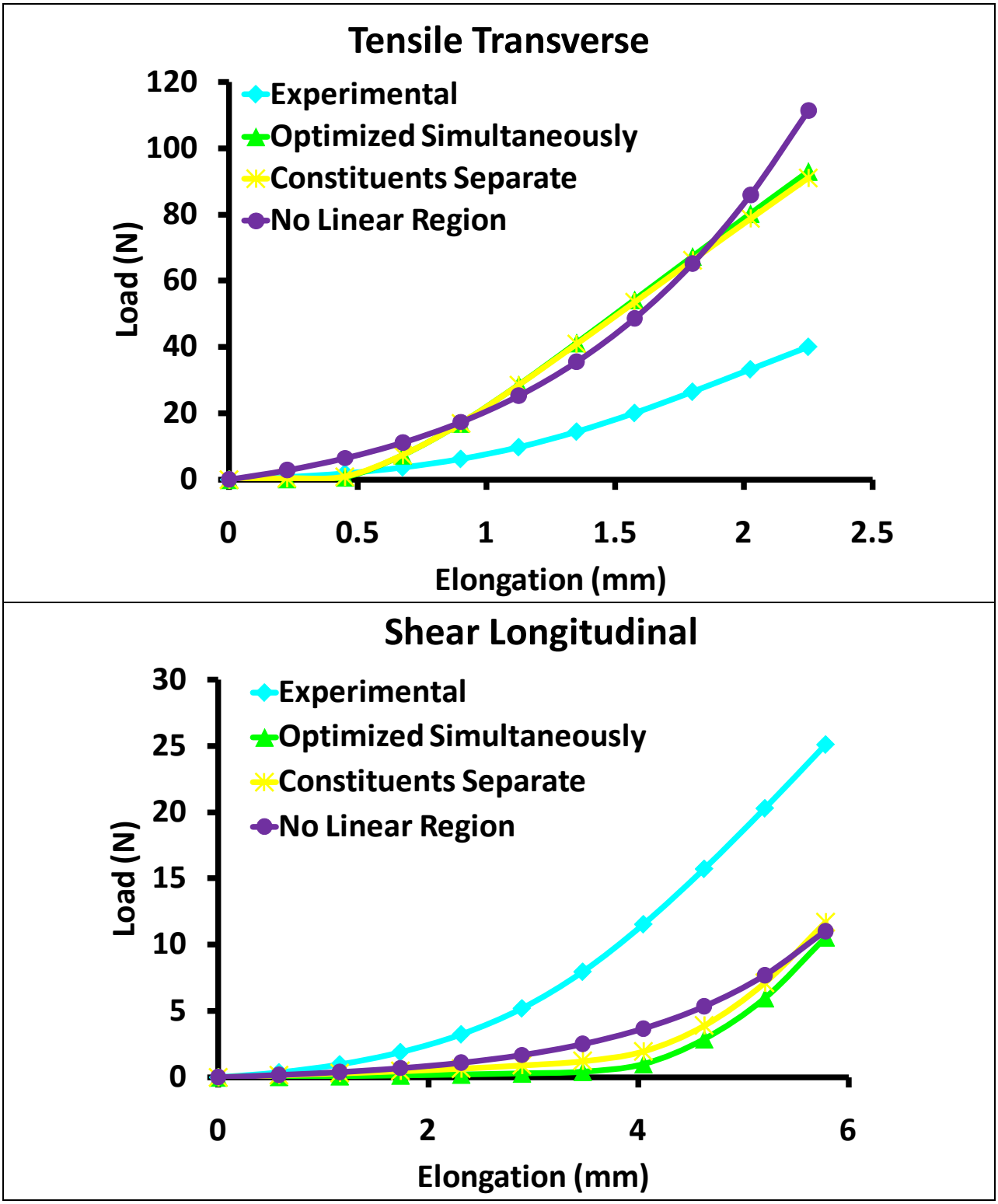

Figure 6.25 Load-elongation curves for Specimen 04-09040R showing the ability of the structural model to predict the tissue response in tension (top) and in shear (bottom) for the three sets of optimized material coefficients.

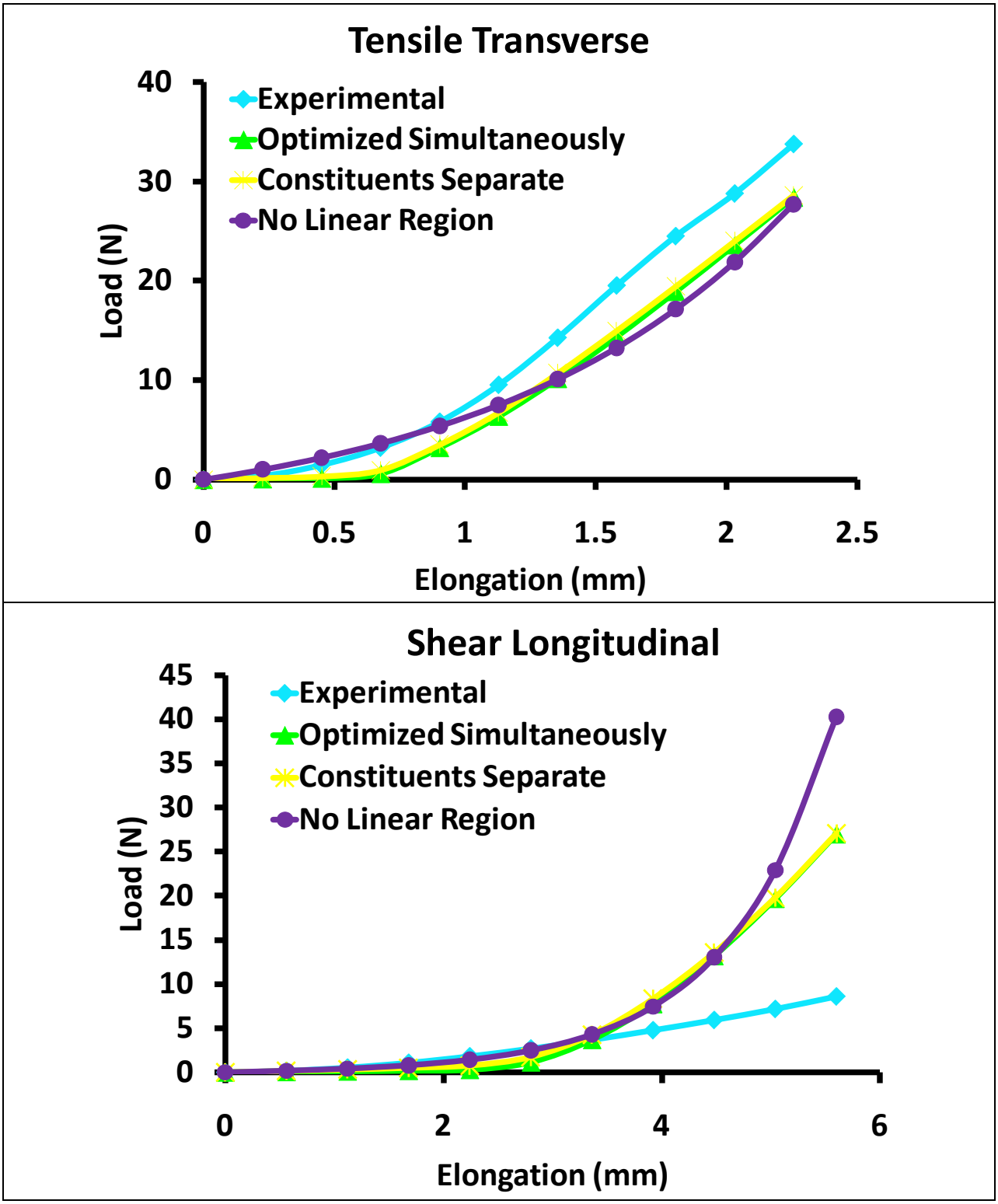

Figure 6.26 Load-elongation curves for Specimen 05-06046R showing the ability of the structural model to predict the tissue response in tension (top) and in shear (bottom) for the three sets of optimized material coefficients.

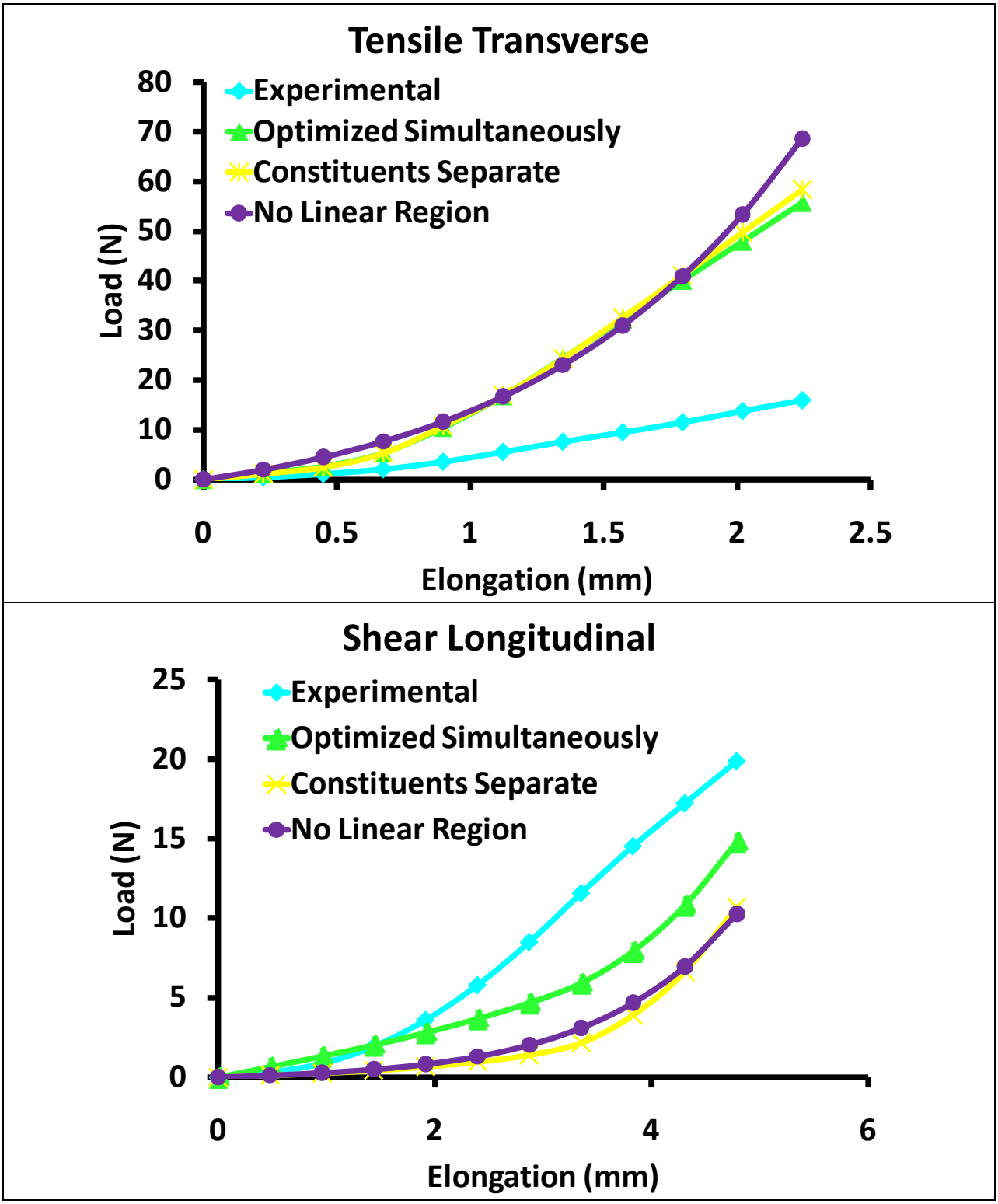

Figure 6.27 Load-elongation curves for Specimen 05-08024R showing the ability of the structural model to predict the tissue response in tension (top) and in shear (bottom) for the three sets of optimized material coefficients.

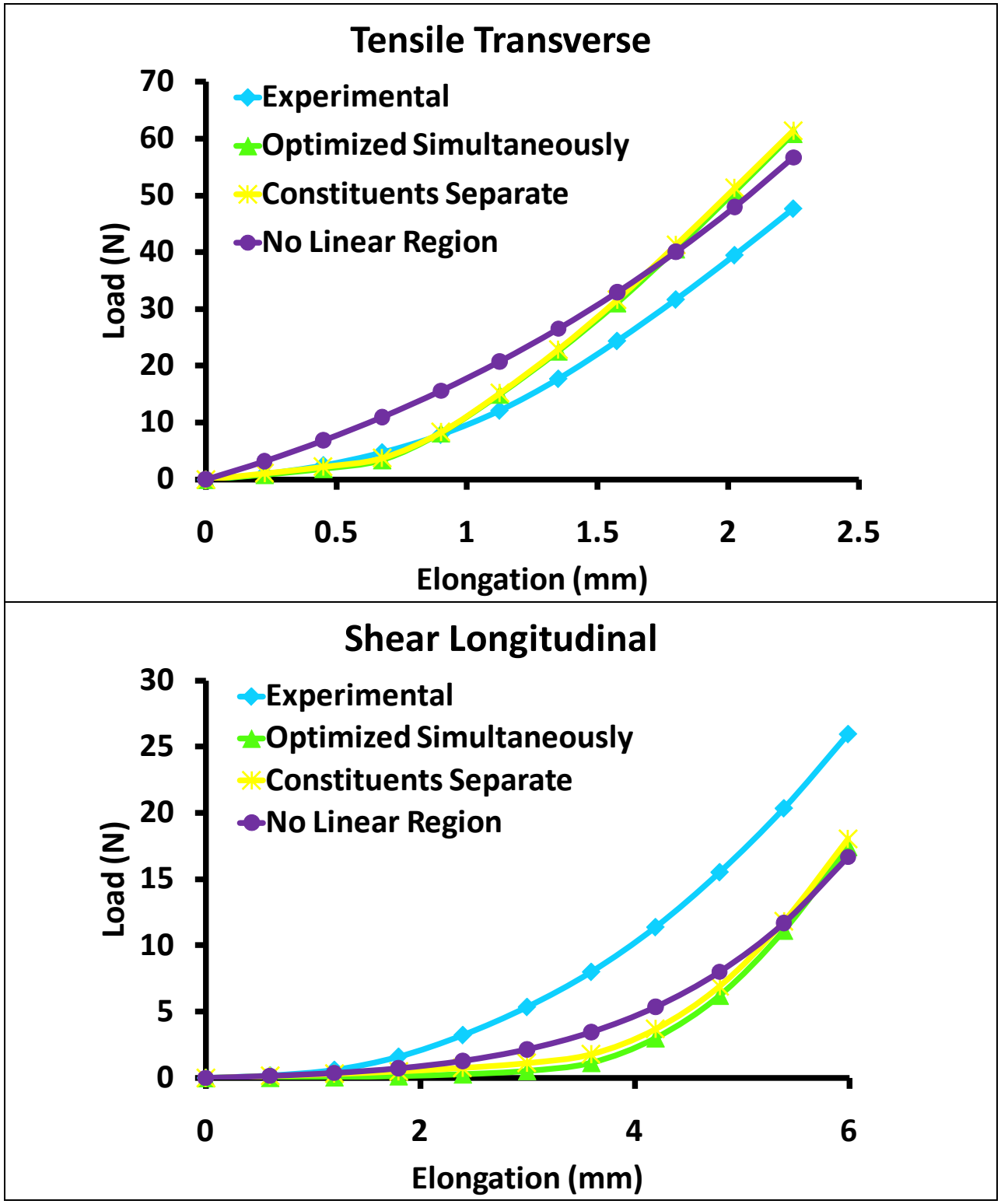

Figure 6.28 Load-elongation curves for Specimen 05-11001R showing the ability of the structural model to predict the tissue response in tension (top) and in shear (bottom) for the three sets of optimized material coefficients.

6.2.3 Alternative Model for Ground Substance

In most cases the structural model under-predicted the response of the tissue during shear loading. Since the tissue response in shear is governed more by the ground substance, especially under small elongations, it was hypothesized that a non-linear model for the ground substance would improve predictive capability over the linear Neo-Hookean model.

6.2.3.1 Methods

The phenomenological constitutive model (Equation 1) was used to describe the response of the ground substance (F_1). This introduced yet another parameter to be optimized therefore the ground substance and fiber coefficients were optimized separately similar to Section 6.2.1 for the structural model. As previously described, the experimental data from the shear transverse loading condition up to 1 mm of elongation was used to determine the ground substance coefficients (C_1 and C_2). These coefficients were then held constant and the tensile longitudinal loading condition was used to determine the optimized fiber coefficients. All five parameters were used to predict the response of four tissue samples to the tensile transverse and shear longitudinal loading conditions. The RMSE% was computed between the model predictions and the experimental data and was used to compare the phenomenological model, the structural model with the linear (Neo-Hookean) model for the ground substance, and the structural model with the non-linear (phenomenological) model for the ground substance.

6.2.3.2 Results

Using a nonlinear model to describe the response of the ground substance exhibited poor results.

Table 6.6 Root-mean-squared error percentages (RMSE%) between the experimental and model predicted load-elongation curves during the tensile transverse loading condition.

SPECIMEN #	Phenomenological Model (%)	Structural Model – Linear Ground Substance (%)	Structural Model - Nonlinear Ground Substance (%)
04-09040R	101.1	71.9	78.5
05-06046R	1074.3	11.1	11.3
05-08024R	140.7	127.7	132.2

Table 6.7 Root-mean-squared error percentages (RMSE%) between the experimental and model predicted load-elongation curves during the shear longitudinal loading condition.

SPECIMEN #	Phenomenological Model (%)	Structural Model – Linear Ground Substance (%)	Structural Model - Nonlinear Ground Substance (%)
04-09040R	353.5	33.7	83.8
05-06046R	1435.2	83.4	1094.0
05-08024R	449.2	19.3	19.3

The RMSE% values for the structural model with the linear (70.2 ± 58.3%) and nonlinear (74.0 ± 60.6%) ground substance were similar when the models were used to predict the tissue response to tension. However, when predicting shear elongations, the structural model with the non-linear (399.0 ± 602.7%) ground substance yielded RMSE% values which were substantially larger than when the linear (45.5 ± 33.6%) model was used for the ground substance. In fact, the non-linear ground substance predicted tissue responses in shear that were similar to those predicted by the phenomenological model (746.0 ± 598.8%). Therefore, the structural model with the linear model (Neo-Hookean) for the ground substance provides the best predictions of the material behavior of the glenohumeral capsule in tension and shear; using a nonlinear model for the ground substance actually made the predictions worse. As a result, model predictions were not performed on the fourth tissue sample.

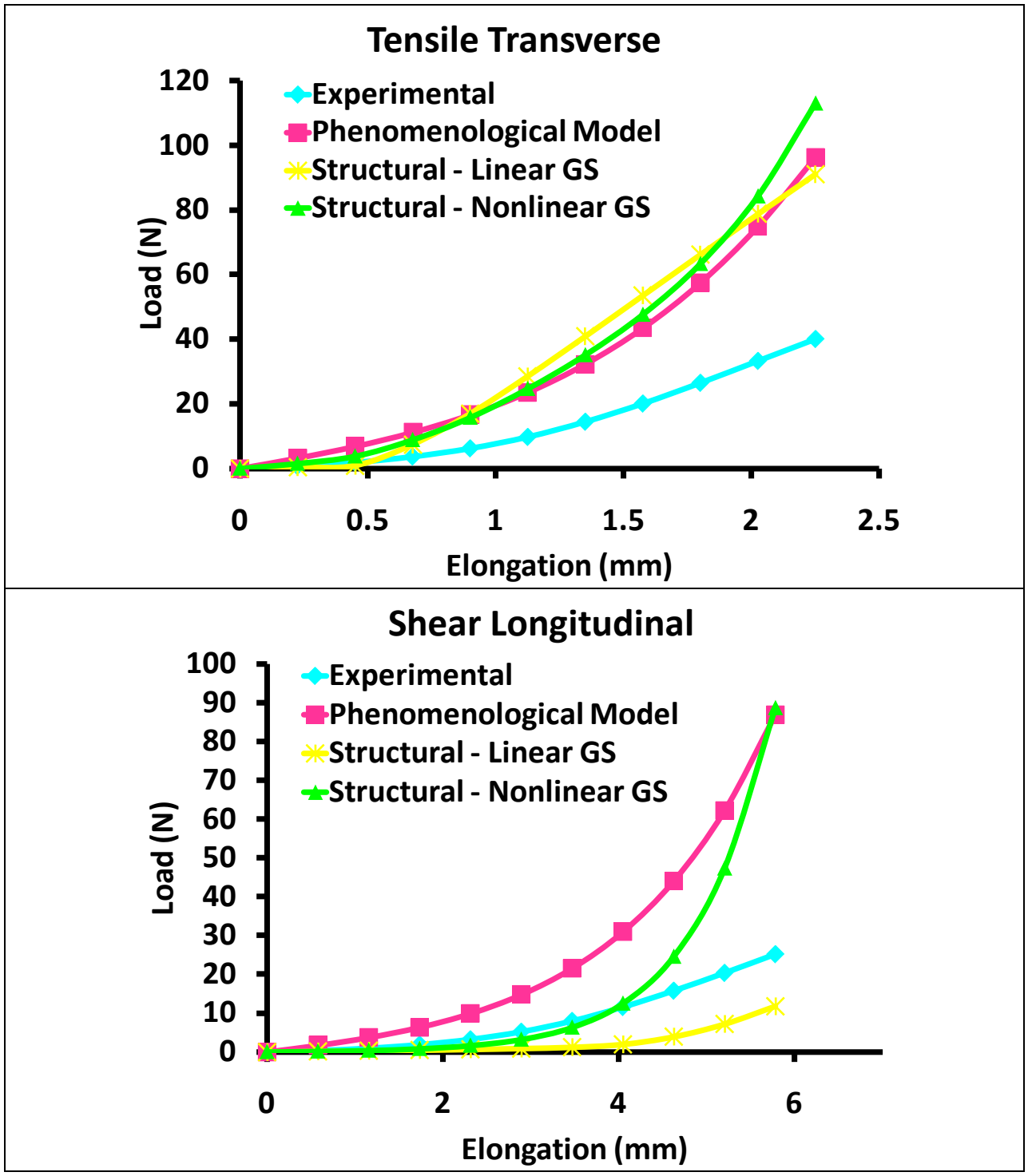

Figure 6.29 Load-elongation curves for Specimen 04-09040R showing the ability of the phenomenological model, structural model with the linear model of the ground substance, and structural model with the nonlinear model for the ground substance to predict the tissue response in tension (top) and in shear (bottom).

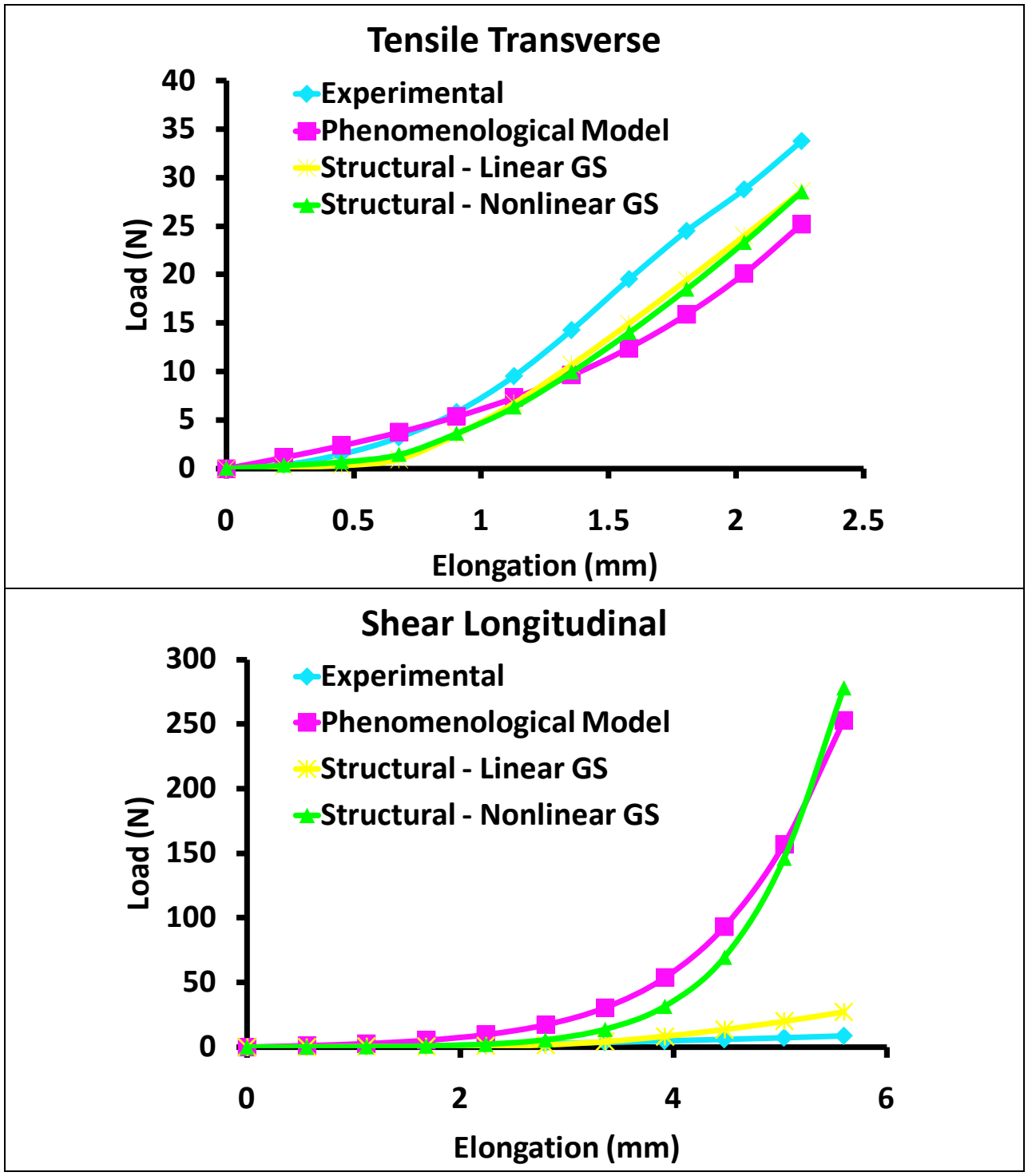

Figure 6.30 Load-elongation curves for Specimen 05-06046R showing the ability of the phenomenological model, structural model with the linear model of the ground substance, and structural model with the nonlinear model for the ground substance to predict the tissue response in tension (top) and in shear (bottom).

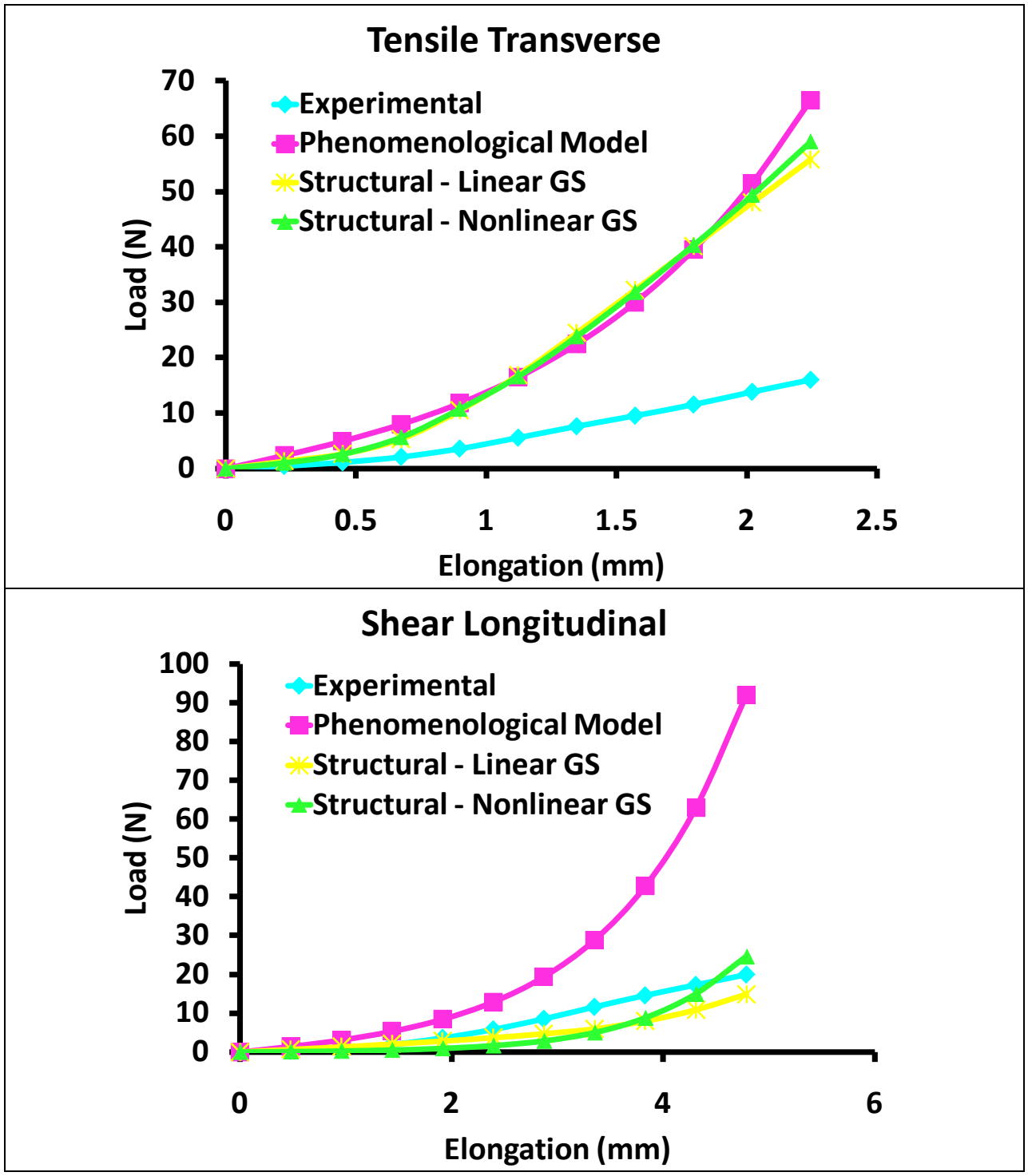

Figure 6.31 Load-elongation curves for Specimen 05-08024R showing the ability of the phenomenological model, structural model with the linear model of the ground substance, and structural model with the nonlinear model for the ground substance to predict the tissue response in tension (top) and in shear (bottom).

6.2.4 Introduce Slight Anisotropy

The constitutive framework of both the phenomenological and structural constitutive models assumes that the glenohumeral capsule has a completely random collagen fiber distribution and that its material symmetry is isotropic. This assumption led to the development of the structural model which was a great improvement over the phenomenological model with RMSE% values between the experimental and model predicted load-elongation curves of ~40% in both tension and shear. Slight changes to the loading conditions used for parameter optimization did not affect the predictive capability of the structural model and describing the response of the ground substance using a nonlinear model provided worse predictions. One final attempt was made to improve the predictive capability of the structural constitutive model by evaluating the assumption that the glenohumeral capsule is completely isotropic.

Previous work in our laboratory has characterized the bi-directional material properties of the axillary pouch and posterior capsule. [40, 41] Results of this work suggest that while the capsule is much more isotropic than typical uniaxial ligaments such as the MCL, it is not perfectly isotropic. For the axillary pouch, the ratio of the longitudinal to transverse moduli was found to be 3.3 ± 2.8, suggesting that the capsule has different material properties when loaded in two perpendicular directions. [41] Therefore, the most accurate description of the capsule would be one which incorporates this slight anisotropy. As the linear region coefficient, C_5, represents the modulus of the straightened collagen fibers anisotropy can be manually induced by manipulating this parameter between longitudinal and transverse loading conditions. This section of the work presents a preliminary study to evaluate the effect of accounting for the slight anisotropy of the capsule on the predictive capability of the structural model.

6.2.4.1 Methods

As indicated by the previous work [41], the longitudinal direction (with respect to the AB-IGHL) of the axillary pouch has a modulus that is, on average, 3.3 times larger than the transverse direction. Therefore, if the tensile longitudinal loading condition is used to determine the optimized value of C_5, then the value of C_5 in the tensile transverse loading condition should be C_5 divided by 3.3. The same concept is true for the shear loading conditions and thus the value of C_5 used in the predictions of the shear longitudinal loading condition should be divided by 3.3 as well.

The same four tissue samples were used to evaluate the assumption of anisotropy. The material coefficients of the structural model were optimized as previously described from the shear transverse and tensile longitudinal loading conditions by separating the response of the ground substance and collagen fibers, respectively. These material coefficients were then used to predict the response of each tissue sample to the tensile transverse and shear longitudinal loading conditions but the value of C_5 was divided by 3.3. The RMSE% was used to quantify differences between the experimental and finite element model-predicted load-elongation curves.

6.2.4.2 Results

In response to the tensile transverse loading condition, introducing anisotropy into the structural model greatly reduced the RMSE% between the experimental and predicted load-elongation curves from 59.1 ± 57.7% to 23.2 ± 11.3% for these four tissue samples. A significant reduction in the RMSE% was seen in two of the four tissue samples. (Table 6.8) In the other two tissue samples the RMSE% increased.

Table 6.8 Root-mean-squared error percentages (RMSE%) between the experimental and model predicted load-elongation curves during the tensile transverse loading condition.

SPECIMEN #	Phenomenological Model (%)	Structural Model (%)	Structural Model – Anisotropy (%)
04-09040R	101.1	78.5	8.6
05-06046R	1074.3	11.3	36.0
05-08024R	140.7	132.2	25.3
05-11001R	59.7	14.4	22.8

Introducing anisotropy into the structural model also improved its ability to predict the response of the capsule to shear loading. The RMSE% was reduced from 304.6 ± 527.1% to 30.8 ± 13.5% in these four tissue samples. Again, significant reductions in the RMSE% values were found in two of the four tissue samples, although these did not correspond to the tissue samples whose predicted tensile responses were improved. (Table 6.9) Increases in the RMSE% values were seen in the other two tissue samples but these increases were much smaller. Therefore, incorporating anisotropy into a structural constitutive model may better describe and predict the complex material behavior of the glenohumeral capsule.

Table 6.9 Root-mean-squared error percentages (RMSE%) between the experimental and model predicted load-elongation curves during the shear longitudinal loading condition.

SPECIMEN #	Phenomenological Model (%)	Structural Model (%)	Structural Model – Anisotropy (%)
04-09040R	353.5	83.8	38.5
05-06046R	1435.2	1094.0	10.9
05-08024R	449.2	19.3	39.8
05-11001R	401.0	21.2	33.9

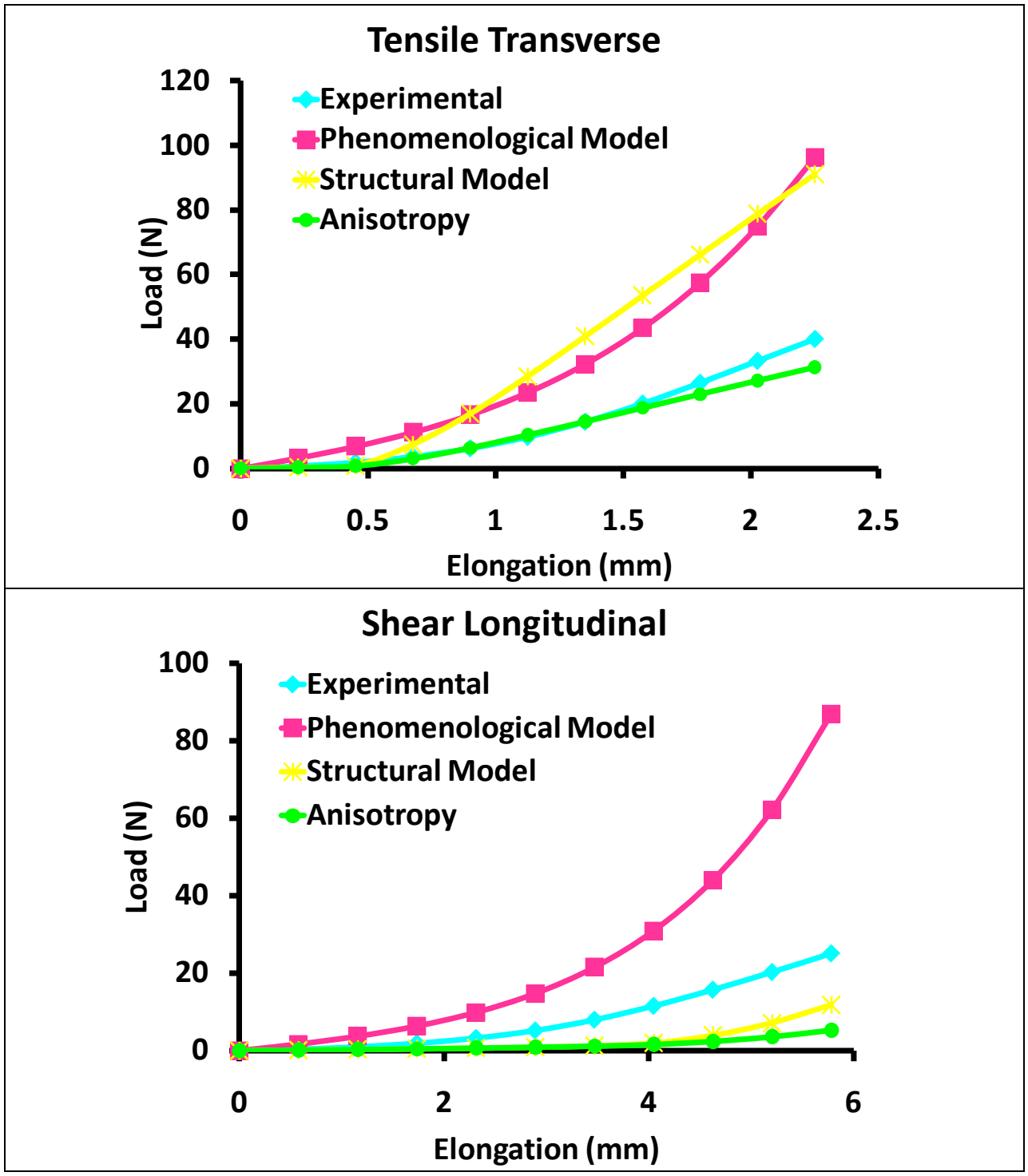

Figure 6.32 Load-elongation curves for Specimen 04-09040R showing the ability of the phenomenological model, structural model, and structural model with induced anisotropy to predict the tissue response in tension (top) and in shear (bottom).

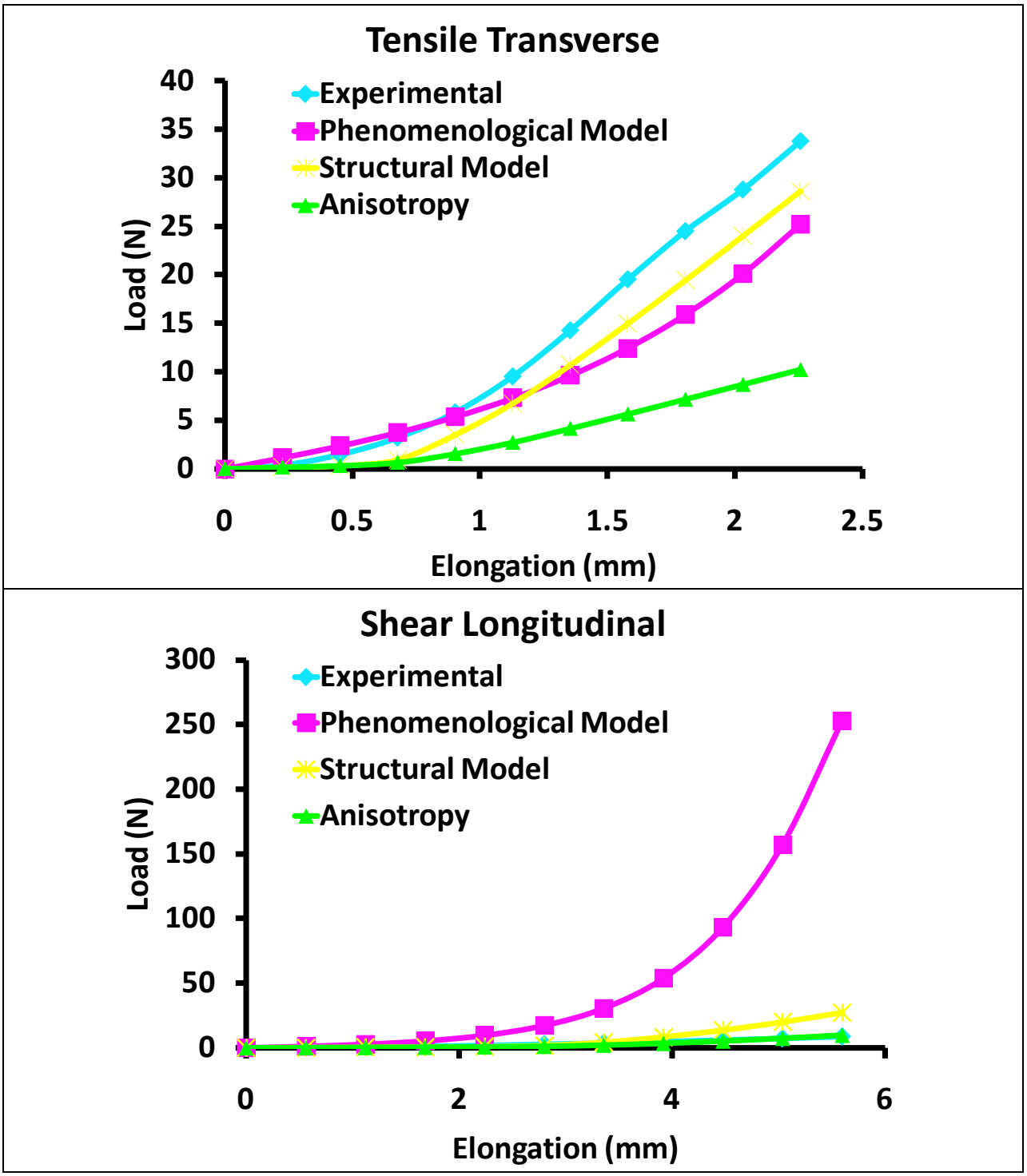

Figure 6.33 Load-elongation curves for Specimen 05-06046R showing the ability of the phenomenological model, structural model, and structural model with induced anisotropy to predict the tissue response in tension (top) and in shear (bottom).

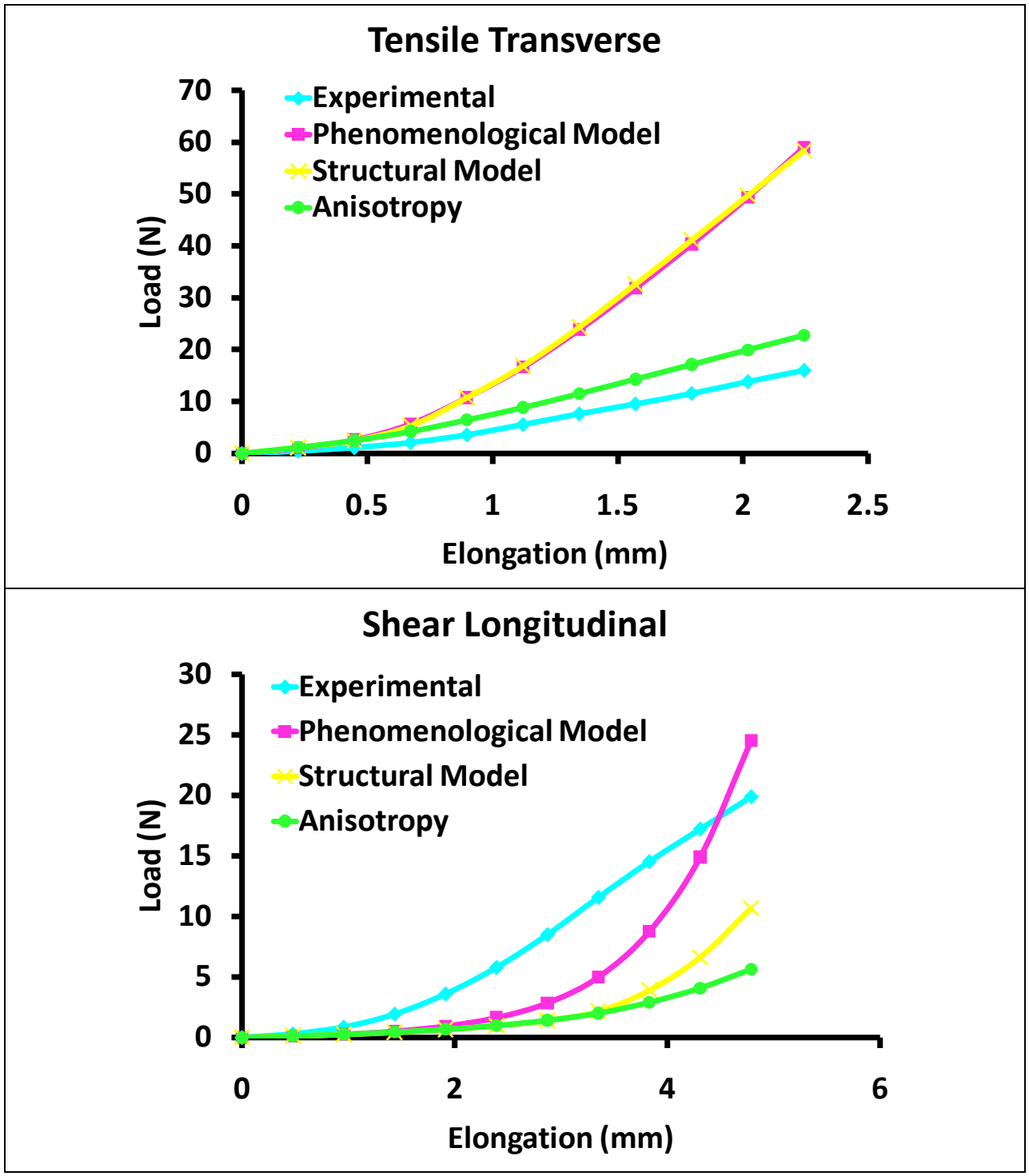

Figure 6.34 Load-elongation curves for Specimen 05-08024R showing the ability of the phenomenological model, structural model, and structural model with induced anisotropy to predict the tissue response in tension (top) and in shear (bottom).

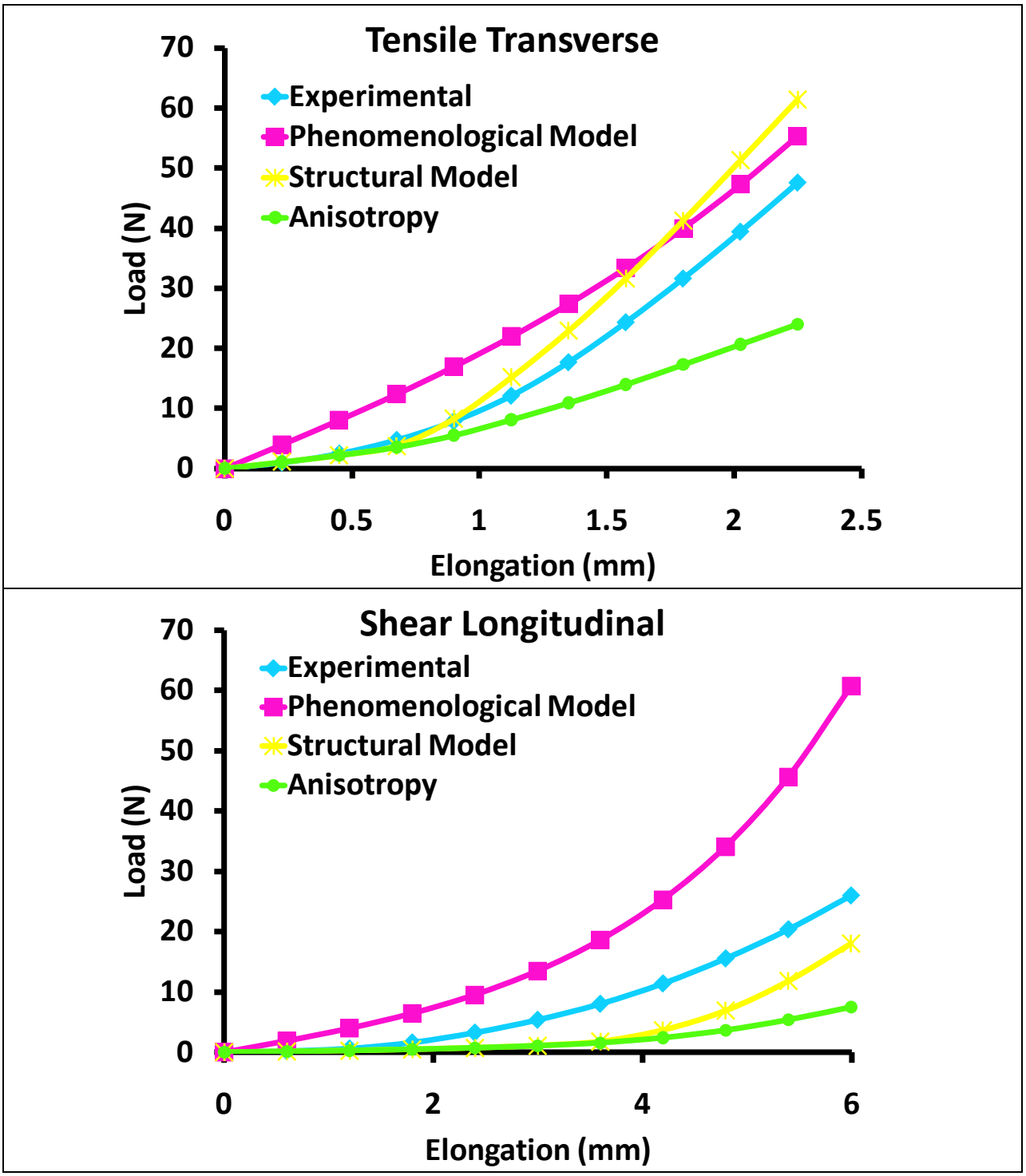

Figure 6.35 Load-elongation curves for Specimen 05-11001R showing the ability of the phenomenological model, structural model, and structural model with induced anisotropy to predict the tissue response in tension (top) and in shear (bottom).

6.2.5 Significance of Results

This section of the dissertation performed four preliminary analyses in order to suggest improvements to the structural constitutive model which could result in a better description of the complex capsule behavior. Using two loading conditions to determine the optimized material parameters for the ground substance and collagen fibers separately proved to be beneficial. Reducing the number of parameters optimized simultaneously cut down on computational time but the uniqueness of the parameters still needs to be determined. The ability of the structural model to predict tensile and shear elongations was unaltered by this spearation. Eliminating the linear region coefficient reducted the physical meaning behind the material coefficients and the predicted load-elongation curves no longer exhibited the distinct toe and linear region typical of biologic soft tissues. Describing the ground substance using a non-linear model was not successful and resulted in RMSE% values between the experimental and predicted load-elongation curves which were closer to those of the phenomenological model than the structural model. Finally, incorporating anisotropy into the structural constitutive model improved its predictive capability and reduced the average RMSE% values in tension and shear for the four representative tissue samples.

The results of this work suggest that the material parameters of the structural constitutive model should be optimized based on their individual contributions to the strain energy function. The ground substance coefficients should be determined separately from the fiber coefficients which will reduce the number of coefficients optimized simultaneously. As there are three fiber coefficients the uniqueness of these parameters should still be determined as described in Section 6.1.5. If parameter uniqueness is an issue, fitting the toe- and linear-regions separately to the tensile longitudinal load-elongation data may be beneficial as it would allow C_3 and C_4 to be

optimized separately from C_5. Another approach for determining unique material coefficients would be to design a new experimental loading condition which was capable of loading only the ground substance. This experiment could then be used to determine the ground substance coefficient(s). One advantage of using a structural constitutive model over a phenomenological model is that the material coefficients have direct physical meaning; however, this is only true if unique parameters are obtained. Therefore, if the structural model is to be used to further understand the material properties of the normal glenohumeral capsule and how they change when the capsule is injured, then unique parameters must be determined.

Introducing anisotropy improved the predictive capability of the structural model in tension and shear. This suggests that a structural model which incorporates the anisotropy of the glenohumeral capsule may be more appropriate than an isotropic model. Introducing a parameter to scale the degree of anisotropy throughout the tissue would be a reasonable first step. In two of the four specimens evaluated in this section of the work, introducing anisotropy decreased the ability of the model to predict the tissue response to tension and shear. These losses were much smaller than the gains in predictive ability of the other two tissue samples but still suggest that a tissue-specific fiber distribution may need to be utilized due to biologic variability. The degree of anisotropy is variable from sample to sample; therefore, depending on the desired accuracy of the constitutive model, the SALS device could be used to collect fiber alignment data in order to give tissue-specific fiber distributions to be incorporated into each finite element model. This would provide anisotropy in the the initial, unloaded configuration and would likely improve the ability of the model to describe capsule behavior.

Before a significant amount of time is spent trying to further improve the predictive capability of the structural model it should be implemented into the finite element models of the

glenohumeral joint in its present state. The purpose of developing a new constitutive model for the capsule was to validate the finite element models of the glenohumeral joint on an element-by-element basis so that the model could be used appropriately to predict local capsule behavior. For this application, parameter uniqueness is not an issue as no inferences will be made as to the properties of each tissue constituent. As the predictive capability of the structural model is significantly improved over the phenomenological model, which was initially used to validate the finite element models, localized validation may be possible with the structural model in its current state.

6.2.6 Limitations

Each of the modifications to the structural model were only evaluated on four tissue samples and other variations from the results found here may be present when more tissue samples are evaluated. Further, the manually induced anisotropy was based on the average ratio of longitudinal to transverse moduli previously reported for dog-boned tissue samples taken from the axillary pouch. [41] Tissue samples with a larger or smaller modulus ratio would result in increased or decreased predictive capability as was seen in the four tissue samples evaluated here. The degree of anisotropy in the square tissue samples used in the combined experimental and computational methodology of the current work may not be the same as more collagen fibers remain intact and contribute to the overall response to applied load. Further, the AB-IGHL has been shown to have slightly more aligned collagen fibers in localized regions compared to the axillary pouch which made lead to different degrees of anisotropy between regions. Therefore, the most appropriate constitutive model for the capsule would take into account the specific fiber distribution throughout the entire capsule.

6.2.7 Implications

The improved constitutive model for the glenohumeral capsule developed in this section of the dissertation has both modeling and clinical implications. The results of this work show that a structural model which accounts for the random fiber organization in the plane of the tissue is a significant improvement over an isotropic phenomenological constitutive model for the glenohumeral capsule. The structural model better describes and predicts the complex material behavior of the capsule and should be used in the future to improve the accuracy of finite element models of the glenohumeral joint. This work also demonstrated the large variability in the material properties and thus the level of difficulty associated with modeling biologic soft tissues. Average properties can be used to address macro-scale research questions but to truly understand the structure and mechanisms responsible for capsule behavior on a local level; tissue specific models must be generated. The most appropriate way to understand the material behavior of the glenohumeral capsule would be to build a population of tissue-specific models.

Previous aims in this dissertation found that changes in collagen fiber alignment were associated with tissue damage and suggested that injured capsule may contain a more anisotropic reference state than normal capsule. Differences in the material properties of the normal and injured capsule are likely due to these differences in collagen fiber alignment. In this aim, it was found that a structural model which accounts for the anisotropy of the normal capsule will improve the predictive capability even further. As the degree of anisotropy is the link between the normal and injured glenohumeral capsule, a structural model which includes a parameter describing the degree of anisotropy could be used to model permanent deformation of the capsule. This parameter could then be altered to increase the degree of anisotropy when the tissue stretch reaches a certain threshold. [202] A structural damage model for tendon has been

developed and employs similar concepts including a damage parameter, D, which ranges from 0 to 1 with an increasing damage effect. In this model, the Helmholtz free energy function, $\Psi(C,D)$, was expressed as a coupling of the stored energy function, W(C), and a fiber damage function, g(D). Where the damage function is based on the damage parameter, D, and the fiber stretch, λ, and only contributes to the free energy function when the fiber stretch has reached a certain threshold. A similar constitutive framework may be capable of modeling normal and injured capsular tissue and should be evaluated in the future.

Clinically, this work stresses the importance of the contributions of each constituent to the overall tissue response. In order to appropriately predict the mechanical properties of the capsule the response of both the ground substance and collagen fibers must be accounted for. As the structural model provided better predictions than the phenomenological model, and accounting for tissue anisotropy further improved model predictions, surgeons may need to be conscious of the collagen fibers and how their orientation changes following injury during repair procedures. Simple plication techniques which do not address changes in tissue anisotropy may not be restoring the normal material properties of the capsule.

6.3 EVALUATION OF THE AFFINE ASSUMPTION

6.3.1 Introduction

As previously discussed, validated finite element models of the glenohumeral capsule may be able to improve diagnostic and repair techniques; however, improving the accuracy of these models requires adequate constitutive models to describe the behavior of both normal and

injured capsular tissue. As the normal capsule can withstand loading in any direction, the collagen fibers in the anteroinferior capsule are globally randomly oriented despite localized areas of alignment. [3] Therefore, an isotropic hyperelastic phenomenological constitutive model was initially used to characterize the material properties of the normal glenohumeral capsule. [42, 124] This model was later found to poorly predict capsule behavior under shear loading, which may be more representative of the complex loading conditions experienced by the sheet-like ligament in vivo. Further, as shown in the previous section, a structural constitutive model consisting of an isotropic matrix embedded with randomly aligned collagen fibers proved to better predict the complex capsule behavior than the isotropic model [204] indicating that structural models accounting for fiber distributions may improve the accuracy of finite element models of the glenohumeral joint.

Structural models are based on specific tissue constituents thus understanding the collagen fiber kinematics is imperative for developing an appropriate constitutive model to describe capsule behavior. Specific Aim 1 of this dissertation demonstrated that the collagen fiber alignment in the glenohumeral capsule becomes more aligned under load with localized areas of high fiber alignment eventually leading to tissue failure. [139] These changes in the degree of anisotropy which exist following injury suggest that the same constitutive model may not be capable of describing the behavior of both normal and injured capsular tissue. However, a model that is capable of describing the collagen fiber kinematics of the glenohumeral capsule throughout the entire load-elongation curve would be ideal.

Many structural models make the affine assumption, i.e. that the local fiber kinematics follow the global tissue deformation. Conversely, an approach to account for non-affine fiber kinematics in structural models has been recently developed [128] as evidence for non-affine

fiber kinematics have been observed in other biologic tissues such as bovine pericardium and porcine aortic heart valves [164], small intestine submucosa (SIS) [125], human annulus fibrosus [142], porcine skin [205], and most recently human supraspinatus tendon [190]. Determining whether the affine assumption can be applied to the collagen fiber kinematics of the glenohumeral capsule would aid in the development of an adequate structural constitutive model to be used in finite element models of the glenohumeral joint. Therefore, the objective of this section of the work was to evaluate the affine assumption of fiber kinematics in the normal and injured anteroinferior glenohumeral capsule by comparing experimentally measured preferred fiber directions to the affine-predicted fiber directions.

6.3.2 Methods

The same experimental protocol used for Specific Aim 1 (Section 3.2) was used in this section of the work and is briefly described here.

6.3.2.1 Specimen Preparation

Five fresh-frozen cadaveric shoulders (70 ± 5 yrs, 3 females, 3 males) were stored at -20°C and thawed for 24 hours at room temperature prior to testing. The protocol was approved by the University of Pittsburgh Committee for Oversight of Research Involving the Dead (CORID no. 131). The shoulders were dissected down to the scapula, humerus, and glenohumeral capsule. Each joint was examined using radiographs and dissection, and determined to be free of pathology, osteoarthritis and any visible signs of injury. The inferior glenohumeral ligament complex was identified by determining the margins of the AB-IGHL and PB-IGHL, whose locations were determined by applying distraction and external or internal rotation, respectively,

to the joint. These positions were chosen as they are the positions in which the bands are most visible. [166] A 20 x 10 mm section was excised from the AB-IGHL and axillary pouch, embedded in OCT compound, and frozen with liquid nitrogen. [3] Each sample was then sliced into 400 μm thick sections using a cryostat (MICROM, Model #: HM 505 E). This thickness was chosen as it was thin enough for accurate data collection in the small angle light scattering (SALS) device [46, 156] while still maintaining as many intact collagen fibers as possible.

6.3.2.2 Elongation Protocol

Small angle light scattering has been used extensively in the past to investigate the collagen fiber organization in biologic soft tissues and detailed descriptions have been reported. [3, 46, 152-163] Briefly, a 4 mW continuous unpolarized laser (λ = 632.8 nm) was passed through each tissue sample with a spatial resolution of 250 μm and the resulting angular distribution of the scattered light pattern was examined. The local preferred fiber direction can be determined from the scattered light pattern as it represents the distribution of fiber angles within the light beam at any given point on the tissue sample. Based on preliminary analyses, for this experimental set-up, the SALS device is capable of determining the local preferred fiber direction with a repeatability of ±2°.

One 400 μm slice was taken from each region of the anteroinferior capsule and placed in custom soft tissue clamps. A 3 x 4 grid of graphite strain markers was attached to the surface of each sample using cyanoacrylate for strain tracking. Each sample was then elongated in the longitudinal direction using a materials testing machine (Thumler, Model #TH2730) with load cell (Interface, Scottsdale, AZ, Model #SM-1000N, range: 0 – 1000 N, resolution: 0.015 N) until a 0.1 N preload was achieved. The tissue width and clamp-to-clamp distance were then

measured using a ruler. The clamp-tissue sample-clamp complex was mounted in a custom stretching chamber designed to integrate with the small angle light scattering (SALS) device. [46, 156] As a load cell is not currently incorporated into the SALS device, the preload was re-established in the stretching chamber by restoring the clamp-to-clamp distance. Once the tissue was preloaded, the positions of the strain markers were captured and served as the reference state (ε_0) for Lagrangian strain calculations. Tissue samples were kept hydrated using physiologic saline solution throughout the entire testing protocol. Each tissue sample was elongated in increments of 5% of the clamp-to-clamp distance at preload and the strain markers positions and the collagen fiber alignment data were collected using the SALS device following each increment. This process was repeated until visible tissue failure (hole) occurred.

The graphite strain markers were used to divide the midsubstance of each tissue sample into six elements: two elements across the width and three elements along the length. Each element was approximately 3 x 4 mm. The experimental and affine-predicted fiber kinematics were compared within each of the six elements for all tissue samples from the AB-IGHL and axillary pouch. (Figure 3.13) The fiber direction ranged from -90° to 90° where 0° was parallel to the axis of loading. (Figure 3.15) The preferred fiber direction was evaluated in two deformed states: 10% of the clamp-to-clamp distance (ε_l) and 5% increment of elongation just prior to failure (ε_d). These deformed points were chosen to represent the fiber distribution in the early linear-region and the plastic region of the load-elongation curve in order to determine the ability of the affine model to predict the fiber distribution of normal (ε_l) and injured (ε_d) capsular tissue.

The comparison of experimental and affine-predicted fiber kinematics is similar to an analysis reported previously. [190] Histograms at each state ε_0, ε_l, and ε_d and the circular variance (VAR) in the reference state (ε_0) were computed for each of the six elements in each

tissue sample. The deformation gradient tensor, F, was computed from the strain marker positions, using a four node finite element technique [206], for the normal (ε_l) and injured (ε_d) tissue. Using the assumption of affine fiber kinematics **(**Equation 11), the preferred fiber directions of each element in the preloaded state (ε_0) were used to compute the distribution of fiber directions in the deformed states for the normal (ε_l) and injured (ε_d) anteroinferior capsule.

$$\theta_p = \tan^{-1}\left[\frac{F_{22}\sin\theta + F_{21}\cos\theta}{F_{11}\cos\theta + F_{12}\sin\theta}\right] \tag{11}$$

Where θ is the experimentally measured preferred fiber direction in the reference state (ε_0), θ_p is the affine-predicted preferred fiber direction in the deformed state (ε_l, and ε_d), and F_{11}, F_{12}, F_{21}, and F_{22} are the components of the 2D deformation gradient computed from the position of the strain makers in the reference (ε_0) and deformed states (ε_l, and ε_d).

6.3.2.3 Data Analysis

The experimentally measured preferred fiber direction distributions in the normal (ε_l) and injured (ε_d) capsule were compared to those predicted by the affine assumption using projection plots. [189] Projection plots are a method for comparing two distributions and allow for thorough evaluation of differences between the distributions with regard to location, shape and spread. The experimental and predicted preferred fiber direction values were grouped into 100 quantiles (1% increments) and projection plots were created by plotting the difference in quantile values (experimental – predicted) vs. the average quantile values (at each increment). If both distributions are identical, all of the data will fall along the x-axis. In order to evaluate the agreement between the experimental and predicted preferred fiber directions the mean and range of the quantile differences were computed. The range was defined as the maximum – minimum

quantile difference where the larger the range value, the poorer the agreement between the experimental and affine-predicted distributions.

Mean and range values were computed for all six elements in each normal (ε_l) and injured (ε_d) tissue sample and were non-normally distributed. Comparisons of the mean quantile difference, range, and VAR values were made between the AB-IGHL and axillary pouch using Mann-Whitney tests. In addition, Spearman rank correlation coefficients were computed between the mean quantile difference, range, and VAR values for each capsule region. In order to compare the ability of the affine model to predict the fiber distributions of normal (ε_l) and injured (ε_d) capsular tissue, Wilcoxon signed rank tests were used to compare the mean quantile difference and range in the normal and injured tissue of each capsule region. Significance was set at $\alpha = 0.05$ for all comparisons.

6.3.3 Results

The ability of the affine model to predict the fiber distributions in the normal and injured capsule varied between elements and tissue samples. Differences between the experimental and affine-predicted fiber direction distributions were evident from the histograms and corresponding projection plots for both capsule regions. On the projection plots, the fiber distribution data was nonlinear in most elements and the mean quantile difference and range values varied from element to element. Overall, the affine model provided poor predictions of the fiber distributions in the normal and injured anteroinferior capsule.

6.3.3.1 Affine-Prediction for Normal Capsule

The ability of the affine model to predict the fiber distributions in the deformed state varied between elements and tissue samples. Disagreement between the experimental and affine-predicted fiber direction distributions occurred in both the AB-IGHL and axillary pouch at 10% elongation. Differences between the experimental and affine-predicted fiber direction distributions were evident from the histograms and corresponding projection plots for both regions of the anteroinferior capsule. The histograms and projection plots for each element of one tissue sample from the AB-IGHL and one from the axillary pouch of the same shoulder are shown below. The remaining tissue samples are shown in Appendix K.

Table 6.10 Preferred fiber direction histogram and corresponding projection plot comparing the experimental and affine-predicted fiber distribution in the normal AB-IGHL for Specimen 07-10874L.

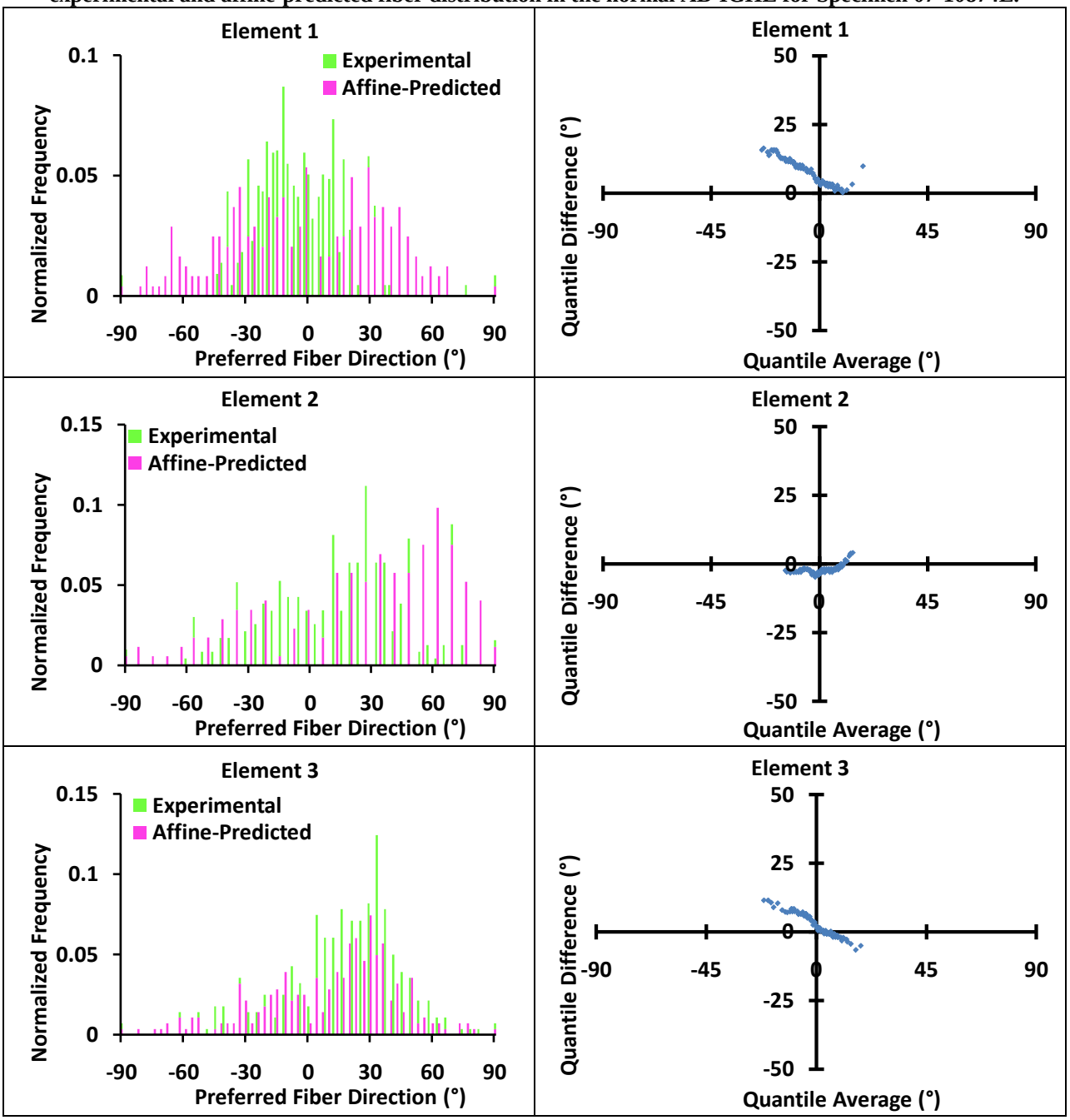

Table 6.10 (Continued).

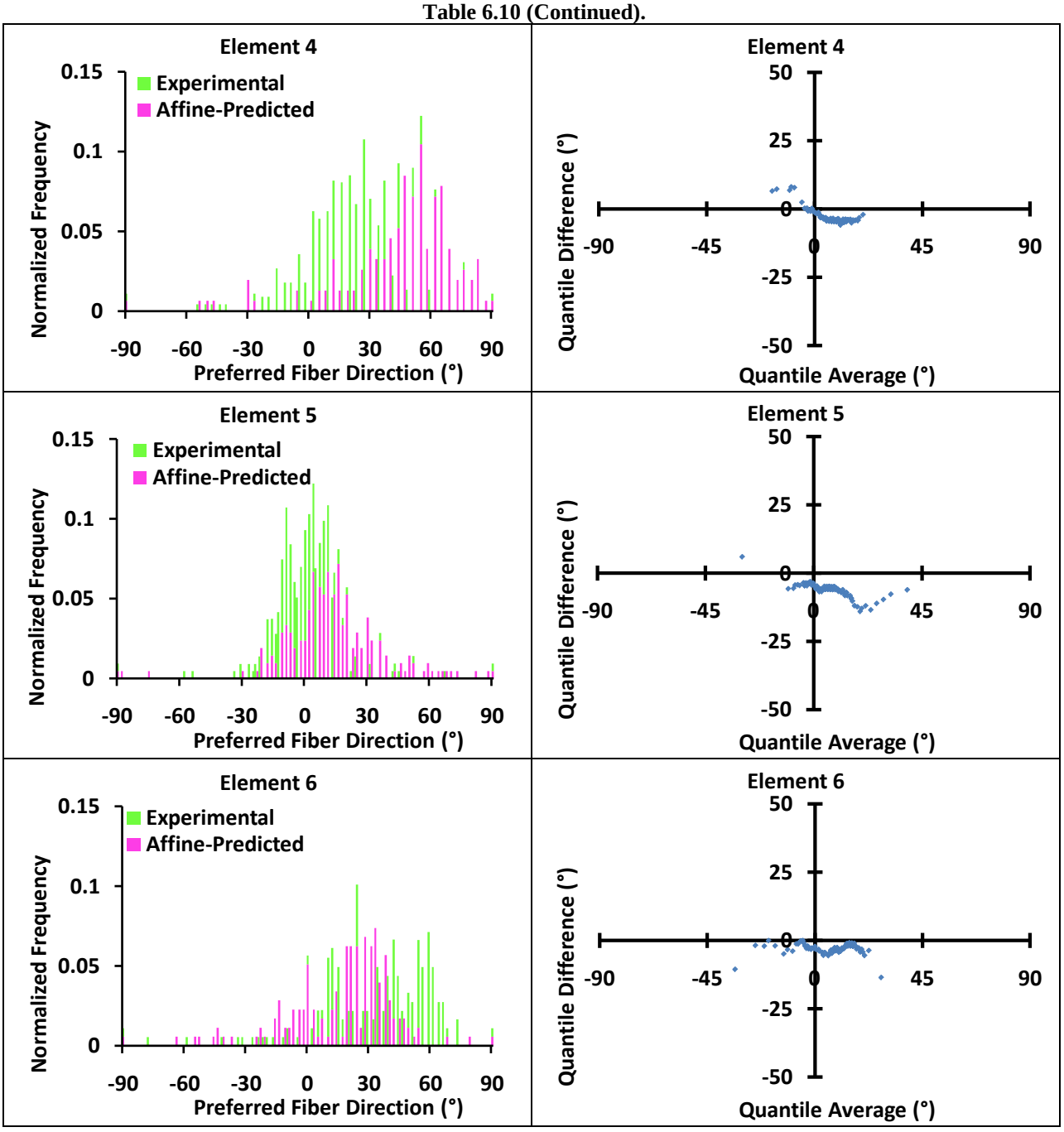

Table 6.11 Preferred fiber direction histogram and corresponding projection plot comparing the experimental and affine-predicted fiber distribution in the normal axillary pouch for Specimen 07-10874L.

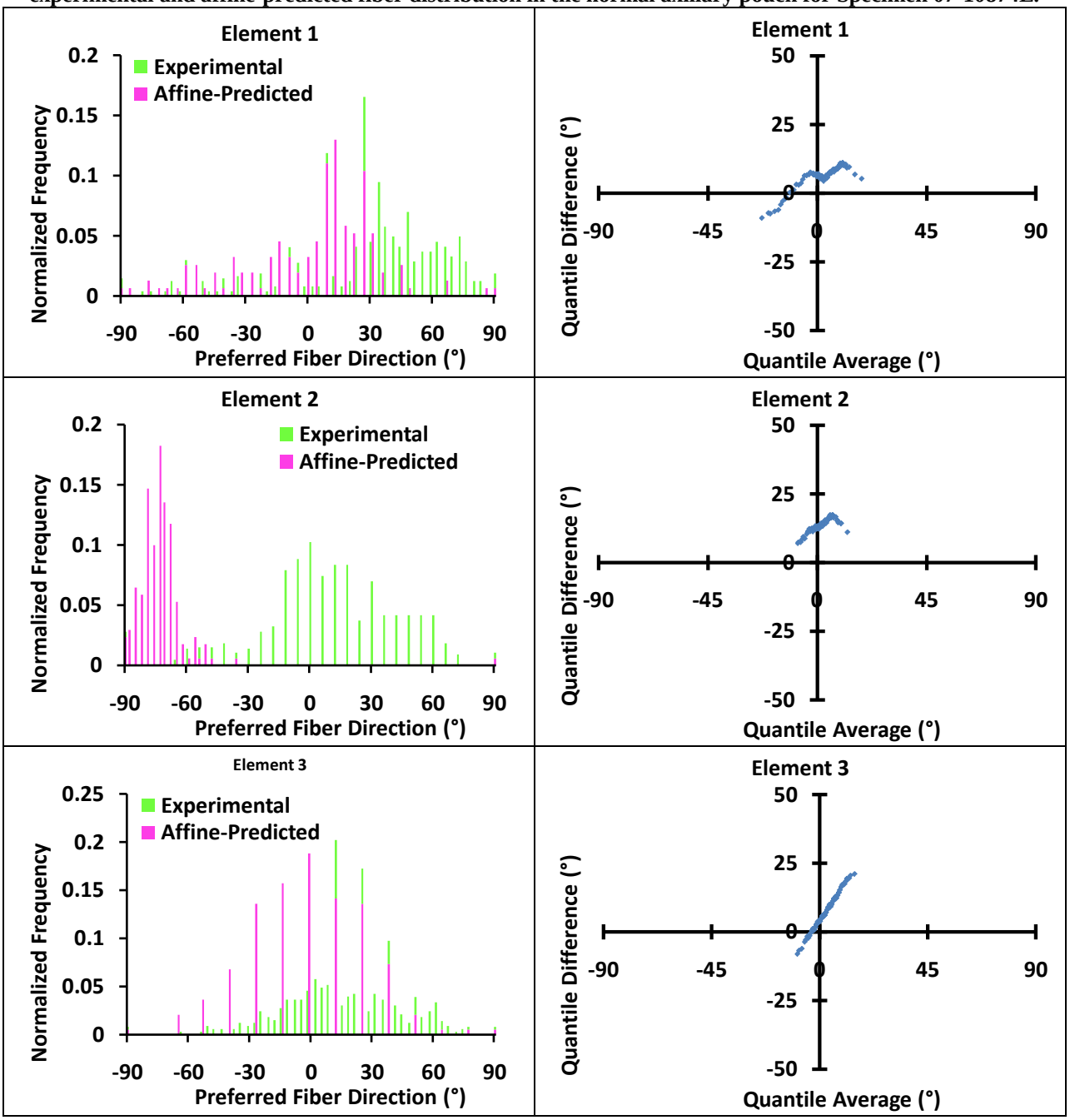

Table 6.11 (Continued).

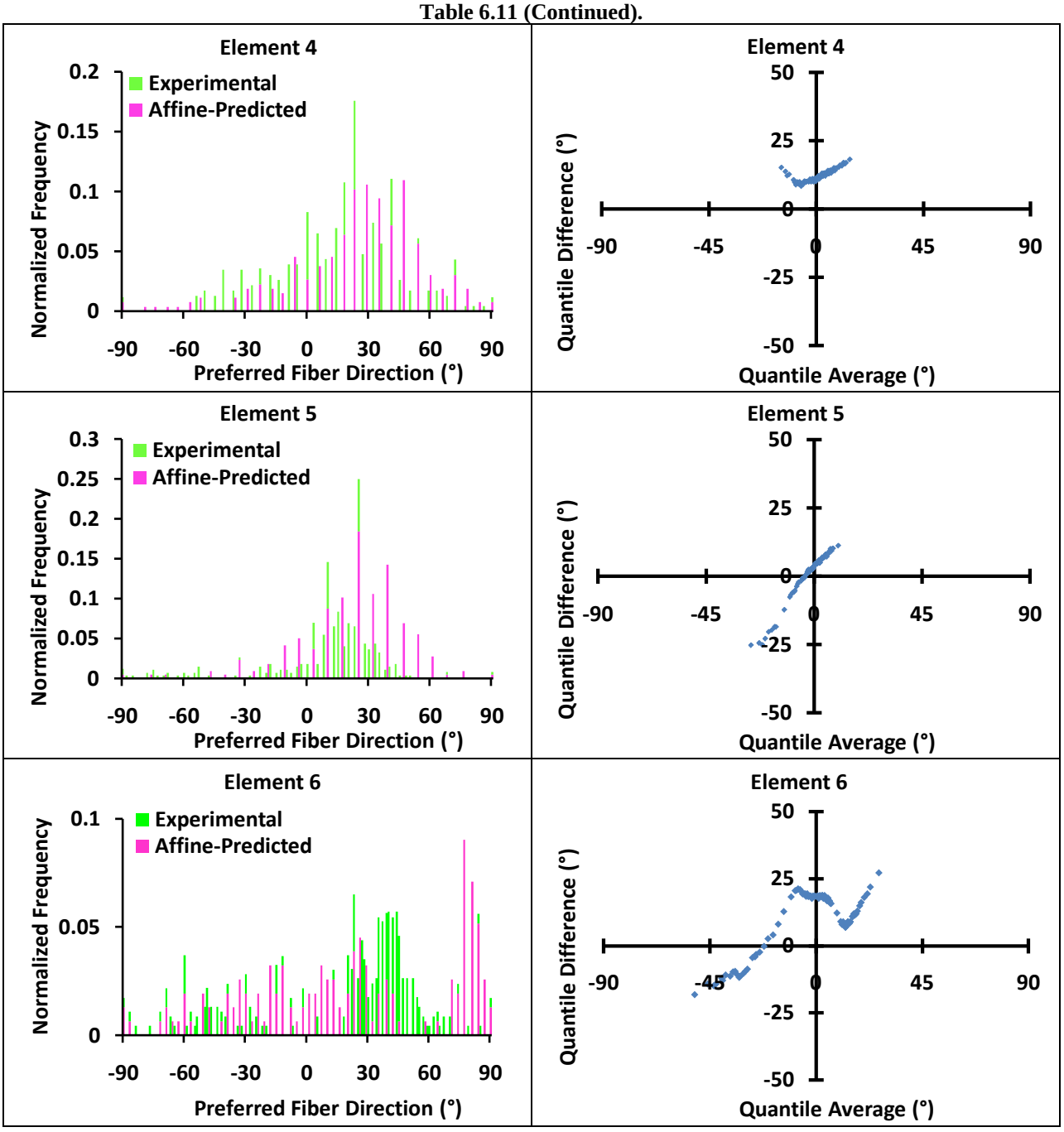

Differences in the mean quantile difference were close to significance ($p = 0.06$) between the normal AB-IGHL (1.6° ± 6.3°) and axillary pouch (4.8° ± 6.8°). The mean quantile difference was 67% lower in the AB-IGHL compared to the axillary pouch. Although the range and VAR values were larger in the axillary pouch (31.5° ± 26.2°, 0.42 ± 0.24) compared to the AB-IGHL

(28.7° ± 23.4°, 0.38 ± 0.24), these differences were not statistically significant. In the AB-IGHL, the Spearman's correlation between the mean quantile difference and circular variance was close to significance ($p = 0.07$). No significant correlations were found in the axillary pouch.

6.3.3.2 Affine Prediction for Injured Capsule

The ability of the affine model to predict the fiber distributions in the deformed state varied between elements and tissue samples. Disagreement also occurred between the experimental and affine-predicted fiber direction distributions in the injured AB-IGHL and axillary pouch at the 5% elongation just prior to failure. Differences between the experimental and affine-predicted preferred fiber direction distributions were evident from the histograms and corresponding projection plots for both regions of the anteroinferior capsule. The histograms and projection plots for one tissue sample from the AB-IGHL and one from the axillary pouch of the same shoulder are shown below. The remaining histograms and projection plots are shown in Appendix L.

Table 6.12 Preferred fiber direction histogram and corresponding projection plot comparing the experimental and affine-predicted fiber distribution in the injured AB-IGHL for Specimen 07-10874L.

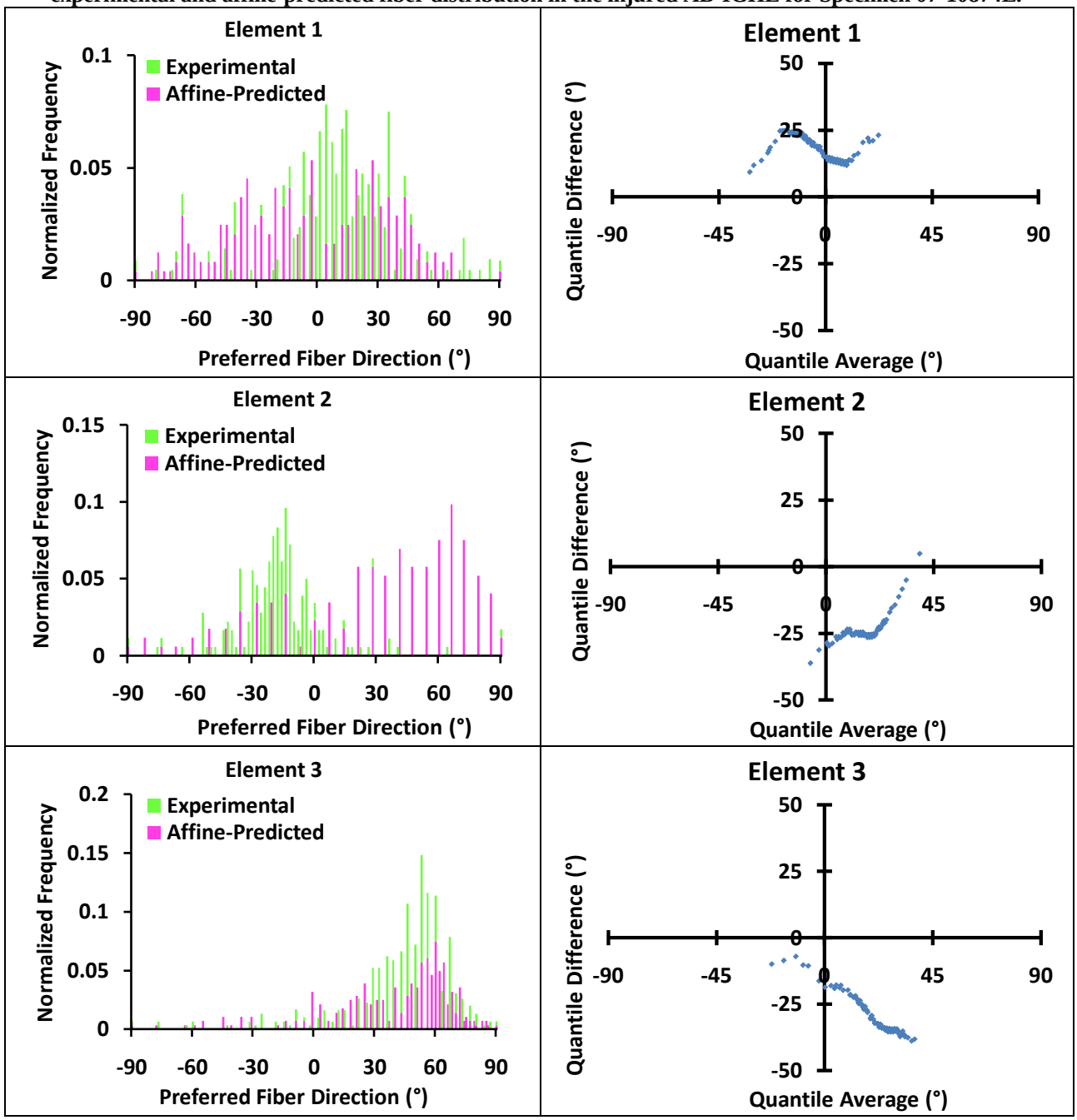

Table 6.12 (Continued).

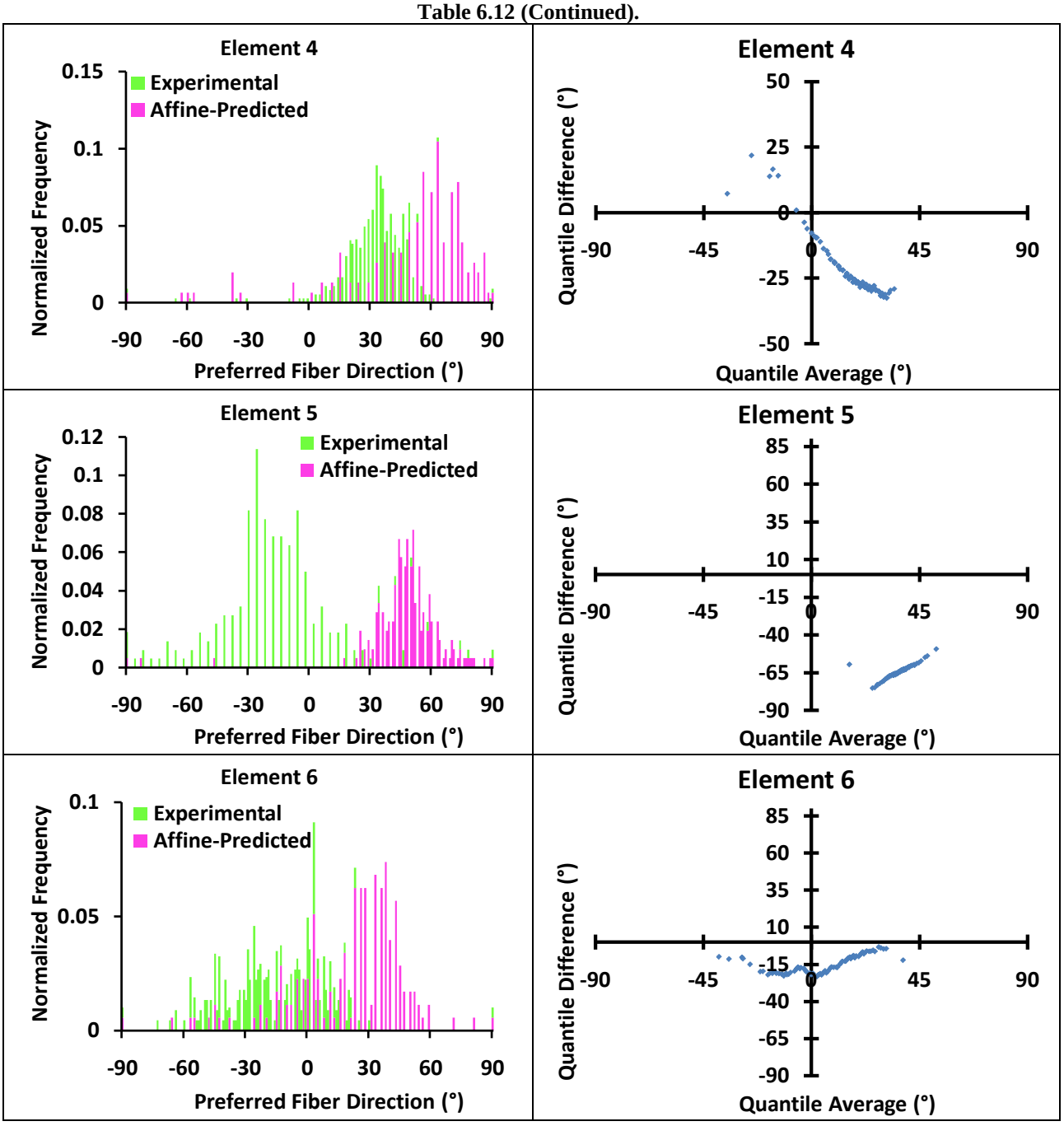

Table 6.13 Preferred fiber direction histogram and corresponding projection plot comparing the experimental and affine-predicted fiber distribution in the injured axillary pouch for Specimen 07-10874L.

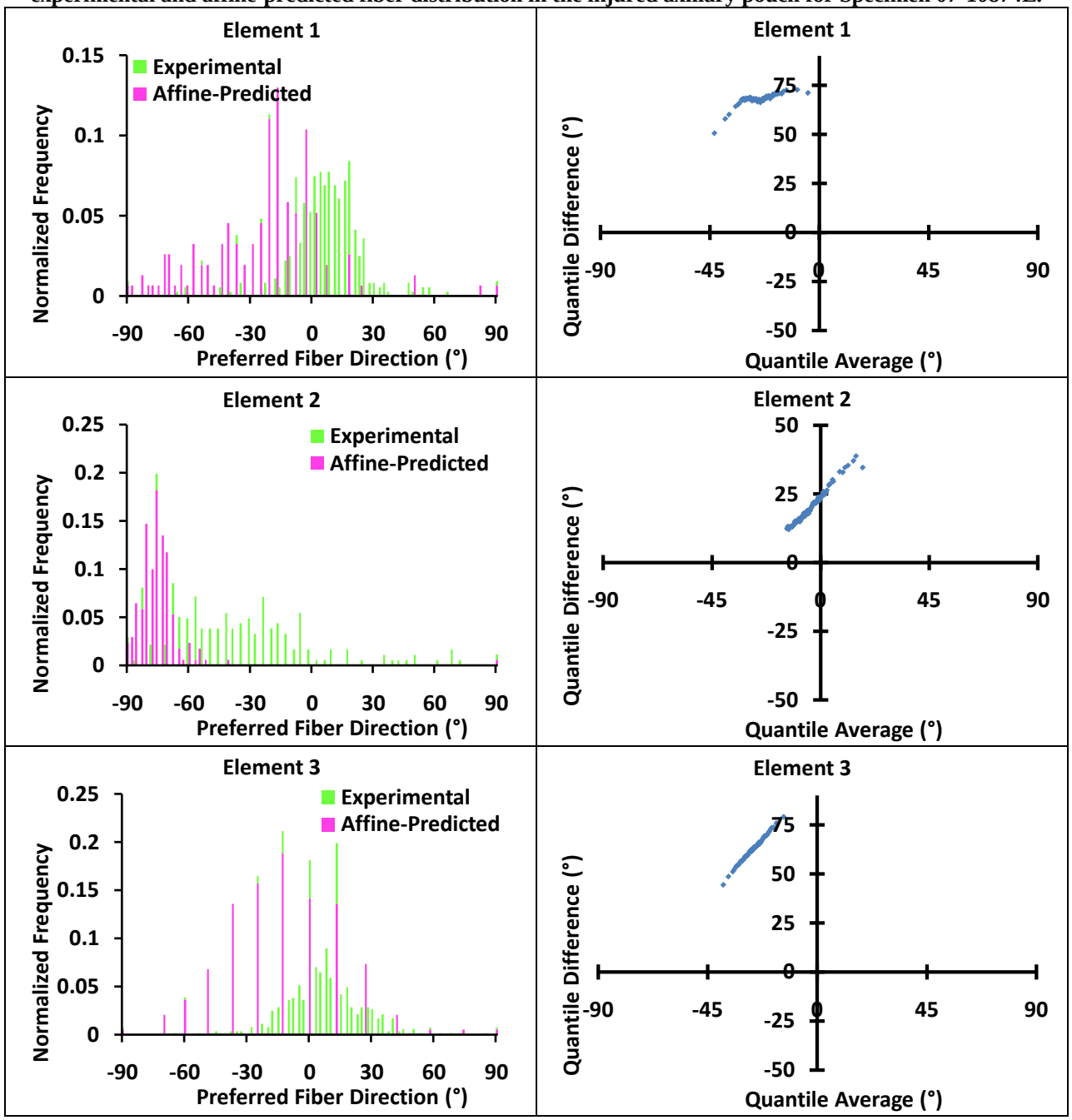

Table 6.13 (Continued).

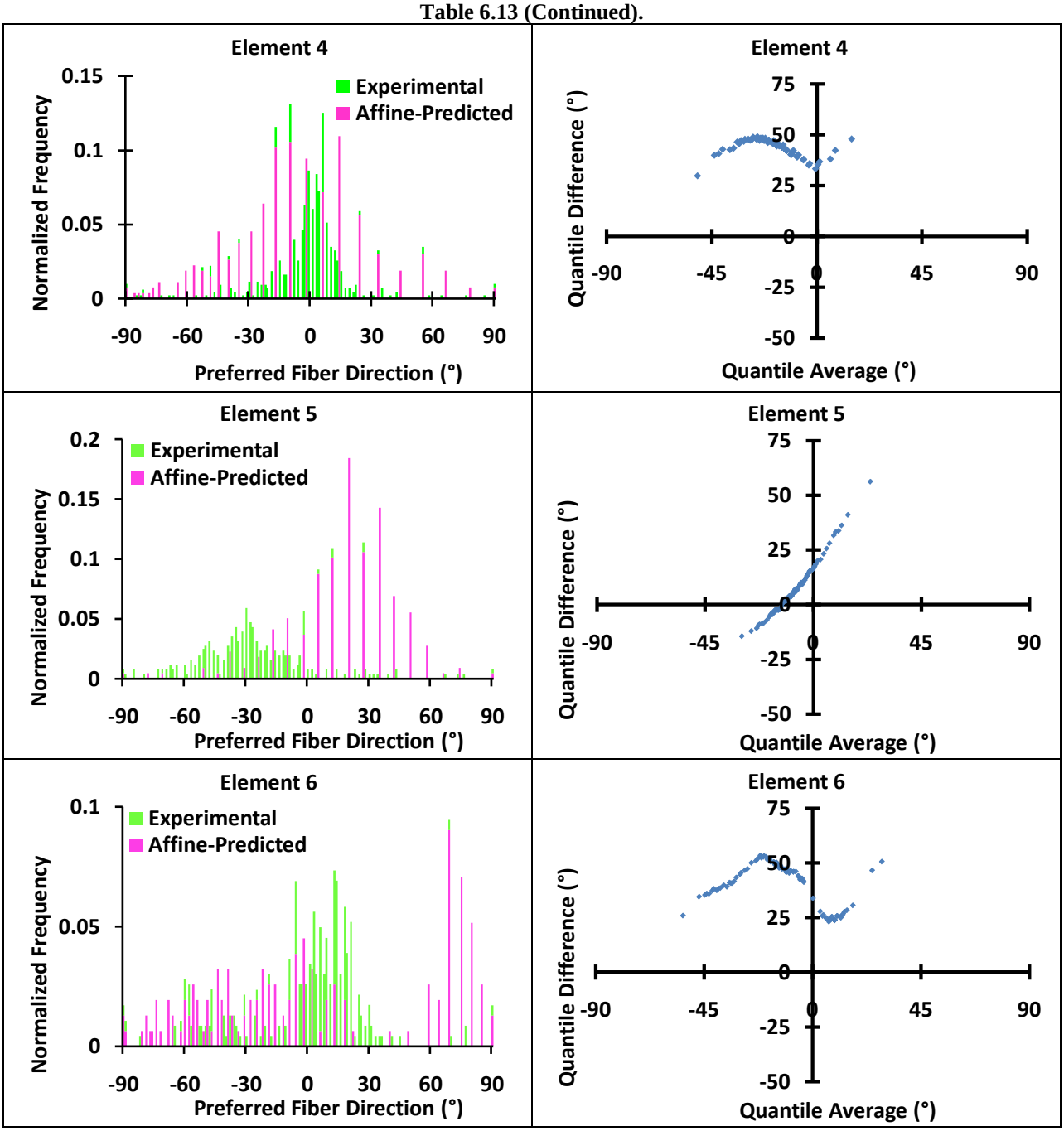

Results for the injured anteroinferior capsule exhibited the same patterns as the normal capsule. A significant difference in the mean quantile difference ($p = 0.02$) was found between the injured AB-IGHL (-1.0° ± 21.2°) and axillary pouch (14.9° ± 21.4°). The mean quantile difference was 93% lower in the AB-IGHL compared to the axillary pouch. No significant differences were

found in the range values between the AB-IGHL (46.0° ± 29.2°) and axillary pouch (49.6° ± 35.9°). No significant correlations were found between the mean or range and the VAR values either capsular region.

The affine model provided better predictions for the fiber distributions in the normal compared to the injured anteroinferior capsule. The mean quantile difference, range values and nonlinearity of the data on the projection plots were larger in the injured tissue. In the axillary pouch, the mean quantile difference ($p = 0.02$) and range values ($p < 0.001$) were significantly larger in the injured (14.9° ± 21.4°, 49.6° ± 35.9°) when compared to the normal (4.8° ± 6.8°, 31.5° ± 26.2°) tissue. The range was also significantly larger ($p < 0.001$) in the injured (45.9° ± 29.2°) compared to the normal (28.7° ± 23.4°) AB-IGHL, however, no differences were found between the mean quantile difference ($p = 0.53$).

Table 6.14 Mean quantile difference in the normal and injured AB-IGHL for each tissue sample.

	Specimen 1		Specimen 2		Specimen 3		Specimen 4		Specimen 5	
Element	**Normal**	**Injured**	**Normal**	**Injured**	**Normal**	**Injured**	**Normal**	**Injured**	**Normal**	**Injured**
1	7.8	18.2	-5.9	-11.0	7.0	19.7	17.6	-2.7	10.4	9.9
2	-2.0	-24.2	-0.8	-1.4	-1.3	-15.0	12.2	3.9	1.1	4.4
3	2.1	-29.5	-4.8	-5.4	10.7	48.7	-4.6	17.6	3.3	8.4
4	-3.1	-22.4	2.9	9.8	-7.0	-20.0	10.1	12.2	-1.3	-0.6
5	-6.2	-64.6	0.9	0.5	4.6	39.3	-1.9	-4.6	3.5	0.4
6	-3.0	-15.3	-0.1	6.6	-4.1	-19.2	5.6	10.1	-6.1	-2.8

Table 6.15 Mean quantile difference in the normal and injured axillary pouch for each tissue sample.

	Specimen 1		Specimen 2		Specimen 3		Specimen 4		Specimen 5	
Element	**Normal**	**Injured**	**Normal**	**Injured**	**Normal**	**Injured**	**Normal**	**Injured**	**Normal**	**Injured**
1	6.1	68.0	2.3	25.4	-2.0	-5.0	13.4	25.7	4.6	28.0
2	13.3	20.6	10.0	-2.9	5.5	38.6	3.9	-4.4	10.5	6.5
3	7.8	62.5	-0.6	13.6	-0.3	-7.5	16.2	41.1	3.9	-13.1
4	12.2	43.9	0.1	-3.3	1.8	8.5	1.1	9.1	5.2	-1.1
5	1.5	7.2	-2.5	-14.7	1.5	-4.3	23.7	15.2	-4.4	-4.8
6	9.9	39.7	-6.6	21.3	1.9	5.6	8.1	22.4	-5.2	3.7

Table 6.16 Range values in the normal and injured AB-IGHL for each tissue sample.

	Specimen 1		Specimen 2		Specimen 3		Specimen 4		Specimen 5	
Element	**Normal**	**Injured**	**Normal**	**Injured**	**Normal**	**Injured**	**Normal**	**Injured**	**Normal**	**Injured**
1	16.0	15.6	55.7	84.5	57.5	76.2	21.3	43.2	41.8	83.6
2	8.9	41.1	39.4	61.0	90.8	116.2	32.8	35.0	19.6	45.3
3	18.0	31.7	13.8	30.1	9.2	30.3	8.7	21.3	16.5	81.3
4	13.8	54.4	27.9	58.9	78.0	73.2	33.2	32.8	26.6	23.9
5	20.0	25.7	44.6	51.6	12.0	10.9	10.0	8.7	14.0	32.6
6	13.6	20.3	84.1	115.2	7.3	7.8	18.5	33.2	6.8	32.1

Table 6.17 Range values in the normal and injured axillary pouch for each tissue sample.

	Specimen 1		Specimen 2		Specimen 3		Specimen 4		Specimen 5	
Element	**Normal**	**Injured**	**Normal**	**Injured**	**Normal**	**Injured**	**Normal**	**Injured**	**Normal**	**Injured**
1	20.1	21.9	9.7	7.5	53.8	75.6	40.3	56.5	104.3	97.5
2	10.4	26.7	17.7	20.3	19.3	62.9	27.7	55.9	55.7	72.9
3	29.0	34.6	8.6	36.7	9.2	12.3	27.6	68.8	113.5	114.2
4	9.8	19.2	8.4	30.3	4.6	11.5	23.5	30.6	34.6	126.9
5	36.4	70.6	20.4	18.1	6.1	6.9	47.5	50.6	44.5	122.1
6	45.4	30.4	43.2	22.0	9.5	9.4	45.6	81.7	18.1	93.4

6.3.4 Significance of Results

This study evaluated the affine assumption for fiber kinematics in the normal and injured anteroinferior glenohumeral capsule. Experimental fiber direction distributions were compared to those predicted by the affine model using projection plots at points in the linear region and plastic region of the load-elongation curve. If two distributions are identical the data on the projection plot will fall along the line $y = 0$. Any differences in the distributions will be manifested as y-axis offsets, non-zero slopes or non-linear data. [189] Values of the mean or range of the quantile differences which define an acceptable cutoff for the affine assumption have not been established. However, the larger the mean or range value, the less accurate the affine assumption. Based on the large range values and the non-linear data, the affine model provides poor predictions of the fiber kinematics in the anteroinferior capsule which become increasingly worse as the tissue is elongated into the plastic region of the load-elongation curve.

6.3.4.1 Discussion of Results and Comparison to Literature

Poor affine-predictions have also been shown in porcine small intestine submucosa under large uniaxial strains, particularly when elongated perpendicular to the axis of predominant fiber orientation. [125] In addition, Lake and coworkers reported larger range values in the normal supraspinatus tendon when it was elongated in the transverse compared to the longitudinal direction. [190] They hypothesized that this was due the inability of the collagen fibers to rotate sufficiently in the extracellular matrix under loading in the direction perpendicular to the predominant fiber direction. This concept is supported by the current work. As the unloaded glenohumeral capsule does not have a preferred fiber orientation, loading in any direction requires substantial fiber rotation to support tensile load. In addition, the collagen fiber cross-links or fiber-fiber interactions may hinder fiber rotation. This likely leads to local fiber kinematics which are different from the global tissue deformation as indicated by differences between the experimental and affine-predicted fiber distributions.

The affine model assumes that each fiber acts independently and that there are no other interactions within the tissue during loading. The poor affine model predictions of the fiber kinematics suggest that the collagen fibers in the glenohumeral capsule do not act independently but rather there are other interactions as the collagen fibers uncrimp, rotate, and stretch. These interactions could be between collagen fibers, collagen cross-links or between the fibers and the ground substance. These results demonstrate that many factors influence the complex material behavior of the glenohumeral capsule.

The circular variance of the preferred fiber direction in the reference state (VAR) was larger in the axillary pouch indicating that the fiber direction distribution was less tightly centered on the mean when compared to the AB-IGHL. This is consistent with the literature

which suggests that the AB-IGHL contains areas of local fiber alignment within the globally randomly aligned tissue. [3] As a result, the affine prediction may be slightly better in the AB-IGHL as indicated by the lower means. Further, correlations between the circular variance of the initial fiber distribution and mean values were close to significance in the AB-IGHL but not in the axillary pouch. Therefore, the relationship between the initial fiber alignment and the ability of the affine model to predict fiber kinematics is stronger in the AB-IGHL than the axillary pouch, which again may be due to the AB-IGHL having slightly more aligned collagen fibers than the axillary pouch. Fiber distributions which were initially more aligned were better predicted by the affine model than less aligned distributions in the supraspinatus tendon as well. [190]

The affine model provided better predictions for the normal than it did for the injured anteroinferior capsule as indicated by the larger mean quantile difference and range values. As the tissue samples are loaded into the plastic region of the load-elongation curve permanent damage occurs. Change in mean fiber rotation has been used to predict damage in the cervical capsular ligament [127] suggesting that individual collagen fibers break and undergo sudden large rotations when partial tissue failure occurs. Once damage ensues, the local fiber kinematics are much different than the global tissue deformation as exhibited by the poor agreement between the experimental and affine-predicted fiber kinematics in the injured anteroinferior capsule. The poor model predictions demonstrate that even more interactions between the collagen fibers, collagen cross-links, and ground substance are occurring as the tissue becomes damaged and a simple model which assumes the fibers act independently is not sufficient.

The structural variability of biologic tissues, particularly human tissue, makes modeling their behavior extremely difficult. One model may describe a tissue sample from one specimen

very well and another very poorly even though they are from the same biologic structure. In the current work, the affine model provided reasonable predictions for a few tissue samples and extremely poor predictions for others, with the majority of samples somewhere in between. As there are no cut and dry definitions of what constitutes an acceptable prediction for the affine model, its use should be evaluated based on the research question being addressed and the predictive ability desired. When modeling the glenohumeral capsule a structural model which accounts for non-affine fiber kinematics may provide a more accurate description of the tissue response than one that makes the affine assumption.

6.3.5 Limitations

Due to capsule thickness, tissue slicing was required for accurate use of the SALS device. However, most collagen fibers remained intact and changes in alignment with elongation were detected. In vivo, the capsule functions as a continuous sheet of tissue rather than discrete uniaxial ligaments and therefore experiences more complex loading conditions than applied to the tissue samples in this study.

6.3.6 Implications

The affine model provided poor predictions of the fiber kinematics in the anteroinferior glenohumeral capsule under uniaxial extension. These results demonstrate that many factors influence the complex material behavior of the glenohumeral capsule making computational modeling of this tissue extermemly difficult. A structural constitutive model which accounts for

non-affine fiber kinematics could improve the accuracy of finite element models of the glenohumeral joint and should be investigated.

7.0 DISCUSSION

7.1 IMPLICATIONS OF FINDINGS

7.1.1 Engineering

The data presented in this dissertation are extremely relevant to the field of engineering and orthopaedic biomechanics. This work clearly demonstrates that anterior glenohumeral dislocation causes permanent deformation of the anteroinferior capsule. This injury can be characterized by changes in collagen fiber alignment and material properties and results in a loss of joint stability provided by the glenohumeral capsule.

The experimental model to dislocate the glenohumeral joint developed in this work has numerous experimental implications. This novel model applied an excessive force in the anterior direction using robotic technology and the joint was allowed to translate freely in all three directions as it would in vivo. As a result permanent deformation of the glenohumeral capsule was successfully achieved as evidenced by the presence of nonrecoverable strain in the anteroinferior capsule and a significant decrease in the in situ force in the capsule during intact kinematics collected in response to three simulated clinical exams. In addition, significant an increase in anterior translation, but no change in posterior translation, was observed during three simulated clinical exams. Therefore, this experimental dislocation model successfully simulates

a glenohumeral joint suffering from anterior instability. This model can be used in future experiments to simulate the state of the glenohumeral joint following anterior dislocation when evaluating other joint pathologies such as Hill-Sachs lesions. This model can also be used to assess the efficacy of various repair techniques. For example, the ability of capsular plication procedures to restore joint kinematics and glenohumeral contact forces could be evaluated.

Previous work has reported the in situ force in the discrete capsule regions [27]; however, this work presents the first data of in situ forces in the entire glenohumeral capsule during simulated clinical exams and during dislocation. Recent studies have shown that the glenohumeral capsule should be evaluated as a continuous sheet of tissue and thus the in situ forces reported here are more appropriate. [9, 69, 136] These values can be used as a basis for comparison when evaluating the efficacy of various capsular repair techniques and pull-out strength of bone fixations during Bankart repairs.

The data presented in this work also have implications with regards to modeling the glenohumeral capsule and other biologic soft tissues. When describing the material behavior of the glenohumeral capsule a structural constitutive model should be used. A model which accounts for the fiber organization in the plane of the tissue will significantly improve the strain distribution predicted in finite element models of the glenohumeral joint compared to the currently used isotropic phenomenological model. As a result these finite element models can be used to predict capsule behavior on a local level. The structural model developed in this work is capable of predicting capsule behavior in tension and shear with a root-mean-squared error of 40%. However, preliminary analyses have suggested that incorporating the anisotropy of the glenohumeral capsule into the structural model may further improve its predictive capability. Finite element models with tissue-specific fiber distributions will provide the most accurate

description of capsule behavior. Further, the material parameters of this structural model can be used to gain additional insight into the material behavior of the capsule and used as a basis of comparison when modeling other biologic soft tissues with dispersed fiber organization.

The structural organization of the normal and injured glenohumeral capsule are different; increases in collagen fiber alignment and stiffness associated with injury suggest that the injured capsule is more anisotropic. As a result of the structural re-organization during permanent deformation, the material properties of the tissue are altered. Therefore the structural constitutive model developed in this work serves as a first step toward the development of a damage model for the glenohumeral capsule which could be implemented into finite element models to simulate glenohumeral dislocation.

This dissertation also presented further evidence of non-affine fiber kinematics in biologic soft tissues which warrants the development of constitutive models which do not make the affine assumption to describe biologic tissues. A structural model which accounts for the non-affine fiber kinematics may also be able to improve finite element models of the glenohumeral joint.

7.1.2 Clinical

The data presented in this dissertation have many clinical implications. On the microstructural level collagen fiber alignment was found to predict the location of tissue failure. It was found that areas of the capsule which have extreme high or low collagen fiber alignment under low strains are at risk for injury under high strains. Further, the location of tissue failure may be independent of loading direction as failure occurred in locations of high fiber alignment even when the fibers were not aligned in the direction of applied elongation. Therefore, the

degree of collagen fiber alignment in the glenohumeral capsule under small loads may be used to identify regions of the capsule that could potentially be damaged or torn under extreme multi-axial loading conditions. Locating regions of the capsule at risk for tears and determining joint positions which would apply excessive strains to these regions would enable rehabilitation techniques to be developed to strengthen the muscles that stabilize the joint at these positions. This may help limit injury to the glenohumeral capsule. Devices could be developed to aid surgeons in this task. For example, the development of a device to image or map the properties of soft tissues in vivo could allow surgeons to identify potential failure sights in the capsule prior to injury. Patients could be warned of their increased risk and given specific exercises to increase muscle strength appropriately.

The increase in collagen fiber alignment, stiffness and material properties of tissue samples from the capsule were found to be associated with tissue damage. These changes in tissue properties imply that its reference state may contain more aligned collagen fibers following injury. As a result, surgical repair techniques which simply tighten the capsule to eliminate excessive tissue elongation may only be addressing part of the problem and changes in tissue properties may still affect the ability of the capsule to support the wide range of motion at the glenohumeral joint. In order to restore the normal material properties, surgeons need to be cognizant of the initial anisotropy of the capsule and how it is altered following injury when they are performing repair procedures to tighten the capsule following dislocation. Again, a device to image the collagen fiber alignment of the capsule in vivo would be helpful as surgeons would be aware of the properties of the injured tissue and would know exactly how it should be altered to restore normal properties. For example, instead of plicating tissue along the glenoid rim,

plicating in the perpendicular direction (from glenoid to humerus) or at a diagonal may better restore tissue properties.

This work found higher strains on the glenoid side compared to the humeral side of the anteroinferior capsule during anterior dislocation. These high strains correspond to the location of common capsular tears known as Bankart lesions and are consistent with results found in this work which demonstrated that areas of greatest strain corresponded to the location of tissue failure during uniaxial extension. Even though high strains during dislocation correspond to the location of capsular tears, the greatest amount of permanent deformation occurs to the posterior side of the axillary pouch. As a result, the ability of this region of the capsule to stabilize the glenohumeral joint in its functional position of abduction and external rotation is compromised. Therefore, while Bankart repairs to the anterior capsule may be necessary to fix capsular tears, plication of the glenohumeral capsule following anterior dislocation should occur also in the posterior axillary pouch.

Anterior glenohumeral dislocation resulted in nonrecoverable strain the anteroinferior capsule. These results exemplify the circle concept which has been applied to the glenohumeral capsule. This concept implies that changes to one portion of the capsule affect its response in all other regions. Due to the continuous structure and function of the capsule excessive translation in the anterior direction resulted in permanent deformation throughout the capsule, and in fact, injury was the greatest to the opposite side, the posterior inferior region of the capsule. This work further demonstrates that the capsule should be treated as a continuous structure as altering its boundary conditions affects all portions of the capsule.

The experimental dislocation model developed in this work resulted in changes in anterior translation of only a few millimeters. When similar forces were applied to the intact and

injured joint during the simulated clinical exams, these small differences were detected. However, during current clinical exams surgeons apply manual maximum loads to the humerus of the injured and contralateral joint and compare the resutling translations. Depending on the experience of the examiner or hand dominance, consistent loads may not be applied to both joints. Differences in translation on the order of millimeters may go undetected if similar forces are not applied to the normal and injured joints.

Even if increased anterior translation is detected, the specific region of the capsule most at risk for damage following anterior dislocation was identified as the posterior axillary pouch. Therefore, repair procedures which plicate the anterior capsule based on increased anterior translation during pre-operative physical exams are not addressing the appropriate region of the capsule. Due to the complex, multi-axial function of the capsule current physical examinations which demonstrate increased translations in a particular direction may not be capable of identifying the specific location of tissue damage. This issue may contribute to failed surgical repair due to misdiagnosis. Therefore, developing standardized clinical exams to diagnose damage in specific capsule regions may lead surgeons to repair the appropriate capsule regions, thus improving patient outcome following traumatic anterior dislocation.

This work also demonstrated the need for clinical exams to be standardized for joint position. Following anterior dislocation damage occurred throughout the anteroinferior glenohumeral capsule. However, changes in the function of different regions of the capsule were detected at different joint positions. Damage to the AB-IGHL was detected when clinical exams were performed with the joint at low- and mid-ranges of external rotation whereas damage to the anterior axillary pouch was only detected when the joint was in extreme external rotation. Changes in the function of the posterior axillary pouch were detected at all joint positions. As the

most damage was found in the posterior axillary pouch, followed by the AB-IGHL and finally the anterior axillary pouch, further work needs to be done in order to determine if these joint positions are specific to capsule region or amount of damage. In other words, can large amounts of permanent deformation always be detected at any joint position and increasing the amount of external rotation will allow detection of moderate damage in other portions of the capsule? Or is it that damage to the anterior axillary pouch can only be detected at extereme external rotiaton? Regardless, the results of this dissertation suggest that specific joint positions exist at which clinical exams can be performed in order to detect permanent deformation in specific sub-regions of the glenohumeral capsule.

Therefore, based on the work presented in this dissertation, one ideal clinical exam may not exist, but rather the most appropriate diagnosis would come from performing a series of clinical exams which would identify the specific amount of permament deformation in each region of the capsule. This would allow surgeons to fully understand the location and extent of tissue damage on a patient-by-patient basis enabling them to design the most appropriate repair. Anterior-posterior loads should be applied to the humerus at multiple joint positions to detect damage in various capsule regions. In addition, inferior loads may also be necessary to fully map the location and extent of tissue damage and should be investigated in future studies. When performing these exams it is imparitive that clinicians apply a consistent amount of force to the injured and contralateral joint, regardless of the joint position. Devices could be developed to provide surgeons with force feedback during the exams and aid them in learning to apply consistent loads.

Anterior dislocation of the glenohumeral joint also resulted in increased glenohumeral contact forces which could lead to abnormal wear on the articular cartilage of the glenohumeral

joint. Although specific contact locations were not identified in the current work, the increase in anterior translation suggests that the location of contact between the humeral head and glenoid is altered following dislocation. If the proper diagnostic and repair techniques are not performed in order to restore normal joint kinemtaics, patients are at risk for the development of glenohumeral osteoarthritis and other injuries. As many dislocations occur in the younger athletic population, these patients could be suffering as they get older.

7.2 UNDERSTANDING INJURY TO THE GLENOHUMERAL CAPSULE

7.2.1 Advancements

Through this dissertation, significant contributions to the scientific literature were made in terms of the understanding of normal and injured capsule behavior as well as experimental and computational methodologies.

This work increased understanding of the effect of injury on the glenohumeral capsule. Previous work in our laboratory [3] and others [4, 5, 123] evaluated the collagen fiber alignment in the unloaded capsule and the collagen fiber kinematics in response to uniaxial and bi-axial loading conditions has been evaluated in other biologic tissues [125, 127, 140, 164]. However, results shown here were the first to quantify the collagen fiber alignment in the glenohumeral capsule under load and demonstrate its ability to predict tissue failure.

Other researchers have developed models to create permanent deformation in the glenohumeral capsule by forcing the humeral head into external rotation beyond the normal range of motion to simulate the increase in external rotation found in overhead athletes. [71]

Joint kinematics following injury were evaluated and increases in anterior translation and external rotation were found. [71] Although this model created injury to the capsule as seen by the increased joint translations and rotations, the amount of permanent deformation was not quantified. Another group quantified the amount of permanent deformation in the anteroinferior capsule resulting from glenohumeral subluxation. [68] The maximum principal strain in the anteroinferior capsule during subluxation was also quantified [69] and later related to the resulting amount of nonrecoverable strain [33]. However, this model did not evaluate the effect of this dislocation on the function of the capsule. The extensive dislocation model developed in the current work quantifies the amount of permanent deformation in the capsule resulting from anterior dislocation and links that damage to changes in capsule function via strain distributions, joint kinematics, in situ forces, and glenohumeral contact forces. Specific joint positions were identified which are capable of detecting permanent deformation and changes in function in specific regions of the glenohumeral capsule. Performing clinical exams at multiple joint positions and applying consistent loads to the injured and contralateral joint can provide clinicians with a better understanding as to the specific location and extent of tissue damage following anterior dislocation.

The development of the experimental dislocation model required significant experimental advancements to be made. As this was the first time the robotic/UFS testing system had been used to dislocate a glenohumeral joint in a controlled manner several modifications to existing protocols had to be made. First, the methodology for determining the reference strain configuration had been developed previously. [7, 9, 69] However, as this position had to be repeated following anterior dislocation in order to quantify the amount of nonrecoverable strain, the reference strain configuration had to be determined while the joint was mounted on the

robotic/UFS testing system. This required an additional reference path (reference strain path) to be determined by applying a 10 N distractive force and 1 N-m torque about the humerus. This established a path of internal/external rotation with the joint distracted so that the hose could be inserted into the capsule for inflation. Second, the code responsible for controlling motion of the robotic/UFS testing system had to be modified such that a glenohumeral joint could be dislocated anteriorly in a controlled manner. An excessive anterior force was applied to the humerus and the joint was allowed to translate in all three degrees of freedom. The code was modified such that the user has the option to stop motion when the anterior translation reached the amount desired by our definition of dislocation. These modifications to the experimental protocol can be used in future studies which require glenohumeral dislocation using the robotic/UFS testing system.

Finally, this dissertation made advancements with regards to modeling the glenohumeral capsule. Previous work in our laboratory initially characterized the material properties of the normal glenohumeral capsule using an isotropic phenomenological constitutive model. [42] However, this model was unable predict the capsule response to more complex loading conditions as would be experienced by the capsule in vivo. [42, 173] When implemented into finite element models of the glenohumeral joint, this model only allowed for the models to be validated for the AB-IGHL. When comparing the experimental and predicted strains on a local level (based on the experimental elements defined by the grid of strain markers), differences were much larger than the experimental repeatability. In order to use these finite element models appropriately to predict local capsule behavior a structural constitutive model was developed and found to provide better predictions of the complex capsule behavior. This structural model

should be used to describe the material behavior of the capsule in future finite element models of the glenohumeral joint.

In addition to the development of a new constitutive model for the capsule the affine assumption of fiber kinematics was evaluated for the glenohumeral capsule. Evidence of non-affine fiber kinematics has been observed in other biologic tissues such as bovine pericardium and porcine aortic heart valves [164], small intestine submucosa (SIS) [125], human annulus fibrosus [142], porcine skin [205], and most recently human supraspinatus tendon [190], but has never been evaluated in the capsule. This work further demonstrated that the assumption that fiber kinematics in soft tissue is affine should be evaluated for individual tissues. It was also observed that the ability of the affine model to predict the fiber distribution is worse when the tissue is damaged. Therefore, it is suggested that a constitutive model which accounts non-affine fiber kinematics, similar to the one recently developed [128], be used to describe capsule behavior.

7.2.2 Limitations

Despite the numerous implications and advancements resulting from this work it is important to note that this work is not without limitations. As the limitations of each Specific Aim were discussed previously, only major limitations of the dissertation as a whole will be discussed here.

The work presented in this dissertation utilized a human cadaver model. This model investigated the time-zero response of the glenohumeral capsule to injury but did not account for the healing response which begins to take place immediately afer injury. The healing response may alter the structural and material properties of the glenohumeral capsule, particularly as scar tissue forms. In order to investigate the effect of healing animal models must be used.

The cadaver model used in this work did not include the contributions from the muscles which cross the glenohumeral joint such as the deltoid and rotator cuff. These muscles play a significant role in maintaining glenohumeral stability and can also be injured during joint dislocation. Inclusion of muscle contributions may make detecting small increases in translation due to dislocation difficult to detect.

The clinical exams performed during this work consisted of applying anterior-posterior loads at 60° abduction and 0°, 30° and 60° of external rotation. In order to truly develop a set of standardized clinical exams for diagnosing injury to various regions of the capsule, other clinical exams will have to be investigated. For example, applying inferior loads to the joint may demonstrate changes in inferior translation and other abduction angles may prove to be easier for detecting differences in anterior translation following dislocation.

This dissertation did not include any histological analyses of the glenohumeral capsule. Examining the microstructure of the capsule may demonstrate other differences between the normal and injured tissue which were not found here and could help explain may of the hypotheses made in this dissertation regarding how structural changes influence the mechanical response. In addition, histology could help explain the conclusion that the collagen fibers in the capsule are not affine predicted by demonstrating interactions between the fibers, collagen cross-links, and ground substance. These analyses should be performed in the future.

7.3 FUTURE DIRECTIONS

The data presented in this dissertation serve as a foundation for future research to further understand the effect of dislocation on the structure and function of the glenohumeral capsule.

The simulated injury model, developed in Specific Aim 2, to create permanent deformation in tissue samples from the capsule could be used to verify that permanent changes in the collagen fiber alignment exist following injury. Using the SALS device, the collagen fiber alignment before and after simulated injury can be quantified. In addition, the collagen fiber kinematics of the glenohumeral capsule should be evaluated under bi-axial loading as this loading condition better simulates in vivo boundary conditions applied to the capsule.

The experimental dislocation model developed in this dissertation will lead to numerous studies. The model can be used to simulate the state of the glenohumeral joint following anterior dislocation when evaluating other joint pathologies such as Hill-Sachs lesions and also assess the efficacy of various repair techniques. For example, the ability of capsular plication to the posterior inferior capsule to restore joint kinematics and glenohumeral contact forces will be evaluated. In addition, this model will be used to determine the effect of anterior dislocation on the collagen fiber alignment mechanical properties of the injured capsule.

This dissertation also serves as a foundation for standardizing clinical exams to diagnose instability. Results of this work imply that by performing clinical exams at specific joint positions and with consistent applied loads, the location and extent of damage to the glenohumeral capsule can be detected. Through further experimental and computational studies these joint positions can be further standardized and other clinical exams can be developed in order to help surgeons map permament deformation in the glenohumeral capsule resulting dislocation and improve patient outcome following repair.

The next step in terms of the modeling efforts discussed in this work would be to determine unique parameters for the structural constitutive model. Developing a new experiment to determine the response of the ground substance independently of the collagen fibers or

optimizing for the toe and linear region coefficients separately should be investigated. The experimental data collected in Specific Aim 2 can serve as a starting point for determining if changes in the material properties of the capsule can be detected in the coefficients of the structural model. Based on the increased stiffness and modulus following simulated injury, changes in the linear region coefficient (C_5) are expected. The structural model should also be implemented into the finite element models of the glenohumeral joint in order to determine if this model increases their predictive capability enough to validate them based on local capsule strains. Other improvements to the structural model should be evaluated in the future such as incorporating tissue-specific fiber distributions and non-affine fiber kinematics if further improvement is necessary.

This dissertation suggested that specific joint positions exist at which injury to explicit regions of the glenohumeral capsule can be detected by performing clinical exams at multiple joint positions. However, this work evaluated cadaveric shoulders which only included the glenohumeral capsule. The next step towards standardizing clinical exams for shoulder instability would be to apply these concepts in vivo. Physical exams should be performed on human subjects with one normal shoulder and one shoulder which suffered an anterior dislocation. Since such small changes in translations were observed in the current work, it needs to be determined whether or not these differences can be detected in vivo, when muscles and other soft tissues are present, by performing exams at multiple joint positions. Performing clinical exams at multiple joint positions could then identify the location and extent of capsule damage and used to direct capsular plication. The success of these surgeries could be then be tracked over an extended period of time.

This work also suggested that applying consistent forces to the injured and contralateral joint during clinical exams is essential for detecting differences in translation. In order to propertly standardize clinical exams the magnitude of force which will result in the greatest difference in translation thereby making injury easiest to detect, must be determined. Differences in translation between the intact and injured joints were only a few millimeters when 25N was applied to each joint. Applying larger loads will likely be necessary to detect differences in translation when the muscles and other soft tissue are present.

In order to determine if the standardized clinical exams are identifying the appropriate regions of the capsule to be plicated during repair, finite element models of glenohumeral dislocation and injured capsular tissue could be utilized. A model could be dislocated in the anterior direction and the capsule injured. By performing simulated clinical exams the strain distributions in the injured capsule could be used to determine the appropriate region for repair. A plication procedure could be simulated in the model by adjusting properties of the finite element mesh and the clinical exams performed again. The strain distributions in the capsule following the simulated repair could be compared to those of the normal capsule to determine if the appropriate region was targeted. This would serve as validation for the standardized clinical exams used to diagnose injury.

7.4 SUMMARY

Anterior glenohumeral dislocation results in permanent deformation of the anteroinferior glenohumeral capsule. Current rehabilitation and repair techniques aimed to address this injury are subjective and many patients suffer recurrent dislocation and other problems following

treatment. Validated finite element models combined with a better understanding of how the structure and function of the glenohumeral capsule is altered following dislocation could advance current treatment options and improve patient outcomes. Therefore, the objective of this work was to evaluate the effect of anterior dislocation on the structure and function of the capsule from three levels: microstructure, tissue, and joint; and to suggest improvements to a constitutive model for the capsule.

At the microstructural level, collagen fiber alignment in the capsule increased with applied load and was found to predict the location of tissue failure. Simulated injury of tissue samples from the capsule provided complementary results as increased stiffness and modulus of stress-stretch curves were found suggesting that the capsule has a more aligned reference state following injury. However, these changes in material properties were not detectable in the parameters of an isotropic phenomenological constitutive model. An experimental model of anterior dislocation successfully caused permanent deformation to the glenohumeral capsule. Changes in the strain distribution in the anteroinferior capsule, joint kinematics, and glenohumeral contact forces during simulated clinical exams suggest that the stabilizing function of the capsule was compromised following dislocation. Finally, a structural constitutive model was found to better predicted complex capsule behavior than the phenomenological model. However, several improvements can be made to the model such as accounting for tissue anisotropy or the non-affine fiber kinematics to improve the accuracy of computational models even further.

The results of this work suggest that surgical repair procedures targeting the anterior capsule based on increased anterior translation during pre-operative physical exams are not addressing the appropriate region of the capsule; rather the posterior axillary pouch suffers the

most damage following anterior dislocation. Therefore, current physical examinations may not be capable of identifying specific locations of tissue damage and future research to standardize physical exams is warranted. Based on this work it is recommended that clinicians perform clinical exams at multiple joint positions and with consistent force in order to detect differences in translation and to identify damage in specific regions of the glenohumeral capsule. In addition, a structural constitutive model should be used in future work to describe the material properties of the capsule in finite element models of the glenohumeral joint.

APPENDIX A

DIGITAL CAMERA IMAGES

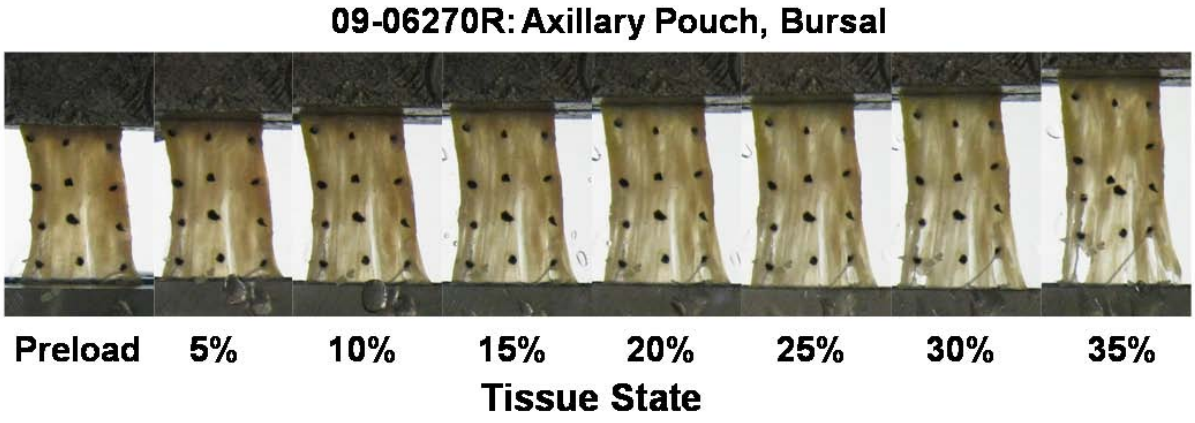

Figure 7.1 Digital camera images for each increment of elongation from which the strain marker coordinates were determined for Specimen 09-06270R: axillary pouch.

Figure 7.2 Digital camera images for each increment of elongation from which the strain marker coordinates were determined for Specimen 09-06270R: posterior capsule.

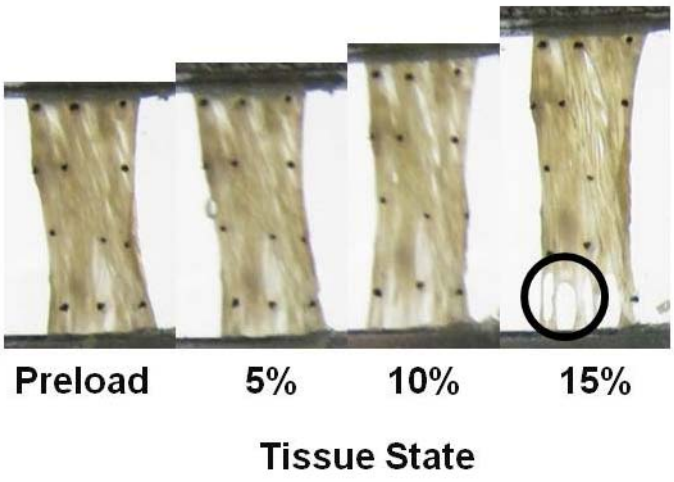

Figure 7.3 Digital camera images for each increment of elongation from which the strain marker coordinates were determined for Specimen 09-06270R: AB-IGHL.

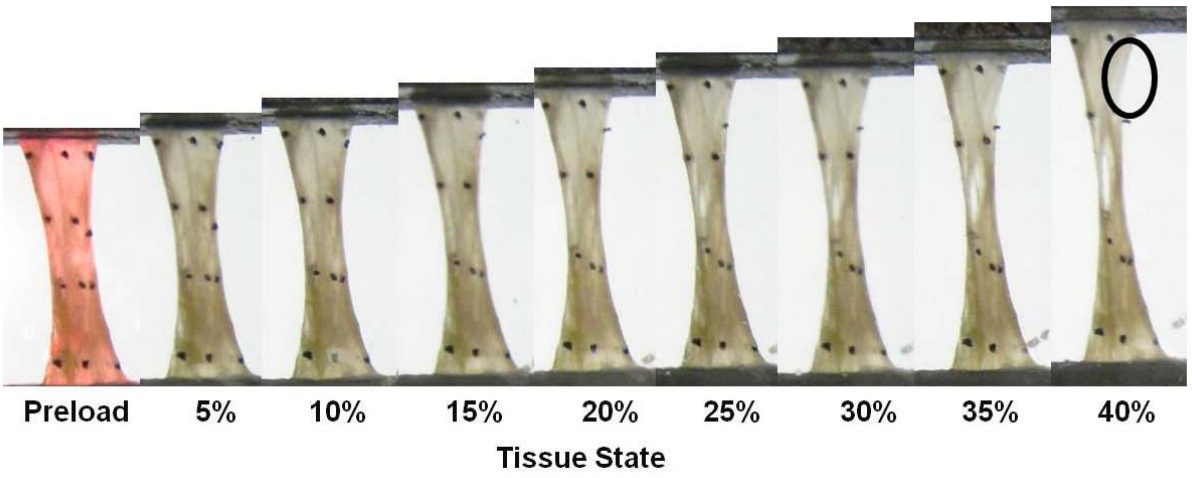

Figure 7.4 Digital camera images for each increment of elongation from which the strain marker coordinates were determined for Specimen 09-06270R: PB-IGHL.

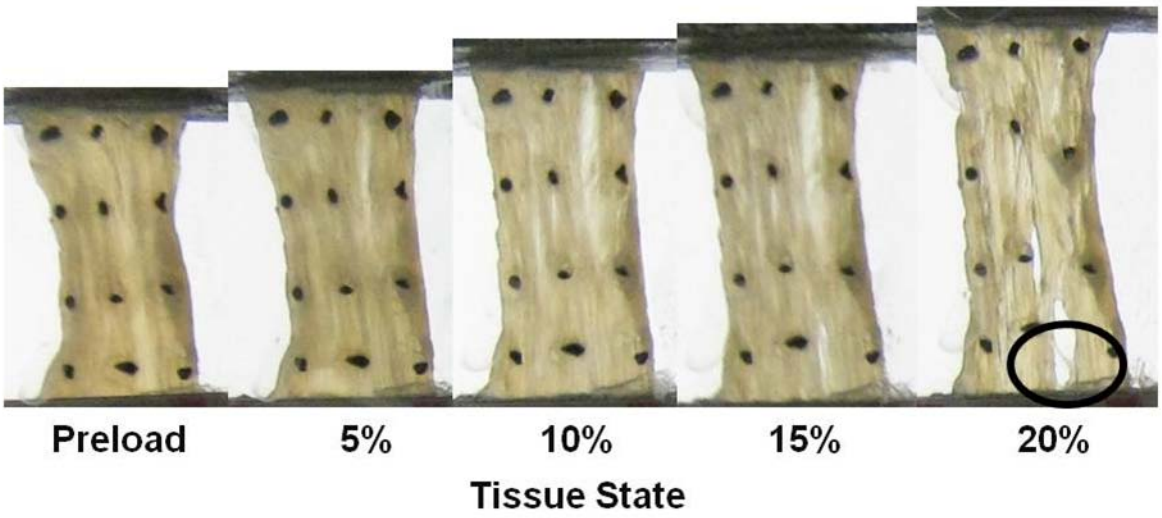

Figure 7.5 Digital camera images for each increment of elongation from which the strain marker coordinates were determined for Specimen 09-06270R: Anterosuperior Capsule.

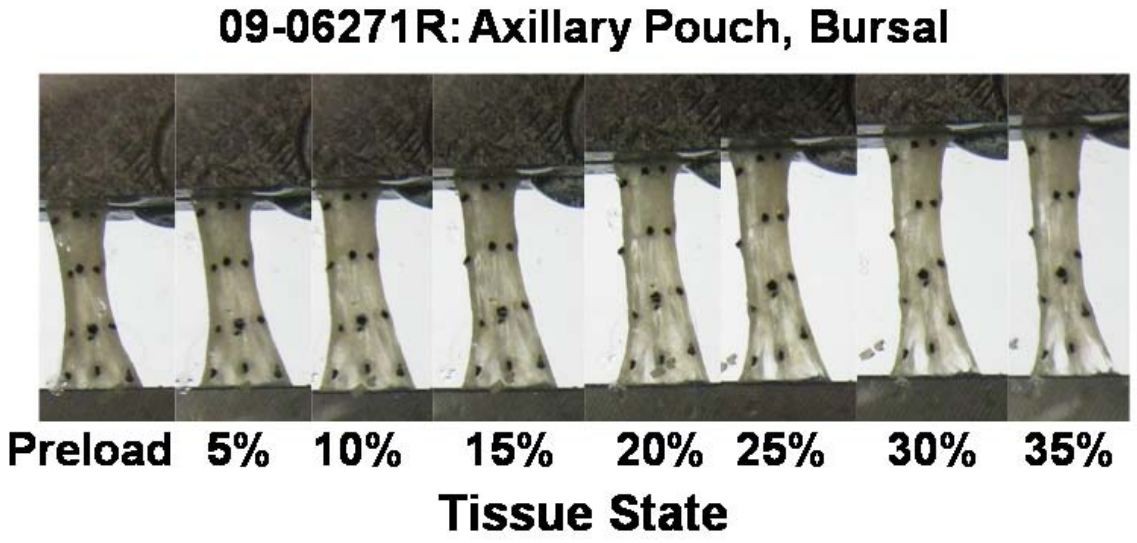

Figure 7.6 Digital camera images for each increment of elongation from which the strain marker coordinates were determined for Specimen 09-06271R: axillary pouch.

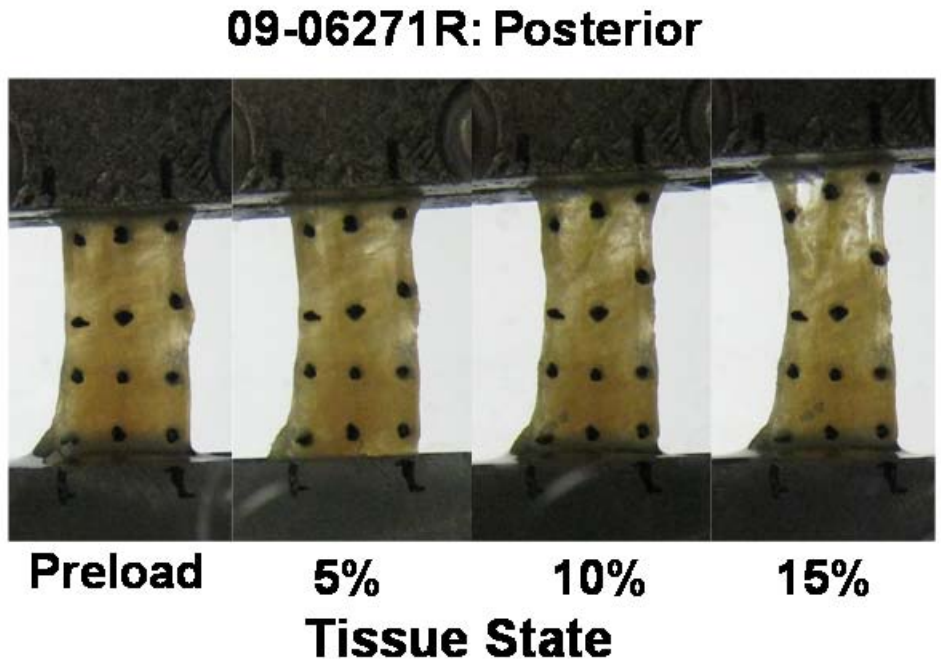

Figure 7.7 Digital camera images for each increment of elongation from which the strain marker coordinates were determined for Specimen 09-06271R: posterior capsule.

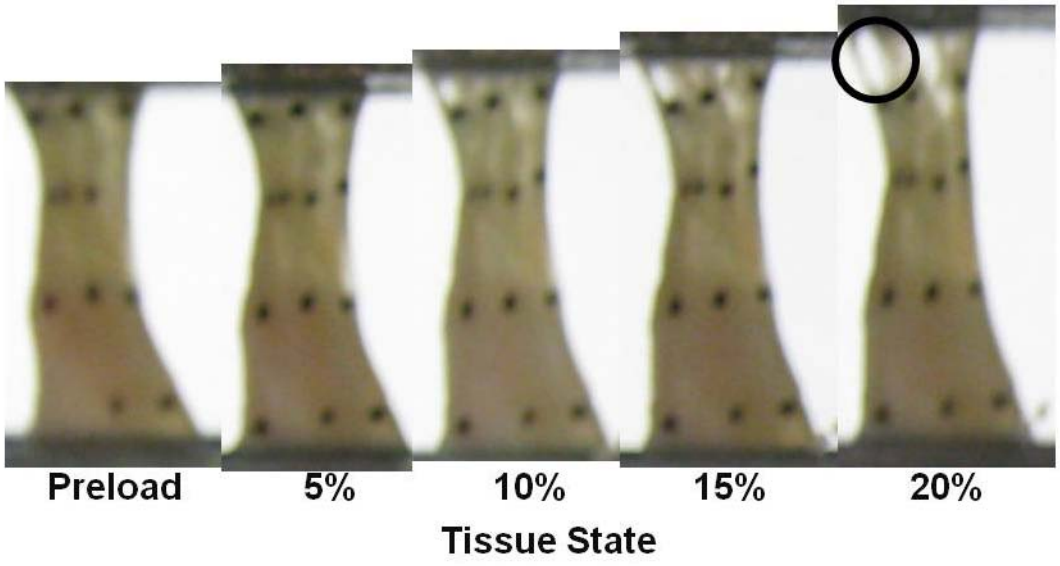

Figure 7.8 Digital camera images for each increment of elongation from which the strain marker coordinates were determined for Specimen 09-06271R: AB-IGHL.

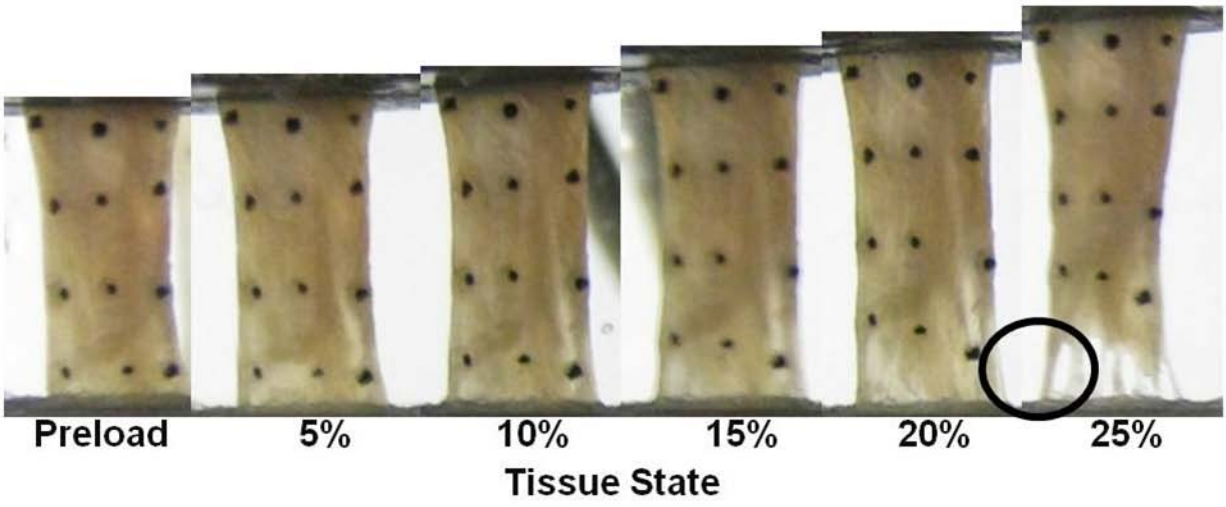

Figure 7.9 Digital camera images for each increment of elongation from which the strain marker coordinates were determined for Specimen 09-06271R: PB-IGHL.

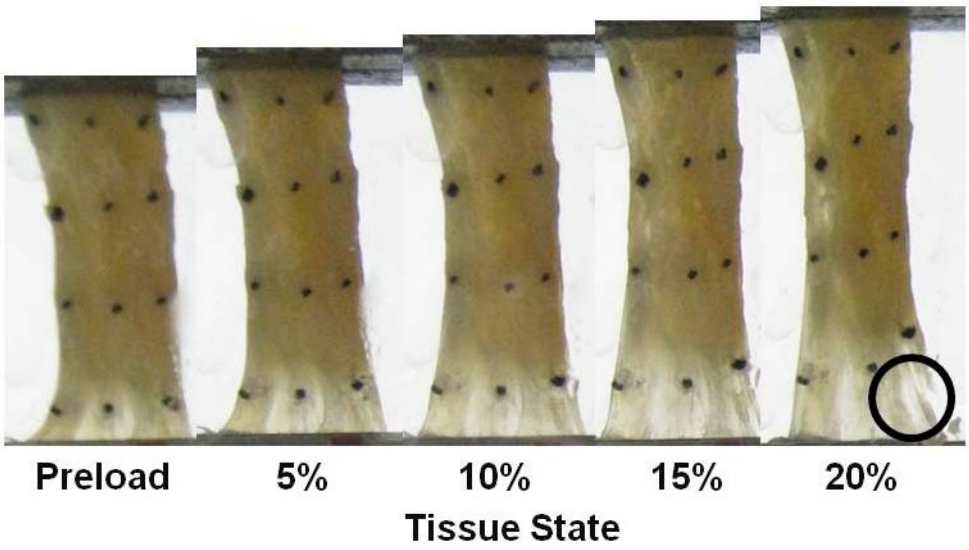

Figure 7.10 Digital camera images for each increment of elongation from which the strain marker coordinates were determined for Specimen 09-06271R: Anterosuperior Capsule.

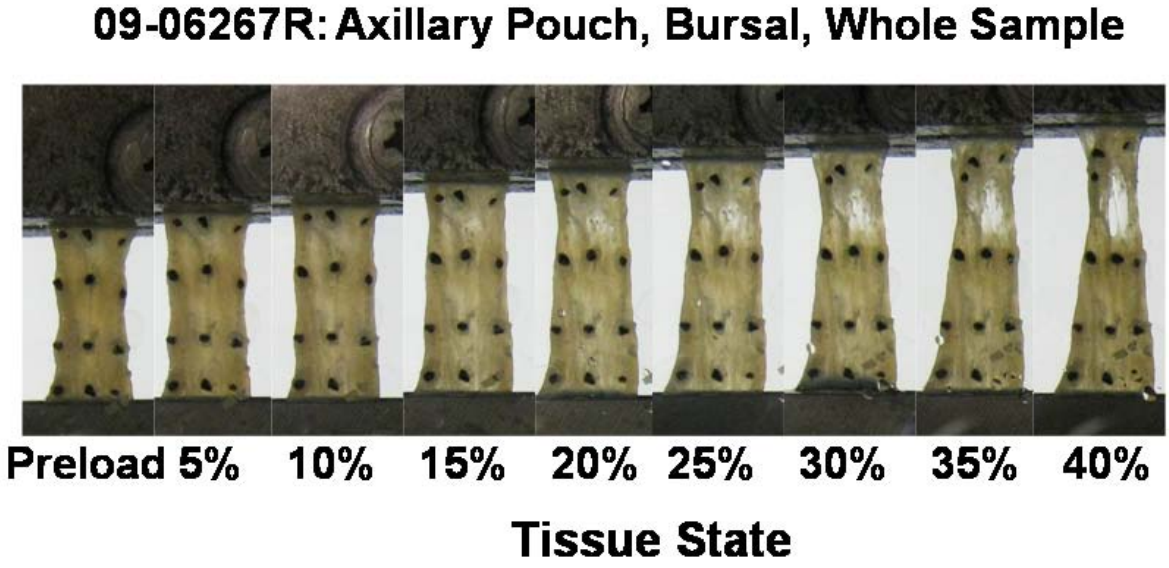

Figure 7.11 Digital camera images for each increment of elongation from which the strain marker coordinates were determined for Specimen 09-06267R: axillary pouch.

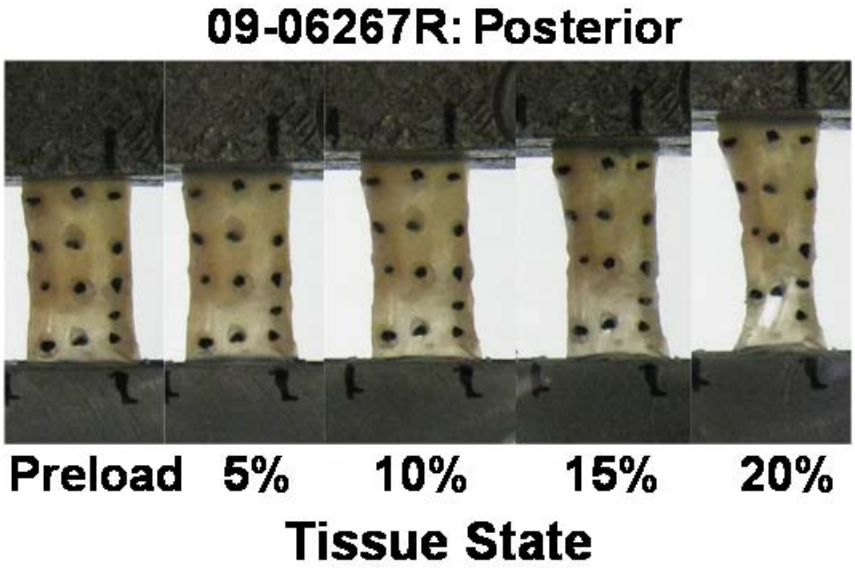

Figure 7.12 Digital camera images for each increment of elongation from which the strain marker coordinates were determined for Specimen 09-06267R: posterior capsule.

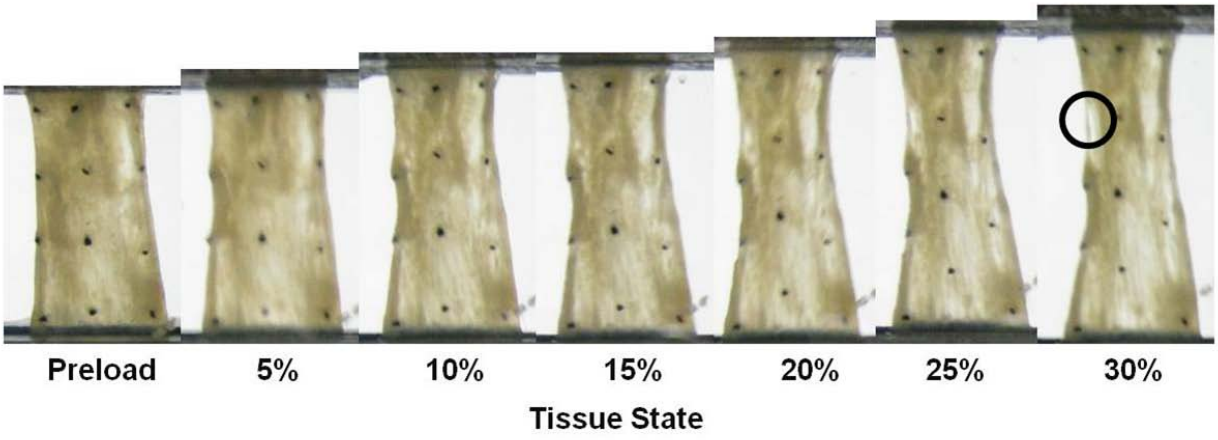

Figure 7.13 Digital camera images for each increment of elongation from which the strain marker coordinates were determined for Specimen 09-06267R: AB-IGHL.

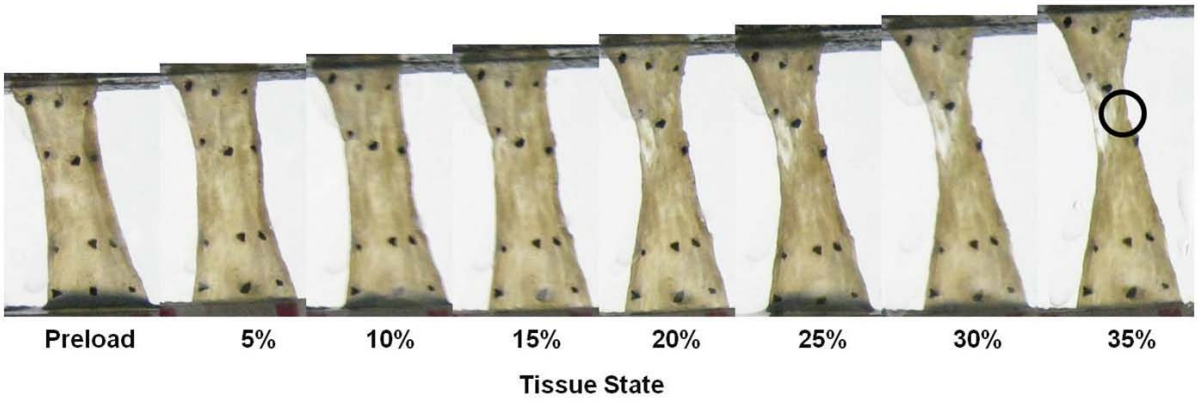

Figure 7.14 Digital camera images for each increment of elongation from which the strain marker coordinates were determined for Specimen 09-06267R: Anterosuperior Capsule.

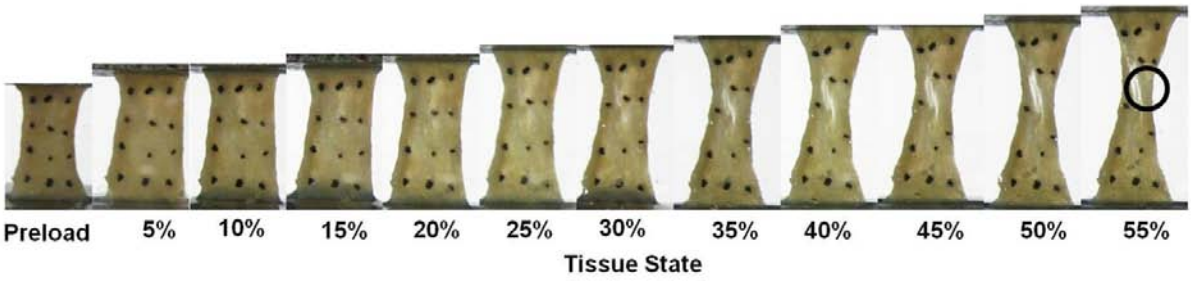

Figure 7.15 Digital camera images for each increment of elongation from which the strain marker coordinates were determined for Specimen 07-10874L: Axillary Pouch.

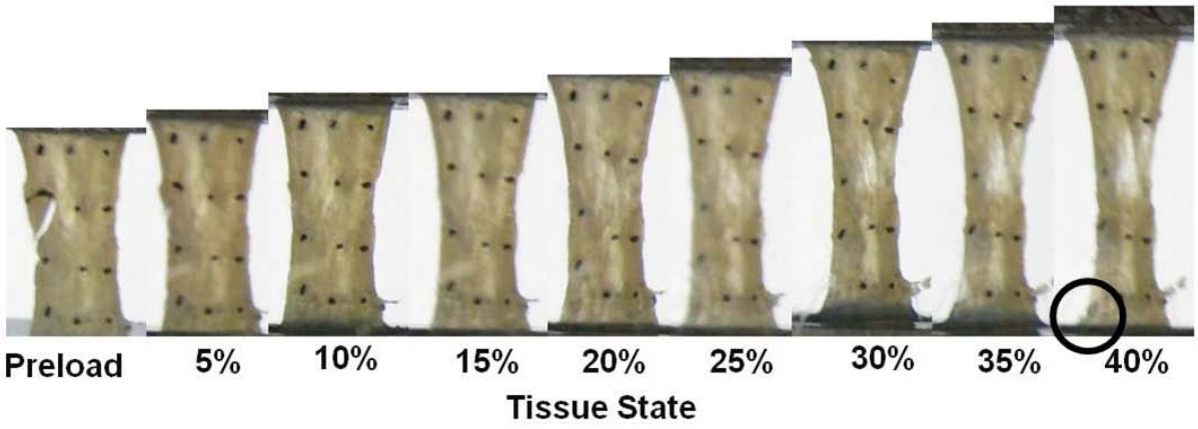

Figure 7.16 Digital camera images for each increment of elongation from which the strain marker coordinates were determined for Specimen 07-10874L: AB-IGHL.

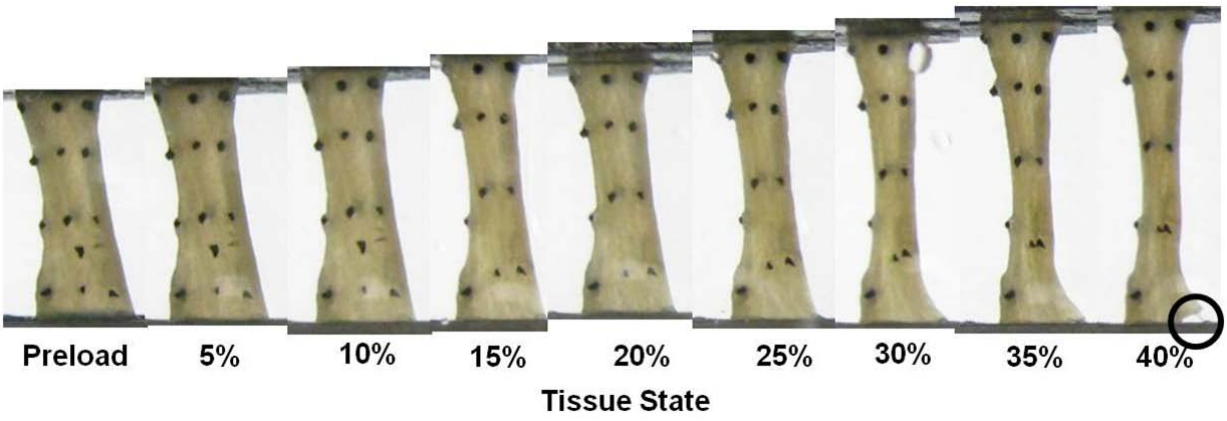

Figure 7.17 Digital camera images for each increment of elongation from which the strain marker coordinates were determined for Specimen 07-10874L: PB-IGHL.

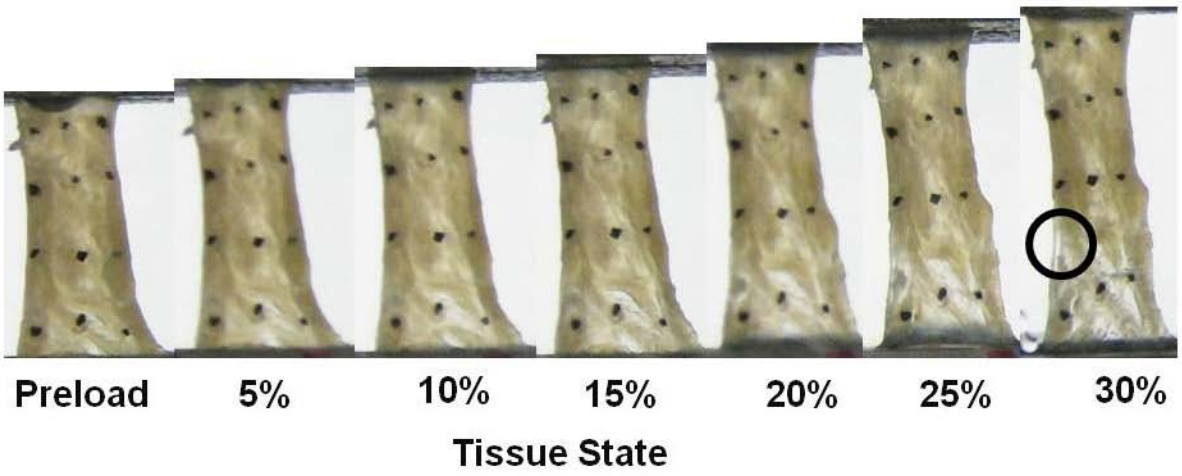

Figure 7.18 Digital camera images for each increment of elongation from which the strain marker coordinates were determined for Specimen 07-10874L: Anterosuperior Capsule.

Figure 7.19 Digital camera images for each increment of elongation from which the strain marker coordinates were determined for Specimen 08-12366R: posterior capsule.

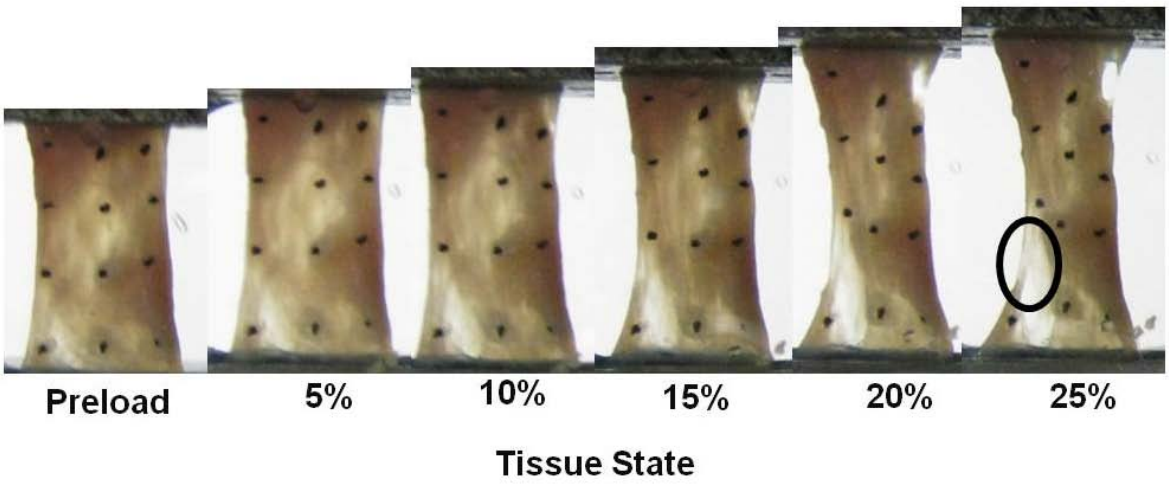

Figure 7.20 Digital camera images for each increment of elongation from which the strain marker coordinates were determined for Specimen 08-12366R: AB-IGHL.

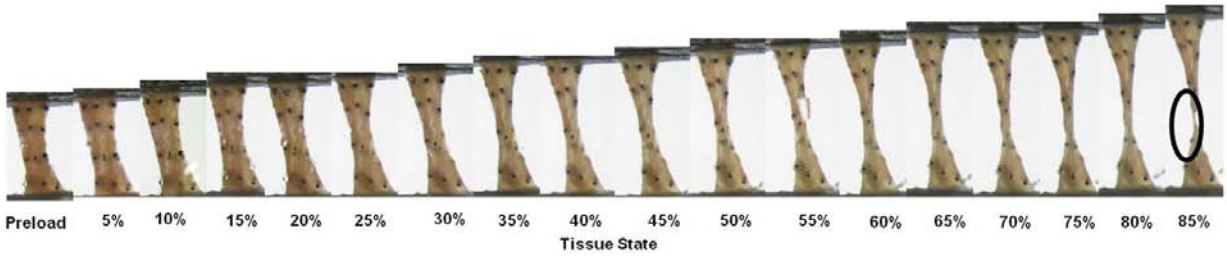

Figure 7.21 Digital camera images for each increment of elongation from which the strain marker coordinates were determined for Specimen 08-12366R: PB-IGHL.

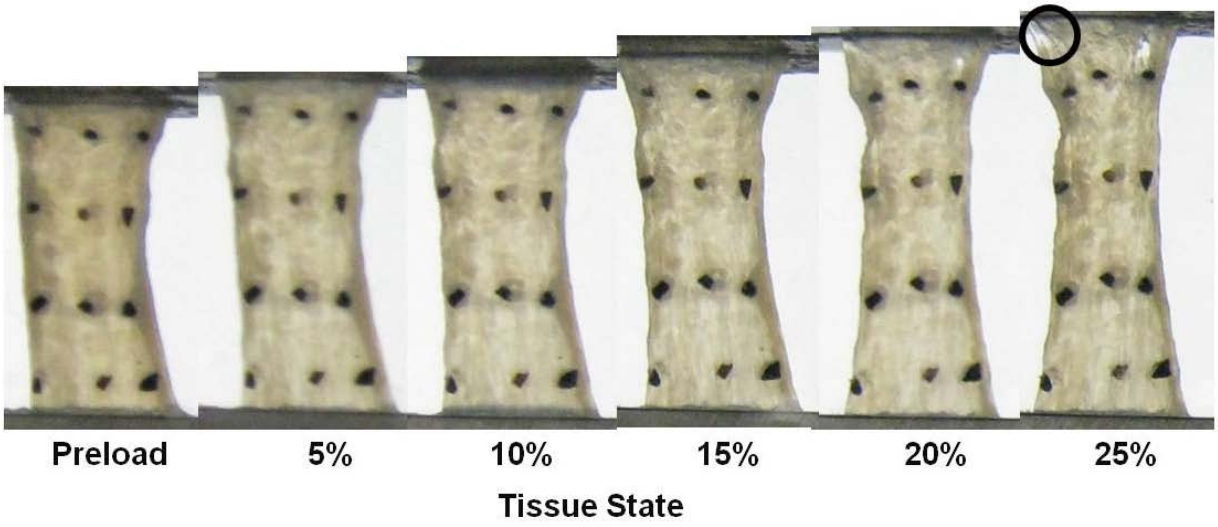

Figure 7.22 Digital camera images for each increment of elongation from which the strain marker coordinates were determined for Specimen 09-06278R: Axillary Pouch.

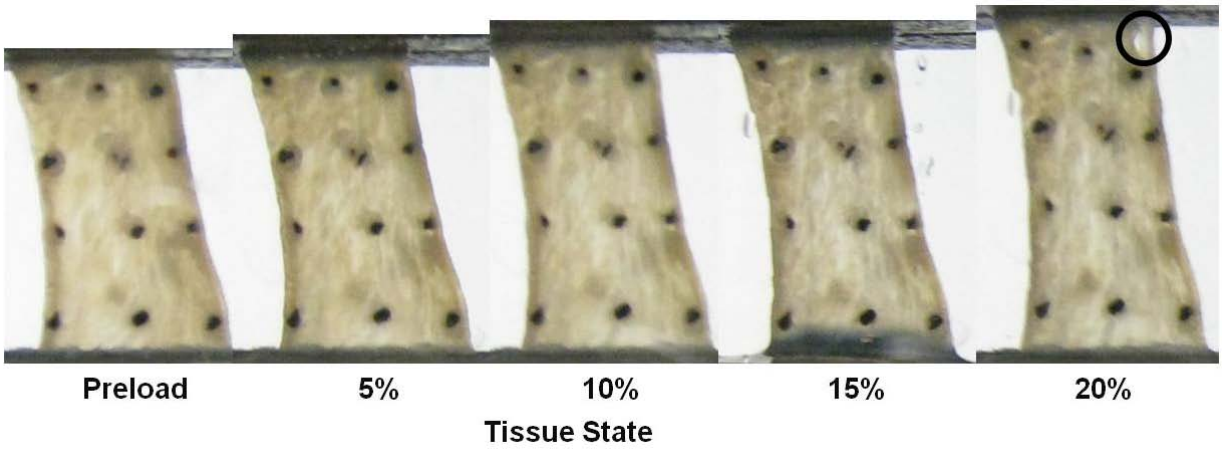

Figure 7.23 Digital camera images for each increment of elongation from which the strain marker coordinates were determined for Specimen 09-06278R: AB-IGHL.

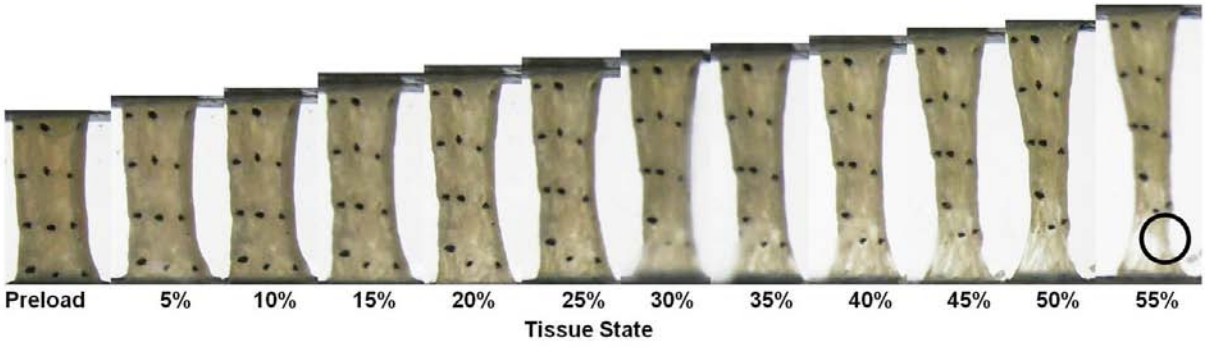

Figure 7.24 Digital camera images for each increment of elongation from which the strain marker coordinates were determined for Specimen 09-06278R: Anterosuperior Capsule.

APPENDIX B

NOI DISTRIBUTIONS

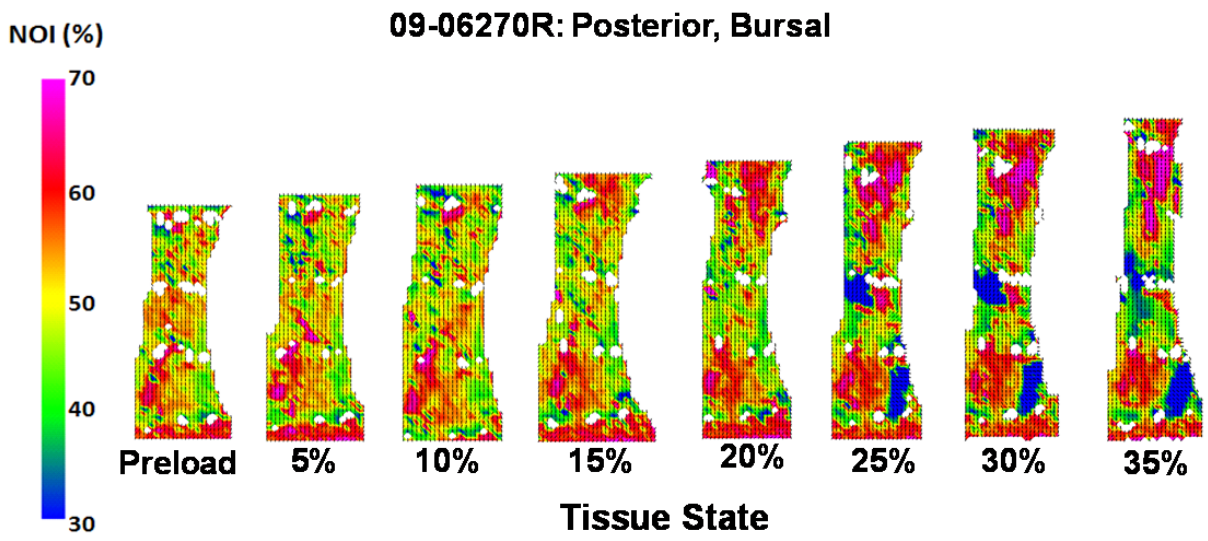

Figure 7.25 NOI distribution at each increment of elongation for Specimen 09-06270R: Posterior Capsule.

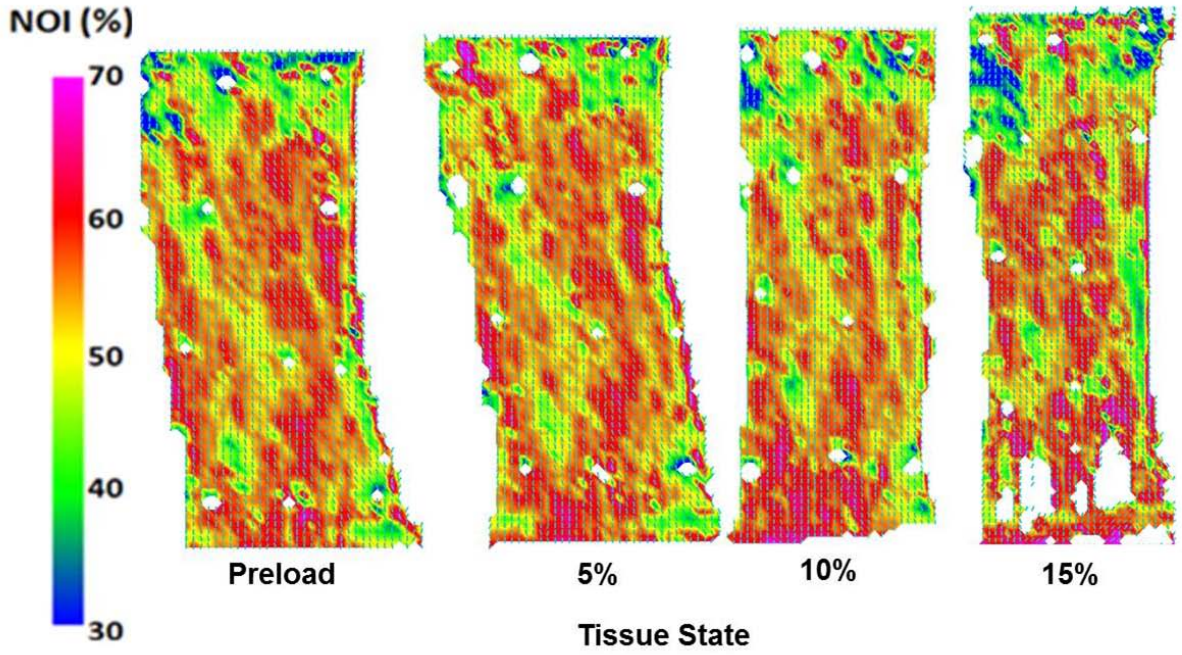

Figure 7.26 NOI distribution at each increment of elongation for Specimen 09-06270R: AB-IGHL.

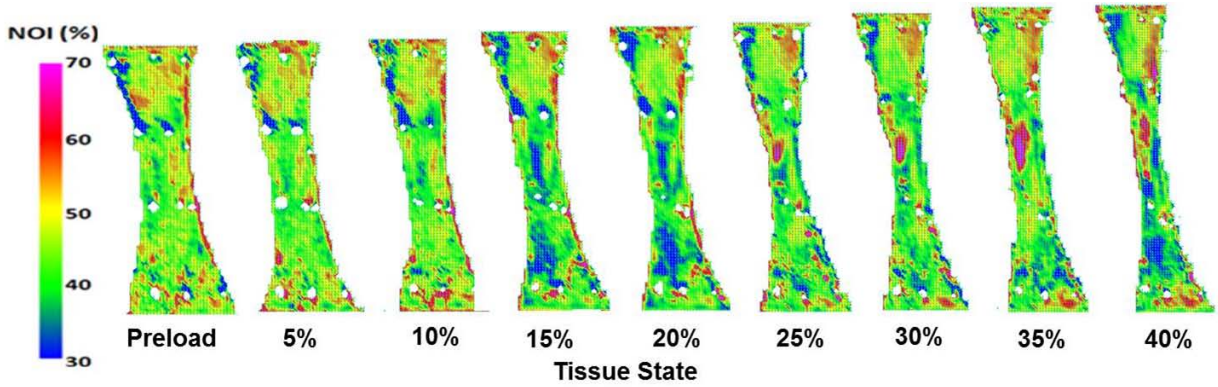

Figure 7.27 NOI distribution at each increment of elongation for Specimen 09-06270R: PB-IGHL.

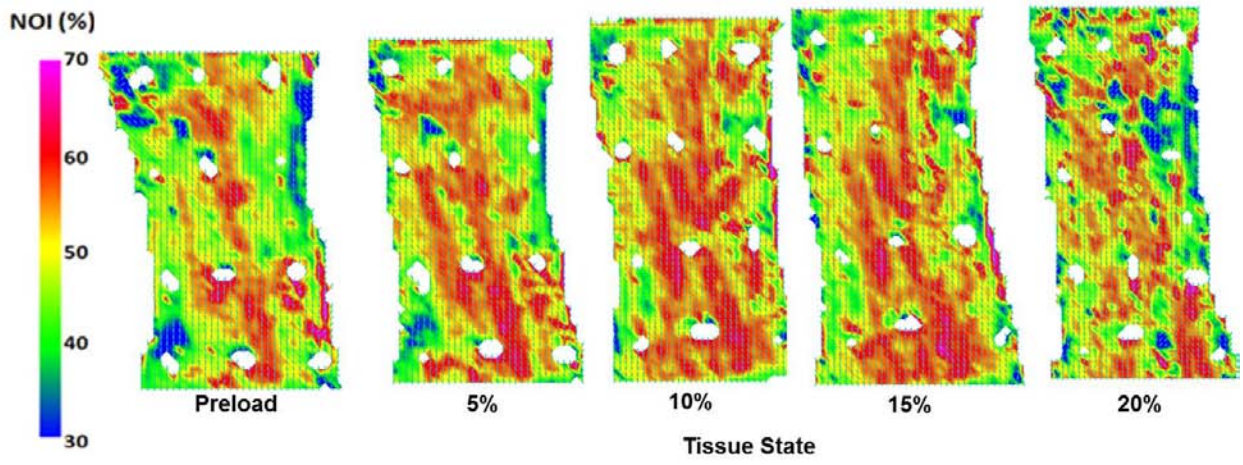

Figure 7.28 NOI distribution at each increment of elongation for Specimen 09-06270R: Anterosuperior Capsule.

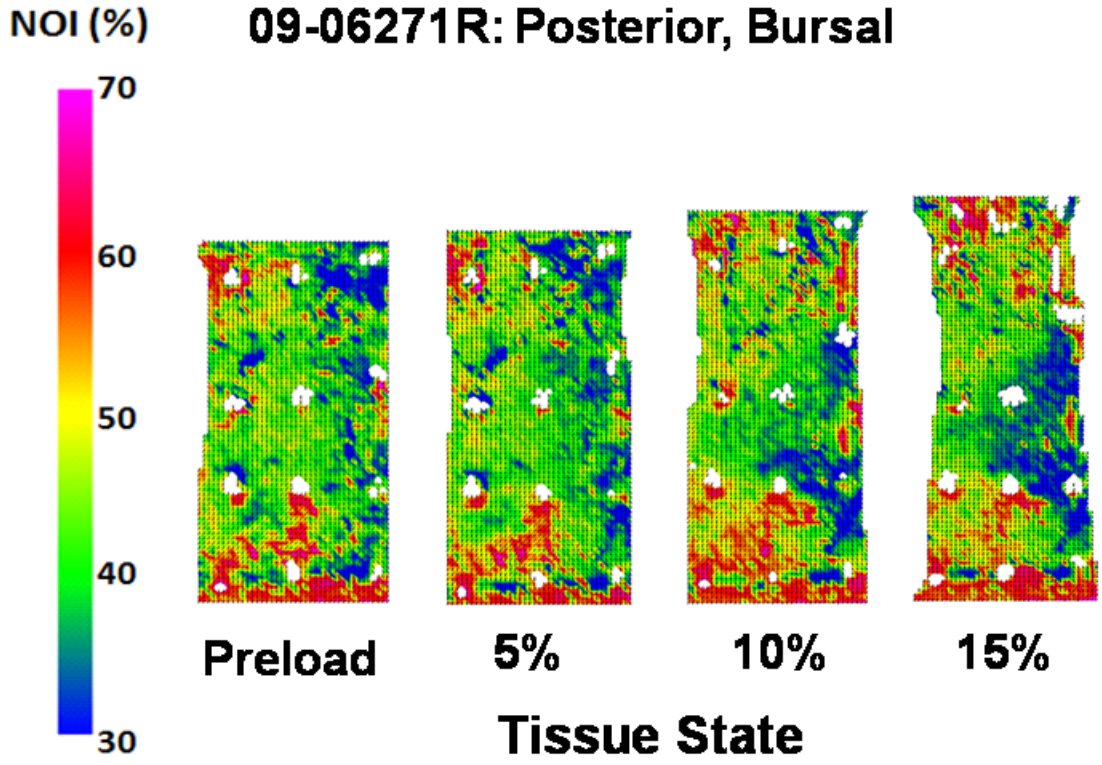

Figure 7.29 NOI distribution at each increment of elongation for Specimen 09-06271R: Posterior Capsule.

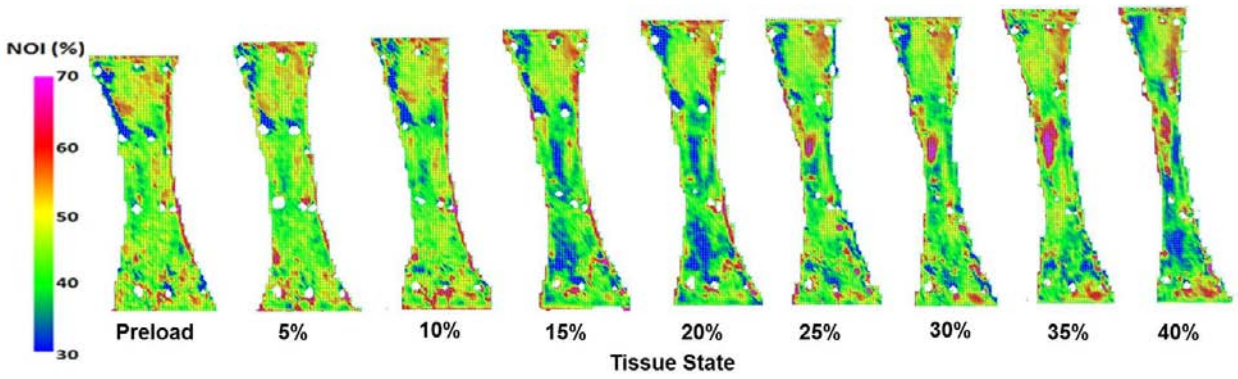

Figure 7.30 NOI distribution at each increment of elongation for Specimen 09-06271R: AB-IGHL.

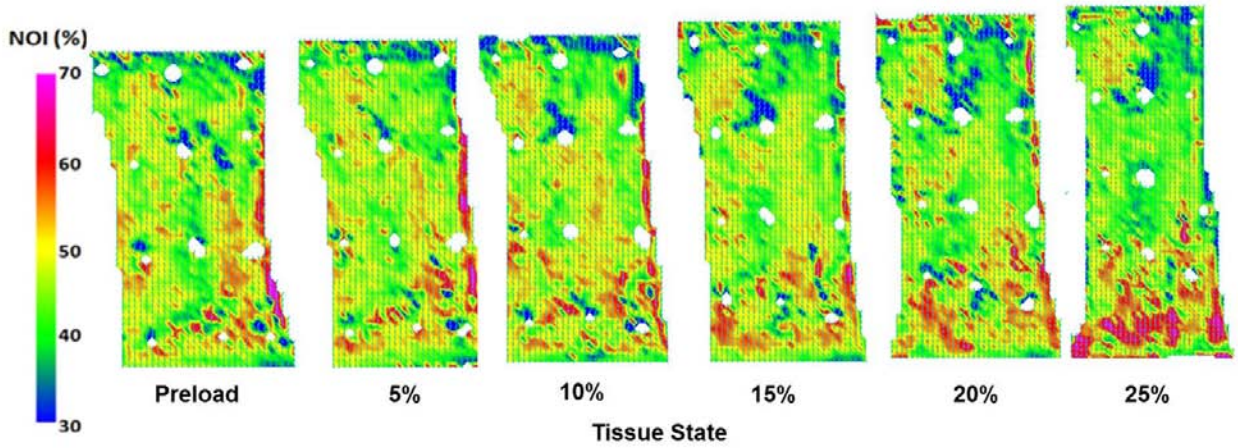

Figure 7.31 NOI distribution at each increment of elongation for Specimen 09-06271R: PB-IGHL.

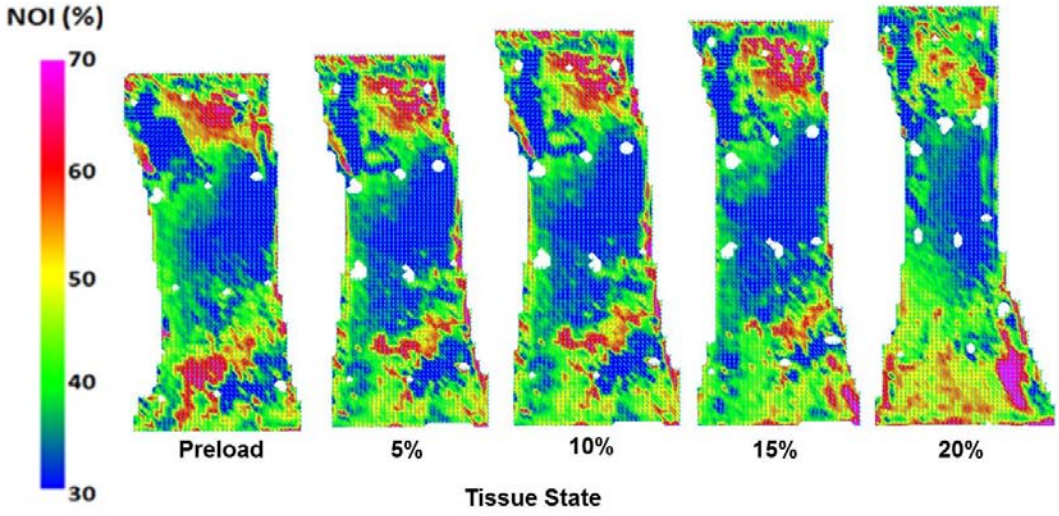

Figure 7.32 NOI distribution at each increment of elongation for Specimen 09-06271R: Anterosuperior Capsule.

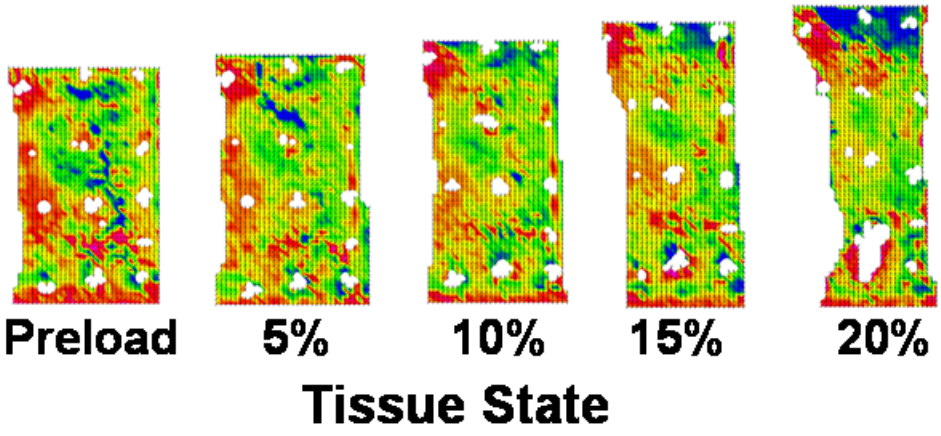

Figure 7.33 NOI distribution at each increment of elongation for Specimen 09-06267R: Posterior Capsule.

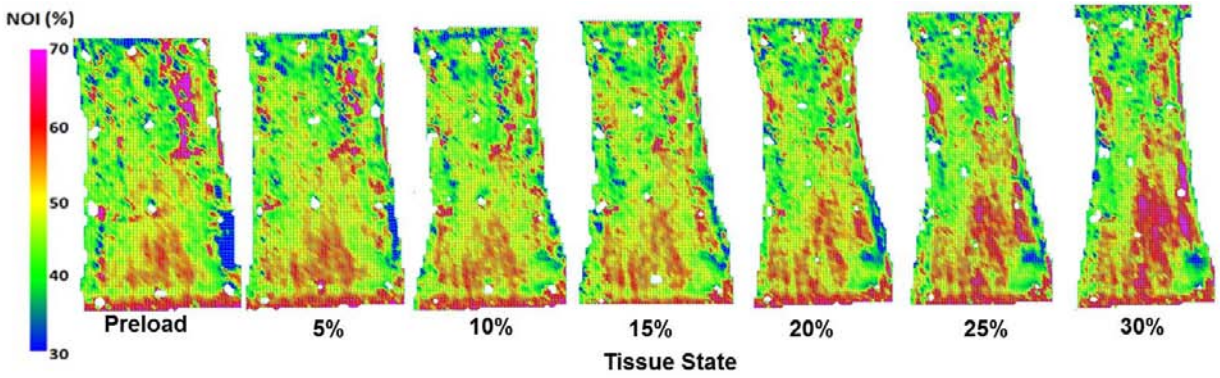

Figure 7.34 NOI distribution at each increment of elongation for Specimen 09-06267R: AB-IGHL.

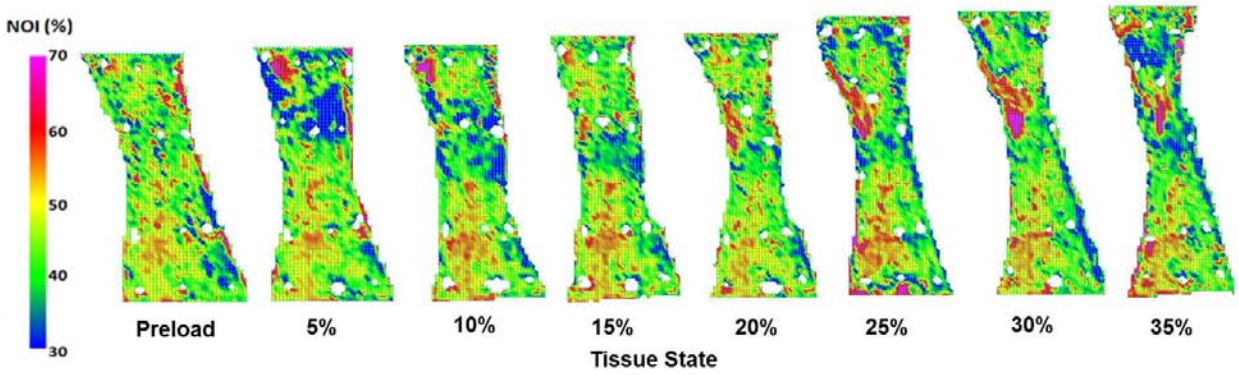

Figure 7.35 NOI distribution at each increment of elongation for Specimen 09-06267R: Anterosuperior Capsule.

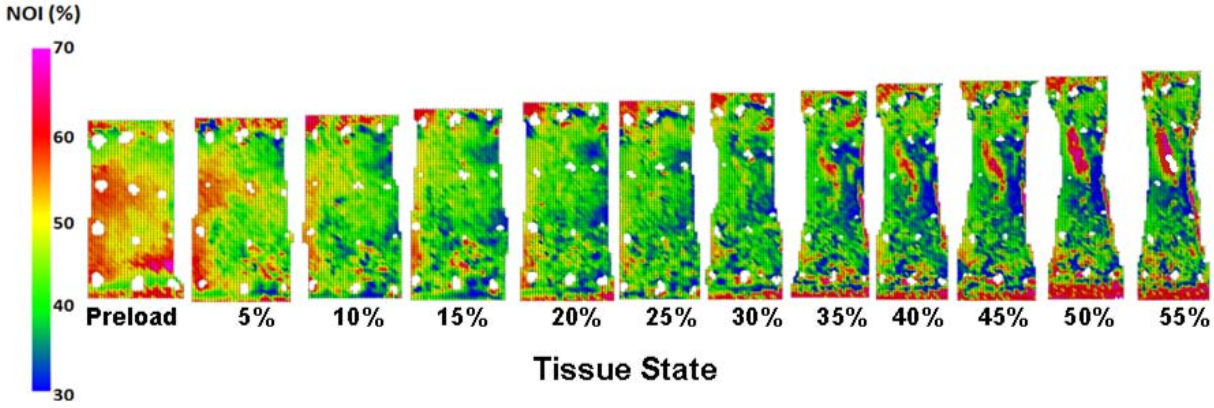

Figure 7.36 NOI distribution at each increment of elongation for Specimen 07-10874L: Axillary Pouch.

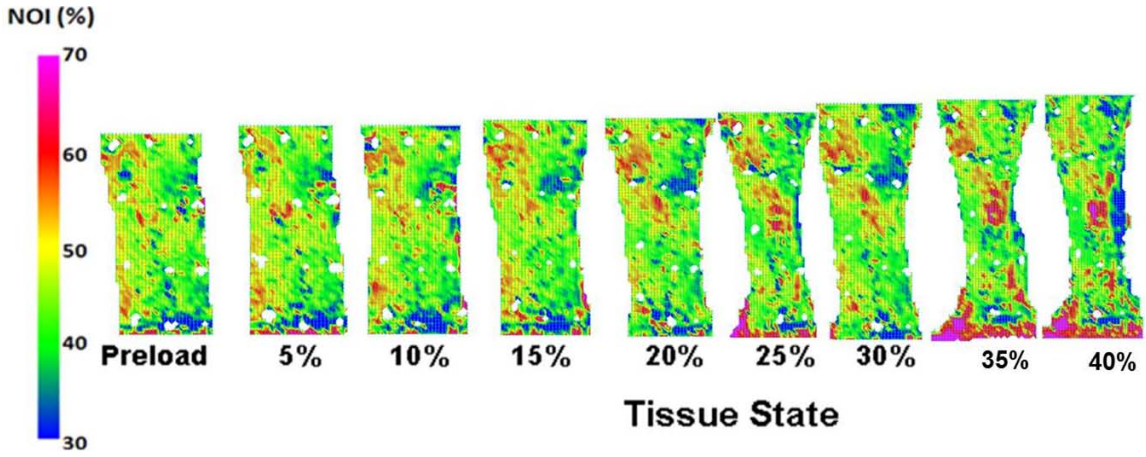

Figure 7.37 NOI distribution at each increment of elongation for Specimen 07-10874L: AB-IHGL.

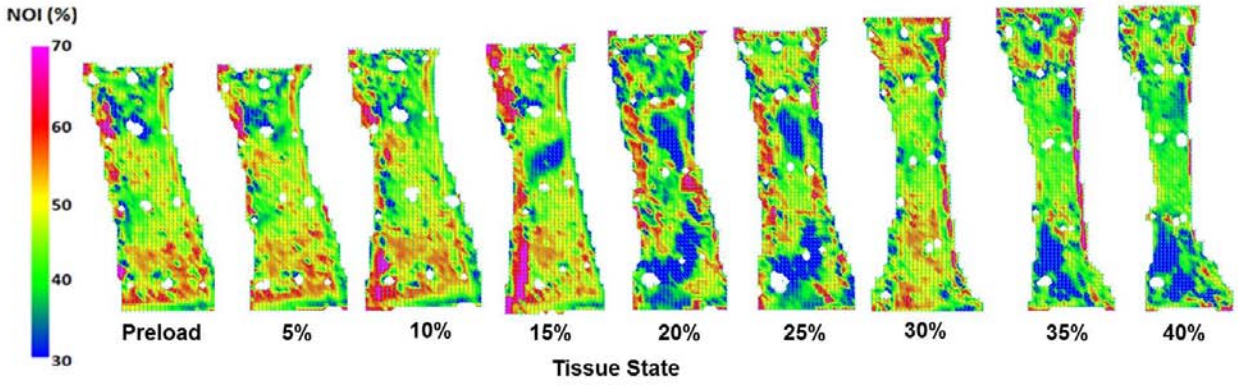

Figure 7.38 NOI distribution at each increment of elongation for Specimen 07-10874L: PB-IHGL.

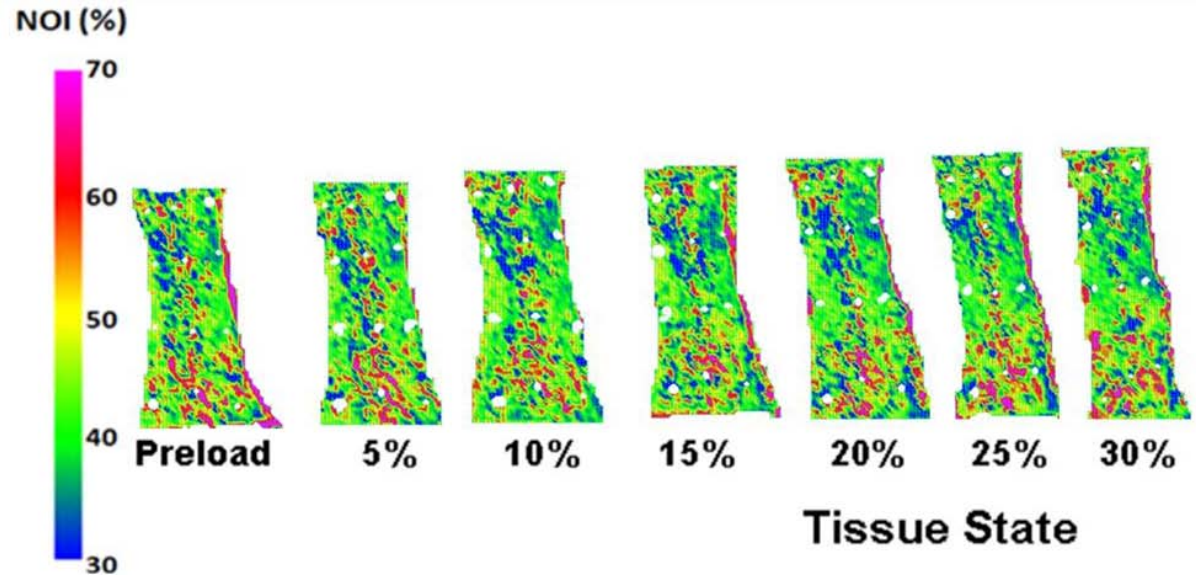

Figure 7.39 NOI distribution at each increment of elongation for Specimen 07-10874L: Anterosuperior Capsule.

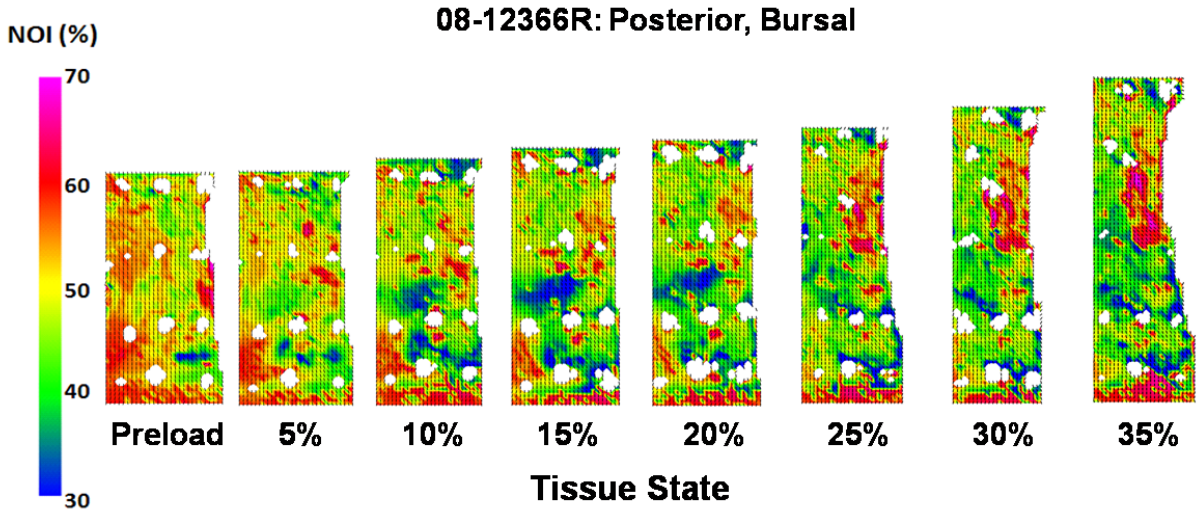

Figure 7.40 NOI distribution at each increment of elongation for Specimen 08-12366R: Posterior Capsule.

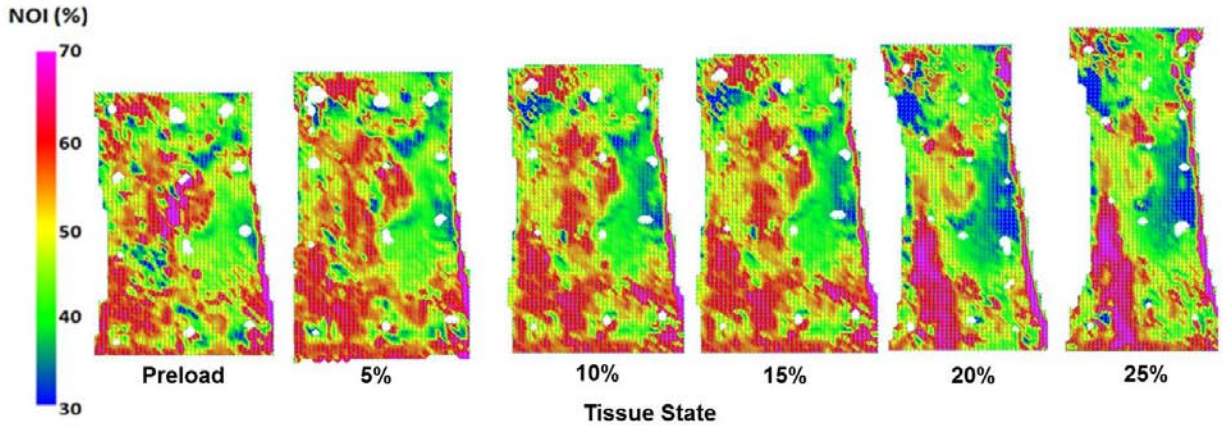

Figure 7.41 NOI distribution at each increment of elongation for Specimen 08-12366R: AB-IGHL.

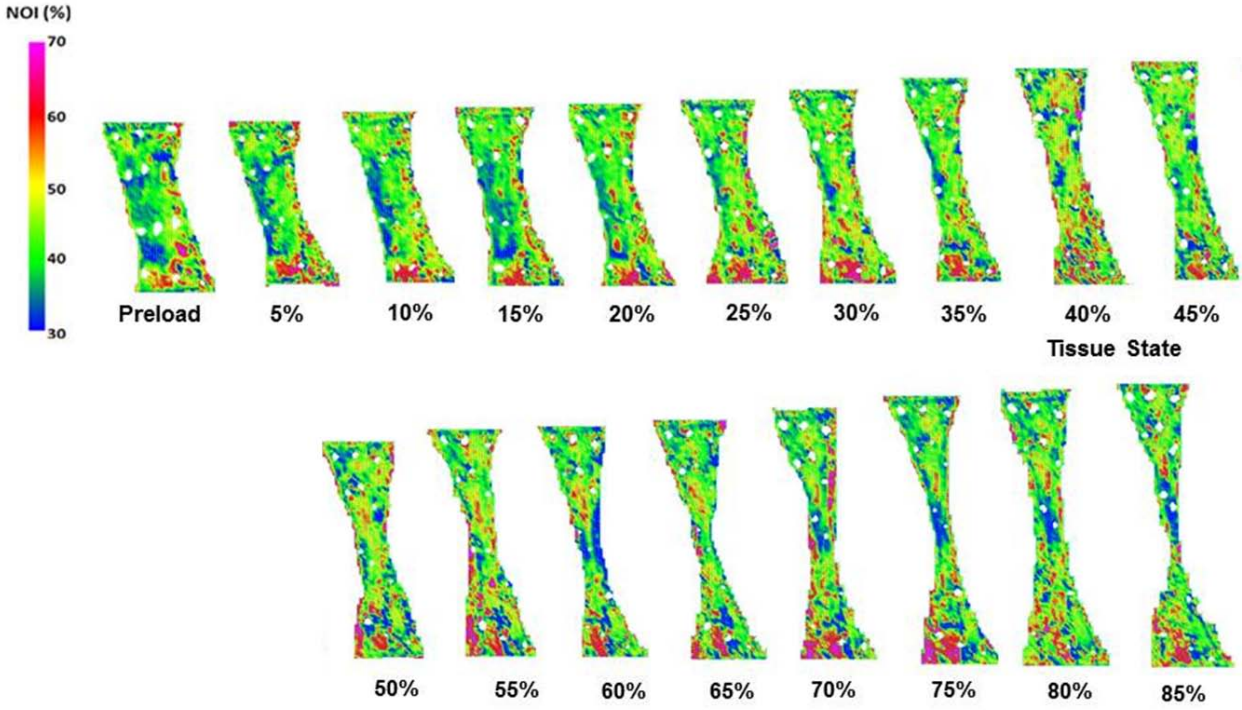

Figure 7.42 NOI distribution at each increment of elongation for Specimen 08-12366R: PB-IGHL.

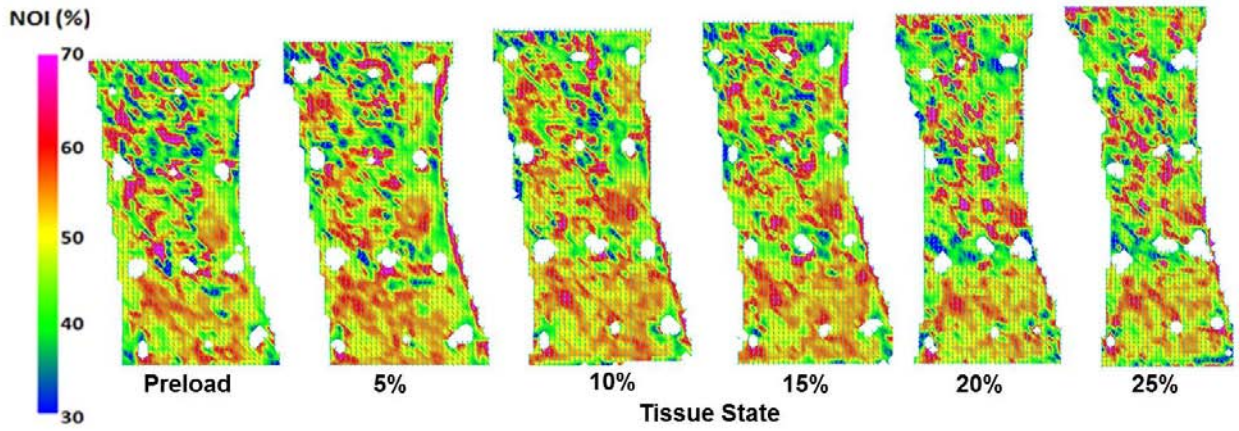

Figure 7.43 NOI distribution at each increment of elongation for Specimen 09-06278R: Axillary Pouch.

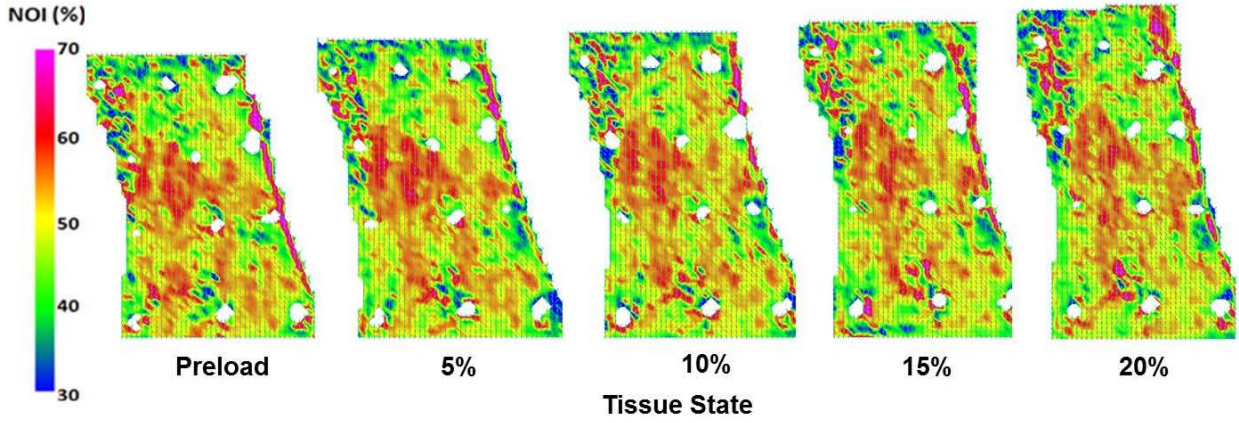

Figure 7.44 NOI distribution at each increment of elongation for Specimen 09-06278R: AB-IGHL.

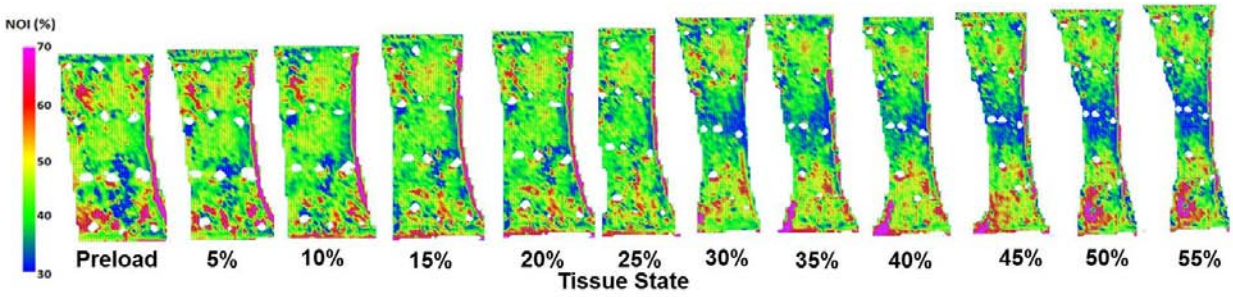

Figure 7.45 NOI distribution at each increment of elongation for Specimen 09-06278R: Anterosuperior Capsule.

APPENDIX C

MODIFIED ROBOT CODE

```
263 ;-------------------------------------------------------------
;Save passive GHIE angle (should be zero)
z.pghie = ghie
z.cycles = -3*(z.draw < 4)-(z.draw > 3)
SPEED 20  ALWAYS
TYPE /C1, /I3, 90-w.now, " Deg, Code", /I4, z.draw+600
TYPE "Cycle Load    ---- Forces, N  ----   Moments, N-m -- Rotate, deg   Keepers"
TYPE "   #   %   Left  Super  Proxim   mGHIE   GHIE     ", /F8.2, dleft, /S
8/18/10: CAV changed “dant” to “dleft” (dleft is anterior direction for shoulder)
FOR i = 0 TO 39
  z.best[207] = 9999
END
FOR z.cyc = 1 TO z.cycles
  FOR i = 0 TO 4
    z.stiff[i] = 100*(-(i < 3))-10*(i > 2)
  END
  FOR z.h = 1 TO -1 STEP -2; Positive\Negative
    TIMER 1 = 0
    FOR b = 0 TO 5
      z.flag[b] = 0; skips at discontinuity
      z.zero[b] = 0
    END
;deleted code   MOVE #knee[20+w.now]
;delete more code   BREAK
    FOR z.s = 1 TO 19; Step
IF z.s == 1 THEN
  z.ghie = z.pghie
ELSE
  z.ghie = ghie
END
```

```
z.step = 20+z.s*z.h
IF (z.cyc > 1) AND (z.draw < 4) THEN; go to previous pt. & stiffness
  IF z.flag[11]==2 THEN
    MOVE #z[z.step]
    BREAK
  ELSE
    MOVE #a[z.step]
  END
  FOR l = 0 TO 4
    z.stiff[208] = z.sti[l]
  END
END
z.ct = 0

266 ;-----------------------------------------------------------
z.d = DISTANCE(z.p0, z.p1)
z.e = ABS(ghie-z.t)
IF (TIMER(1) < ABS(z.d)/w.rate) AND (z.draw > 3) GOTO 264
IF (TIMER(1) < ABS(z.d)/w.rate) AND (z.cyc > 1) AND (z.draw < 4) GOTO 264
z.rfa = SQRT(SQR(fa[0])+SQR(fa[1])+SQR(fa[207])); resultant
z.rma = fa[208]
IF z.draw < 4 THEN; evaluate
IF z.ct < -5*(z.cyc == 1)-6*(z.cyc > 1)-10*(z.s == 0) GOTO 264
FOR l = 0 TO 4
  z.sti[l] = z.stiff[l]
END
IF (z.cyc < 3) OR (z.rfa+z.rma*z.minf/z.minm < z.best[z.step]) THEN
  HERE #z[z.step]
  HERE #a[z.step]  ;for ER/IR (step to extreme) loop
END
END; code 1 or 2 or 3
i = (per[ABS(z.step-20)])*(SIGN(z.step-20))
CASE ABS(z.step-20) OF
  VALUE 1, 3, 5, 7, 9, 11, 13, 15, 17, 19:
  TYPE " ", /C1, /I5, z.cyc, i, /F8.1, fleft, fant, fdist, /S
  TYPE /F8.2, mghie, ghie, /I5, z.ct, "x", /F8.2, dleft
```

8/18/10 CAV changed “dant” to “dleft” (“dleft” is anterior for shoulder), prints out anterior translation after each loading step

```
  PROMPT "Carrie, Do you want to proceed? (0 = Proceed, 1 = STOP)", z.proceed1
  IF z.proceed1 == 1 THEN
    HALT
  END
```

8/4/10 CAV & RED added this code to ask the user whether or not they want to continue after each loading step. Enter yes (0) if the anterior translation does not equal the translation required for dislocation. Enter no (1) if desired anterior translation has been reached to exit program.

```
END
IF (z.cyc < 3) OR (z.rfa+z.rma*z.minf/z.minm < z.best[z.step]) GOTO 269
```

APPENDIX D

JOINT KINEMATICS DURING DISLOCATION

Table 7.1 Joint kinematics during dislocation for specimen H00915L.

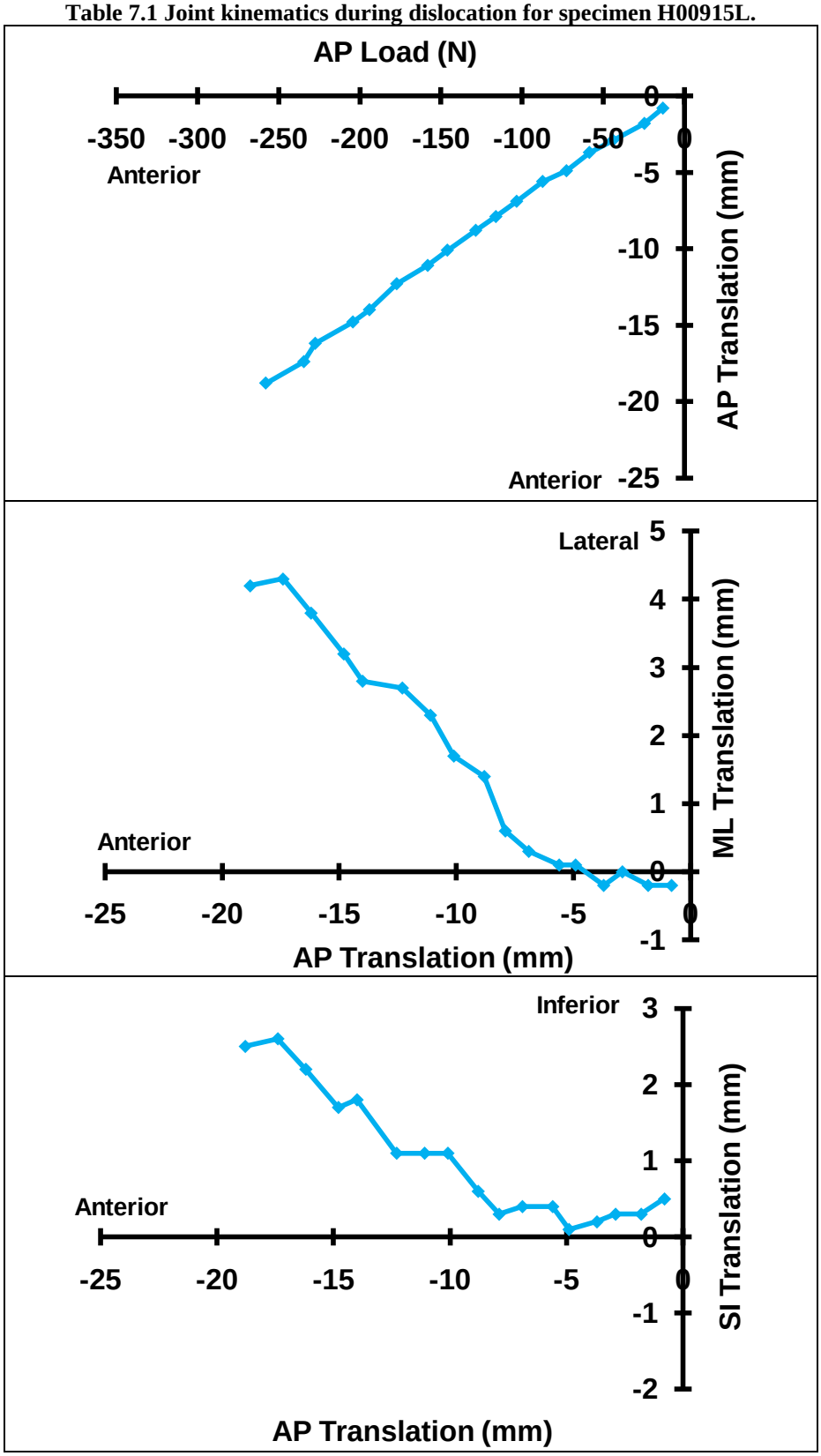

Table 7.2 Joint kinematics during dislocation for specimen H00925R.

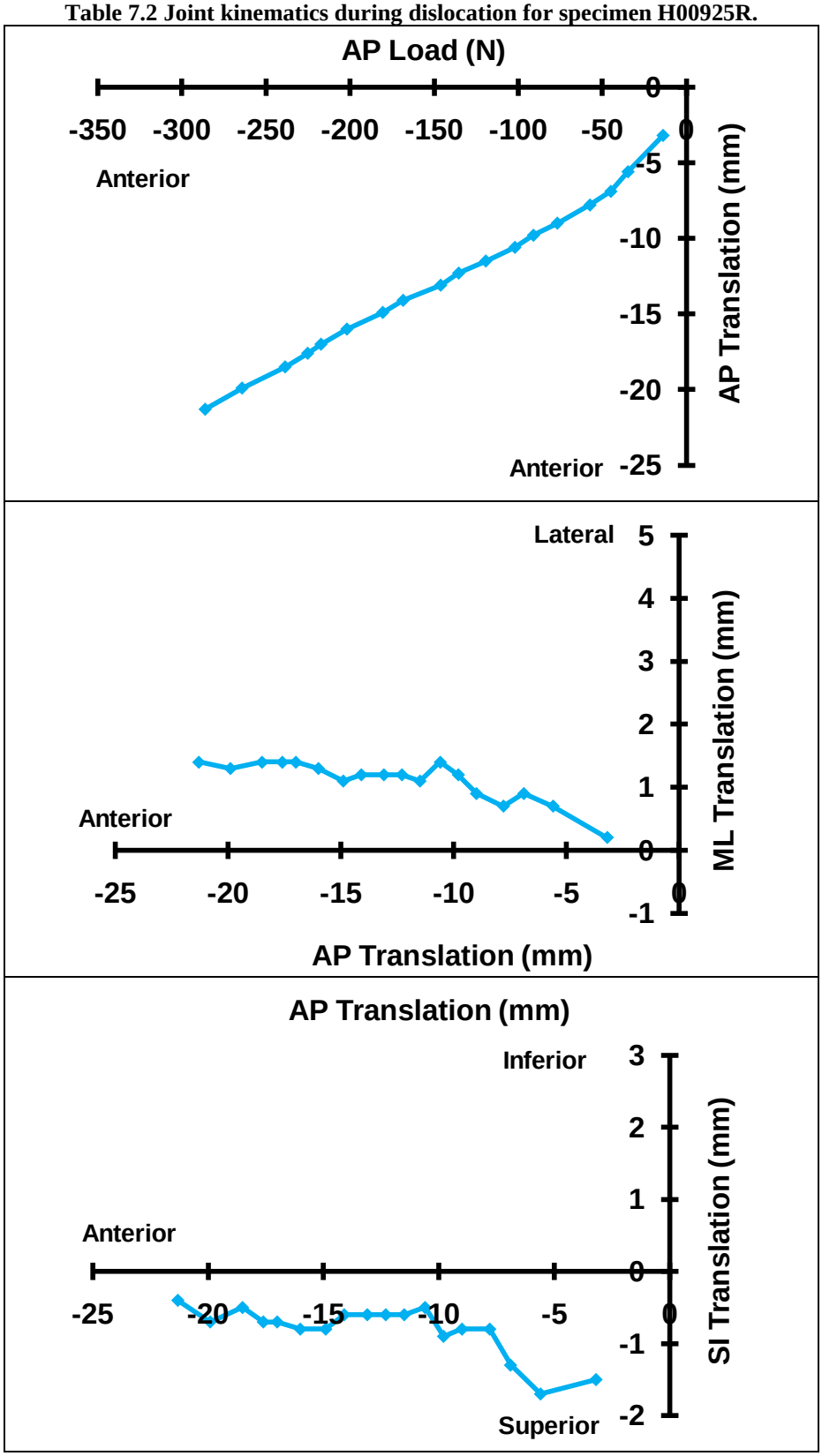

Table 7.3 Joint kinematics during dislocation for specimen H01015R.

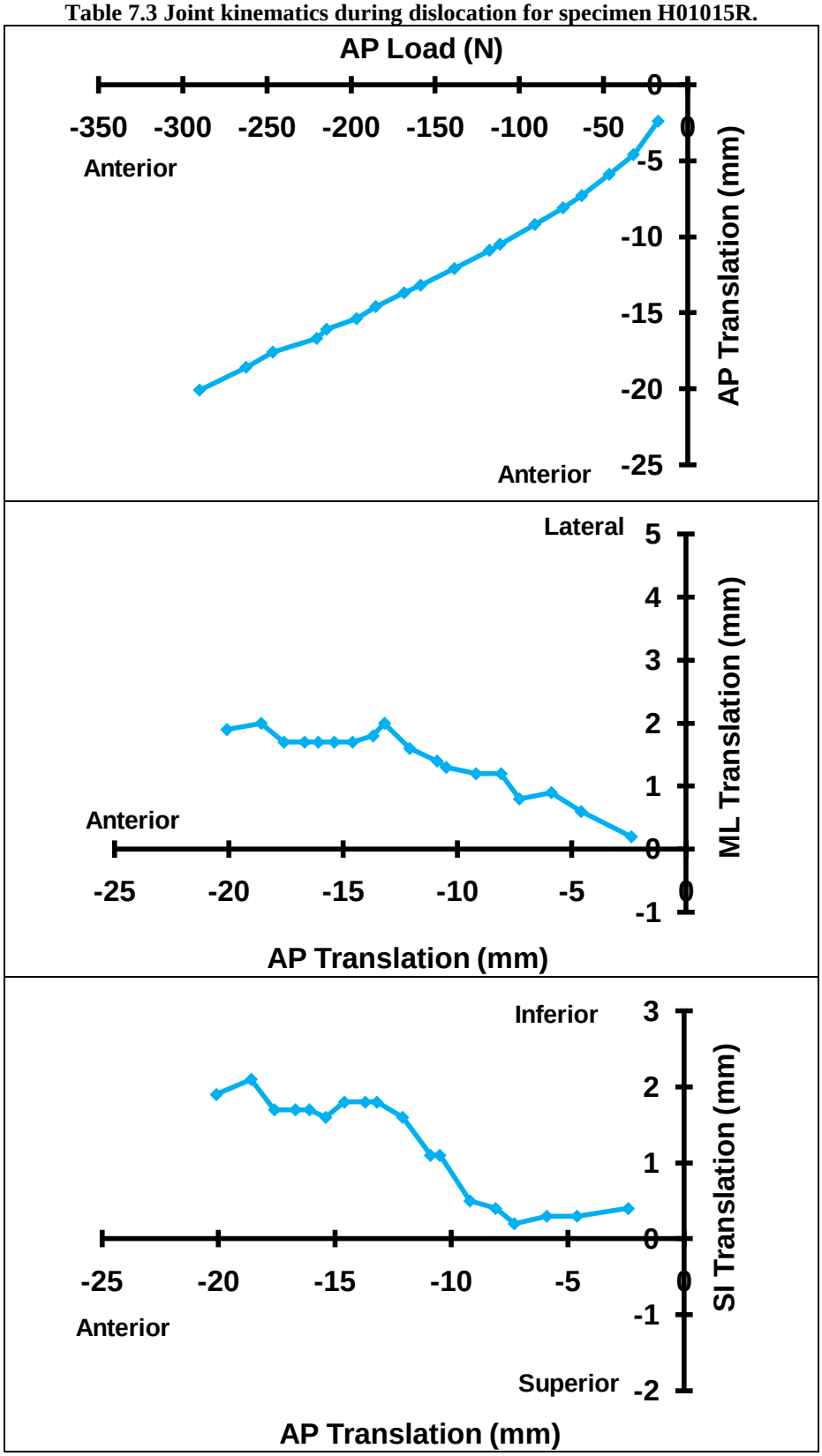

Table 7.4 Joint kinematics during dislocation for specimen H01022L.

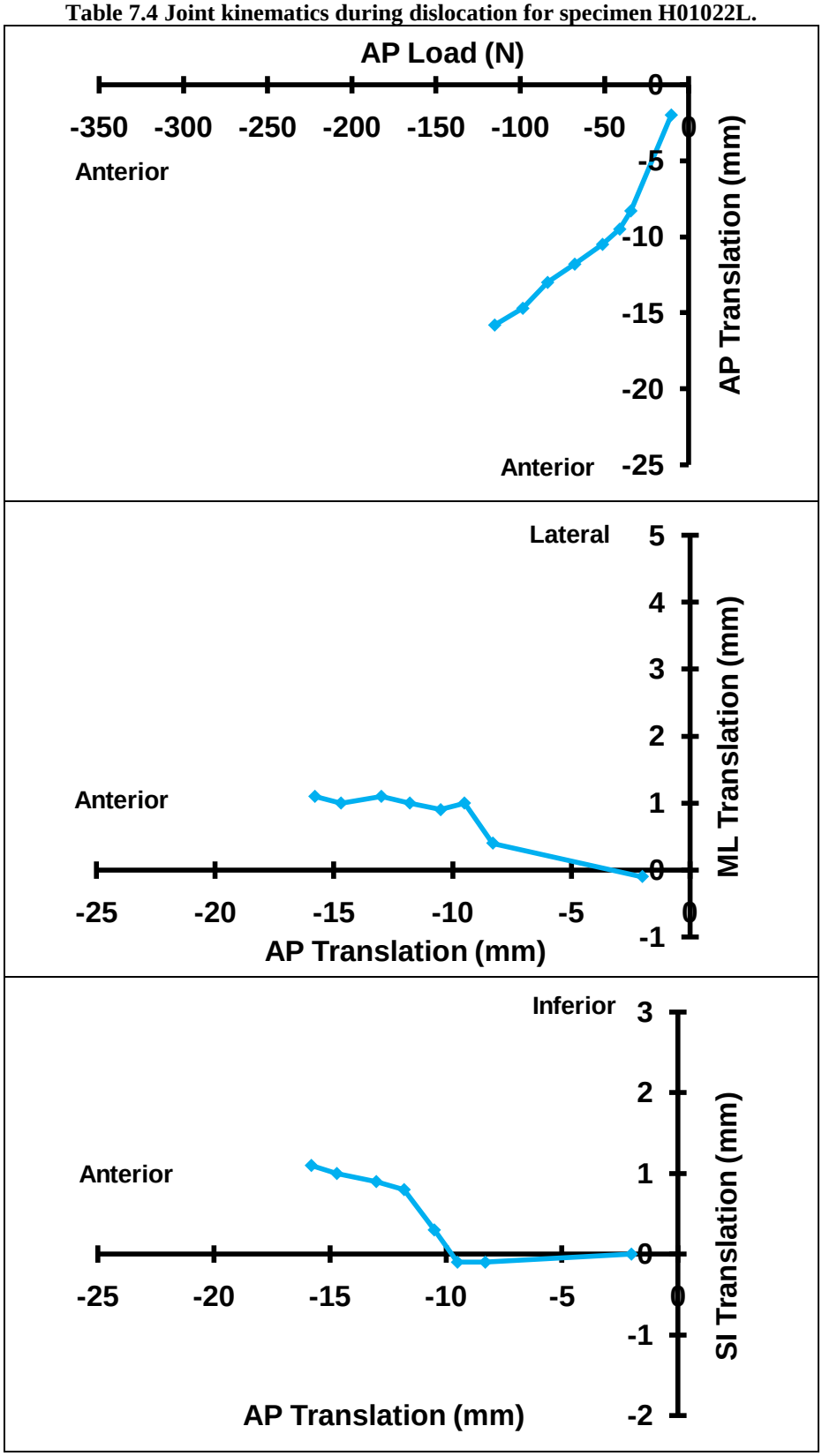

Table 7.5 Joint kinematics during dislocation for specimen H01029L.

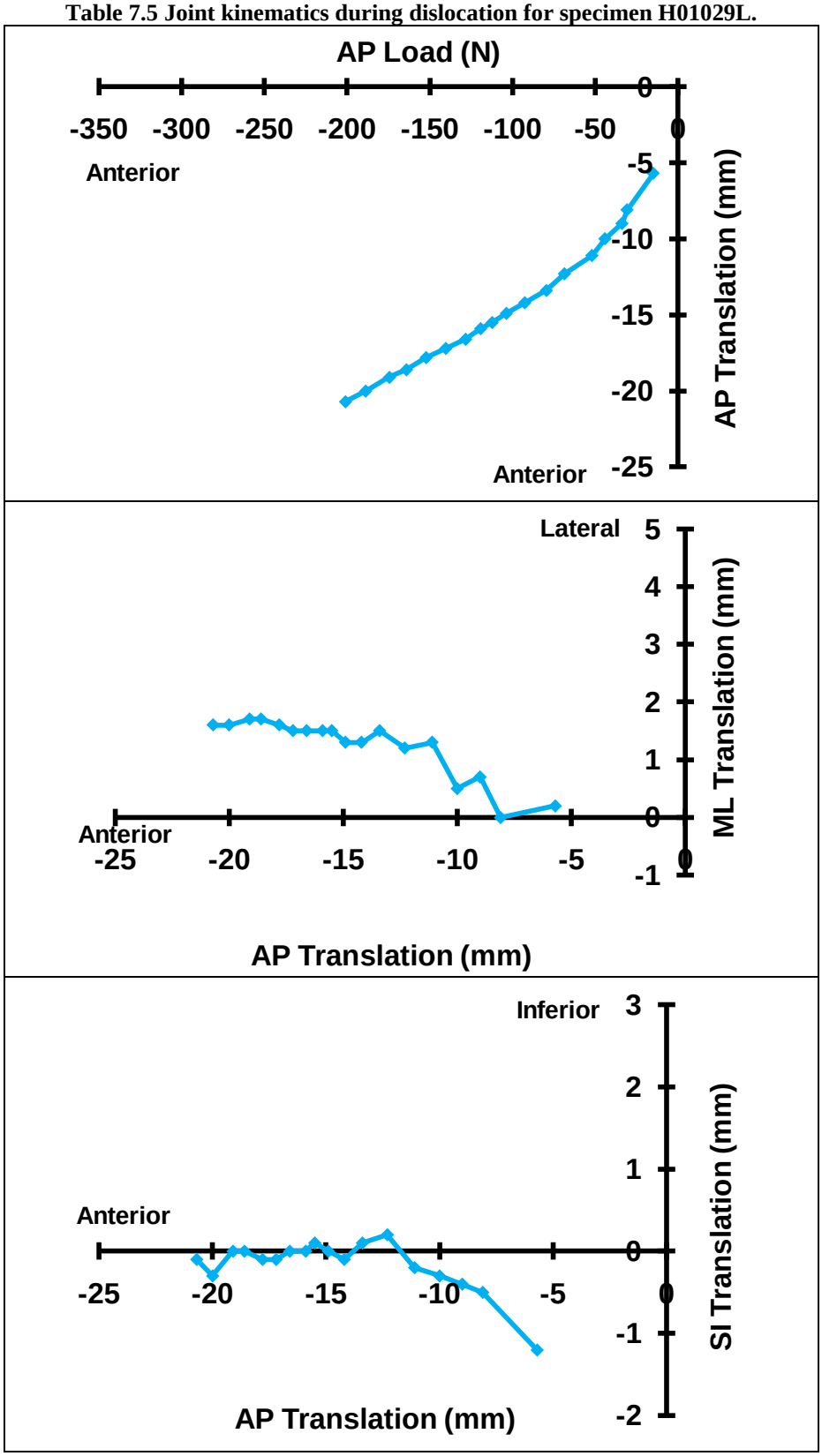

Table 7.6 Joint kinematics during dislocation for specimen H01107R.

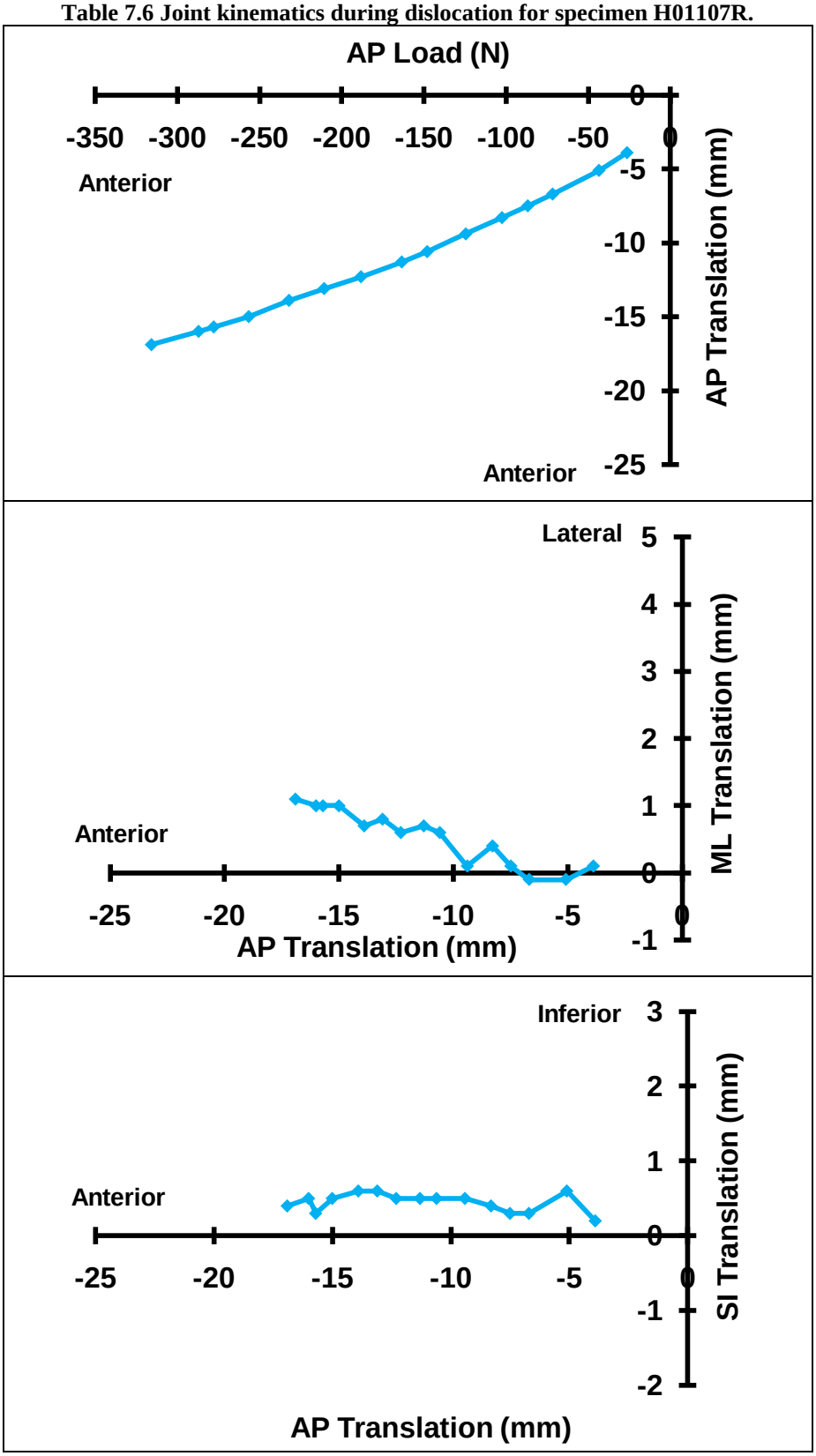

APPENDIX E

ANTERIOR-POSTERIOR JOINT KINEMATICS

Table 7.7 Anterior-posterior translation versus anterior-posterior load at 60° of abduction and 0°, 30° and 60° of external rotation for Specimen H00915L.

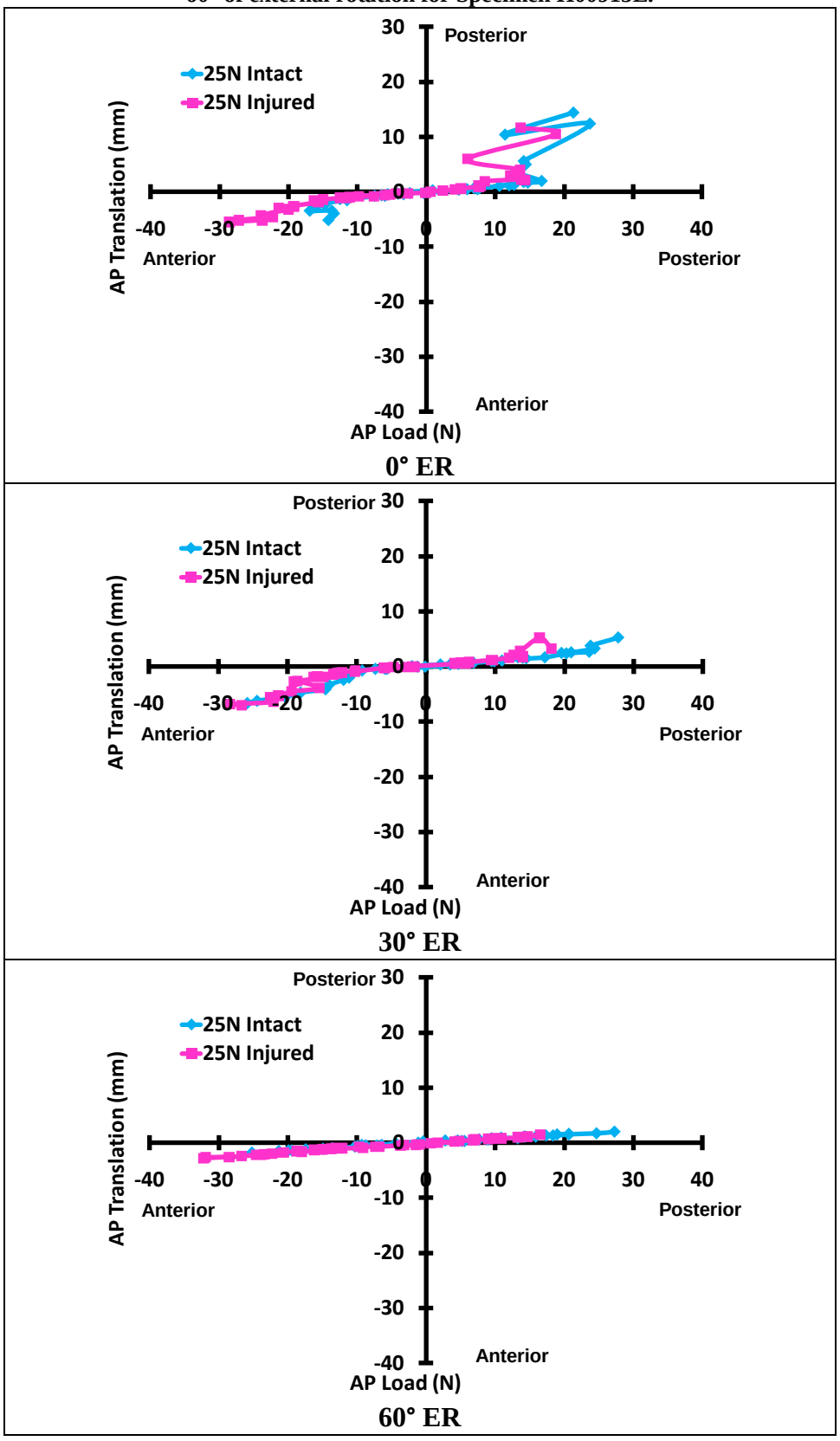

Table 7.8 Anterior-posterior translation versus anterior-posterior load at 60° of abduction and 0°, 30° and 60° of external rotation for Specimen H00925R.

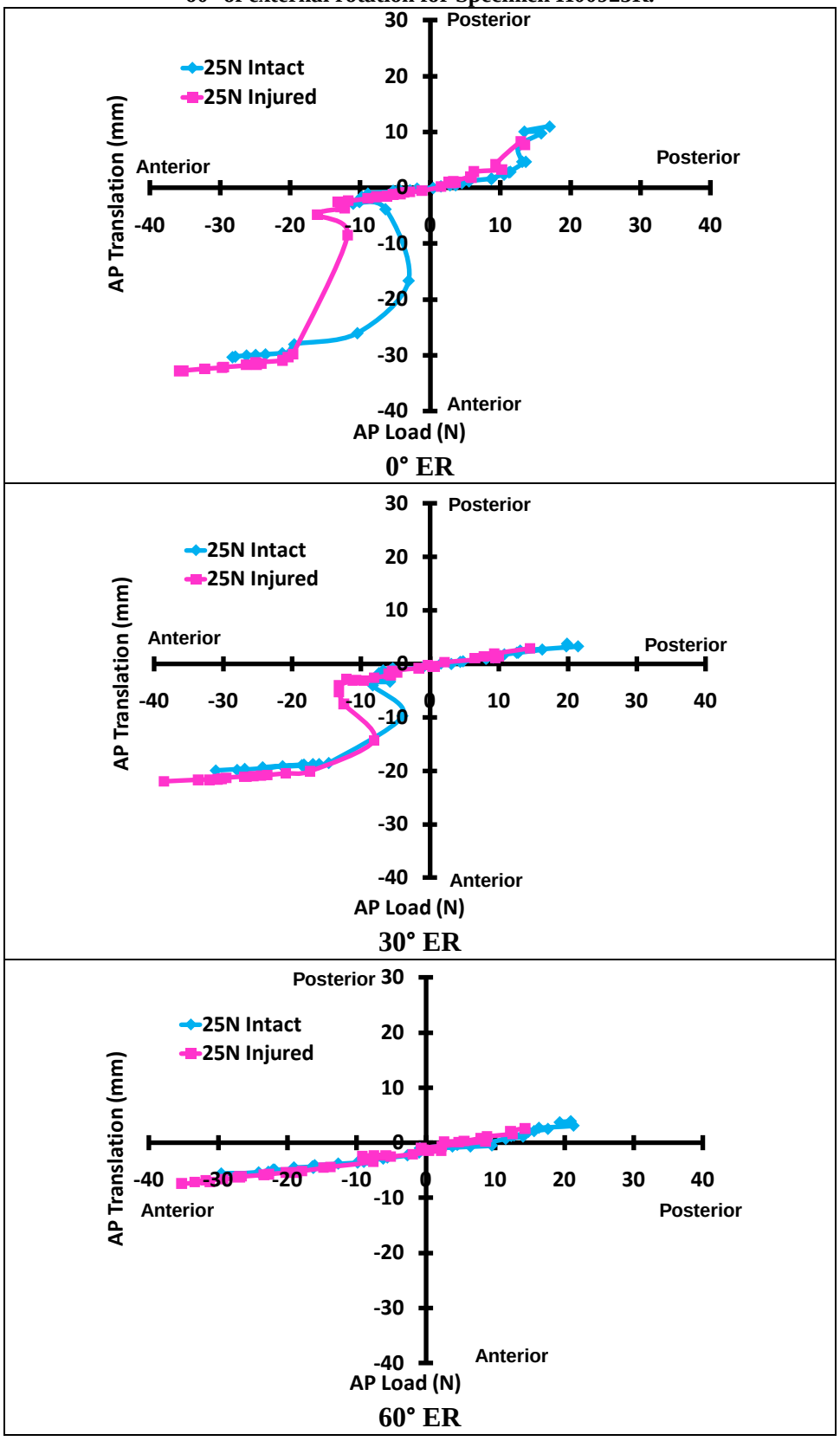

Table 7.9 Anterior-posterior translation versus anterior-posterior load at 60° of abduction and 0°, 30° and 60° of external rotation for Specimen H01015R.

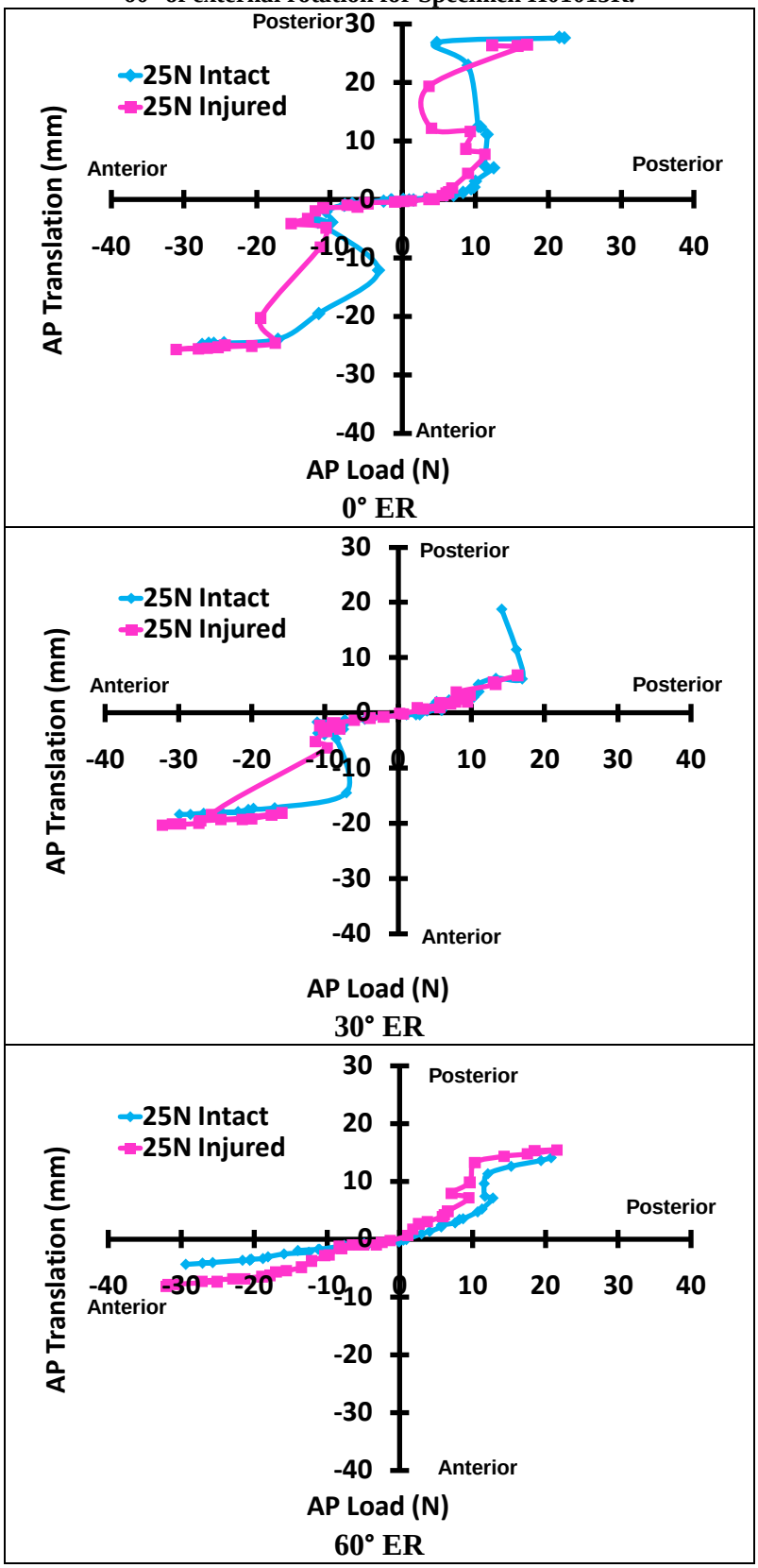

Table 7.10 Anterior-posterior translation versus anterior-posterior load at 60° of abduction and 0°, 30° and 60° of external rotation for Specimen H01022L.

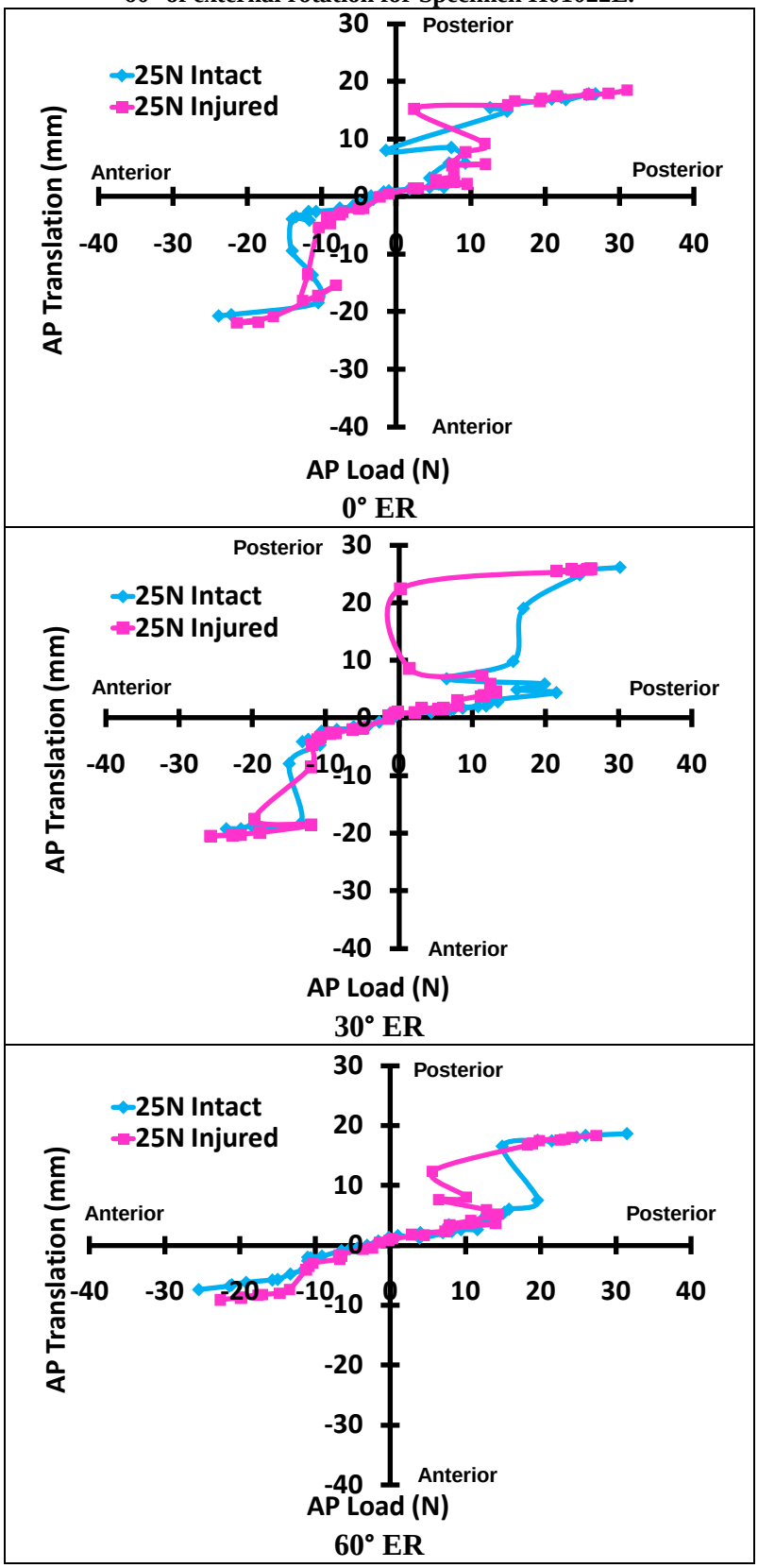

Table 7.11 Anterior-posterior translation versus anterior-posterior load at 60° of abduction and 0°, 30° and 60° of external rotation for Specimen H01029L.

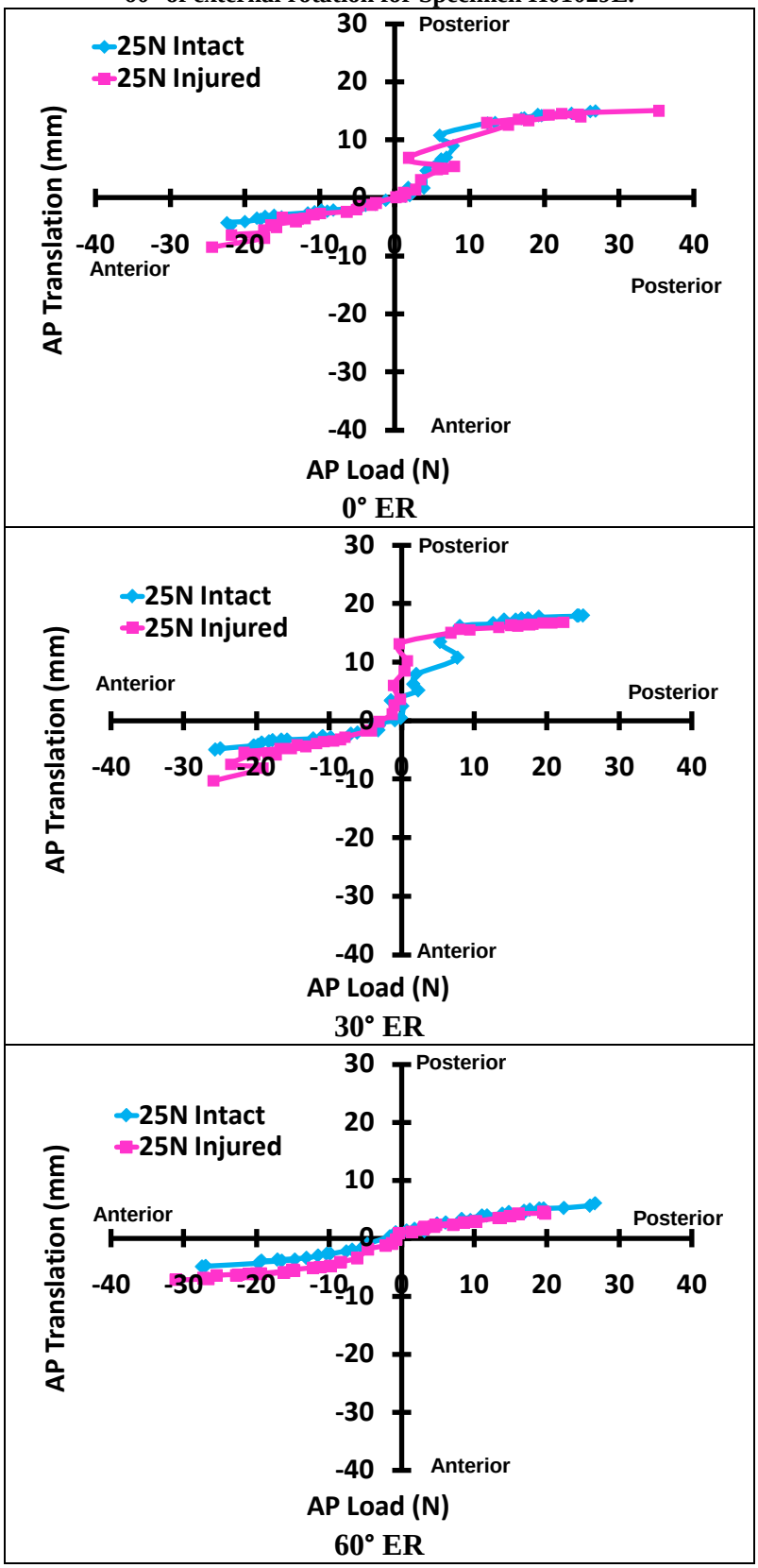

Table 7.12 Anterior-posterior translation versus anterior-posterior load at 60° of abduction and 0°, 30° and 60° of external rotation for Specimen H01107R.

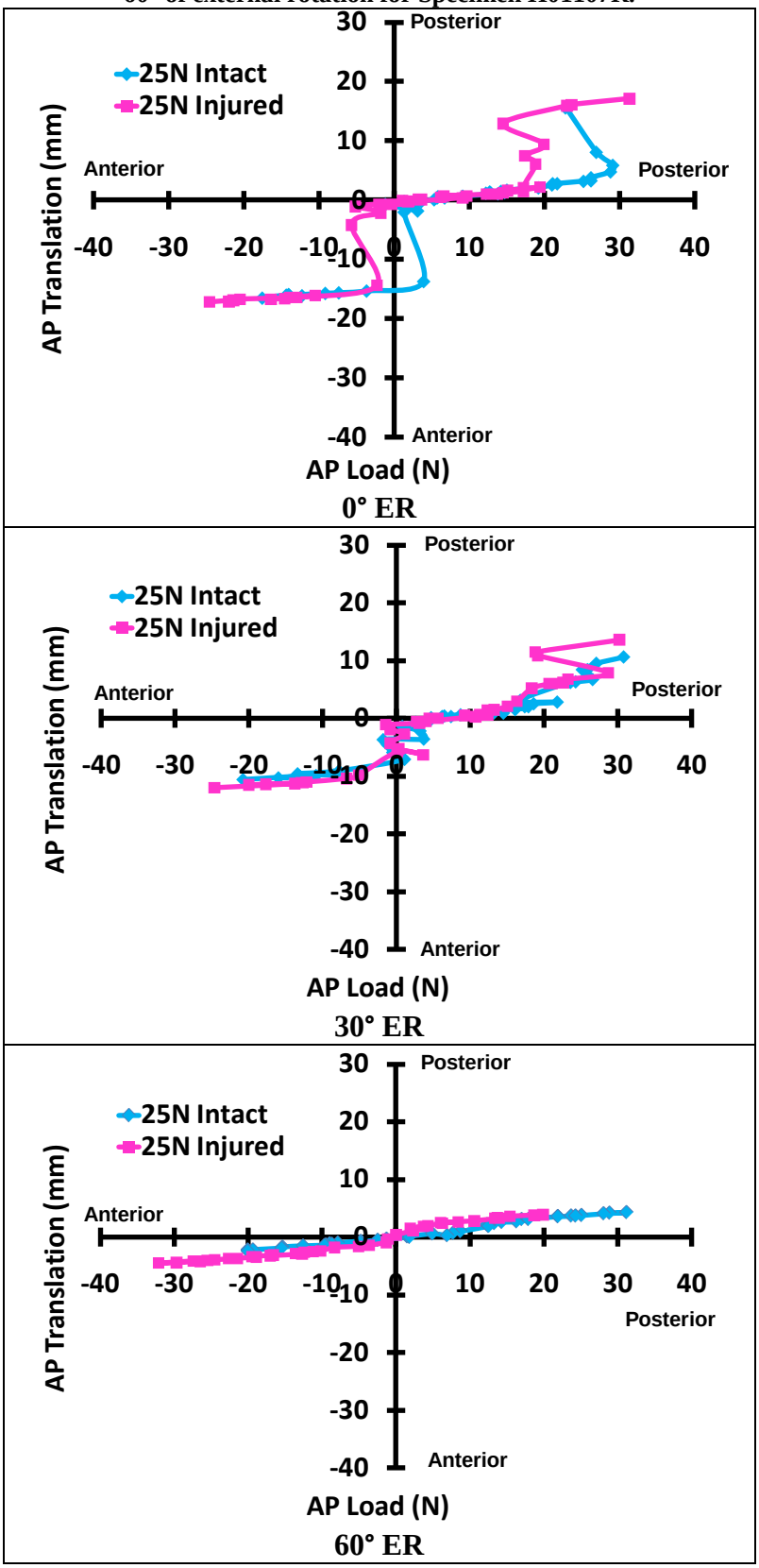

APPENDIX F

SUPERIOR-INFERIOR JOINT KINEMATICS

Table 7.13 Superior-inferior translation versus anterior-posterior load at 60° of abduction and 0°, 30° and 60° of external rotation for Specimen H00915L.

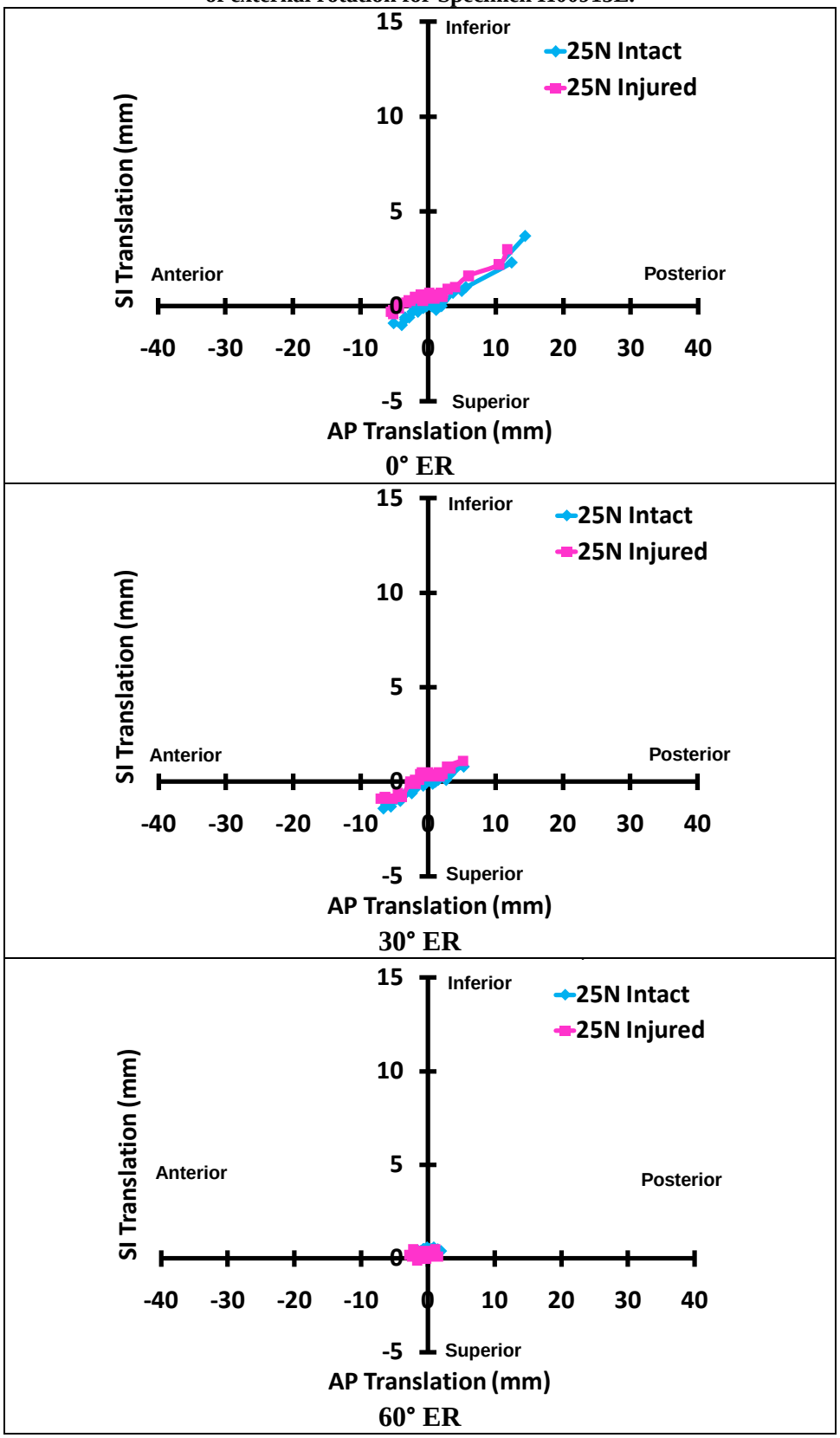

Table 7.14 Superior-inferior translation versus anterior-posterior load at 60° of abduction and 0°, 30° and 60° of external rotation for Specimen H00925R.

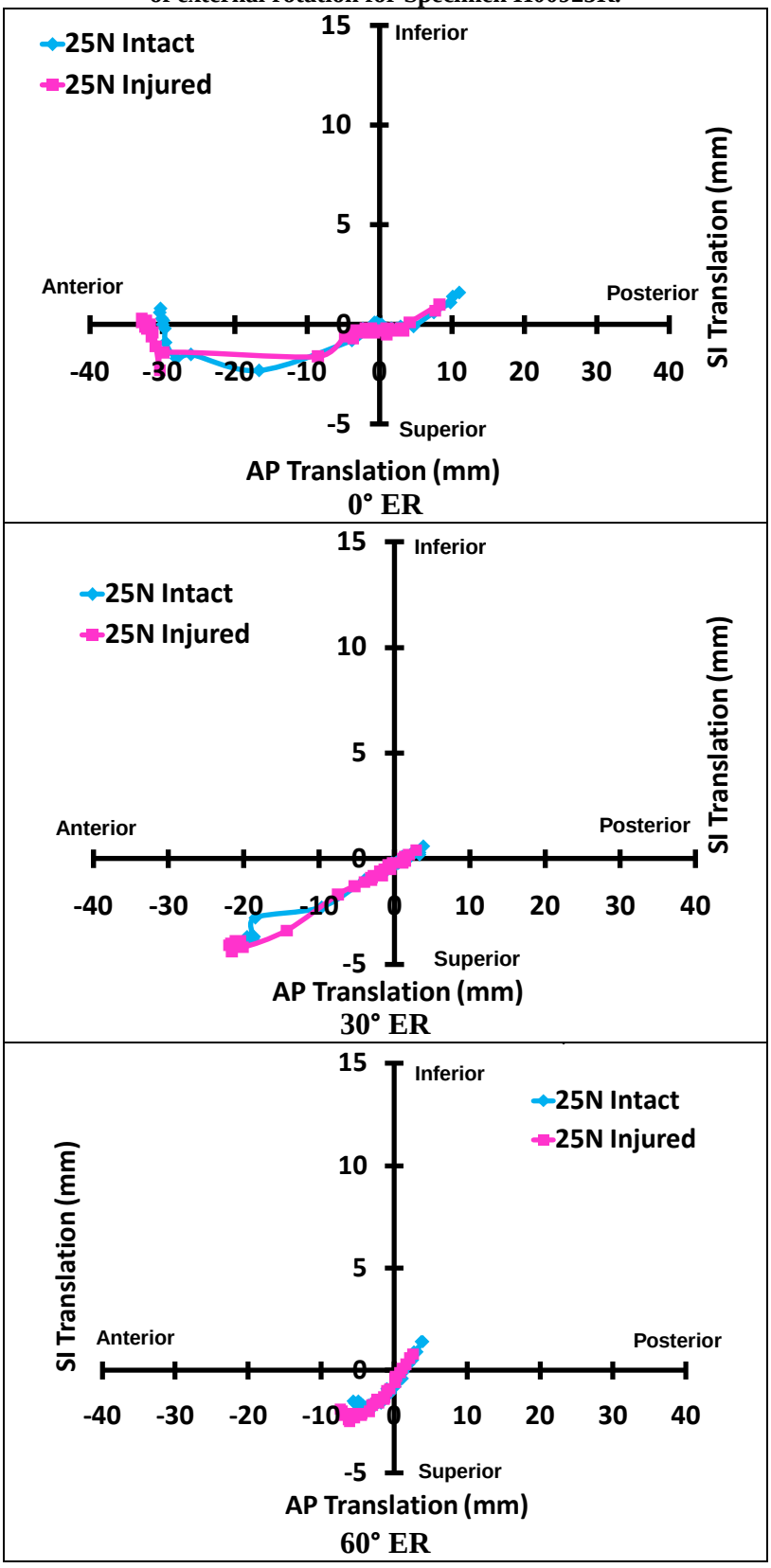

Table 7.15 Superior-inferior translation versus anterior-posterior load at 60° of abduction and 0°, 30° and 60° of external rotation for Specimen H01015R.

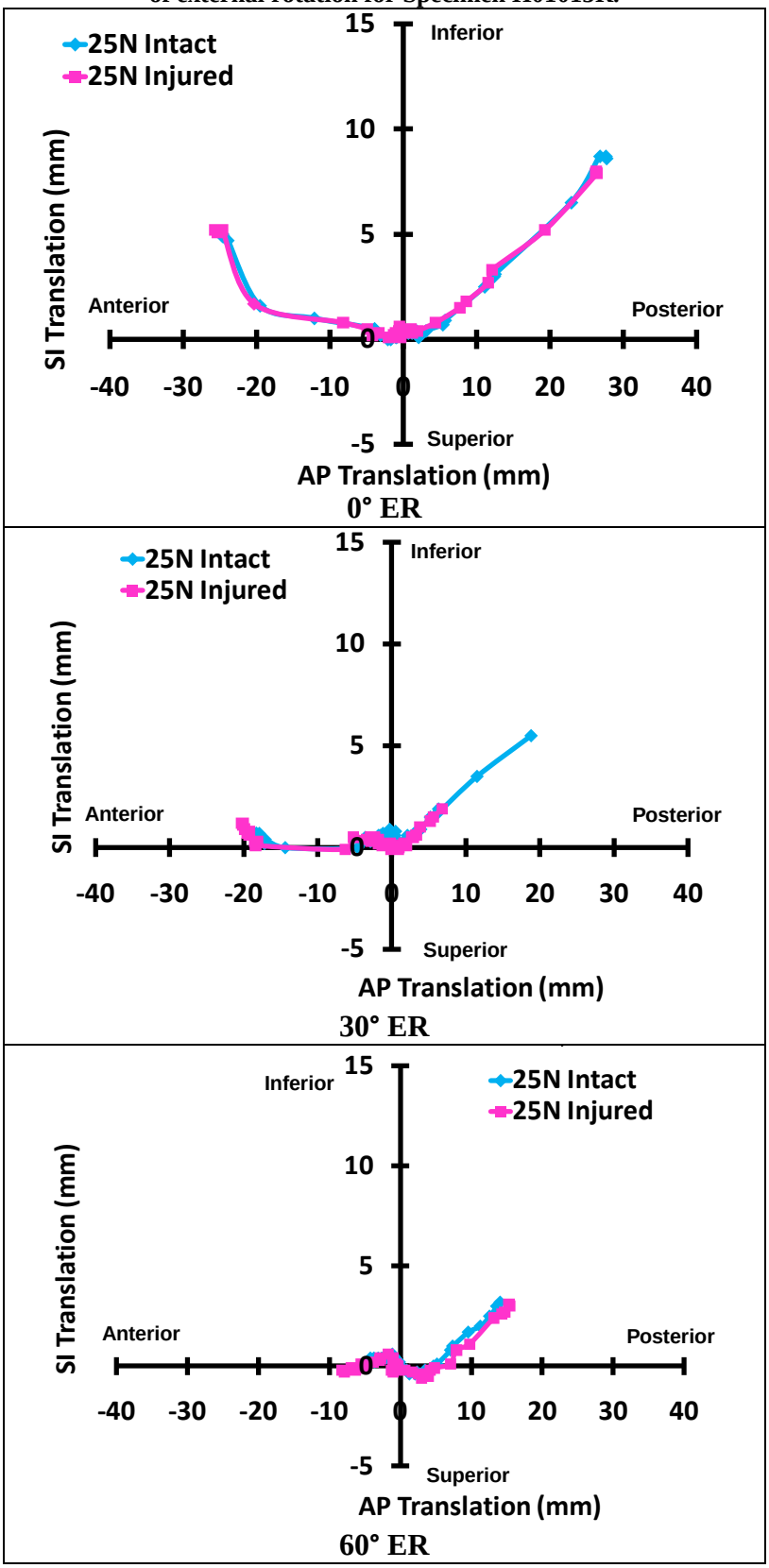

Table 7.16 Superior-inferior translation versus anterior-posterior load at 60° of abduction and 0°, 30° and 60° of external rotation for Specimen H01022L.

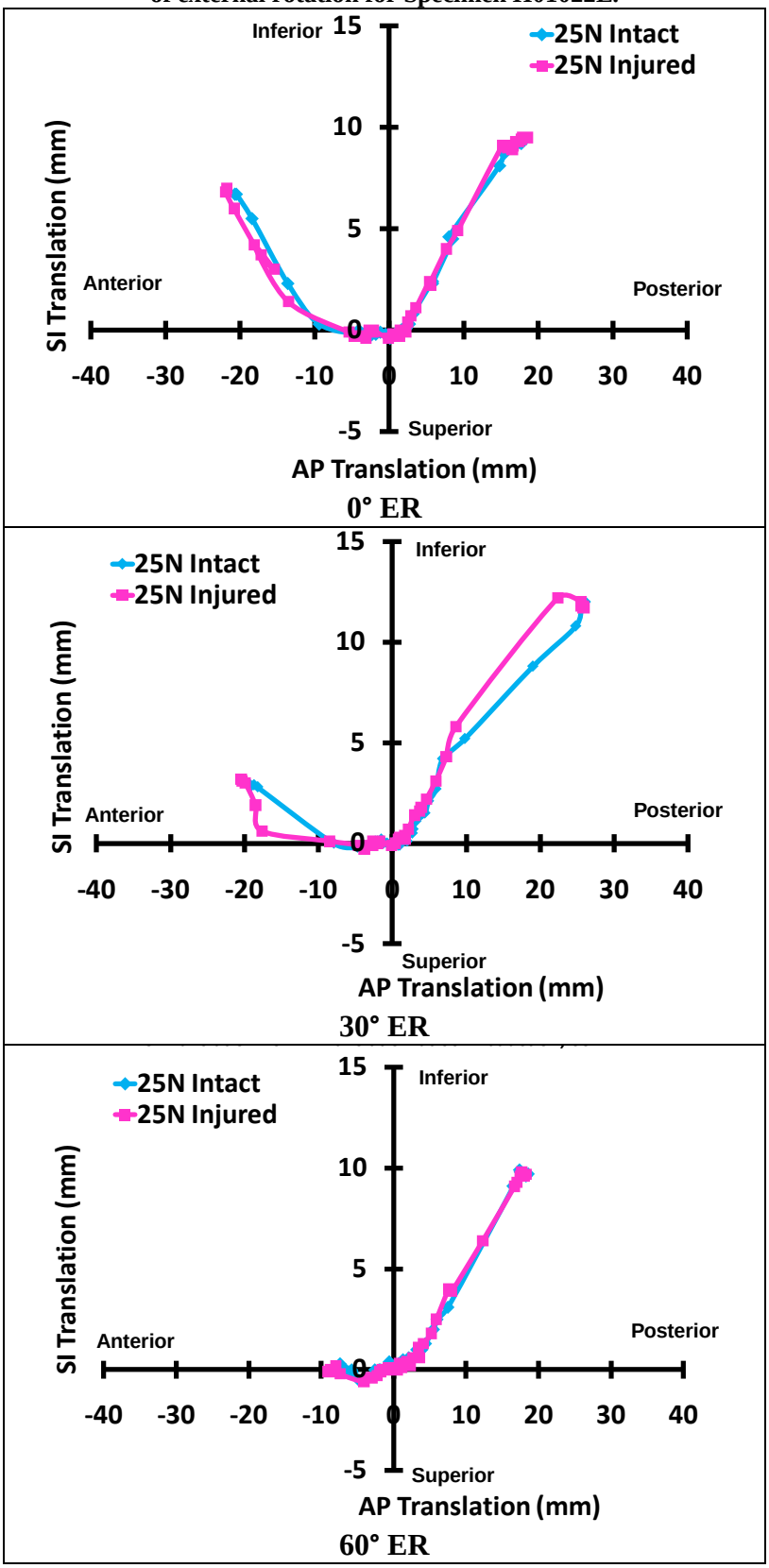

Table 7.17 Superior-inferior translation versus anterior-posterior load at 60° of abduction and 0°, 30° and 60° of external rotation for Specimen H01029L.

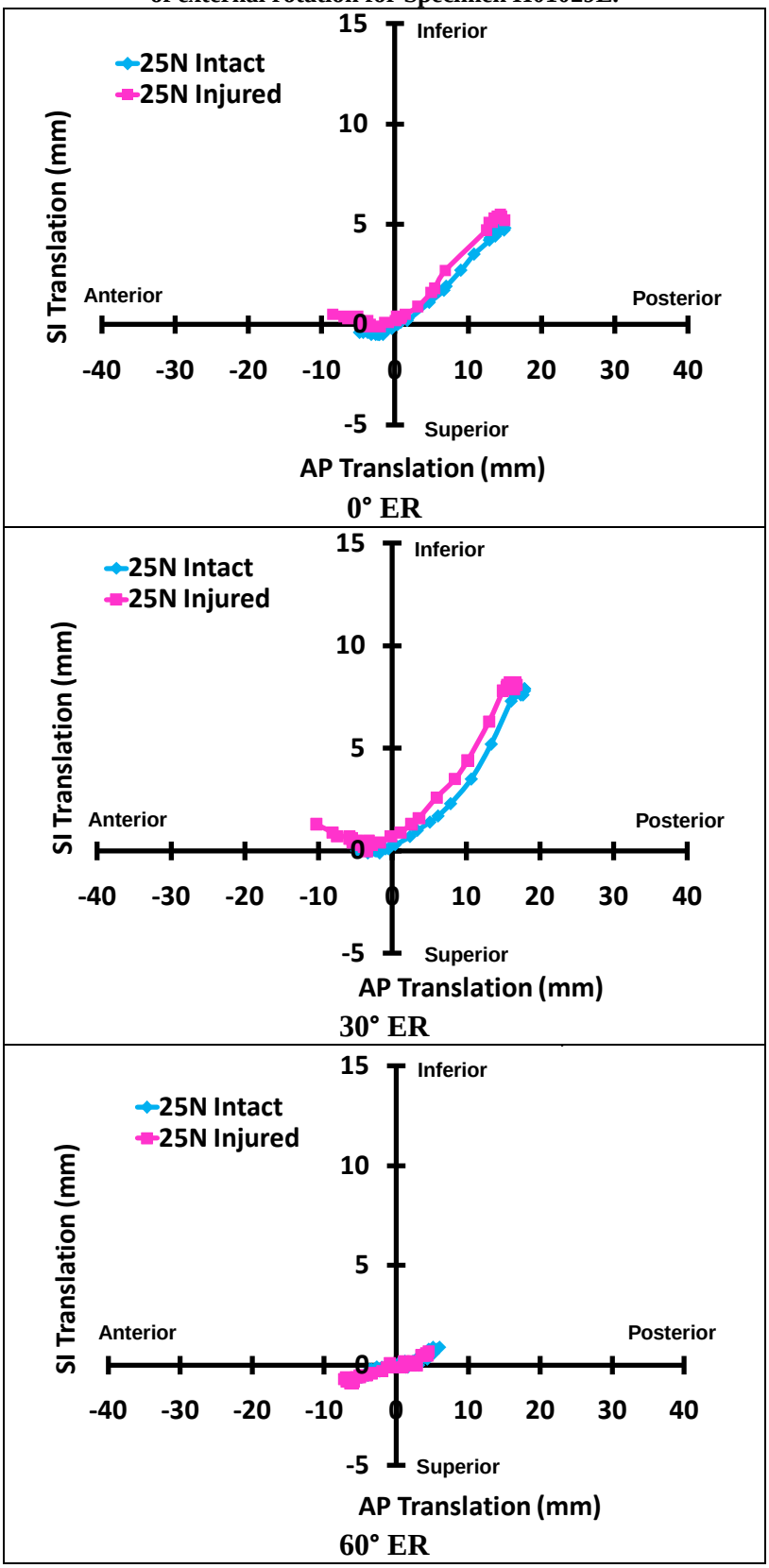

Table 7.18 Superior-inferior translation versus anterior-posterior load at 60° of abduction and 0°, 30° and 60° of external rotation for Specimen H01107R.

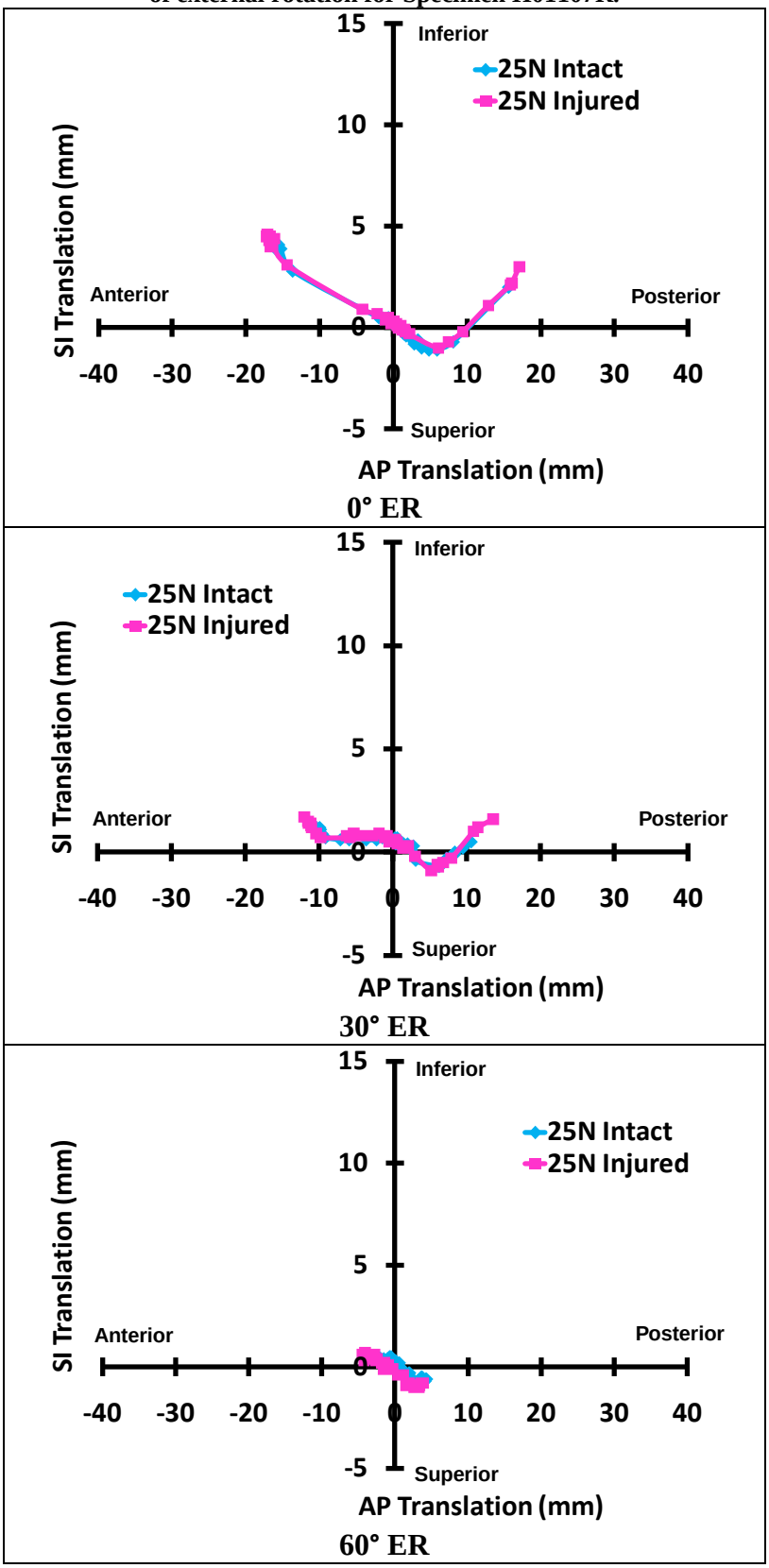

APPENDIX G

MEDIAL-LATERAL JOINT KINEMATICS

Table 7.19 Medial-lateral translation versus anterior-posterior load at 60° of abduction and 0°, 30° and 60° of external rotation for Specimen H00915L.

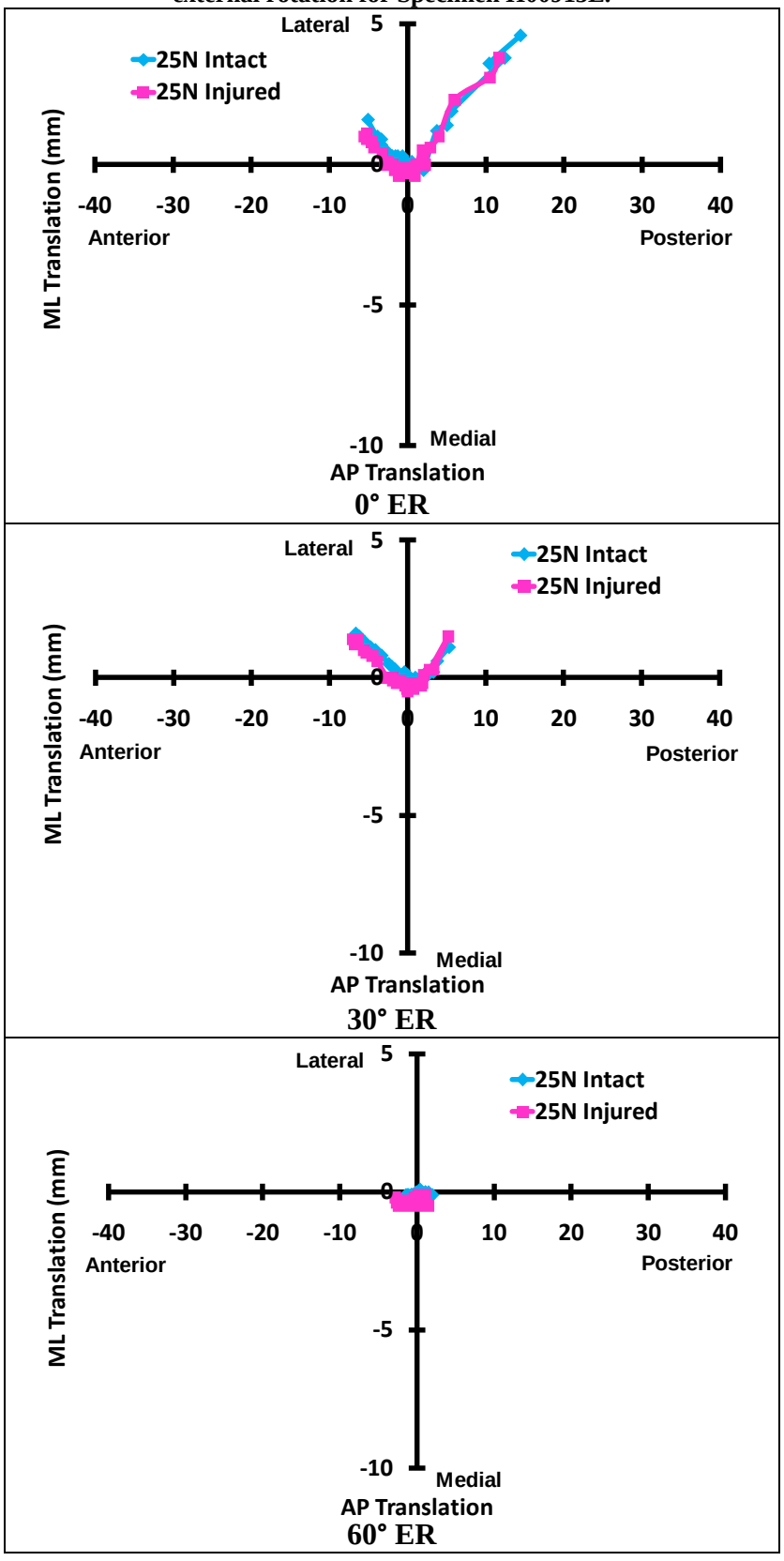

Table 7.20 Medial-lateral translation versus anterior-posterior load at 60° of abduction and 0°, 30° and 60° of external rotation for Specimen H00925R.

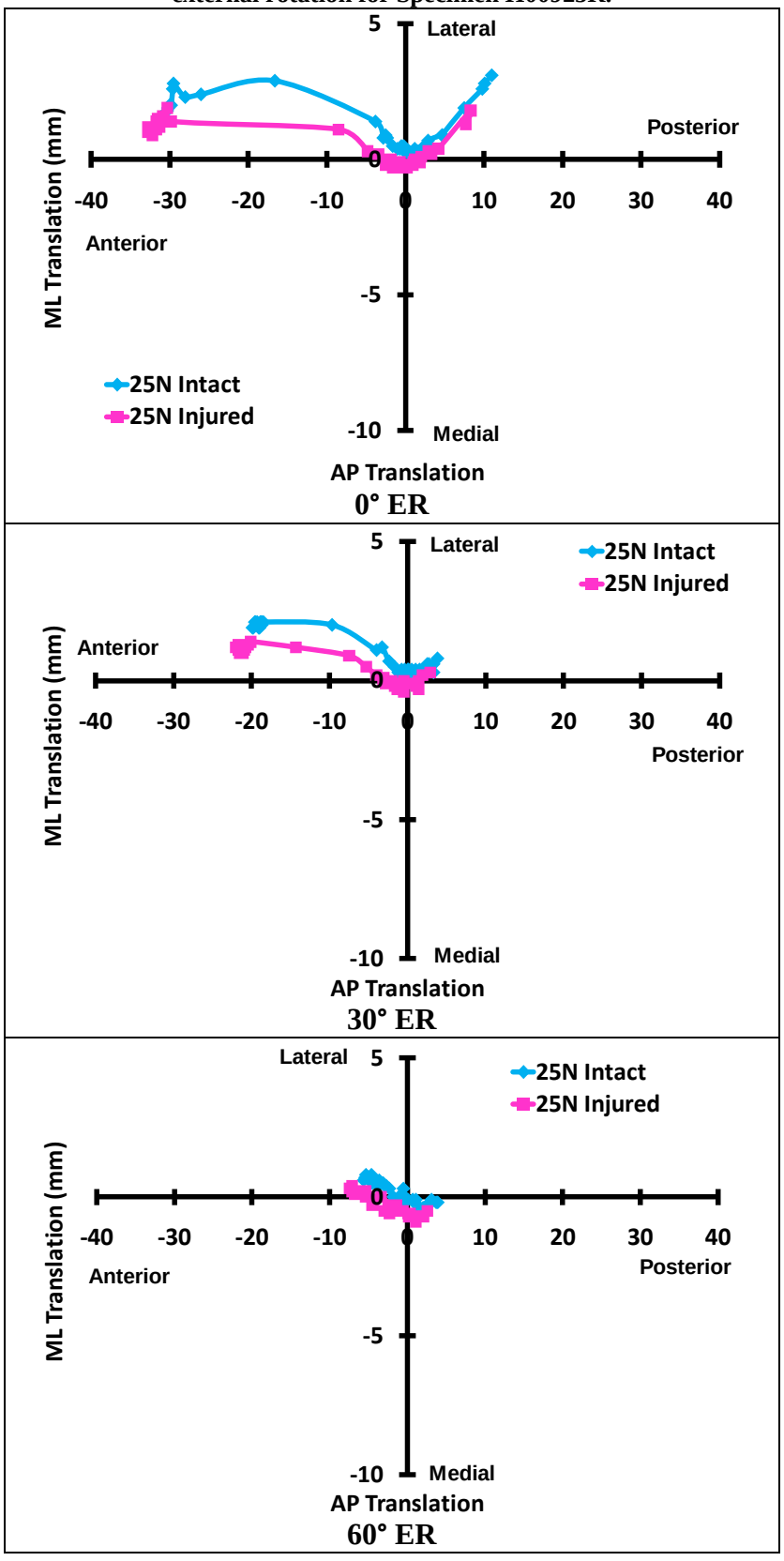

Table 7.21 Medial-lateral translation versus anterior-posterior load at 60° of abduction and 0°, 30° and 60° of external rotation for Specimen H01015R.

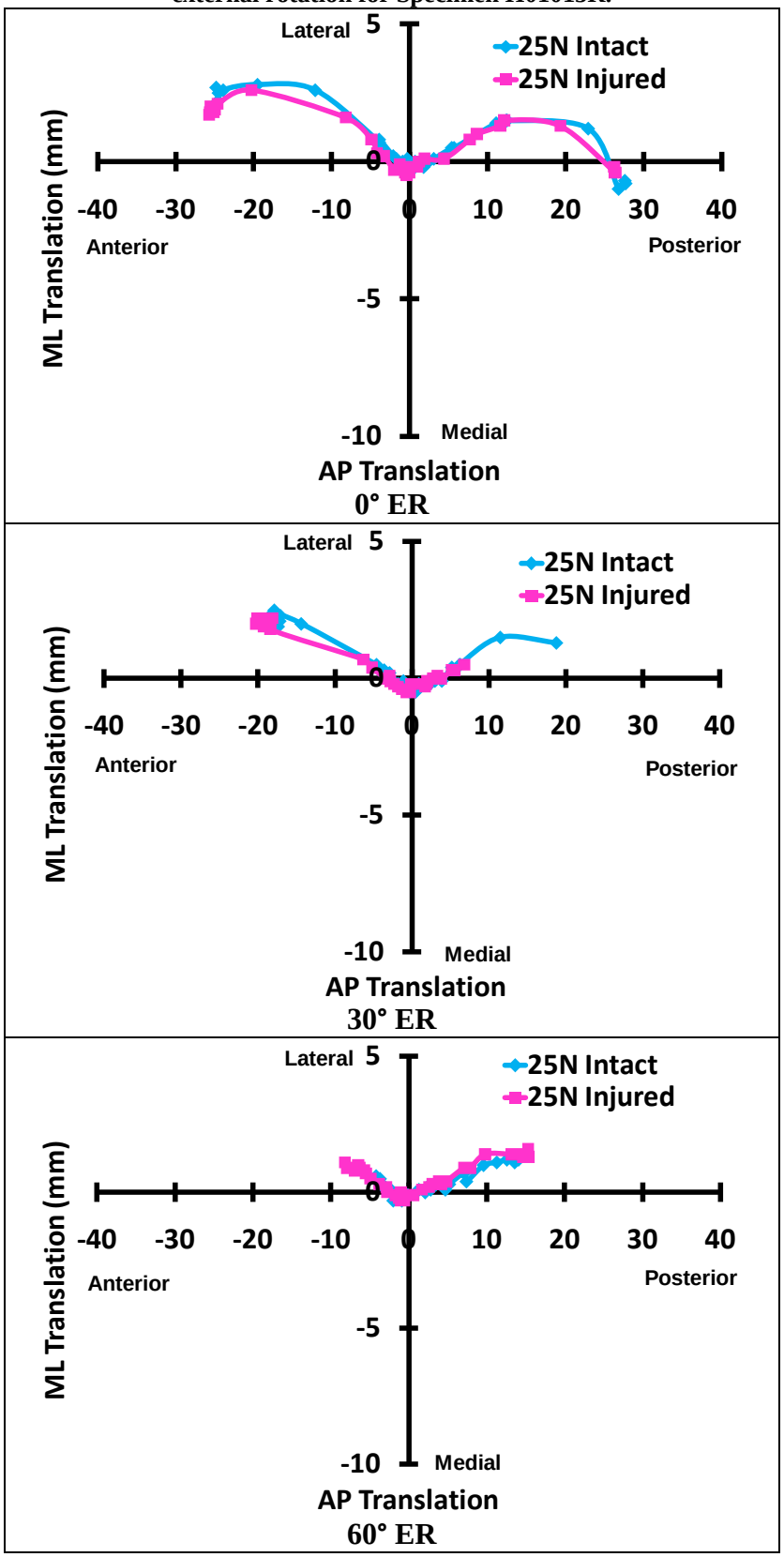

Table 7.22 Medial-lateral translation versus anterior-posterior load at 60° of abduction and 0°, 30° and 60° of external rotation for Specimen H01022L.

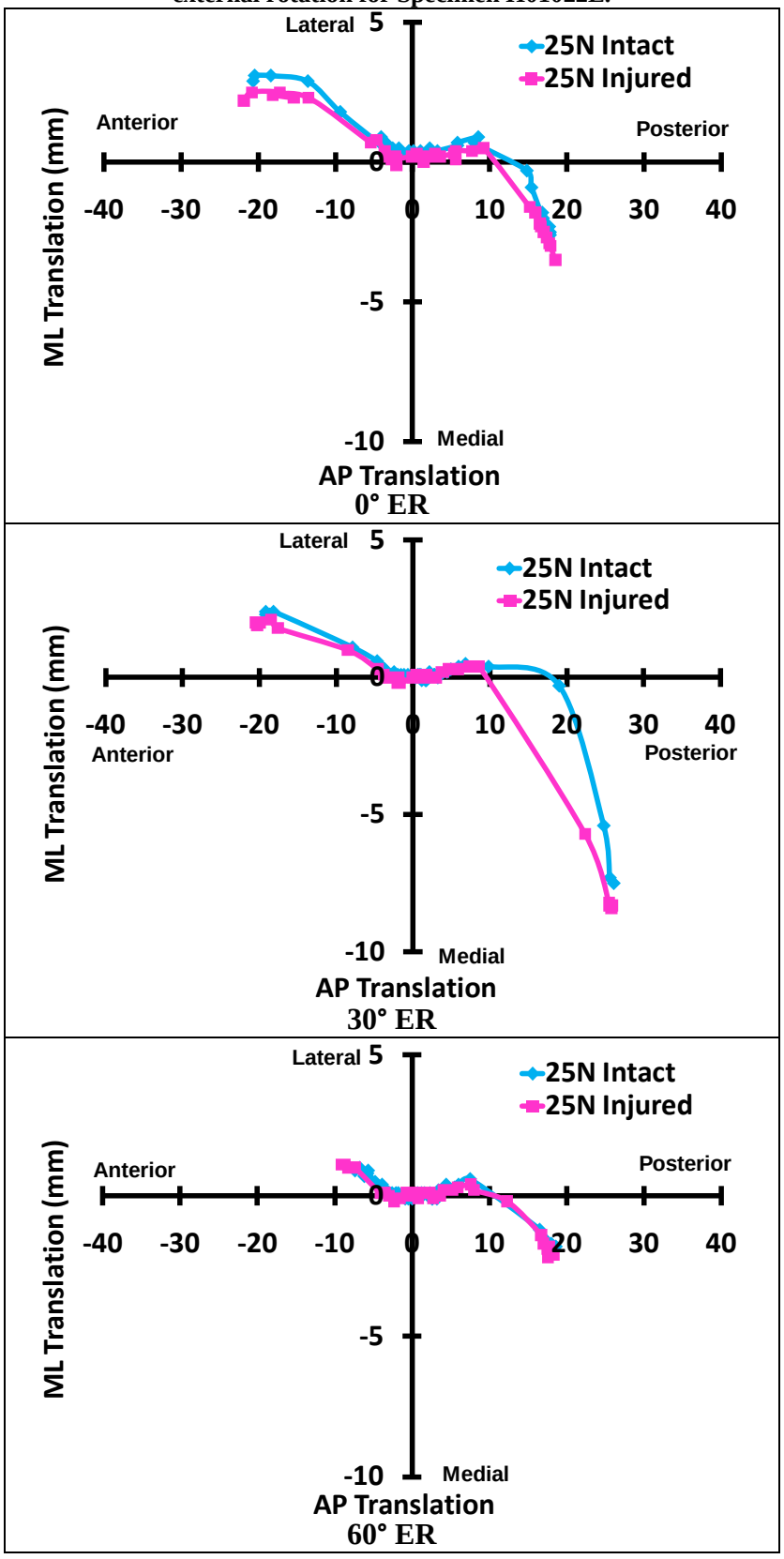

Table 7.23 Medial-lateral translation versus anterior-posterior load at 60° of abduction and 0°, 30° and 60° of external rotation for Specimen H01029L.

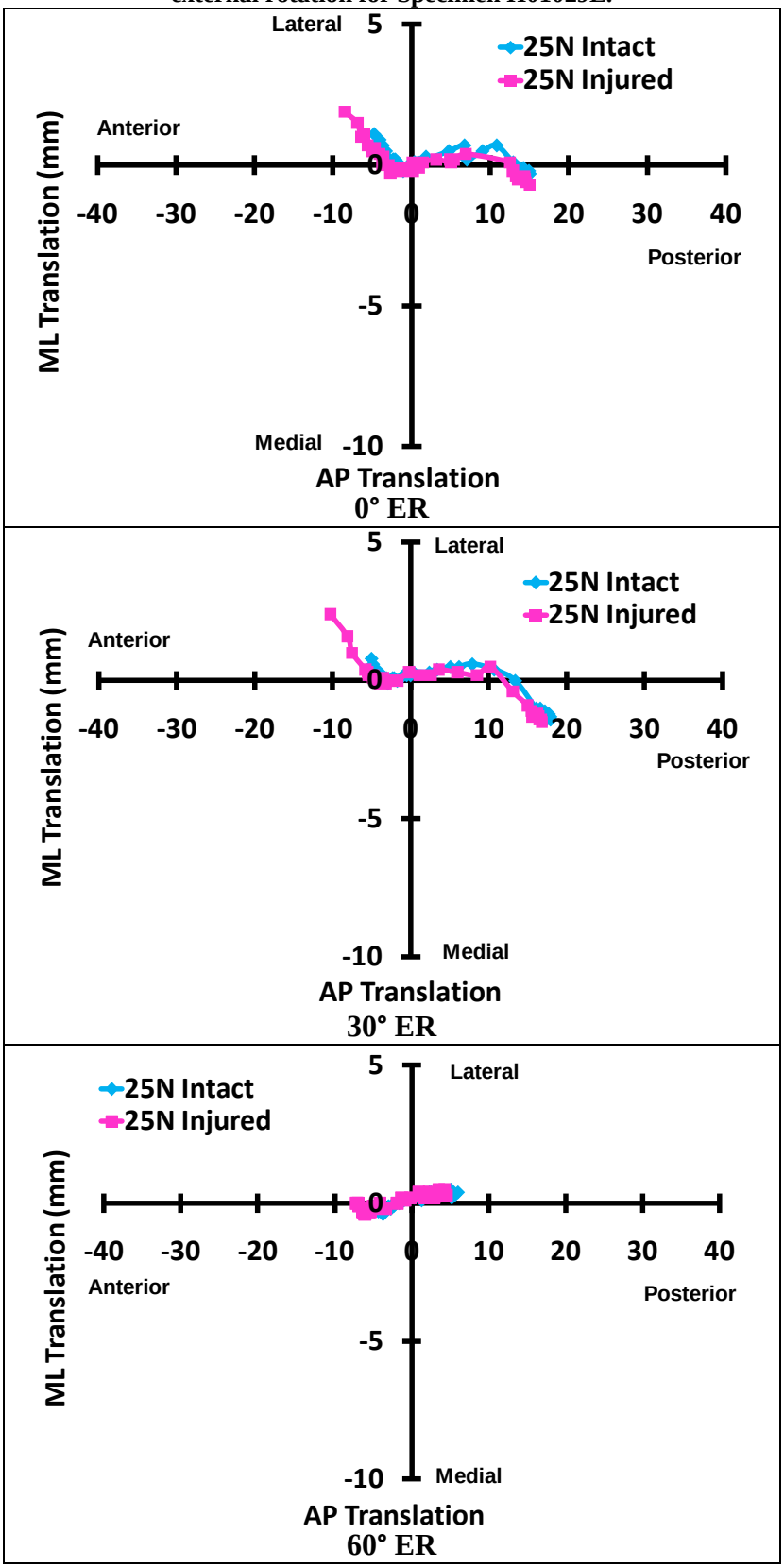

Table 7.24 Medial-lateral translation versus anterior-posterior load at 60° of abduction and 0°, 30° and 60° of external rotation for Specimen H01107R.

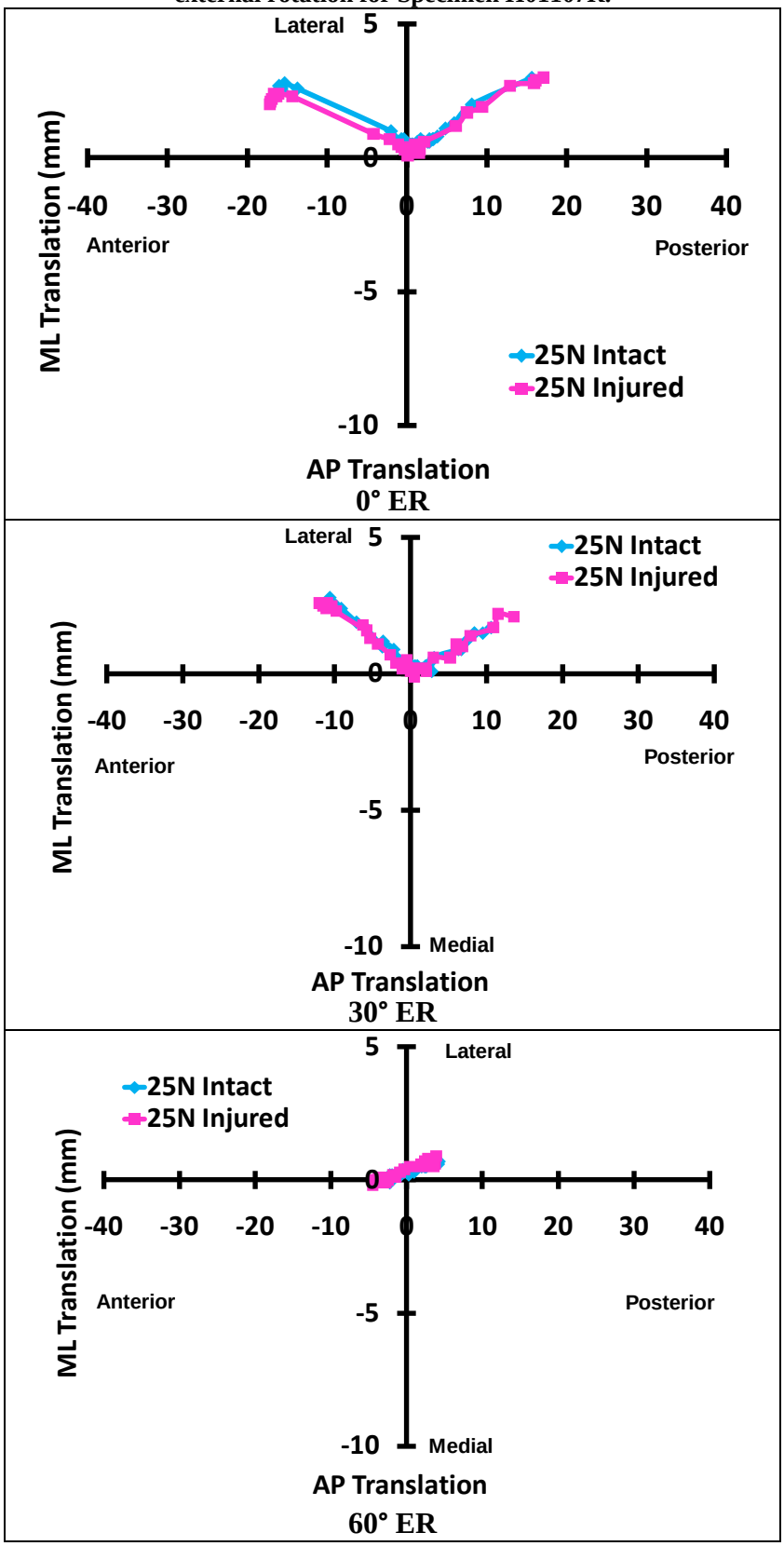

APPENDIX H

MATERIAL PARAMETERS FOR CONSTITUTIVE MODELS

Table 7.25 Material parameters of the phenomenological and structural models for Specimen 04-09040R in response to the four loading conditions.

Loading Condition	Phenomenological Model		Structural Model			
	C1 (MPa)	C2	C1 (MPa)	C3 (MPa)	C4	C5 (MPa)
SL	0.37	3.2	0.27	5.30	16.4	56.2
ST	0.17	2.8	0.14	1.37	2.0	60.9
TL	0.47	5.4	0.03	0.03	33.4	147.1
TT	0.31	4.0	0.03	0.04	0.9	55.5

Table 7.26 Material parameters of the phenomenological and structural models for Specimen 05-06046R in response to the four loading conditions.

Loading Condition	Phenomenological Model		Structural Model			
	C1 (MPa)	C2	C1 (MPa)	C3 (MPa)	C4	C5 (MPa)
SL	0.79	0.6	0.11	2.43	6.1	8.3
ST	0.44	0.7	0.07	2.34	5.1	5.9
TL	0.21	5.8	0.03	0.15	1.1	68.7
TT	0.33	5.3	0.40	0.001	66.7	62.6

Table 7.27 Material parameters of the phenomenological and structural models for Specimen 05-08013L in response to the four loading conditions.

Loading Condition	Phenomenological Model		Structural Model			
	C1 (MPa)	C2	C1 (MPa)	C3 (MPa)	C4	C5 (MPa)
SL	0.05	11.0	0.14	3.40	21.6	0.01
ST	0.11	11.5	0.06	25.4	17.8	95.8
TL	0.12	13.4	0.10	1.54	5.3	136.7
TT	0.06	8.4	0.11	0.24	9.8	20.5

Table 7.28 Material parameters of the phenomenological and structural models for Specimen 05-08022Lin response to the four loading conditions.

Loading Condition	Phenomenological Model		Structural Model			
	C1 (MPa)	C2	C1 (MPa)	C3 (MPa)	C4	C5 (MPa)
SL	0.06	10.1				
ST	0.25	5.3	0.45	24.23	5.8	0.01
TL	0.31	8.1	0.54	0.001	121.6	102.8
TT	0.15	8.8	0.24	0.04	50.4	48.7

Table 7.29 Material parameters of the phenomenological and structural models for Specimen 05-08024R in response to the four loading conditions.

Loading Condition	Phenomenological Model		Structural Model			
	C1 (MPa)	C2	C1 (MPa)	C3 (MPa)	C4	C5 (MPa)
SL	0.58	2.0	0.03	21.47	3.8	0.04
ST	0.06	4.1	0.07	0.94	16.5	45.1
TL	0.22	7.4	0.38	0.17	11.3	71.1
TT	0.19	3.5	0.09	0.04	31.1	18.2

Table 7.30 Material parameters of the phenomenological and structural models for Specimen 05-08038Lin response to the four loading conditions.

Loading Condition	Phenomenological Model		Structural Model			
	C1 (MPa)	C2	C1 (MPa)	C3 (MPa)	C4	C5 (MPa)
SL	0.07	9.1	0.09	5.38	19.8	1.0
ST	0.28	5.6				
TL	0.11	14.5	0.01	0.16	18.8	176.3
TT	0.12	8.1	0.23	0.04	43.5	32.3

Table 7.31 Material parameters of the phenomenological and structural models for Specimen 05-10043Rin response to the four loading conditions.

Loading Condition	Phenomenological Model		Structural Model			
	C1 (MPa)	C2	C1 (MPa)	C3 (MPa)	C4	C5 (MPa)
SL	0.17	8.4	0.35	18.76	13.4	0.03
ST	0.07	9.5	0.18	22.63	5.4	0.1
TL	0.13	11.7	0.05	0.54	14.9	109.5
TT	0.24	7.1	0.12	0.11	29.9	40.2

Table 7.32 Material parameters of the phenomenological and structural models for Specimen 05-10071R in response to the four loading conditions.

Loading Condition	Phenomenological Model		Structural Model			
	C1 (MPa)	C2	C1 (MPa)	C3 (MPa)	C4	C5 (MPa)
SL	0.09	3.6	0.03	7.18	5.0	25.6
ST	0.20	4.0	0.07	4.88	13.5	91.8
TL	0.06	15.6	0.31	0.01	0.02	75.5
TT	0.09	11.1				

Table 7.33 Material parameters of the phenomenological and structural models for Specimen 05-10072R in response to the four loading conditions.

Loading Condition	Phenomenological Model		Structural Model			
	C1 (MPa)	C2	C1 (MPa)	C3 (MPa)	C4	C5 (MPa)
SL	0.06	10.3	0.10	1.07	59.4	75.4
ST	0.51	3.8	0.15	15.3	5.0	0.01
TL	0.49	8.3	0.21	0.001	87.6	41.4
TT						

Table 7.34 Material parameters of the phenomenological and structural models for Specimen 05-11001R in response to the four loading conditions.

Loading Condition	Phenomenological Model		Structural Model			
	C1 (MPa)	C2	C1 (MPa)	C3 (MPa)	C4	C5 (MPa)
SL	0.36	2.7	0.09	1.80	23.4	41.5
ST	0.07	3.0	0.06	0.23	19.0	18.5
TL	0.82	2.8	0.01	0.61	10.5	84.3
TT	0.14	7.8	0.04	0.42	13.2	60.6

Table 7.35 Material parameters of the phenomenological and structural models for Specimen 05-11007R in response to the four loading conditions.

Loading Condition	Phenomenological Model		Structural Model			
	C1 (MPa)	C2	C1 (MPa)	C3 (MPa)	C4	C5 (MPa)
SL	0.48	3.7	0.36	20.26	8.4	1.6
ST	0.42	3.8	0.36	20.14	7.2	20.5
TL	0.15	8.2	0.32	0.02	56.8	41.1
TT	0.07	11.5	0.01	0.64	8.7	61.2

Table 7.36 Material parameters of the phenomenological and structural models for Specimen 06-10218L in response to the four loading conditions.

Loading Condition	Phenomenological Model		Structural Model			
	C1 (MPa)	C2	C1 (MPa)	C3 (MPa)	C4	C5 (MPa)
SL	0.04	4.7	0.05	1.34	12.2	11.6
ST	0.08	4.1	0.07	0.75	20.9	43.6
TL	0.09	10.7	0.04	1.56	4.5	59.7
TT	0.08	10.9	0.13	0.03	57.3	35.1

Table 7.37 Material parameters of the phenomenological and structural models for Specimen 06-11284R in response to the four loading conditions.

Loading Condition	Phenomenological Model		Structural Model			
	C1 (MPa)	C2	C1 (MPa)	C3 (MPa)	C4	C5 (MPa)
SL	0.17	3.1	0.15	1.06	22.1	32.1
ST	0.20	2.9	0.15	3.46	9.0	6.3
TL	0.51	3.9	0.05	0.74	0.5	86.2
TT	2.18	1.5	1.04	0.03	0.01	53.5

Table 7.38 Material parameters of the phenomenological and structural models for Specimen 07-03466L in response to the four loading conditions.

Loading Condition	Phenomenological Model		Structural Model			
	C1 (MPa)	C2	C1 (MPa)	C3 (MPa)	C4	C5 (MPa)
SL	0.16	1.3	0.07	8.69	1.4	3.0
ST	0.29	1.2	0.14	7.58	1.6	8.6
TL	0.07	3.6	0.01	0.05	0.6	11.1
TT	0.13	3.3	0.01	0.08	2.8	16.6

Table 7.39 Material parameters of the phenomenological and structural models for Specimen 07-03471L in response to the four loading conditions.

Loading Condition	Phenomenological Model		Structural Model			
	C1 (MPa)	C2	C1 (MPa)	C3 (MPa)	C4	C5 (MPa)
SL	0.08	3.9	0.05	4.05	8.4	1.2
ST	0.16	4.3	0.27	2.29	16.8	74.8
TL	0.11	5.0	0.01	0.25	0.2	28.9
TT	0.16	4.9	0.03	4.15	0.04	42.1

Table 7.40 Material parameters of the phenomenological and structural models for Specimen 07-03472R in response to the four loading conditions.

Loading Condition	Phenomenological Model		Structural Model			
	C1 (MPa)	C2	C1 (MPa)	C3 (MPa)	C4	C5 (MPa)
SL	0.29	1.4	0.14	0.27	20.5	17.2
ST	0.09	2.5	0.08	2.51	4.9	3.7
TL	0.19	3.3	0.01	0.40	1.8	26.9
TT	0.32	4.0	0.01	0.80	6.9	52.6

APPENDIX I

CONSTITUTIVE MODEL PREDICTIONS

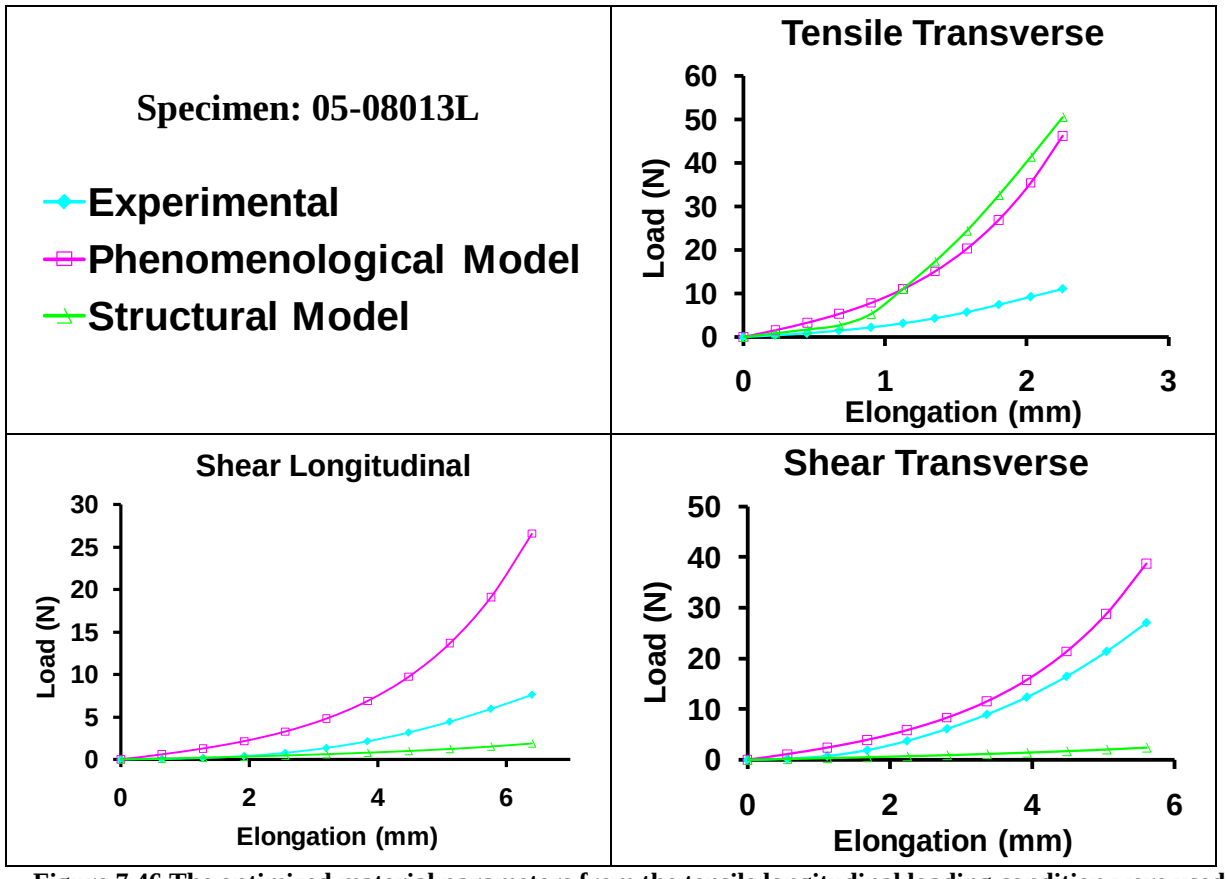

Figure 7.46 The optimized material parameters from the tensile longitudinal loading condition were used to predict the response of the capsule to the 1) tensile transverse (top right), 2) shear longitudinal (bottom left), and 3) shear transverse (bottom right) loading conditions for Specimen 05-08013L.

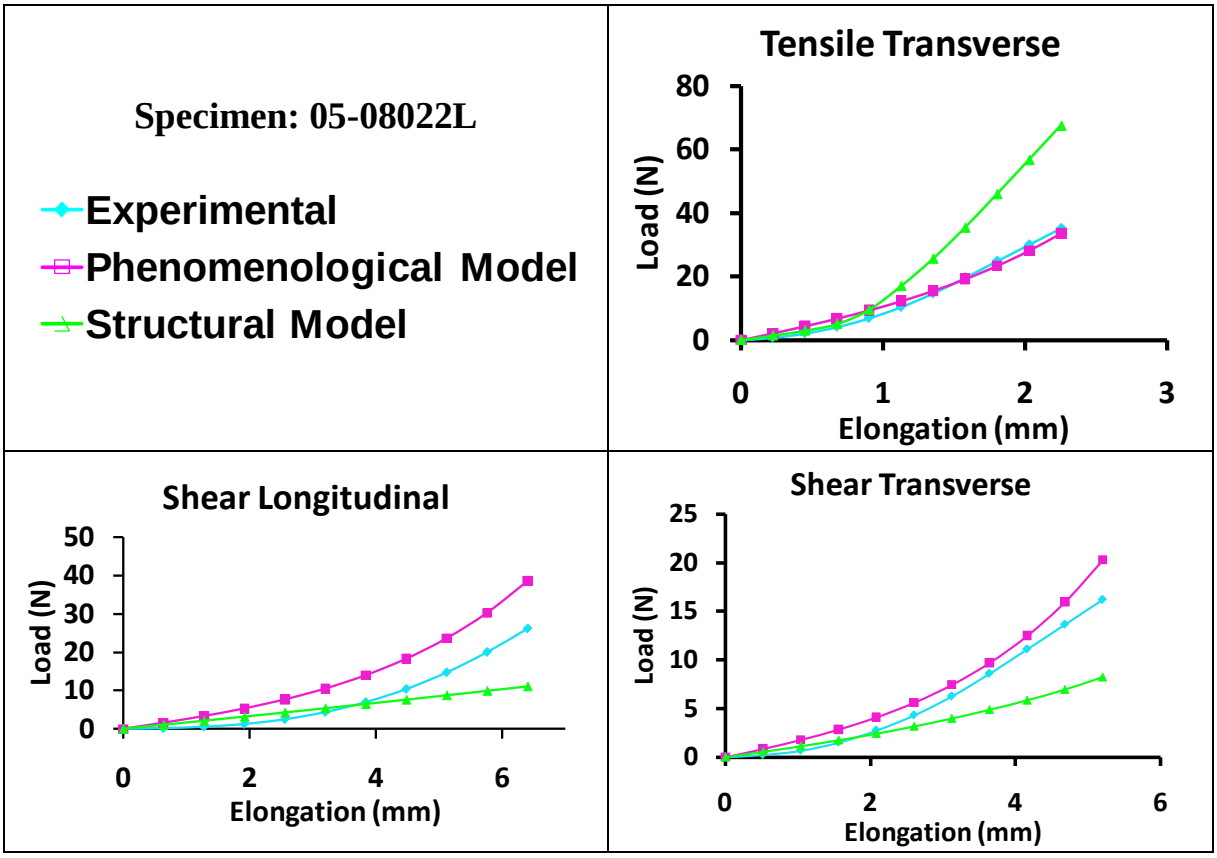

Figure 7.47 The optimized material parameters from the tensile longitudinal loading condition were used to predict the response of the capsule to the 1) tensile transverse (top right), 2) shear longitudinal (bottom left), and 3) shear transverse (bottom right) loading conditions for Specimen 05-08022L.

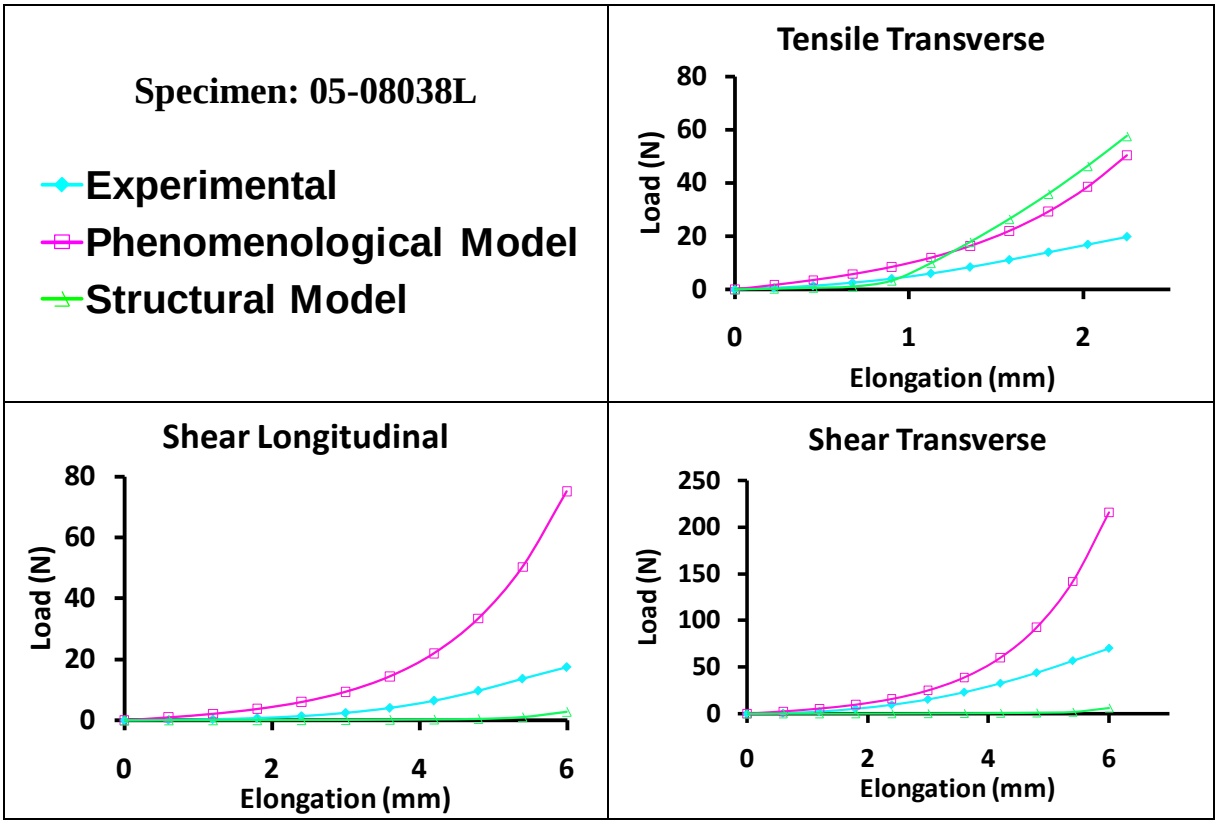

Figure 7.48 The optimized material parameters from the tensile longitudinal loading condition were used to predict the response of the capsule to the 1) tensile transverse (top right), 2) shear longitudinal (bottom left), and 3) shear transverse (bottom right) loading conditions for Specimen 05-08038L.

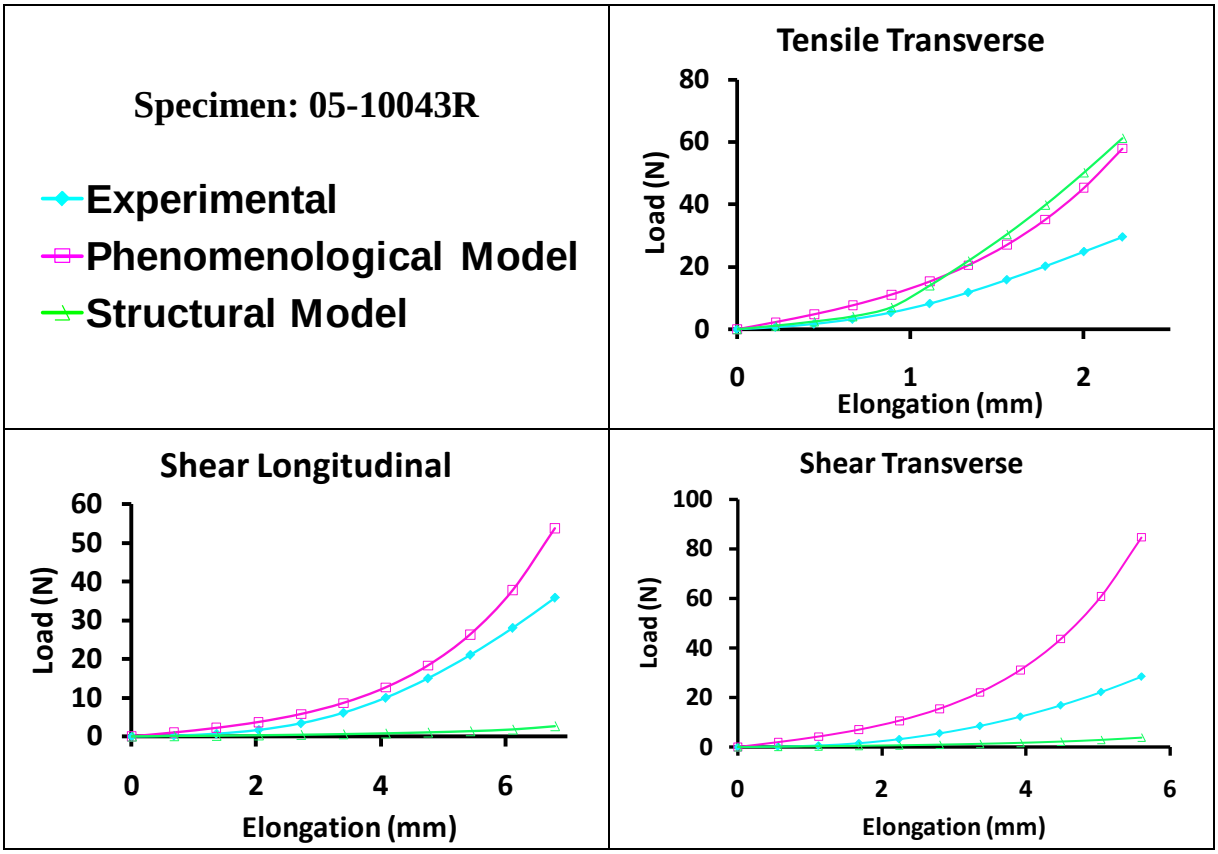

Figure 7.49 The optimized material parameters from the tensile longitudinal loading condition were used to predict the response of the capsule to the 1) tensile transverse (top right), 2) shear longitudinal (bottom left), and 3) shear transverse (bottom right) loading conditions for Specimen 05-10043R.

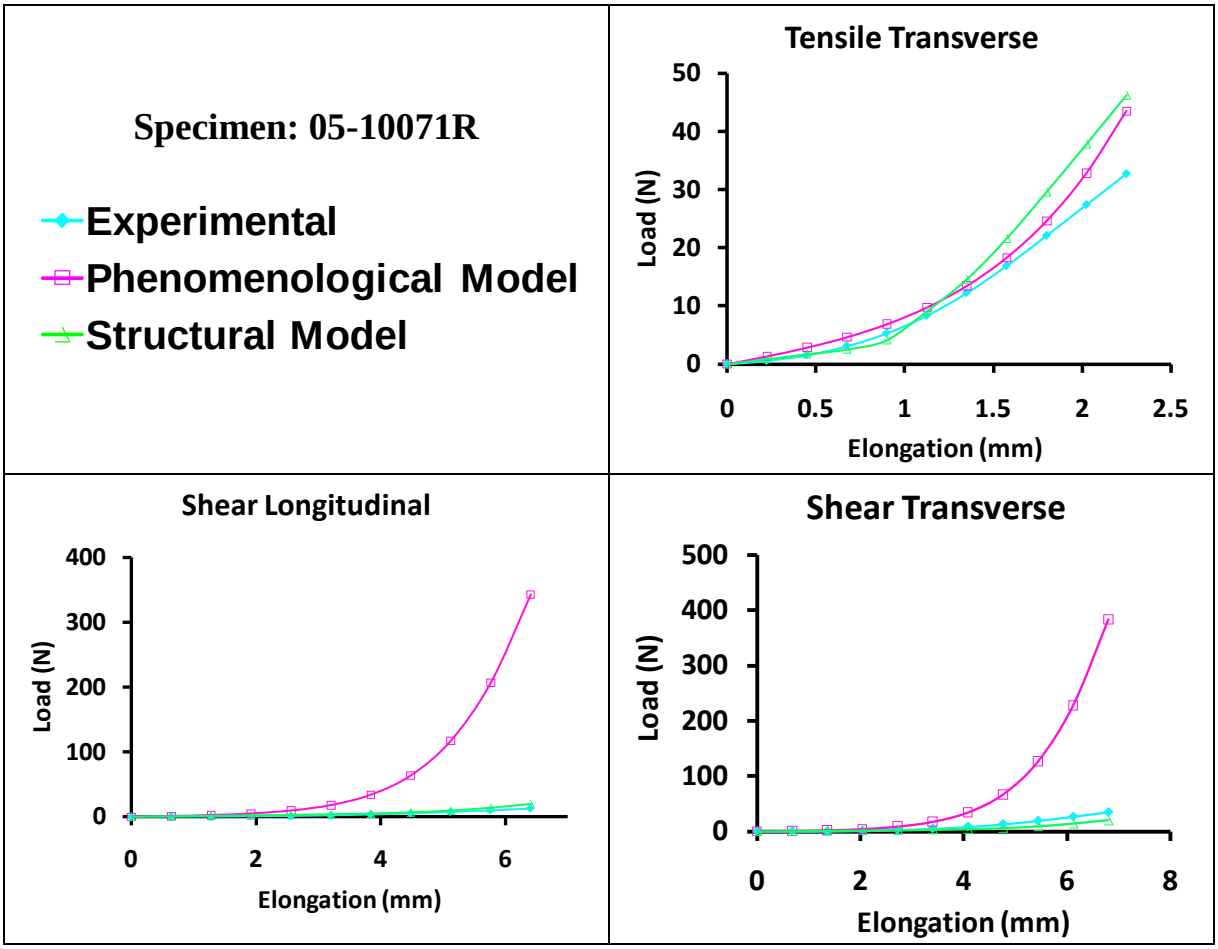

Figure 7.50 The optimized material parameters from the tensile longitudinal loading condition were used to predict the response of the capsule to the 1) tensile transverse (top right), 2) shear longitudinal (bottom left), and 3) shear transverse (bottom right) loading conditions for Specimen 05-10071R.

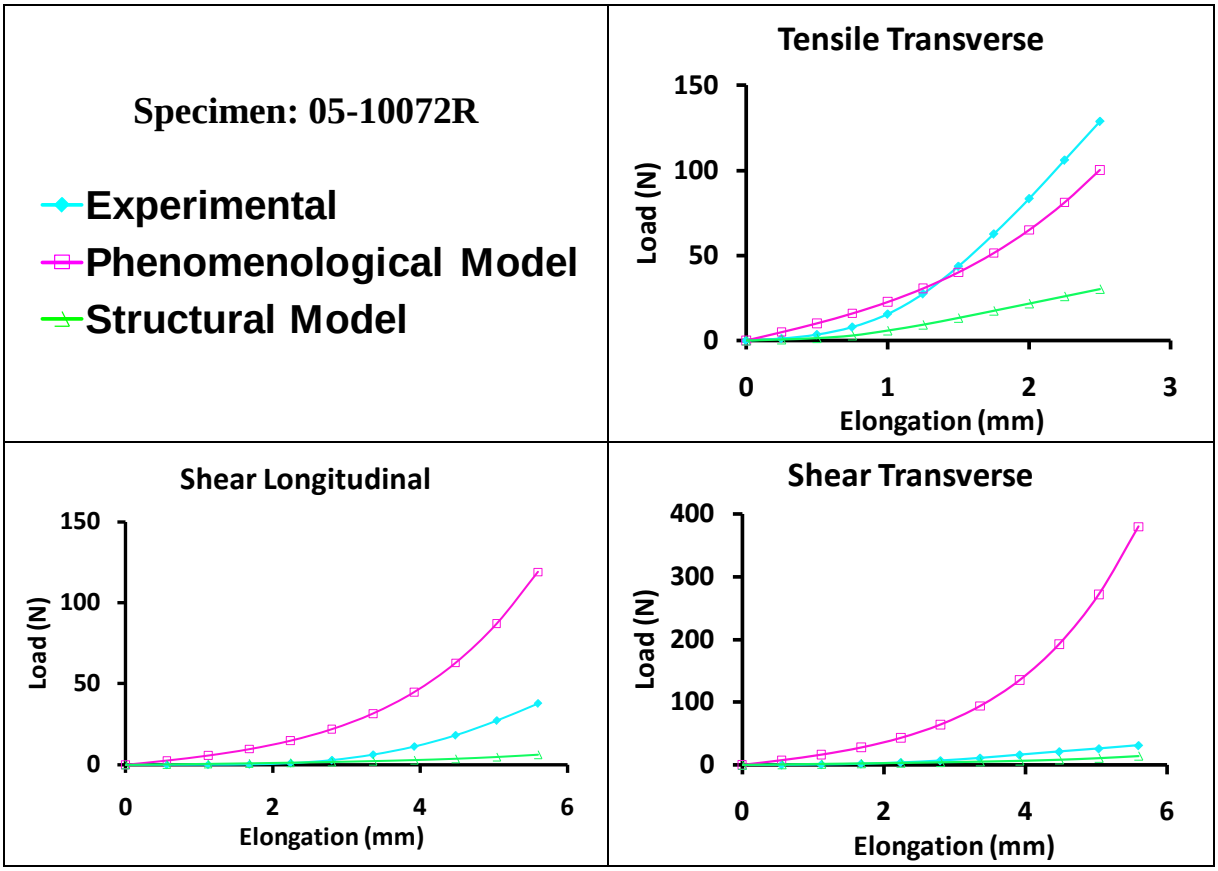

Figure 7.51 The optimized material parameters from the tensile longitudinal loading condition were used to predict the response of the capsule to the 1) tensile transverse (top right), 2) shear longitudinal (bottom left), and 3) shear transverse (bottom right) loading conditions for Specimen 05-10072R.

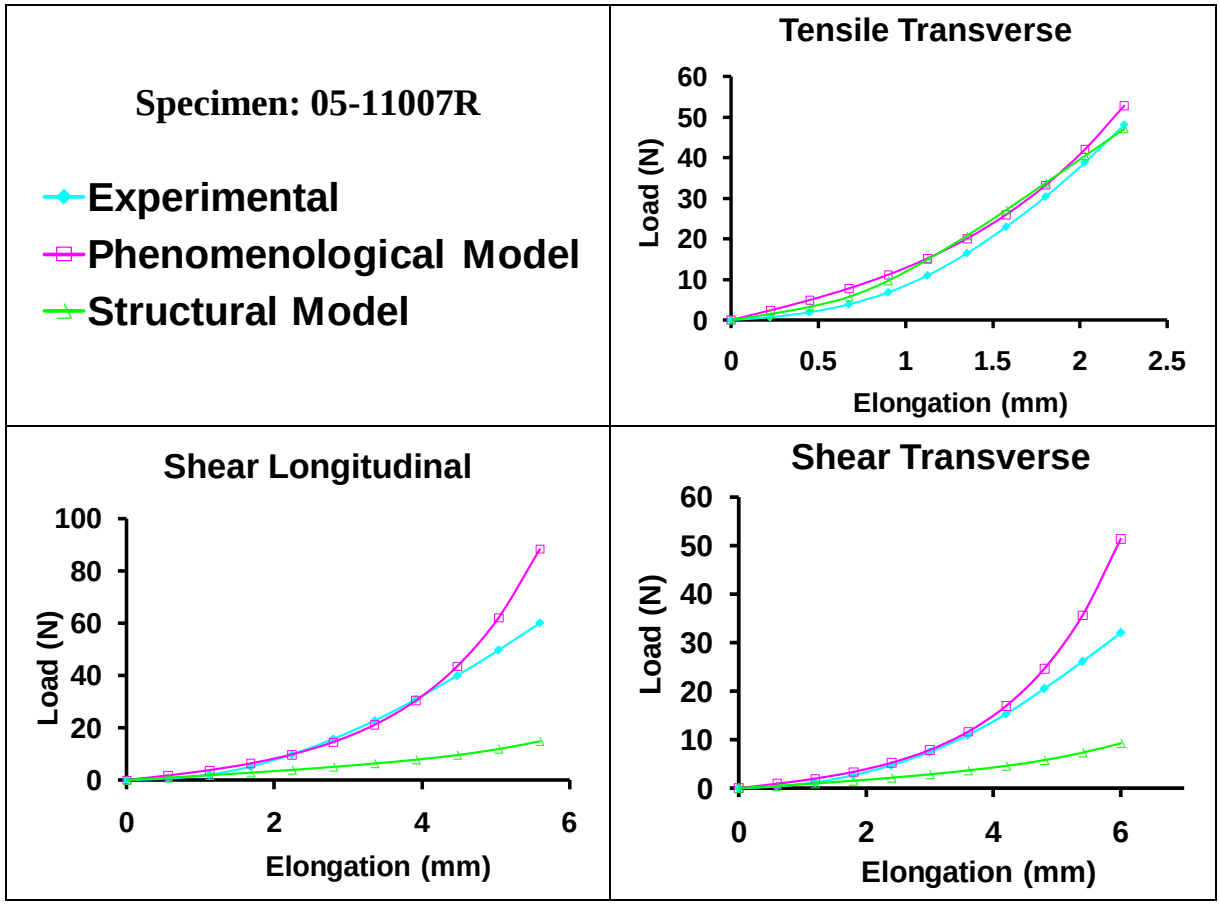

Figure 7.52 The optimized material parameters from the tensile longitudinal loading condition were used to predict the response of the capsule to the 1) tensile transverse (top right), 2) shear longitudinal (bottom left), and 3) shear transverse (bottom right) loading conditions for Specimen 05-11007R.

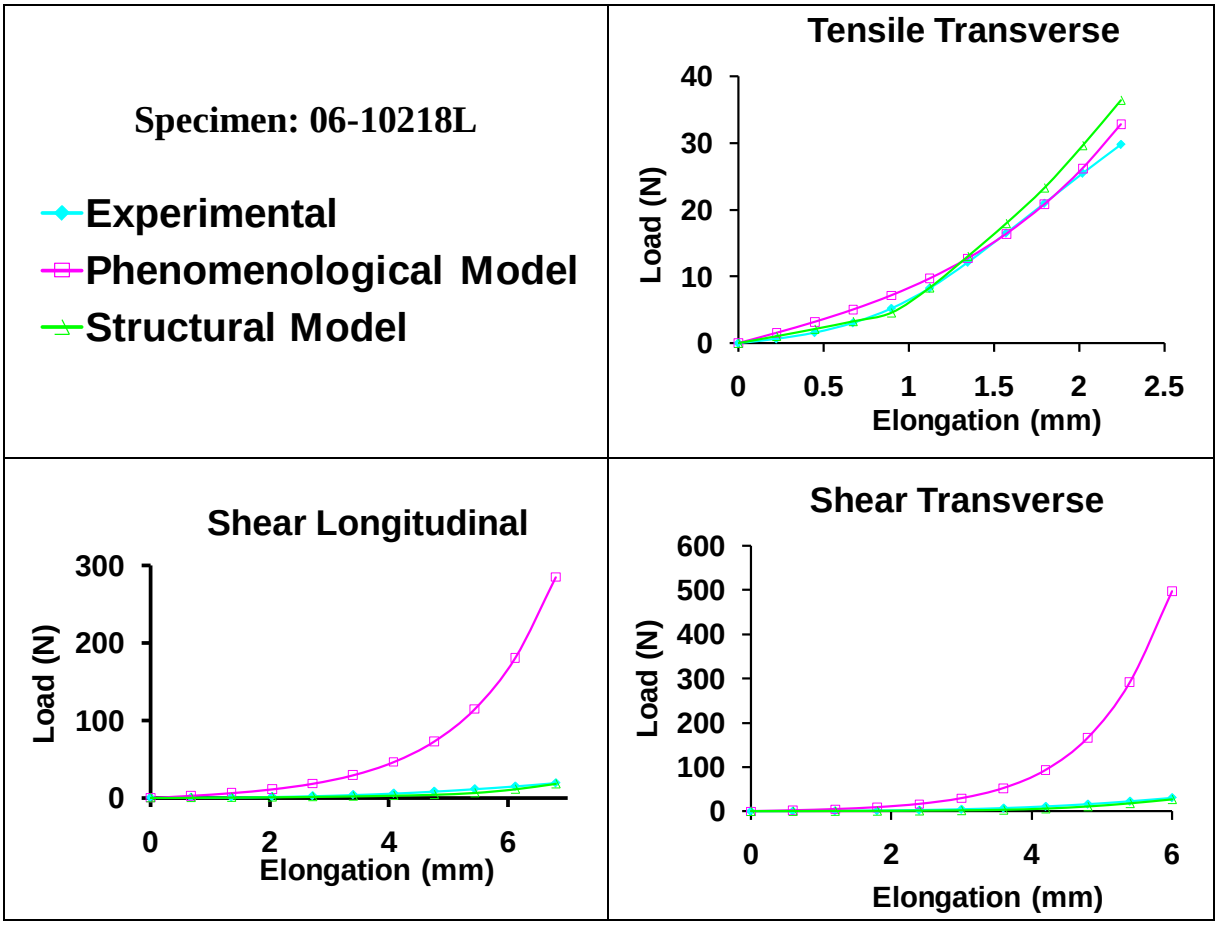

Figure 7.53 The optimized material parameters from the tensile longitudinal loading condition were used to predict the response of the capsule to the 1) tensile transverse (top right), 2) shear longitudinal (bottom left), and 3) shear transverse (bottom right) loading conditions for Specimen 06-10218L.

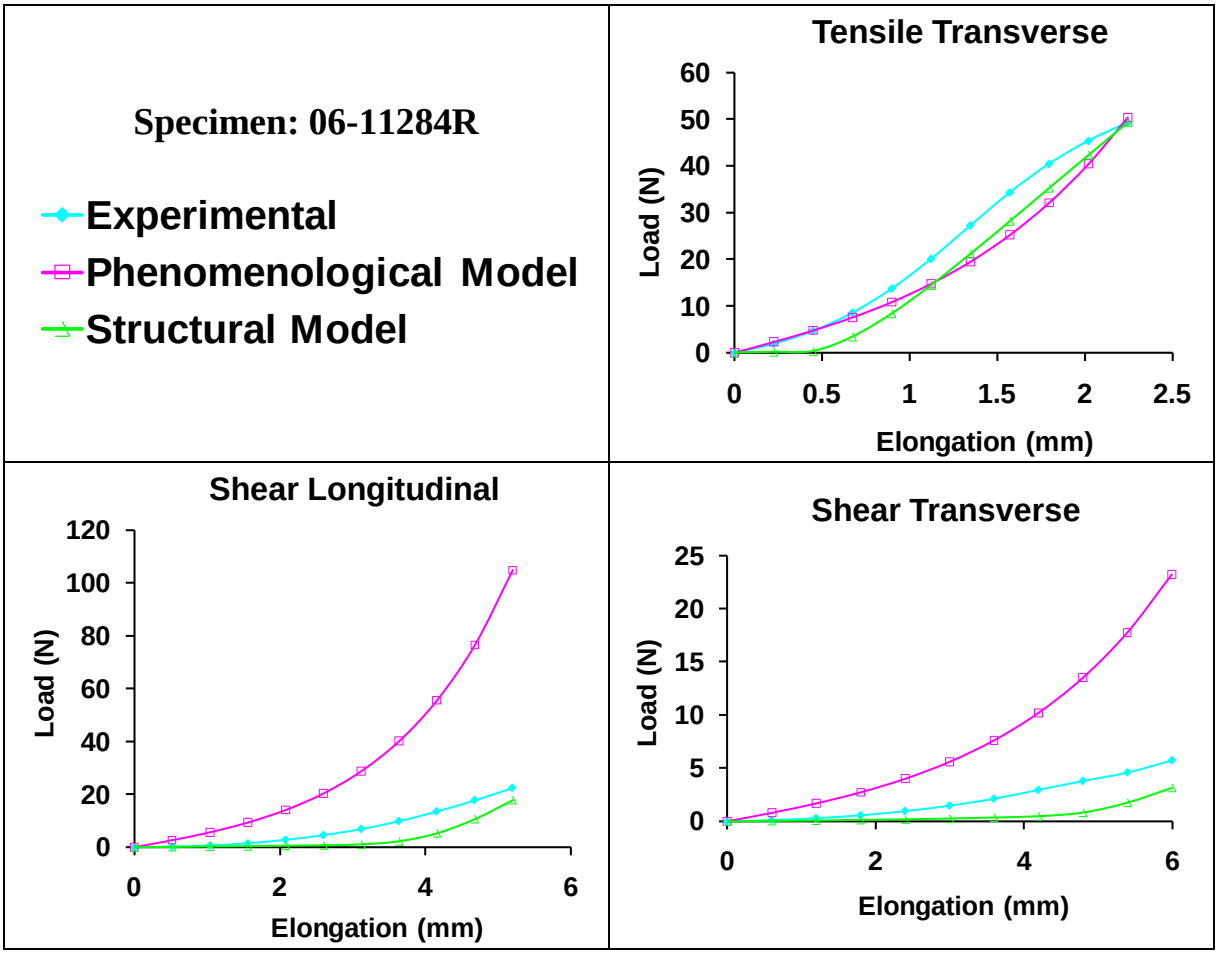

Figure 7.54 The optimized material parameters from the tensile longitudinal loading condition were used to predict the response of the capsule to the 1) tensile transverse (top right), 2) shear longitudinal (bottom left), and 3) shear transverse (bottom right) loading conditions for Specimen 06-11284R.

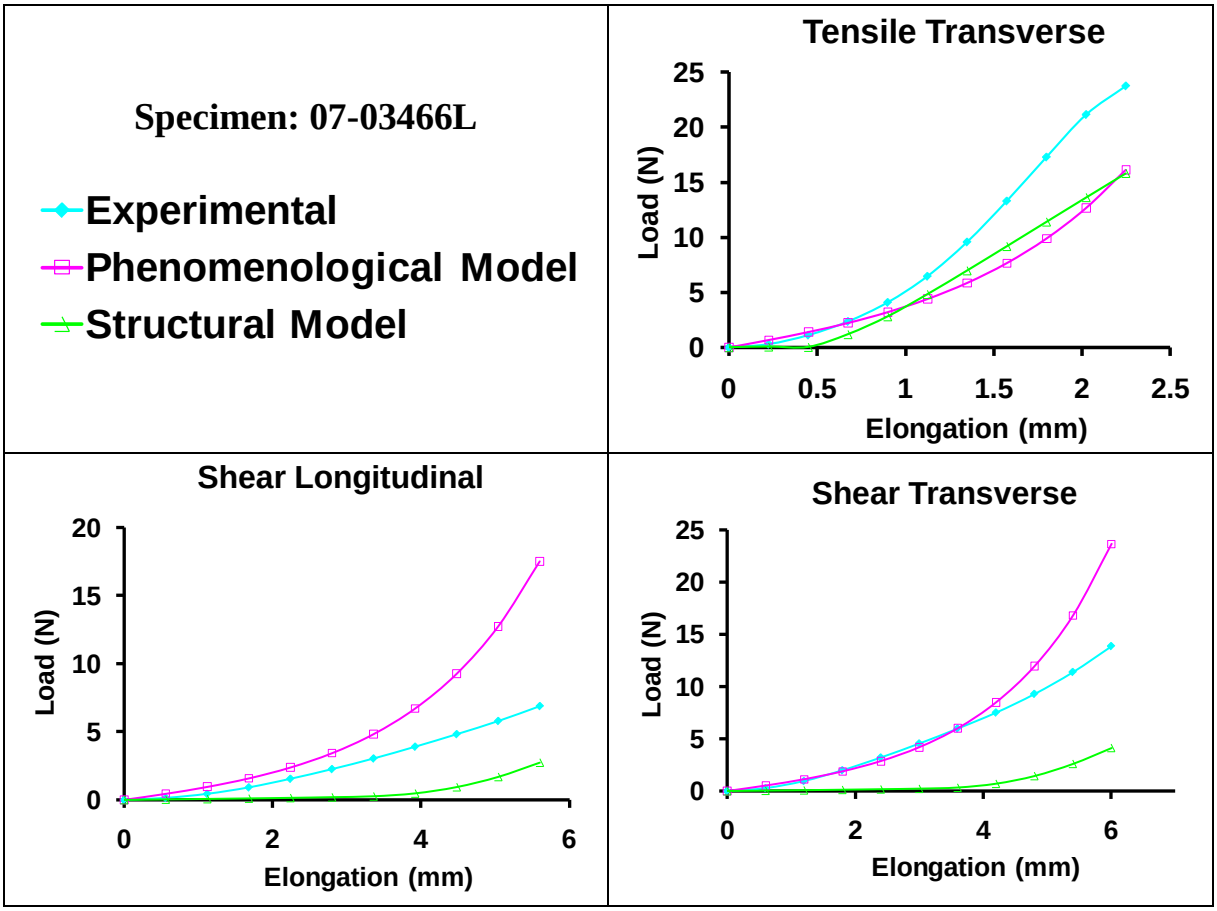

Figure 7.55 The optimized material parameters from the tensile longitudinal loading condition were used to predict the response of the capsule to the 1) tensile transverse (top right), 2) shear longitudinal (bottom left), and 3) shear transverse (bottom right) loading conditions for Specimen 07-03466L.

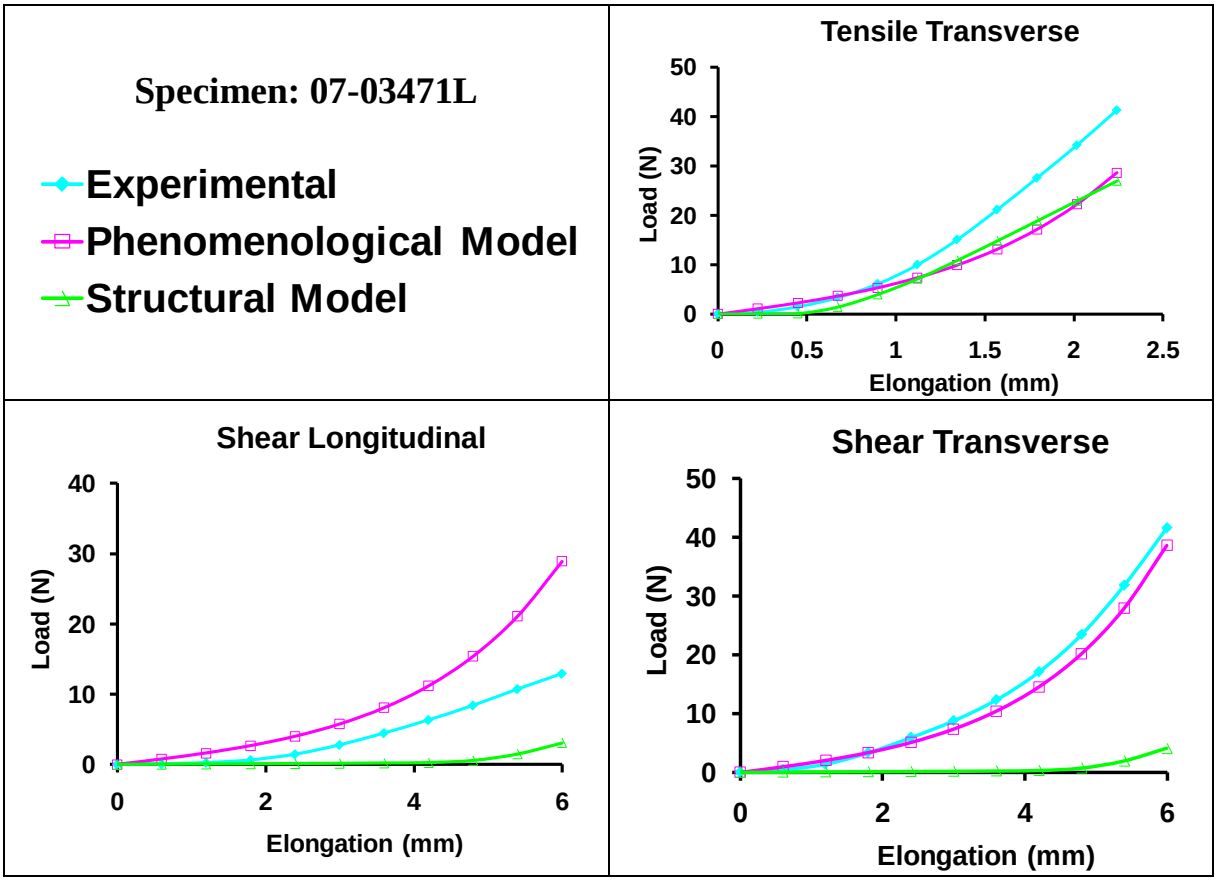

Figure 7.56 The optimized material parameters from the tensile longitudinal loading condition were used to predict the response of the capsule to the 1) tensile transverse (top right), 2) shear longitudinal (bottom left), and 3) shear transverse (bottom right) loading conditions for Specimen 07-03471L.

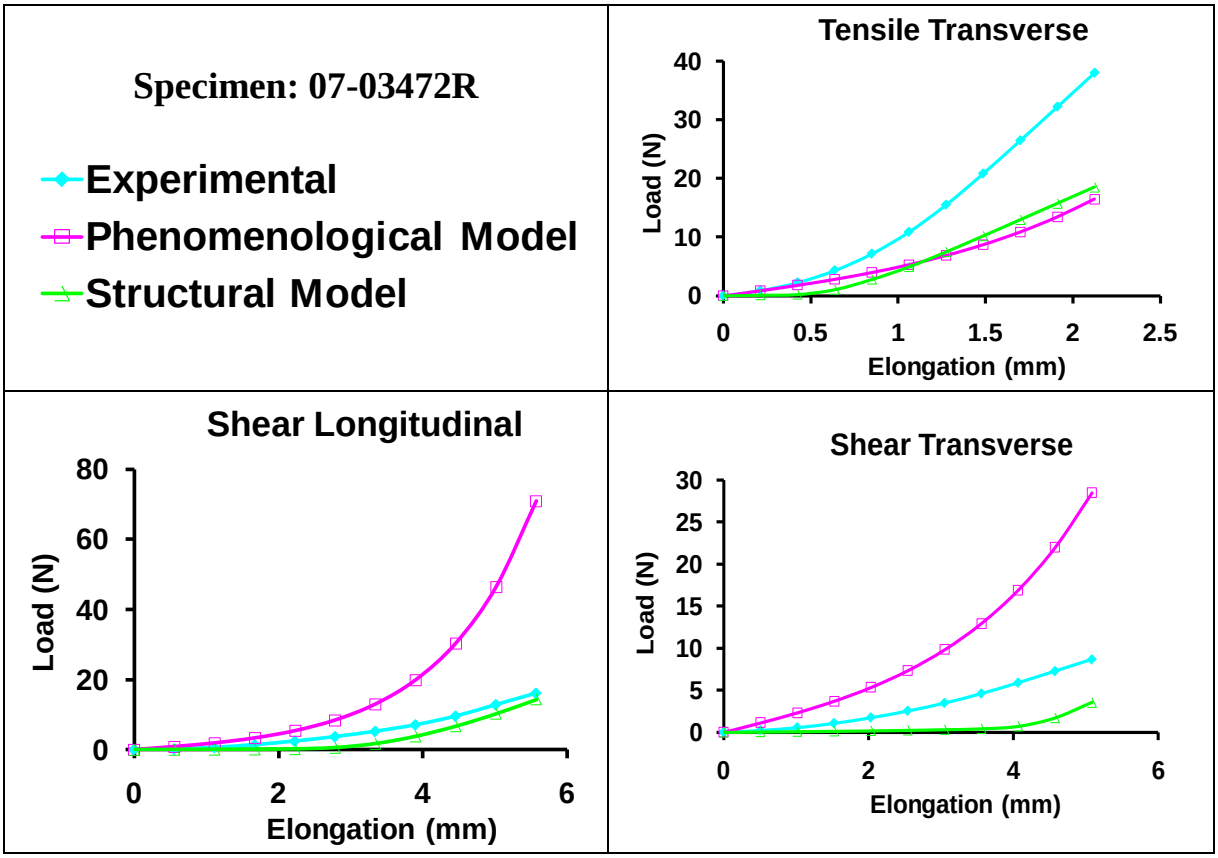

Figure 7.57 The optimized material parameters from the tensile longitudinal loading condition were used to predict the response of the capsule to the 1) tensile transverse (top right), 2) shear longitudinal (bottom left), and 3) shear transverse (bottom right) loading conditions for Specimen 07-03472R.

APPENDIX J

MATLAB CODE FOR AFFINE MODEL PREDICTIONS

```
% Chris Carruthers
% 07-15-2010
% Stretch Calculator
% Objective: Calculates principal stretches from two or more 4 node images.
% Uses a 4 node FE approach for computing marker strains for biaxial test.
% x is axis 1, y is axis 2

% Modified by Carrie Voycheck 12/1/11 to be used as a function with the
% initial and final coordinates of 4 markers as inputs. The deformation
% gradient for one element will be calculated and returned.

function F = calcF(X, Y, x, y)

% Define input variables [top right, top left, bottom left, bottom right]

% X=[1,0,0,1]; % initial
% Y=[1,1,0,0]; % initial
% x=[1,0,0,1]; % final
% y=[2,2,0,0]; % final

% Compute the displacements
for i=1:4;
    u(i)=x(i)-X(i);
    v(i)=y(i)-Y(i);
end

% Compute shape functions and their derivatives for r and s = 0
r=0;s=0;
h(1)=(1+r)*(1+s)/4;
```

```
h(2)=(1-r)*(1+s)/4;
h(3)=(1-r)*(1-s)/4;
h(4)=(1+r)*(1-s)/4;
dhdr(1)=(1+s)/4;
dhdr(2)=-(1+s)/4;
dhdr(3)=-(1-s)/4;
dhdr(4)=(1-s)/4;
dhds(1)=(1+r)/4;
dhds(2)=(1-r)/4;
dhds(3)=-(1-r)/4;
dhds(4)=-(1+r)/4;

% Compute derivatives wrt isoparametric coords at r=s=0
dxdr=X(1)*dhdr(1)+X(2)*dhdr(2)+X(3)*dhdr(3)+X(4)*dhdr(4);
dxds=X(1)*dhds(1)+X(2)*dhds(2)+X(3)*dhds(3)+X(4)*dhds(4);
dydr=Y(1)*dhdr(1)+Y(2)*dhdr(2)+Y(3)*dhdr(3)+Y(4)*dhdr(4);
dyds=Y(1)*dhds(1)+Y(2)*dhds(2)+Y(3)*dhds(3)+Y(4)*dhds(4);

dudr=u(1)*dhdr(1)+u(2)*dhdr(2)+u(3)*dhdr(3)+u(4)*dhdr(4);
duds=u(1)*dhds(1)+u(2)*dhds(2)+u(3)*dhds(3)+u(4)*dhds(4);
dvdr=v(1)*dhdr(1)+v(2)*dhdr(2)+v(3)*dhdr(3)+v(4)*dhdr(4);
dvds=v(1)*dhds(1)+v(2)*dhds(2)+v(3)*dhds(3)+v(4)*dhds(4);

detJ=dxdr*dyds-dxds*dydr;

% Compute displacement derivatives wrt x and y
dudx=(1/detJ)*(dyds*dudr-dydr*duds);
dudy=(1/detJ)*(-dxds*dudr+dxdr*duds);
dvdx=(1/detJ)*(dyds*dvdr-dydr*dvds);
dvdy=(1/detJ)*(-dxds*dvdr+dxdr*dvds);

% Compute F
F11=dudx+1;
F12=dudy;
F21=dvdx;
F22=dvdy+1;
F = [F11 F12; F21 F22];

% Compute E and perform polar decomposition to compute rigid body angle
% theta, and U
th = atan2(F21-F12, F11+F22);
U11=(F11*cos(th)+F21*sin(th));
U12=(F12*cos(th)+F22*sin(th));
U22=(F22*cos(th)-F12*sin(th));

E11=(dudx+0.5*(dudx^2+dvdx^2));
E12=(0.5*(dudy+dvdx+dudx*dudy+dvdx*dvdy));
E22=(dvdy+0.5*(dvdy^2+dudy^2));
alpha=asin(2*E12/(sqrt(1+2*E11)*sqrt(1+2*E22)));



% Carrie Voycheck
% 12/1/10
% This code calculates the deformation gradient for an entire tissue sample
(6
```

```
% elements) by repeatedly calling calcF.m to calculate F in each element.
% The F's for each element are returned. The initial and finial marker
% positions (pixel positions identified in ImageJ) must be placed in a
% text file (markerpositions.txt) where the first column is the x data and
% the second column is the y data. The first 12 rows are initial marker
% positions and the second 12 rows are the final (or deformed) marker
positions.

function [F1 F2 F3 F4 F5 F6] = multipleF_6;

% load marker positions from ImageJ data
data = load('markerpositions_6.txt');

% initial marker coordinates
Xi1 = data(1,1);
Yi1 = data(1,2);
Xi2 = data(2,1);
Yi2 = data(2,2);
Xi3 = data(3,1);
Yi3 = data(3,2);
Xi4 = data(4,1);
Yi4 = data(4,2);
Xi5 = data(5,1);
Yi5 = data(5,2);
Xi6 = data(6,1);
Yi6 = data(6,2);
Xi7 = data(7,1);
Yi7 = data(7,2);
Xi8 = data(8,1);
Yi8 = data(8,2);
Xi9 = data(9,1);
Yi9 = data(9,2);
Xi10 = data(10,1);
Yi10 = data(10,2);
Xi11 = data(11,1);
Yi11 = data(11,2);
Xi12 = data(12,1);
Yi12 = data(12,2);

% final marker coordinates
Xf1 = data(13,1);
Yf1 = data(13,2);
Xf2 = data(14,1);
Yf2 = data(14,2);
Xf3 = data(15,1);
Yf3 = data(15,2);
Xf4 = data(16,1);
Yf4 = data(16,2);
Xf5 = data(17,1);
Yf5 = data(17,2);
Xf6 = data(18,1);
Yf6 = data(18,2);
Xf7 = data(19,1);
Yf7 = data(19,2);
Xf8 = data(20,1);
Yf8 = data(20,2);
```

```
Xf9 = data(21,1);
Yf9 = data(21,2);
Xf10 = data(22,1);
Yf10 = data(22,2);
Xf11 = data(23,1);
Yf11 = data(23,2);
Xf12 = data(24,1);
Yf12 = data(24,2);

% Define input variables [top right, top left, bottom left, bottom right]
% Calculate F for each element by calling calcF function

% Element 1 (markers 2,1,4,5)
F1 = calcF([Xi2, Xi1, Xi4, Xi5],[Yi2, Yi1, Yi4, Yi5], [Xf2, Xf1, Xf4,
Xf5],[Yf2, Yf1, Yf4, Yf5]);

% Element 2 (markers 3,2,5,6)
F2 = calcF([Xi3, Xi2, Xi5, Xi6],[Yi3, Yi2, Yi5, Yi6], [Xf3, Xf2, Xf5,
Xf6],[Yf3, Yf2, Yf5, Yf6]);

% Element 3 (markers 5,4,7,8)
F3 = calcF([Xi5, Xi4, Xi7, Xi8],[Yi5, Yi4, Yi7, Yi8], [Xf5, Xf4, Xf7,
Xf8],[Yf5, Yf4, Yf7, Yf8]);

% Element 4 (markers 6,5,8,9)
F4 = calcF([Xi6, Xi5, Xi8, Xi9],[Yi6, Yi5, Yi8, Yi9], [Xf6, Xf5, Xf8,
Xf9],[Yf6, Yf5, Yf8, Yf9]);

% Element 5 (markers 8,7,10,11)
F5 = calcF([Xi8, Xi7, Xi10, Xi11],[Yi8, Yi7, Yi10, Yi11], [Xf8, Xf7, Xf10,
Xf11],[Yf8, Yf7, Yf10, Yf11]);

% Element 6 (markers 9,8,11,12)
F6 = calcF([Xi9, Xi8, Xi11, Xi12],[Yi9, Yi8, Yi11, Yi12], [Xf9, Xf8, Xf11,
Xf12],[Yf9, Yf8, Yf11, Yf12]);



% Carrie Voycheck
% 12/1/2010
% This code was written to process the SALS and strain data in order to
% compare the experimental and affine-predicted fiber kinematics in the
% glenohumeral capsule similar to the work done by Lake et al. on the
% supraspinatus tendon (Abstract #: SBC2010-19234). The strain marker
% positions are used to calculate the deformation gradient for each
% element. The deformation gradient is then used to predict the fiber
% orientations at the 5% elongation just prior to failure using the fiber
% orientations from the preloaded state and the assumption of affine fiber
% kinematics. This code will work for all tissue samples where failure
% occurred in elements 7 or 8 near the bottom clamp.

% You will need:
% 1) SALS data in a text file - a separate file for each element (these
%   must be named appropriately (pre_1.txt, fail_1.txt)
% 2) initial and final marker positions (pixel positions
%   identified in ImageJ) placed in a text file where the first column is the
```

```
%   x data and the second column is the y data. The first 15 rows are inital
%   marker positions and the second 15 rows are the final (or deformed)
%   marker positions.
% 3) AffinePredictions_PFD_8.m, calcF.m, multipleF_8.m in the same folder as
%   your data

clear all
clc

% Calculate deformation gradient for uniaxial extension using multipleF.m
[F1 F2 F3 F4 F5 F6] = multipleF_6;

% % Set F12 = 0 because the loading axis for all samples is in the
% % 2-direction resulting in very small F12 values
% F12 = 0;

% Calculate F11, F21, F22 for each element

% Element 1
F11_1 = F1(1,1);
F21_1 = F1(2,1);
F22_1 = F1(2,2);
F12_1 = F1(1,2);

% Element 2
F11_2 = F2(1,1);
F21_2 = F2(2,1);
F22_2 = F2(2,2);
F12_2 = F2(1,2);

% Element 3
F11_3 = F3(1,1);
F21_3 = F3(2,1);
F22_3 = F3(2,2);
F12_3 = F3(1,2);

% Element 4
F11_4 = F4(1,1);
F21_4 = F4(2,1);
F22_4 = F4(2,2);
F12_4 = F4(1,2);

% Element 5
F11_5 = F5(1,1);
F21_5 = F5(2,1);
F22_5 = F5(2,2);
F12_5 = F5(1,2);

% Element 6
F11_6 = F6(1,1);
F21_6 = F6(2,1);
F22_6 = F6(2,2);
F12_6 = F6(1,2);

% SALS data was processed separately in order to separate the fiber
```

```
% alignment data for each element from the whole tissue sample

% Load SALS Data - Element 1
data_pre_elm1 = load('pre_1.txt');
data_fail_elm1 = load('fail_1.txt');
Centroid_Pre_elm1 = data_pre_elm1(:,5);
Centroid_Fail_elm1 = data_fail_elm1(:,5);

Cent_Pre_1 = Centroid_Pre_elm1;
Cent_Fail_1 = Centroid_Fail_elm1;

% Load SALS Data - Element 2
data_pre_elm2 = load('pre_2.txt');
data_fail_elm2 = load('fail_2.txt');
Centroid_Pre_elm2 = data_pre_elm2(:,5);
Centroid_Fail_elm2 = data_fail_elm2(:,5);

Cent_Pre_2 = Centroid_Pre_elm2;
Cent_Fail_2 = Centroid_Fail_elm2;

% Load SALS Data - Element 3
data_pre_elm3 = load('pre_3.txt');
data_fail_elm3 = load('fail_3.txt');
Centroid_Pre_elm3 = data_pre_elm3(:,5);
Centroid_Fail_elm3 = data_fail_elm3(:,5);

Cent_Pre_3 = Centroid_Pre_elm3;
Cent_Fail_3 = Centroid_Fail_elm3;

% Load SALS Data - Element 4
data_pre_elm4 = load('pre_4.txt');
data_fail_elm4 = load('fail_4.txt');
Centroid_Pre_elm4 = data_pre_elm4(:,5);
Centroid_Fail_elm4 = data_fail_elm4(:,5);

Cent_Pre_4 = Centroid_Pre_elm4;
Cent_Fail_4 = Centroid_Fail_elm4;

% Load SALS Data - Element 5
data_pre_elm5 = load('pre_5.txt');
data_fail_elm5 = load('fail_5.txt');
Centroid_Pre_elm5 = data_pre_elm5(:,5);
Centroid_Fail_elm5 = data_fail_elm5(:,5);

Cent_Pre_5 = Centroid_Pre_elm5;
Cent_Fail_5 = Centroid_Fail_elm5;

% Load SALS Data - Element 6
data_pre_elm6 = load('pre_6.txt');
data_fail_elm6 = load('fail_6.txt');
Centroid_Pre_elm6 = data_pre_elm6(:,5);
Centroid_Fail_elm6 = data_fail_elm6(:,5);

Cent_Pre_6 = Centroid_Pre_elm6;
```

```
Cent_Fail_6 = Centroid_Fail_elm6;

% Process Data - Element 1
% Calculate PFD for Preload
PFD_Pre_elm1 = zeros(length(Centroid_Pre_elm1),1);
for i = 1:length(Centroid_Pre_elm1)
    if Centroid_Pre_elm1(i)>90
        PFD_Pre_elm1(i) = Centroid_Pre_elm1(i)-180;
    else
        PFD_Pre_elm1(i) = Centroid_Pre_elm1(i);
    end
end

%PFD_Pre_elm1 = PFD_Pre_elm1';

% Calculate PFD at elongation just before failure just before failure
PFD_Fail_elm1 = zeros(length(Centroid_Fail_elm1),1);
for i = 1:length(Centroid_Fail_elm1)
    if Centroid_Fail_elm1(i)>90
        PFD_Fail_elm1(i) = Centroid_Fail_elm1(i)-180;
    else
        PFD_Fail_elm1(i) = Centroid_Fail_elm1(i);
    end
end

%PFD_Fail_elm1 = PFD_Fail_elm1';

% Process Data - Element 2
% Calculate PFD for Preload
PFD_Pre_elm2 = zeros(length(Centroid_Pre_elm2),1);
for i = 1:length(Centroid_Pre_elm2)
    if Centroid_Pre_elm2(i)>90
        PFD_Pre_elm2(i) = Centroid_Pre_elm2(i)-180;
    else
        PFD_Pre_elm2(i) = Centroid_Pre_elm2(i);
    end
end

%PFD_Pre_elm2 = PFD_Pre_elm2';

% Calculate PFD at elongation just before failure just before failure
PFD_Fail_elm2 = zeros(length(Centroid_Fail_elm2),1);
for i = 1:length(Centroid_Fail_elm2)
    if Centroid_Fail_elm2(i)>90
        PFD_Fail_elm2(i) = Centroid_Fail_elm2(i)-180;
    else
        PFD_Fail_elm2(i) = Centroid_Fail_elm2(i);
    end
end

%PFD_Fail_elm2 = PFD_Fail_elm2';

% Process Data - Element 3
% Calculate PFD for Preload
PFD_Pre_elm3 = zeros(length(Centroid_Pre_elm3),1);
```

```
for i = 1:length(Centroid_Pre_elm3)
    if Centroid_Pre_elm3(i)>90
        PFD_Pre_elm3(i) = Centroid_Pre_elm3(i)-180;
    else
        PFD_Pre_elm3(i) = Centroid_Pre_elm3(i);
    end
end

%PFD_Pre_elm3 = PFD_Pre_elm3';

% Calculate PFD at elongation just before failure just before failure
PFD_Fail_elm3 = zeros(length(Centroid_Fail_elm3),1);
for i = 1:length(Centroid_Fail_elm3)
    if Centroid_Fail_elm3(i)>90
        PFD_Fail_elm3(i) = Centroid_Fail_elm3(i)-180;
    else
        PFD_Fail_elm3(i) = Centroid_Fail_elm3(i);
    end
end

%PFD_Fail_elm3 = PFD_Fail_elm3';

% Process Data - Element 4
% Calculate PFD for Preload
PFD_Pre_elm4 = zeros(length(Centroid_Pre_elm4),1);
for i = 1:length(Centroid_Pre_elm4)
    if Centroid_Pre_elm4(i)>90
        PFD_Pre_elm4(i) = Centroid_Pre_elm4(i)-180;
    else
        PFD_Pre_elm4(i) = Centroid_Pre_elm4(i);
    end
end

%PFD_Pre_elm4 = PFD_Pre_elm4';

% Calculate PFD at elongation just before failure just before failure
PFD_Fail_elm4 = zeros(length(Centroid_Fail_elm4),1);
for i = 1:length(Centroid_Fail_elm4)
    if Centroid_Fail_elm4(i)>90
        PFD_Fail_elm4(i) = Centroid_Fail_elm4(i)-180;
    else
        PFD_Fail_elm4(i) = Centroid_Fail_elm4(i);
    end
end

%PFD_Fail_elm4 = PFD_Fail_elm4';

% Process Data - Element 5
% Calculate PFD for Preload
PFD_Pre_elm5 = zeros(length(Centroid_Pre_elm5),1);
for i = 1:length(Centroid_Pre_elm5)
    if Centroid_Pre_elm5(i)>90
        PFD_Pre_elm5(i) = Centroid_Pre_elm5(i)-180;
    else
        PFD_Pre_elm5(i) = Centroid_Pre_elm5(i);
```

```
    end
end

%PFD_Pre_elm5 = PFD_Pre_elm5';

% Calculate PFD at elongation just before failure just before failure
PFD_Fail_elm5 = zeros(length(Centroid_Fail_elm5),1);
for i = 1:length(Centroid_Fail_elm5)
    if Centroid_Fail_elm5(i)>90
        PFD_Fail_elm5(i) = Centroid_Fail_elm5(i)-180;
    else
        PFD_Fail_elm5(i) = Centroid_Fail_elm5(i);
    end
end

%PFD_Fail_elm5 = PFD_Fail_elm5';

% Process Data - Element 6
% Calculate PFD for Preload
PFD_Pre_elm6 = zeros(length(Centroid_Pre_elm6),1);
for i = 1:length(Centroid_Pre_elm6)
    if Centroid_Pre_elm6(i)>90
        PFD_Pre_elm6(i) = Centroid_Pre_elm6(i)-180;
    else
        PFD_Pre_elm6(i) = Centroid_Pre_elm6(i);
    end
end

%PFD_Pre_elm6 = PFD_Pre_elm6';

% Calculate PFD at elongation just before failure just before failure
PFD_Fail_elm6 = zeros(length(Centroid_Fail_elm6),1);
for i = 1:length(Centroid_Fail_elm6)
    if Centroid_Fail_elm6(i)>90
        PFD_Fail_elm6(i) = Centroid_Fail_elm6(i)-180;
    else
        PFD_Fail_elm6(i) = Centroid_Fail_elm6(i);
    end
end

%PFD_Fail_elm6 = PFD_Fail_elm6';

%convert to radians
PFD_Pre_elm1 = PFD_Pre_elm1.*pi./180;
PFD_Fail_elm1 = PFD_Fail_elm1.*pi./180;
Centroid_Pre_elm1 = Cent_Pre_1.*pi./180;
Centroid_Fail_elm1 = Cent_Fail_1.*pi./180;

PFD_Pre_elm2 = PFD_Pre_elm2.*pi./180;
PFD_Fail_elm2 = PFD_Fail_elm2.*pi./180;
Centroid_Pre_elm2 = Cent_Pre_2.*pi./180;
Centroid_Fail_elm2 = Cent_Fail_2.*pi./180;

PFD_Pre_elm3 = PFD_Pre_elm3.*pi./180;
PFD_Fail_elm3 = PFD_Fail_elm3.*pi./180;
```

```
Centroid_Pre_elm3 = Cent_Pre_3.*pi./180;
Centroid_Fail_elm3 = Cent_Fail_3.*pi./180;

PFD_Pre_elm4 = PFD_Pre_elm4.*pi./180;
PFD_Fail_elm4 = PFD_Fail_elm4.*pi./180;
Centroid_Pre_elm4 = Cent_Pre_4.*pi./180;
Centroid_Fail_elm4 = Cent_Fail_4.*pi./180;

PFD_Pre_elm5 = PFD_Pre_elm5.*pi./180;
PFD_Fail_elm5 = PFD_Fail_elm5.*pi./180;
Centroid_Pre_elm5 = Cent_Pre_5.*pi./180;
Centroid_Fail_elm5 = Cent_Fail_5.*pi./180;

PFD_Pre_elm6 = PFD_Pre_elm6.*pi/180;
PFD_Fail_elm6 = PFD_Fail_elm6.*pi./180;
Centroid_Pre_elm6 = Cent_Pre_6.*pi./180;
Centroid_Fail_elm6 = Cent_Fail_6.*pi./180;

% Compute circular variance

% Element 1
circ_pre_1 = circ_var(Centroid_Pre_elm1,[],[],1);
circ_fail_1 = circ_var(Centroid_Fail_elm1,[],[],1);

% Element 2
circ_pre_2 = circ_var(Centroid_Pre_elm2,[],[],1);
circ_fail_2 = circ_var(Centroid_Fail_elm2,[],[],1);

% Element 3
circ_pre_3 = circ_var(Centroid_Pre_elm3,[],[],1);
circ_fail_3 = circ_var(Centroid_Fail_elm3,[],[],1);

% Element 4
circ_pre_4 = circ_var(Centroid_Pre_elm4,[],[],1);
circ_fail_4 = circ_var(Centroid_Fail_elm4,[],[],1);

% Element 5
circ_pre_5 = circ_var(Centroid_Pre_elm5,[],[],1);
circ_fail_5 = circ_var(Centroid_Fail_elm5,[],[],1);

% Element 6
circ_pre_6 = circ_var(Centroid_Pre_elm6,[],[],1);
circ_fail_6 = circ_var(Centroid_Fail_elm6,[],[],1);

% Calculate Affine Prediction based on PFD at Preload and Deformation
Gradient
thetaP_elm1 = atan2((F22_1.*sin(PFD_Pre_elm1) +
F21_1.*cos(PFD_Pre_elm1)),(F11_1.*cos(PFD_Pre_elm1) +
F12_1.*sin(PFD_Pre_elm1)));
thetaP_elm2 = atan2((F22_2.*sin(PFD_Pre_elm2) +
F21_2.*cos(PFD_Pre_elm2)),(F11_2.*cos(PFD_Pre_elm2) +
F12_2.*sin(PFD_Pre_elm2)));
thetaP_elm3 = atan2((F22_3.*sin(PFD_Pre_elm3) +
F21_3.*cos(PFD_Pre_elm3)),(F11_3.*cos(PFD_Pre_elm3) +
F12_3.*sin(PFD_Pre_elm3)));
```

```
thetaP_elm4 = atan2((F22_4.*sin(PFD_Pre_elm4) +
F21_4.*cos(PFD_Pre_elm4)),(F11_4.*cos(PFD_Pre_elm4) +
F12_4.*sin(PFD_Pre_elm4)));
thetaP_elm5 = atan2((F22_5.*sin(PFD_Pre_elm5) +
F21_5.*cos(PFD_Pre_elm5)),(F11_5.*cos(PFD_Pre_elm5) +
F12_5.*sin(PFD_Pre_elm5)));
thetaP_elm6 = atan2((F22_6.*sin(PFD_Pre_elm6) +
F21_6.*cos(PFD_Pre_elm6)),(F11_6.*cos(PFD_Pre_elm6) +
F12_6.*sin(PFD_Pre_elm6)));

%convert back to degrees
PFD_Pre_elm1 = PFD_Pre_elm1.*180./pi;
PFD_Fail_elm1 = PFD_Fail_elm1.*180./pi;
Centroid_Pre_elm1 = Centroid_Pre_elm1.*180./pi;
Centroid_Fail_elm1 = Centroid_Pre_elm1.*180./pi;
thetaP_elm1 = thetaP_elm1.*180./pi;

PFD_Pre_elm2 = PFD_Pre_elm2.*180./pi;
PFD_Fail_elm2 = PFD_Fail_elm2.*180./pi;
Centroid_Pre_elm2 = Centroid_Pre_elm2.*180./pi;
Centroid_Fail_elm2 = Centroid_Pre_elm2.*180./pi;
thetaP_elm2 = thetaP_elm2.*180./pi;

PFD_Pre_elm3 = PFD_Pre_elm3.*180./pi;
PFD_Fail_elm3 = PFD_Fail_elm3.*180./pi;
Centroid_Pre_elm3 = Centroid_Pre_elm3.*180./pi;
Centroid_Fail_elm3 = Centroid_Pre_elm3.*180./pi;
thetaP_elm3 = thetaP_elm3.*180./pi;

PFD_Pre_elm4 = PFD_Pre_elm4.*180./pi;
PFD_Fail_elm4 = PFD_Fail_elm4.*180./pi;
Centroid_Pre_elm4 = Centroid_Pre_elm4.*180./pi;
Centroid_Fail_elm4 = Centroid_Pre_elm4.*180./pi;
thetaP_elm4 = thetaP_elm4.*180./pi;

PFD_Pre_elm5 = PFD_Pre_elm5.*180./pi;
PFD_Fail_elm5 = PFD_Fail_elm5.*180./pi;
Centroid_Pre_elm5 = Centroid_Pre_elm5.*180./pi;
Centroid_Fail_elm5 = Centroid_Pre_elm5.*180./pi;
thetaP_elm5 = thetaP_elm5.*180./pi;

PFD_Pre_elm6 = PFD_Pre_elm6.*180./pi;
PFD_Fail_elm6 = PFD_Fail_elm6.*180./pi;
Centroid_Pre_elm6 = Centroid_Pre_elm6.*180./pi;
Centroid_Fail_elm6 = Centroid_Pre_elm6.*180./pi;
thetaP_elm6 = thetaP_elm6.*180./pi;

bins = -90:1:90;
bins = bins';

% Generate Histograms - normalize frequency to number of data points
thetaP_Hist_elm1 = hist(thetaP_elm1,181)'./length(thetaP_elm1);
PFD_Fail_Hist_elm1 = hist(PFD_Fail_elm1, 181)'./length(PFD_Fail_elm1);

thetaP_Hist_elm2 = hist(thetaP_elm2,181)'./length(thetaP_elm2);
```

```
PFD_Fail_Hist_elm2 = hist(PFD_Fail_elm2, 181)'./length(PFD_Fail_elm2);

thetaP_Hist_elm3 = hist(thetaP_elm3,181)'./length(thetaP_elm3);
PFD_Fail_Hist_elm3 = hist(PFD_Fail_elm3, 181)'./length(PFD_Fail_elm3);

thetaP_Hist_elm4 = hist(thetaP_elm4,181)'./length(thetaP_elm4);
PFD_Fail_Hist_elm4 = hist(PFD_Fail_elm4, 181)'./length(PFD_Fail_elm4);

thetaP_Hist_elm5 = hist(thetaP_elm5,181)'./length(thetaP_elm5);
PFD_Fail_Hist_elm5 = hist(PFD_Fail_elm5, 181)'./length(PFD_Fail_elm5);

thetaP_Hist_elm6 = hist(thetaP_elm6,181)'./length(thetaP_elm6);
PFD_Fail_Hist_elm6 = hist(PFD_Fail_elm6, 181)'./length(PFD_Fail_elm6);

% compute quantiles
quant_Pred_1 = quantile(thetaP_elm1,100)';
quant_Exp_1 = quantile(PFD_Fail_elm1,100)';

quant_Pred_2 = quantile(thetaP_elm2,100)';
quant_Exp_2 = quantile(PFD_Fail_elm2,100)';

quant_Pred_3 = quantile(thetaP_elm3,100)';
quant_Exp_3 = quantile(PFD_Fail_elm3,100)';

quant_Pred_4 = quantile(thetaP_elm4,100)';
quant_Exp_4 = quantile(PFD_Fail_elm4,100)';

quant_Pred_5 = quantile(thetaP_elm5,100)';
quant_Exp_5 = quantile(PFD_Fail_elm5,100)';

quant_Pred_6 = quantile(thetaP_elm6,100)';
quant_Exp_6 = quantile(PFD_Fail_elm6,100)';

% Quantile Average & Difference

quant_ave_1 = zeros(length(100),1);
quant_ave_2 = zeros(length(100),1);
quant_ave_3 = zeros(length(100),1);
quant_ave_4 = zeros(length(100),1);
quant_ave_5 = zeros(length(100),1);
quant_ave_6 = zeros(length(100),1);

quant_diff_1 = zeros(length(100),1);
quant_diff_2 = zeros(length(100),1);
quant_diff_3 = zeros(length(100),1);
quant_diff_4 = zeros(length(100),1);
quant_diff_5 = zeros(length(100),1);
quant_diff_6 = zeros(length(100),1);

for i = 1:100
    quant_ave_1(i) = (quant_Pred_1(i) + quant_Exp_1(i))/2;
    quant_ave_2(i) = (quant_Pred_2(i) + quant_Exp_2(i))/2;
    quant_ave_3(i) = (quant_Pred_3(i) + quant_Exp_3(i))/2;
    quant_ave_4(i) = (quant_Pred_4(i) + quant_Exp_4(i))/2;
```

```
    quant_ave_5(i) = (quant_Pred_5(i) + quant_Exp_5(i))/2;
    quant_ave_6(i) = (quant_Pred_6(i) + quant_Exp_6(i))/2;

    quant_diff_1(i) = quant_Exp_1(i) - quant_Pred_1(i);
    quant_diff_2(i) = quant_Exp_2(i) - quant_Pred_2(i);
    quant_diff_3(i) = quant_Exp_3(i) - quant_Pred_3(i);
    quant_diff_4(i) = quant_Exp_4(i) - quant_Pred_4(i);
    quant_diff_5(i) = quant_Exp_5(i) - quant_Pred_5(i);
    quant_diff_6(i) = quant_Exp_6(i) - quant_Pred_6(i);

end

quant_ave_1 = quant_ave_1';
quant_ave_2 = quant_ave_2';
quant_ave_3 = quant_ave_3';
quant_ave_4 = quant_ave_4';
quant_ave_5 = quant_ave_5';
quant_ave_6 = quant_ave_6';

quant_diff_1 = quant_diff_1';
quant_diff_2 = quant_diff_2';
quant_diff_3 = quant_diff_3';
quant_diff_4 = quant_diff_4';
quant_diff_5 = quant_diff_5';
quant_diff_6 = quant_diff_6';

% Write Data to Excel

xlswrite('Affine_Prediction_ALL', median(quant_diff_1), 'Summary', 'B2');
xlswrite('Affine_Prediction_ALL', mean(quant_diff_1), 'Summary', 'B3');
xlswrite('Affine_Prediction_ALL', std(quant_diff_1), 'Summary', 'B4');
xlswrite('Affine_Prediction_ALL', 2*std(quant_diff_1), 'Summary', 'B5');
xlswrite('Affine_Prediction_ALL', max(quant_diff_1), 'Summary', 'B6');
xlswrite('Affine_Prediction_ALL', min(quant_diff_1), 'Summary', 'B7');
xlswrite('Affine_Prediction_ALL', range(quant_diff_1), 'Summary', 'B8');
xlswrite('Affine_Prediction_ALL', circ_pre_1, 'Summary','B9');
xlswrite('Affine_Prediction_ALL', circ_fail_1, 'Summary','B10');

xlswrite('Affine_Prediction_ALL', median(quant_diff_2), 'Summary', 'C2');
xlswrite('Affine_Prediction_ALL', mean(quant_diff_2), 'Summary', 'C3');
xlswrite('Affine_Prediction_ALL', std(quant_diff_2), 'Summary', 'C4');
xlswrite('Affine_Prediction_ALL', 2*std(quant_diff_2), 'Summary', 'C5');
xlswrite('Affine_Prediction_ALL', max(quant_diff_2), 'Summary', 'C6');
xlswrite('Affine_Prediction_ALL', min(quant_diff_2), 'Summary', 'C7');
xlswrite('Affine_Prediction_ALL', range(quant_diff_2), 'Summary', 'C8');
xlswrite('Affine_Prediction_ALL', circ_pre_2, 'Summary','C9');
xlswrite('Affine_Prediction_ALL', circ_fail_2, 'Summary','C10');

xlswrite('Affine_Prediction_ALL', median(quant_diff_3), 'Summary', 'D2');
xlswrite('Affine_Prediction_ALL', mean(quant_diff_3), 'Summary', 'D3');
xlswrite('Affine_Prediction_ALL', std(quant_diff_3), 'Summary', 'D4');
xlswrite('Affine_Prediction_ALL', 2*std(quant_diff_3), 'Summary', 'D5');
xlswrite('Affine_Prediction_ALL', max(quant_diff_3), 'Summary', 'D6');
xlswrite('Affine_Prediction_ALL', min(quant_diff_3), 'Summary', 'D7');
xlswrite('Affine_Prediction_ALL', range(quant_diff_3), 'Summary', 'D8');
```

```
xlswrite('Affine_Prediction_ALL', circ_pre_3, 'Summary','D9');
xlswrite('Affine_Prediction_ALL', circ_fail_3, 'Summary','D10');

xlswrite('Affine_Prediction_ALL', median(quant_diff_4), 'Summary', 'E2');
xlswrite('Affine_Prediction_ALL', mean(quant_diff_4), 'Summary', 'E3');
xlswrite('Affine_Prediction_ALL', std(quant_diff_4), 'Summary', 'E4');
xlswrite('Affine_Prediction_ALL', 2*std(quant_diff_4), 'Summary', 'E5');
xlswrite('Affine_Prediction_ALL', max(quant_diff_4), 'Summary', 'E6');
xlswrite('Affine_Prediction_ALL', min(quant_diff_4), 'Summary', 'E7');
xlswrite('Affine_Prediction_ALL', range(quant_diff_4), 'Summary', 'E8');
xlswrite('Affine_Prediction_ALL', circ_pre_4, 'Summary','E9');
xlswrite('Affine_Prediction_ALL', circ_fail_4, 'Summary','E10');

xlswrite('Affine_Prediction_ALL', median(quant_diff_5), 'Summary', 'F2');
xlswrite('Affine_Prediction_ALL', mean(quant_diff_5), 'Summary', 'F3');
xlswrite('Affine_Prediction_ALL', std(quant_diff_5), 'Summary', 'F4');
xlswrite('Affine_Prediction_ALL', 2*std(quant_diff_5), 'Summary', 'F5');
xlswrite('Affine_Prediction_ALL', max(quant_diff_5), 'Summary', 'F6');
xlswrite('Affine_Prediction_ALL', min(quant_diff_5), 'Summary', 'F7');
xlswrite('Affine_Prediction_ALL', range(quant_diff_5), 'Summary', 'F8');
xlswrite('Affine_Prediction_ALL', circ_pre_5, 'Summary','F9');
xlswrite('Affine_Prediction_ALL', circ_fail_5, 'Summary','F10');

xlswrite('Affine_Prediction_ALL', median(quant_diff_6), 'Summary', 'G2');
xlswrite('Affine_Prediction_ALL', mean(quant_diff_6), 'Summary', 'G3');
xlswrite('Affine_Prediction_ALL', std(quant_diff_6), 'Summary', 'G4');
xlswrite('Affine_Prediction_ALL', 2*std(quant_diff_6), 'Summary', 'G5');
xlswrite('Affine_Prediction_ALL', max(quant_diff_6), 'Summary', 'G6');
xlswrite('Affine_Prediction_ALL', min(quant_diff_6), 'Summary', 'G7');
xlswrite('Affine_Prediction_ALL', range(quant_diff_6), 'Summary', 'G8');
xlswrite('Affine_Prediction_ALL', circ_pre_6, 'Summary','G9');
xlswrite('Affine_Prediction_ALL', circ_fail_6, 'Summary','G10');

xlswrite('Affine_Prediction_ALL', PFD_Pre_elm1, 'Element1','A:A');
xlswrite('Affine_Prediction_ALL', thetaP_elm1, 'Element1','B:B');
xlswrite('Affine_Prediction_ALL', PFD_Fail_elm1, 'Element1','C:C');
xlswrite('Affine_Prediction_ALL', thetaP_Hist_elm1, 'Element1','D1:D181');
xlswrite('Affine_Prediction_ALL', PFD_Fail_Hist_elm1, 'Element1','E1:E181');
xlswrite('Affine_Prediction_ALL', bins, 'Element1', 'F1:F181')
xlswrite('Affine_Prediction_ALL', quant_Pred_1, 'Element1', 'G1:G100');
xlswrite('Affine_Prediction_ALL', quant_Exp_1, 'Element1', 'H1:H100');
xlswrite('Affine_Prediction_ALL', quant_ave_1, 'Element1', 'I1:I100');
xlswrite('Affine_Prediction_ALL', quant_diff_1, 'Element1', 'J1:J100');

xlswrite('Affine_Prediction_ALL', PFD_Pre_elm2, 'Element2','A:A');
xlswrite('Affine_Prediction_ALL', thetaP_elm2, 'Element2','B:B');
xlswrite('Affine_Prediction_ALL', PFD_Fail_elm2, 'Element2','C:C');
xlswrite('Affine_Prediction_ALL', thetaP_Hist_elm2, 'Element2','D1:D181');
xlswrite('Affine_Prediction_ALL', PFD_Fail_Hist_elm2, 'Element2','E1:E181');
xlswrite('Affine_Prediction_ALL', bins, 'Element2', 'F1:F181')
xlswrite('Affine_Prediction_ALL', quant_Pred_2, 'Element2', 'G1:G100');
xlswrite('Affine_Prediction_ALL', quant_Exp_2, 'Element2', 'H1:H100');
xlswrite('Affine_Prediction_ALL', quant_ave_2, 'Element2', 'I1:I100');
xlswrite('Affine_Prediction_ALL', quant_diff_2, 'Element2', 'J1:J100');

xlswrite('Affine_Prediction_ALL', PFD_Pre_elm3, 'Element3','A:A');
```

```
xlswrite('Affine_Prediction_ALL', thetaP_elm3, 'Element3','B:B');
xlswrite('Affine_Prediction_ALL', PFD_Fail_elm3, 'Element3','C:C');
xlswrite('Affine_Prediction_ALL', thetaP_Hist_elm3, 'Element3','D1:D181');
xlswrite('Affine_Prediction_ALL', PFD_Fail_Hist_elm3, 'Element3','E1:E181');
xlswrite('Affine_Prediction_ALL', bins, 'Element3', 'F1:F181')
xlswrite('Affine_Prediction_ALL', quant_Pred_3, 'Element3', 'G1:G100');
xlswrite('Affine_Prediction_ALL', quant_Exp_3, 'Element3', 'H1:H100');
xlswrite('Affine_Prediction_ALL', quant_ave_3, 'Element3', 'I1:I100');
xlswrite('Affine_Prediction_ALL', quant_diff_3, 'Element3', 'J1:J100');

xlswrite('Affine_Prediction_ALL', PFD_Pre_elm4, 'Element4','A:A');
xlswrite('Affine_Prediction_ALL', thetaP_elm4, 'Element4','B:B');
xlswrite('Affine_Prediction_ALL', PFD_Fail_elm4, 'Element4','C:C');
xlswrite('Affine_Prediction_ALL', thetaP_Hist_elm4, 'Element4','D1:D181');
xlswrite('Affine_Prediction_ALL', PFD_Fail_Hist_elm4, 'Element4','E1:E181');
xlswrite('Affine_Prediction_ALL', bins, 'Element4', 'F1:F181')
xlswrite('Affine_Prediction_ALL', quant_Pred_4, 'Element4', 'G1:G100');
xlswrite('Affine_Prediction_ALL', quant_Exp_4, 'Element4', 'H1:H100');
xlswrite('Affine_Prediction_ALL', quant_ave_4, 'Element4', 'I1:I100');
xlswrite('Affine_Prediction_ALL', quant_diff_4, 'Element4', 'J1:J100');

xlswrite('Affine_Prediction_ALL', PFD_Pre_elm5, 'Element5','A:A');
xlswrite('Affine_Prediction_ALL', thetaP_elm5, 'Element5','B:B');
xlswrite('Affine_Prediction_ALL', PFD_Fail_elm5, 'Element5','C:C');
xlswrite('Affine_Prediction_ALL', thetaP_Hist_elm5, 'Element5','D1:D181');
xlswrite('Affine_Prediction_ALL', PFD_Fail_Hist_elm5, 'Element5','E1:E181');
xlswrite('Affine_Prediction_ALL', bins, 'Element5', 'F1:F181')
xlswrite('Affine_Prediction_ALL', quant_Pred_5, 'Element5', 'G1:G100');
xlswrite('Affine_Prediction_ALL', quant_Exp_5, 'Element5', 'H1:H100');
xlswrite('Affine_Prediction_ALL', quant_ave_5, 'Element5', 'I1:I100');
xlswrite('Affine_Prediction_ALL', quant_diff_5, 'Element5', 'J1:J100');

xlswrite('Affine_Prediction_ALL', PFD_Pre_elm6, 'Element6','A:A');
xlswrite('Affine_Prediction_ALL', thetaP_elm6, 'Element6','B:B');
xlswrite('Affine_Prediction_ALL', PFD_Fail_elm6, 'Element6','C:C');
xlswrite('Affine_Prediction_ALL', thetaP_Hist_elm6, 'Element6','D1:D181');
xlswrite('Affine_Prediction_ALL', PFD_Fail_Hist_elm6, 'Element6','E1:E181');
xlswrite('Affine_Prediction_ALL', bins, 'Element6', 'F1:F181')
xlswrite('Affine_Prediction_ALL', quant_Pred_6, 'Element6', 'G1:G100');
xlswrite('Affine_Prediction_ALL', quant_Exp_6, 'Element6', 'H1:H100');
xlswrite('Affine_Prediction_ALL', quant_ave_6, 'Element6', 'I1:I100');
xlswrite('Affine_Prediction_ALL', quant_diff_6, 'Element6', 'J1:J100');
```

APPENDIX K

AFFINE PREDICTIONS FOR NORMAL CAPSULE

Table 7.41 Preferred fiber direction histogram and corresponding projection plot comparing the experimental and affine-predicted fiber distribution in the normal AB-IGHL for Specimen 08-12389L.

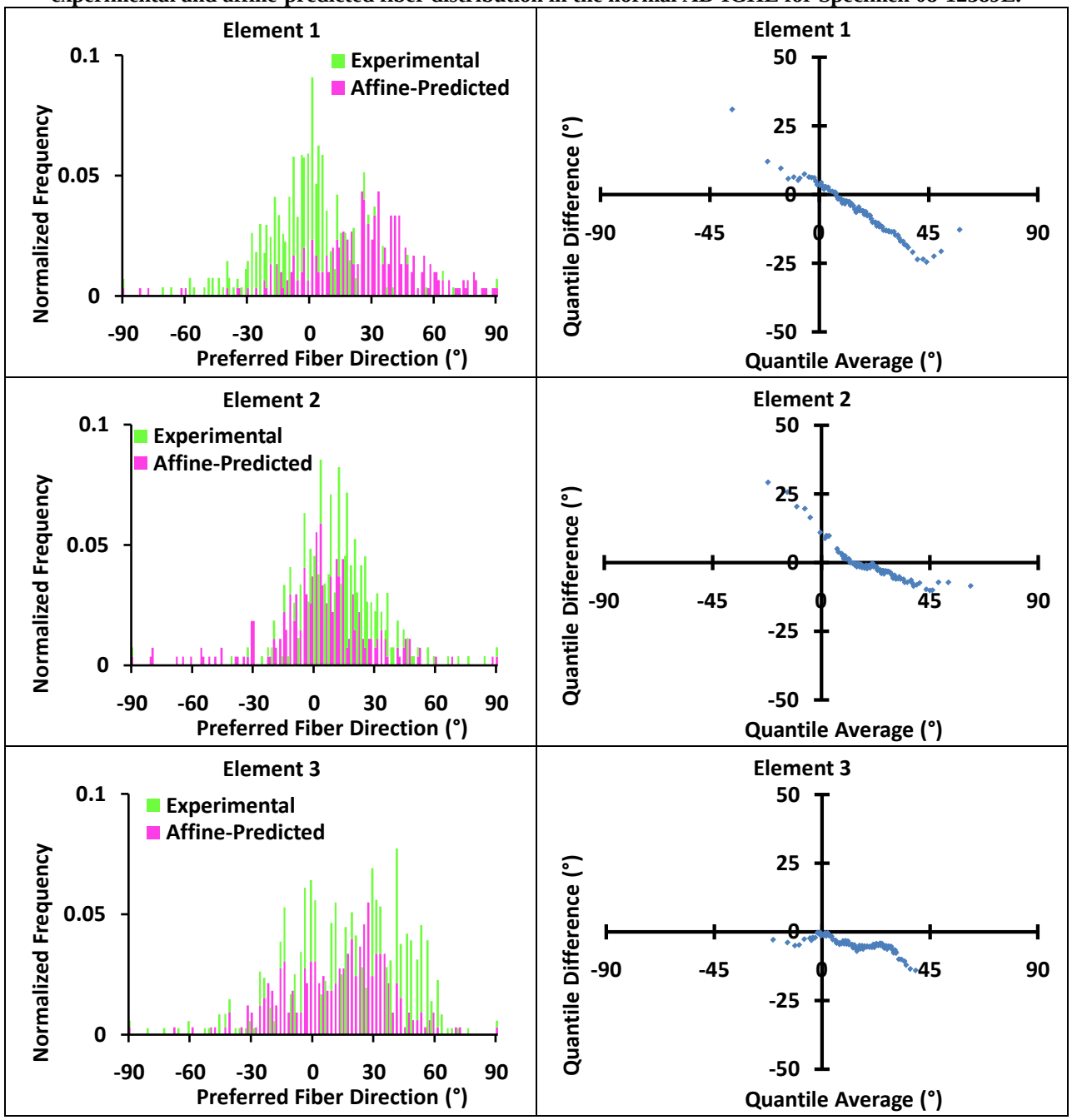

Table 7.41 (Continued).

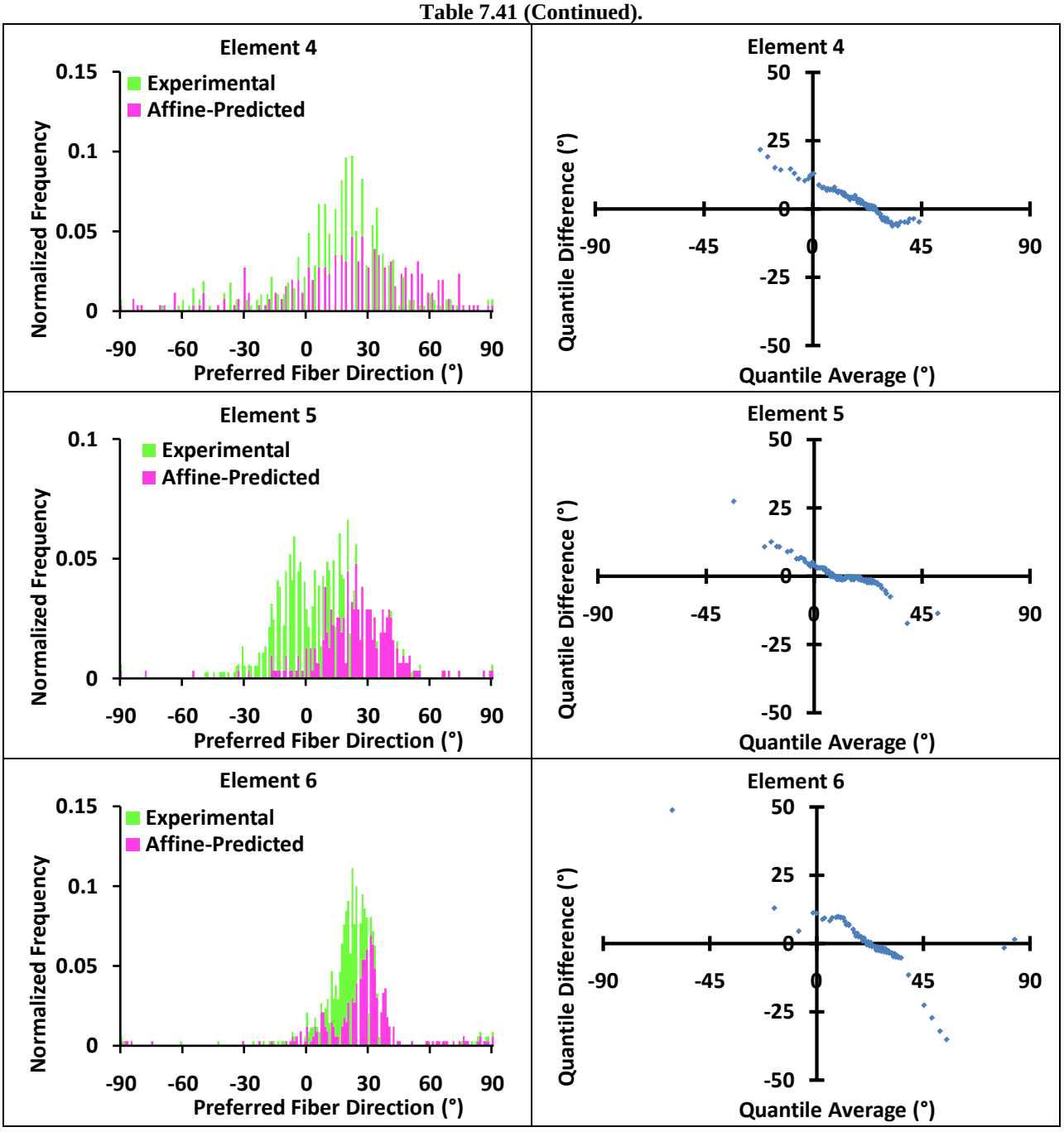

Table 7.42 Preferred fiber direction histogram and corresponding projection plot comparing the experimental and affine-predicted fiber distribution in the normal axillary pouch for Specimen 08-12389L.

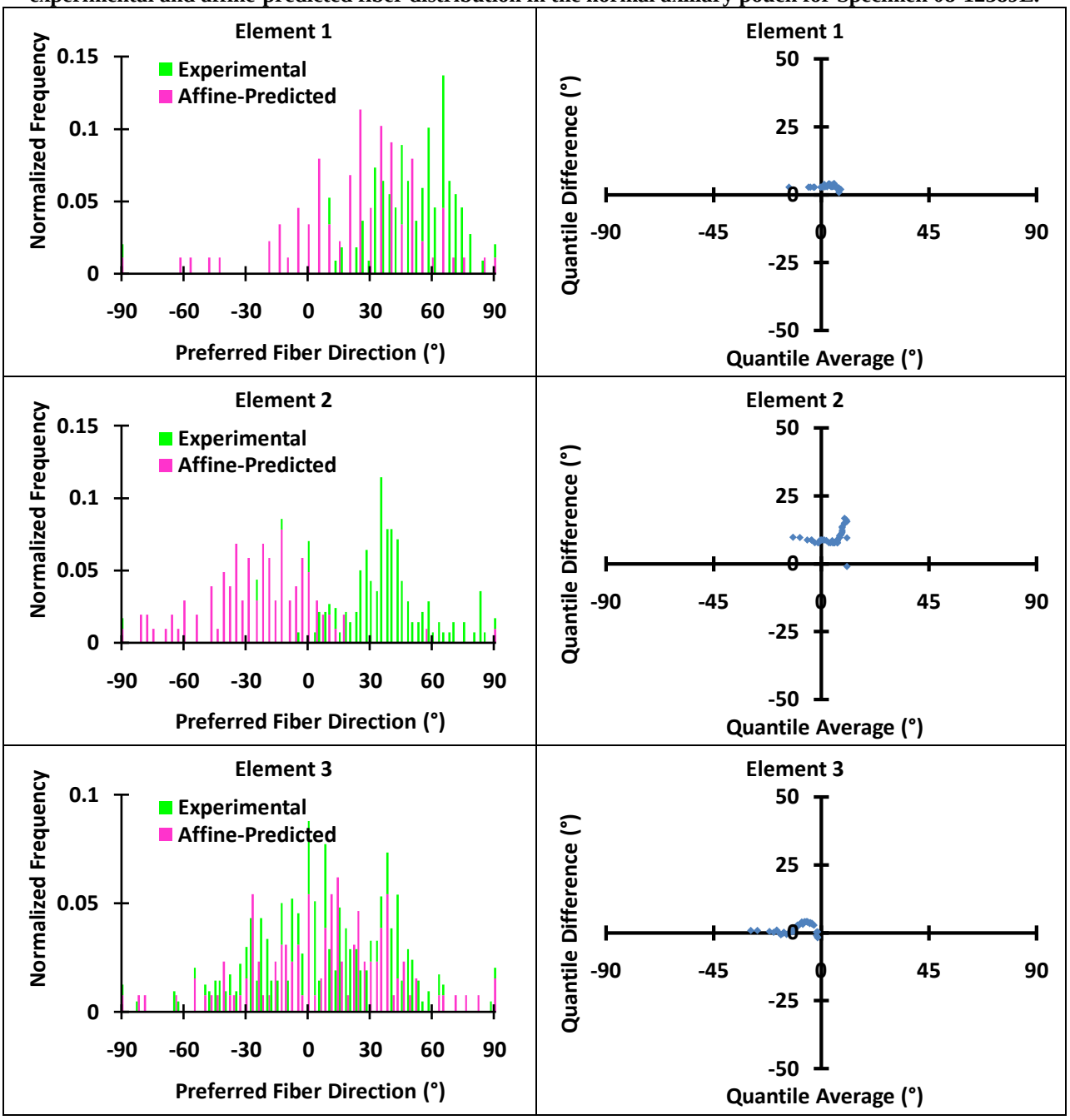

Table 7.42 (Continued).

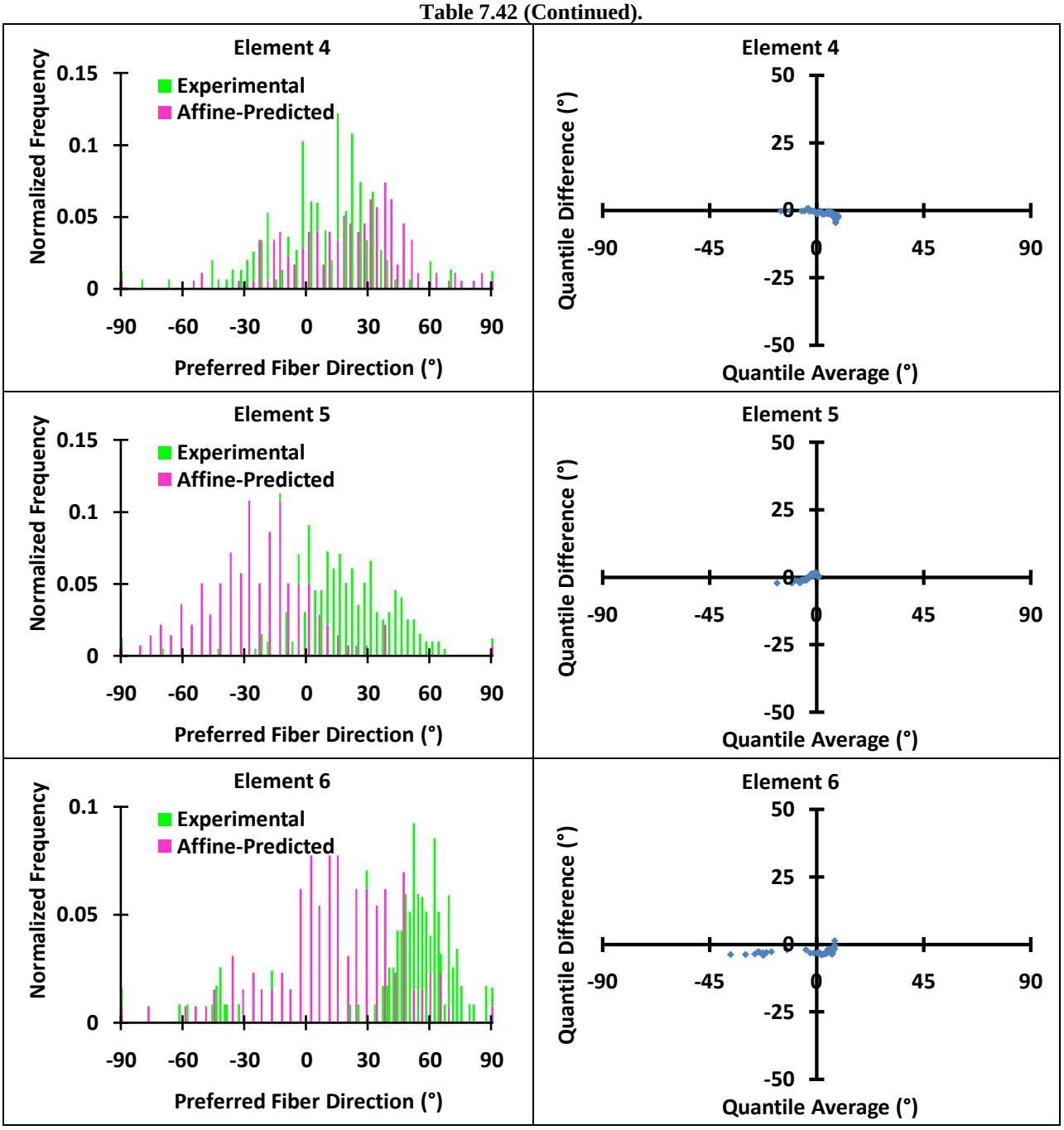

Table 7.43 Preferred fiber direction histogram and corresponding projection plot comparing the experimental and affine-predicted fiber distribution in the normal AB-IGHL for Specimen 09-06267R.

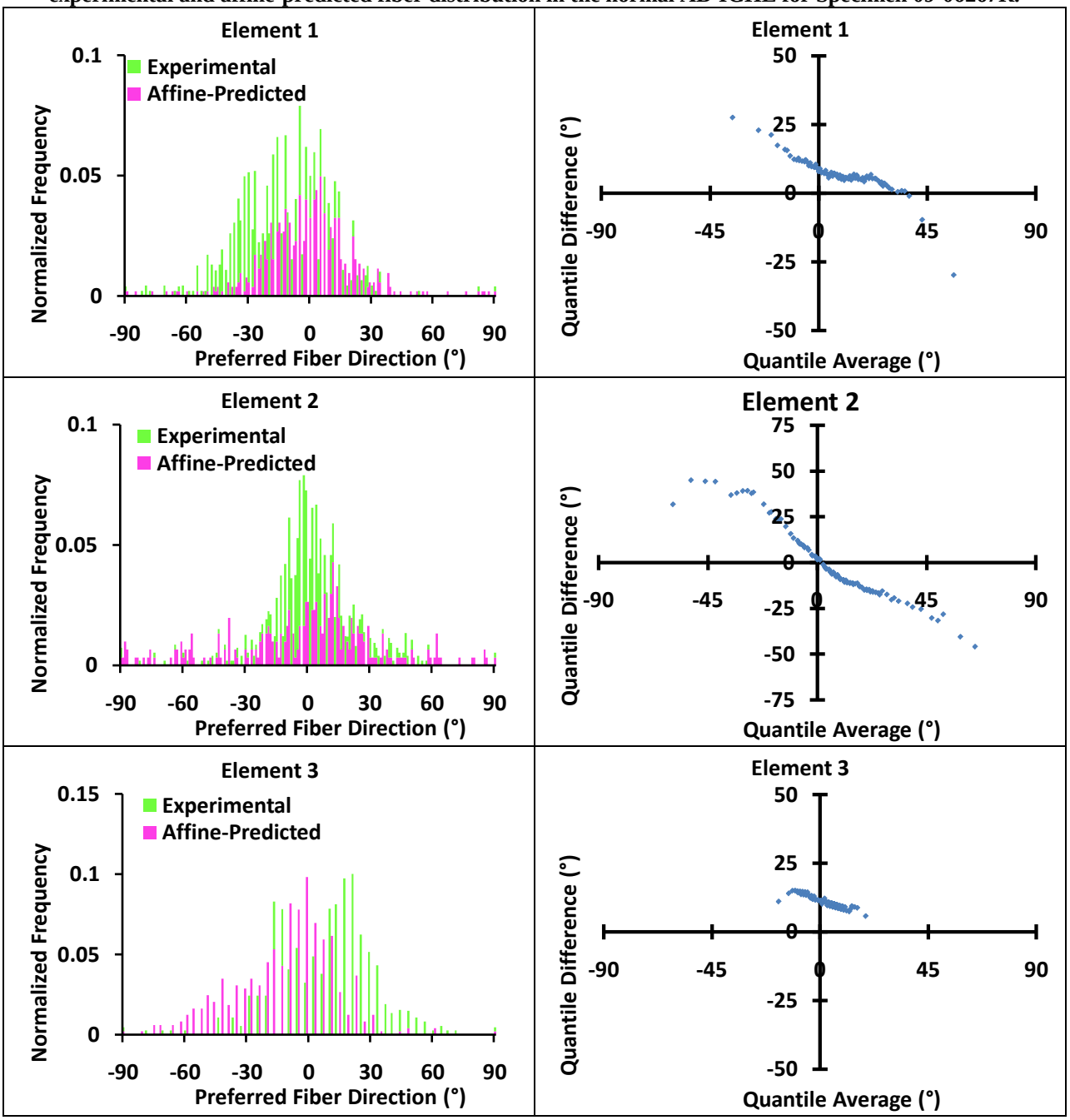

Table 7.43 (Continued).

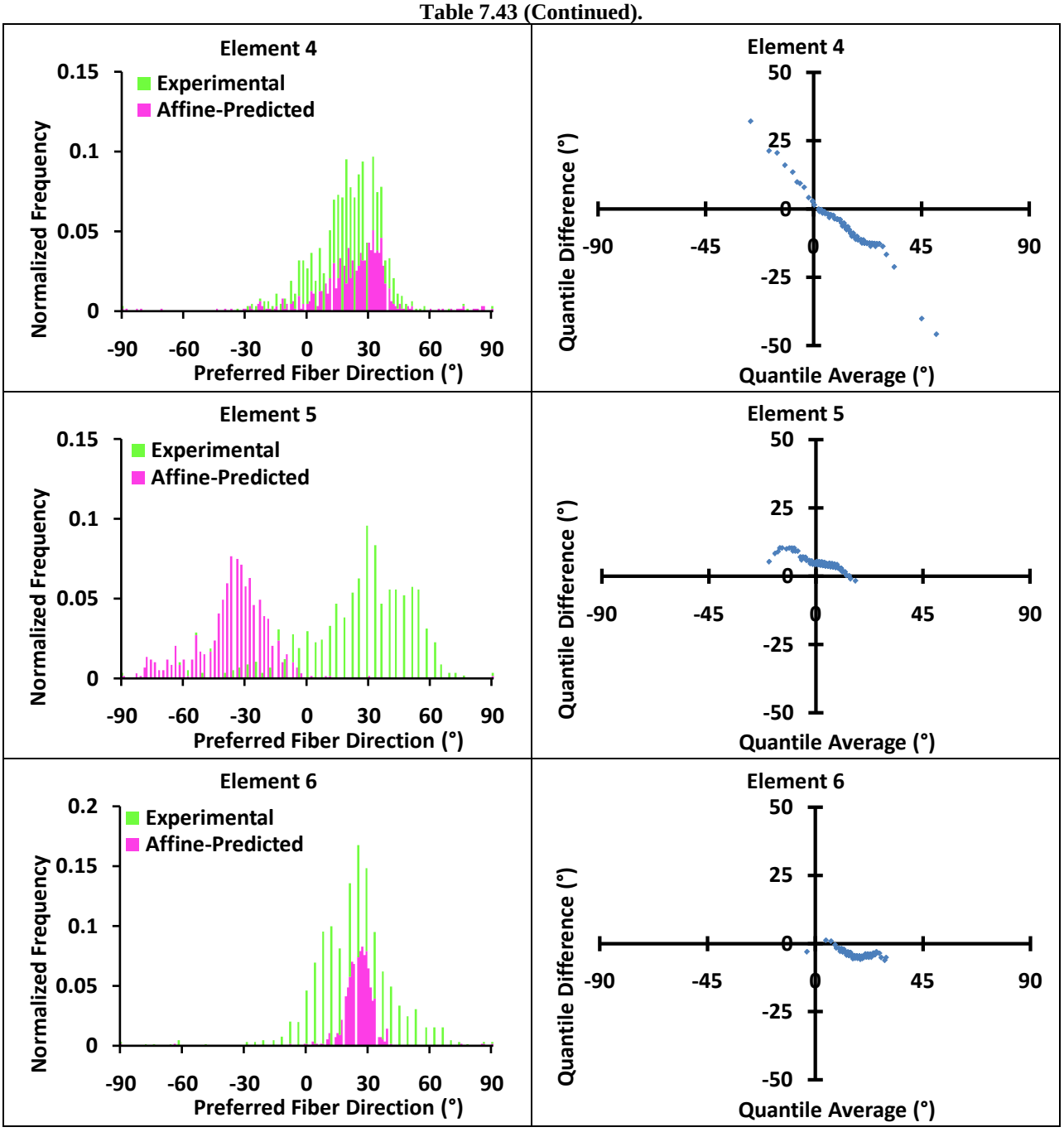

Table 7.44 Preferred fiber direction histogram and corresponding projection plot comparing the experimental and affine-predicted fiber distribution in the normal axillary pouch for Specimen 09-06267R.

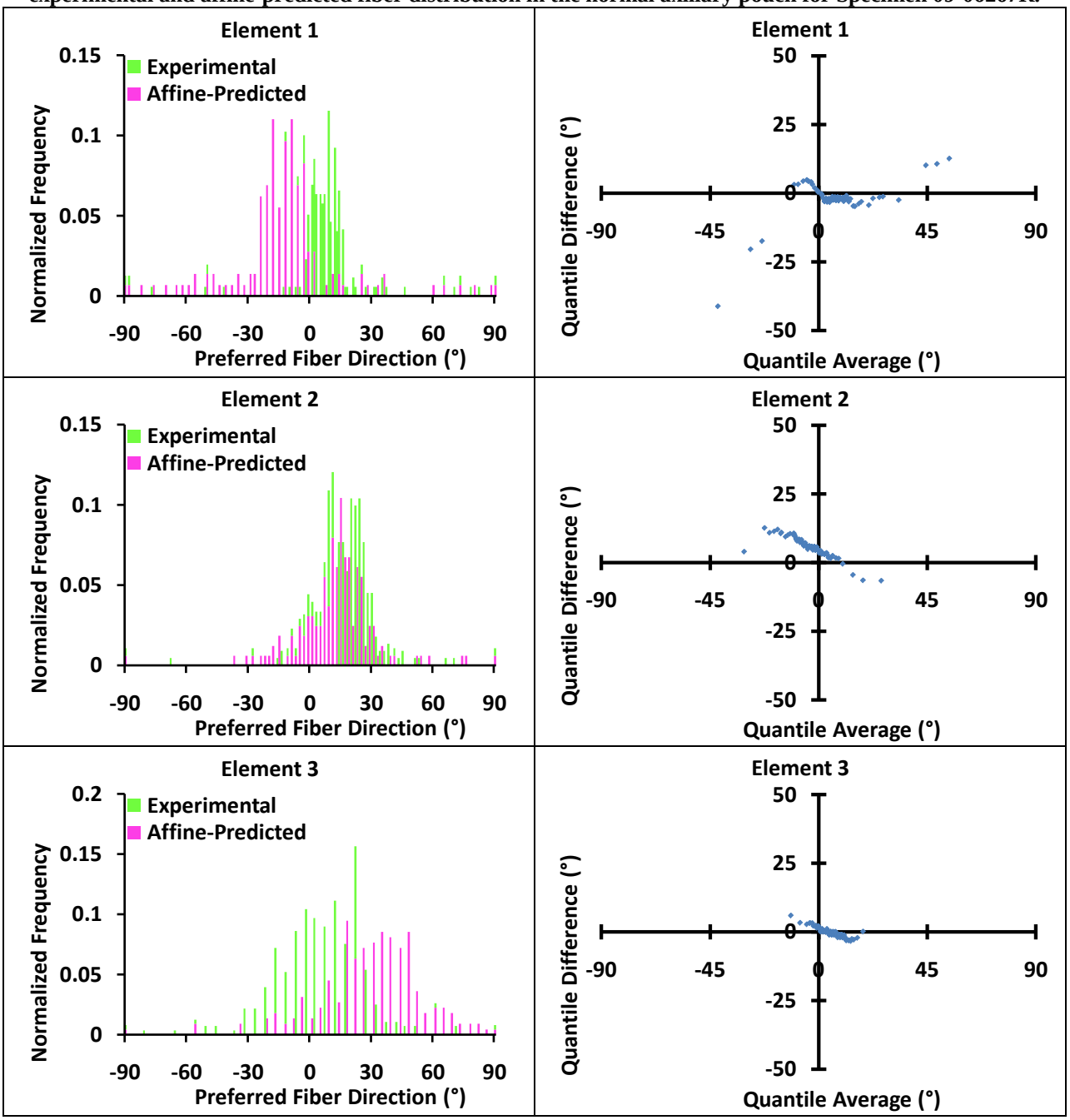

Table 7.44 (Continued).

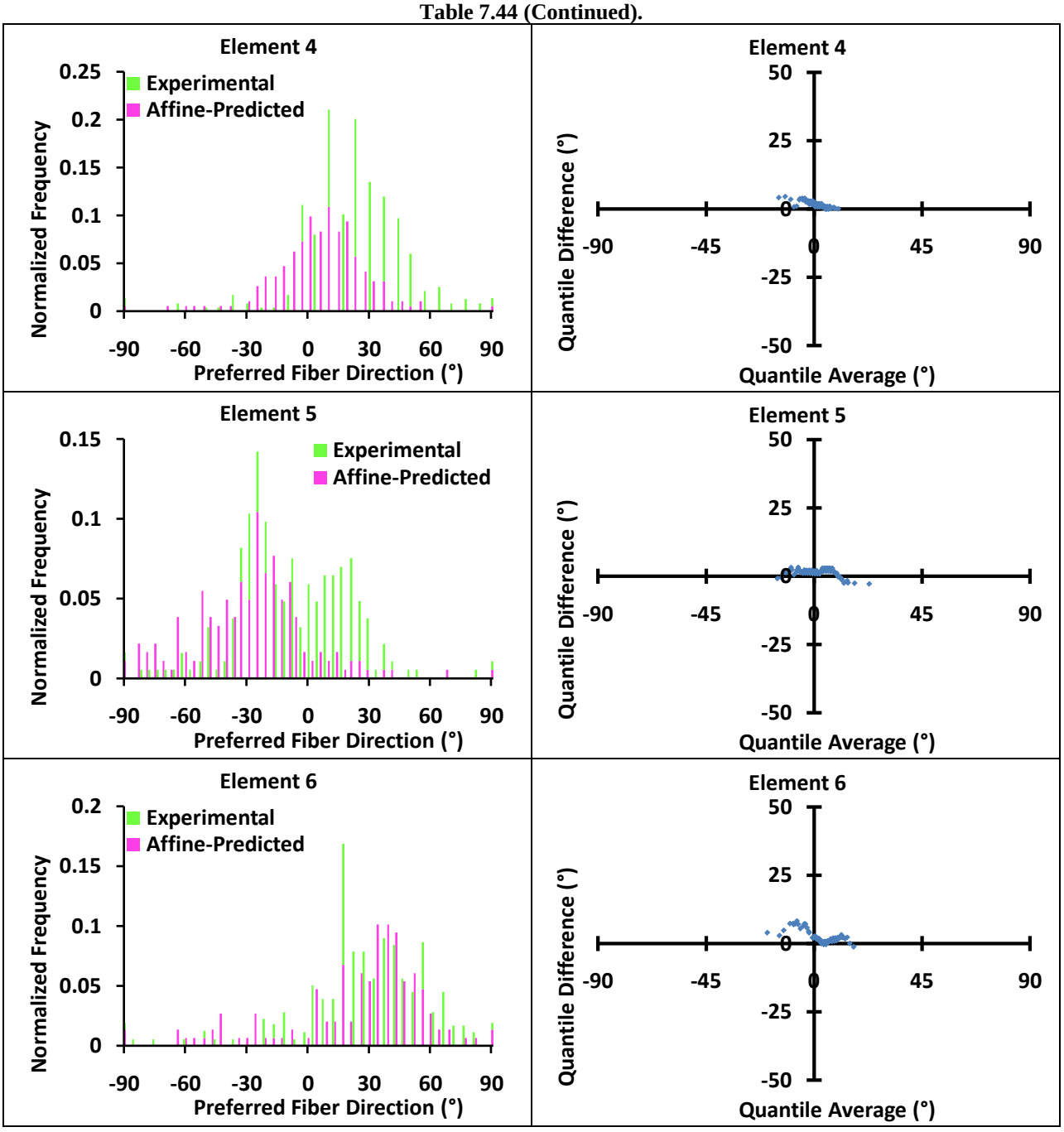

Table 7.45 Preferred fiber direction histogram and corresponding projection plot comparing the experimental and affine-predicted fiber distribution in the normal AB-IGHL for Specimen 09-06271R.

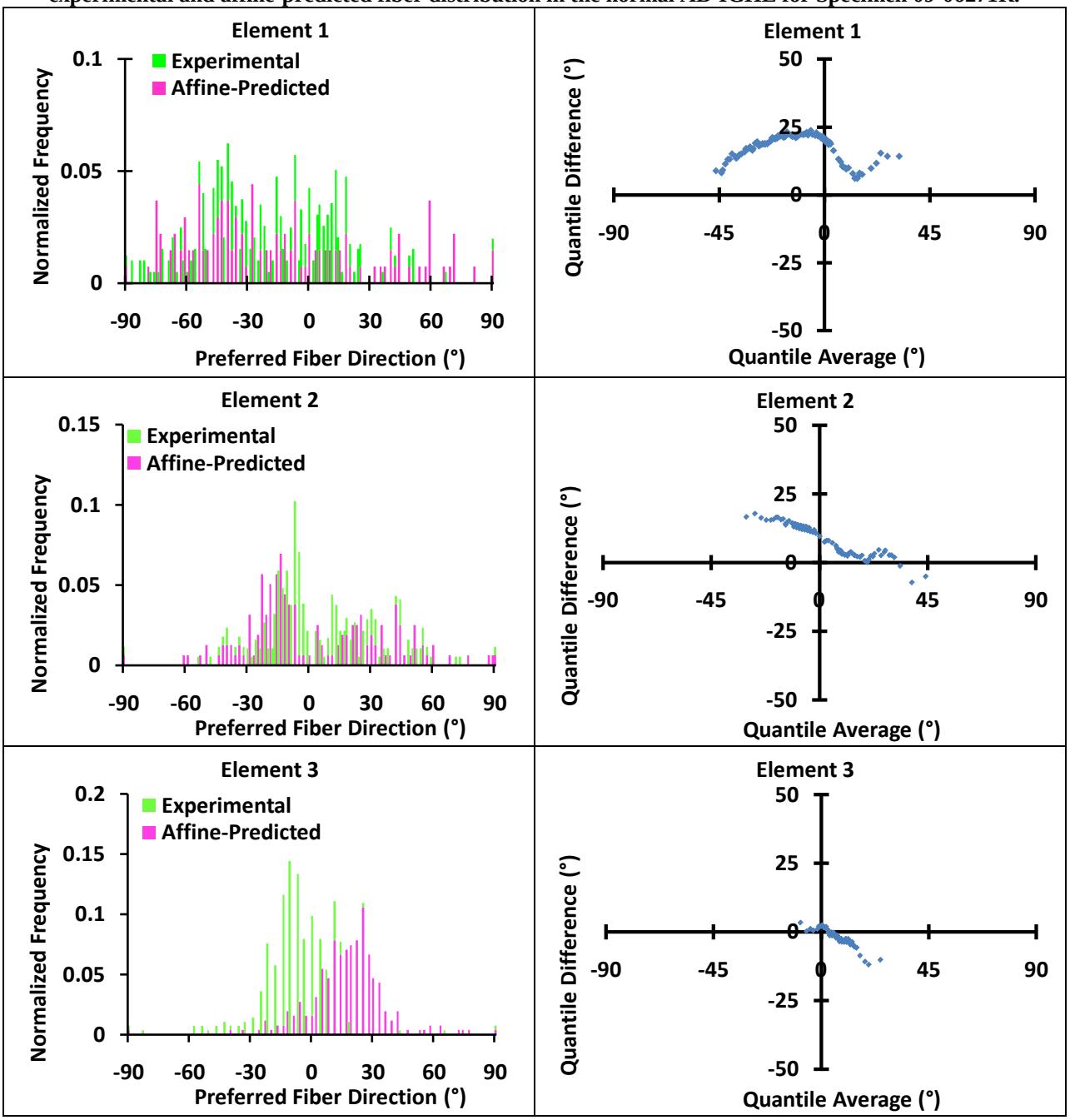

Table 7.45 (Continued).

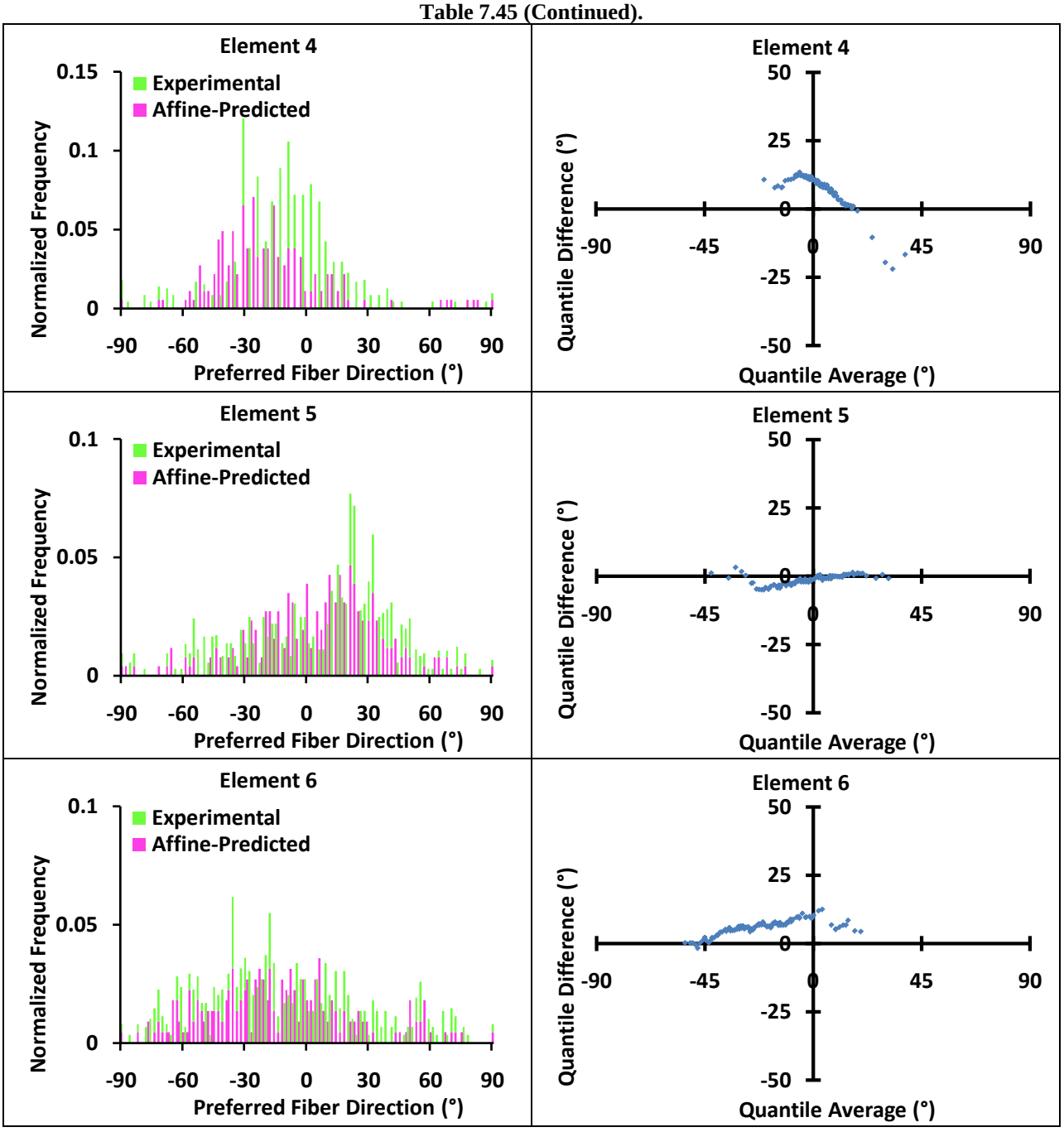

Table 7.46 Preferred fiber direction histogram and corresponding projection plot comparing the experimental and affine-predicted fiber distribution in the normal axillary pouch for Specimen 09-06271R.

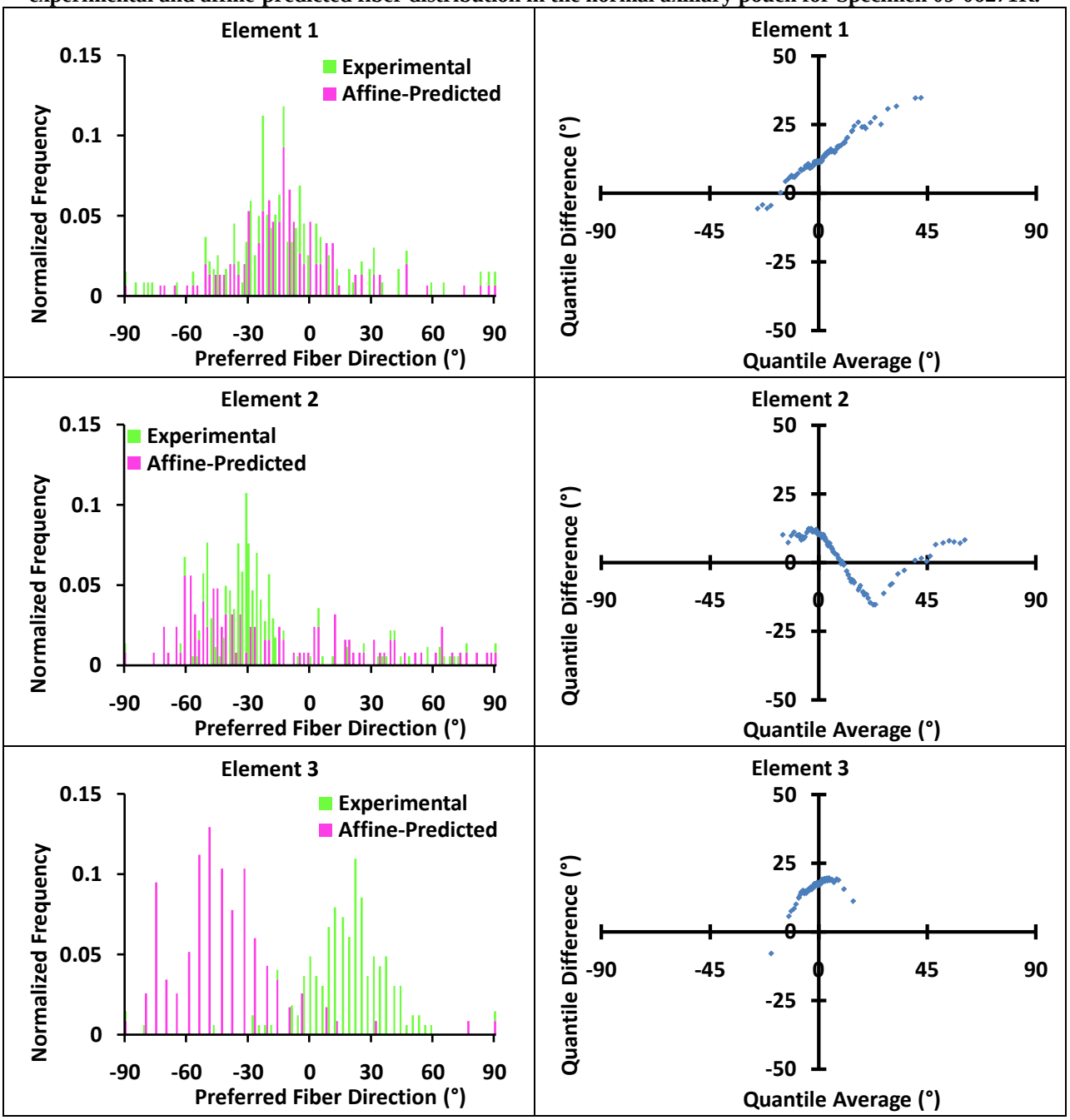

Table 7.46 (Continued).

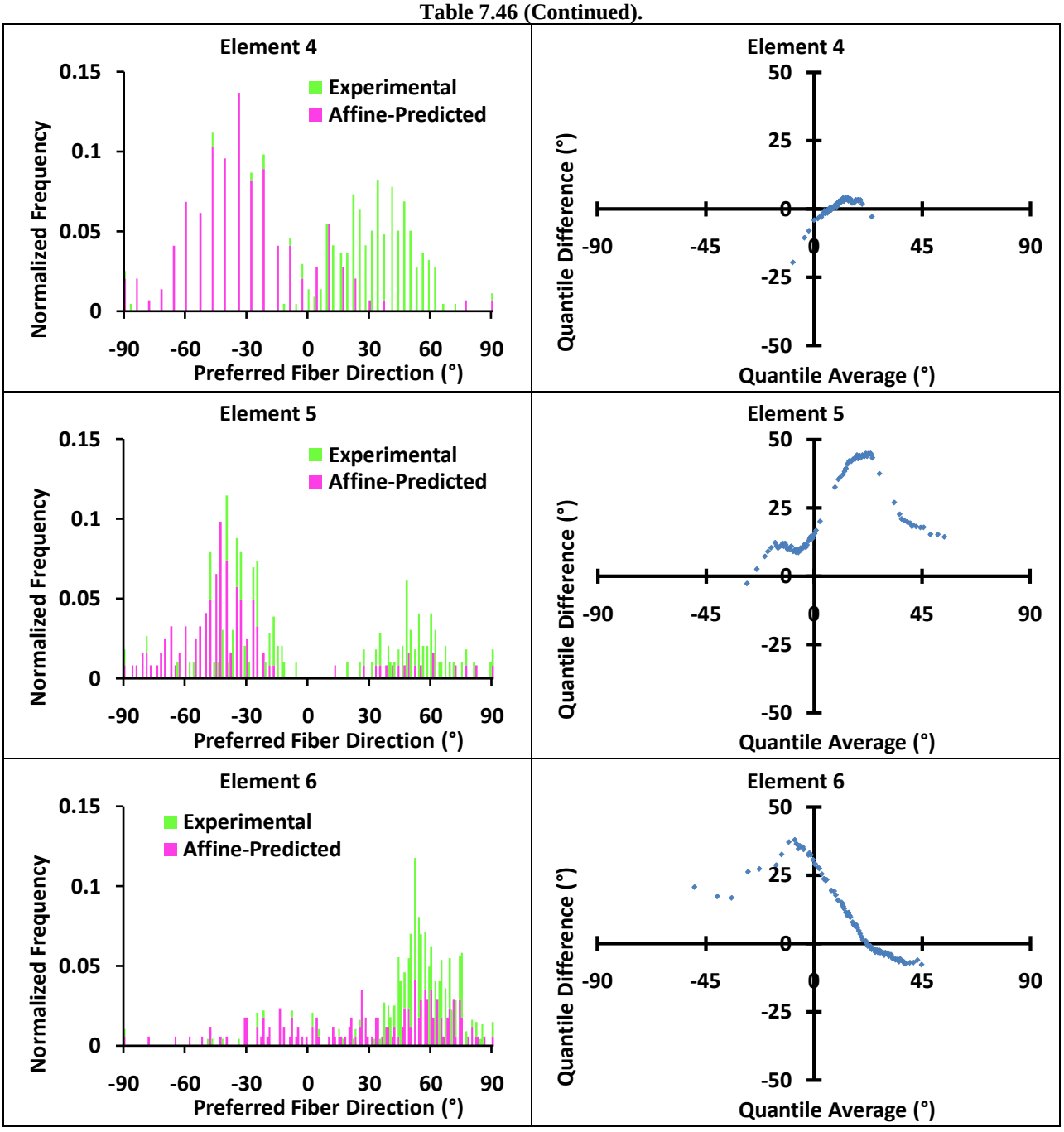

Table 7.47 Preferred fiber direction histogram and corresponding projection plot comparing the experimental and affine-predicted fiber distribution in the normal AB-IGHL for Specimen 09-06278R.

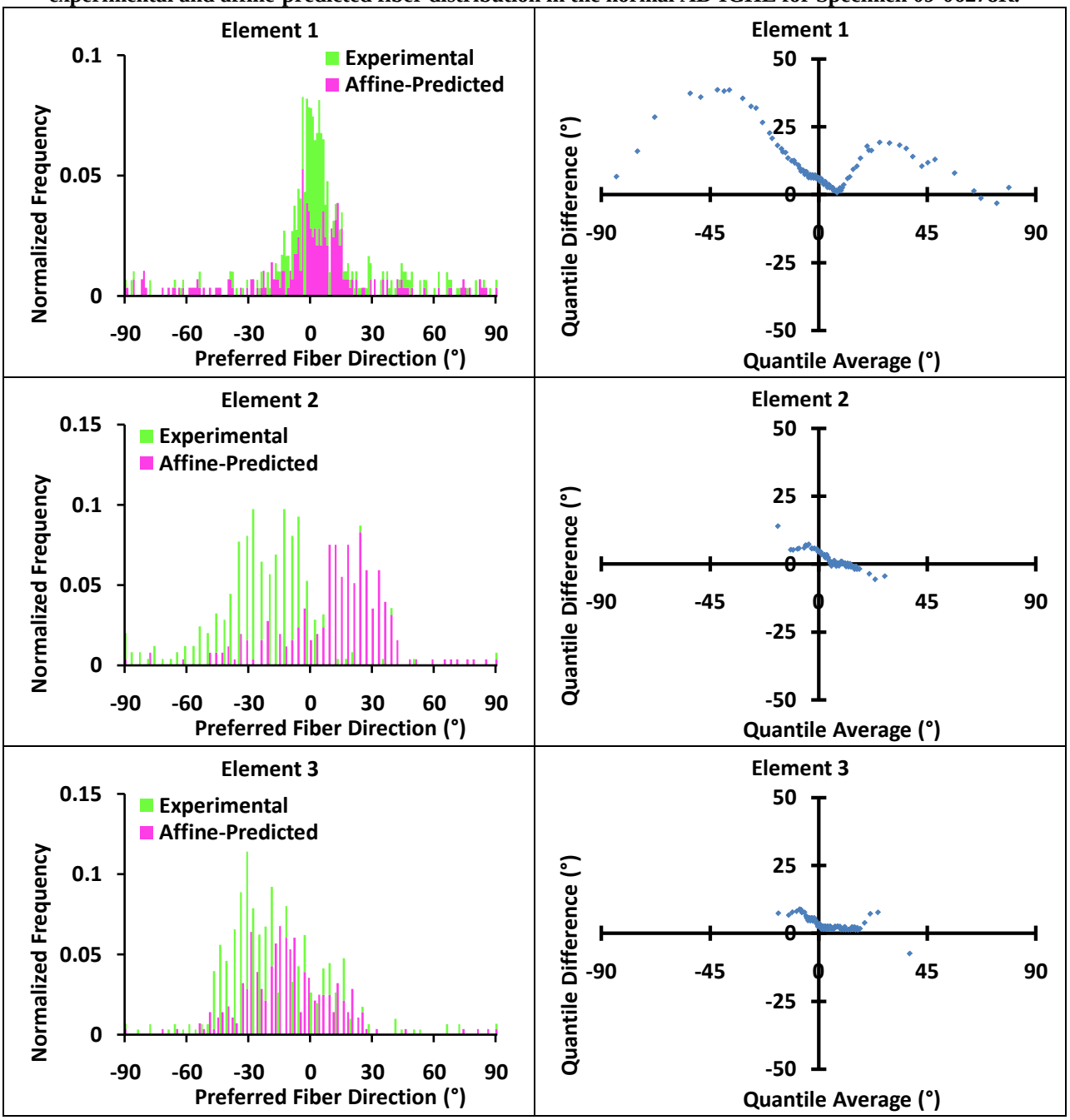

Table 7.47 (Continued).

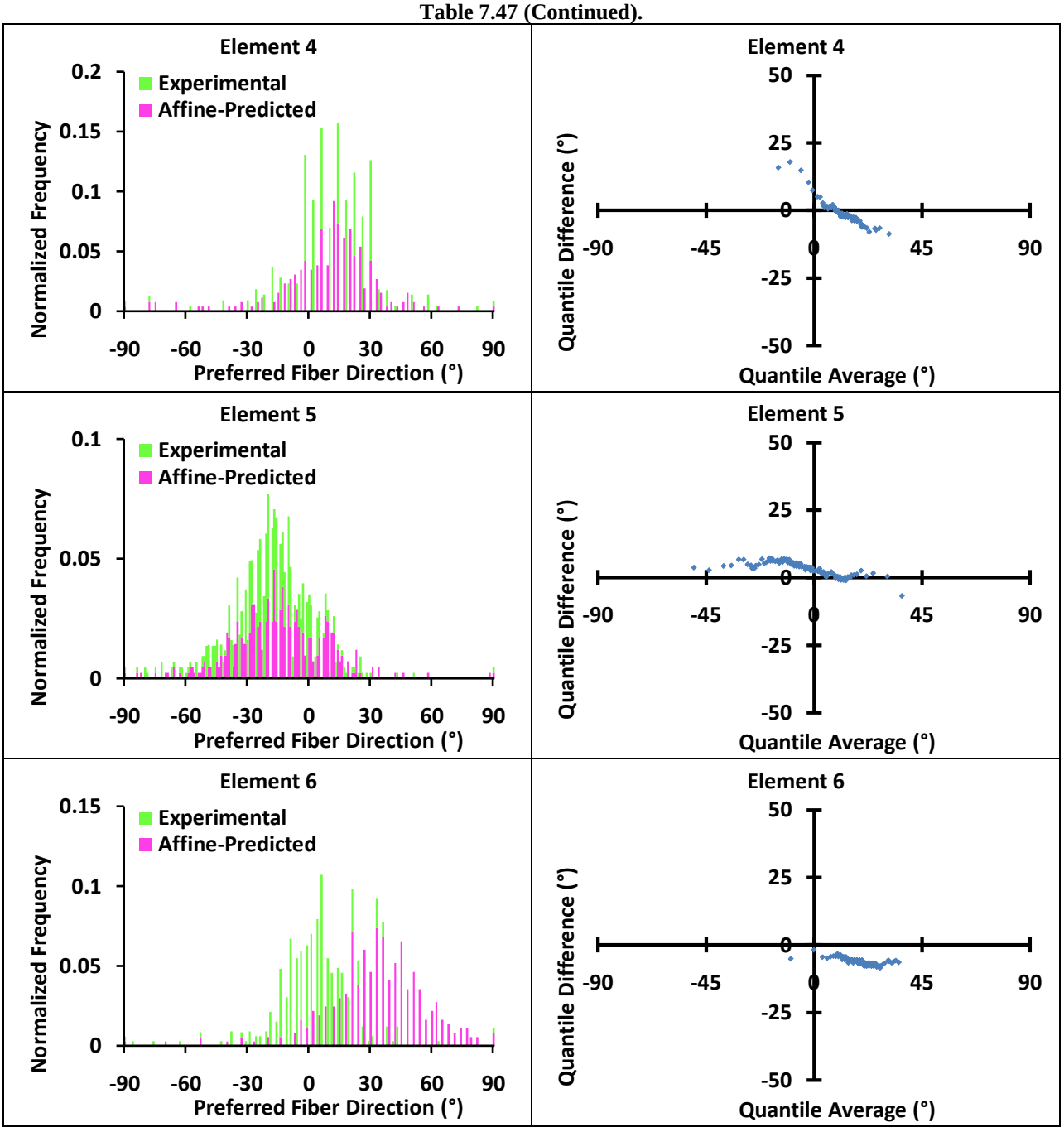

Table 7.48 Preferred fiber direction histogram and corresponding projection plot comparing the experimental and affine-predicted fiber distribution in the normal axillary pouch for Specimen 09-06278R.

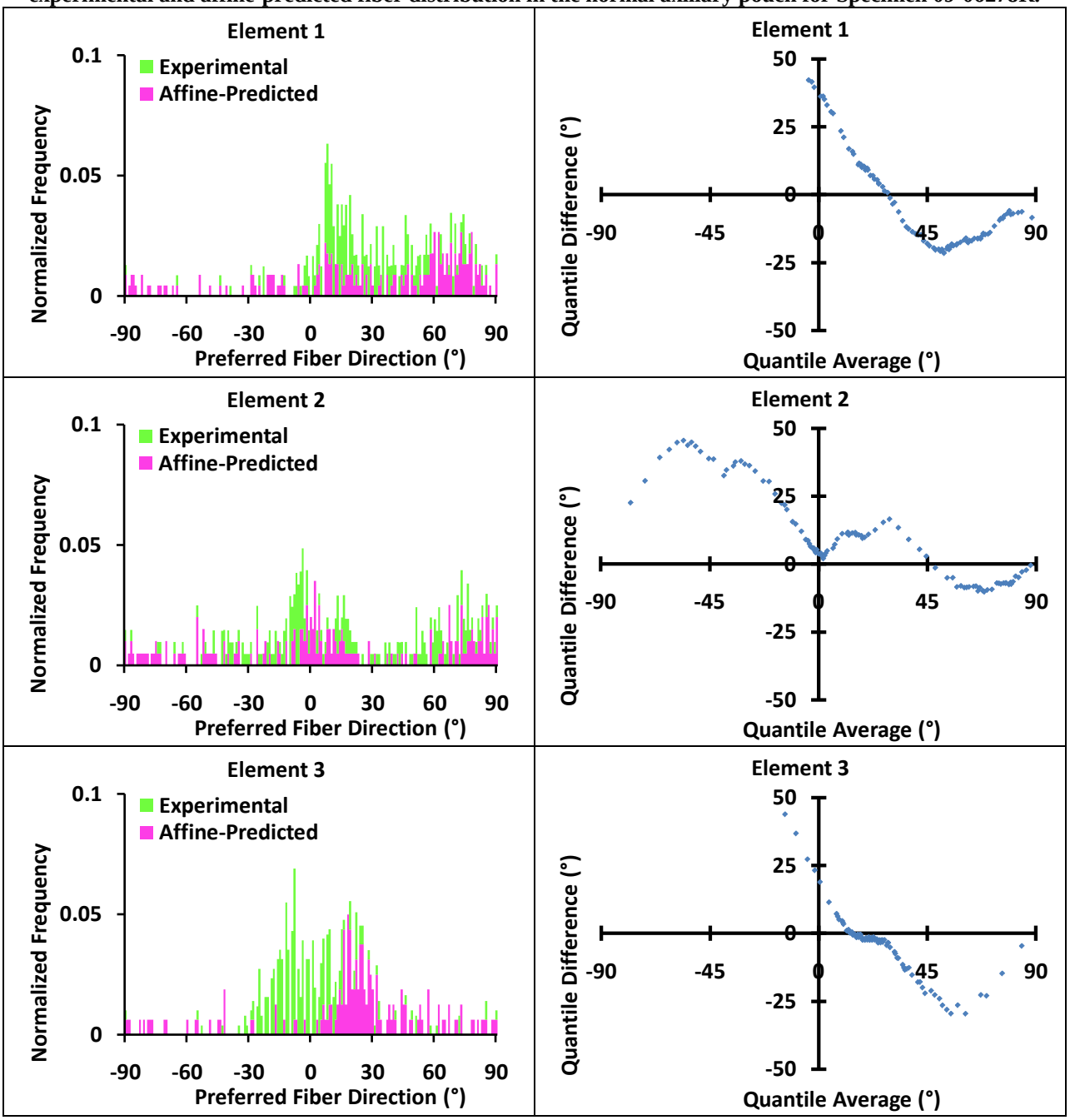

Table 7.48 (Continued).

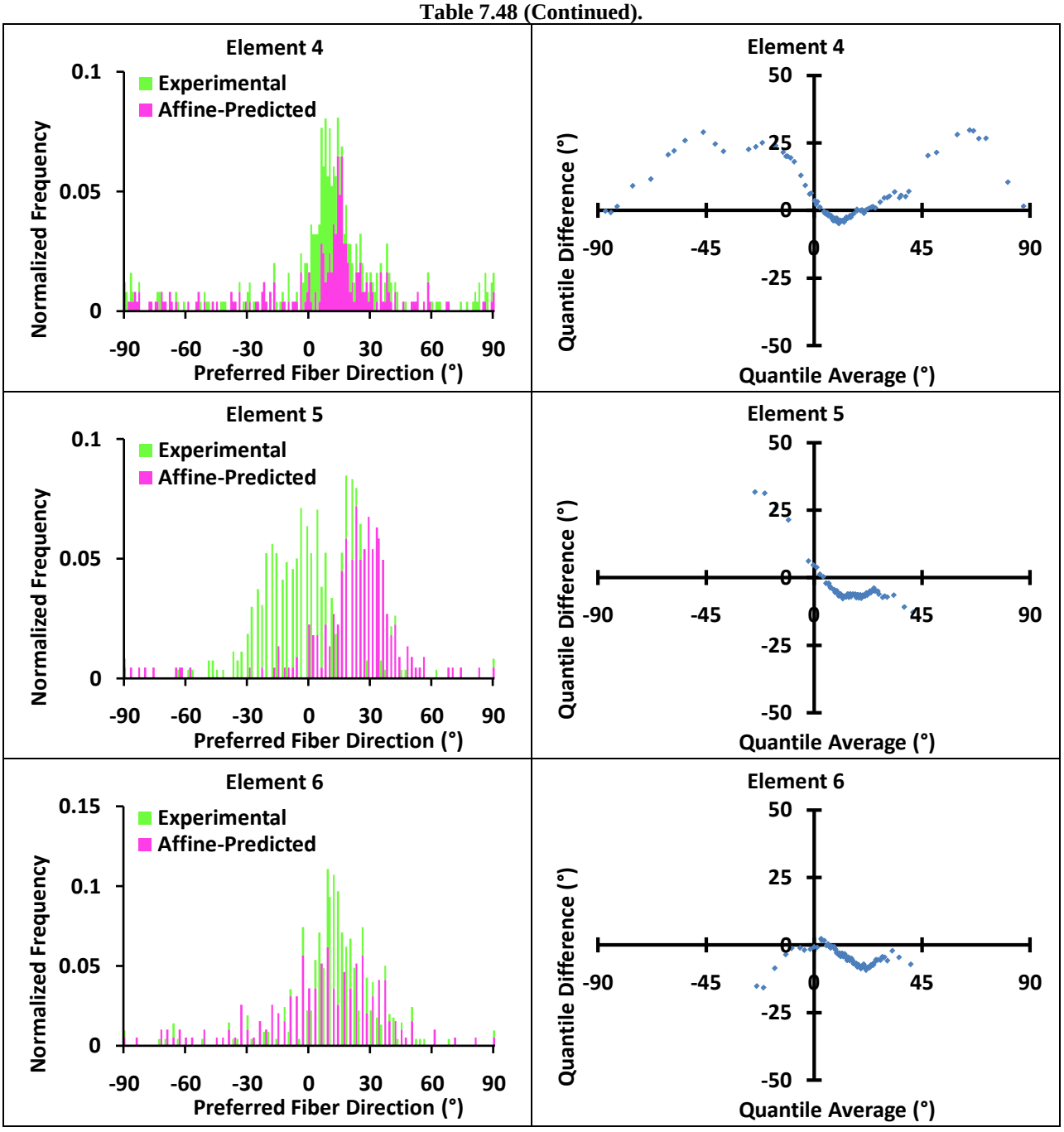

APPENDIX L

AFFINE PREDICTIONS FOR INJURED CAPSULE

Table 7.49 Preferred fiber direction histogram and corresponding projection plot comparing the experimental and affine-predicted fiber distribution in the injured AB-IGHL for Specimen 08-12389L.

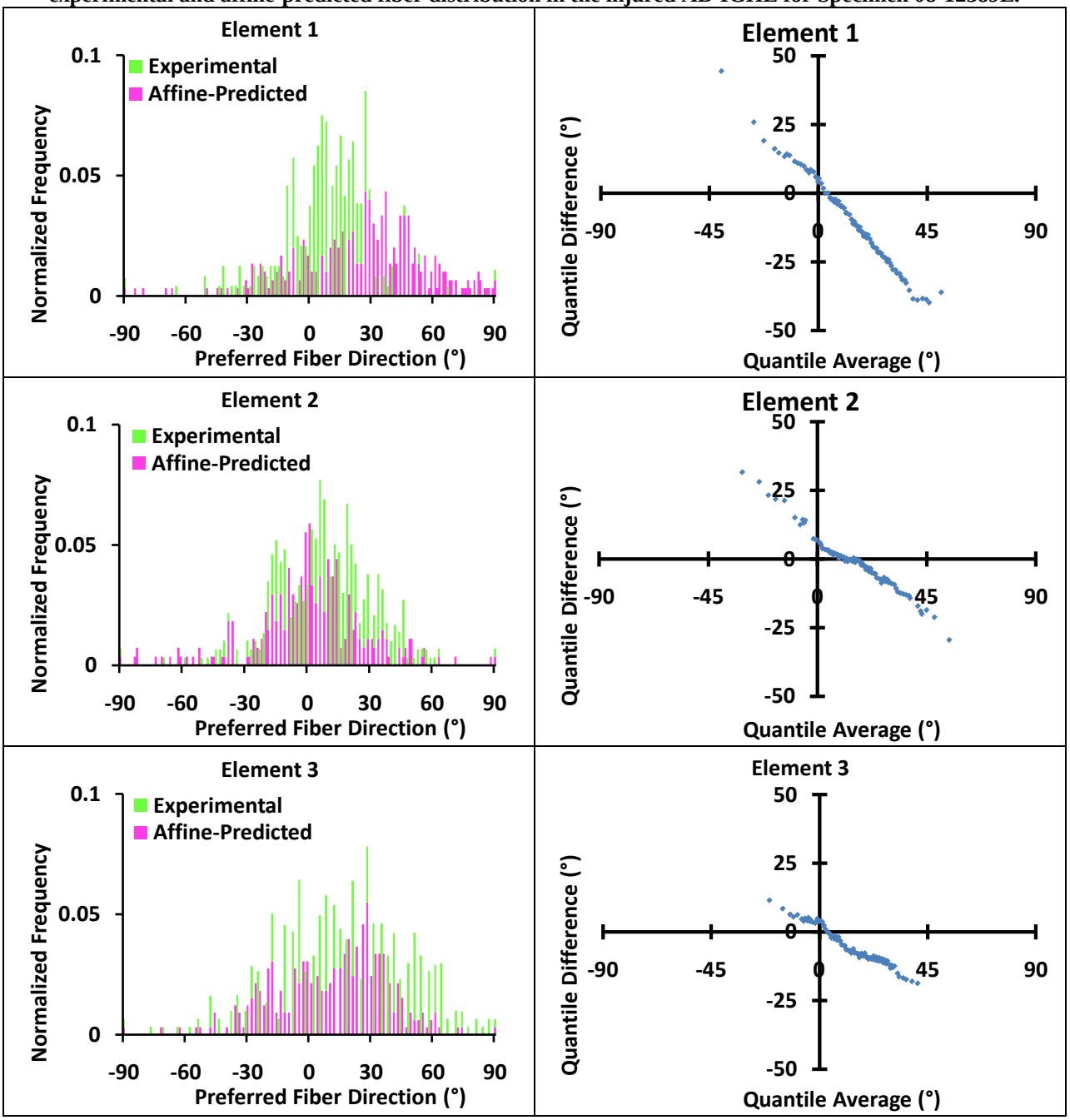

Table 7.49 (Continued).

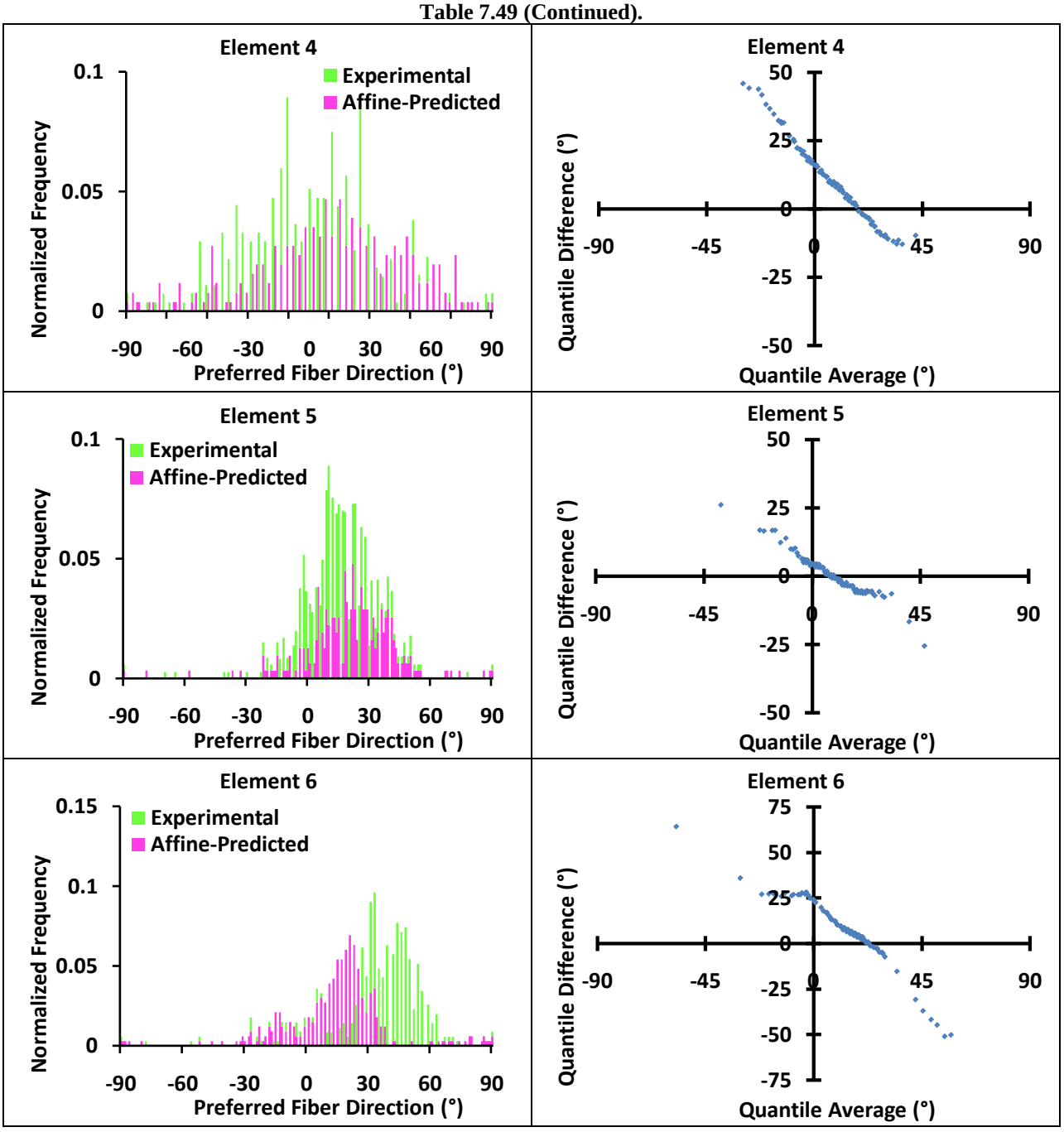

Table 7.50 Preferred fiber direction histogram and corresponding projection plot comparing the experimental and affine-predicted fiber distribution in the injured axillary pouch for Specimen 08-12389L.

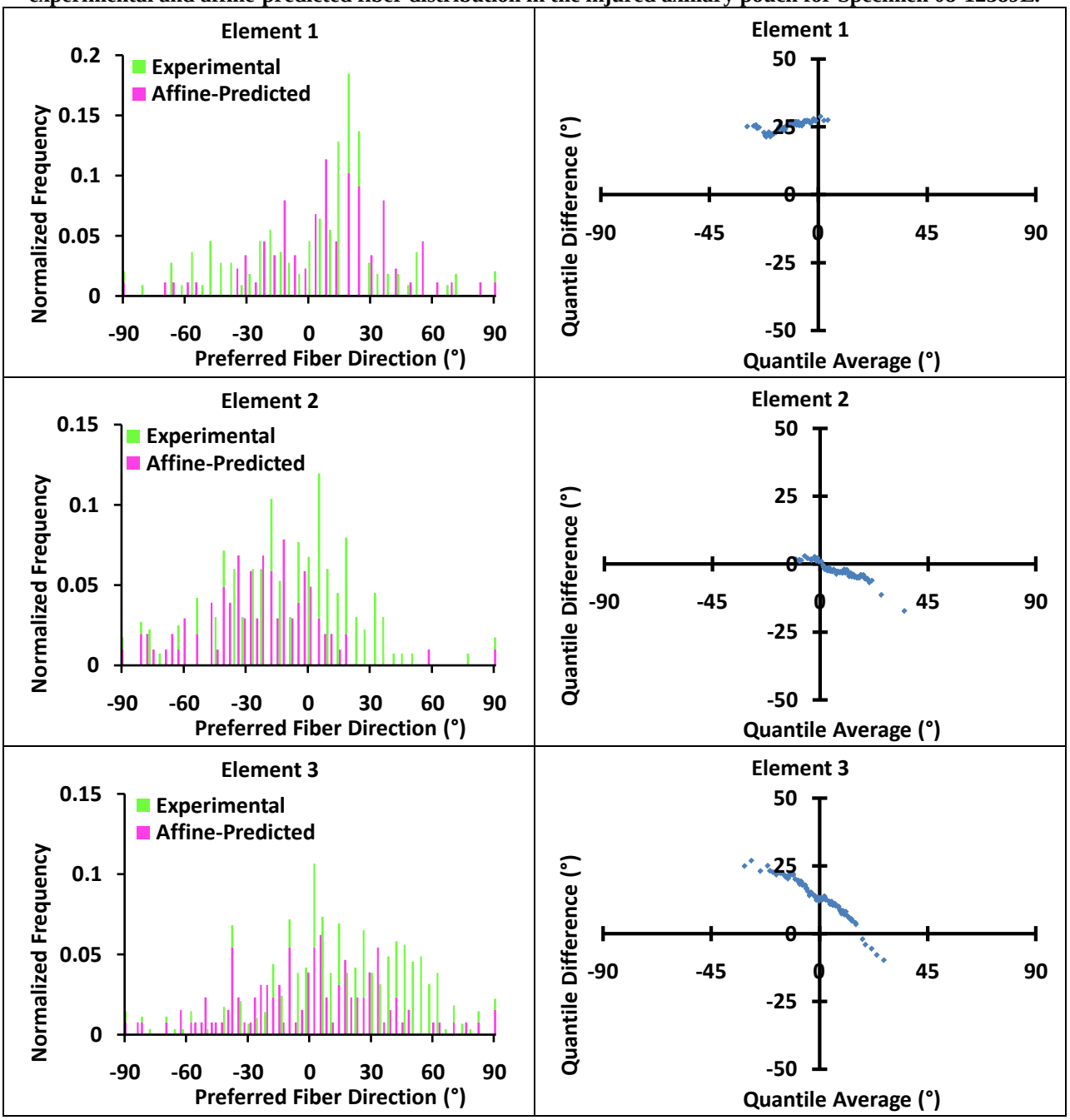

Table 7.50 (Continued).

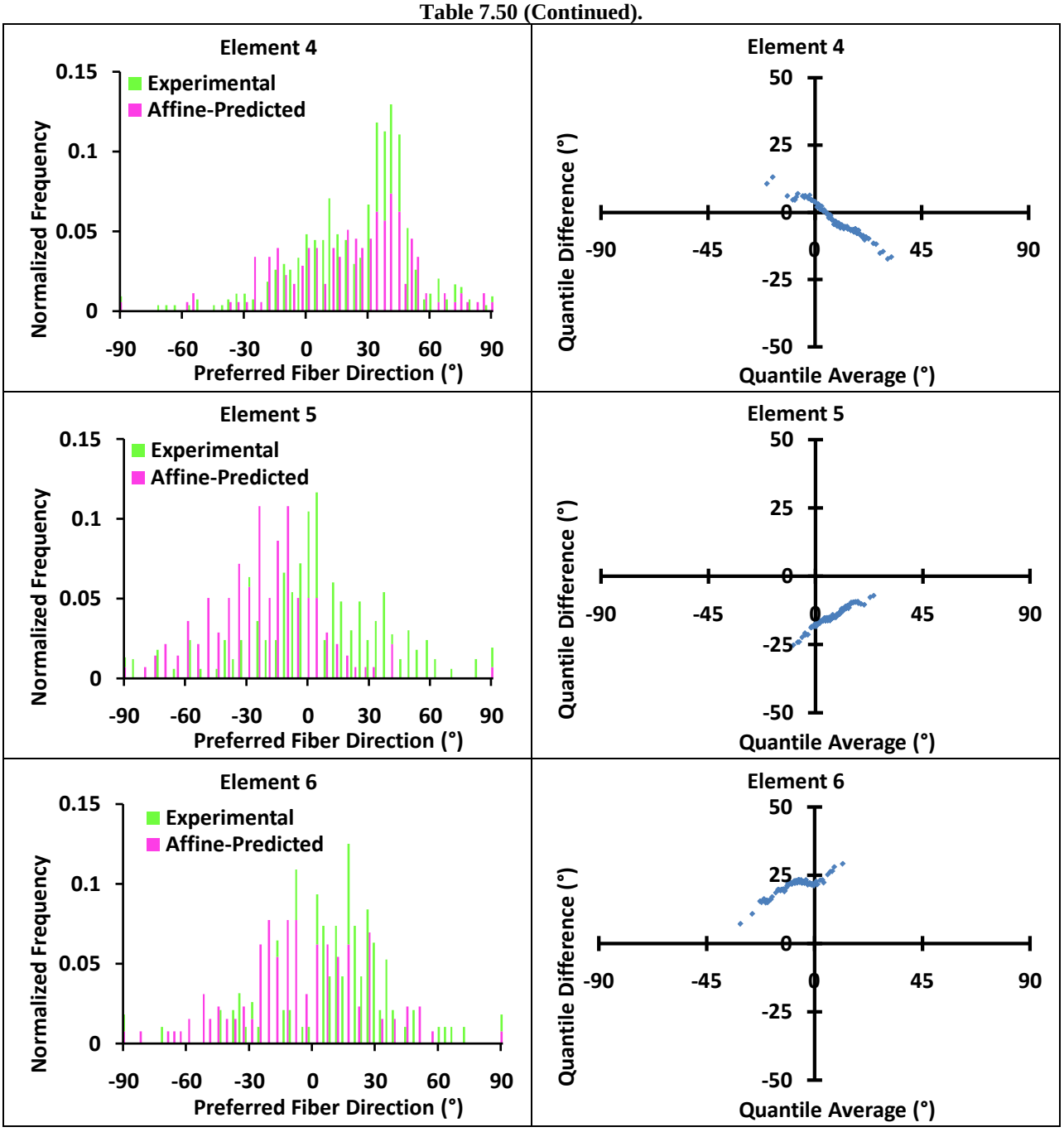

Table 7.51 Preferred fiber direction histogram and corresponding projection plot comparing the experimental and affine-predicted fiber distribution in the injured AB-IGHL for Specimen 09-06267R.

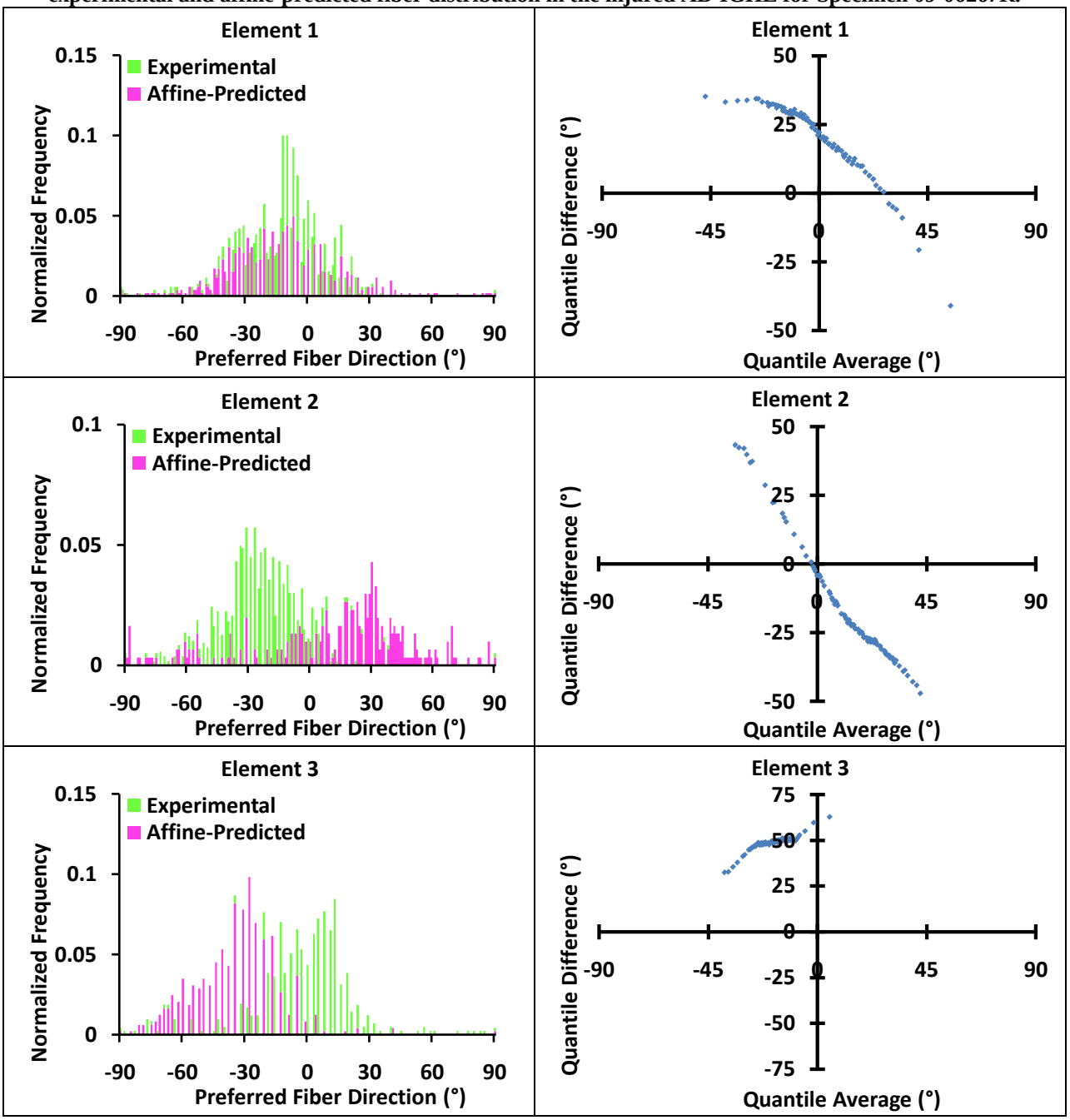

Table 7.51 (Continued).

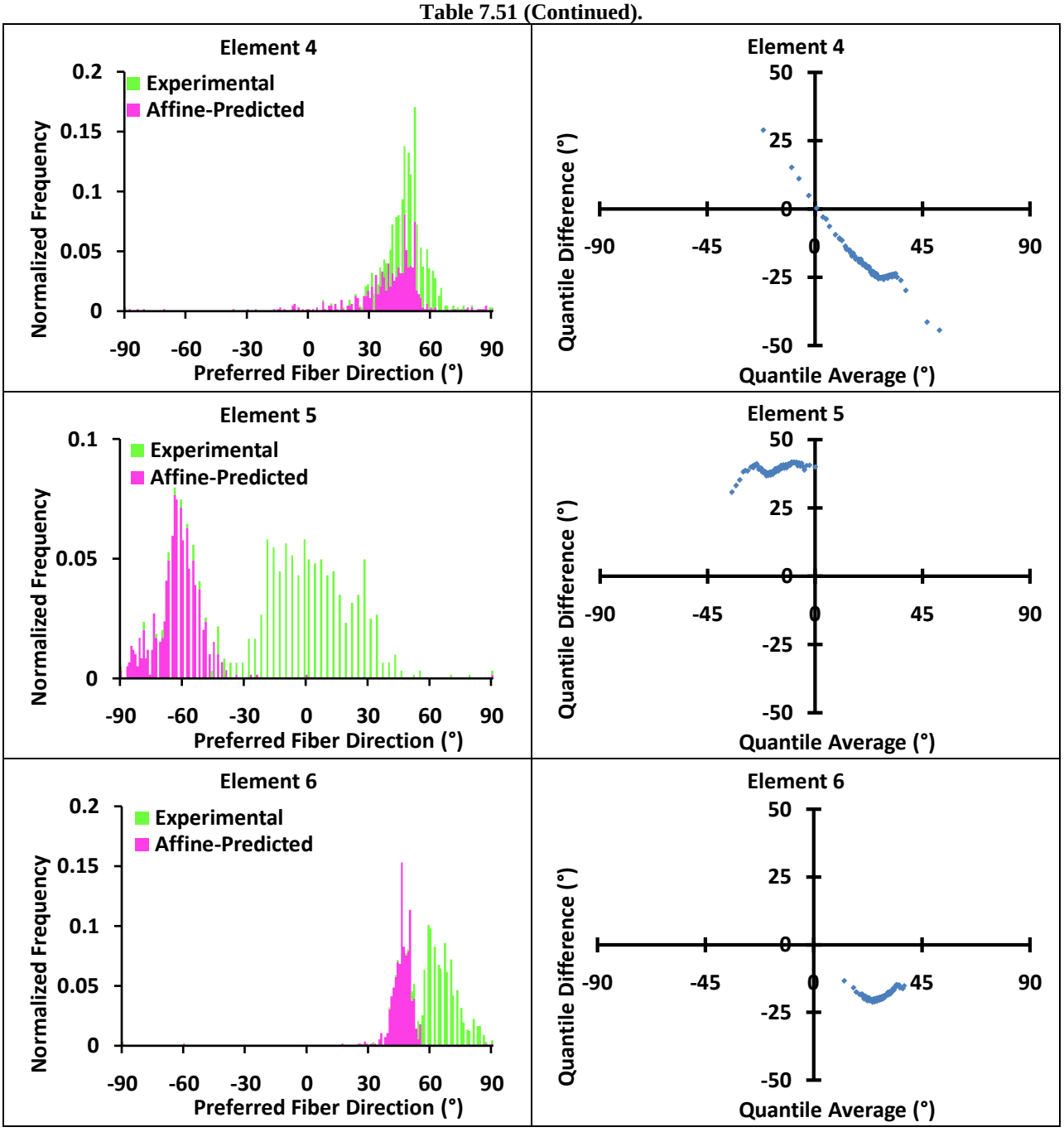

Table 7.52 Preferred fiber direction histogram and corresponding projection plot comparing the experimental and affine-predicted fiber distribution in the injured axillary pouch for Specimen 09-06267R.

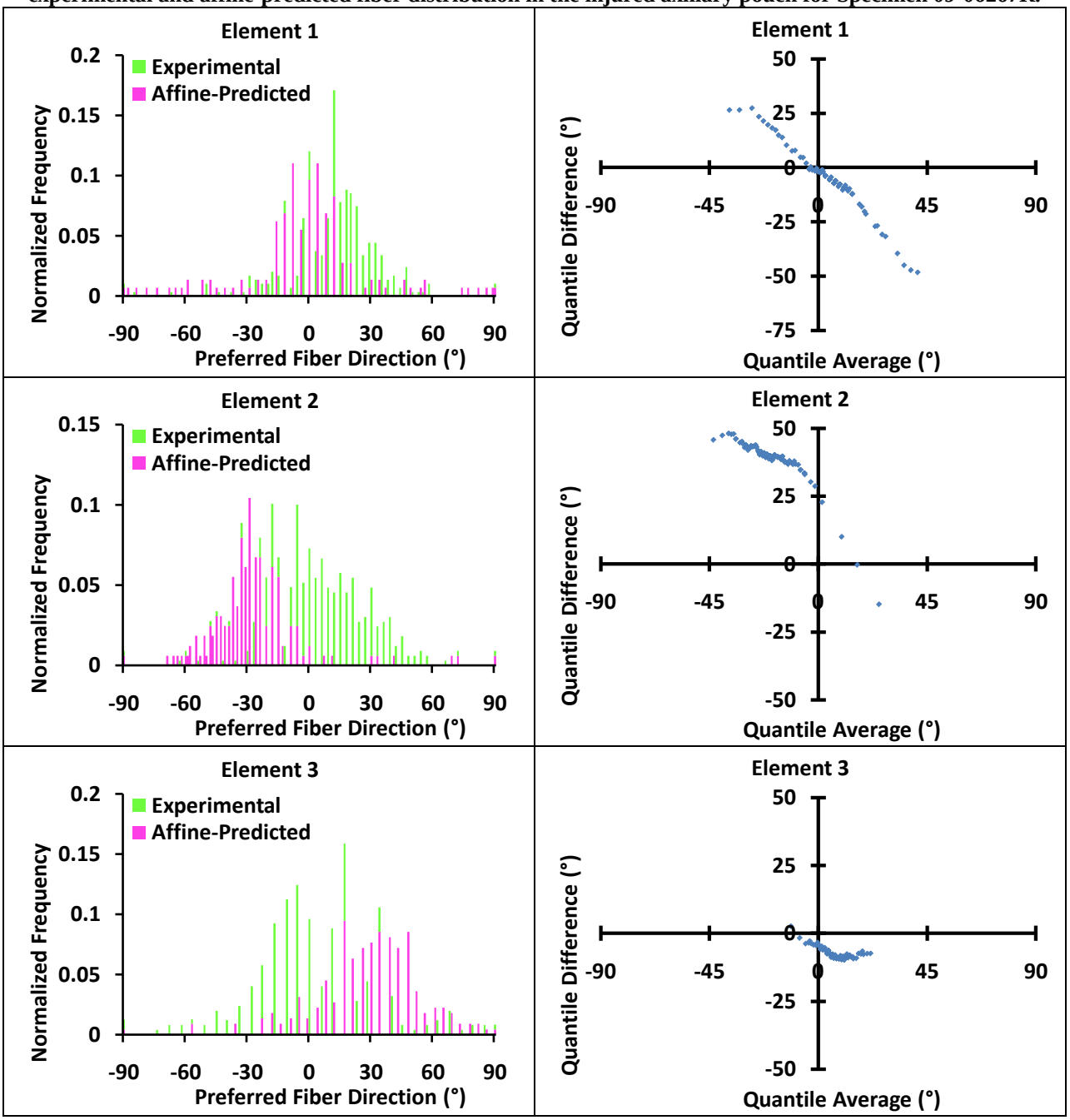

Table 7.52 (Continued).

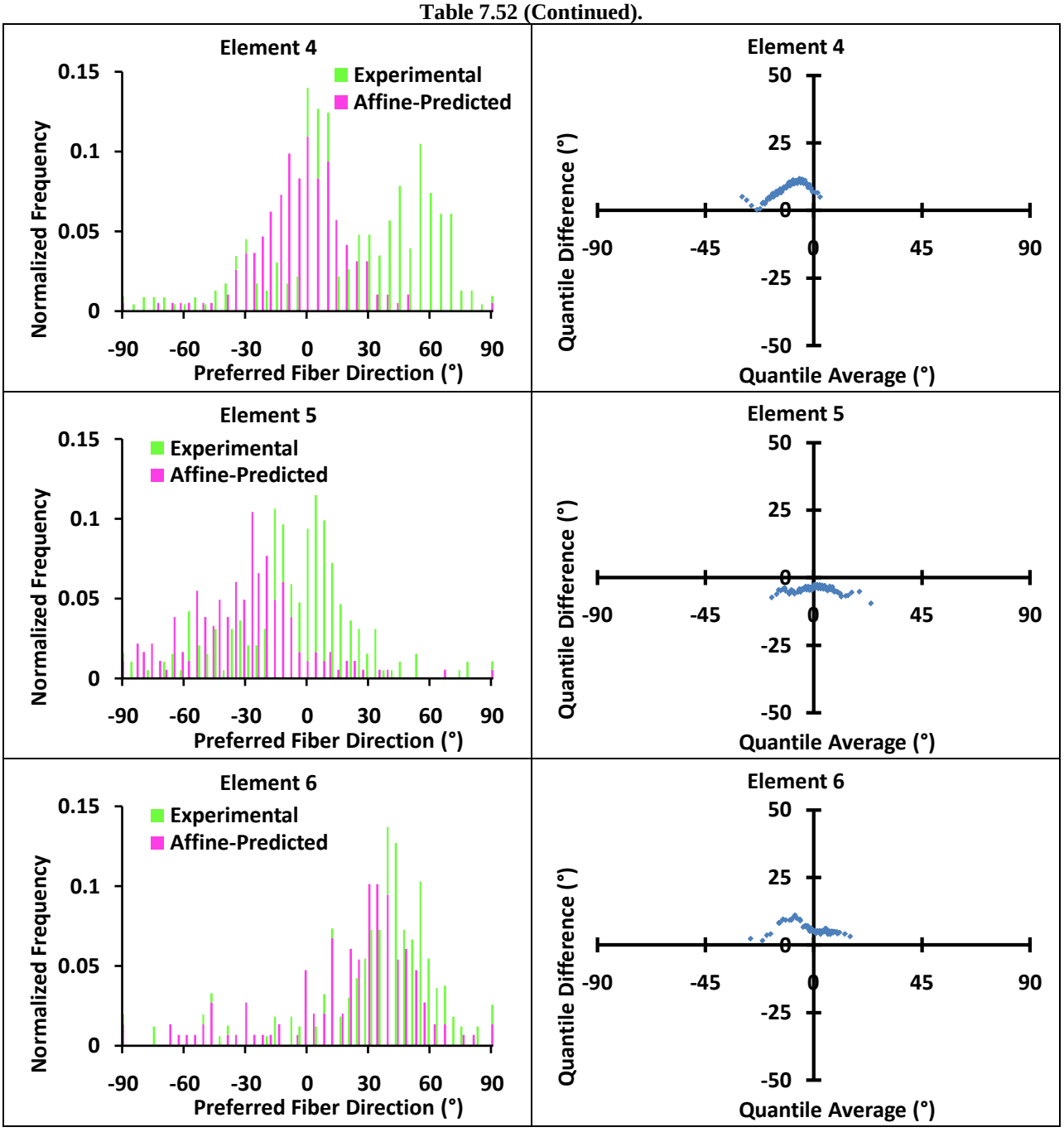

Table 7.53 Preferred fiber direction histogram and corresponding projection plot comparing the experimental and affine-predicted fiber distribution in the injured AB-IGHL for Specimen 09-06271R.

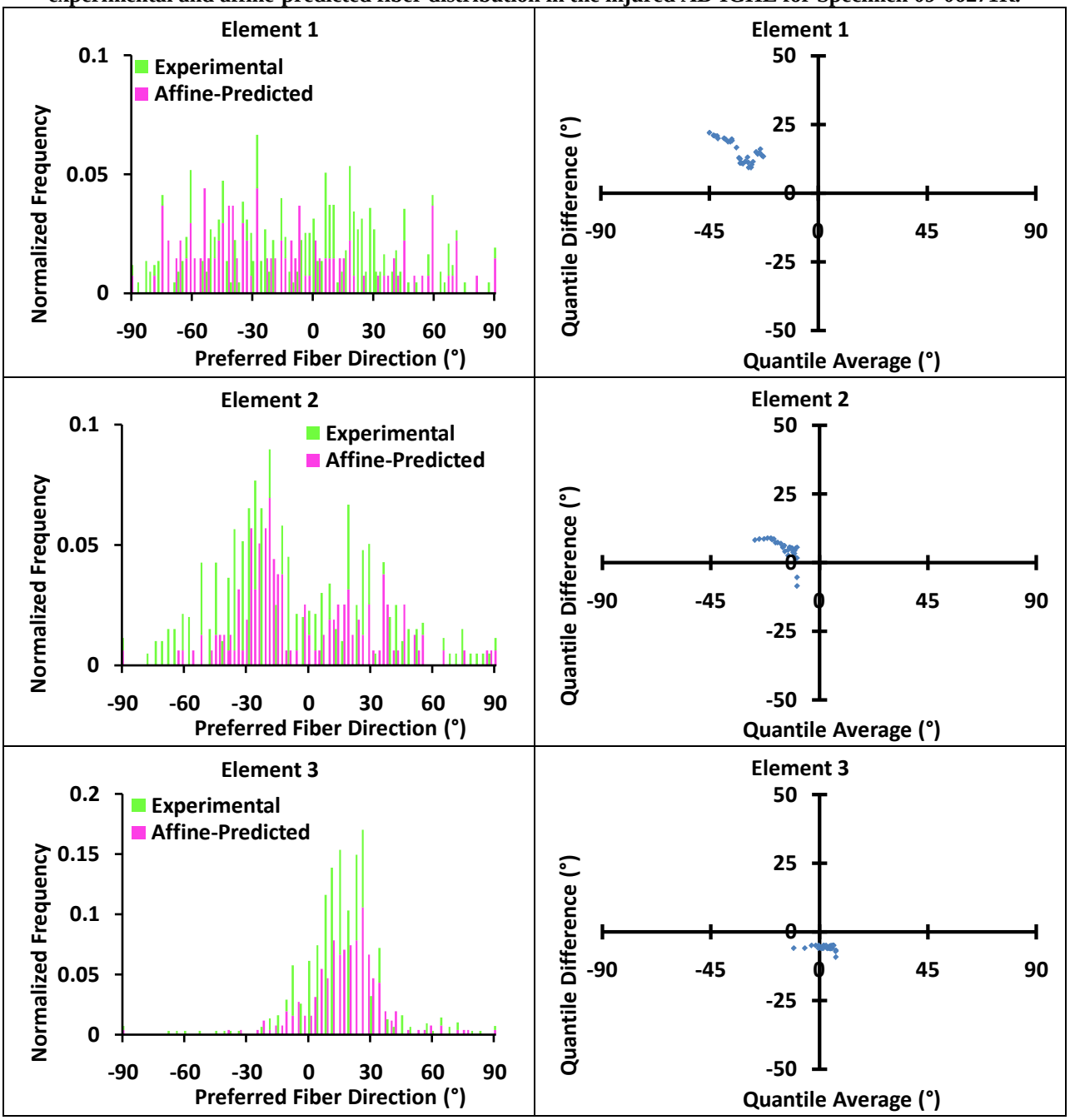

Table 7.53 (Continued).

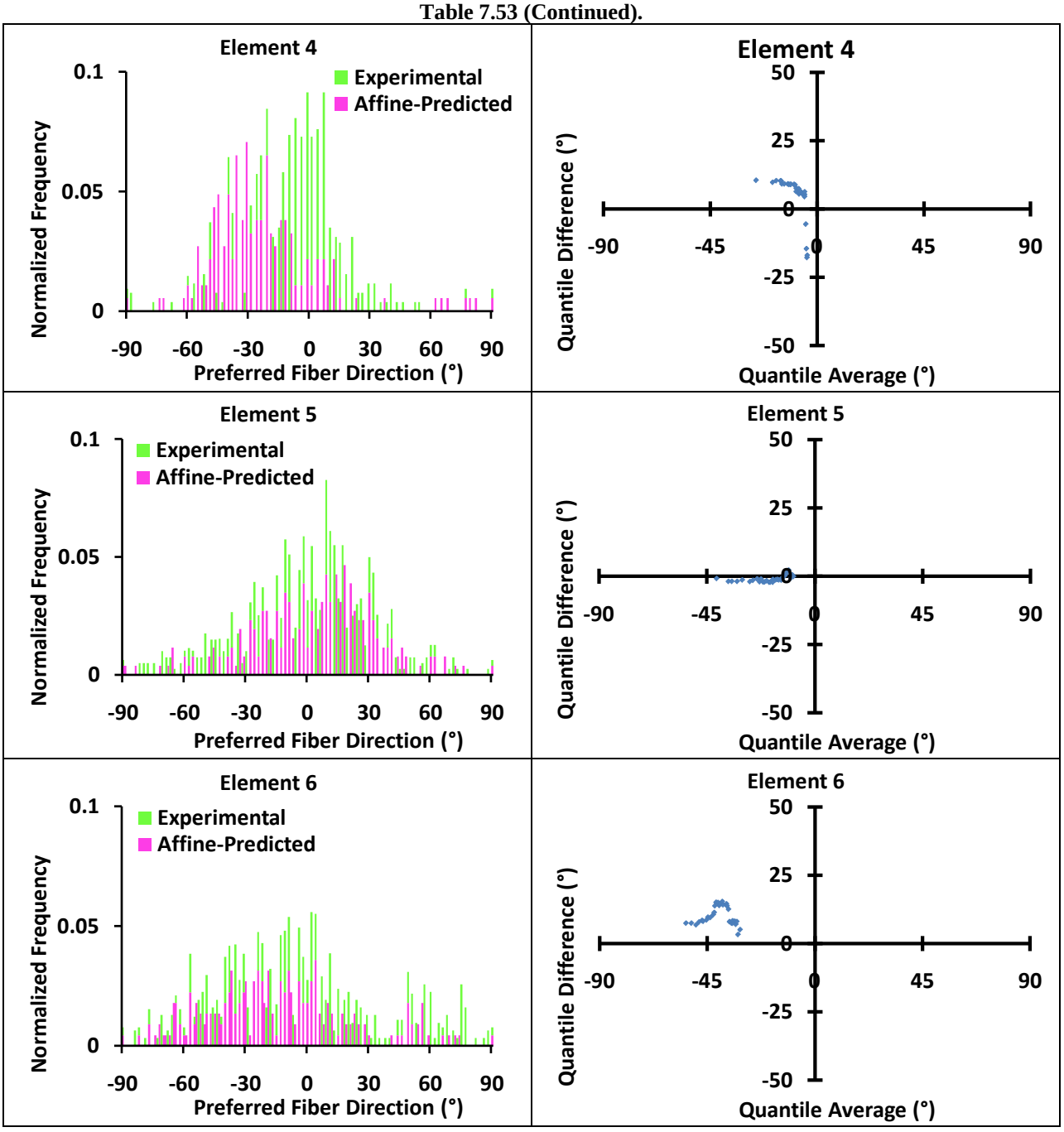

Table 7.54 Preferred fiber direction histogram and corresponding projection plot comparing the experimental and affine-predicted fiber distribution in the injured axillary pouch for Specimen 09-06271R.

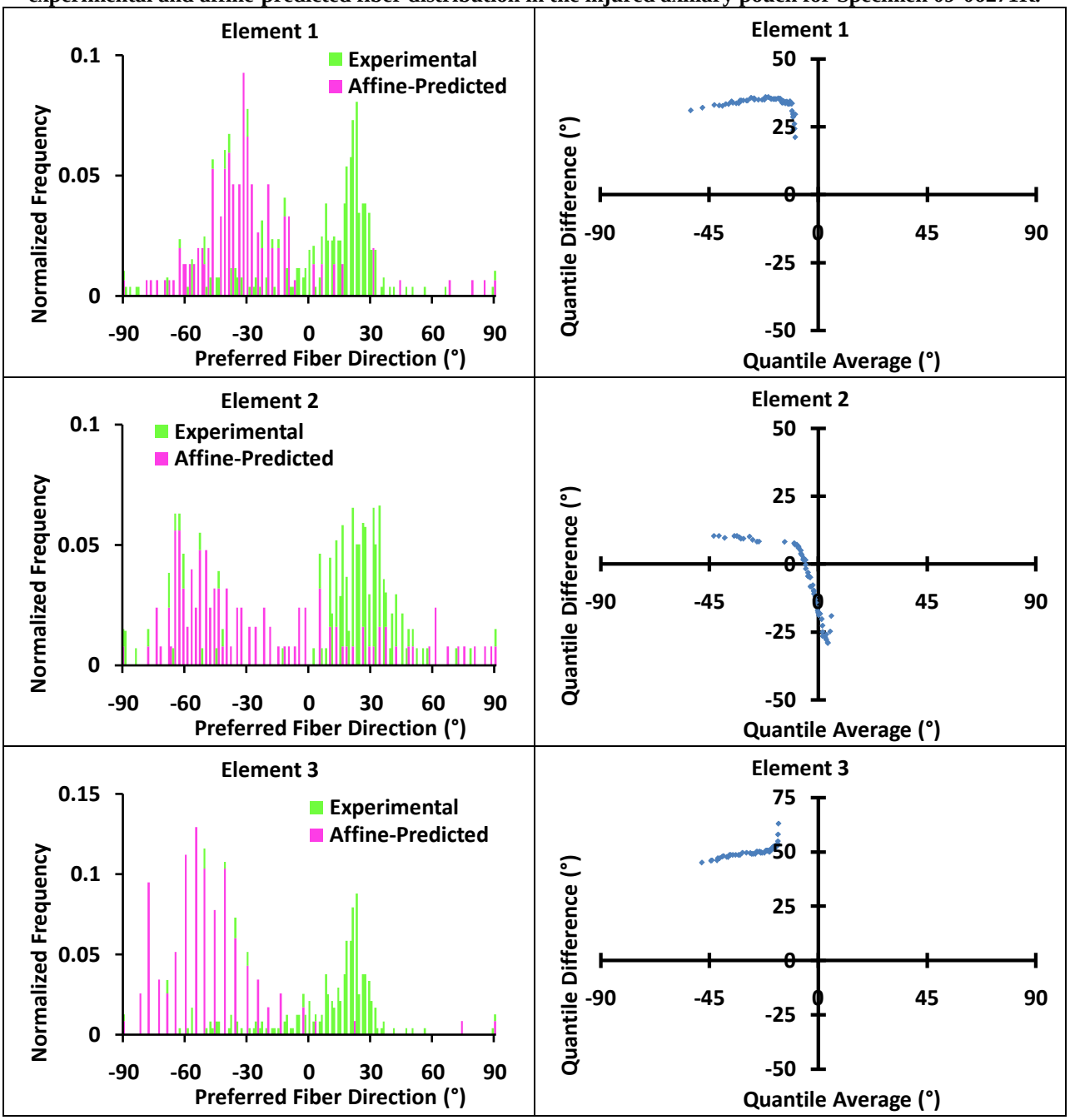

Table 7.54 (Continued).

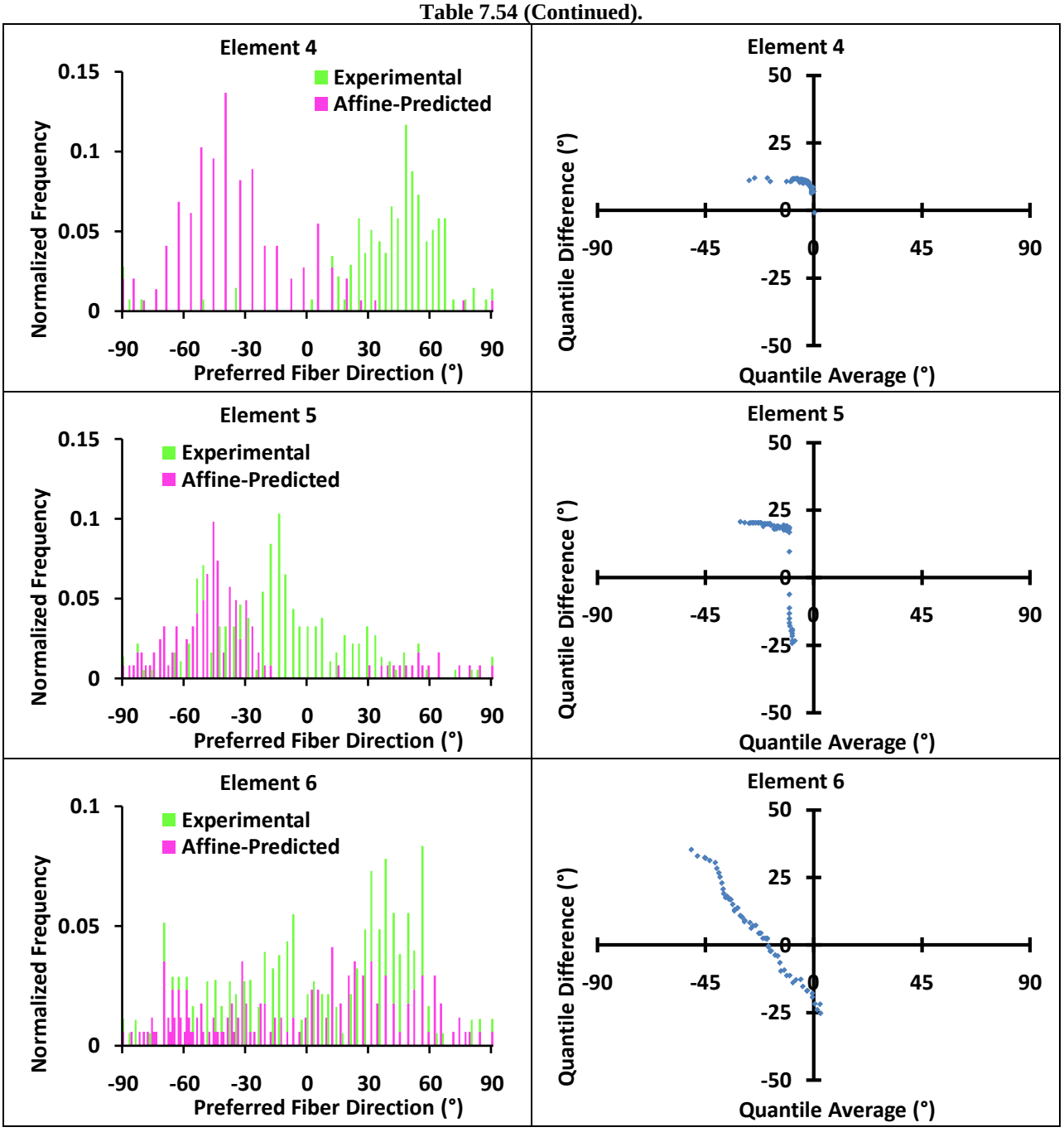

Table 7.55 Preferred fiber direction histogram and corresponding projection plot comparing the experimental and affine-predicted fiber distribution in the injured AB-IGHL for Specimen 09-06278R.

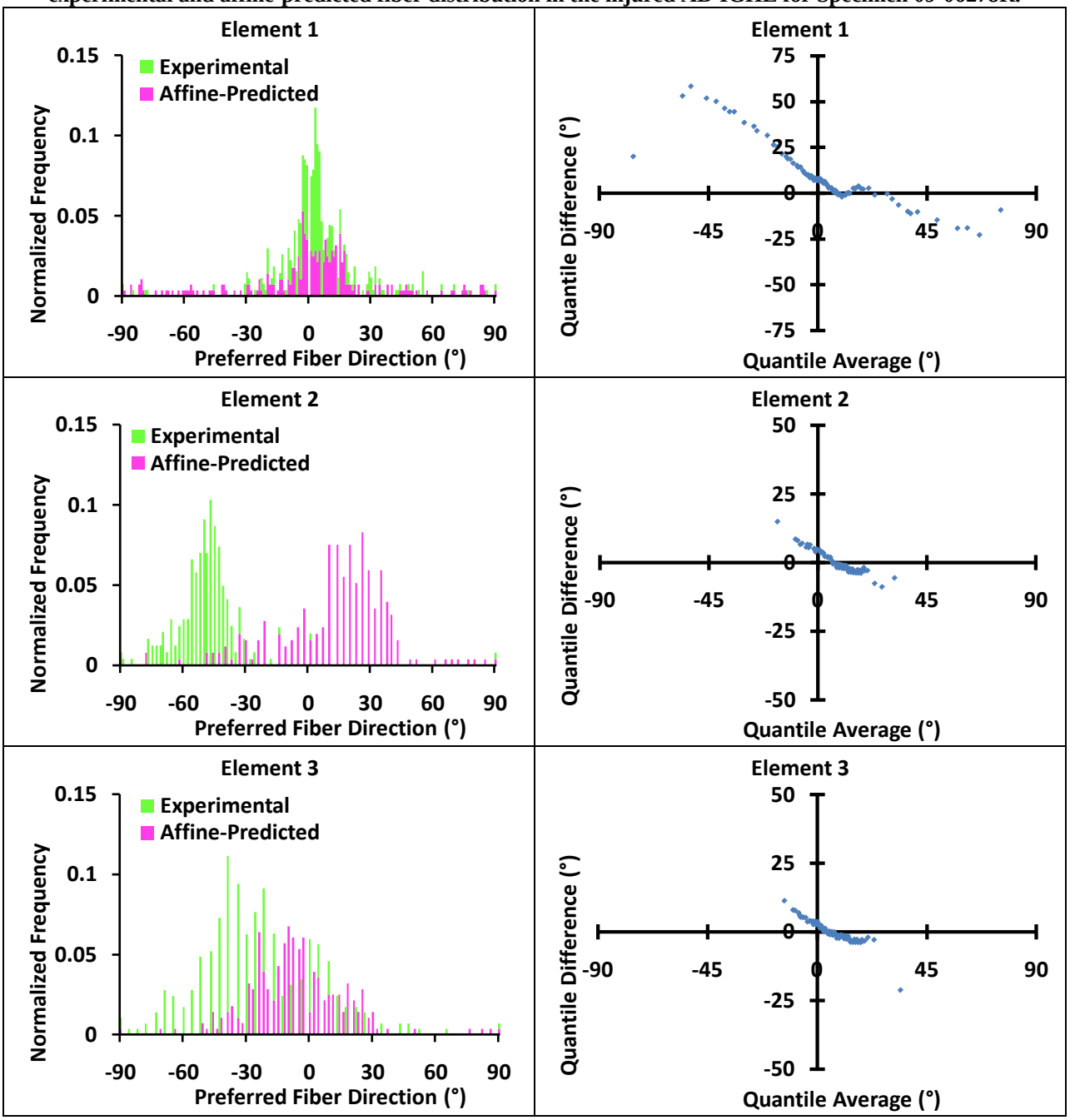

Table 7.55 (Continued).

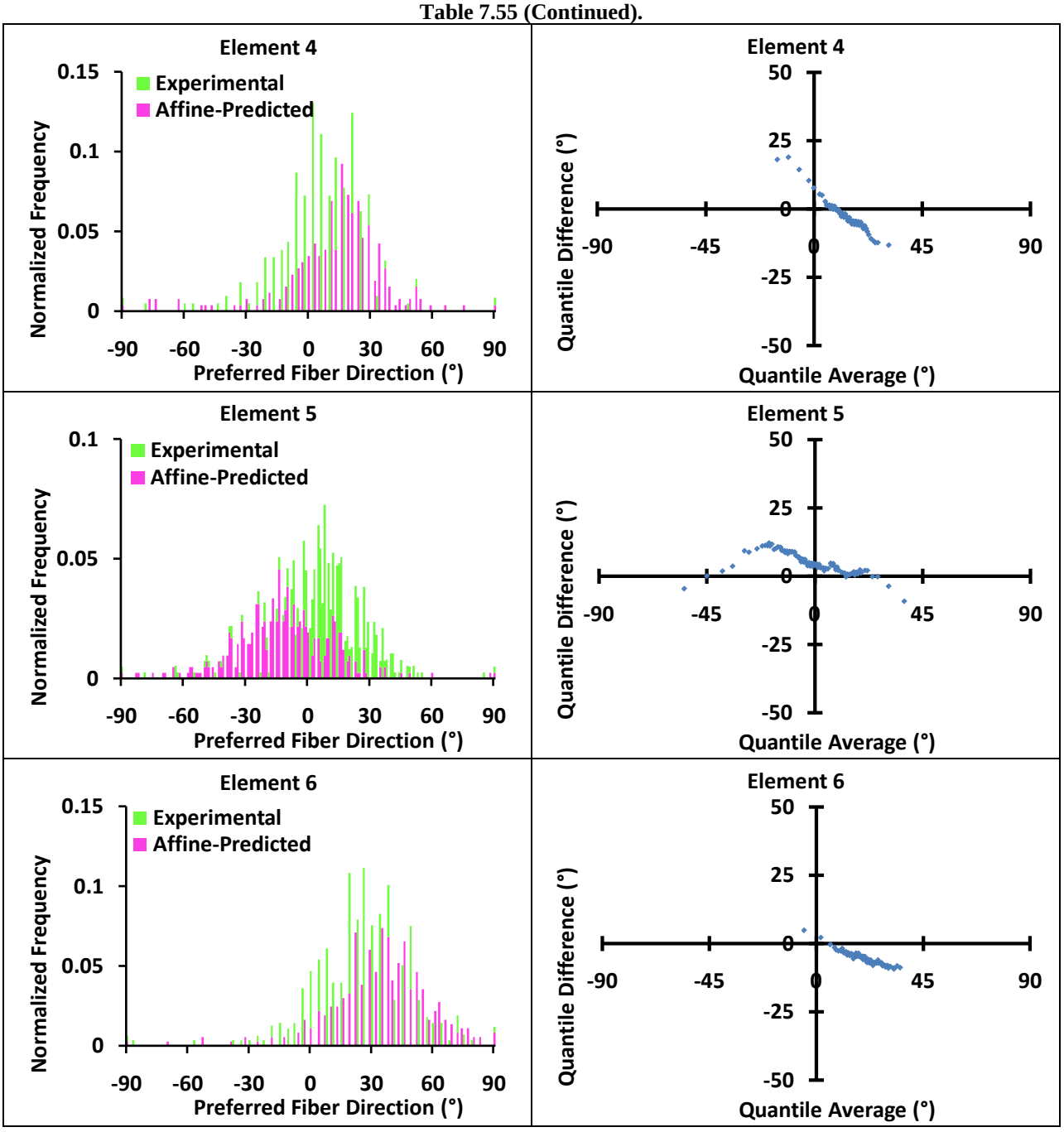

Table 7.56 Preferred fiber direction histogram and corresponding projection plot comparing the experimental and affine-predicted fiber distribution in the injured axillary pouch for Specimen 09-06278R.

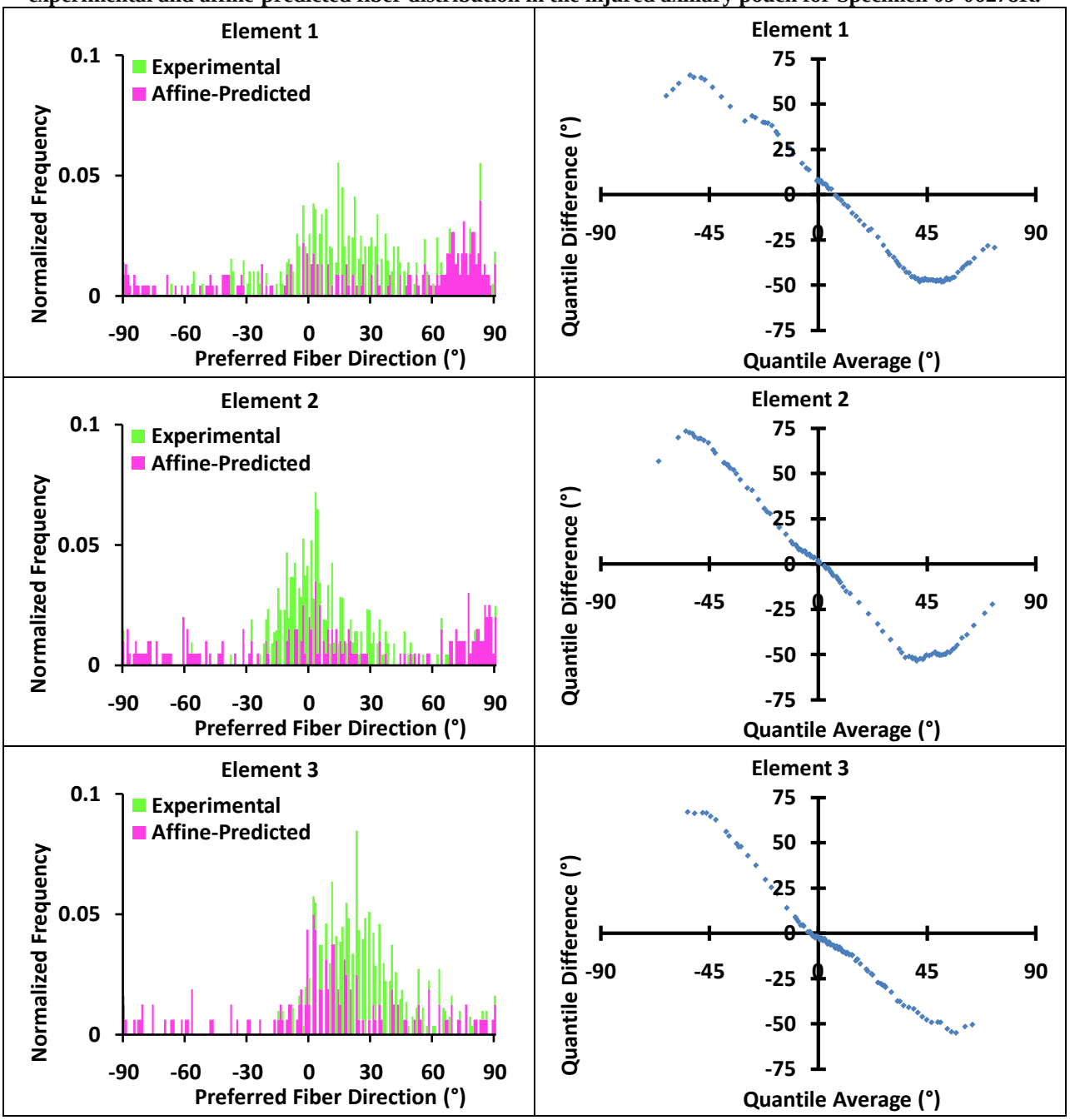

Table 7.56 (Continued).

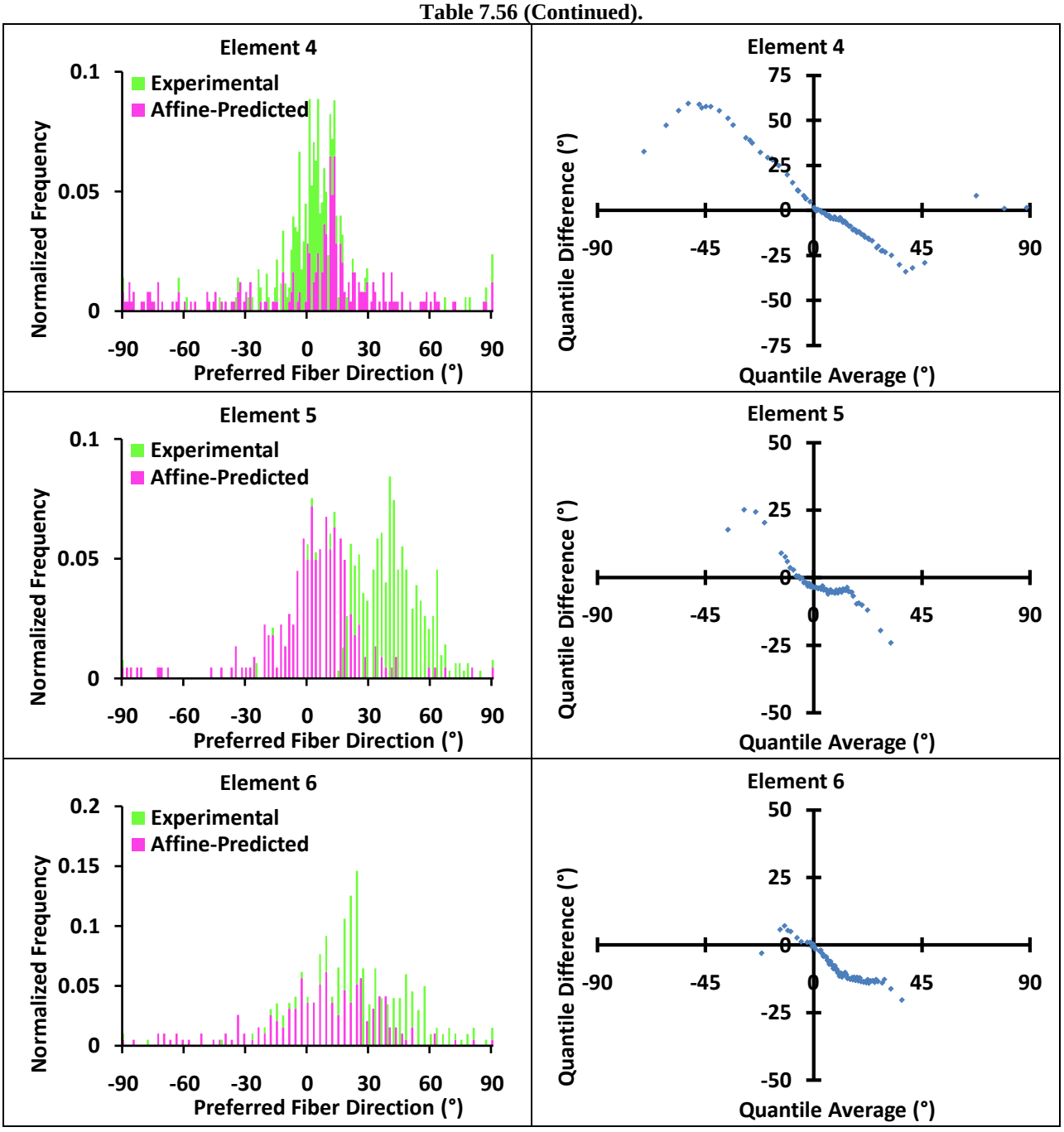

BIBLIOGRAPHY

1. Fung, Y.C., *Mechanical Properties of Living Tissues*. 2nd ed. Biomechanics, ed. 2nd. 2004, New York, NY: Springer. 568.

2. Kastelic, J., A. Galeski, and E. Baer, *The multicomposite structure of tendon.* Connect Tissue Res, 1978. **6**(1): p. 11-23.

3. Debski, R.E., et al., *The collagen fibers of the anteroinferior capsulolabrum have multiaxial orientation to resist shoulder dislocation.* J Shoulder Elbow Surg, 2003. **12**(3): p. 247-52.

4. Gohlke, F., B. Essigkrug, and F. Schmitz, *The patterns of the collagen fiber bundles of the capsule of the glenohumeral joint.* J Shoulder Elbow Surg, 1994. **3**(3): p. 111-28.

5. O'Brien, S.J., et al., *The anatomy and histology of the inferior glenohumeral ligament complex of the shoulder.* Am J Sports Med, 1990. **18**(5): p. 449-56.

6. Woo, S.L., et al., *Biomechanics of knee ligaments.* Am J Sports Med, 1999. **27**(4): p. 533-43.

7. Moore, S.M., *Glenohumeral Capsule Should be Evaluated as a Sheet of Fibrous Tissue: A Study in Functional Anatomy*, in *Bioengineering*. 2006, University of Pittsburgh: Pittsburth. p. 212.

8. Moore, S.M., et al., *The Glenohumeral Capsule Should be Evaluated as a Sheet of Fibrous Tissue: A Validated Finite Element Model.* Ann Biomed Eng, 2009.

9. Moore, S.M., et al., *The current anatomical description of the inferior glenohumeral ligament does not correlate with its functional role in positions of external rotation.* J Orthop Res, 2008. **26**(12): p. 1598-604.

10. Matsen, F.A., F.H. Fu, and R.J. Hawkins, *The Shoulder : a balance of mobility and stability : workshop, Vail, Colorado, September 1992*. 1993, Rosemont, IL: American Academy of Orthopaedic Surgeons. xviii, 653.

11. Hovelius, L., et al., *Primary anterior dislocation of the shoulder in young patients. A ten-year prospective study.* J Bone Joint Surg Am, 1996. **78**(11): p. 1677-84.

12. Bey, M.J., et al., *Structural and mechanical properties of the glenohumeral joint posterior capsule.* J Shoulder Elbow Surg, 2005. **14**(2): p. 201-6.

13. Bigliani, L.U., et al., *Tensile properties of the inferior glenohumeral ligament.* J Orthop Res, 1992. **10**(2): p. 187-97.

14. Ticker, J.B., et al., *Inferior glenohumeral ligament: geometric and strain-rate dependent properties.* J Shoulder Elbow Surg, 1996. **5**(4): p. 269-79.

15. Voycheck, C.A., et al., *Effects of region and sex on the mechanical properties of the glenohumeral capsule during uniaxial extension.* J Appl Physiol, 2010. **108**(6): p. 1711-8.

16. Flood, V., *Discovery of a new ligament of the shoulder joint.* Lancet, 1829: p. 671.

17. Sarrafian, S.K., *Gross and functional anatomy of the shoulder.* Clin Orthop, 1983(173): p. 11-9.

18. Ferrari, D.A., *Capsular ligaments of the shoulder. Anatomical and functional study of the anterior superior capsule.* Am J Sports Med, 1990. **18**(1): p. 20-4.

19. Bost, F.C. and V.T. Inman, *The pathological changes in recurrent dislocation of the shoulder.* J Bone Joint Surg Am, 1942. **24A**: p. 595.

20. Rowe, C.R., D. Patel, and W.W. Southmayd, *The Bankart procedure: a long-term end-result study.* J Bone Joint Surg Am, 1978. **60**(1): p. 1-16.

21. Neer, C.S., 2nd and C.R. Foster, *Inferior capsular shift for involuntary inferior and multidirectional instability of the shoulder. A preliminary report.* J Bone Joint Surg Am, 1980. **62**(6): p. 897-908.

22. Clark, J.M. and D.T. Harryman, 2nd, *Tendons, ligaments, and capsule of the rotator cuff. Gross and microscopic anatomy.* J Bone Joint Surg Am, 1992. **74**(5): p. 713-25.

23. Cooper, D.E., et al., *Anatomy, histology, and vascularity of the glenoid labrum. An anatomical study.* J Bone Joint Surg Am, 1992. **74**(1): p. 46-52.

24. Turkel, S.J., et al., *Stabilizing mechanisms preventing anterior dislocation of the glenohumeral joint.* J Bone Joint Surg Am, 1981. **63**(8): p. 1208-17.

25. Ovesen, J. and S. Nielsen, *Stability of the shoulder joint. Cadaver study of stabilizing structures.* Acta Orthop Scand, 1985. **56**(2): p. 149-51.

26. Malicky, D.M., et al., *Anterior glenohumeral stabilization factors: progressive effects in a biomechanical model.* J Orthop Res, 1996. **14**(2): p. 282-8.

27. Debski, R.E., et al., *In situ force distribution in the glenohumeral joint capsule during anterior-posterior loading.* J Orthop Res, 1999. **17**(5): p. 769-76.

28. Warner, J.J.P., et al., *Dynamic capsuloligamentous anatomy of the glenohumeral joint.* J Shoulder Elbow Surg, 1993. **2**: p. 115-33.

29. Hoffmeyer, P., et al., *Stabilizing mechanism of the glenohumeral ligaments.* Biomed Sci Instrum, 1990. **26**: p. 49-52.

30. O'Connell, P.W., et al., *The contribution of the glenohumeral ligaments to anterior stability of the shoulder joint.* Am J Sports Med, 1990. **18**(6): p. 579-84.

31. Terry, G.C., et al., *The stabilizing function of passive shoulder restraints.* Am J Sports Med, 1991. **19**(1): p. 26-34.

32. Miller, M.C., et al., *A mathematical and experimental model of length change in the inferior glenohumeral ligament in the late cocking phase of pitching.* Transcripts of the Orthopaedic Research Society, 1991. **16**: p. 609.

33. Malicky, D.M. and L.J. Soslowsky, *Relationships between total and non-recoverable strain fields in glenohumeral capsule during shoulder subluxation.* Ann Biomed Eng, 2009. **37**(12): p. 2547-55.

34. Lew, W.D., J.L. Lewis, and E.V. Craig, *Stabilization by capsule, ligaments, and labrum: Stability at the extremes of motion*, in *The Shoulder: A Balance of Mobility and Stability*, F.A. Matsen, 3rd, F.H. Fu, and R.J. Hawkins, Editors. 1993, American Academy of Orthopaedic Surgeons: Rosemont, IL. p. 69-90.

35. Moseley, H. and B. Overgaard, *The anterior capsular mechanism in recurrent anterior dislocation of the shoulder: Morphological and clinical studies with special reference to the glenoid labrum and glenohumeral ligaments.* J Bone Joint Surg Br, 1962. **44**: p. 913-27.

36. Peat, M., *Functional anatomy of the shoulder complex.* Phys Ther, 1986. **66**(12): p. 1855-65.

37. Novotny, J.E., B.D. Beynnon, and C.E. Nichols, *Modeling the stability of the human glenohumeral joint during external rotation.* J Biomech, 2000. **33**(3): p. 345-54.

38. Debski, R.E., et al., *An analytical approach to determine the in situ forces in the glenohumeral ligaments.* J Biomech Eng, 1999. **121**(3): p. 311-5.

39. Lee, T.Q., et al., *Age related biomechanical properties of the glenoid-anterior band of the inferior glenohumeral ligament-humerus complex.* Clin Biomech (Bristol, Avon), 1999. **14**(7): p. 471-6.

40. Moore, S.M., et al., *Bi-directional mechanical properties of the posterior region of the glenohumeral capsule.* J Biomech, 2005. **38**(6): p. 1365-9.

41. Moore, S.M., P.J. McMahon, and R.E. Debski, *Bi-directional Mechanical Properties of the Axillary Pouch of the Glenohumeral Capsule: Implications for Surgical Repair.* J Biomech Eng, 2004. **126**(2): p. 284-288.

42. Rainis, E.J., et al., *Material properties of the axillary pouch of the glenohumeral capsule: is isotropic material symmetry appropriate?* J Biomech Eng, 2009. **131**(3): p. 031007.

43. Ellis, B., Drury, NJ, Moore, SM, Weiss, JA, Debski, RE, *Finite Element Modeling of the Inferior Glenohumeral Ligament Can Assess the Location of Injury being Diagnosed by a Clinical Exam.* Computer Methods in Biomechanics and Biomedical Engineering, 2009. **Submitted**.

44. Ellis, B.J., et al., *Methodology and Sensitivity Studies for Finite Element Modeling of the Inferior Glenohumeral Ligament Complex.* J Biomech, 2006. **In Press**.

45. Sacks, M., *Small-Angle Light Scattering Methods for Soft Connective Tissue Structural Analysis*, in *Encyclopedia of Biomaterials and Biomedical Engineering*. 2004, Marcel Dekker, Inc. p. 1371-1384.

46. Sacks, M.S., D.B. Smith, and E.D. Hiester, *A small angle light scattering device for planar connective tissue microstructural analysis.* Ann Biomed Eng, 1997. **25**(4): p. 678-89.

47. Quapp, K.M. and J.A. Weiss, *Material characterization of human medial collateral ligament.* Journal of Biomechanical Engineering, 1998. **120**(6): p. 757-63.

48. Weiss, J.A., J.C. Gardiner, and C. Bonifasi-Lista, *Ligament material behavior is nonlinear, viscoelastic and rate-independent under shear loading.* J Biomech, 2002. **35**(7): p. 943-50.

49. Hovelius, L., et al., *Recurrences after initial dislocation of the shoulder. Results of a prospective study of treatment.* Journal of Bone and Joint Surgery. American Volume, 1983. **65**(3): p. 343-9.

50. Kaltsas, D.S., *Comparative study of the properties of the shoulder joint capsule with those of other joint capsules.* Clin Orthop, 1983(173): p. 20-6.

51. Matsen, F.A., 3rd, et al., *Glenohumeral instability*, in *The Shoulder*, C.A. Rockwood, et al., Editors. 1998, W. B. Saunders Co.: Philadelphia, PA. p. 611-755.

52. Rowe, C.R., B. Zarins, and J.V. Ciullo, *Recurrent anterior dislocation of the shoulder after surgical repair. Apparent causes of failure and treatment.* J Bone Joint Surg Am, 1984. **66**(2): p. 159-68.

53. Bigliani, L.U., et al., *Shoulder motion and laxity in the professional baseball player.* Am J Sports Med, 1997. **25**(5): p. 609-13.

54. Fitzpatrick, M.J., et al., *Development of cadaveric models of a thrower's shoulder.* J Shoulder Elbow Surg, 2005. **14**(1 Suppl S): p. 49S-57S.

55. Wilk, K.E., K. Meister, and J.R. Andrews, *Current concepts in the rehabilitation of the overhead throwing athlete.* Am J Sports Med, 2002. **30**(1): p. 136-51.

56. Borsa, P.A., E.L. Sauers, and D.E. Herling, *Patterns of glenohumeral joint laxity and stiffness in healthy men and women.* Med Sci Sports Exerc, 2000. **32**(10): p. 1685-90.

57. Borsa, P.A., E.L. Sauers, and D.E. Herling, *Glenohumeral Stiffness Response Between Men and Women for Anterior, Posterior, and Inferior Translation.* J Athl Train, 2002. **37**(3): p. 240-245.

58. Brown, G.A., J.L. Tan, and A. Kirkley, *The lax shoulder in females. Issues, answers, but many more questions.* Clin Orthop Relat Res, 2000(372): p. 110-22.

59. Chandrashekar, N., et al., *Sex-based differences in the tensile properties of the human anterior cruciate ligament.* J Biomech, 2006. **39**(16): p. 2943-50.

60. Charlton, W.P., L.M. Coslett-Charlton, and M.G. Ciccotti, *Correlation of estradiol in pregnancy and anterior cruciate ligament laxity.* Clin Orthop Relat Res, 2001(387): p. 165-70.

61. Kubo, K., H. Kanehisa, and T. Fukunaga, *Gender differences in the viscoelastic properties of tendon structures.* Eur J Appl Physiol, 2003. **88**(6): p. 520-6.

62. McFarland, E.G., G. Campbell, and J. McDowell, *Posterior shoulder laxity in asymptomatic athletes.* Am J Sports Med, 1996. **24**(4): p. 468-71.

63. Pollard, C.D., B. Braun, and J. Hamill, *Influence of gender, estrogen and exercise on anterior knee laxity.* Clin Biomech (Bristol, Avon), 2006. **21**(10): p. 1060-6.

64. Debski, R.E., et al., *Stress and strain in the anterior band of the inferior glenohumeral ligament during a simulated clinical examination.* J Shoulder Elbow Surg, 2005. **14**(1 Suppl S): p. 24S-31S.

65. Hovelius, L., *Incidence of shoulder dislocation in Sweden.* Clin Orthop, 1982(166): p. 127-31.

66. Nelson, B.J. and R.A. Arciero, *Arthroscopic management of glenohumeral instability.* Am J Sports Med, 2000. **28**(4): p. 602-14.

67. Cave, E., J. Burke, and R. Boyd, *Trauma Management*. 1974, Chicago, IL: Year Book Medical Publishers. 437.

68. Malicky, D.M., et al., *Neer Award 2001: nonrecoverable strain fields of the anteroinferior glenohumeral capsule under subluxation.* J Shoulder Elbow Surg, 2002. **11**(6): p. 529-40.

69. Malicky, D.M., et al., *Total strain fields of the antero-inferior shoulder capsule under subluxation: a stereoradiogrammetric study.* J Biomech Eng, 2001. **123**(5): p. 425-31.

70. McMahon, P.J., et al., *A novel cadaveric model for anterior-inferior shoulder dislocation using forcible apprehension positioning.* J Rehabil Res Dev, 2003. **40**(4): p. 349-59.

71. Grossman, M.G., et al., *A cadaveric model of the throwing shoulder: a possible etiology of superior labrum anterior-to-posterior lesions.* J Bone Joint Surg Am, 2005. **87**(4): p. 824-31.

72. Remia, L.F., et al., *Biomechanical evaluation of multidirectional glenohumeral instability and repair.* Clin Orthop Relat Res, 2003(416): p. 225-36.

73. Schneider, D.J., et al., *Biomechanical evaluation after five and ten millimeter anterior glenohumeral capsulorrhaphy using a novel shoulder model of increased laxity.* J Shoulder Elbow Surg, 2005. **14**(3): p. 318-23.

74. Widjaja, A.B., et al., *Correlation between Bankart and Hill-Sachs lesions in anterior shoulder dislocation.* ANZ J Surg, 2006. **76**(6): p. 436-8.

75. Bankart, A.S., *Recurrent or habitual dislocation of the shoulder-joint.* Br Med J, 1923. **2**: p. 1132-3.

76. Bach, B.R., R.F. Warren, and J. Fronek, *Disruption of the lateral capsule of the shoulder. A cause of recurrent dislocation.* J Bone Joint Surg Br, 1988. **70**(2): p. 274-6.

77. Speer, K.P., et al., *Biomechanical evaluation of a simulated Bankart lesion.* J Bone Joint Surg Am, 1994. **76**(12): p. 1819-26.

78. Pouliart, N., S. Marmor, and O. Gagey, *Simulated capsulolabral lesion in cadavers: dislocation does not result from a bankart lesion only.* Arthroscopy, 2006. **22**(7): p. 748-54.

79. Pouliart, N. and O. Gagey, *Simulated humeral avulsion of the glenohumeral ligaments: a new instability model.* J Shoulder Elbow Surg, 2006. **15**(6): p. 728-35.

80. Pollock, R.G., et al., *Effects of repetitive subfailure strains on the mechanical behavior of the inferior glenohumeral ligament.* J Shoulder Elbow Surg, 2000. **9**(5): p. 427-35.

81. McMahon, P.J., et al., *Deformation and strain characteristics along the length of the anterior band of the inferior glenohumeral ligament.* J Shoulder Elbow Surg, 2001. **10**(5): p. 482-8.

82. Rodeo, S.A., et al., *Analysis of collagen and elastic fibers in shoulder capsule in patients with shoulder instability.* Am J Sports Med, 1998. **26**(5): p. 634-43.

83. van Grinsven, S., et al., *MR arthrography of traumatic anterior shoulder lesions showed modest reproducibility and accuracy when evaluated under clinical circumstances.* Arch Orthop Trauma Surg, 2007. **127**(1): p. 11-7.

84. Brenneke, S.L., et al., *Glenohumeral kinematics and capsulo-ligamentous strain resulting from laxity exams.* Clin Biomech (Bristol, Avon), 2000. **15**(10): p. 735-42.

85. Matsen, F.A., 3rd, D.T. Harryman, 2nd, and J.A. Sidles, *Mechanics of glenohumeral instability.* Clin Sports Med, 1991. **10**(4): p. 783-8.

86. Pollock, R.G. and L.U. Bigliani, *Recurrent posterior shoulder instability. Diagnosis and treatment.* Clin Orthop Relat Res, 1993(291): p. 85-96.

87. Rockwood, C.A., et al., *The Shoulder*. 2nd ed. 1998, Philadelphia, PA: W. B. Saunders Co.

88. Gerber, C. and R. Ganz, *Clinical assessment of instability of the shoulder. With special reference to anterior and posterior drawer tests.* J Bone Joint Surg Br, 1984. **66**(4): p. 551-6.

89. Millett, P.J., et al., *Recurrent posterior shoulder instability.* J Am Acad Orthop Surg, 2006. **14**(8): p. 464-76.

90. Silliman, J.F. and R.J. Hawkins, *Classification and physical diagnosis of instability of the shoulder.* Clin Orthop Relat Res, 1993(291): p. 7-19.

91. Harryman, D.T., 2nd, et al., *Laxity of the normal glenohumeral joint: A quantitative in vivo assessment.* J Shoulder Elbow Surg, 1992. **1**: p. 66-76.

92. May, S., et al., *Reliability of physical examination tests used in the assessment of patients with shoulder problems: a systematic review.* Physiotherapy, 2010. **96**(3): p. 179-90.

93. Drury, N.J., et al., *Finding consistent strain distributions in the glenohumeral capsule between two subjects: Implications for development of physical examinations.* J Biomech, 2011.

94. Rowe, C.R., *Prognosis in dislocations of the shoulder.* J Bone Joint Surg Am, 1956. **38**: p. 957-77.

95. Arciero, R.A. and D.C. Taylor, *Primary anterior dislocation of the shoulder in young patients. A ten-year prospective study.* J Bone Joint Surg Am, 1998. **80**(2): p. 299-300.

96. Postacchini, F., S. Gumina, and G. Cinotti, *Anterior shoulder dislocation in adolescents.* J Shoulder Elbow Surg, 2000. **9**(6): p. 470-4.

97. Rowe, C.R., *The Results of Operative Treatment of Recurrent Dislocations of the Shoulder.* Surg Clin North Am, 1963. **43**: p. 1667-70.

98. Itoi, E., et al., *A new method of immobilization after traumatic anterior dislocation of the shoulder: a preliminary study.* J Shoulder Elbow Surg, 2003. **12**(5): p. 413-5.

99. Itoi, E., et al., *Immobilization in external rotation after shoulder dislocation reduces the risk of recurrence. A randomized controlled trial.* J Bone Joint Surg Am, 2007. **89**(10): p. 2124-31.

100. Itoi, E., et al., *Position of immobilization after dislocation of the shoulder. A cadaveric study.* J Bone Joint Surg Am, 1999. **81**(3): p. 385-90.

101. Itoi, E., et al., *Position of immobilization after dislocation of the glenohumeral joint. A study with use of magnetic resonance imaging.* J Bone Joint Surg Am, 2001. **83-A**(5): p. 661-7.

102. Miller, B.S., et al., *Should acute anterior dislocations of the shoulder be immobilized in external rotation? A cadaveric study.* J Shoulder Elbow Surg, 2004. **13**(6): p. 589-92.

103. Seybold, D., et al., *[Immobilization in external rotation after primary shoulder dislocation]*. Chirurg, 2006. **77**(9): p. 821-6.

104. Seybold, D., et al., *Which labral lesion can be best reduced with external rotation of the shoulder after a first-time traumatic anterior shoulder dislocation?* Arch Orthop Trauma Surg, 2009. **129**(3): p. 299-304.

105. Arciero, R.A., et al., *Arthroscopic Bankart repair versus nonoperative treatment for acute, initial anterior shoulder dislocations.* Am J Sports Med, 1994. **22**(5): p. 589-94.

106. Henry, J.H. and J.A. Genung, *Natural history of glenohumeral dislocation--revisited.* Am J Sports Med, 1982. **10**(3): p. 135-7.

107. Hovelius, L., *Anterior dislocation of the shoulder in teen-agers and young adults. Five-year prognosis.* J Bone Joint Surg Am, 1987. **69**(3): p. 393-9.

108. McLaughlin, H.L. and D.I. MacLellan, *Recurrent anterior dislocation of the shoulder. II. A comparative study.* J Trauma, 1967. **7**(2): p. 191-201.

109. Simonet, W.T. and R.H. Cofield, *Prognosis in anterior shoulder dislocation.* Am J Sports Med, 1984. **12**(1): p. 19-24.

110. Wheeler, J.H., et al., *Arthroscopic versus nonoperative treatment of acute shoulder dislocations in young athletes.* Arthroscopy, 1989. **5**(3): p. 213-7.

111. Safran, O., et al., *Accuracy of the anterior apprehension test as a predictor of risk for redislocation after a first traumatic shoulder dislocation.* Am J Sports Med. **38**(5): p. 972-5.

112. Bigliani, L.U., et al., *Inferior capsular shift procedure for anterior-inferior shoulder instability in athletes.* Am J Sports Med, 1994. **22**(5): p. 578-84.

113. Neer, C.S., 2nd and C.R. Foster, *Inferior capsular shift for involuntary inferior and multidirectional instability of the shoulder: a preliminary report. 1980.* J Bone Joint Surg Am, 2001. **83-A**(10): p. 1586.

114. Ozbaydar, M.U., et al., *[Arthroscopic treatment of anterior-inferior shoulder instability]*. Acta Orthop Traumatol Turc, 2007. **41**(2): p. 120-6.

115. Sekiya, J.K., *Arthroscopic labral repair and capsular shift of the glenohumeral joint: technical pearls for a multiple pleated plication through a single working portal.* Arthroscopy, 2005. **21**(6): p. 766.

116. Westerheide, K.J., R.M. Dopirak, and S.J. Snyder, *Arthroscopic anterior stabilization and posterior capsular plication for anterior glenohumeral instability: a report of 71 cases.* Arthroscopy, 2006. **22**(5): p. 539-47.

117. Wiley, W.B., V.K. Goradia, and S.E. Pearson, *Arthroscopic capsular plication-shift.* Arthroscopy, 2005. **21**(1): p. 119-21.

118. Chiang, E.R., et al., *Arthroscopic posteroinferior capsular plication and rotator interval closure after Bankart repair in patients with traumatic anterior glenohumeral instability-A minimum follow-up of 5 years.* Injury, 2010.

119. Kirkley, A., et al., *Prospective randomized clinical trial comparing the effectiveness of immediate arthroscopic stabilization versus immobilization and rehabilitation in first traumatic anterior dislocations of the shoulder: long-term evaluation.* Arthroscopy, 2005. **21**(1): p. 55-63.

120. Moore, S.M., et al., *Multidirectional kinematics of the glenohumeral joint during simulated simple translation tests: impact on clinical diagnoses.* J Orthop Res, 2004. **22**(4): p. 889-94.

121. Bonnevialle, N., et al., *Selective capsular repair for the treatment of anterior-inferior shoulder instability: review of seventy-nine shoulders with seven years' average follow-up.* J Shoulder Elbow Surg, 2009. **18**(2): p. 251-9.

122. Hawkins, R.H. and R.J. Hawkins, *Failed anterior reconstruction for shoulder instability.* J Bone Joint Surg Br, 1985. **67**(5): p. 709-14.

123. Pouliart, N. and O. Gagey, *Reconciling arthroscopic and anatomic morphology of the humeral insertion of the inferior glenohumeral ligament.* Arthroscopy, 2005. **21**(8): p. 979-84.

124. Voycheck, C.A., et al., *Effects of region and sex on the mechanical properties of the glenohumeral capsule during uniaxial extension.* J Appl Physiol. **108**(6): p. 1711-8.

125. Gilbert, T.W., et al., *Fiber kinematics of small intestinal submucosa under biaxial and uniaxial stretch.* J Biomech Eng, 2006. **128**(6): p. 890-8.

126. Lake, S.P., et al., *Effect of fiber distribution and realignment on the nonlinear and inhomogeneous mechanical properties of human supraspinatus tendon under longitudinal tensile loading.* J Orthop Res, 2009. **27**(12): p. 1596-1602.

127. Quinn, K.P. and B.A. Winkelstein, *Altered collagen fiber kinematics define the onset of localized ligament damage during loading.* J Appl Physiol, 2008. **105**(6): p. 1881-8.

128. Sacks, M.S. *A Novel Approach to Account for Non-Affine Fiber Kinematics in Structural Continuum Models for Heart Valve Leaflets*. in *American Society of Mechanical Engineers Summer Bioengineering Conference*. 2010. Naples, FL.

129. Baker, C.L., J.W. Uribe, and C. Whitman, *Arthroscopic evaluation of acute initial anterior shoulder dislocations.* Am J Sports Med, 1990. **18**(1): p. 25-8.

130. Caspari, R.B., *Arthroscopic reconstruction for anterior shoulder instability.* Techniques in Orthopaedics, 1988. **3**: p. 59-66.

131. Field, L.D., D.J. Bokor, and F.H. Savoie, 3rd, *Humeral and glenoid detachment of the anterior inferior glenohumeral ligament: a cause of anterior shoulder instability.* J Shoulder Elbow Surg, 1997. **6**(1): p. 6-10.

132. Morgan, C.D. and A.B. Bodenstab, *Arthroscopic Bankart suture repair: technique and early results.* Arthroscopy, 1987. **3**(2): p. 111-22.

133. Jakobsen, B.W., et al., *Primary repair versus conservative treatment of first-time traumatic anterior dislocation of the shoulder: a randomized study with 10-year follow-up.* Arthroscopy, 2007. **23**(2): p. 118-23.

134. Drury, N.J., *Evaluating the Anterior Stability Provided by the Glenohumeral Capsule: A Finite Element Approach*, in *Bioengineering*. 2008, University of Pittsburgh: Pittsburgh. p. 253.

135. Ellis, B.J., et al., *Methodology and sensitivity studies for finite element modeling of the inferior glenohumeral ligament complex.* J Biomech, 2007. **40**(3): p. 603-12.

136. Moore, S.M., et al., *The glenohumeral capsule should be evaluated as a sheet of fibrous tissue: a validated finite element model.* Ann Biomed Eng, 2009. **38**(1): p. 66-76.

137. Refior, H.J. and D. Sowa, *Long tendon of the biceps brachii: sites of predilection for degenerative lesions.* J Shoulder Elbow Surg, 1995. **4**(6): p. 436-40.

138. Lake SP, M.K., Soslowsky LJ. *Fiber Re-alignment under Load Contributes to Human Supraspinatus Tendon Nonlinearity and Inhomogeneity*. in *55th Annual Meeting of the Orthopaedic Research Society*. 2009. Las Vegas, NV.

139. Voycheck, C.A., McMahon, P. J., Debski, R. E., *Collagen Fiber Alignment and Maximum Principal Strain in the Axillary Pouch Predict Location of Failure During Uniaxial Extension*, in *ASME 2010 Summer Bioengineering Conference*. 2010: Grande Beach Resort, Naples Florida, USA.

140. Lake, S.P., et al., *Tensile properties and fiber alignment of human supraspinatus tendon in the transverse direction demonstrate inhomogeneity, nonlinearity, and regional isotropy.* J Biomech. **43**(4): p. 727-32.

141. Lake, S.P., et al., *Effect of fiber distribution and realignment on the nonlinear and inhomogeneous mechanical properties of human supraspinatus tendon under longitudinal tensile loading.* J Orthop Res, 2009. **27**(12): p. 1596-602.

142. Guerin, H.A. and D.M. Elliott, *Degeneration affects the fiber reorientation of human annulus fibrosus under tensile load.* J Biomech, 2006. **39**(8): p. 1410-8.

143. Whittaker, P. and P.B. Canham, *Demonstration of quantitative fabric analysis of tendon collagen using two-dimensional polarized light microscopy.* Matrix, 1991. **11**(1): p. 56-62.

144. Whittaker, P., et al., *Quantitative assessment of myocardial collagen with picrosirius red staining and circularly polarized light.* Basic Res Cardiol, 1994. **89**(5): p. 397-410.

145. Chaudhuri, S., et al., *A Fourier domain directional filtering method for analysis of collagen alignment in ligaments.* IEEE Trans Biomed Eng, 1987. **34**(7): p. 509-18.

146. Frank, C., et al., *A quantitative analysis of matrix alignment in ligament scars: a comparison of movement versus immobilization in an immature rabbit model.* J Orthop Res, 1991. **9**(2): p. 219-27.

147. Liu, Z.Q., R.M. Rangayyan, and C.B. Frank, *Statistical analysis of collagen alignment in ligaments by scale-space analysis.* IEEE Trans Biomed Eng, 1991. **38**(6): p. 580-8.

148. Sasaki, N. and S. Odajima, *Stress-strain curve and Young's modulus of a collagen molecule as determined by the X-ray diffraction technique.* J Biomech, 1996. **29**(5): p. 655-8.

149. Hilbert, S.L., V.J. Ferrans, and W.M. Swanson, *Optical methods for the nondestructive evaluation of collagen morphology in bioprosthetic heart valves.* J Biomed Mater Res, 1986. **20**(9): p. 1411-21.

150. Tower, T.T. and R.T. Tranquillo, *Alignment maps of tissues: II. Fast harmonic analysis for imaging.* Biophys J, 2001. **81**(5): p. 2964-71.

151. Tower, T.T. and R.T. Tranquillo, *Alignment maps of tissues: I. Microscopic elliptical polarimetry.* Biophys J, 2001. **81**(5): p. 2954-63.

152. Bowes, L.E., et al., *Collagen fiber orientation as quantified by small angle light scattering in wounds treated with transforming growth factor-beta2 and its neutalizing antibody.* Wound Repair Regen, 1999. **7**(3): p. 179-86.

153. Engelmayr, G.C., Jr., et al., *Guidance of engineered tissue collagen orientation by large-scale scaffold microstructures.* J Biomech, 2006. **39**(10): p. 1819-31.

154. Joyce, E.M., et al., *Functional collagen fiber architecture of the pulmonary heart valve cusp.* Ann Thorac Surg, 2009. **87**(4): p. 1240-9.

155. Liao, J., et al., *Molecular orientation of collagen in intact planar connective tissues under biaxial stretch.* Acta Biomater, 2005. **1**(1): p. 45-54.

156. Sacks, M., *Small-Angle Light Scattering Methods for Soft Connective Tissue Structural Analysis*, in *Encyclopedia of Biomaterials and Biomedical Engineering*. 2004, Marcel Dekker, Inc. p. 1371-1384.

157. Sacks, M.S., *Biaxial mechanical evaluation of planar biological materials.* Journal of Elasticity, 2000. **61**: p. 199-246.

158. Sacks, M.S., *Incorporation of experimentally-derived fiber orientation into a structural constitutive model for planar collagenous tissues.* J Biomech Eng, 2003. **125**(2): p. 280-7.

159. Sacks, M.S. and C.J. Chuong, *Biaxial mechanical properties of passive right ventricular free wall myocardium.* Journal of Biomechanical Engineering, 1993. **115**(2): p. 202-5.

160. Sacks, M.S., C.J. Chuong, and R. More, *Collagen fiber architecture of bovine pericardium.* Asaio J, 1994. **40**(3): p. M632-7.

161. Sacks, M.S. and D.C. Gloeckner, *Quantification of the fiber architecture and biaxial mechanical behavior of porcine intestinal submucosa.* J Biomed Mater Res, 1999. **46**(1): p. 1-10.

162. Sacks, M.S. and F.J. Schoen, *Collagen fiber disruption occurs independent of calcification in clinically explanted bioprosthetic heart valves.* J Biomed Mater Res, 2002. **62**(3): p. 359-71.

163. Wells, S.M., T. Sellaro, and M.S. Sacks, *Cyclic loading response of bioprosthetic heart valves: effects of fixation stress state on the collagen fiber architecture.* Biomaterials, 2005. **26**(15): p. 2611-9.

164. Billiar, K.L. and M.S. Sacks, *A method to quantify the fiber kinematics of planar tissues under biaxial stretch.* J Biomech, 1997. **30**(7): p. 753-6.

165. Sacks, M.S. and C.J. Chuong, *Orthotropic mechanical properties of chemically treated bovine pericardium.* Ann Biomed Eng, 1998. **26**(5): p. 892-902.

166. O'Brien, S.J., et al., *Developmental anatomy of the shoulder and anatomy of the glenohumeral joint*, in *The Shoulder*, F.A. Matsen, 3rd and C.A. Rockwood, Editors. 1990, W. B. Saunders Co.: Philadelphia, PA. p. 1-33.

167. Voycheck, C.A., McMahon, P. J., Debski, R. E., *Mechanical Properties of the Glenohumeral Capsule Change with Siumlated Injury*, in *ASME 2010 Summer Bioengineering Conference*. 2010: Grande Beach Resort, Naples Florida, USA.

168. DePalma, A.F., G. Callery, and G.A. Bennett, *Variational anatomy and degenerative lesions of the shoulder joint.* American Academy of Orthopaedic Surgery Instructional Course Lecture Series, 1949. **6**: p. 225-81.

169. Provenzano, P.P., et al., *Subfailure damage in ligament: a structural and cellular evaluation.* J Appl Physiol, 2002. **92**(1): p. 362-71.

170. Panjabi, M.M., et al., *Subfailure injury of the rabbit anterior cruciate ligament.* J Orthop Res, 1996. **14**(2): p. 216-22.

171. Chiang, E.R., et al., *Arthroscopic posteroinferior capsular plication and rotator interval closure after Bankart repair in patients with traumatic anterior glenohumeral instability-A minimum follow-up of 5 years.* Injury.

172. Bigliani, L.U., et al., *Glenohumeral stability. Biomechanical properties of passive and active stabilizers.* Clin Orthop Relat Res, 1996(330): p. 13-30.

173. Rainis, E.J., *Characterizing the Mechanical Properties of the Glenohumeral Capsule: Implications for Finite Element Modeling*, in *Bioengineering*. 2006, University of Pittsburgh: Pittsburgh. p. 146.

174. Ellis, B.J., et al., *Finite element modelling of the glenohumeral capsule can help assess the tested region during a clinical exam.* Comput Methods Biomech Biomed Engin, 2009: p. 1.

175. Veronda, D.R. and R.A. Westmann, *Mechanical characterization of skin-finite deformations.* Journal of Biomechanics, 1970. **3**: p. 111-124.

176. Weiss, J.A., B.N. Maker, and S. Govindjee, *Finite element implementation of incompressible, transversely isotropic hyperelasticity.* Comp Meth Appl Mech Eng, 1996. **135**: p. 107-28.

177. Gardiner, J.C. and J.A. Weiss, *Simple shear testing of parallel-fibered planar soft tissues.* J Biomech Eng, 2001. **123**(2): p. 170-5.

178. Marsden, J.E. and T.J.R. Hughes, *Mathematical Foundations of Elasticity.* 1994.

179. Gardiner, J.C. and J.A. Weiss, *Simple shear testing of parallel-fibered planar soft tissues.* Journal of Biomechanics, 2001. **123**: p. 1-5.

180. Triola, M.F., *Elementary Statistics*. 8th ed, ed. D. Lynch. 2001, New York, NY: Addison Wesley Longman, Inc. 855.

181. Edvore, J.L., *Probability and Statistics for Engineering and the Sciences*. 6th ed, ed. C. Crockett. 2004, Toronto, Ontario, Canada: Brooks/Cole, Thompson Learning. 795.

182. Rudy, T.W., et al., *A combined robotic/universal force sensor approach to determine in situ forces of knee ligaments.* J Biomech, 1996. **29**(10): p. 1357-60.

183. Burkart, A., et al., *Glenohumeral translations are only partially restored after repair of a simulated type II superior labral lesion.* Am J Sports Med, 2003. **31**(1): p. 56-63.

184. Burkart, A.C. and R.E. Debski, *Anatomy and function of the glenohumeral ligaments in anterior shoulder instability.* Clin Orthop, 2002(400): p. 32-9.

185. Li, G., et al., *A validated three-dimensional computational model of a human knee joint.* J Biomech Eng, 1999. **121**(6): p. 657-62.

186. Li, G., J. Suggs, and T. Gill, *The effect of anterior cruciate ligament injury on knee joint function under a simulated muscle load: a three-dimensional computational simulation.* Ann Biomed Eng, 2002. **30**(5): p. 713-20.

187. Livesay, G.A., et al., *Determination of the in situ forces and force distribution within the human anterior cruciate ligament.* Ann Biomed Eng, 1995. **23**(4): p. 467-74.

188. Livesay, G.A., et al., *Evaluation of the effect of joint constraints on the in situ force distribution in the anterior cruciate ligament.* J Orthop Res, 1997. **15**(2): p. 278-84.

189. Jones, C.P., *Living beyond our "means": new methods for comparing distributions.* Am J Epidemiol, 1997. **146**(12): p. 1056-66.

190. Lake, S.P., Cortes, D. H., Kadlowec, J. A., Elliot, D. M., Soslowsky, L. J. *Comparison of Experimental and Affine-Predicted Fiber Kinematics in Human Supraspinatus Tendon*. in *American Society of Mechanical Engineers Summer Bioengineering Conference*. 2010. Naples, FL.

191. Luke, T.A., et al., *Volumetric change in the shoulder capsule after open inferior capsular shift versus arthroscopic thermal capsular shrinkage: a cadaveric model.* J Shoulder Elbow Surg, 2004. **13**(2): p. 146-9.

192. Cohen, S.B., et al., *Anterior capsulorrhaphy: an in vitro comparison of volume reduction--arthroscopic plication versus open capsular shift.* Arthroscopy, 2005. **21**(6): p. 659-64.

193. Wang, V.M., et al., *Comparison of glenohumeral mechanics following a capsular shift and anterior tightening.* J Bone Joint Surg Am, 2005. **87**(6): p. 1312-22.

194. Voycheck, C.A., Brown, A. J., McMahon, P.J., Debski, R. E. *Are the mechanical properties of the anterior band of the inferior glenohumeral ligament and the axillary pouch similar?* in *International Symposium on Ligaments & Tendons VIII*. 2008. Stanford University, Stanford CA.

195. Musahl, V., et al., *Orientation feedback during simulated simple translation tests has little clinical significance on the magnitude and precision of glenohumeral joint translations.* Knee Surg Sports Traumatol Arthrosc, 2006. **14**(11): p. 1194-9.

196. Terrier, A., et al., *Effect of supraspinatus deficiency on humerus translation and glenohumeral contact force during abduction.* Clin Biomech (Bristol, Avon), 2007. **22**(6): p. 645-51.

197. Nikooyan, A.A., et al., *Validation of the Delft Shoulder and Elbow Model using in-vivo glenohumeral joint contact forces.* J Biomech. **43**(15): p. 3007-14.

198. Van de Velde, S.K., et al., *Increased tibiofemoral cartilage contact deformation in patients with anterior cruciate ligament deficiency.* Arthritis Rheum, 2009. **60**(12): p. 3693-702.

199. Puso, M.A. and J.A. Weiss, *Finite element implementation of anisotropic quasi-linear viscoelasticity using a discrete spectrum approximation.* J Biomech Eng, 1998. **120**(1): p. 62-70.

200. Rivlin, R.S.a.S., D.W., *Large Elastic Deformations of Isotropic Materials VII. Experiments on the Deformation of Rubber.* Philosophical Transactions of the Royal Society of London, series A, 1951. **243**: p. 251-288.

201. Weiss, J.A., D.A. Schauer, and J.C. Gardiner. *Modeling contact in biological joints using penalty and augmented Lagrangian methods*. in *ASME Winter Annual Meeting*. 1996.

202. Natali, A.N., et al., *Anisotropic elasto-damage constitutive model for the biomechanical analysis of tendons.* Med Eng Phys, 2005. **27**(3): p. 209-14.

203. Simo, J.C., *On the dynamics in space of rods undergoing large motions: A geometrically exact approach.* Comp Meth Appl Mech Eng, 1988. **66**: p. 125-161.

204. Voycheck, C.A., Maas, S. A., Weiss, J. A., McMahon, P. J., Debski, R. E. *A Structural Model Describes and Predicts the Material Behavior of the Glenhoumeral Capsule*. in *55th Annual Meeting of the Orthopaedic Research Society*. 2009. Las Vegas, NV.

205. Hepworth, D.G., et al., *Affine versus non-affine deformation in soft biological tissues, measured by the reorientation and stretching of collagen fibres through the thickness of compressed porcine skin.* J Biomech, 2001. **34**(3): p. 341-6.

206. Humphrey, J.D., D.L. Vawter, and R.P. Vito, *Quantification of strains in biaxially tested soft tissues.* J Biomech, 1987. **20**(1): p. 59-65.

207. *United States Census 2000*. 2000, United States Census Bureau.

208. Abboud, J.A. and L.J. Soslowsky, *Interplay of the static and dynamic restraints in glenohumeral instability.* Clin Orthop, 2002(400): p. 48-57.